SYSTEMATIC STUDY OF MUTUAL NEUTRALIZATION REACTIONS BETWEEN ATOMIC SPECIES USING THE MERGED BEAM METHOD AND AN ASYMPTOTIC MODEL

Thèse présentée en vue de l'obtention du grade de Docteur en Sciences

ARNAUD DOCHAIN

SUPERVISORS:

Xavier Urbain

MEMBERS OF THE JURY:

Arnaud Delcorte (chairman)
Clément Lauzin (secretary)
Paul S. Barklem
Arnaud Le Padellec
Bernard Piraux
Nathalie Vaeck

UCLouvain
Institute of Condensed Matter
and Nanosciences

January 2022

Abstract

The mutual neutralization reaction $A^+ + B^- \rightarrow A^0 + B^0$ plays an important role whenever an anion populated plasma is involved (interstellar molecular clouds, ionospheres, stellar atmospheres, etc.), and modifies its radiative emissions, used for estimating their elemental composition, e.g. stars metallicities. Additionally, the measurement of mutual neutralization can serve as a benchmark for the numerical models of estimation of inelastic collisions used in these models of reaction dynamics.

In this manuscript, we present results for several low energy mutual neutralization reactions measured with the UCLouvain single pass merged beam apparatus: He^+/Li^++H^-/D^-, $C^+/N^+/O^+$+$D^-/C^-/O^-/Si^-/P^-/S^-$, Na^++O^-/S^-, and Ne^++$C^-/O^-/S^-$. We detail how a pair of time and position sensitive detectors allows us to obtain accurate branching ratios and partial differential cross sections.

In order to rationalize the branching ratios we have measured, we developed a multi-channel Landau-Zener model combined with an updated version of the anion centered asymptotic (analytical) model (ACAM). The overall agreement between theory and experiment allows us to use this model to describe the mutual neutralization process. The ACAM validity domain is also studied, revealing additional processes responsible for the discrepancies between theory and experiment, such as the production of Rydberg series of the neutral atoms.

The differential cross section was also computed using two models: the interrupted Rutherford scattering model and the impact parameter method. The former is analytical and describes well the collision energy dependency of the differential cross section while the latter gives quantitative results. It is also shown how differential cross section analysis provides a better insight into the mutual neutralization process, e.g. which molecular states are temporarily populated.

As a conclusion, this manuscript suggests several ideas for improving both the theoretical models and the experimental setup.

Remerciements

Avant d'entamer la discussion scientifique, j'aimerais remercier l'ensemble des personnes qui m'ont aidé durant cette période.

Premièrement, je remercie Xavier Urbain, mon promoteur de thèse. C'est une chance que j'ai eue de pouvoir faire de la recherche avec toi. Grâce à toi, je n'ai pas réalisé cette thèse sous la houlette d'un directeur de laboratoire, mais je l'ai réalisée en collaboration avec un chercheur qui n'a pas peur de mettre les mains dans le cambouis : autant pour dompter les humeurs des sources d'ions que pour détecter du premier coup d'œil pourquoi un modèle ne marche pas. C'est grâce à toi, et à nos nombreuses discussions que j'ai acquis une grande partie de mon bagage en physique atomique, moléculaire et optique.

J'aimerais remercier Paul Barklem, Arnaud Delcorte, Clément Lauzin, Arnaud Le Padellec, Bernard Piraux et Nathalie Vaeck d'avoir accepté de faire partie de mon jury de thèse. Un tout grand merci pour le regard neuf que vous avez porté sur ce manuscrit, du temps que vous avez consacré à sa relecture et de m'avoir incité à pousser mes raisonnement jusqu'au bout.

Merci à Thibault Launoy et Jérôme Loreau pour vos calculs. Sans vous, je n'aurais jamais réussi à débroussailler le modèle asymptotique. Merci à Nathalie de Ruette (sans toi, la source à sputtering n'aurait jamais fonctionné), Richard Thomas, Thibault Launoy, Rodrigo Nascimento, Mark Stockett et Magdalena Kaminska pour votre participation aux différentes campagnes de mesures. Merci à Mariko Dunseath-Terao et Kevin Dunseath de m'avoir aidé à comprendre comment construire correctement un atome. Je remercie aussi Mathias Poline (ainsi que le reste de l'équipe de DESIREE à Stockholm) pour nos discussions sur l'interprétation des résultats, merci de m'avoir forcé à la clarifier.

Je remercie les personnes avec qui j'ai pu collaborer lors d'autres projets de recherche : Baptiste Fabre (et tes calculs kilométriques), Clément Lauzin, André Nauts (pour nos discussions sur les fondements de la mécanique quantique), Benoît Hackens (et ton intuition sur les propriétés du graphène), Raphaël Marion (et ta grande rigueur mathématique), Matthieu Génévriez (et la circularisation des données), Aigar Znotins, Denisse Cruz, ainsi que les mémorants avec qui j'ai travaillé. Ceci me permet de glisser ici une petite men-

tion à mes collègues de bureau Matthieu Génévriez et Raphaël Marion pour m'avoir supporté et aidé à clarifier mes idées (mais aussi pour tout le reste).

L'équipe technique aussi, bien sûr : autant les électroniciens Guilhem Vanlancker, Feliz Kapita et Jean-Pierre Van Roy, que les mécaniciens Thomas Corbo, Luca Azzola, Daniel Dedouaire et Hervé Laurent (ainsi que les autres membres de l'atelier de mécanique) sans qui la machine n'aurait pu être mise à jour et réparée à de nombreuses reprises.

Mais aussi, l'équipe administrative : Laurence Lenoir, Fabienne Richard, Fabienne Delbrouck et Nicole Coismann. Merci de votre patience envers ma faible compétence administrative, mais aussi d'avoir accepté mes demandes improbables (fournitures de bricolage et informatiques).

Sans oublier l'ensemble des autres membres du pôle NAPS-MDH, dont la liste est trop longue pour être citée explicitement ici. Merci de m'avoir accueilli et pour ces bons moments passés ensemble.

Pour clôturer, je remercie aussi les membres d'Eristic Fuel, car il n'y a pas que la science dans la vie, il y a aussi la musique. Ceci me donne l'occasion d'adresser ma dernière pensée à Morgane qui a supporté mes zines durant toutes ces années. Merci de t'y être intéressée plus que de raison.

Publications

All the publications authored during this PhD thesis are listed below, ordered by publication date.

- **Peer reviewed**
  - Dochain, A., de Ruette, N., Thomas, R. D. and Urbain, X., Differential Cross Sections for Na^+ + O^- Mutual Neutralization, *in preparation* (2022)
  - Poline, M., A. Dochain, Rosén, S., Ji, M., Larsson, M. , Ard, S., Shuman,N. , Viggiano, A. A., Grumer, J., Urbain, X., Barklem, P. S. and Thomas, R. D., Mutual neutralisation of N^+ with O^-, *in preparation* (2022)
  - M. Poline, A. Dochain, S. Rosén, J. Grumer, M. Ji, G. Eklund, A. Simonsson, P. Reinhed, M. Blom, N. S. Shuman, S. G. Ard, A. A. Viggiano, M. Larsson, H. Cederquist, H. T. Schmidt, H. Zettergren, X. Urbain, P. S. Barklem and R. D. Thomas, Mutual neutralisation of O^+ with O^-: investigation of the role of metastable ions in a combined experimental and theoretical study, *Physical Chemistry Chemical Physics* **23**, 24607 (2021)
  - Urbain, X., Dochain, A., Marion, R., Launoy, T., Loreau, J. Photodissociation as a probe of the H_3^+ avoided crossing seam, *Philosophical Transactions of the Royal Society A: Mathematical, Physical and Engineering Sciences* **377**, 20180399 (2019)
  - Launoy, T., Loreau, J., Dochain, A., Liévin, J., Vaeck, N., Urbain, X. Mutual Neutralization in Li^+–D^- Collisions: A Combined Experimental and Theoretical Study, *Astrophysical Journal* **883**, 85 (2019)
  - Génévriez, M., Dunseath, K.M., Terao-Dunseath, M., Hibbert, A., Dochain, A., Marion, R., Urbain, X. Absolute total, partial, and differential cross sections for photodetachment of O^-, *Physical Review A* **98**, 033410 (2018)

- De Ruette, N., Dochain, A., Launoy, T., Nascimento, R.F., Kaminska, M., Stockett, M.H., Vaeck, N., Schmidt, H.T., Cederquist, H., Urbain, X. Mutual Neutralization of O^- with O^+ and N^+ at Subthermal Collision Energies, *Physical Review Letters* **121**, 083401 (2018)
- Le Padellec, A., Launoy, T., Dochain, A., Urbain, X. Investigation of critical parameters controlling the efficiency of associative ionization, *Journal of Physics B: Atomic, Molecular and Optical Physics* **50**, 095202 (2017)
- Génévriez, M., Urbain, X., Dochain, A., Cyr, A., Dunseath, K.M., Terao-Dunseath, M. One- and two-photon detachment of O^-, *Physical Review A* **94**,023407 (2016)
- Dochain, A., Urbain, X. Production of a rovibrationally selected O_2^+ beam for dissociative recombination studies, *EPJ Web of Conferences* **84**, 05001 (2015)

- **Proceedings**

  - Urbain, X., Dochain, A., Marion, R., Launoy, T., Loreau, J., Non-adiabatic transitions in the near-UV photodissociation of H_3^+, *Journal of Physics: Conference Series* **1412**, 102007 (2020)
  - Urbain, X., De Ruette, N., Dochain, A., Launoy, T., Nascimento, R.F., Kaminska, M., Stockett, M.H., Loreau, J., Liévin, J., Vaeck, N., Thomas, R.D., Schmidt, H.T., Cederquist, H. Merged beam studies of mutual neutralization at subthermal collision energies, *Journal of Physics: Conference Series* **1412**, 062009 (2020)
  - Dochain, A., Urbain, X. Vibrational and electronic branching ratios of the molecular oxygen ion produced in collisions between atmospheric molecular oxygen and solar wind ions, *ISPC23 Proceedings*, 587 (2018)
  - Urbain, X., Dochain, A., Lauzin, C., Fabre, B. Absence of entanglement effect on the decay dynamics of H($2p$) pairs produced by VUV photodissociation of H_2, *Journal of Physics: Conference Series* **635**,112085 (2015)
  - Nascimento, R.F., De Ruette, N., Dochain, A., Kaminska, M., Stockett, M.H., Schmidt, H.T., Cederquist, H., Urbain, X. State-resolved measurements of mutual neutralization at subthermal collision energies, *Journal of Physics: Conference Series* **635**, 022043 (2015)

- **Oral Communications**
  - BPS, General Scientific Meeting of the Belgian Physical Society, 2021: Differential Cross Sections for Na^+ + O^- mutual neutralization
  - BPS, General Scientific Meeting of the Belgian Physical Society, 2019: Mutual Neutralization Studies of S^-/O^- and Na^+/Ne^+ at Low Collision Energies
  - UCLouvain Young Minds Seminar 2019: Imaging of wavefunctions
  - 8e journée scientifique de l'école doctorale thématique METAMORPHOSE (2018): State-to-state study of Mutual Neutralization in Low Energy Collisions

Contents

1 Introduction **1**

1.1 The mutual neutralization 1
1.2 A brief description of the process 3
1.2.1 Semi-classical description 3
1.2.2 Classical version of the Landau-Zener model 3
1.2.3 Two-state model 6
1.3 Experimental setups 11
1.3.1 Plasma measurements 11
1.3.2 Measurements using ion beams 16
1.3.3 Plasma/beam technique comparison 21
1.4 Theoretical models 25
1.4.1 How to treat the reaction 25
1.4.2 Perturbed stationnary states method 26
1.4.3 Impact parameter method 28
1.4.4 Discussion about electronic wavefunctions 30
1.4.5 Exchange at the crossing of the potential curves 31
1.4.6 Some basics of electronic wavefunctions 33
1.4.7 A list of theoretical predictions 36

2 Experimental setup **39**

2.1 Working principle 39
2.2 Preparation of beams 40
2.3 Beams transport 41
2.4 Mixing beams 41
2.5 Observation cell 43
2.6 Separation of ion beams from neutral signal 44
2.7 Beams overlap 45
2.8 Extracting the relative kinetic energy 48
2.9 Effects of residual pressure 50
2.10 Cleaning background 53

3 Theory **57**
3.1 Collision dynamics: The Landau-Zener Model 57
3.1.1 Adiabatic and diabatic basis 57
3.1.2 Evolution of the molecular wavefunction through an avoided crossing 61
3.1.3 Full description of the collision 63
3.1.4 Effect of the Molecular Symmetries 66
3.1.5 Cross section 69
3.1.6 Limitations of the Landau-Zener Model 74
3.2 Interaction potential: ACAM 79
3.2.1 Introduction 79
3.2.2 Surface integral method 80
3.2.3 Definition of the surface to integrate 82
3.2.4 One-electron exchange approximation 83
3.2.5 Electron wavefunction for the covalent state 89
3.2.6 Electron wavefunction for the ionic state 92
3.2.7 Result of the surface integral 93
3.2.8 Diabatic basis of antisymmetrized wavefunctions . . . 95
3.2.9 Limitations of the Anion Centered Asymptotic Model 98
3.3 Validity of the LZ model for the MN reaction 100
3.4 MN at low collision energy 101

4 Differential cross section **105**
4.1 Geometric detection probability 105
4.1.1 Trajectories of neutralized ions 106
4.1.2 Derivation of the acceptance 110
4.1.3 Acceptance map 117
4.2 Beam modeling 120
4.2.1 Collisions distribution 121
4.3 Modeling of the differential cross section 128
4.3.1 Methodology 128
4.3.2 Interrupted Rutherford scattering 129
4.3.3 Impact parameter model 136
4.4 Signal modeling 146
4.4.1 Convolution with the angular distribution of collisions 148
4.4.2 Effects of the geometry of the observation cell 151
4.4.3 Peak width of experimental spectra 156
4.4.4 Correction of the branching ratios 161

5 Results and interpretation **167**
5.1 Preamble . . . 167
5.2 Checking the model validity . . . 173
5.2.1 Asymptotic extent of the anion wavefunction . . . 173
5.2.2 Comparison with experimental spectra . . . 177
5.2.3 Comparison with other theoretical predictions . . . 180
5.3 Differential cross section . . . 183
5.4 States not predicted by the model . . . 189
5.4.1 $2s2p^{N_{A+}+2}$ configurations . . . 189
5.4.2 Excited states of the neutralized anion . . . 191
5.4.3 Fractional parentage coefficients of Rydberg states . . . 194
5.4.4 Rydberg series . . . 196
5.4.5 Mutual neutralization into autoionizing states . . . 200
5.4.6 The unidentified peak . . . 202

6 Conclusion and perspectives **203**
6.1 Ongoing improvements . . . 203
6.1.1 Experimental setup . . . 203
6.1.2 Theoretical model . . . 204
6.1.3 Calibration of another setup . . . 205
6.2 Areas for improvement . . . 205
6.2.1 Measuring differential cross section at minimum collision energy . . . 205
6.2.2 Another method for measuring branching ratios . . . 206
6.2.3 Comparison with plasma measurements . . . 207
6.3 Conclusion . . . 208

A Ion beams and plasma physics **215**
A.1 Elements of corpuscular optics . . . 215
A.1.1 Characteristics of ion beams . . . 215
A.1.2 Emittance of the beams . . . 216
A.1.3 Extracting a beam from an ion source . . . 217
A.1.4 Electrostatic lens . . . 219
A.1.5 Planar deflector . . . 221
A.1.6 Cylindrical deflector . . . 222
A.1.7 Spherical deflector . . . 223
A.1.8 Magnetic deflector . . . 223
A.1.9 Wien filter . . . 224
A.1.10 Faraday Cup . . . 225
A.1.11 Position sensitive detector . . . 226
A.2 Ion sources . . . 228
A.2.1 Thermionic emission source . . . 229

A.2.2 Sputter ion source . . . 229
A.2.3 ECR Ion Source . . . 233
A.2.4 Duoplasmatron ion source . . . 240

B Data treatement **251**
B.1 Acquisition system . . . 251
B.1.1 Scaling . . . 251
B.2 Mass missattribution . . . 253

C Theory: Derivation details **257**
C.1 Collision dynamics: The Landau-Zener Model . . . 257
C.1.1 Landau-Zener transition probability . . . 257
C.1.2 Two-channel Landau-Zener cross section . . . 261
C.1.3 Pedestrian approach of the MLZ model . . . 263
C.2 Interaction potential: ACAM . . . 265
C.2.1 Firsov surface integral . . . 265
C.2.2 Angular momentum algebra identities . . . 266
C.2.3 Coefficients of fractional parentage for excited states . 267
C.2.4 Antisymmetrization and normalization . . . 270
C.2.5 Covalent wavefunction around atom B . . . 279
C.2.6 Alternate resolution of the ionic wavefunction . . . 289
C.2.7 Comment on the selection rules . . . 290

D Theory: Asymptotic model parameters **291**

E Results: Differential cross section **297**
E.1 $He^+ + D^-$ . . . 298
E.2 $Li^+ + D^-$ . . . 300
E.3 $Na^+ + O^-$ . . . 301
E.4 $C^+ + C^-$ . . . 304
E.5 $C^+ + O^-$ . . . 305
E.6 $N^+ + O^-$ . . . 306
E.7 $O^+ + O^-$ . . . 307
E.8 $Ne^+ + C^-$ . . . 309

F Results: Branching ratios **311**
F.1 Helium . . . 313
F.1.1 Deuterium . . . 313
F.2 Lithium . . . 318
F.2.1 Hydrogen . . . 319
F.2.2 Deuterium . . . 322
F.3 Sodium . . . 326
F.3.1 Deuterium . . . 327

F.3.2 Oxygen 328
F.3.3 Sulfur 331
F.4 Carbon 334
F.4.1 Phosphorus 336
F.4.2 Deuterium 345
F.4.3 Silicon 351
F.4.4 Carbon 356
F.4.5 Oxygen 361
F.4.6 Sulfur 366
F.4.7 Hydroxide 372
F.5 Nitrogen 374
F.5.1 Phosphorus 376
F.5.2 Deuterium 389
F.5.3 Silicon 397
F.5.4 Carbon 405
F.5.5 Oxygen 412
F.5.6 Sulfur 420
F.6 Oxygen 428
F.6.1 Phosphorus 430
F.6.2 Deuterium 437
F.6.3 Silicon 444
F.6.4 Carbon 450
F.6.5 Oxygen 458
F.6.6 Sulfur 464
F.7 Neon 470
F.7.1 Carbon 471
F.7.2 Oxygen 475
F.7.3 Sulfur 479

Bibliography **499**

Acronyms

KER	Kinetic energy release
MN	Mutual neutralization
IRSM	Interrupted Rutherford scattering model
IPM	Impact parameter method
PSS	Perturbed stationnary states method
LZ	Single channel Landau-Zener method
MLZ	Multi-channel Landau-Zener method
AMLZ	Adiabatic Multi-channel Landau-Zener method
ACAM	Anion centered asymptotic model
FCI	Full configuration interaction
MCSCF	Multi-configuration self-consistent field
LCAO	Linear conbination of atomic orbitals
MCP	Micro-channel plates
ADC	Analog-to-digital converter
ECR	Electron cyclotron resonnance
FALP	Flowing Afterglow/Langmuir Probe
DESIREE	Double electrostatic ion ring experiment

Chapter 1

Introduction

1.1 The mutual neutralization

Suppose two atoms: one misses an electron – this is a positive ion, a cation A^+ – the other has an electron surplus – this is a negative ion, an anion B^-. When they meet, several chemical reactions can occur:

$$\begin{aligned}
A^+ + B^- &\rightarrow A + B && \text{(Mutual neutralization)} && (1.1)\\
&\rightarrow A^+ + B + e^- && \text{(Collisional detachment)} && (1.2)\\
&\rightarrow A + B^+ + e^- && \text{(Transfer ionization)} && (1.3)\\
&\rightarrow AB^* \rightarrow AB^+ + e^- && \text{(Associative ionization)} && (1.4)\\
&\rightarrow A^- + B^+ && \text{(Double charge exchange)} && (1.5)
\end{aligned}$$

This thesis is an attempt to describe the first reaction. The basic concepts needed to understand the process are exposed in the following section.

A first question then arises: why study this reaction?

A first set of answers is given by [1] (and references therein): anion-cation reactions are the most important mechanism for destroying negative ions. The high efficiency of neutralization reactions is explained by several factors: first, cations and anions attract each other by Coulomb interaction. This attraction having an infinite range, it increases the reactivity enormously. In the limit of low center-of-mass collision energy $E_{r,i}$ (the kinetic energy available in the center-of-mass-frame – section 4.1.1), the cross section is diverging as $E_{r,i}^{-1}$ (section 3.1.5), while the rate coefficient diverges as $E_{r,i}^{-1/2}$ (section 4.2.1) as a consequence of Wigner's threshold law [2]. Then, this reaction is exothermic without passing through a potential barrier. This means that the reaction releases energy, that the reaction can take place even if the ions approach slowly.

This explains why the mutual neutralization is the most important mechanism for destroying negative ions: because the other reactions involving

an atomic anion and cation are either endothermic (reaction 1.2), happen at smaller interatomic distance (reactions 1.3, 1.5) or need more than one electron to be exchanged – by either a sequential one-electron process of by a multi-electron process – (reactions 1.5,1.3). Those reactions are briefly discussed in sections 3.1.6, 5.4.2, 5.4.4 and 5.4.5.

From this answer emerges another question: why discuss negative ions? To answer this question, it helps to define what a plasma is.

A plasma is a globally neutral gas of which at least some of the atoms / molecules that compose it are ionized. Ionization processes generate cations, anions and electrons – mostly cations and electrons –. However, since electrons are much lighter than ions and hence more mobile, they will quickly react with cations. Once this first set of reactions is ended, only cations and anions remain in the plasma. The chemical dynamics of the system are then dominated by mutual neutralization and interaction with photons.

Thus, mutual neutralization plays an important role whenever an anion populated plasma is involved (interstellar molecular clouds, ionospheres, etc.), e.g. it has been shown recently that the $O^+ + O^-$ mutual neutralization leads to a significant part of the UV tropical nightglow of O I at 135.6 nm [1, 3, 4].

The mutual neutralization also plays a significant role in the estimation of metallicity of stars (i.e. estimating the abundance of elements heavier than hydrogen and helium). This abundance is infered from the measurement of the intensity of the spectral lines associated to those elements. It requires non-local thermal equilibrium modeling of the star atmosphere in order to correlate the elemental abundance in the volume of the star with the spectra emitted at its surface. It has been shown recently that, e.g., neglecting mutual neutralization does in fact have a significant impact on spectral line profiles and on inferred lithium and sodium abundances [5]. This explains why a large number of calculations has been performed recently for mutual neutralization involving the hydrogen anion (section 1.4.7).

Let us add to this that the measurement of mutual neutralization can serve as a benchmark for the numerical models of estimation of inelastic collisions $A + B \rightarrow A^\star + B$ [6–8]. As the excited states involved in those collisions are coupled by the ionic curve of the system, if the mutual neutralization reaction is correctly described – as it requires an accurate description of the same excited states involved in the inelastic collision system – then the inelastic collisions have a better chance to be accurately described. This in turn validates the use of those predicted inelastic collision rates in stellar atmosphere modelling [9, 10].

One should note that all these processes take place at temperatures below 10,000 K, i.e. with a center of mass collision energy below 1 eV. Which is the collision energy range studied in this thesis.

Another interest in the study of mutual neutralization is directly linked to

the ITER project: a tokamak in which the plasma is heated using an intense beam of D^-, whose main destruction process in the ion beam source is the mutual neutralization with D^+, D_2^+ and D_3^+ which had to be bypassed.

But my main interest in the study of mutual neutralization is its apparent simplicity. It could be summed up in a simplistic way: "If I am an atom with an extra electron, I will give it to this atom which is missing one". Yet this seemingly simple reaction is difficult to reproduce with rigorous models that take into account all the electrons in the system. And this for a obvious reason: when the anion "gives" its electron, this electron weakly attaches to the cation. In order to describe the reaction rigorously, it is then necessary to consider all the excited states of the diatomic quasi-molecule associated with the reaction. As these excited states quickly become numerous, the calculation of the properties of this quasi-molecule is not always possible to perform (with reasonable computer resources).

Thus, this reaction, which is at the same time simple to explain qualitatively and very complex to describe quantitatively, makes it a fascinating subject of study. This is why a certain number of cation-anion combinations selected in this thesis have no direct application, but this great variety of reagents makes it possible to obtain an overview of the reaction, to identify the various mechanisms at play, and to find an efficient method to describe the processes involved.

1.2 A brief description of the process

1.2.1 Semi-classical description

Mutual neutralization is a process of electron transfer from a negative ion to a positive ion. The objective of this section is to describe this process in a simple way, following a semi-classical representation. This process will initially be described from a kinematic point of view – in other words, the study of the trajectory of the particles involved in the process –. It will then be presented from an energy point of view – using a two-state model – in order to complete this description.

1.2.2 Classical version of the Landau-Zener model

Suppose two ions, one positive (a cation A^+) and the other negative (an anion B^-). Let us take a reference frame such that the anion is fixed at the center of the frame. These two ions are initially attracted to each other by the Coulomb force. But as the anion is assumed to be fixed, only the cation moves within the chosen frame.

The cation comes from a position initially sufficiently far from the anion to consider these two ions as isolated from each other. However, the two ions are still close enough to consider them isolated from the outside environment[1].

As the cation approaches, it is subjected to the Coulomb force of the anion. The cation and the anion are of opposite charge, therefore, the Coulomb force is an attractive force. The cation will be accelerated towards the center of the coordinate system.

As the Coulomb force derives from a central potential, the trajectory of the cation will be a conical function. As the cation has a non-zero initial velocity, otherwise there would be no encounter, its trajectory is a hyperbola (see figure 1.1).

As the cation approaches the anion, it is possible that the latter will "donate" its supernumerary electron to the cation. The two ions A^+ and B^- become neutral atoms A^0 and B^0. Consequently, these are said to be neutralized. This explains why this reaction is called the mutual neutralization reaction.

Since the atoms are each of zero charge, the Coulomb force no longer acts on them. The cation then leaves its hyperbolic trajectory to follow a simple uniform rectilinear trajectory. Its velocity remains the one it had just before his neutralization.

In order to model this process, some assumptions must be made. The model used here was devised in 1932 by Landau and Zener [11]. The main hypothesis of this model is to assume that the anion can donate its supernumerary electron to the cation only for a single very precise separation distance of the cation. This distance between the two ionized atoms is called the critical interatomic distance R_c.

The determination of this distance is described in the section dedicated to the two-state model (next section).

Within the framework of this model, the complete kinematics of the reaction (presented by the figure 1.1), is as follows:

As the anion is fixed at the center of the frame, it is possible to draw a circle of radius R_c around it. This circle is called the critical circle. When the cation enters the critical circle, there is a certain probability P that the anion will donate an electron to the cation. Indeed, at this instant, the distance between the cation and the anion is the critical interatomic distance R_c.

If the atom A or the cation A^+ is inside the critical circle, then, it must leave it. In doing so, it crosses the critical circle again - with a probability of

[1] This reaction is a so-called gas phase binary reaction. All atoms and molecules are considered isolated – they do not interact with each other – except in a collision between two of these atoms.

The external environment is therefore the set of other molecules that make up the gas, this one containing the two ions that interest us.

In addition, it is considered highly unlikely that three particles will meet at the same time.

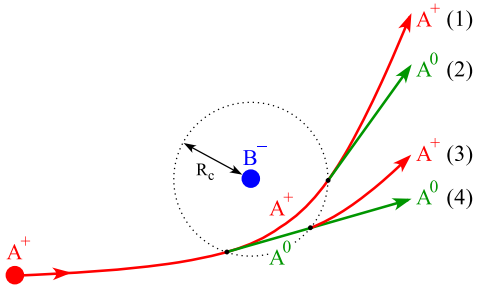

Figure 1.1: Classical mutual neutralization trajectories as described by the Landau-Zener model. Trajectories (1), (2), (3) and (4) are described in the text.

electron exchange with the atom B (or the anion B^- depending on the location of the electron around A^+ or B).

In order to determine the total probability of mutual neutralization $\mathscr{P}_{\text{tot}}$, the set of possible trajectories must be taken into account (see figure 1.1):

(1) If the cation was not neutralized on its first pass through the critical circle (↙, with a probability $1-P$) and the cation was not neutralized on its second pass through of the critical circle (↗, with a probability $1-P$), then the total probability that the ion remains an ion along this trajectory is $(1-P)\times(1-P)$.

(2) If the cation has not been neutralized on its first passage through the critical circle (↙, with a probability $1-P$) and the cation is neutralized on its second passage through the critical circle (↗↔, with a probability P), then the total probability for the ion to neutralize along this trajectory is $(1-P)\times P$.

(3) If the cation was neutralized on its first passage through the critical circle (↔↙, with a probability P) and the neutralized cation ionizes again on its second passage through the critical circle (→↗, with a probability P) [2], then the total probability that the ion remains an ion following this trajectory is $P\times P$.

(4) If the cation was neutralized on its first passage through the critical circle (↔↙, with a probability P) and the neutralized cation remains neutral on its second passage through the critical circle (→↔, with a probability $1-P$). then the total probability for the ion to neutralize along this trajectory is $P\times(1-P)$.

[2] Indeed, the probability P is the probability of electron transfer. It does not depend on the direction of transfer of this electron: It is valid for both ionization and neutralization. Furthermore, this definition shows that the sum over all the possible path is equal to 1.

Only the trajectories (2) and (4) end up with the neutralized ions. Therefore, the total probability of mutual neutralization will be the sum of the probabilities of borrowing each of these paths [3]. This gives a total probability $\mathscr{P}$ of

$$\mathscr{P} = 2\,P \times (1-P). \tag{1.6}$$

Quantum mechanics requires to consider the phase relationship of those two trajectories leading to interferences between them. This question will be addressed later on. It should be noted that the probability of electron exchange P depends on the angle with which the cation (or neutralized cation) enters or leaves the critical circle. This is why a more rigorous calculation of the total probability requires taking into account the set of possible initial trajectories of A^+.

Mutual neutralization will now be approached according to another representation, that of the two-state model.

1.2.3 Two-state model

This representation provides results equivalent to those of the kinematic representation. Nevertheless, although it is more difficult to understand, it allows to approach in a much simpler way the rest of the development. Moreover, this representation is compatible with quantum mechanics.

This representation implies that the two atoms – or the two ions – are no longer considered as isolated particles, but as a system, a whole. This system can be in two different states: an ionic state and a covalent state.

These states are characterized by their internal energy, also called potential energy. Potential energy is an amount of energy stored inside the system.

As the total energy of a system is conserved, when the potential energy of the system decreases, it transforms into kinetic energy, or energy of displacement (see figure 1.2).

The kinetic energy of the system E_k is proportional to the square of the speed of the particles in the center-of-mass frame

$$E_k = \frac{\mu v^2}{2} \tag{1.7}$$

where $\mu = \left(\frac{1}{m_A} + \frac{1}{m_B}\right)^{-1}$ is the reduced mass, m_A is the mass of the atom A and m_B is the mass of the atom B.

The potential energy depends only on the position of the particles. In addition, as the system is made up of only two particles, it is possible to express

[3] If the system is initially in the ionic state $(A^+ + B^-)$, the total probability of mutual neutralization is the probability of obtaining the system in the end in the covalent state $(A^0 + B^0)$, by taking into account all the possible trajectories.

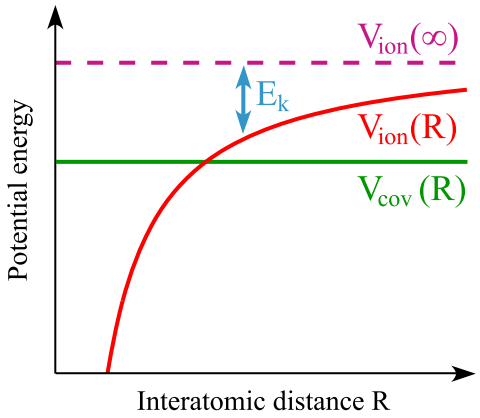

Figure 1.2: Illustration as curves of potential energy and kinetic energy.

the set of all possible positions of these two particles using a single variable: the distance between the two particles – also called interatomic distance R.

The initial state of the system composed of the anion and the cation is called the ionic state. As stated earlier, these two ions are attracted to each other by the Coulomb force. If the two ions are at a sufficiently large distance from each other for this distance to be considered infinite, the potential energy of this state $V_{\text{ion}}(\infty)$ is the sum of the internal energies V_{A^+} and V_{B^-} of each of the ions A^+ and B^- taken separately. When the two ions approach, the potential energy of the system $V_{\text{ion}}(R)$ will decrease (see figure 1.2). This decrease – given by the Coulomb potential – is inversely proportional to the interatomic distance (atomic units are adopted here):

$$V_{\text{ion}}(R) = V_{\text{ion}}(\infty) - \frac{1}{R}. \tag{1.8}$$

The other possible state of the system is composed of the two neutralized ions and is called the covalent state. Since atoms A and B have zero charge, the Coulomb force does not act on them [4]. Neglecting the polarization forces (van der Waals), the potential energy $V_{\text{cov}}(R)$ of the system in this state is constant,

[4] In practice, each atom is made up of several electrons and a nucleus. Those particles are not located in the same positions, each electron and each nucleus gives a different Coulomb attraction/repulsion to the nucleus and each electron of the other atom. When the atoms are far from each other, the average Coulomb force of one atom on the other is null. But when the atoms are close to each other, the Coulomb force applied to an electron/nucleus of the other atom should take into account the slight position difference, resulting in a net Coulomb force. This force could polarize the atoms (and form a dipole) which, in return, could also apply a force on the former atom. This interaction, which takes into account all the sub-elements of atoms, is called a multipolar interaction, the simplest component of which is dipolar attraction.

However, the mutual neutralization reaction takes place at large interatomic distances which

independent of the interatomic distance (see figure 1.2). Its value is the sum of the internal energies V_{A^0} and V_{B^0} of each of the atoms A^0 or B^0 taken separately.

Still following this model, the potential energy cannot suddenly change in value. The variation of potential energy over time must therefore be continuous. Therefore, the transition from one state to another is possible only when the potential energy curves of the ionic state and covalent state coincide which only occurs when they intersect (figure 1.3). The interatomic distance at which this crossing takes place is the same critical interatomic distance R_c described in the kinematic representation [5].

To better visualize the transition between two states, the mutual neutralization reaction is shown both as trajectories and as potential energy curves in figure 1.3.

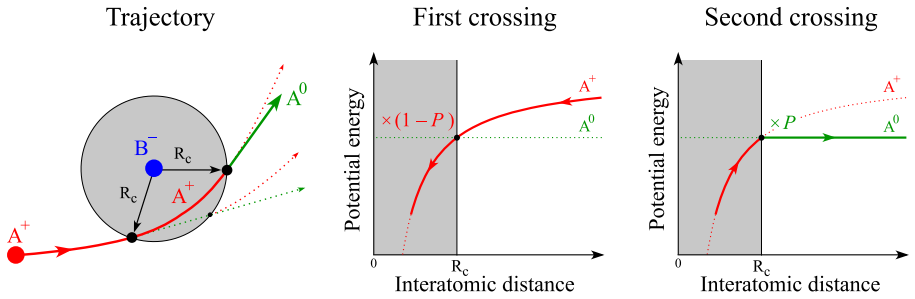

Figure 1.3: Mutual neutralization reaction paths. The different reaction paths are defined by the different trajectories given by figure 1.1. These are represented with the help of potential energy diagrams. The transition between the ionic state $(A^+ + B^-)$ and the covalent state $(A^0 + B^0)$ is possible only when the potential energy curves of these two states intersect at the interatomic distance R_c.

Thus, this model makes it possible to determine the distance at which the two ions interact. However, a problem persists: How to be sure that the covalent state produced during a mutual neutralization reaction is indeed what is expected?

Is it possible to determine, by an experimental measurement, if the neutral atoms produced during the mutual neutralization reaction are indeed those whose potential energy is given by the figures 1.3 and 1.4 ?

Indeed, the covalent state is composed of two neutral atoms. When these two atoms are far enough apart, they can be considered isolated from each other. Each of these atoms is in a given quantum state (depending on how the

means that the multipolar interaction is negligible. Nevertheless, these interactions must be considered to have a more detailed description of the reaction (section 3.2).

[5] The probability of changing curve is given by the behavior of potential curves at the crossing point. This behavior is too complex to be detailed here, but is described in detail in the following sections.

electrons are arranged around the nucleus, called the terms of an electronic configuration), to which there is a corresponding potential energy. Thus, the measurement of the potential energy of the covalent state makes it possible to determine the state of each of the atoms produced by this reaction of mutual neutralization A^0 and B^0.

A similar reasoning holds for the ionic state, except that one must take into account the decrease in potential energy when the distance between atoms decreases (equation 1.8).

Since the potential energy of the system before the reaction is greater than that after the reaction, this difference in potential energies is released in the form of kinetic energy, called KER (for Kinetic Energy Release - figure 1.4).

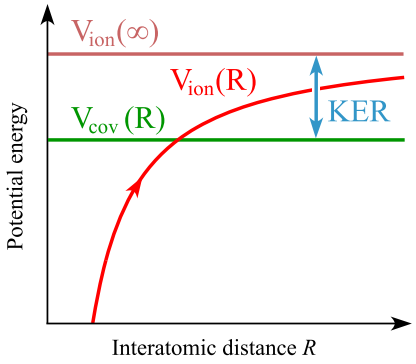

Figure 1.4: Illustration in the form of potential energy curves of the kinetic energy release (KER).

Thus, measuring the kinetic energy released during a mutual neutralization reaction makes it possible to determine the difference between the potential energy of the two ions (A^+ and B^-) before the reaction and the potential energy of the two neutral atoms (A^0 and B^0) after the reaction.

A priori, it does not seem obvious that measuring an energy difference leads to the identification of both initial and final states. However, there is in general a finite number of accessible states, which is possible to count. These states are said to be quantized (hence the name quantum physics). In addition, each atomic state has its own unique potential energy.

Therefore, only a finite set of kinetic energies can be released in a mutual neutralization reaction. It corresponds to the energy gained of the electron capture by the cation minus the energy needed to extract the electron from the anion as shown on figure 1.5.

As a consequence, the measurement of the released kinetic energy makes it possible to determine the state of the ions (A^+ and B^-) before the reaction and the state of the two neutral atoms (A^0 and B^0) after the reaction.

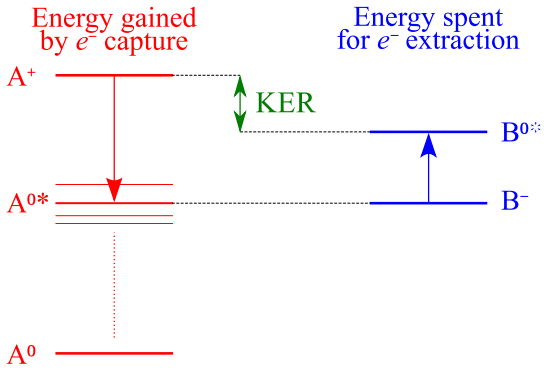

Figure 1.5: Schematic definition fo the kinetic energy released during a mutual neutralization reaction.

Furthermore, if the number and density of initial ions, the number of neutralized ions produced and the kinetic energy release are known, it is possible to determine the total probability of mutual neutralization from each ionic state to each covalent state.

The experimental method used to carry out these measurements will be the subject of a later chapter.

1.3 Experimental setups

The experimental device presented in this thesis is far from being the only one that have been used to study the mutual neutralization reaction. A wide variety of experimental devices which allow this reaction to be studied have been constructed from the late 1930s until recently. This section aims to give an overview of these various setups and then briefly explain their operating principles.

These experimental setups can be divided into two categories: one measures the reaction rate within a plasma, the other uses ion beams propagating in a vacuum in order to perform cross section measurements. The present review of experiments follows this logic.

1.3.1 Plasma measurements

Let us start with all the techniques of mutual neutralization measurements carried out within a plasma. The descriptions below are broadly based on those given by [12–14] in their literature reviews.

Charges collection

The first type of setups used to reliably measure the mutual neutralization reaction rate used a charge collection system (positive and negative) synchronized with the pulsed plasma ionization source. This type of measurement is performed in a chamber where a plasma is generated: At a given time, the energy source that generates the plasma is interrupted. The measurement of the evolution of the number of charges (positive and negative) within the plasma makes it possible to deduce the mutual neutralization reaction rate constant. This technique works as follows:

A gas is injected between two parallel plane electrodes. Part of this gas is then ionized using X [15, 16] or UV [17, 18] radiation. After a determined waiting time, a voltage V is applied to one of the electrodes. The ions are then collected on the different plates.

This waiting time allows, on the one hand, the electrons to either attach themselves to a gas molecule (dissociative or radiative attachment) or to diffuse to the walls. As the (negative) ions are heavier, the time required for their diffusion to the walls is longer. Thus, after a certain time, all the electrons are eliminated from the plasma, while the anions have not yet had time to diffuse [6].

[6] In order to verify these hypotheses, several precautions are put in place: in order to reduce the diffusion of the gas mixture studied, a buffer gas (supposedly inert) is injected. Its pressure (about 100 mbar) is much greater than that of the gas studied (about 0.1 mbar). The wavelength of the light pulse ($\sim$ 10 eV) is large enough to ionize the gas of interest, but not the buffer gas (typically helium). The composition of the plasma is independently established using a mass

If this initial diffusion to the walls is neglected, and we assume that it does not influence the neutralization dynamics [7], then the evolution of the ion density (n_- and n_+) is given by:

$$\frac{dn_{+,-}}{dt} = -\alpha n_+ n_- \text{ with } n_+ \simeq n_- \tag{1.9}$$

where α is the reaction rate coefficient, determined experimentally.

Measuring the dielectric constant of the gas

This second type of device has many similarities with the previous one. It mainly differs by the potential applied to the electrodes. In this case, the objective is no longer to collect the charges contained in the plasma, but to estimate the number of charges present within it by measuring the dielectric constant of the plasma κ. This constant is measured by applying an oscillating electric field of known frequency. This method was used by [19, 20].

The principle of the reaction rate constant measurement is as follows: an electric field of frequency ω is applied to the plasma: as the two plates form a capacitor, it is possible to measure its capacity and to deduce the dielectric constant of the plasma. As the theory [19, 20] indicates that this dielectric constant is given by:

$$\kappa = 1 - \frac{e^2}{\varepsilon_0} \sum_k \frac{N_k}{m_k(\omega^2 + \nu_k^2)} \left(1 + i\frac{\nu_k}{\omega}\right) \tag{1.10}$$

with N_k, m_k, ν_k the density, mass and collision frequency[8] of each compound k present in the plasma. Using this information, it is possible, using the time dependance of κ, to deduce the ion density as a function of time, and finally to obtain the reaction rate constant.

Note that, as the collision frequency is difficult to estimate, the frequency of oscillation of the electric field is chosen so as to be much higher (several MHz) than the frequency of collisions. This greatly simplifies the expression above.

Flowing Afterglow with Langmuir Probe (FALP)

The two previous types of setups are pulsed setups. This component intrinsic to the devices, combined with the difficulty (at the time) of measuring the time dependence of a current made it necessary to measure the integral of the current

spectrometer. This makes it possible to identify the cations and anions which react.

[7] If diffusion is taken into account, it complicates this equation, but does not invalidate the reasoning.

[8] The inverse of the time between two collisions for a given atom/ion.

for several delay times corresponding to time in the evolution equation. These methods therefore required a large number of repetitions of the measurement. The use of a post-discharge plasma flow (flowing afterglow) made it possible to carry out the experiment continuously and to greatly improve the (statistical) quality of the measurements. Its operating principle is as follows:

Suppose a flow of gas passes through a discharge and forms a plasma. As the flow within a tube which confines the plasma has a constant velocity, each position after the discharge in the tube corresponds to a time after the discharge. Within the post-discharge plasma, as electrons have a much greater mobility than anions, they quickly escape from the plasma to the walls [9]. So the only remaining charged particles are cations $(+)$ and anions $(-)$. By arranging so that there is only one anion and a single cation species present in the plasma (see the Ar^++Cl^- example below), it is possible (using a Langmuir probe [10]) to measure the density of anions and cations within this plasma. And as the plasma forms a flow of given speed, the position of the probe within this flow gives a temporal indication of the evolution of the neutralization of the ions. In other words, the reaction rate of mutual neutralization.

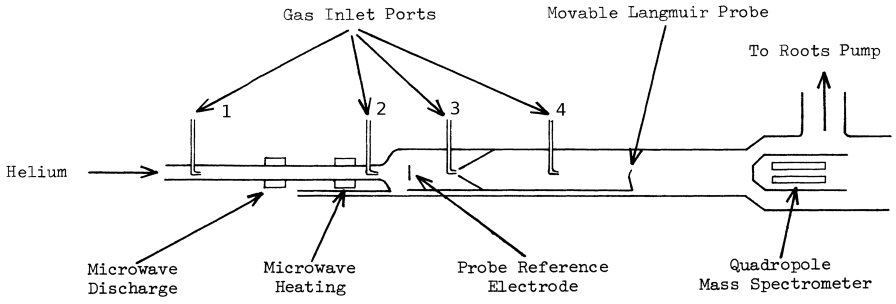

Figure 1.6: Schematic diagram of the Flowing Afterglow/Langmuir Probe apparatus [12]

A version of this device is shown in figure 1.6: a buffer gas (usually helium) is injected into a 10 cm diameter glass tube. The gas then passes through one or two RF discharges. Then propagates over a meter before being extracted through a small opening at the tube outlet, to be mass analyzed using a quadrupole and finally evacuated from the system. Several gas injection points are possible along the tube (before or after the discharges). Within the tube, a

[9] In the post-discharge regime, when there is no anion in the plasma, as the plasma is quasineutral and the total current in the plasma is null, the electron (e) diffusion current in the plasma equals the cation $(+)$ current. In such case, the density of the charged particles $n_{+,e}$ is driven by the ambipolar diffusion $\dot{n}_{+,e} = D_a \nabla^2 n_{+,e}$ where D_a is the ambipolar diffusion coefficient which is inversely proportional to the total gas pressure. In order to inhibit the ions/electrons diffusion to the wall, the setup is operated at a suitably high pressure.

[10] An electrode whose plasma current is read as a function of its polarization. The geometry of this probe may vary.

movable Langmuir probe measures the density of positive and negative ions.

The order of the different injection and discharge steps used for the Ar^+ + Cl^- reaction helps to understand the interest of these different injection points:

1. Injection of helium.
2. First RF discharge: generation of He^+, e^- and He^*.
3. Second RF discharge: of sufficient intensity to heat the plasma electrons, but of insufficient intensity to ionize the helium [21]. This process accelerates the ambipolar diffusion of ions and electrons, leaving only He^* ($2\,^3S$ and $2\,^1S$) in the plasma.
4. Injection of a noble gas (Ar, Kr or Xe — inlet 2). It will convert all the excited helium atoms into atomic ions (Ar^+, Kr^+ or Xe^+) and into electrons (no He^+ is produced as its ionization potential is greater).
5. A halogen gas is injected (Cl_2 or F_2 — inlet 3). This gas forms atomic anions by dissociative attachment. The ionization potential of noble gases is too low to ionize halogens[11].

As dissociative attachment is faster than mutual neutralization, the result is a compound plasma whose cations are only rare gases and anions are only halogens.

This reaction example shows the complexity of preparing the plasma. This explains the few mutual neutralization reactions between two atomic ions measured using this method. However, it made it possible to measure a number of reactions involving molecules and clusters of molecules (see [12, 22] and references therein).

The VENDAMS setup

The device which closes this section on techniques for measuring reaction rate within a plasma is a device which was recently developed [14] and produced several measurements of mutual neutralization between atomic species (H/D/He/C/N/O/Ne/Ar/Kr/Xe^+ + Cl/Br/I^- — see [23–27]). It reuses the principle of FALPs by modifying certain aspects and is called VENDAMS (for Variable Electron and Neutral Density Attachment Mass Spectroscopy). The elements included are:

- Helium buffer plasma (double RF discharges)
- Argon injection after RF discharges.

[11] The density of neutral elements is low enough to neglect collisions between ions and neutrals. Collisions with helium do not modify the ions charge.

- The quadrupole mass spectrum at the oulet (only measures anions).

While the modified elements are:

- The Langmuir probe, which becomes fixed: It is placed after the injection of argon (or other gas which generates the cation of the reaction). It only measures the electron density.
- There is only one gas injection point generating the anion. This is positioned after the probe (this injection may contain a mixture of gases).

These modifications entailed a change in the operating principle of the device: as the Langmuir probe is no longer mobile, there is no longer any question here of observing the evolution of the ion density along the tube in order to measure directly the reaction rate. This reaction rate is derived according to another method.

The idea is to modify the initial density of the ions before reaction, to let them react during the passage of the tube and to measure the density of ions at the outlet. This change in the initial ion density serves as a time scale. Thus, within this device, the RF discharge conditions and the flux of argon (or other gas generating the cation) are modified in order to control the density of electrons within the initial plasma while the second injection of gas is kept constant. The gas mixture is chosen so that two types of negative ions are produced: one of which the rate constant of mutual neutralization is known, while the other product has an unknown rate constant of neutralization. The mass spectrometer then measures the ratio between the two negative ions at the tube outlet for each electron density before gas injection.

Obtaining the reaction rate constant is then deduced by injecting all possible reactions into a numerical model, then by performing a non-linear fit of the experimental data using a dynamical reaction model.

Characteristics of measurements in a plasma

One of the peculiarities of the devices presented above is that the plasma is always confined by the walls of the plasma chamber. This interaction (of the buffer gas with the walls and of the buffer gas with the rest of the elements of the plasma) makes it possible to heat the plasma at the temperature of the walls.

Thus, the temperature of the walls imposes the distribution of the populations of the internal energy levels (electronic, vibrational and rotational) of the reactants, that is to say of the charged particles which make up the plasma. This makes it impossible to select a specific initial energy level [12]. In addition,

[12] In the case of atomic ions, this problem does not really exist: the distribution of electronic levels at room temperature gives a population exclusively in the ground state.

the collision energy also follows a thermal distribution.

Since the reaction rate coefficient by definition includes an energy distribution, it is not possible to obtain the cross section of the reaction for a given collision energy (while the reverse is possible, by averaging over the collision energy).

1.3.2 Measurements using ion beams

Measurements principle

The devices described here are devices which cross two ion beams. All these devices follow the same operating principle: they cross a beam of cations and a beam of anions. Each of these beams is a beam of a single ions species obtained by selection in mass and kinetic energy. As a reminder, an ion beam is a set of charged particles propagating in a vacuum in the same average direction at the same average speed. The methods used to generate and characterize these beams are described throughout chapter 2 and section 4.2. For the purposes of this introduction, we will assume that the particles all have the same direction and speed of propagation (unless otherwise indicated). Note however that, as the density of ions within a beam is low (typically 10^4–10^5 cm^{-3}), they do not collide with each other, hence cannot exchange internal energy (thermalize). Thus, the transverse kinetic energy distribution and the internal energy distribution (electronic, vibrational and rotational) remain unchanged throughout the beam path unless rapid spontaneous decay takes place [13].

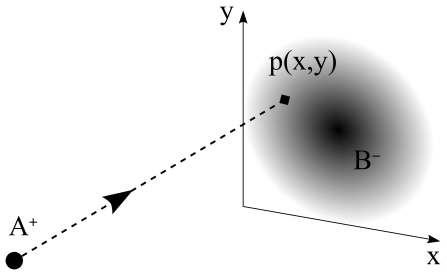

Figure 1.7: Representation of the probability of reaction $p(x,y)$ of a particle A^+ with another particle B^- when the latter crosses the plane transverse to its trajectory which includes B^-.

As the ions of each beam are considered to be isolated from each other, it is possible to consider binary collisions only, i.e. collision-by-collision reactions. Thus, when the ion A^+ crosses the plane transverse to its trajectory including B^- (figure 1.7), it crosses this plane according to a position (x,y).

[13] There are, however, various techniques for modifying these distributions. It nevertheless requires storing the ions for a relatively long time.

As the probability of reaction depends on this position (x,y), and since it is not possible to know this position experimentally [14], we integrate all of these probabilities, which produces a surface: the cross section $\sigma = \int p(x,y)\ \mathrm{d}x\mathrm{d}y$.

This approach to measuring cross sections is very different from that adopted by the plasma physics which describes the reaction in volumetric terms. The ion beam methods still provide the result of the reaction rate by averaging the cross section [28]:

$$\alpha(T) = \sqrt{\frac{8}{\pi\mu(k_B T)^3}} \int \sigma(E_{r,i}) \times E_{r,i} e^{-E_{r,i}/k_B T}\ \mathrm{d}E_{r,i} \tag{1.11}$$

where $E_{r,i}$ is the collision energy in the center-of-mass frame, μ is the reduced mass of the two atoms, k_B is the Boltzmann constant and T is the temperature.

Beam crossing

Crossed-beam cross section measurement methods require a positive ion beam and a negative ion beam in order to measure the cross section of the mutual neutralization. Thus, it is necessary to have two sources of ions, one producing cations and the other anions in sufficient quantity [15].

Once the two ion beams have been produced, there are four ways to cross these beams: perpendicularly ($\theta = 90°$), at an acute angle ($\theta < 90°$), an obtuse angle ($\theta > 90°$) or in confluence ($\theta \simeq 0°$). These different methods allow different collision energy ranges to be sampled. Indeed, the collision energy $E_{r,i}$ in the reference frame of the center-of-mass is given by:

$$E_{r,i} = \mu \left(\frac{E_+}{m_+} + \frac{E_-}{m_-} - 2\sqrt{\frac{E_+}{m_+}\frac{E_-}{m_-}} \cos\theta \right) \tag{1.12}$$

where μ is the reduced mass of the system, E_+, m_+ (E_-, m_-) are the energy and mass of the compounds of the cation (anion) beam. Thus, the smaller the angle between the beams, the lower the collision energy.

Crossed-beam devices (perpendicular or at 45°) have the advantage of having well-defined beam overlap geometry. It is even possible to do away with

[14] The surface for which the probability of collision is non-zero is a sphere with a maximum radius of a few nanometers. This is much lower than the spatial distribution of the beams, which is of the order of a millimeter.

[15] The first mutual neutralization measurements carried out using beams — which were set up at the Stanford Research Institute in 1967 [29, 30] — were carried out shortly after the development of an intense negative ion source [31] whose optimal operating principle was discovered shortly before. This principle is described in the section A.2.4.

the geometry of the beams [16] by using the method of animated beams [32]. However, since it is difficult to obtain and maintain stable beams with low kinetic energy (less than 1 keV), the minimum collision energy is of the order of 250 eV (for ions of identical masses and an angle of 90°). The upper limit is for its part limited by the maximum kinetic energy of the beams, this method made it possible to obtain collision energies in the center-of-mass frame going up to 40 keV [33] (for a angle of $-45°$). Which is higher than the other two methods presented below.

To decrease the collision energy, one method is to tilt the two beams relative to each other [17]. Once the geometry of each of the beams is well determined, the overlap between the two beams is possible to estimate [34]. This method made it possible to lower the collision energy to 20 eV (in the center-of-mass frame) while keeping a kinetic energy for each beam greater than 1 keV.

To go even lower in collision energy, the last method places the beams in confluence (the beams are aligned hence at an angle $\theta = 0$). In this case, the collision energy given by the equation 1.12 becomes:

$$E_{r,i} = \mu \left(\sqrt{\frac{E_+}{m_+}} - \sqrt{\frac{E_-}{m_-}} \right)^2 \tag{1.13}$$

This method has several advantages: firstly, by finely adjusting the kinetic energy of each of the beams, this method theoretically makes it possible to achieve zero collision energy. In practice, the kinetic energy dispersion of each of the beams (imposed by the ion sources and the emittance of each of the beams) limits the minimum collision energy. Then, as the beams are parallel, the overlap volume between the two beams is much greater. Thus, for the same beam diameter, many more reactions will take place (their numer being proportional to the volume of overlap of the beams). This method hence makes it possible to measure smaller cross sections.

This method would therefore appear to be ideal. However, it presents a number of difficulties. The first is directly related to the overlap of the beams. Indeed, it is complicated to estimate the length of the overlap region. To overcome this problem, one method consists in carrying out the confluence in two stages: initially placing the beams in confluence while adjusting the kinetic energy of the two beams so that the relative kinetic energy minimizes the signal.

[16] This beam overlap problem is as follows: suppose that we pass an ion beam through a circular diaphragm, so that the beam is cylindrical at the exit. However, it is not certain that the density of the ions within this cylinder is uniform. In addition, the distribution of speed and direction of the particles that make up this beam indicates that the beam is not exactly symmetrical and modifies the density of the ions throughout the path of the beam.

[17] The angle between the two beams can be 20° [34–36], 8.5° [37] or 15° [38, 39].

Next, bringing the two beams into a cell biased at a potential that accelerates one beam (the slower) and slows down the other (the faster), thus matching their velocities so that the signal generated within the cell is much larger than that generated outside of it [18].

Another intrinsic difficulty with this method comes from the fact that it is necessary to measure the profile of each of the beams separately before carrying out a measurement [40–42], and to make sure that the beams remain stable throughout the overlap region. However, a method has been developed to work around the problem. This method is an extension of the animated crossed beam [43]) method to the merged beam geometry.

Detecting the neutralized atoms

Once the ions have been neutralized, they must be detected to estimate their production rate and deduce the cross section. As only the primary ions are sensitive to static electric or magnetic fields, it suffices to deflect them to recover only the neutral atoms in a straight line. However, several problems arise: how to treat the ions neutralized with the residual gas within the interaction cell? How to ensure that the studied reaction is indeed mutual neutralization, and not collisional detachment (reaction 1.2) or transfer ionization (reaction 1.3)?

And finally, when the two beams are brought together, how to distinguish the neutralized cations from the neutralized anions? This issue is particularly important when the two atoms are identical. Thus, when the two ions are associated with the same atom to give a reaction of the type:

$$A^+_{(1)} + A^-_{(2)} \rightarrow A_{(1)} + A_{(2)}, \tag{1.14}$$

The only possible method to differentiate them is by time of flight: if $A^+_{(1)}$ is faster than $A^-_{(2)}$ then there is a good chance that $A_{(1)}$ is faster than $A_{(2)}$. However, when the collision energy tends towards 0 (the collision energy between the ions is dominated by the kinetic energy distribution of the two beams), it is impossible to experimentally differentiate $A_{(1)}$ from $A_{(2)}$.

As the two beams of neutralized atoms overlap, the technique used for crossed beams, which is to ensure that the detection of an atom $A_{(1)}$ from the cation beam coincides with the detection of an atom $A_{(2)}$ coming from the anion beam, becomes inapplicable directly. Thus, if only the combination of $A_{(1)}$ and/or $A_{(2)}$ of the reaction is measured, it is difficult to separate the

[18] This assumption is valid when the interaction cell is sufficiently long. Indeed, the change of potential is not abrupt, but gradual. Consequently, if the length of the interaction cell is of the same order of magnitude as the rise / fall of the electric potential, it is no longer possible to take the length of the cell directly into account. This point is discussed in more detail in section 4.4.2

mutual neutralization from the combined competing processes (a combination of reactions 1.2 and 1.3) [19].

Two methods, which ensure that neutrals are produced only during the mutual neutralization reaction, were developed: one modulates the intensity of the ion beams and observes the effect of this modulation on the neutral atoms count rate [20]. The other method is to measure the pairs of neutrals produced in coincidence. This is used at the Stockholms Universitet and the Université catholique de Louvain under two versions: using a single detector [41, 42, 47] [21], or a pair of detectors [22]. This last scheme offers the advantage of bypassing the problem of dead time of the detection system (when a detector detects a particle, there is post-detection remanence - physical or electronic - which prevents the detection of a second particle immediately after).

Branching ratio measurements

These two methods (beams modulation and coincidences) were used to study the reaction:

$$H^+ + H^- \rightarrow H + H \tag{1.15}$$

However, the results obtained using coincidence measurements [42] differed from those using beams modulation [44]. To explain this difference, the Louvain-la-Neuve team attempted to measure the excited states produced during the reaction by reproducing the method used by the University of Chicago [52, 53], i.e. to measure the emission of photons by atoms excited by the mutual neutralization process. Thus, an attempt to measure the excited states produced during the reaction $H^+ + H^-$ by detection of the Lyman$-\alpha$ [54] and

[19] Note that the first tilted beam measurements only measured the neutral atoms coming from the cation beam [34, 37, 44]. These measures are subject to the same biases.

[20] This first method, developed at the Stanford Research Institute [40] was the first used. It blocked the two beams upstream using choppers. This method had the advantage of not requiring rapid electronics, essential for measuring coincident events. It was still used for an experiment in the 90s on the mutual neutralization of water clusters at Ohio State University [45, 46].

[21] This technique has the advantage of detecting the whole emission sphere (in the center-of-mass frame). However, the dead time induced by the detection of an event imposes an upper limit on the collision energy (approximately 5 eV). This is to ensure that the flight time difference between the two neutral products is long enough [41, 42, 48, 49].

To counter this undesirable effect, the system used in Stockholm separates the detector into independent detection bands. Thus, if two events occur on two different bands, the two particles are detected [50]. However, if the two neutral atoms arrive on the same band, there is no coincident detection.

[22] This method — used by [1, 4, 51] and described in detail in the B.1 section — has the advantage of measuring very close coincidences. It is therefore not limited by a minimum collision energy. However, this method has a lower geometric probability of detection (taken into account in sections 4.1 and 4.2.1).

Balmer$-\alpha$ photons [55] within the interaction region was set up. Another attempt tackled the detection of possible autoionizing states [56, 57] whose ionization would have occurred after leaving the observation cell. These measures were unfortunately not conclusive. It was not until 2012 that a time-of-flight difference technique measured these [48] electronic branching ratios. Against all expectations, it was the repetition of the measurement by the modulation of beams of the University of Newcastle in 1985 [38] which closed the debate: the reason for this difference would come from the transfer ionization (reaction 1.3) which was unintentionally counted during modulation measurements [58].

Thus, the only experiments measuring branching ratios (or partial cross sections) preceding this thesis were (in chronological order): on the one hand the Chicago experiment related to the mutual neutralization of Na^+ with O^- which measured the de-excitation of Sodium Na($3s4p\ ^2P^o$), Na($3s3d\ ^2D$) and Na($3s3p\ ^2P$) (the lifetime of O(^1D) was too long to be measured). Their comparison with the total cross-section measurements [59] suggests that only the radiations emitted by Na($3s3p\ ^2P^o$) correspond to the mutual neutralization (which corroborates the measurements data in this manuscript - section F.3.2). And the time-of-flight measurements of $H^+ + H^-$ [48].

The branching ratio measurements presented in this thesis allow a step forward in the understanding of the mutual neutralization process (which includes [4, 51]). These measurements can be combined with recent experimental studies carried out at Stockholms Universitet [5, 60–62].

1.3.3 Plasma/beam technique comparison

Potential flaws inherent to the beam methods

The ion beams measurement has the following inherent flaws:

1. It is difficult to estimate the temperature of the collision, which comes from several reasons, first the collision energy distribution does not follow a thermal distribution (except at the lowest collision energy).

2. The internal temperature (electronic distribution) does not follow the collision energy distribution.

3. For mutual neutralization involving molecular ions, the electronic, vibrational and rotational temperatures are difficult to obtain, as the vibrational distribution differs from the rotational distribution, which also differs from the electronic distribution. The plasma in ion sources is generally not in thermal equilibrium, due to limited residence time and low gas density.

The first problem is already taken into account: as the collision energy distribution is known, it is easy to average the theoretical cross section and compare it to the experiment [23] (sections 4.2 and 4.4.2).

The second flaw could be subdivided in two: Taking into account only the *LS* terms of the atoms and extending this analysis to the *J* value of each term. Using the recent development of the merged beam setups, it is possible – by the kinetic energy release measurement and/or by storing the ions in a storage ring (such as DESIREE [47]) – to separate the signal coming from each electronic *LS* state of the ions. This is not especially possible for the *J* splitting of those levels.

Then, when the MN reaction happens in a plasma whose temperature is sufficiently low so that the *J* distribution of the initial ions should no longer be statistical, one needs to take into account this *J* distribution of the reactants and should provide the J' distribution of the neutral products. This is where the problems arise for the merged beam setups: The electronic temperature in the ion sources – around thousands of kelvins – cannot be lowered and always generate statistical *J* distributions. This problem is difficult, but not impossible, to avoid. It requires advance in two domains: The ability to experimentally measure the *J* dependency on a subset of mutual neutralization reactions – e.g. the Ne^++S^- (appendix F.7.3) have *J* splitting large enough to allow identifying those states in the kinetic energy release spectra – and the inclusion of this *J* splitting in the theoretical models. Once it is done, it should be possible to assign the amount of signal for each *J* in the experimental data and therefore to infer the cross section at lower temperatures.

One last problem still remains: the vibrational and rotational populations for the molecular ions. One solution, developed at the double electrostatic storage ring DESIREE, is to store the ions long enough to radiatively cool (and thermalize) before measuring mutual neutralization cross sections. Another solution is the characterization of each distribution (rotational, vibrational and electronic) using some diagnosis setup and later ensuring that the ion source conditions remain the same. Such a setup exists for molecular cations at UCLouvain, which is based on the dissociative charge exchange with potassium [63]. For the atomic anions beam, it is also possible to use the photodetachement data measured with the same ion source operated under the same conditions [64–66]. Only the atomic cation diagnosis remains, which could be achieved – using electron impact ionization – once the UCLouvain merged beam setup update is complete. The last solution would be the production of a well-defined electronic and rovibrational state-selected beams, e.g. producing the beam by resonant multiphoton ionization of a gas [63]. However, this example used a 30 Hz laser and produced a beam that was too thin to

[23] It is a best practice to compare two convoluted signals as the deconvolutions algorithms are inherently numerically unstable, i.e. highly sensitive to the statistical errors.

be usable for a mutual neutralization study.

Potential flaws inherent to the plasma methods

The plasma measurement also has some inherent potential flaws. The first one is that there is no actual technique which would allow to determine the state of the products, only the ion density and the mass of the neutral product.

Also, as there are several compounds in the plasma, it is difficult to ensure that only the mutual neutralization reaction is the cause of the destruction of the ions and the production of the neutral products, e.g., the remaining electrons and the buffer gas could catalyze the reaction if the density is too high, i.e. it is difficult to ensure that there is no other reaction happening in the setup. Two methods – in addition to the variation of the ions density parameters – have been used: The first one, applied to the FALP experiments, was a complete diagnosis of the other possible processes which could happen, which reduces drastically the number of MN reactions studied. The other method, used in the VENDAMS method, supposes that all the other reactions involved during the process are well known and then – using a dynamic model of the plasma – infers the remaining(s) reaction rate(s).

One of the hypotheses underlying those techniques is that the ions are thermalized (by collisions with the buffer gas) before the MN reaction happens. But, as it will be shown later in this manuscript, the neutral electronic population produced by the MN reaction widely differs from the Boltzmann distribution, which invalidates this primary hypothesis. This flaw could be avoided by a non-local thermal equilibrium simulation of the plasma, in order to extract the MN reaction rate. But again, as the inelastic collisions between the neutrals are driven by the ionic potential energy curve, there is a need for the MN reaction rate to be known in order to obtain the inelastic collision reaction rates.

One could argue that this problem is not necessarily one, as the MN reaction rate measurement is performed within the plasma, meaning the measured MN rate would correspond to the anion/cation destruction in the plasma. This argument is valid for similar plasmas, but does not especially apply to astronomical plasma whose density and temperature may largely vary.

Comparison example

The two measurement techniques, presented above, follow radically different measurement principles. But since they both measure the same process, the results should be equivalent (despite their potential flaws). To be sure, it would suffice to compare the results of a reaction whose measurement was carried out with the two types of instruments.

Unfortunately, one of the few measurements made using both plasma [67] and beams [68]

$$NO^+ + NO_2^- \rightarrow NO + NO_2 \tag{1.16}$$

shows significant discrepancies in their results. The reaction rate obtained by the beam technique is substantially larger than that obtained using plasma. The difference between these two measurements comes from the internal energy distribution of the initial molecular ions: while this distribution was controlled (thermalized by collisions with the buffer gas or the walls) during the experiment carried out in plasma, the rovibrational distribution was unknown during the measurement carried out using beams [24].

Recent measurements of atomic mutual neutralization within plasma provide a new set of measurements which could be reproduced with the merged beam technique and therefore answer the question: Are the two techniques compatible?

[24] In a complementary article [69] taken up in [12], the Stanford team explains that the rovibrational excitation of the positive beam must have a weak influence on the measurement of the cross section. However, the excitation of the negative beam should have a non-negligible effect on the measurement of the cross section by significantly lowering the electron affinity of the anion.

Note also that other cross sections of mutual neutralization seem to be overestimated. An example is the cross section of the reaction between H^+ and H^- mentioned above.

1.4 Theoretical models

1.4.1 How to treat the reaction

The theoretical study of the mutual neutralization reaction is also tackled with difficulties. In principle, it would "suffice" to solve the (dynamic) Schrödinger equation of the total wavefunction of the system from an initial infinite approach distance to an infinite final distance away and repeat the operation for each possible combination of initial wavefunctions and all possible impact parameter. The probability of occurrence of such initial conditions must of course be weighted.

Therefore, if it is possible to describe the final wavefunction using those of the two isolated atoms, then the probability of mutual neutralization of the two atoms is given by the square of the projection of the total wavefunction on the product of wavefunctions of the two neutralized atoms.

However, the operation described above is incredibly complex for all the systems that interest us here. For example, for the C^+-O^- system, this calculation requires solving a 30-body Schrödinger equation!

Thus, to solve all the systems, certain approximations are essential to introduce. The first is to suppose that the wavefunction is, at each instant, a linear combination of the wavefunctions of the static system (obtained within the context of the Born-Oppenheimer approximation). In addition, that the collision speed is slow enough to consider that the electrons have time to readjust as the collision progresses. These two conditions are justified when the collision energy is low (cases studied in this thesis), but need to be treated with more caution when the collision energy increases [70, 71].

This assumption makes it possible to separate the problem in two: on the one hand the evaluation of each wavefunction $\psi_i(R)$ possible for the system at each interatomic distance R and the associated potential energy $V_i(R)$ (description of the quasi-molecule), on the other hand the estimation of the collision dynamics. This collision dynamics is then an evolution over time of the wavefunction projected onto the "static" Born-Oppenheimer states of the system. This projection attributes to each "static" state a coefficient which changes during the collision.

The set of theories that have addressed mutual neutralization separate the problem in the same way. The specificity of each of these theories comes from the method used to describe the quasi-molecule. Thus, to simplify the review of different theories, it is useful to briefly describe the different methods of collision dynamics as well as the different methods of evaluation of electronic wavefunctions.

1.4.2 Perturbed stationnary states method

Formally [72], the Hamiltonian of a diatomic system *A*-*B* is written:

$$H^{tot} = (1/2\mu)\vec{p}^{nu} \cdot \vec{p}^{nu} + H^{el} + Z_A Z_B / R \tag{1.17}$$

where Z_A (Z_B) is the charge of the nucleus A (B), R the interatomic distance, $\vec{p}^{nu}$ the momentum of the nuclei in the center-of-mass frame and H^{el} is the electronic Hamiltonian defined as

$$H^{el} = -(\hbar/2m_e)\sum_i \nabla_i^2 + V^{el}(\vec{R},\vec{r}) \tag{1.18}$$

where $\vec{R}$ are the nuclear coordinates, $\vec{r}$ the electronic coordinates, ∇_i^2 is the Laplacian operator according to the ith electronic coordinates and $V^{el}(\vec{R},\vec{r})$ is the potential energy of electron-electron and electron-nucleus interactions. Thus, if $\Psi(\vec{R},\vec{r})$ is the total wavefunction of the system, the general Schrödinger equation of the system is written:

$$(H^{tot} - E)\Psi(\vec{R},\vec{r}) = 0 \tag{1.19}$$

The Born-Oppenheimer approximation makes it possible to decompose this wavefunction according to its nuclear component and its electronic component. In order to perform this decomposition, it must be assumed that the nuclei are slow enough to allow the electrons to minimize their energy before the nuclei move.

Therefore, it is possible to separate the total wavefunction according to:

$$\Psi(\vec{R},\vec{r}) = \sum_k \phi_k^{nu}(\vec{R})\chi_k^{el}(\vec{r};\vec{R}) \tag{1.20}$$

where ϕ^{nu} is the nuclear wavefunction which does not depend on electronic coordinates and χ^{el} is the total electron wavefunction — solutions of the electronic Hamiltonian — for which the nuclear coordinates are parameters [25] and the electronic coordinates are the variables. So that :

$$\int \chi_k^{el*}(H^{tot} - E)\phi_j^{nu}\chi_j^{el}\,\mathrm{d}\vec{r} = 0 \tag{1.21}$$

[25] If the collision energy is high, then it is no longer technically valid to make the separation between electronic wavefunction and nuclear wavefunction. This is because the speed of the nuclei is so important that the electrons do not have time to adjust their wavefunction before the nuclei change position. There is a ripple effect on the electronic wavefunction. To counter this effect, one method consists in modifying the electronic wavefunctions by multiplying them by a plane wave term which moves at the initial relative speed of the nuclei [70, 71]. However, this method has a flaw: the electronic wavefunctions are no longer the solution of the electronic Hamiltonian. In addition, they are no longer orthogonal. These faults can nevertheless be avoided. This subject was treated in detail by Schneiderman & Russek [73], it is then taken up again for the calculations of cross-sections of mutual neutralization at high collision energy (for example up to 20 keV for H^++H^- [70]).

As the integral only applies to the electronic wavefunction and its result does not depend on k, it is possible to rewrite the Schrödinger equation for the nuclear wavefunction as:

$$\left(T_{jk} + U_{jk} + \delta_{j,k}E\right)\phi_k^{nu}(\vec{R}) = 0 \tag{1.22}$$

with

$$T_{jk} = (1/2\mu)\left(\vec{p}^{nu}\delta_{jk} + \int \chi_j^{el*}\vec{p}^{nu}\chi_k^{el}\,\mathrm{d}\vec{r}\right)^2 \tag{1.23}$$

and

$$U_{jk} = \int \chi_j^{el*}(H^{el} + Z_A Z_B/R)\chi_j^{el}\,\mathrm{d}\vec{r}. \tag{1.24}$$

Before continuing, several elements should be noted:

- Each nuclear wavefunction is associated with an electronic wavefunction. This means that an electronic transition induces the passage from one nuclear wavefunction to another, and explains why the solutions of this equation depend on the choice of the representation chosen to describe the electronic wavefunctions χ_k^{el}. This choice of representation deserves a specific treatment. It will be detailed in section 1.4.4.

- It seems strange, at first glance, to treat a collision as a stationary solution, to use a "static" treatment to characterize a dynamical system. The use of this method is justified by the intrinsically quantum character of the treatment of the collision [26]: During an atomic collision, the two atoms are initially in a given stable state (or in a very long-lived metastable state). Therefore, their binding energy is fixed. Likewise, the experimental set-up fixes the collision energy "exactly". Thus, the energy of the collision (as well as the momentum) is known exactly. Therefore, the Heisenberg uncertainty relation indicates that the temporal (spatial) dependence of the wavefunction follows a much wider distribution than the duration (trajectory) of the collision. Thus, if we took a picture of the nuclear wavefunction at a given moment, part of it would still be far from arriving in the interaction region while another part would have already left away, after interacting. This means that during a period much longer than the interaction duration, the wavefunction is in a "stationary" state which includes both the component before interaction, the component in interaction and the component having interacted. It is this "stationary" situation which is described by the preceding equation. However, this equation has one flaw: it contains all the components (incoming and outgoing) of the reaction. To obtain the effective section, it will be necessary to isolate the outgoing component.

[26] This description uses a summary version of the argument given by Joachain [74, §3.5].

- It follows from the discussion that the nuclear wavefunction must satisfy the following asymptotic conditions: the initial state is composed of a plane wave (incoming component) and outgoing spherical waves. All the states produced are asymptotically outgoing spherical waves, because at a great interatomic distance, it is no longer possible to determine the source point with precision (this does not prevent this spherical wave from having an angular dependence) [27].

To solve this equation, one method is to expand $\phi_k^{nu}(\vec{R})$ in the form of partial waves:

$$\phi_k^{nu}(\vec{R}) = R^{-1} \sum_l u^l(R) P_l(\cos\theta) \tag{1.25}$$

where $P_l(\cos\theta)$ are the Legendre polynomials and $u_l(R)$ are the radial component of the wavefunction.

The stationary Schrödinger equation applied to the nuclear wavefunction then becomes:

$$\left[\frac{\mathrm{d}^2}{\mathrm{d}r^2} - \frac{l(l+1)}{R^2} + 2\mu\left[E - U_{kk}(R)\right]\right] u_k^l(R) = 2\mu U_{jk}(R) u_j^l(R) \tag{1.26}$$

This system of coupled equations can then be integrated numerically from the asymptotic conditions in order to obtain the cross section (given by the spherical component of each wavefunction).

Therefore, as the probability of transition p_j to the state j depends on the angular momentum of the incoming plane wave l, the cross section is obtained by integrating over all possible values of l multiplying by the multiplicity associated with l. This gives:

$$\sigma_j = \frac{4\pi}{2\sqrt{2\mu E}} \sum_{l=0}^{\infty} (2l+1) p_j \tag{1.27}$$

with $\sqrt{2\mu E}$ the incident wave vector.

1.4.3 Impact parameter method

Let us suppose now that the trajectory of the pseudo-particle of reduced mass μ associated to the diatomic nuclei[28] can be considered in a classical way. The ions trajectory is (section 4.3.3), in spherical coordinates (R, θ, φ):

$$\dot{R} = \pm\sqrt{1 - [b/R^2] - V(R)/E} \tag{1.28}$$

[27] One could also use wavepacket propagation method [75] but, as it was not used for the mutual neutralization reaction, this method is not described here.

[28] The name "pseudo-particle" comes from the idea that it is neither nuclei A or B, but the trajectory of both atoms can be derived from the trajectory of this pseudo particle (section 4.3.2).

$$\dot{\theta} = v_0 b/R^2 \tag{1.29}$$

$$\dot{\varphi} = 0 \tag{1.30}$$

where b is the impact parameter [29] and v_0 is the initial relative speed of approach between the two atoms. Thus, for a given collision energy, the trajectory depends only on the impact parameter.

Therefore, the internuclear distance is known at each instant $R = R(t)$. The temporal evolution of the electronic wavefunction makes it possible to establish whether the electron transfer has indeed taken place.

The Hamiltonian applies to this electronic wavefunction as [30]:

$$(-i\frac{\partial}{\partial t} + H^{el} + \frac{Z_A Z_B}{R(t)})\chi^{el}(\vec{r},\vec{R}) = 0 \tag{1.31}$$

that it is possible to develop at any time on the basis of the stationnary states of the system [31] [32]:

$$\left|\chi^{el}(\vec{r};t)\right\rangle = \sum_j a_j(t)\left|\chi_j(\vec{r})\right\rangle \exp\left\{-i\int_{-\infty}^{t}\left\langle\chi_j(\vec{r})\right| H^{el} + \frac{Z_A Z_B}{R(t')}\left|\chi_j(\vec{r})\right\rangle \, \mathrm{d}t'\right\} \tag{1.32}$$

By defining $E_{jk}(t) = \left\langle\chi_j(\vec{r})\right| H^{el} + \frac{Z_A Z_B}{R(t)}\left|\chi_k(\vec{r})\right\rangle$ and by projecting on a state $\left\langle\chi_k^{el}\right|$, this Schrödinger equation becomes: [33]:

$$\dot{a}_k = -\sum_{j\neq k} a_j \left\langle\chi_k\right| \frac{\partial}{\partial t}\left|\chi_j\right\rangle \exp\left\{-i\int_{-\infty}^{t}(E_{jj} - E_{kk})\,\mathrm{d}t'\right\} \tag{1.33}$$

[29] Minimum distance between the two nuclei if their trajectories were straight.

[30] To achieve such a result, it is not necessary to use the time derivative directly. Suppose first that the kinetic term of the nuclei $(1/2\mu)\nabla^2_{nu}$ is negligible (because the reduced mass of the nuclei is large, compared to the mass of the electrons). It is then necessary to establish what the movement of the nuclei implies for the electronic wavefunctions: if the wavefunction of the nuclei is constant ($\partial/\partial t_{nu} = 0$), the displacement of these causes a displacement of the electronic wavefunction at the relative speed of the nuclei which gives a term $\vec{v}\cdot\vec{\nabla}_{nu}$. As this speed indicates the speed of movement of the nuclei $v = d\vec{R}/dt$ and the temporal variation of the position of the electronic wavefunction, it is possible to simplify the term $d\vec{R}$ with $\vec{\nabla}_R$, which makes the time derivative term reappear in the equation.

[31] The imaginary exponential term can be explained as follows: the electronic wavefunctions χ_j are stationary solutions of the system. In other words, if $R(t)$ evolves slowly as a function of time (it is assumed to be constant), the time evolution of a stationary state of the system, between t and $t+\delta t$, is given by $\chi_j(t+\delta t) = \chi_j \exp\left\{-i\int_t^{t+\delta t} E_{jj}(t')\,\mathrm{d}t'\right\}$. This gives a phase oscillation of the stationary solutions.

[32] The quasi-classical approach follows a similar development, except that the evolution of the electronic wavefunction is carried out directly, instead of being projected on a basis of stationary solutions.

[33] The method used to detail the term $\left\langle\chi_k\right| \frac{\partial}{\partial t}\left|\chi_j\right\rangle$ is beyond the scope of this brief description. Let us simply recall that the temporal term $\partial/\partial t = \dot{R}\partial/\partial R + (v_0 b/R^2)\partial/\partial\theta$ expresses the radial coupling and the rotational coupling, respectively.

Thus, the probability of transition to the state k is given by $p_k = |a_k(\infty)|^2$.

As the transition probability depends on the trajectory, and the trajectory depends on the impact parameter, the transition probability also depends on the impact parameter. Thus, the effective section is given by:

$$\sigma_k = 2\pi \int p_k(b) b \, \mathrm{d}b \tag{1.34}$$

1.4.4 Discussion about electronic wavefunctions

Before proceeding, it is useful to dwell briefly on the basis of electronic wavefunctions χ_j. Indeed, it can be complicated to evaluate the term $\langle \chi_k | \frac{\partial}{\partial t} | \chi_j \rangle$ [34]. Another representation of electronic wavefunctions may be useful. This other representation is chosen such that $\langle \tilde{\chi}_k | \partial/\partial t | \tilde{\chi}_j \rangle = 0$. Nevertheless, the wavefunctions given by this representation are no longer eigenfunctions of the electronic Hamiltonian, that is to say $\langle \tilde{\chi}_k | H^{tot} | \tilde{\chi}_j \rangle \neq 0$. This means that it is necessary to repeat the above development from the equation 1.21 to find again a system of coupled equations similar to the one presented here. This system reveals the potential for interaction $E_{jk}(R) = \langle \tilde{\chi}_k | H^{tot} | \tilde{\chi}_j \rangle$ as follows:

$$\dot{\tilde{c}}_j = -i\tilde{c}_k(t) E_{jk} \exp\left\{ -i \int_{-\infty}^{t} E_{jj}(t') - E_{kk}(t') \, \mathrm{d}t' \right\} \tag{1.35}$$

These two representations are called the adiabatic basis $\chi_j = \chi_j^a$ and the diabatic basis $\tilde{\chi}_j = \chi_j^d$.

One of the big differences between these two representations is the shape of the curves of interatomic potentials $E_j(R)$. Indeed, as the adiabatic wavefunctions χ_j^a are eigenstates of the system, the different curves do not intersect (the

[34] Note that, the molecular operators $\hat{L}_z$ (projection of the orbital angular momentum on the interatomic axis), $\hat{S}^2$ (spin), $\hat{S}_z$ (projection of the spin) and $\hat{\sigma}_0$ (exchange symmetry) commute with the electronic Hamiltonian of the system (which defines the molecular state). In addition, the operator $\partial/\partial R$ only applies to nuclear coordinates. This operator therefore also commutes with the Hamiltonian.

By defining the operator $\hat{A}$ as one of the electronic operators mentioned above (whose eigenvalue for a state χ_j is α_j), we find:

$$0 = \langle \chi_j | [\hat{A}, \partial/\partial R] | \chi_k \rangle = (\alpha_j - \alpha_k) \langle \chi_j | \partial/\partial R | \chi_k \rangle$$

So, if $\alpha_j \neq \alpha_k$ then $\langle \chi_j | \partial/\partial R | \chi_k \rangle = 0$. In other words, there is no exchange between two states of different molecular symmetries. This is why the collision is always treated within the same molecular symmetry.

Note that this notion of molecular symmetry is discussed by [70, 71] within the framework of the reaction $H^+ + H^-$: they note that the separation according to symmetries $g - u$ is not possible in this type of collision. Indeed, as the model has an electron centered either around H^+, or centered around H($1s$), and this electron cannot be confused with the electron $1s$ of H^0, the two atoms are not equivalent. Therefore, it is not possible to establish a $g - u$ exchange symmetry of atoms. This argument can obviously be extended to other homonuclear systems.

diagonalization of the Hamiltonian orders the states, even if it means modifying the properties of the different atoms). Thus, adiabatic wavefunctions preserve the molecular properties of the collision at the expense of atomic properties. The general choice of diabatic wavefunctions χ_j^d for its part preserves the atomic properties of the wavefunction to the detriment of the molecular properties of the system. The Hamiltonian is not diagonal. Diabatic potential curves can intersect, while this crossing is avoided in the adiabatic basis.

These two ways of representing the reaction are equivalent, each representation has its advantages and its drawbacks. For example, it is difficult to obtain an orthonormal basis, at short interatomic distance, for the diabatic representation (by taking into account the overlap of atomic wavefunctions). Moreover this representation is not unique, it is difficult to treat precisely the dynamics of the coupling between two adiabatic states [35].

Let us also note before continuing that the electronic wavefunctions are complex to compute. This complexity increases for each electron added to the system. To work around this problem, one method is to process only a subset of the electrons. These electrons are the ones that are assumed to play a role in the reaction (called the active electron or valence electron), while the rest are considered spectators (called spectator electrons or core electrons). The core electrons are then "attached" to a nucleus and included in the internuclear potential. This makes it possible to drastically reduce the number of electrons included in the electronic wavefunction. However, this method modifies the potential to which these active electrons are subjected. This new potential is called "effective potential". All the numerical models presented here use this technique [36].

1.4.5 Exchange at the crossing of the potential curves

In order to simplify the solution of the system of coupled equations given by equation 1.33 (or its diabatic equivalent), several methods were implemented. The first, the Landau-Zener model (sections 3.1 and 3.2.5 for the model with two-state "LZ" and section 3.1.5 for the multi-channel model "MLZ") supposes that the transition of an electronic state occurs only during an avoided crossing (i.e. during a crossing between diabatic potential energy curves, the resonance between the two states leads to a state degeneracy which is exponentially less likely away from resonance – section 3.1.2). This model treats the crossing of the curves pairwise in an analytically isolated way: it solves

[35] Indeed, as the adiabatic coupling term varies greatly around the avoided crossing (approximately according to a Lorentzian), it is difficult to treat it precisely. The term diabatic interaction, on the other hand, varies little. This makes it easier to process numerically.

[36] With the exception of the H^++H^- reaction, where it is possible to treat the two electrons of the system.

the system by assuming a constant interaction potential E_{jk} and a difference between the diabatic potentials $E_j - E_k$ linearly varying in the vicinity of the crossing. This method is considered efficient for low collision energies (see [70] or section 3.3 [37]). Note the existence of an adiabatic version of the model (AMLZ [76] [38]).

Another model is that of Demkov [77]. It too assumes that the transition from one state to another occurs at a given interatomic distance. However, the selected diabatic basis does not especially assume that a crossing in the diabatic basis takes place. As this model applies to larger collision energies, this assumption is not necessary. In this model, the change of diabatic state occurs when the difference between two diabatic levels and the coupling matrix element satisfy the condition $|E^d_{jj} - E^d_{kk}| \simeq |E^d_{jk}|$. Demkov then solves the system assuming that E^d_{jj} and E^d_{kk} are constant and that E^d_{jk} is exponentially decreasing at the chosen interatomic distance.

Collision method	Abbreviation
Perturbated stationnary states	PSS
Impact parameter method	IPM
Two-state Landau-Zener	LZ
Multi-channel Landau-Zener method	MLZ
Adiabatic Multi-channel Landau-Zener method	AMLZ

Table 1.1: Abbreviations for the different models of dynamics used.

[37] Note that only one reaction invalidates the pairwise crossing hypothesis within this thesis (see section 5.4.2.

[38] This version of the model transforms the term ζ included in the transition probability through an avoided crossing (equation 3.28):

$$P_{1,c} = 1 - \exp\zeta = 1 - \exp\left(-\frac{2\pi E_{ic}^2}{\hbar v_R \Delta F}\right)$$

The transformation of ζ in the adiabatic basis is carried out using the following assumptions: the energy difference between two adiabatic levels $\Delta E(R)$ is only useful at the crossing radius; the diabatic interaction potential between the two states E_{ic} is constant; the difference in potential energy between the two diabatic states $\Delta V = V_i - V_c$ is zero during the avoided crossing; the following equality is satisfied $\Delta E(R_c) = 2E_{ic}$ at the intersection radius R_c. In this case, the equation which links the curves of diabatic and adiabatic potential $[\Delta E(R)]^2 = [\Delta V(R)]^2 + 4E_{ic}^2$ can be rewritten, in order to simplify the notations, like $g^2(x) = f^2(x) - f^2(x_0)$ (using $x = R$, $x_0 = R_c$, $g(x) = \Delta V(R)$, $f(x) = \Delta E(R)$). It is then possible to write $f(x)f''(x) = g(x)g''(x) + \frac{f^2(x)g'^2(x)}{g^2(x)+f^2(x_0)}$. And remembering that $g(x_0) = \Delta V(R_c) = 0$, one finds $f(x_0)f''(x_0) = g'(x_0)$, or $\partial|\Delta V|/\partial R(R_c) = \sqrt{\Delta E(\partial^2 \Delta E/\partial R^2)}$ and – by inserting the radial speed $v_R = \partial R/\partial t$ in the radial derivative, one obtains:

$$\zeta = -\frac{\pi}{2\hbar}\sqrt{\frac{\Delta E^3}{\partial^2 \Delta E/\partial t^2}}$$

evaluated at $R = R_c$.

1.4.6 Some basics of electronic wavefunctions

In order to facilitate the review of the calculations of the mutual neutralization cross sections, it is interesting to quickly describe the different methods used to obtain the electronic wavefunctions, as well as the methods used to obtain the interaction potential (diabatic) or the coupling term (adiabatic) between the different states of the quasi-molecule.

A first approach, the simplest, consists in carrying out an atomic processing of the electronic wavefunctions. These developments start from a diabatic basis for which electrons are attached to an atom. Thus, each diabatic state is described by the combination of the wavefunctions of each atom [39].

In order to simplify the development, only the valence electrons are taken into account (this is justified when one considers a long-distance or asymptotic interaction. In this case, the electrons close to their nucleus play a minor role). So, under the one-electron asymptotic model, one of the valence electrons of atom B^- is transferred to atom A^+ to form A^0. The transferred electron is then on a valence configuration of A^0 [40].

To describe these wavefunctions, the method generally used consists in considering the valence orbital of the main configuration of the atomic state studied (as a first approximation, the other configurations that make up the state of the atom are neglected). To achieve this, it is necessary to describe the wavefunction of the atomic configuration within each molecular symmetry present (such an expansion is presented in the section 3.2.4). Note that the result of this development (equation 3.114) supposes that each energy level is associated with a single electronic configuration. This development assumes that some transitions are prohibited by fractional parentage coefficients while these states are experimentally produced (e.g. $2s^2 2p^2\ ^3P \rightarrow 2s2p^4\ ^4P$). To explain these transitions, two methods exist: one assumes that these processes fall under two electron processes during a single crossing ("2e" – an interaction which involve two active electrons – in this case, the interaction potential $\tilde{H}^{2e}_{ic}$ becomes $\tilde{H}^{1e}_{ic'} R_c \tilde{H}^{1e}_{c'c}$ with c' the covalent state intermediary [78]). The other method invalidates the association of a single and unique configuration for each energy level, so there are multiple configurations associated with each state ("MC") — an atomic configuration interaction calculation provides the linear combination of the state configurations [4].

Several alternatives exist to represent these wavefunctions: firstly the

[39] It should be noted that when the atoms are sufficiently close, it is necessary to take into account the overlap between the wavefunctions of A^0 and B^- (sections C.2.4 and 3.2.8).

[40] This one-electron transfer model applies for each avoided crossing in isolation. As each collision involves, at a minimum, two passes through an avoided crossing, the result of the collision may give the impression that two-electron processes are present, while the collisional process involves two consecutive one-electron exchange processes (more details are given in section 5.4).

asymptotic method which uses the long-distance analytical development of atomic functions (an electron subjected to a Coulomb potential for $A^0(B^-)$ and an atomic wavefunction disturbed by a *polarization* given by Coulomb potential external to the atom for $B^0(A^+)$ – sections 3.2.5 and 3.2.6). The second consists in using numerical methods to approximate the wavefunction (such as the "scaled Thomas-Fermi-Dirac" (TFD) method described in [79]).

Finally, it remains to evaluate the volume integral which determines the interaction potential: It can be obtained analytically (B&L – Bates and Lewis [80]) using a two centers integral [81], by integrating numerically around the center B (vdB – van den Bos [82]) or any other numerical method, or using Green's theorem which replaces the volume integral by an analytically resolved surface integral (this surface can be a plane halfway between the two atoms, whose solution is given by Smirnov [83, 84], or a sphere centered around the atom B, whose solution is given by Davidovitć [85]).

Diabatic methods

Name	$\|A^0\rangle$	$\|B^-\rangle$	$\langle A^0\|H\|B^-\rangle$
B&L [80]	Asymptotic[86, 87]	Asymptotic	Two centers integral [81]
G&H [88]	Asymptotic	Asymptotic	Numeric integral
vdB [82]	Hartree-Fock-Slater (HFS)	polarized HFS	Numeric: Legendre expansion around B
AM_S [83]	Polarized asymptotic	Polarized asymptotic	Analytic surface integral (plane between A and B)
AM_J [89]	Polarized asymptotic	Polarized asymptotic	Analytic surface integral (sphere around B)[85]
1e-Sidis [70]	Hydrogen wavefunction	Analytic 1-e polarized by A^+	Analytical elliptic integrals [71]
$LCAO_B$ [90]	scaled Thomas-Fermi-Dirac [79]	Asymptotic 2-e wavefunction	Numeric

Forbiden transition processes

Method Name	Abbreviation
Two-electron process	2e
Multiconfiguration description	MC

Molecular approaches

Method Name	Abbreviation
Full Configuration Interaction	FCI
Multi-Configuration Self-Consistent Field	MCSCF
Internally Contracted Multi-Reference Configuration Interaction	IC-MRCI

Table 1.2: Compilation of the methods used to obtain the interaction potential (see text for details).

All of these models can then be used to obtain the adiabatic energy potential curves: once the potential energy curves $E_{jk}(R) = \langle j|H|k\rangle$ obtained using

an diabatic model, it is possible to obtain the adiabatic potential energy curves by diagonalizing the matrix $E_{jk}(R)$ at each interatomic distance. And find the associated potential energy curves for each adiabatic state.

A second approach considers the molecular electronic wavefunction as a whole, as a Slater determinant [41]. This approach satisfies the antisymmetry requirement of the electronic wavefunction. Since the electronic wavefunction of the molecule depends on the electronic interaction, and the electronic interaction depends on the electronic wavefunction of the molecule (field A depends on field B, which depends on field A), then one needs to use a self-consistent field method (SCF [91]) in order to obtain – iterativelly from an initial guess – the electronic wavefunction as a whole. This method could be extended by the Multi-Configuration Self-Consistent Fields method (MCSCF [92]): rather than minimizing the energy of a single Slater determinant, the wavefunction is expanded over several Slater determinants (configurations). The expansion coefficients (configurations mixing) are determined by diagonalizing the Hamiltonian matrix while the molecular orbitals parameters (called expansion coeficients) are obtained iteratively (the orbitals are optimized by the configuration interaction).

When the number of excited states to take into account is large, a Full Configuration Interaction (FCI) approach becomes computationally prohibitive. The size of the matrix to diagonalize can be reduced by using the "Internally Contracted Multi-Reference Configuration Interaction" (IC-MRCI) method which consists in selecting several subsets of configurations (called references) to be optimized. One strategy is to first consider internally contracted subsets of configurations, with parameters and linear coefficients of references already optimized, then to apply the configuration interaction method to the set of references.

The last approach is the one applied as a last resort. When it is too complex to obtain the potential energy curves (either by the atomic or molecular approach), why not fit all the other results already obtained with an empirical formula, and then apply this result to the reaction studied? This is what Olson

[41] The Slater determinant is a antisymetrization method for the electronic wavefunction: if one obtains the wavefunction χ_i for each orbital of the electronic configuration of each atom, and $\vec{x}_j$ are the coordinate of the jth electron, the Slater determinant is defined as

$$|\psi\rangle = \frac{1}{\sqrt{N!}} \det \begin{pmatrix} \chi_1(\vec{x}_1) & \cdots & \chi_N(\vec{x}_1) \\ \vdots & \ddots & \vdots \\ \chi_1(\vec{x}_N) & \cdots & \chi_N(\vec{x}_N) \end{pmatrix}$$

where $\det(\cdots)$ is the determinant.

The choice of the orbitals is still critical (see [51]). Nevertheless, for a better readability of this review, the choice of the basis set is omitted in the description of the calculations (the reference is indicated so that the reader can find this choice of basis set).

et al. [93, 94] did to obtain an approximate version of the interaction term as a function of the interatomic distance (using data from [80, 82, 88, 95]):

$$H_{ic} = \gamma_{B^-}^2 \left(8.0e^{-0.91\gamma_B R_c} - 7.5e^{-0.99\gamma_B R_c}\right) \tag{1.36}$$

where $\gamma_b^2/2$ is the electron affinity of the negative ion and R_c is the intersection radius of the diabatic curves. In a later paper [96], he then modifies this equation (while keeping the principle of fit on the interaction terms obtained by other methods) so that it takes the form:

$$H_{ic} = 1.044\gamma_A\gamma_B(\gamma_A + \gamma_b)R_c e^{-0.429(\gamma_A+\gamma_B)R_c} \tag{1.37}$$

where $\gamma_A^2/2$ is the binding energy of the valence electron of the neutralized cation [42].

1.4.7 A list of theoretical predictions

It is now possible to list a significant part of the calculations for the cross sections (and partial cross sections) of mutual neutralization between atomic ions. These are classified by reaction then by chronology of publication.

A large number of reactions involve the hydrogen (deuterium) anion:

- H^+-H^- :
  - B&L-LZ [80],
  - AM_S-LZ [83, 84],
  - Olson's fit-LZ [93],
  - Sidis-1e-(MLZ+IPM+PSS) [70, 99],
  - MCSCF-FCI-PSS [100],
  - There are several other theories for this reaction, they can be found in the references above.
- He^+-H^- :
  - Olson's fit-LZ [93],
  - MCSCF-MRCI-PSS [101],
- Li^+-H^- :
  - B&L-LZ [95],
  - G&H [88, 102]
  - AM_J-LZ [103],
  - MCSCF-FCI[104]-PSS [105, 106],
  - MCSCF-FCI[104]-PSS+MLZ, [107, 108],
  - $LCAO_B$-2e-(AMLZ+MLZ) [90],
  - MCSCF-MRCI-MLZ [51],

[42] On the basis of this approximate interaction potential, Hickman [97] completes the model by combining the formula previously cited by Miller & Morgner [98] of the Landau-Zener model. It assumes that the probability of switching from an ionic curve to a covalent curve during an avoided crossing is very low and that the density of covalent states is high. Thus, during the approach phase, before reaching the state n, the probability of remaining on the diabatic curve is given by

$$P_{tot} = \prod_{i=1}^{n}(1-p_i) = \prod e^{-\alpha_i} = e^{-\Sigma\alpha_i} = e^{-\int_{\infty}^{R_c}\alpha_i(R)d\rho/dR\ \mathrm{d}R}$$

where ρ is the density of states. This model then calculates the total cross section according to a form of the Landau-Zener model which uses the angular momentum instead of the impact parameter.

- Be^+-H^- :
  - AM_J-LZ [109].
  - Olson's fit-AMLZ [110],
- C^+-H^- :
  - $LCAO_B$-2e-(AMLZ+MLZ) [7],
- N^+-H^- :
  - $LCAO_B$-2e-(AMLZ+MLZ) [7],
- O^+-H^- :
  - $LCAO_B$-2e-(AMLZ+MLZ) [8],
  - MCSCF-ICMRCI-AMLZ [6, 111],
- Na^+-H^- :
  - B&L-LZ [95],
  - G&H [88, 102]
  - AM_J-LZ [103],
  - MCSCF-PSS [112]
  - MCSCF[113]-MLZ [114]
  - MCSCF-FCI-PSS [115],
  - MCSCF-FCI[115]-PSS+MLZ [116, 117],
  - MCSCF-FCI[115]-AMLZ [76],
  - $LCAO_B$-2e-(AMLZ+MLZ) [90],
- Mg^+-H^- :
  - (MCSCF-MRCI+AM)-PSS [118–120],
  - MCSCF-MRCI-PSS [121],
  - $LCAO_B$-2e-(AMLZ+MLZ) [90],
  - Olson's fit-2e-AMLZ [122],
- Al^+-H^- :
  - Olson's fit-2e-AMLZ [123, 124],
- Si^+-H^- :
  - Olson's fit-2e-AMLZ [125],
- S^+-H^- :
  - Olson's fit-2e-AMLZ [126],
- K^+-H^- :
  - B&L-LZ [95],
  - G&H [88, 102],
  - AM_J-LZ [103],
  - (Olson's fit+$LCAO_B$)-AMLZ [127],
- Ca^+-H^- :
  - $LCAO_B$-2e-(AMLZ+MLZ) [90],
  - Olson's fit-2e-AMLZ [128],
  - MCSCF-ICMRCI[129]-PSS [130],
- Ti^+-H^- :
  - $LCAO_B$-2e-(AMLZ+MLZ) [131],
- Mn^+-H^- :
  - $LCAO_B$-2e-(AMLZ+MLZ) [131],
- Fe^+-H^- :
  - Olson's fit-AMLZ [132],
- Co^+-H^- :
  - Olson's fit-2e-AMLZ[126],
- Rb^+-H^- :
  - G&H [88, 102],
  - AM_J-LZ [103],
  - (Olson's fit+$LCAO_B$)-AMLZ [127],
- Cs^+-H^- :
  - G&H [88, 102],
  - AM_J-LZ [103],
  - MCSCF-PSS [133],
  - MCSCF[134]-AMLZ [135],
- Ba^+-H^- :
  - Olson's fit-2e-AMLZ[136],

some reactions involve the oxygen anion:

- H^+-O^- :
  - $LCAO_B$-2e-(AMLZ+MLZ) [8],
  - MCSCF-ICMRCI-AMLZ [6, 111],
- Li^+-O^- :
  - G&H [88],
  - AM_J [89],
- N^+-O^- :
  - Olson's fit-LZ [93],
  - AM_J-MLZ [137],
  - AM_J-MC-MLZ [4],
- O^+-O^- :
  - Olson's fit-LZ [93],
  - AM_J-MLZ [137],
  - AM_J-MC-MLZ [4],
- Na^+-O^- :
  - vdB-LZ [82],
  - Olson's fit-LZ [93],
  - vdB-IPM [138, 139],
  - G&H [88],
  - AM_J [89],
  - AM_J-MLZ [140],
- K^+-O^- :
  - vdB-LZ [82],
  - vdB-IMP [138, 139],
  - G&H [88]
  - AM-J [89],
- Rb^+-O^- :
  - vdB-LZ [82],
  - G&H [88],
  - vdB-IMP [138, 139],
  - AM_J [89],
- Cs^+-O^- :
  - vdB-LZ [82],
  - G&H [88],
  - vdB-IMP [138, 139],
  - AM_J [89],

or halogens:

- Li/Na/K/Rb/Cs^+-F/Cl/Br/I^- :
  - G&H [88],
  - AM_J-LZ [141],
- Li^+-F^- :
  - MCSCF-FCI-PSS [142],
- H^+-F^- :
  - MCSCF-MRCI[143]-PSS [144],
- Li^+-F^- :
  - MCSCF-MRCI-MLZ [145],
- H^+-Cl^- :
  - MCSCF-MRCI(semi-empirical spin-orbit coupling)-PSS [146],
- C^+-Cl^- :
  - MCSCF-MRCI-PSS [26].

Note that few of these calculations cover experimental data (partial cross section) and even less the measurements presented during this thesis. It is therefore difficult to deal with the validity of the different models proposed here (apart from the discussion on the H^++H^- reaction). However, this discussion will be presented in the section 5.2 for the few calculations which overlap the new experimental measurements presented in this manuscript (those are shown in section 5.2.3).

Chapter 2

Experimental setup

2.1 Working principle

The experimental set-up used to study the different mutual neutralization reactions presented here is a device that uses the confluent beam method. The principle of operation of this device is to bring two beams parallel to the same place, at the same speed and in the same direction. This makes it possible to achieve a relative speed close to zero between the particles of each of the beams.

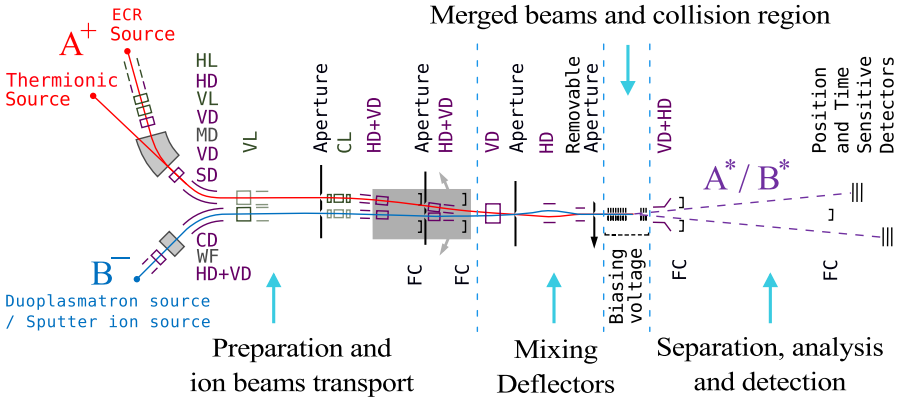

Figure 2.1: Schematic representation of the experimental setup. Ion sources - the entire source including the acceleration column - are represented by a dot (see appendix A for more details). The proportions have not been preserved in order to improve readability. All the elements that make up the device are described in this chapter (and appendix A). HL: Horizontal lens; VL: Vertical lens; CL: Cylindrical lens; HD: Horizontal deflector; VD: Vertical deflector; CD: Cylindrical deflector; SD: Spherical deflector; MD: Magnetic deflector (vertical magnetic field); WF: Wien filter; FC: Faraday cavity; Aperture: Circular diaphragm.

To achieve this (figure 2.1), the device is equipped with two ion sources,

one for positive ions and the other for negative ions. From each of these sources is extracted an ion beam, the acceleration potential being chosen such that their speeds differ slightly.

These beams are then shaped before being brought into confluence within an observation cell. An observation voltage (intended to select the region in which the reactions that we observe occur) is applied to this cell: it will slow down the fastest beam and accelerate the slower beam so that the relative speed between those is almost zero.

Some of the ions will react to form pairs of neutral particles.

At the exit of this cell, the ions are deflected towards probes while the pairs of neutral atoms continue their way towards a detector. This detector measures the magnitude and direction of the relative velocity between the neutralized particles.

2.2 Preparation of beams

The ions production in the ions sources used by the merged beam setup are details in appendix A.2. Once the ion are extracted from an ion source, the generated ion beam is composed of several types of ions (with the exception of the lithium / sodium thermionic source). The mixture of ions that compose it has a velocity and angular distribution. These distributions depend on the type of ion source used.

In addition, the beam is not always extracted exactly on the axis of the source. Indeed, for the duoplasmatron source, the ion beam comes from a plasma. The geometry of the source makes it possible to extract the negative ions [1] from a volume off-axis within the source: Since negative ions in a plasma tend to be on the outer part of it (positive ions tend to be in the center), negative ions are extracted from a volume in the source that depends on the state of the plasma and have a slightly different extraction direction [2]. A similar phenomenon exists in the sputter ion source. As the ions that form the beam are stripped from the cathode, the cathode hole will widen progressively as the device extracts the ions. Consequently, the initial point of extraction of the ions varies over time. Additionally, the way electrons ionize cesium and the impact position of cesium ions on the cathode influence the ion extraction zone. This influences the initial point of the ions extraction, and therefore the

[1] In the context of the experimental setup presented here, only this operating mode was used. However, this source also makes it possible to extract positive ions.

[2] It is also possible that the negative ions are extracted from two different locations of the source. As the electrostatic potential varies spatially in the source, it may happen that the beam extracted from the source has two components in its velocity distribution. These two components can not be separated during the preparation of the beams, however they can still be extracted in the data analysis.

initial direction of the beam emission.

Additionally, for these two sources, a magnetic field is used in order to confine the electrons within the source. This magnetic field will also slightly deflect the extracted negative ions [3].

All of these physical phenomena require placing at the output of the sources two pairs of deflection electrodes. These electrodes positioned after the first lens direct the beam in the desired direction. However, it is still made up of different ions, with a velocity and angular distribution.

2.3 Beams transport

Once the ions are extracted from the sources and accelerated, a mass selection is applied to each beam (a Wien filter for the negative ions and a magnetic deflector for the positive ions coming from the ECR), followed by a selection in kinetic energy (cylindrical deflector for negative ions and spherical deflector for the positive beam).

Once the mass and kinetic energy of the beams are selected, we now need to control their emittances (see section 4.2.1). To do this, both beams pass through an electrostatic lens then two diaphragms [4]. Consequently, as the geometry of the beam is entirely defined by the passage of the beam through two diaphragms, without intermediate focusing, the emittance of each of the beams is known.

2.4 Mixing beams

Once both beam are collimated, they can be mixed. To achieve this, they are directed to the same diaphragm. They cross it with a different trajectory [5].

The two beams then move apart freely over a short distance to be brought together by a first horizontal deflector (in practice, two segments of cylinders). Then, when the two beams are close to axis, they are aligned in the same

[3] This magnetic field is adjusted to properly confine the electrons, without deviating too much the ions.

[4] In practice, the lens of the positive beam is placed just after the first diaphragm. However, this is close enough to the diaphragm to consider that the lens modifies the emittance of the beam directly at the level of the diaphragm.

[5] As the two beams have a different trajectory, the relative velocity between the ions of each of the beams is large. Therefore, as the cross section of mutual neutralization is approximately inversely proportional to the relative kinetic energy between the reactants, this component does not contribute to the recorded signal. In addition, since the center-of-mass of the beams is not directed on the axis between the detectors, the mutual neutralization events related to this crossing of beams do not contribute (or in a negligible way) to the reaction rate.

direction by a second horizontal deflector. These deflectors (called mixers) act on both beams at once.

Since the charge of the particles that make up the two beams is of opposite sign, the mixers deflect the beams in opposite directions. Therefore, it would be tempting to assume that the deflection of the two beams is symmetrical. However, the kinetic energy differs from one beam to another, and so does the deflection angle.

This dictates the initial direction of the beams through the common diaphragm. As the kinetic energy of the beams is imposed by the mass ratio between the positive ion and the negative ion, the position of the last diaphragms specific to each beam must be adjusted for every mutual neutralization reaction we want to measure.

In order to adjust the position of these diaphragms, they are placed on a rotating table. The ideal position of that table was previously measured for each kinetic energy ratio between the two beams (2.2).

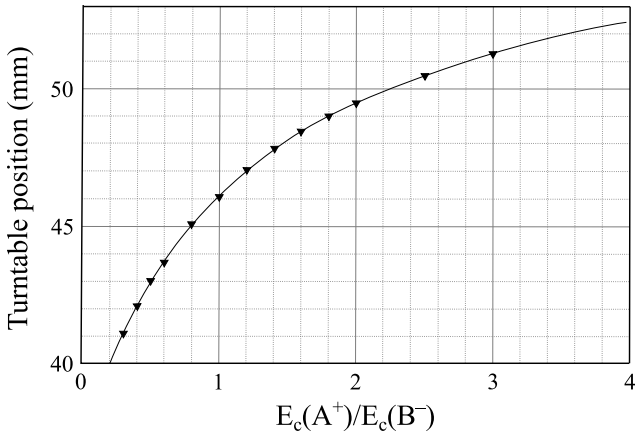

Figure 2.2: Turntable position according to the ratio between the kinetic energy of positive and negative beam. Triangles: Experimental measurements (taken from the lab notebook [43, 147]); Curve: fit.

Therefore, since the position of the second pair of diaphragms varies according to the kinetic energy ratio (similar to the mass ratio) of the ions, it is necessary to deflect the beams at the exit of the first pair of diaphragms. This deflection is applied to each beam using a pair of planar deflectors.

Likewise, a pair of planar deflectors is placed behind each of the second diaphragms in order to direct the beams with the correct angle through the common diaphragm.

In order to ensure that the beams pass well through the diaphragms, probes (Faraday cups) are placed after each pair of diaphragms.

It should be noted in figure 2.1 that the negative ion beam - at the output of

the cylindrical deflector (CD) - is oriented on the axis of the observation cell (OBS). This particularity has two effects:

On the one hand, the negative ion beam can be neutralized voluntarily (for example by using a laser). This makes it possible to measure reactions between neutrals and ions.

On the other hand, when the cation/anion mass ratio is greater than 12/1, the position of the turntable is such that the diaphragms of the negative beam are aligned on the DC-OBS axis (in particular the diaphragm located on the turntable [6]). Therefore, the neutralization of the anion beam with the residual gas generates neutral atoms which propagate in the direction of the coincident detectors. These neutrals cannot be deflected.

As the pressure at the level of the cylindrical deflector is 1000 times higher than the pressure inside the observation cell, and the distance traveled by the negative beam on the axis of the detector more than 10 times longer, the number of non-coincident neutral particles arriving at the detectors is 10 000 times larger. It is then impossible to extract the real coincidences from the signal measured by the detectors. They are drowned in the statistical noise of fortuitous coincidences [7].

This limits the mutual neutralization reactions one can measure with this device. For example, it was impossible to measure the mutual neutralization of the systems $N^+ + H^-$ and $O^+ + H^-$.

2.5 Observation cell

The beams are superimposed before having the same speed. To adjust the relative speed between the beams, they enter the observation cell. This cell is made up of a set of ten plates perpendicular to the beams, with holes in their centers, each one centimeter apart. The first, second, and the last plate are grounded. A movable diaphragm slides against the second plate [8]. For each of the other plates, a voltage can be applied independently.

When a voltage V_{obs} is applied to one of the plates, the energy of the posi-

[6] The other diaphragms – the fixed diaphragms – are always ion the DC-OBS axis, in order to allow the confluence of a possible beam of neutrals.

[7] In addition, the number of particles arriving on the detectors is so high that it would be dangerous to install the MCPs on axis otherwise they would be roasted.

[8] This diaphragm with a diameter smaller than the previous diaphragms ensures that the two beams overlap well at the entrance to the observation cell. It makes it possible to estimate the overlap of the beams. However, because of its smaller diameter, the ions that make up the beams neutralize each other if they are close enough to the diaphragm, which generates a large amount of noise on position-sensitive detectors, and greatly reduces the signal to noise ratio. Therefore, this mobile diaphragm is removed during the measurements.

tive beam around the plate becomes (e is the unsigned elementary charge):

$$E'_{c,A^+} = E_{c,A^+} - eV_{obs} \tag{2.1}$$

while the kinetic energy of the negative beam becomes

$$E'_{c,B^-} = E_{c,B^-} + eV_{obs} \tag{2.2}$$

It is then possible to adjust the relative speed between the beams (see section A.1.3).

The independent voltage applied to the different plates of the observation cell makes it possible to determine the length of the path of the beams on which the observation voltage is applied, also called the interaction length. The grounded plates at the input and at the output of the observation cell ensure that this voltage is effectively applied only within the cell [9].

The difference in speed between the beams outside the observation cell is considered to be sufficiently large for the cross-section of mutual neutralization to be negligible outside the observation cell.

2.6 Separation of ion beams from neutral signal

From the observation cell come out the neutral particles resulting from the mutual neutralization, but also the ions which have not reacted.

In order to separate the three types of outgoing particles, a segmented conical deflector is placed after the observation cell. This deflects the positive ions towards a first probe (Faraday cup with guard anode), the negative ions towards a second probe (Faraday cup with guard anode), and lets the neutral particles continue their trajectory in straight line. These neutral particles propagate through a tube of adjustable length (with magnetic $\mu-$metal shielding), towards a detection system. The latter measures the position and time of impact of pairs of coincident neutral particles (see section A.1.11). Alignment of the detection system with the axis of the observation cell is critical (see section 4.1). This alignment can be modified by mechanically adjusting the vertical and horizontal position of the detection system perpendicular to the axis of propagation of the beam of neutrals.

The intensity of the current measured on the two probes corresponds to the intensity of each of the beams at the entry into the observation cell, typically tens of nanoamperes, i.e. 10^{11} particles per second. This is to be contrasted with the rate of mutual neutralization measured by the coincident detection system, which is about 25 events per second (they are always coincident). As the geometry of the detectors makes it possible to measure about 10 % of the

[9] The limitations of this claim are described in section 4.4.2.

events (see section 4.1), while the detection efficiency of MCPs is about 50 %, it means that a thousand ions react every second, which is negligible compared to the number of ions (both positive and negative) which cross the observation cell during that same second.

2.7 Beams overlap

A couple of mixers allows the two beams to be superimposed. The quality of this overlap is critical. Two types of misalignment are possible (figure 2.3).

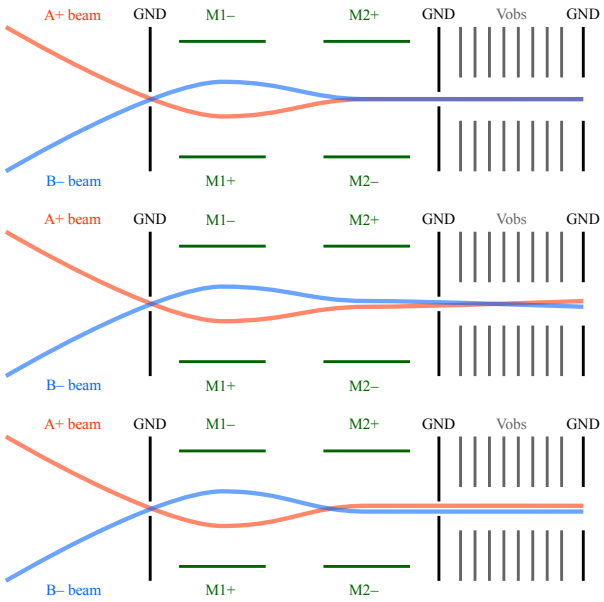

Figure 2.3: Various cases of beam alignment

First, if the beams do not have exactly the same direction, the relative kinetic energy between the cations and the anions, expressed as the square of the vector difference of the velocities, will always be non-zero, directed perpendicular to the main beam axis. This implies an increase in the minimum collision energy, and an inability to have a uniform collision angular distribution.

Second, if the beams have the same direction, but are not exactly on the same axis, the overlap between the two beams is lower than predicted. Only some of the ions that make up each beam can react. This leads to a reduction of the number of events.

As the beams are maintained in the same horizontal plane from their exit from the sources, the overlap and alignment of the beams along the vertical axis is very good (of the order of 1 mrad). The reason for this assertion comes

from the voltages applied to the vertical deflectors which are always small - maximum around 10 Volts (on the deflectors V1 and V2 used when transporting the beams through the diaphragms [10]). Therefore, only one vertical mixing deflector is required. A very slight deflection is sufficient to align the two beams vertically. This constraint which requires the beams to remain in the same horizontal plane facilitates their alignment and overlap.

To ensure alignment and overlap of the beams, several methods are applied. The first consists in verifying the alignment of each of the beams independently from the observation cell to the coincident detection system. The second allows for fine adjustment of the alignment and overlap of the two beams.

The alignment method for each of the beams independently depends on the type of ions that make up the beam (cation or anion). However, these methods make it possible to circumvent the same constraint: When the ions leave the observation cell, if they are not separated at the exit of the cell, continue their trajectories almost in a straight line towards the detection system. The intensity of the ion beams is too large for this detection system. Therefore, a mobile probe (Faraday cup with guard cathode) is placed in front of the position sensitive detectors. Its reduced diameter, however, is barely large enough to contain the entire beam. Therefore, when the current measured on this probe is the same as that measured on the probe linked to the separator, the entire beam is on the axis which connects the input diaphragm of the observation cell to the probe placed in front of the detector. If the two beams pass through this axis, they overlap perfectly.

However, the ions do not propagate perfectly in a straight line between the observation cell and the detectors, as they are subjected to Earth's magnetic field, despite a magnetic shielding arranged around the vacuum chamber. Their trajectories are thus slightly curved. This slight curvature has an effect on the trajectory of several meters which separate the observation cell from the position sensitive detectors.

To counter this problem, it is necessary to evaluate the trajectory of each beam – neutralized in the observation cell – separately, and to ensure that the neutralized ions actually propagate along the same axis. This neutralization must be done within the observation cell.

- The neutralization of the negative beam is obtained by photodetachment:

$$B^- + h\nu \rightarrow B + e^- \tag{2.3}$$

  This photodetachment is carried out in crossed beams using a continuous wave diode laser (with a wavelength of 1064 nm, 778 nm, 532 nm or

[10] If this is not the case, it is necessary to re-evaluate the alignment of the beams through the diaphragms by adjusting the vertical deflection V0 applied at the source output and thus to minimize the voltages applied to V1 and V2.

406 nm) focused on the ion beam. The wavelength of this laser must be greater than the electron affinity of the atom or molecule. To ensure the alignment of the beam, it suffices to look at the impact position of the neutrals on the position sensitive detectors.

- The neutralization of a beam of atomic cations is not possible by laser (a cation from which an electron is extracted remains a cation). Neutralization by charge exchange with the residual gas is not sufficiently effective to determine the orientation of the positive beam, given the high vacuum which prevails within the cell. The contribution of this reaction is small compared to the rest of the background present on the detectors, with too wide an angular distribution.

  However, all of the corpuscular optical elements which bring the positive ion beam are electrostatic, with the exception of the magnetic deflector. If the field of the magnetic deflector is set to pass the H_2^+ molecule instead of the A^+ ion, (or any other homonuclear molecule, like N_2^+ or O_2^+ – one of those always exist as a trace at the output of the ions source) then, as the rest of the setup is electrostatic, the ion beam becomes a beam of H_2^+ whose trajectory is identical to that of A^+, without modifying any other parameter (see appendix A.1). This molecule can interact with the residual gas present on the beam trajectory, and undergo dissociative charge exchange

$$H_2^+ + X \rightarrow H + H + X^+ + KER \tag{2.4}$$

  which produces two hydrogen atoms with some excess energy (KER) whose center-of-mass follows the trajectory of the parent molecular ion.

  Therefore, the center-of-mass is aligned with the position sensitive system only within the observation cell. If a data acquisition is performed with only the H_2^+ beam, the direction of the positive beam is obtained by measuring the position of the center-of-mass of the two hydrogen atoms on the detectors (see section 4.1.2). A short acquisition (1000 coincidences) is enough to determine this position.

Once the two beams are aligned independently, the overlap between the beams is relatively good. But it can be improved by optimizing the coincidence rate on the detectors. Since the cross section of mutual neutralization is inversely proportional to the collision energy between atoms, the more the alignment is optimized, the more the count rate increases. Thus, the iterative optimization of the voltages of M1, M2 and Vobs drastically improves the number of coincidences linked to the measured signal (generally by a factor of

10). It is then possible to optimize the overlap of the beams by optimizing the pair of electrodes M1/M2 without modifying their voltage ratio [11].

2.8 Extracting the relative kinetic energy

To determine the velocity of the two particles in the laboratory fixed frame (with a static detection system), it must be remembered that neutral particles are in uniform rectilinear motion from their neutralization until their impact on the detectors:

$$\vec{d_1} = \vec{v}_1 \cdot t_{d1} \text{ et } \vec{d_2} = \vec{v}_2 \cdot t_{d2} \tag{2.5}$$

therefore the difference in impact time is

$$\tau = t_{d2} - t_{d1} = \frac{d_2}{v_2} - \frac{d_1}{v_1} \tag{2.6}$$

This gives the first equation which makes it possible to determine the two speeds. The second assumes that the velocity of the center-of-mass of the particles is known:

$$(m_1 + m_2)\vec{v}_{cm} = m_1\vec{v}_1 + m_2\vec{v}_2 \tag{2.7}$$

whose square gives:

$$(m_1 + m_2)^2 v_{cm}^2 = m_1^2 v_1^2 + m_2^2 v_2^2 + 2m_1 m_2 v_1 v_2 \cos\alpha_{12} \tag{2.8}$$

the second equation which allows to determine v_1 and v_2.

In order find v_1 and v_2, one method consists of first defining the distance p traveled by particle 1 when particle 2 is detected, as well as the distance q that particle 2 would have traveled when particle 1 is detected. These distances are given by:

$$p = v_1 t_{d2} = d_1 + v_1\tau \text{ and } q = v_2 t_{d1} = d_2 - v_2\tau \tag{2.9}$$

Therefore, by isolating v_1 and v_2 from equation 2.6, these speeds are expressed as

$$v_1 = \frac{d_1}{q} v_2 \text{ and } v_2 = \frac{d_2}{p} v_1 \tag{2.10}$$

which once replaced in equation 2.8 give

$$v_1 = \frac{(m_1 + m_2) p v_{cm}}{\sqrt{m_1^2 p^2 + m_2^2 d_2^2 + 2m_1 m_2 p d_2 \cos\alpha}} \tag{2.11}$$

$$v_2 = \frac{(m_1 + m_2) q v_{cm}}{\sqrt{m_1^2 q^2 + m_2^2 d_1^2 + 2m_1 m_2 q d_1 \cos\alpha}} \tag{2.12}$$

[11] This sequence of optimizations requires great finesse. It is sensitive to a change of a fraction of a Volt when the total voltage is 150 V (M1, M2) or even 500 V (V_{obs}).

This system of equations allows to find $\{v_1, v_2\}$ assuming $\{p, q\}$ known, while equations 2.9 determine $\{p, q\}$ by knowing $\{v_1, v_2\}$. Therefore, these are found by iterating over the two equations 2.9 and 2.12 starting with $v_1 = v_2 = v_{cm}$ as initial conditions [12].

In order to check the convergence of this algorithm, we verify that the value obtained for v_2 remains stable between two iterations, this check is made with equation 2.9. In other words, the algorithm is deemed to have converged if

$$\frac{v_2 - \frac{d_2}{q} v_1}{v_2} < 10^{-10} \tag{2.13}$$

If this condition is satisfied, it is possible to extract the position values of the center-of-mass when particle 1 collides with detector 1:

$$x_{cm} = \frac{m_1 x_1 + m_2 x_2'}{m_1 + m_2} \text{ et } y_{cm} = \frac{m_1 y_1 + m_2 y_2'}{m_1 + m_2} \tag{2.14}$$

where $\{x_2', y_2'\} = (1 - \tau v_2 / d_2)\{x_2', y_2'\}$ is the position of particle 2 when particle 1 comes in contact with detector 1.

The position of the center-of-mass along the axis $\hat{z}$ at the time of impact of particle 1 on detector D1 with respect to the position of detector 1 is [13]

$$z_{cm,D1} = z_1 - \frac{m_1 z_1 + m_2 z_2'}{m_1 + m_2} \tag{2.15}$$

where z_2' is defined in the same way that x_2' and y_2'.

The relative speed between the 2 particles is

$$\begin{aligned} v_r &= \|\vec{v}_1 - \vec{v}_2\| \\ &= \sqrt{(\vec{v}_1 - \vec{v}_2) \cdot (\vec{v}_1 - \vec{v}_2)} \end{aligned}$$

[12] Initially, the initial conditions on $\{v_1, v_2\}$ were chosen as being a slight deviation from the velocity of the center-of-mass

$$v_{1,i} = v_{cm} \sqrt{1 \pm \frac{14 \text{ eV}}{E_{cm}}} \text{ and } v_{2,i} = v_{cm} \sqrt{1 \mp \frac{14 \text{ eV}}{E_{cm}}}$$

The direct use of the center-of-mass velocity does not modify the resulting value of the algorithm nor its convergence. This algorithm converges in less than 10 iterations, but 20 iterations are used in order to ensure it.

[13] In practice, the position values according to $\hat{z}$ used in our code are relative to detector 2. Consequently, the position is relative to detector 2, when particle 2 collides with detector 2:

$$z_{cm,D2} = z_2 - \frac{m_1 z_1'' + m_2 z_2}{m_1 + m_2}$$

where $z_1'' = (1 + \tau v_1 / d_1) z_1$ is the position according to $\hat{z}$ of particle 1 when particle 2 comes in contact with detector 2. Both center-of-mass calculation are valid, as they are computed in the same z plane.

$$= \sqrt{v_1^2 + v_2^2 - 2v_1 v_2 \cos(\alpha_{12})} \tag{2.16}$$

The zenith angle between the relative velocity and the velocity of the center-of-mass (c.m.) is obtained using the scalar product between these two velocities [14] which gives

$$\cos(\theta_r) = \frac{v_1^2 - v_2^2 + \frac{m_1 - m_2}{m_1 + m_2} v_r^2}{2 v_{cm} v_r} \tag{2.17}$$

The relative kinetic energy after collision is simply

$$E_{r,f} = \frac{\mu v_r^2}{2} \tag{2.18}$$

This analysis is performed for each of the two possible combinations of mass, the particle 1 being given a mass m_1 or m_2, and vice versa for the particle 2. Even if this algorithm should only converge in one of the cases only, it is possible that it converges in both cases (see appendix B.2). The method used to select only the correct analysis among the two is described below.

2.9 Effects of residual pressure

The intensity of the current I of a beam is given by:

$$I = \rho \cdot v \cdot e \cdot S \tag{2.19}$$

with ρ the ion density, v the beam speed, e the elementary charge and S the section of the beam.

[14] The scalar product between the relative and c.m. velocities can be written either as a function of the cosine of the angle between the two, but can also be decomposed according to the speed of the two particles:

$$\begin{aligned}
\vec{v}_r \cdot \vec{v}_{cm} &= v_r v_{cm} \cos(\theta_r) \\
&= (\vec{v}_1 - \vec{v}_2) \cdot \left(\frac{m_1 \vec{v}_1 + m_2 \vec{v}_2}{m_1 + m_2} \right) \\
&= \frac{1}{m_1 + m_2} \left(m_1 v_1^2 + m_2 v_2^2 + (m_2 - m_1) v_1 v_2 \cos(\alpha_{12}) \right)
\end{aligned}$$

Therefore, remembering the definition of the square of the relative velocity norm:

$$v_1 v_2 \cos(\alpha_{12}) = \frac{1}{2} \left(v_1^2 + v_2^2 - v_r^2 \right)$$

we obtain:

$$(m_1 + m_2) \vec{v}_r \cdot \vec{v}_{cm} = \frac{1}{2}(m_1 + m_2) v_1^2 - \frac{1}{2}(m_1 + m_2) v_2^2 + \frac{1}{2}(m_1 - m_2) v_r^2$$

that must be replaced in the equation of the scalar product to be able to isolate the zenith angle and obtain its expression.

Therefore, in a positive oxygen beam – whose current is 30 nA, the kinetic energy is 7500 eV and the diameter is 1 mm – the density of ions is about 8 10^5 ions/cm^3.

This ion density within the beam is to be compared with the density of particles of the residual gas within the experimental device.

This device is made up of several chambers with differential pumping. For example, the chamber in which the beams are shaped is at a pressure of about 10^{-7} mbar, i.e. a density of about 2.7 10^9 particles/cm^3.

It can be seen that the density of the residual gas is much greater than the density of the ion beam that is being studied. However, the density of the residual gas is low enough not to affect the experiment (or at least not significantly). Indeed, it interacts little with the detectors and does not influence the properties of the beam. However, the interaction of the beam with the residual gas cannot be neglected.

First the residual gas is composed of neutral particles, therefore, it does not influence the current measurements carried out using Faraday cups. Then, as this residual gas is at room temperature, the kinetic energy distribution of this gas is sufficiently low (much lower than the work of extraction of the material) so that most of the particles that make up this gas are in a range energy for which the Micro-Channel Plates (MCP) have zero detection efficiency (figure 2.4).

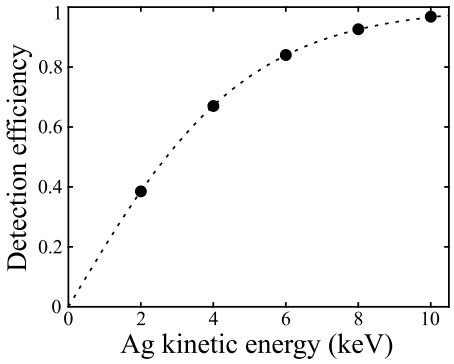

Figure 2.4: Detection efficiency of a channeltron as a function of the incident energy of a silver atom. The points are the experimental measurements, the dotted curve is given by the function $\tanh(E/4922\text{ eV})$. The channeltron is a detector that functions similarly to that of MCPs. Only, it is made up of a single large channel. This allows it to have a detection efficiency close to 100 %, unlike MCPs which have a maximum detection efficiency given by the ratio between the area of the holes and the total area of the wafer (60 % about). The detection efficiency is almost unity when the kinetic energy of the particles is close to that of the beam (10 keV) and almost zero when the energy of the atoms is close to the thermal energy (25 meV). Dark count rates of a few Hz confirm that finding.

On the other hand, the ion beam interacts little enough with the residual

gas not to reduce its intensity. Considering a cross section of neutralization of the negative beam on the residual gas of the order of $\sigma_{\text{gas}} \sim 10^{-15}$ cm^2, a beam traveling a distance of $l \sim 2$ m within the vacuum device, the probability of neutralization by the residual gas of density $\rho_{\text{gas}} \sim 2.7\ 10^9$ particles/cm^3 is of the order of:

$$P_{\text{gas}} = \rho_{\text{gas}} l \sigma_{gas} \sim 5\ 10^{-4} \tag{2.20}$$

Consequently, as the precision of certain elements (for example the current measurements) to be taken into account during the measurement is of the order of one percent, this loss rate is negligible in comparison.

However, these neutralized ions have sufficient kinetic energy for the detection efficiency of these neutralized particles to be high. Therefore, if the ion beam is on the axis of the detectors, since neutralization negligibly modifies the trajectory in the laboratory, these particles collide with the detectors and generate background events.

The count rate on MCP linked to residual gas is relatively easy to estimate: The beams are aligned with the detectors only within the observation cell [15]. This cell has a length of $l = 8$ cm, while the pressure in the chamber is at best $2\ 10^{-10}$ mbar. This gives a rate of about 7500 neutral atoms sent to the detectors every second for a negative ion beam of 30 nA.

This rate is immense compared to 30 events per second of signal [16]. The method used to separate the signal - related to the reaction studied - from the background - generated by the residual gas - is described in section 2.10. However, the coincident background generated on the detectors is quadratic as a function of the pressure. Therefore, reducing the pressure within the observation cell is an important factor for improving the signal-to-noise ratio.

This high background level explains the current arrangement of the detection system (blind near the main axis of the beams). Such an amount of background cannot be tolerated for long by MCPs. This provision unfortunately has several drawbacks, the taking into account and the correction of which are described in chapter 4.1.

Consequently, an update of the device is in progress in order to improve the pressure of the residual gas within the observation cell by a factor of 20 in order to have an acceptable count rate on the detectors. This would make it possible to use another detection system [148] capable of measuring a large number of coincident particles (up to 10 particles). This would make it possible

[15] Certain mutual neutralization reactions (for example $O^+ + H^-$) could not be measured, because the configuration of the experimental setup is such that for these reactions, part of the beam was aligned within the region which prepares the alignment of the beams. As the vacuum is of lower quality within this region, the background on the detectors was more than a hundred times higher. Therefore, the measurement of these reactions was impossible.

[16] This rate of real event count is unfortunately an upper limit. This event rate was 3 Hz for $D_2^+ + D^-$ when the system was perfectly aligned.

to measure molecular dissociation reactions with greater ease.

2.10 Cleaning background

There are two sources of background inherent in the experimental setup. On the one hand, crosstalk appears intermittently during the amplification of the electronic pulses generated by the microchannel wafers, on the other hand the neutralization of the negative beam with the residual gas within the observation cell generates a high non-coincident count rate on each detector.

The first source of noise is easy to remove. Indeed, this source of noise is resonant. The false coincidences linked to this resonance are characterized by a measurement time τ of very low dispersion. The values included in this window are rejected during the analysis.

The window of coincidence within which the events are located is approximately $\Delta t_{coinc} \sim 1\ \mu$s.

The probability of having a second background event within a microsecond of the first (assuming the distribution of background events is uniform over time and the probability of having a second event is low) is the product of the duration of the coincidence window Δt_{coinc} and the frequency of occurrence of the background $f_{bg} \sim 7500$ Hz, which gives $f_{bg} \times \Delta t_{coinc} = 0.75$ % chance of having a second event within the coincidence window. This gives a coincident count rate linked only to the neutralization of the negative beam on the residual gas of approximately

$$f_{bg} \times f_{bg} \times \Delta t_{coinc} \simeq 60 \text{ Hz}. \tag{2.21}$$

Although this coincident count rate is larger than the coincident count rate linked to the events actually measured, it is however low enough to be able to statistically extract the signal from the background generated by the residual gas. However, some reactions lead to a lower count rate (~ 1 Hz). For such reactions, it is necessary to reduce the background. As shown on equation 2.21, this background is proportional to the square of the non-coincident count rate. Therefore, the coincident background is proportional to the square of the pressure of the residual gas within the observation cell. Thus, reducing the pressure by a factor of 10 within this cell would improve the ratio between signal and background by a factor of 100, and would make it possible to measure much less efficient mutual neutralization reactions.

In order to eliminate the second source of background, it is necessary to make several assumptions: The signal of neutralization by the residual gas is not coincident. It is accepted by discriminators, because statistically, it may happen that two fortuitous neutralizations are sufficiently close to be considered as coincident. As the direction of the negative beam is on the axis of the

detectors within the observation cell, the combination of the two positions follows the distribution of the beam before neutralization. However, the combination of two fortuitous neutralizations does not necessarily produce a center-of-mass on the axis between the detectors. Then, the temporal and spatial information is decorrelated.

This hypothesis leads to several results: On the one hand, the temporal distribution of Δt is uniform and the spatial distribution of the center-of-mass is both wider and centered differently compared to the distribution of the center-of-mass of the coincident mutual neutralization events. Therefore, if one obtains during a preliminary analysis the temporal and spatial distribution due to the mutual neutralization, it is then possible to exclude the events which are outside this distribution. This first phase of background subtraction is called cut by the center-of-mass.

On the other hand, the spatial distribution of the center-of-mass is not correlated with its temporal distribution during fortuitous events (unlike truly coincident events). If the coincidence window used to measure the events is large enough (at least twice the time window within which the truly coincident events are found), a modification can be applied to $T_1' = T_1 + \Delta T$ with ΔT greater than the temporal distribution of the truly coincident events (figure 2.5).

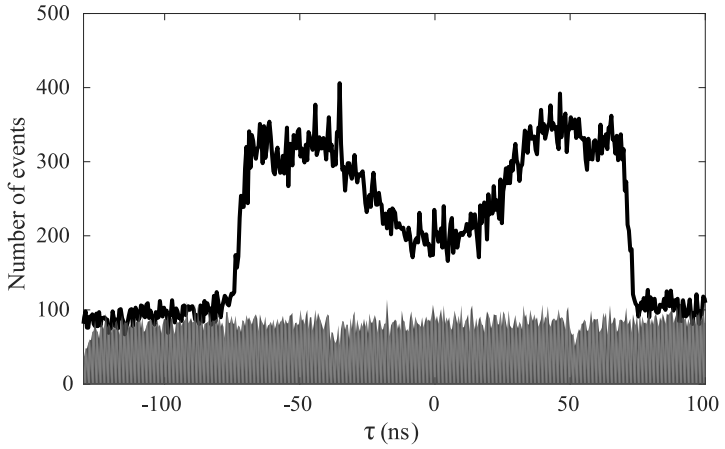

Figure 2.5: Histogram of the distribution of τ for the reaction $C^+ + S^- \rightarrow C + S + KER$, for minimal collision energy. Black curve: raw measurement; Shaded area: reconstruction of the background by the time shift method.

This new distribution of reconstructed events shifted in time – satisfying all the conditions such as the analysis algorithm converges and not affected by the cut linked to the center-of-mass – is formed of exclusively non-coincident events.

This new distribution corresponds to the background component of the

measurement.

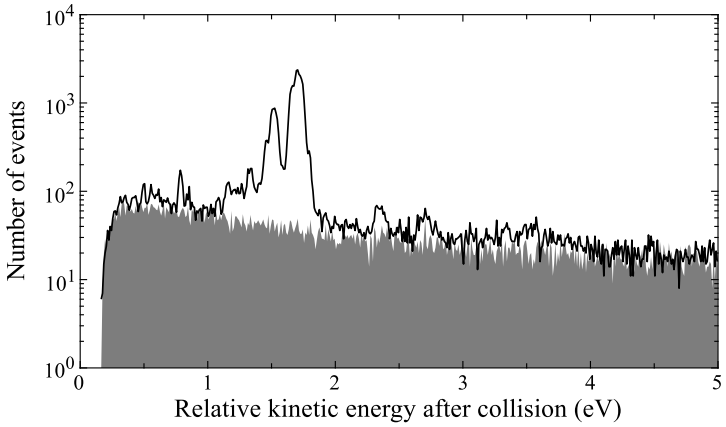

Figure 2.6: Raw histogram of relative kinetic energy after reaction for the reaction $C^+ + S^- \rightarrow C + S + KER$, for minimal collision energy. The solid curve represents the signal measured with the background, the gray area corresponds to the reconstructed background.

The histogram of the signal alone is obtained by subtracting the histogram (or spectrum) of background from the initial histogram (or spectrum – signal + background – figure 2.6). However, since the detection system is composed of two detectors with a finite solid angle, some components $(E_{r,f}, \cos\theta, \phi)$ of the distribution cannot be detected by the system. How these events are taken into account to correct histograms is described in section 4.1.

The error on this corrected histogram takes into account the statistical error of the initial spectrum and of the time-shifted spectrum. This is why the initial filtering by the center-of-mass is important to apply before the calculation of each of the histograms.

Chapter 3

Theory

As stated in section 1.4.1, models for the mutual neutralization may be categorized in two families: One that solve the collision dynamics (section 3.1) and one that solve the potential energy curves (section 3.2). This chapter treats only the total (partial) cross section. The differential cross section will be treated in its own chapter, as it is deeply correlated with the experimental collision distribution.

3.1 Collision dynamics: The Landau-Zener Model

3.1.1 Adiabatic and diabatic basis

The objective of this section is to describe the probability of mutual neutralization between the positive ion A^+ and the negative ion B^- producing the neutral atoms A^0 and B^0. It combines the description made by Zener [11] and Janev & Salin [149].

The first step necessary for this description is the establishment of the studied physical system. This system is composed of a cation A^+, an atom B^0 and a supernumerary electron.

The Hamiltonian of this system (assuming the nuclei are fixed in space) describes the motion of the electron around the cation and the neutral atom. It is composed of the kinetic term, as well as the potential term linked to A^+ and B^0,

$$H = -\frac{1}{2}\nabla^2 + V_{A^+}(\vec{r}_A) + V_{B^0}(\vec{r}_B) \tag{3.1}$$

where $V_{A^+}(\vec{r}_A)$ and $V_{B^0}(\vec{r}_B)$ are the effective potentials of atoms A^+ and B^0 respectively and where the electron is at a position $\vec{r}_A$ and $\vec{r}_B$ respectively.

Solutions of the Hamiltonian with just one of the two potential terms $V_{A^+}(\vec{r}_A)$ or $V_{B^0}(\vec{r}_B)$ are the atomic wavefunctions χ_{A^0} and χ_{B^-}. So, if the electron is located around A only then we have $A^0 + B^0$ and if the electron is around

B then we have $A^+ + B^-$, i.e.

$$\begin{array}{lll} \chi_{\mathrm{A}^0} & \rightarrow & \mathrm{A}^0 + \mathrm{B}^0 \quad \text{covalent state} \\ \chi_{\mathrm{B}^-} & & \mathrm{A}^+ + \mathrm{B}^- \quad \text{ionic state} \end{array} \tag{3.2}$$

These wavefunctions do not form a basis of the system when the interatomic distance is small. But they make it possible to describe it when this distance is large.

Restricting to a two-state system, the solutions of the Hamiltonian are the *adiabatic* wavefunctions ψ_1 and ψ_2 defined such as:

$$\begin{array}{lll} \psi_1 & \xrightarrow[R\to\infty]{} & \chi_{B^-}\left(\vec{r}_B\right) \\ \psi_2 & & \chi_{A^0}\left(\vec{r}_A\right) \end{array} \tag{3.3}$$

where R is the interatomic distance.

The solutions of the Hamiltonian as a function of the interatomic distance then form potential energy curves $E_1(R)$ and $E_2(R)$ given by:

$$E_1 = \langle \psi_1 | H | \psi_1 \rangle \,,\; E_2 = \langle \psi_2 | H | \psi_2 \rangle \tag{3.4}$$

As the states associated with these wavefunctions are solutions of the Hamiltonian, the off-diagonal terms are zero:

$$\langle \psi_1 | H | \psi_2 \rangle = \langle \psi_2 | H | \psi_1 \rangle = 0 \tag{3.5}$$

Now suppose that the wavefunctions ψ_1 and ψ_2 exchange properties around a critical interatomic distance R_c. In the case of mutual mutualization, this property is the location of the supernumerary electron around either the cation A^+, or the atom B^0.

Thus, when $R \gg R_\mathrm{c}$, the wavefunction ψ_1 will have the property of locating the electron around the atom B^0 while ψ_2 will have the property of locating the electron around the ion A^+. Conversely, when $R \ll R_\mathrm{c}$, these properties will be reversed.

If the two atoms are no longer at a fixed interatomic distance, but approach each other infinitely slowly from infinity, the property of locating the electron around one of the atoms will be preserved by the total wavefunction of the system Ψ. As the wavefunctions ψ_1 and ψ_2 form a wavefunction basis, the total wavefunction can be written as a linear combination of them .

As the interatomic distance varies over time, the corresponding states are no longer in a stationary state, then E_1 and E_2 are no longer solutions of the Hamiltonian.

Let ψ_ion be the wavefunction Ψ initially in state 1, this wavefunction is called the wavefunction of the ionic state where the electron is attached to the atom B^0. Let ψ_cov be the wavefunction Ψ initially in state 2, this wavefunction

is called the wavefunction of the covalent state where the electron is attached to the ion A^+. Then the wavefunctions ψ_{ion} and ψ_{cov} form another basis of this two-state system.

This basis set is called the diabatic basis.

When the internuclear distance is large, on the one hand the wavefunction $\psi_{\text{cov}}\left(\vec{r},\vec{R}\right)$ is exponentially small when $r_{\text{A}} \simeq R$, on the other hand the wavefunction $\psi_{\text{ion}}\left(\vec{r},\vec{R}\right)$ is exponentially small when $r_{\text{B}} \simeq R$.

Thus, the wavefunction $\psi_{\text{cov}}\left(\vec{r},\vec{R}\right)$ is zero for a distance from the kernel A^+ of the order of the interatomic distance. In other words, for this state, the electron is located around the ion A^+. This wavefunction corresponds to the configuration of a covalent state $A^0 + B^0$. The energy curve

$$E_{\text{cov}} = \langle \psi_{\text{cov}} | H | \psi_{\text{cov}} \rangle \tag{3.6}$$

varies only slightly according to the interatomic distance.

By the same reasoning, the wavefunction $\psi_{\text{ion}}\left(\vec{r},\vec{R}\right)$ is zero when the distance of the electron from the nucleus B is of the order of the interatomic distance. The electron is then located near the nucleus B. This wavefunction therefore corresponds to a configuration of an ionic state $A^+ + B^-$, whose energy curve

$$E_{\text{ion}} = \langle \psi_{\text{ion}} | H | \psi_{\text{ion}} \rangle \tag{3.7}$$

follows the Coulomb potential curve. This varies little when the interatomic distance is large ($R \gg 1$ a$_0$).

Therefore

$$\begin{array}{l} \psi_{\text{cov}}\left(\vec{r},\vec{R}\right) \\ \psi_{\text{ion}}\left(\vec{r},\vec{R}\right) \end{array} \xrightarrow[R\to\infty]{} \begin{array}{l} \chi_{A^0}\left(\vec{r}_A\right) \\ \chi_{B^-}\left(\vec{r}_B\right) \end{array} \tag{3.8}$$

However, these wavefunctions are not eigenstates of the Hamiltonian. The non-diagonal matrix elements

$$E_{\text{ic}} = \langle \psi_{\text{ion}} | H | \psi_{\text{cov}} \rangle = \langle \psi_{\text{cov}} | H | \psi_{\text{ion}} \rangle \neq 0 \tag{3.9}$$

are therefore not zero, this non-diagonal term is called the interaction term. There is a probability of exchange between these two states. This is why these wavefunctions are called the *diabatic* wavefunctions.

As said previously, the diabatic basis states are not specific states of the system. Therefore, the application of the Schrödinger equation on the system is written:

$$\left\{ \begin{array}{lll} H\psi_{\text{ion}} & = E_{\text{ion}}\psi_{\text{ion}} & + E_{\text{ic}}\psi_{\text{cov}} \\ H\psi_{\text{cov}} & = E_{\text{ic}}\psi_{\text{ion}} & + E_{\text{cov}}\psi_{\text{cov}} \end{array} \right. \tag{3.10}$$

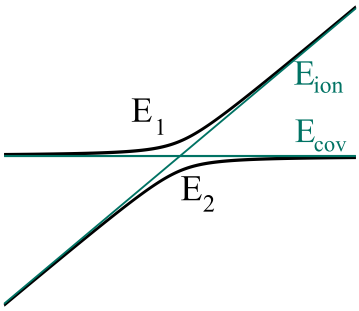

Figure 3.1: Potential energy curves in the adiabatic and diabatic representations. The thick curves represent an avoided crossing in the adiabatic basis, while the light curves represent the curve crossing in the diabatic basis. If the curves in the diabatic representation are straight lines, then those in the adiabatic representation are hyperbolas.

where E_{ion} and E_{cov} are the energy levels in the diabatic basis and $E_{\text{i,c}}$ is the potential for interaction between the two states. A sketch of the potential energy curves is presented in figure 3.1.

As the diabatic wavefunctions vary slightly according to the interatomic distance, they are expressed according to a linear combination of the adiabatic wavefunctions ψ_1 and ψ_2,

$$\begin{cases} \psi_{\text{cov}} &= a_1\psi_1 - a_2\psi_2 \\ \psi_{\text{ion}} &= a_2\psi_1 + a_1\psi_2 \end{cases} \tag{3.11}$$

The transformation parameters from the adiabatic to the diabatic basis a_1 and a_2 are obtained by inserting equation 3.11 to the left and to the right of the equation 3.10 and projecting the result on the adiabatic wavefunctions $\langle\psi_1|$ and $\langle\psi_2|$. This gives the intermediate result:

$$\begin{cases} E_1 a_2 &= E_{\text{ion}} a_2 &+E_{\text{i,c}} a_1 \\ E_2 a_1 &= E_{\text{ion}} a_1 &-E_{\text{i,c}} a_2 \\ E_1 a_1 &= E_{\text{i,c}} a_2 &+E_{\text{cov}} a_1 \\ -E_2 a_2 &= E_{\text{i,c}} a_1 &-E_{\text{cov}} a_2 \end{cases} \tag{3.12}$$

Adding the first and the fourth equation, and subtracting the third from the second,

$$\begin{cases} 2E_{\text{i,c}} a_1 &= [(E_1 - E_2) + (E_{\text{cov}} - E_{\text{ion}})]\, a_2 \\ 2E_{\text{i,c}} a_2 &= [(E_1 - E_2) - (E_{\text{cov}} - E_{\text{ion}})]\, a_1 \end{cases} \tag{3.13}$$

Using the normalization of the transformation parameters $a_1^2 + a_2^2 = 1$, inserting the first of these equations into the second, and assuming that $a_1 \neq 0$, it is possible to obtain a relation between the energies of the adiabatic basis and

those of the diabatic basis,

$$a_1 = \sqrt{\frac{1}{2}\left(1 + \frac{E_{\text{cov}} - E_{\text{ion}}}{\sqrt{(E_{\text{cov}} - E_{\text{ion}})^2 + 4E_{\text{ic}}^2}}\right)}, \tag{3.14}$$

$$a_2 = \sqrt{\frac{1}{2}\left(1 - \frac{E_{\text{cov}} - E_{\text{ion}}}{\sqrt{(E_{\text{cov}} - E_{\text{ion}})^2 + 4E_{\text{ic}}^2}}\right)} \tag{3.15}$$

$$E_1 - E_2 = \sqrt{(E_{\text{cov}} - E_{\text{ion}})^2 + 4E_{\text{ic}}^2} \tag{3.16}$$

and

$$a_1 a_2 = \frac{E_{\text{i,c}}}{E_1 - E_2} \tag{3.17}$$

At the crossing point R_{c} between the diabatic curves, the adiabatic potential energy curves have an avoided crossing ($E_{\text{cov}} - E_{\text{ion}} = 0$). The energy difference between these curves at the crossing, is

$$\Delta(R_{\text{c}}) = E_1 - E_2 = 2E_{\text{ic}}(R_{\text{c}}) \tag{3.18}$$

If E_{ion} and E_{cov} are linear, and E_1 and E_2 are the two branches of a hyperbola whose asymptotes are E_{ion} and E_{cov}, then $E_{\text{i,c}}$ is constant. Its value is identical to that found in the previous paragraph. This type of crossing is exactly the one represented by the figure 3.1.

3.1.2 Evolution of the molecular wavefunction through an avoided crossing

Now that the diabatic basis wavefunctions, as well as some of their properties are described, it is possible to describe the evolution of the total wavefunction for two atoms approaching each other at a non-zero velocity. This speed is greater than previously described [11].

Let Φ be a wavefunction initially in the state ψ_{ion} when the interatomic distance is large ($R >> R_{\text{c}}$). This wavefunction is written in the diabatic basis as follows,

$$\Phi(t) = C_{\text{ion}}(t)\psi_{\text{ion}} + C_{\text{cov}}(t)\psi_{\text{cov}} \tag{3.19}$$

with the following asymptotic conditions on the population coefficients

$$\begin{aligned} |C_{\text{ion}}(t = -\infty)| &= 1 \\ |C_{\text{cov}}(t = -\infty)| &= 0 \end{aligned} \tag{3.20}$$

Suppose that these atoms approach each other with an initial velocity $\vec{v}_i$. The evolution of the wavefunction follows the Schrödinger equation [150] [1]

$$\left[H - i\hbar\frac{\partial}{\partial t}\right]\left\{C_{\text{ion}}(t)\psi_{\text{ion}}e^{\frac{1}{i\hbar}\int_{-\infty}^{t}E_{\text{ion}}(t)\ \mathrm{d}t} + C_{\text{cov}}(t)\psi_{\text{cov}}e^{\frac{1}{i\hbar}\int_{-\infty}^{t}E_{\text{cov}}(t)\ \mathrm{d}t}\right\} = 0 \tag{3.21}$$

In order to solve this equation, several hypotheses are necessary [11]:

First, the interaction potential must be much lower than the relative kinetic energy between the two atoms (at the crossing). This assumption makes it possible to treat this system in the center-of-mass frame, without involving additional parameters. This assumption makes the interatomic distance depend only on time. This hypothesis can be circumvented by taking into account the semi-classical trajectories, described in section 4.3.3.

The second assumption concerns the region of interaction between the ionic and covalent states. If this transition region is short, then one can consider that $E_{\text{cov}} - E_{\text{ion}}$ is a linear function of time [2], and the interaction potential and the wavefunctions of the diabatic basis remains constant (independent of time) during this transition, i.e. the transition happens mostly at (not around) the resonnace between the diabatic curves. In other words:

$$\begin{cases} (E_{\text{cov}} - E_{\text{ion}})/\hbar & = \alpha t \\ \dot{E}_{\text{ic}} = \dot{\psi}_{\text{cov}}(\vec{r}_A) = \dot{\psi}_{\text{ion}}(\vec{r}_B) & = 0 \end{cases} \tag{3.22}$$

Taking the Schrödinger equation (equation 3.21), applying the Hamiltonian on the diabatic wavefunctions (equation 3.10) and projecting the result on the wavefunctions of the diabatic basis $\langle\psi_{\text{cov}}|$ and $\langle\psi_{\text{ion}}|$, the equation of

[1] Zener [11] uses a slightly different version of Schrödinger's equation,

$$\left\{H - \frac{\hbar}{i}\frac{\partial}{\partial t}\right\}\left\{C_{\text{ion}}(t)\psi_{\text{ion}}e^{\frac{i}{\hbar}\int_{-\infty}^{t}E_{\text{ion}}(t)\ \mathrm{d}t} + C_{\text{cov}}(t)\psi_{\text{cov}}e^{\frac{i}{\hbar}\int_{-\infty}^{t}E_{\text{cov}}(t)\ \mathrm{d}t}\right\} = 0$$

It leads, with the help of an identical development, altered by a few changes of signs, to an identical result. In fact, time is reversed in this equation, but as the Landau-Zener formula requires two passages through an avoided crossing, in two opposite directions, the solution is indeed identical.

[2] If one does an analysis of this condition, it leads to

$$\alpha = v_R\frac{\partial}{\partial R}(E_{\text{cov}} - E_{\text{ion}}) >> \dot{\alpha}\Delta t$$

where Δt it the time needed to pass through the crossing. In order to check the validity of this condition, lets assume that, at small collision energies (section 3.4), $v_R \simeq v \simeq \sqrt{2/(\mu R)}$ and $\partial/\partial R(E_{\text{cov}} - E_{\text{ion}}) \simeq 1/R^2$. Then the condition becomes $2R >> 5\Delta t\dot{R}$ which means that the crossing should be shorter than the interatomic distance, i.e. the hypothesis of the model.

In the limit case of the tangent trajectory, $v_R \simeq 0$ then the Landau-Zener approximation is not valid. These cases correspond to partially crossed crossing, i.e., a marginal part of all the possible trajectories. This condition is therefore globally satisfied.

evolution of the populations becomes:

$$\frac{\hbar}{i}\frac{\partial C_{\text{cov}}}{\partial t}(t) = E_{\text{ic}} \exp\left\{-\frac{i}{\hbar}\int_{-\infty}^{t}(E_{\text{cov}} - E_{\text{ion}})\,\mathrm{d}t\right\} C_{\text{ion}}(t) \tag{3.23}$$

$$\frac{\hbar}{i}\frac{\partial C_{\text{ion}}}{\partial t}(t) = E_{\text{ic}} \exp\left\{\frac{i}{\hbar}\int_{-\infty}^{t}(E_{\text{cov}} - E_{\text{ion}})\,\mathrm{d}t\right\} C_{\text{cov}}(t) \tag{3.24}$$

whose resolution is given in appendix C.1.1.

The probability of transition $P_{\text{i,c}}$ from the ionic state to the covalent state through an avoided crossing is given by:

$$P_{\text{i,c}} = \|C_{\text{cov}}(\infty)\|^2 = 1 - e^{-2\pi\gamma} \tag{3.25}$$

By expliciting the parameter $\gamma = E_{\text{ic}}^2/(\hbar\alpha)$ and re-expressing the constant α as:

$$\alpha = v_R \Delta F \tag{3.26}$$

where v_R is the radial velocity and

$$\Delta F = \frac{\mathrm{d}}{\mathrm{d}R}(E_{\text{ion}} - E_{\text{cov}}) \tag{3.27}$$

is the slope of the diabatic potential difference curve, the transition probability at the passage through an avoided crossing given by the Landau-Zener theory is

$$P_{\text{i,c}} = 1 - e^{-2\pi\gamma} = 1 - \exp\left(-\frac{2\pi E_{\text{ic}}^2}{\hbar v_R \Delta F}\right) \tag{3.28}$$

This result can be extended to the case where the interaction term is not constant [151].

3.1.3 Full description of the collision

In the previous section, the probability of passage from the ionic state to the covalent state through an avoided crossing in the diabatic basis was obtained (equation 3.28). This transition probability describes the evolution of the population of states through a single crossing.

The objective of this section is to describe the entire mutual neutralization reaction through the two passages by the avoided crossing: An inward passage and an outward passage. This description follows the the development carried out by D. Fussen [152].

To simplify the development which will follow, the reaction will be divided into three parts: the inward passage, a free oscillation and finally the outward passage.

This process will modify the total wavefunction of the system Ψ. As this wavefunction is a linear combination of the diabatic basis states

$$\Psi = C_{\text{ion}}\,\psi_{\text{ion}} + C_{\text{cov}}\,\psi_{\text{cov}}, \tag{3.29}$$

Each part will be represented by a matrix transformation of the population vector of the states of the diabatic basis $\{C_{\text{ion}}, C_{\text{cov}}\}$. These transformation matrices T are hermitic. This gives transitions of the form

$$\begin{bmatrix} C_{\text{ion}}(\infty) \\ C_{\text{cov}}(\infty) \end{bmatrix} = T \begin{bmatrix} C_{\text{ion}}(-\infty) \\ C_{\text{cov}}(-\infty) \end{bmatrix} \text{ with } T = \begin{bmatrix} a_1 & a_2 \\ -a_2 & a_3 \end{bmatrix} \tag{3.30}$$

The first transformation, the first passage through the crossing, the inward passage, is obtained using the equation 3.28. By choosing phase terms for the initial state, this equation indicates that if

$$\|C_{\text{ion}}(-\infty)\|^2 = 1 \text{ and } \|C_{\text{cov}}(-\infty)\|^2 = 0 \tag{3.31}$$

then

$$\|C_{\text{ion}}(+\infty)\|^2 = 1 - P_{\text{i,c}} \text{ and } \|C_{\text{cov}}(+\infty)\|^2 = P_{\text{i,c}}. \tag{3.32}$$

These conditions imply that $\|a_1\| = \|a_3\| = \sqrt{P_{\text{i,c}}}$ and $\|a_2\| = \sqrt{1 - P_{\text{i,c}}}$. No constraint is given here for the phase factors. However, in order to simplify the notations, the factors a_1 and a_2 will be assumed to be real and positive. The reason for the validity of this choice will be described later in this section. So that the matrix T_{in} of transformation of the populations of the diabatic base states through an avoided crossing (inward) within the framework of the Landau-Zener model is given by:

$$T_{\text{in}} = \begin{bmatrix} \sqrt{1-P} & \sqrt{P} \\ -\sqrt{P} & \sqrt{1-P} \end{bmatrix} \tag{3.33}$$

Once the crossing has been carried out, the total wavefunction will evolve freely between the time of the first passage through the crossing t_1 and the time of the second crossing t_2. During this interval, the interaction potential will be low compared to the energies of the states and will be neglected. Moreover, since the interatomic distance is less than the critical interatomic distance ($R \ll R_{\text{c}}$), then the ionic state corresponds to the adiabatic state 2, while the covalent corresponds to adiabatic state 1 (see figure 3.1). Diabatic states become solutions of Schrödinger's equation,

$$\left(H - i\hbar \frac{\partial}{\partial t} \right) \psi = 0 \tag{3.34}$$

which becomes, once the total wavefunction is expressed in the diabatic basis and projected onto each of the wavefunctions of this same basis

$$\dot{C}_{\text{ion}} = \frac{E_{\text{ion}}}{i\hbar} C_{\text{ion}} \tag{3.35}$$

$$\dot{C}_{\rm cov} = \frac{E_{\rm cov}}{i\hbar} C_{\rm cov} \tag{3.36}$$

whose solutions are, at the end of free evolution:

$$C_{\rm ion}(t_2) = C_{\rm ion}(t_1) \exp\left\{ \frac{1}{i\hbar} \int_{t_1}^{t_2} E_{\rm ion}\, {\rm d}t \right\} \tag{3.37}$$

$$C_{\rm cov}(t_2) = C_{\rm cov}(t_1) \exp\left\{ \frac{1}{i\hbar} \int_{t_1}^{t_2} E_{\rm cov}\, {\rm d}t \right\} \tag{3.38}$$

Therefore, the transformation matrix will be:

$$T_{\rm free} = \begin{bmatrix} e^{i\vartheta_{\rm ion}} & 0 \\ 0 & e^{i\vartheta_{\rm cov}} \end{bmatrix} \tag{3.39}$$

with $\vartheta_{\rm ion} = \int_{t_1}^{t_2} E_{\rm ion}(t'){\rm d}t'$ and $\vartheta_{\rm cov} = \int_{t_1}^{t_2} E_{\rm cov}(t'){\rm d}t'$.

The free oscillation ends with a new passage through the crossing in the opposite direction, the outward passage. By conservation of energy, this crossing takes place at the same speed as during the inward passage.

This transformation is identical to that of the inward passage, except that time is reversed. So, if a wavefunction identical to that obtained by the inward transition passes through the outward avoided crossing, then the wavefunction must return to its initial state before its inward passage. Thus the transformation matrix for the outward passage is the inverse of that for the inward passage.

$$T_{\rm in}^{-1} T_{\rm out} = \begin{bmatrix} 1 & 0 \\ 0 & 1 \end{bmatrix} \tag{3.40}$$

As the transformation matrices are hermitic, the inverse of a transformation matrix whose elements are real is the transpose of this same matrix.

$$T_{\rm out} = T_{\rm in}^{-1} = T_{\rm in}^{t} \tag{3.41}$$

So the matrix which describes the outward passage through the crossing is given by:

$$T_{\rm out} = \begin{bmatrix} \sqrt{1-P_{\rm ic}} & -\sqrt{P_{\rm ic}} \\ \sqrt{P_{\rm ic}} & \sqrt{1-P_{\rm ic}} \end{bmatrix} \tag{3.42}$$

Now that all the transformations applied to the wavefunction during a mutual neutralization reaction have been described, it remains only to apply them in the correct order:

$$\begin{aligned} \begin{bmatrix} C_{\rm ion}(\infty) \\ C_{\rm cov}(\infty) \end{bmatrix} &= T_{\rm out}\; T_{\rm free}\; T_{\rm in} \begin{bmatrix} 1 \\ 0 \end{bmatrix} \\ &= \begin{bmatrix} e^{-i\vartheta_{\rm ion}} \left(1 - P_{\rm i,c}\right) + e^{-i\vartheta_{\rm cov}} P_{\rm i,c} \\ \sqrt{P_{\rm i,c}\left(1 - P_{\rm i,c}\right)} \left(e^{-i\vartheta_{\rm ion}} - e^{-i\vartheta_{\rm cov}} \right) \end{bmatrix} \end{aligned} \tag{3.43}$$

The squared norm of the coefficient $C_{\rm cov}(\infty)$ will therefore correspond to the total probability of neutralization,

$$P_{\rm tot} = \|C_{\rm cov}(\infty)\|^2 = P_{\rm i,c}\,(1-P_{\rm i,c})\left(e^{-i\vartheta_{\rm ion}} - e^{-i\vartheta_{\rm cov}}\right)^2 \tag{3.44}$$

The last quadratic factor can be simplified, by extracting its mean value. The argument may be written as:

$$\left(e^{-i\vartheta_{\rm ion}} - e^{-i\vartheta_{\rm cov}}\right) = e^{-i(\vartheta_{\rm ion}+\vartheta_{\rm cov})/2}\left(e^{-i(\vartheta_{\rm ion}-\vartheta_{\rm cov})/2} - e^{i(\vartheta_{\rm ion}-\vartheta_{\rm cov})/2}\right) \tag{3.45}$$

and using the expression in the form of complex exponential of the sine,

$$\sin x = \frac{e^{ix}-e^{-ix}}{2i}, \tag{3.46}$$

this leads to:

$$\left(e^{-i\vartheta_{\rm ion}} - e^{-i\vartheta_{\rm cov}}\right) = \exp\left\{-i\frac{\vartheta_{\rm ion}+\vartheta_{\rm cov}}{2}\right\}(-2i)\sin\left\{\frac{\vartheta_{\rm ion}-\vartheta_{\rm cov}}{2}\right\} \tag{3.47}$$

This allows to express the transition probability within the Landau-Zener model,

$$P_{\rm tot} = 4\,P_{\rm i,c}\,(1-P_{\rm i,c})\,\sin^2\left(\frac{\vartheta_{\rm ion}-\vartheta_{\rm cov}}{2}\right) \tag{3.48}$$

The sine squared factor oscillates rapidly, giving rise to interference figures. However, these interferences are to rapid to survive the integration over impact parameter. This term can be averaged over a period ($\int_0^{2\pi}\sin^2(x)\,{\rm d}x = 1/2$) [153]. The probability of transition under the Laudau-Zener model is

$$P_{\rm tot} = 2\,P_{\rm i,c}\,(1-P_{\rm i,c}) \tag{3.49}$$

This expression is identical to that obtained following the classical description of the model (section 1.2). This description is valid thanks to a purely quantum phenomenon: the free oscillation of the wavefunctions between the two passages through the crossings of the diabatic potentials. Without this effect, the correspondance between classical and quantum description would not be hold!

3.1.4 Effect of the Molecular Symmetries

The previous discussion of the reaction dynamics makes the assumption that there is only one ionic wavefunction. We have made the hypothesis that, when the ions approach each other, there is only one accessible ionic molecular state. Before the electron exchange process, only one ionic state would play a role

in the reaction. But, as stated initially in section 1.4.4, the potential energy curves can be obtained only within a given molecular symmetry k (in the case of the LS coupling, the molecular symmetry is given by the spin S_k, its projection along the internuclear axis m_{Sk}, the projection of the orbital angular momentum $\Lambda_k = |m_{Lk}|$ and the parity p_k of the molecular state). In order to take into account this effect, this section expands the symmetry considerations introducing section 3.1.2.

Before the collision, the atoms are far away from each other, the total wavefunction is an antisymmetrized product of atomic wavefunctions. This total wavefunctions is normalized,

$$\langle \Phi | \Phi \rangle = 1 \tag{3.50}$$

It is not meaningful to define the molecular symmetry $(S_k, m_{S,k}, \Lambda_k)$. The atoms do not have a defined projection of their (L_A, S_A and L_B, S_B) state yet (i.e. if I create an arbitrary projection axis, the (m_L, m_S) distribution would be statistical). When the two atoms approach each other, the molecular symmetries start to be defined (along the internuclear projection axis). If I want to keep the wavefunction normalized, I should split it into all the molecular symmetries $|\psi_{ion,k}\rangle$ whose potential energy curve ends in the ionic $A^+ - B^-$ asymptotic state as

$$|\Phi\rangle = \sum_k a_k |\psi_{ion,k}\rangle \tag{3.51}$$

where k stands for a given $(S_k, m_{S,k}, \Lambda_k)$ combination, $\langle \psi_{ion,k} | \psi_{ion,k'} \rangle = \delta_{k,k'}$ and $\sum_k (a_k)^2 = 1$. This decomposition of the initial wavefunction into several symmetries modifies equation 3.19 [3]:

$$\Phi(t) = \sum_k [a_k C_{\mathrm{ion,k}}(t) \psi_{\mathrm{ion},k} + b_k C_{\mathrm{cov},k}(t) \psi_{\mathrm{cov},k}] \tag{3.52}$$

where we need to obtain b_k in order to retrieve an equation similar to equation 3.23 and 3.24. In order to achieve this, one must recall the following properties

[3] In order to keep the following development clearer, we have made the assumption that there is only one covalent state for each symmetry. If this is not the case, then the equation needs to sum over all the states n of each symmetry k:

$$\Phi(t) = \sum_k \left[a_k C_{\mathrm{ion,k}}(t) \psi_{\mathrm{ion},k} + \sum_n b_{k,n} C_{\mathrm{cov},k,n}(t) \psi_{\mathrm{cov},k,n} \right]$$

This will lead to $b_{k,n} = b_{k,n'}$ for all n and n', i.e., $b_{k,n} = b_{k,n'} = b_k = a_k$, which gives

$$\Phi(t) = \sum_k a_k \left[C_{\mathrm{ion,k}}(t) \psi_{\mathrm{ion}} + \sum_n C_{\mathrm{cov,k,n}}(t) \psi_{\mathrm{cov,k,n}} \right]$$

the same result as the one obtained at the end of this section.

of the molecular symmetries:

$$\begin{cases} \langle \psi_{ion,k} | H | \psi_{ion,k'} \rangle & = E_{ion,k}\delta_{k,k'} \\ \langle \psi_{cov,k} | H | \psi_{ion,k'} \rangle & = E_{ic,k}\delta_{k,k'} \\ \langle \psi_{cov,k} | H | \psi_{cov,k'} \rangle & = E_{cov,k}\delta_{k,k'} \end{cases} \tag{3.53}$$

Using these hypotheses, we can now apply the Schrödinger equation to $\Phi(t)$

$$\left[H - \frac{\hbar}{i}\frac{\partial}{\partial t}\right] \left\{\sum_k \left[a_k C_{\text{ion}}(t)\psi_{\text{ion}} e^{\frac{i}{\hbar}\int_{-\infty}^{t} E_{\text{ion,k}}(t)\ \mathrm{d}t} + b_k C_{\text{cov}}(t)\psi_{\text{cov}} e^{\frac{i}{\hbar}\int_{-\infty}^{t} E_{\text{cov,k}}(t)\ \mathrm{d}t}\right]\right\} = 0 \tag{3.54}$$

This leads to, when projected on any $\langle \phi_{ion,k'} |$ or $\langle \phi_{cov,k'} |$ wavefunction,

$$\begin{aligned} b_k \frac{\hbar}{i}\frac{\partial C_{\text{cov}}}{\partial t}(t) &= a_k E_{\text{ic}} \exp\left\{-\frac{i}{\hbar}\int_{-\infty}^{t}(E_{\text{cov}} - E_{\text{ion}})\,\mathrm{d}t\right\} C_{\text{ion}}(t) \\ a_k \frac{\hbar}{i}\frac{\partial C_{\text{ion}}}{\partial t}(t) &= b_k E_{\text{ic}} \exp\left\{\frac{i}{\hbar}\int_{-\infty}^{t}(E_{\text{cov}} - E_{\text{ion}})\,\mathrm{d}t\right\} C_{\text{cov}}(t) \end{aligned} \tag{3.55}$$

If we choose $b_k = a_k$, the above equation is the same as equations 3.23 and 3.24. This means that, if the above development remains valid, up to equations 3.25 or 3.44, where the transition probability is obtained, those become

$$P_{i,c} = \|a_k C_{cov,k}\|^2 = a_k^2 \|C_{cov,k}\|^2 \tag{3.56}$$

This means that the partial cross section should be multiplied by a factor a_k^2. In the (L,S) coupling case, this factor is given by

$$a_k^2 = \frac{(2S_k+1)}{(2S_{A+}+1)(2S_{B-}+1)} \frac{(\#\Lambda_k)}{(2L_{A+}+1)(2L_{B-}+1)} \tag{3.57}$$

where $\#\Lambda_k$ is the multiplicity of the orbital angular momentum, given by the Wigner-Witmer rules.

It should be noted that this factor comes from the splitting of the initial diatomic wavefunction into several molecular normalized wavefunctions. The meaning of this factor is not the same as the factor obtained in section 3.2.4 which comes from the expression of the molecular wavefunction in terms of several atomic wavefunctions. This explains why the term obtained in this section takes into account only the ionic terms, as the later takes into account both the ionic and the covalent wavefunction.

3.1.5 Cross section

Two-channel Landau-Zener model: Single curve crossing

The equation 3.49 gives the probability of transition from one state to another for a particular trajectory of the pseudo particle. In order to predict the cross section using this model, it is necessary to average over all the possible trajectories.

As the model assumes that there is no preferred orientation between the ions for the reaction (the atoms are not polarized), the angular component is neglected. Thus, the set of incident trajectories is reduced to a uniform distribution on a plane passing through the target particle. These trajectories have an initial speed perpendicular to this plane:

$$\sigma_{LZ} = \int_{\text{plane}} P_{\text{tot}} \tag{3.58}$$

This integral gives the area of this plane for which the reaction takes place: The cross section.

This plane can be expressed according to a coordinate system characterized by the impact position of the incident particle on the plane, if this had not been deflected: the impact parameter b indicates the distance between the impact in the absence of deflection and the angular position ϕ complete the plane.

$$\sigma_{LZ} = \int_0^{2\pi} \mathrm{d}\phi \int_0^{\infty} b\mathrm{d}b P_{\text{tot}} \tag{3.59}$$

$$= 2\pi \int_0^{\infty} b\mathrm{d}b \left[4\, P_{\text{i,c}} \left(1 - P_{\text{i,c}}\right)\, \sin^2\left(\frac{\vartheta_{\text{ion}} - \vartheta_{\text{cov}}}{2} \right) \right] \tag{3.60}$$

where $P_{\text{i,c}}$ is given by 3.28.

Thus, with the assumption that the term

$$\sin^2\left(\frac{\vartheta_{\text{ion}} - \vartheta_{\text{cov}}}{2} \right) \simeq \frac{1}{2} \tag{3.61}$$

is averaged over the set of possible trajectories [4], the cross section becomes (appendix C.1.2):

$$\sigma_{LZ} = 4\pi R_c^2 \left(1 - \frac{V(R_c)}{E_0} \right) \int_1^{\infty} e^{-\zeta x} \left(1 - e^{-\zeta x} \right) \frac{\mathrm{d}x}{x^3}$$

[4] This hypothesis is less restrictive than the one made at the end of section 3.1.3: Each particle has a unique trajectory for a set of given initial conditions. If this assumption turns out to be false, the particle follows all the trajectories simultaneously, they interfere and interference fringes appear in the differential cross section. These interference fringes come from the particle interfering with itself.

In this case, the average is not carried out on a single trajectory, but on all the possible trajectories. This average is applied to all the sets of possible initial conditions. As each set of initial conditions corresponds to a separate event, they do not interfere with each other. The average is thus valid.

$$= 4\pi R_c^2 \left(1 - \frac{V(R_c)}{E_0}\right) G(\zeta) \tag{3.62}$$

where

$$\zeta = \frac{2\pi E_{ic}^2}{\hbar \Delta F v_0 \sqrt{1 - V(R_c)/E_0}} \tag{3.63}$$

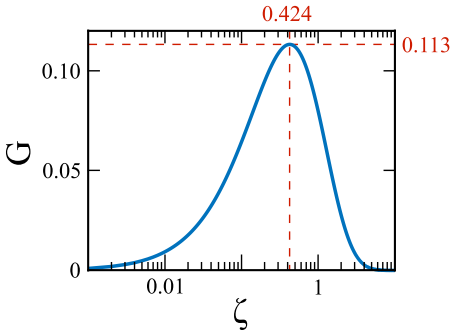

Figure 3.2: Values of the integral $G(\zeta)$ defined in equation 3.62.

The integral $G(\zeta)$ can be solved numerically, and is shown in figure 3.2. This has a maximum when $\zeta = 0.424$, then decreases exponentially to the left and to the right. The evolution of $G(\zeta)$ dominates the variation of the prefactor in the expression of the cross section.

Thus, there is an optimal interaction term for which the cross section is maximum. This is easily explained using the classical expression of the Landau-Zener model. Indeed, as the incident particle passes twice through the crossing between the two potential curves, for the complete reaction to take place, the crossing must be crossed during one passage and be avoided during the other passage. As the interaction potential determines the coupling between two states, it determines the probability of avoiding this crossing. If the interaction potential is too low, the pseudo-molecule remains on its initial diabatic curve. The reaction does not take place. If the interaction potential is too large, then the pseudo-molecule remains on its initial adiabatic curve. The reaction does not take place because of the double exchange.

Likewise, since the integral term dominates the prefactor and the ions are initially subjected to a Coulomb potential ($V \simeq -1/R_c$, $\Delta F \simeq 1/R_c^2$), there exists an optimal crtical distance R_c (see figure 3.3). This interaction distance is most of the time several tens of Bohr radii, far from the equilibrium distance of the molecule. Therefore, it seems reasonable to consider that the potential curves follow their asymptotic forms - constant or Coulomb - during the charge exchange [5]. Similarly, for an initial collision energy and a given interaction

[5] This argument allows to validate – at least partially – the development carried out in section

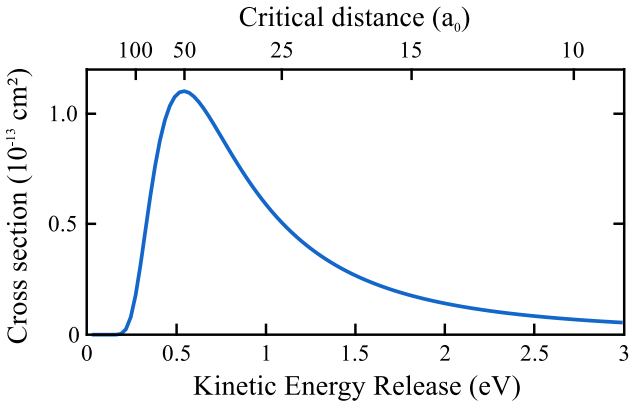

Figure 3.3: Landau-Zener window illustration: Cross section of the mutual neutralization reaction of Li^+ with D^- giving D in its ground state and Li in the configuration 3*s*. The binding energy is adjusted while keeping the interaction term constant in order to modify the interaction distance and the kinetic energy release.

term, there is a window of approximately 1 eV for which the cross section is maximum.

If a final state is accesible for this released kinetic energy, the partial cross section of this state is large. On the other hand, if the binding energy of the final state is outside this window, then its production is much lower [6]. What ultimately controls the reaction probability is the Landau-Zener parameter ζ, the value of which diminishes with radial velocity and increases with the square of the interaction potential. The rapid decrease of the latter with the critical distance R_c sets a maximum distance for the reaction to occur, hence a minimum KER. On the other hand, avoided crossings at short R_c will become more and more diabatic as the collision energy increases, explaining the growing contribution of deeply bound states.

The preceding considerations allow us to understand how it is possible to estimate the atomic states produced during mutual neutralization reactions [7]. This model will be used in order to characterized the total (partial) cross

3.2.

[6] For some mutual neutralization reactions, such as Na^++S^- and C^++Cl^- [26], there is no state within this reaction window (with the neutral atom associated with the anion in its ground state). Therefore, either there exists a state associated with the anion neutralized in an excited state within the Landau-Zener window (Na^++S^-), or the cross section is much smaller (C^++Cl^-).

[7] The passage through several avoided crossings has not yet been taken into account. All covalent states are assumed to be independent. The extension of this model to take into account the combined set of covalent states is described in section 3.1.5. However, this model is no longer analytical.

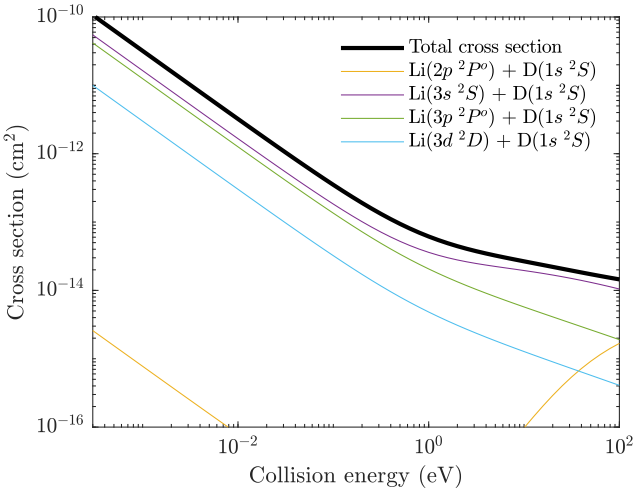

Figure 3.4: Partial (colored curves) and total (black curve) cross sections calculated from the simple Landau-Zener model for the reaction $Li^+ + D^- \rightarrow Li^* + D$.

section at low collision energies in section 3.4.

Multi-state curve crossing model: Multi-state Landau-Zener model

If several covalent states are accessible, it suffices to extend the reasoning developed in section 3.1.3 by including all the states.

If we take the probability of transition from an ionic state to a covalent state given by the equation 3.49:

$$P_1(b) = 2\ p_1(b)\,(1 - p_1(b)) \tag{3.64}$$

where b is the impact parameter, p_1 is the probability of passing from the ionic state to the covalent state 1 (or vice versa) when traversing the crossing and P_1 is the probability that the pseudo-molecule is in the covalent state 1 after the collision.

This result corresponds to the semi-classical vision of the collision represented in figure 3.5: At each crossing between two potential curves, a transition probability is associated. Thus, to obtain the probability that the reaction ends in a given state, it is necessary to sum over all the possible paths through the potential curves of all the states present and to associate a weight with each of these paths. The set of possible paths is described by Cohen [154, 155]. However, simplifying assumptions applied to the potential curves make it possible to greatly limit the possible paths:

As all the potential curves of covalent states are assumed to be constant, they cannot intersect. Therefore, crossings are only possible between the ionic

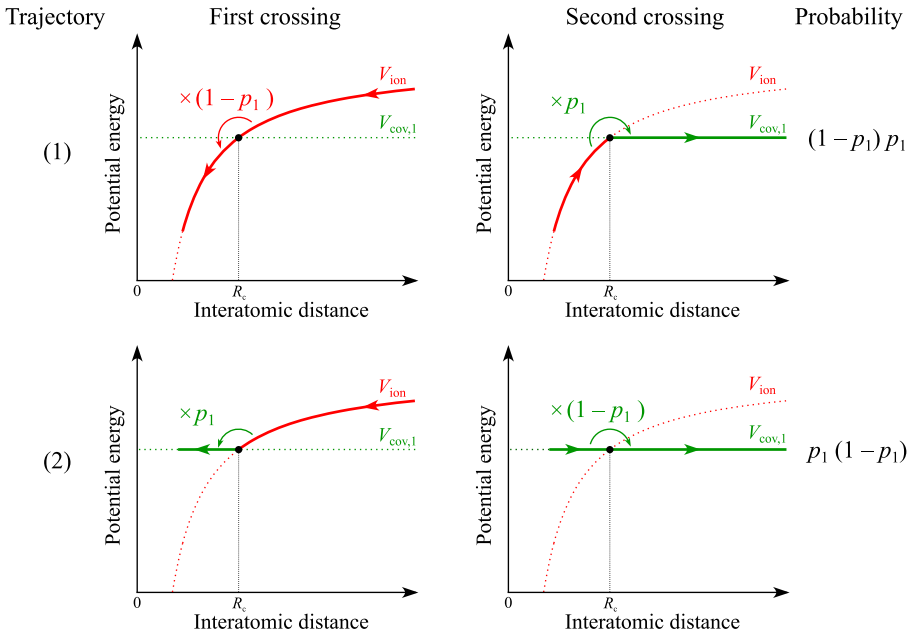

Figure 3.5: Mutual neutralization reaction paths - extended version. Extension of the figure 1.3 representing the two possible trajectories leading to the covalent state.

curve and a covalent curve. If the covalent states are numbered from 1 to N in ascending order of bonding, then it is possible to name p_i the probability of avoiding the crossing between the ionic curve and the i^{th} covalent state.

$$p_i = 1 - \exp\left(-\frac{-2\pi E_{ic}^2(i)}{\hbar v_R(b,i)\Delta F(i)}\right) \tag{3.65}$$

where $E_{ic}(i)$ is the interaction potential between the ionic state and the covalent state i, it should be noted that the radial velocity $v_R(b)$ depends on the impact parameter b.

It is also possible to rename P_i as the probability that the system ends in the i^{th} covalent state after the collision, and obtain (section C.1.3):

$$\begin{aligned} P_i &= \left(\prod_{j=1}^{i}(1-p_j)\right) \times p_i \times \left[1 + p_{i+1}^2 \right. \\ &\quad \left. + \left(\sum_{j=i+1}^{N-1} p_{j+1}^2 \prod_{k=i+1}^{j}(1-p_k)^2\right) + \left(\prod_{j=i+1}^{N}(1-p_j)^2\right)\right] \qquad \text{if } i < N-1 \\ &= \left(\prod_{j=1}^{i}(1-p_j)\right) \times p_i \times \left[1 + p_N^2 + (1-p_N)^2\right] \qquad \text{if } i = N-1 \end{aligned}$$

$$= \left(\prod_{j=1}^{i} (1 - p_j) \right) \times p_i \times 2 \qquad \text{if } i = N \tag{3.66}$$

Therefore, to obtain the partial cross section σ^i_{MLZ} for the state i, it only remains to integrate this transition probability on the appropriate range of impact parameter, in a similar way as for equation 3.59:

$$\sigma^i_{MLZ} = 2\pi \int_0^{b_{max}(i)} P_i(b)\ b \mathrm{d}b \tag{3.67}$$

where the maximum impact parameter $b_{max}(i) = R_c(i)\sqrt{1 - V_i(R_c(i))/E_0}$ is defined following the same logic as in the previous section.

This equation, however, has no analytical solution. However, it is easily integrated using numerical methods [8].

3.1.6 Limitations of the Landau-Zener Model

Before continuing and introducing other concepts, it is important to recall the limitations of the model presented here:

First, the crossings are always between two curves only. To estimate the validity of this hypothesis, we must use the interaction term E_{ic} (equation 3.78). Thus, when the interaction potential of a covalent state is of the order of the difference in energy between two covalent levels, the crossing of a covalent curve with the ionic state implies the crossing with another covalent state.

The estimation of this minimum energy difference between two states is useful only for states whose probability of being populated is not zero. Thus by combining the equation 3.63 with the figure 3.2, the states which have the greatest probability of being populated have an interaction potential whose value is approximately 10^{-3} Hartree. This implies that the states of the molecule may be treated separately when the energy difference between two levels reaches a few tens of meV. Two solutions are then available: Either the states have the same configuration *LS*, in this case, these states are supposed to be mixed, which gives the configuration given by the equation 3.114 [9], either the states come from different terms (or even from different configurations). In such case, it is not possible to correctly process the reaction. It is necessary to carry out a complete calculation of the adiabatic potential energy curves. This

[8] In this case, `trapz` does the job perfectly.

[9] This is also the argument that allows this development. The atomic levels are not given only by the term L and S of the atom, but also of J which is the combination of the two preceding numbers. This treatment – much heavier – is unfortunately necessary for the heaviest atoms presented here (phosphorus, sulfur and neon).

calculation is however much more demanding because of the high sensitivity of the system. This point is discussed in more detail by Launoy *et al.* [51, 156].

Another point to keep in mind is that the partial cross section obtained using the multiple Landau-Zener model is always smaller than that obtained using the two-state Landau-Zener model. This is simply explained: Each state added to the initial (two-state) system generates a potential leakage of the wave function to one of these states which decreases the partial cross section. This is visible in the transition probability equations, since $0 \leq p_j \leq 1$ then

$$\prod_{j=1}^{i-1}(1-p_j) \leq 1 \tag{3.68}$$

and

$$\bar{p}_{i+1}^2 + \left(\sum_{j=i+1}^{N} \bar{p}_{j+1}^2 \prod_{k=i+1}^{j} (1-\bar{p}_k)^2 \right) \leq 1. \tag{3.69}$$

This confirms the previous statement.

This phenomenon implies that if another important process is present (other than mutual neutralization) then the cross section of mutual neutralization decreases. Indeed, this other phenomenon introduces non-negligible escape routes.

Two cases are representative of this leakage phenomenon: $H^+ + H^-$ et $C^+ + Cl^-$. The first case has already been briefly mentioned in the introduction to the experimental methods.

The second case (C^+ + Cl^-) has attracted attention much more recently, with the measurements at the Kirtland Air Force Research Laboratory (AFRL) team in 2019 [26]. It serves as an example for this team to claim that mutual neutralization between two atomic ions is much less likely than mutual neutralization between two molecular ions. Indeed, the cross section of this reaction is much smaller than those measured within this thesis. There are several reasons for this low cross section. The first comes from the anion – chlorine – whose electron affinity is much greater (3.612 eV) than that of the anions studied here (between 0.7 and 1.4 eV). The consequence is that there are fewer states present in the Landau-Zener window. The only state present is $C(2s2p^3\ {}^5S_o) + Cl({}^2P_o)$ whose spin prevents its population. Thus, the only possible states are those which involve the fundamental configuration of neutral carbon (the terms ${}^3P$, ${}^1D$ and ${}^1S$). These states lead to a kinetic energy release greater than 5 eV (figure 3.7).

This has several consequences, on the one hand the reaction takes place at a crossing radius much smaller than usual of 5 to 7 a_0 - figure 3.6. As the distance is very short and the produced states have the same configuration, the interaction potential between the states is very important. Therefore, when the wavefunction arrive near the crossing, the wavefunction tends to remain on

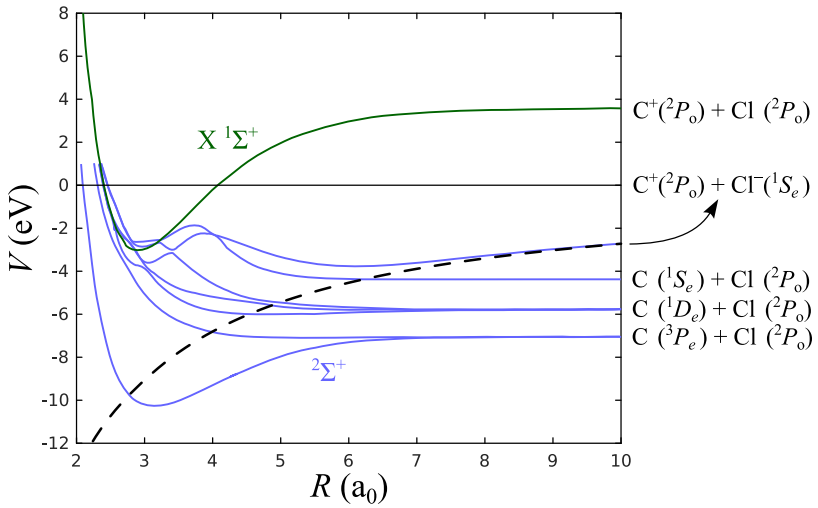

Figure 3.6: Potential curves relating to the mutual neutralization of C^+ with Cl^-. Blue curves: CCl potential in $^2\Sigma^+$ symmetry (normalized to their asymptotic values) [26]. Green curve: ground state potential curve of the CCl^+ ion [157]. Curve in black dashes: $1/R$ potential.

the same adiabatic curve, to avoid the crossing (the probability of changing the diabatic curve is $1-\exp(-aE_{ic})$). Figure 3.7 shows the result of the simulation using the asymptotic model. The signal predicted by this model is about 5 times weaker than the signal predicted for the other reactions studied in this thesis (see chapter 5) [10].

Another important effect linked to this short interaction distance is that of the ionizing association: First, this is energetically permitted. Then, the interaction distance between the potential curves used for mutual neutralization and that of the ground state of the ion CCl^+ extends to 4 a_0. This distance is not much smaller than the interaction distance between the different states of CCl. Therefore, the low probability of mutual neutralization is further reduced by the flight to the ionizing association (multiple Landau-Zener model hypothesis).

Note that this reasoning is valid for most reactions of mutual neutralization between an atomic cation and a negative halogen. In fact, the electronic affinity of halogens is generally greater than that of other atoms. Therefore, during

[10] Note that using the asymptotic model has low predictive power in this case. On the one hand, the approximation that C^0 is in a strongly excited state is no longer valid. It is therefore necessary to modify the normalization term of this wave function.

Then, the interatomic distance is less than 6 a_0, the asymptotic approximation is no longer valid (see the discussion given in the section 3.2.9).

Finally, the interatomic crossing distance is overestimated in the asymptotic model (figure 3.6). This overestimation leads to an underestimation of the interaction potential and therefore an overestimation of the cross section for small interatomic distances.

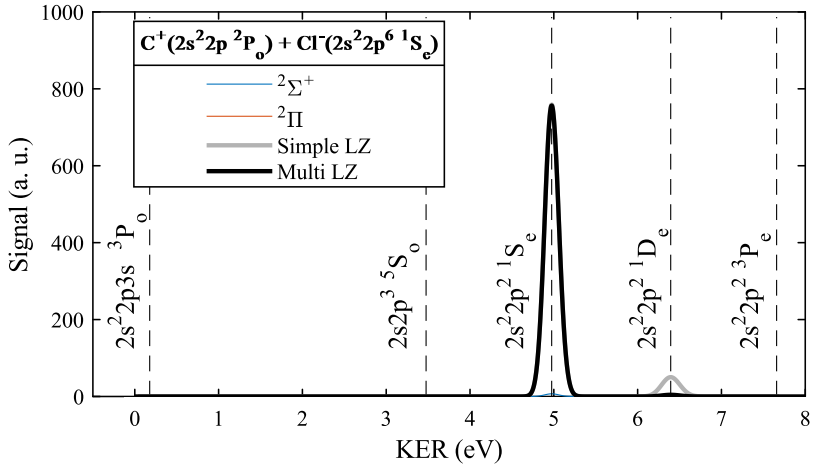

Figure 3.7: Kinetic Energy Released spectrum simulated using the asymptotic method for a relative collision energy of 20 meV. The width of the peaks is generated artificially to correspond to the width obtained experimentally using the device used in Louvain-la-Neuve.

the reaction, the Rydberg series associated with the cation is not energetically accessible [11]. There is then no state within the Landau-Zener window: The cross section is much lower.

Thus, contrary to what the AFRL team affirms [14, 158], there is no reason to think - a priori - that the cross section of mutual neutralization between two atomic ions is weaker than that of two molecular ions [12]. Nevertheless, it is true that molecules have a much greater number of energy levels (vibration and rotation). It is more likely that at least one state is within the Landau-Zener window and maximizes the cross section.

On the other hand, if our multiple Landau-Zener model – combined with an asymptotic exchange model – accurately predicted the partial cross section of each state, this model would only provide an upper bound to the partial cross section. It would then complete the one presented by Le Padellec *et al.* [159] which approximates the equation 3.62 by:

$$\sigma < \frac{\pi}{2} R_c^2 \left(1 + \frac{1}{E_0 R_c}\right) \tag{3.70}$$

[11] The Rydberg series are, in this case, all the states whose are not in the fondamental configuration.

[12] In their explanation, they cite Church & Smith [21] who measured a small cross section for $Ar^+ + Cl^-$. However, in their discussion, Church & Smith indicate – while the cross sections of mutual neutralization between molecules are similar – that the cross section of mutual neutralization between two atomic ions varies greatly depending on the species studied. That is, it is necessary to treat each reaction independently. This argument joins ours (availability of energy levels within the Landau-Zener window), as opposed to the AFRL assertion (the cross section is small for mutual neutralization between two atomic ions).

This model is, on the other hand, perfectly suited to determining the branching ratio between the different product states. Indeed, the Landau-Zener model applied to obtaining the products of the reaction indicates that the states produced must be located within a restricted window of energy levels, i.e. their crossing within a window of restricted interatomic distance. Therefore, assuming that the other processes occur at an interatomic distance outside this window, the modification of the partial cross section induced by those processes is a simple constant factor shared by all the products of the reaction leaving the branching ratio among them unchanged.

3.2 Interaction potential model: Anion Centered Asymptotic Model

3.2.1 Introduction

The probability of transition from one diabatic state to another obtained using the Landau-Zener model (equation 3.28) indicates that this probability depends on the diabatic potential energy curves, the radial velocity between the two atoms, as well as the interaction potential between these two states.

All these parameters can be obtained using advanced numerical methods (such as those described by T. Launoy in his thesis [156]). However, these calculations take time and struggle to accurately reproduce the results obtained experimentally. It is therefore judicious to carry out an estimate of the cross section beforehand.

In the context of mutual neutralization, the radial velocity is easily obtained using the kinematics of the reaction. Likewise, the diabatic potential curve of the ionic state follows that given by the Coulomb potential between A^+ and B^- while the potential curve of the covalent state is assumed to be constant.

The last ingredient to be determined is the interaction potential $E_{\mathrm{i,c}}$. There are several approximate methods to determine this. The chosen method is an asymptotic method (the atoms are far from their position of equilibrium in the molecule) called the Landau-Herring method [149] [13].

This method applies when the critical interatomic distance for which mutual neutralization takes place is much larger than the size of the atomic wavefunction of each of the atoms (on the order of a few a_0) – in practice, this crossing radius is of the order of 10 to 30 a_0. If this condition is satisfied, only the asymptotic component of the wavefunctions is necessary to obtain the interaction term. The same goes for the wavefunctions of the diabatic basis, these are treated here as atomic wavefunctions having undergone a disturbance. The conditions for applying the asymptotic model are explained in detail at the end of the section.

This section therefore sets out to show how to obtain this interaction term

[13] This method is also called the Firsov surface integral method [160], the Holstein-Herring method [161, 162] or the Smirnov method [163].

The development of the method mainly follows that proposed by Janev and Salin [149]

Supplements from various other sources are used in order to clarify the development [83, 109, 160–170]. I would also like to thank Alexander Galstyan for the translation from Russian of the last reference which allowed me to unlock part of the reasoning.

using the asymptotic method [14]:

$$E_{\text{ic}}(R_{\text{c}}) = \langle \psi_{\text{ion}} | H | \psi_{\text{cov}} \rangle \tag{3.71}$$

3.2.2 Surface integral method

To start with, let us take a closed surface S that surrounds the ion A^+, as shown in the figure 3.8. This surface is such that the potential exerted by atom B is negligible compared to the Coulomb potential of the ion A^+. In addition, this surface must be large enough to fully contain the atomic wavefunction of an electron attached to the ion χ_{A^*} [15] and small enough to exclude the atomic wavefunction of the electron attached to the atom χ_B [16]. It is therefore possible to define a volume $\tilde{\mathscr{V}}$ which is outside the surface S.

It is then possible to define the following integral:

$$J \equiv \int_{\tilde{\mathscr{V}}} [\psi_2^* H \psi_1 - \psi_1^* H \psi_2] \, \mathrm{d}\mathscr{V} \tag{3.72}$$

The interest of this method is the possibility of evaluating this integral in two different ways: one makes the interaction term appear, the other evaluates this integral explicitly.

The first evaluation of this integral requires taking into consideration several elements.

First, adiabatic wavefunctions can be re-expressed as a function of diabatic wavefunctions using the equation 3.11, which when inverted gives:

$$\begin{cases} \psi_1 &= +a_1 \psi_{\text{cov}} + a_2 \psi_{\text{ion}} \\ \psi_2 &= -a_2 \psi_{\text{cov}} + a_1 \psi_{\text{ion}} \end{cases} \tag{3.73}$$

Then, since the diabatic wavefunctions are the disturbed atomic wavefunctions, the ion wavefunction $\psi_{\text{ion}} \simeq \chi_{B^-}$ is fully contained within the volume

[14] This detailed demonstration is motivated by several factors:

On the one hand, all the results presented here are the fruit of a development that lasted more than ten years (from the mid-1960s to the end of the 1970s, not to mention the initial development of the principle of Firsov integral). Each published article advances in this theory, taking for granted everything that was said before. A compilation of the whole development is therefore of interest.

In addition, all these posts were intended for an informed audience to whom certain details seem obvious. These "details" sometimes require several pages of mathematical developments calling on the properties of mathematical functions, or of hypotheses not mentioned. Therefore, this complete development includes all the development details and assumptions put in place to arrive at the final result.

Finally, the development detailed in the literature does not take into account the orbital angular momentum of the molecule. The following demonstration adds this element.

A subsection is also reserved to discuss the domain of validity of this model a priori (before comparison with the experimental results).

[15] At least, the wavefunction χ_{A^*} decreases exponentially around this surface.

[16] The wavefunction χ_B decreases exponentially within this surface.

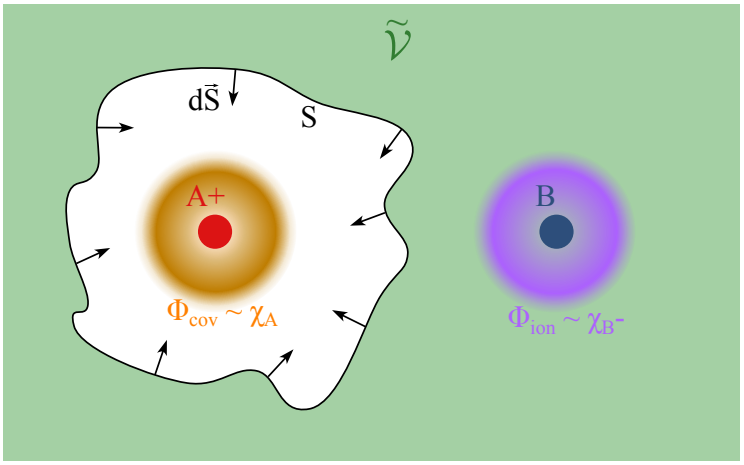

Figure 3.8: Example of volume for integral J. S is the surface whose volume $\tilde{\mathcal{V}}$ is outside. $\mathrm{d}\vec{S}$ is an element of this surface, directed inward. The surface S includes the atomic wavefunction χ_A, but not χ_{B^-}. The volume used in the anion centered asymptotic model is shown in figure 3.9.

$\tilde{V}$. Likewise, the covalent wavefunction $\psi_{\text{cov}} \simeq \chi_A$ is entirely outside the volume $\tilde{\mathcal{V}}$. At least, its contribution will be negligible compared to that of ψ_{ion}. Therefore,

$$\int_{\tilde{\mathcal{V}}} \psi_{\text{ion}}^* \psi_{\text{ion}} \, \mathrm{d}\mathcal{V} \simeq 1 \tag{3.74}$$

$$\int_{\tilde{\mathcal{V}}} \psi_{\text{cov}}^* \psi_{\text{cov}} \, \mathrm{d}\mathcal{V} \simeq 0 \tag{3.75}$$

$$\int_{\tilde{\mathcal{V}}} \psi_{\text{cov}}^* \psi_{\text{ion}} \, \mathrm{d}\mathcal{V} \simeq 0 \tag{3.76}$$

Finally, it is important to remember that since adiabatic wavefunctions are stationary solutions of the Hamiltonian of the system at any point in space – independently of the integral, they satisfy:

$$H\psi_1 = E_1\psi \text{ et } H\psi_2 = E_2\psi_2. \tag{3.77}$$

By taking into account these considerations and the equation 3.17, the integral becomes:

$$\begin{aligned} J &\equiv \int_{\tilde{\mathcal{V}}} [\psi_2^* H\psi_1 - \psi_1^* H\psi_2] \, \mathrm{d}\mathcal{V} \\ &= \int_{\tilde{\mathcal{V}}} [\psi_2^* E_1\psi_1 - \psi_1^* E_2\psi_2] \, \mathrm{d}\mathcal{V} \\ &= (E_1 - E_2) \int_{\tilde{\mathcal{V}}} \psi_1^* \psi_2 \, \mathrm{d}\mathcal{V} \end{aligned}$$

$$
\begin{aligned}
&= (E_1 - E_2) \times \\
&\times \int_{\tilde{\mathscr{V}}} \Big[-a_1 a_2 \overbrace{\psi^*_{\text{cov}} \psi_{\text{cov}}}^{=0} + a_1^2 \overbrace{\psi^*_{\text{cov}} \psi_{\text{ion}}}^{=0} - a_2^2 \overbrace{\psi^*_{\text{ion}} \psi_{\text{cov}}}^{=0} + a_2 a_1 \overbrace{\psi^*_{\text{ion}} \psi_{\text{ion}}}^{=1} \Big] \, \mathrm{d}\mathscr{V} \\
&= (E_1 - E_2) a_1 a_2 \\
&= E_{\text{i,c}} = \frac{\Delta}{2}
\end{aligned}
\tag{3.78}
$$

Now that the integral given by J is directly related to the interaction potential, it remains to find a method to simplify its explicit evaluation (discussed in appendix C.2.1). Once it is done, one obtains:

$$
J = \frac{1}{2} \oint_S \left(\psi^*_{\text{ion}} \vec{\nabla} \psi_{\text{cov}} - \psi^*_{\text{cov}} \vec{\nabla} \psi_{\text{ion}} \right) \cdot \, \mathrm{d}\vec{S}
\tag{3.79}
$$

where the infinitesimal elements $\mathrm{d}\vec{S}$ are directed towards the interior of the volume $\tilde{V}$.

Thus, by combining equation 3.78 and equation 3.79, the interaction term can be calculated according to the following surface integral

$$
E_{\text{i,c}} = \frac{1}{2} \oint_S \left(\psi^*_{\text{ion}} \vec{\nabla} \psi_{\text{cov}} - \psi^*_{\text{cov}} \vec{\nabla} \psi_{\text{ion}} \right) \cdot \, \mathrm{d}\vec{S}
\tag{3.80}
$$

Now that an equation has been found to determine the interaction term, it remains to determine which diabatic wavefunctions to use, as well as the surface on which to integrate these wavefunctions.

3.2.3 Definition of the surface to integrate

If we take as integration surface a sphere centered around the atom B (figure 3.9), and we integrate according to the spherical coordinates centered around this atom $(r_B, \theta_B, \varphi_B)$ (figure 3.10), then only the radial component of the gradient will be non-zero.

$$
E_{\text{i,c}} = \frac{1}{2} \int_{-1}^{1} \mathrm{d}\cos\theta_B \int_0^{2\pi} \mathrm{d}\varphi_B \, r_B^2 \left(\psi^*_{\text{ion}} \frac{\mathrm{d}}{\mathrm{d}r_B} \psi_{\text{cov}} - \psi^*_{\text{cov}} \frac{\mathrm{d}}{\mathrm{d}r_B} \psi_{\text{ion}} \right)
\tag{3.81}
$$

Moreover, in order to simplify the notation, it is useful to introduce the Wronskian [171, §1.13]

$$
\mathscr{W}\big[f(r), g(r)\big] = f'(r) g(r) - f(r) g'(r)
\tag{3.82}
$$

whose properties are used later.

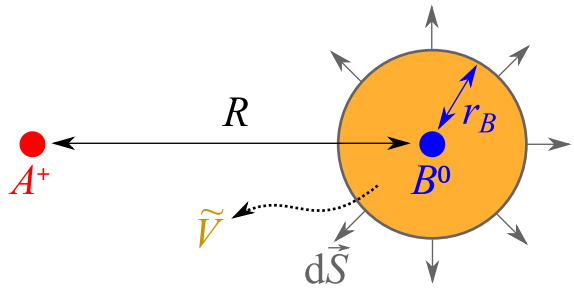

Figure 3.9: Representation of the spherical volume integral used in the anion center asymptotic model.

So, since the phase of ψ_{ion} and the phase of ψ_{cov} are chosen to take a real value, then:

$$E_{\text{i,c}} = \frac{1}{2}\int_{-1}^{1} \mathrm{d}\cos\theta_B \int_0^{2\pi} \mathrm{d}\varphi_B \left\{ r_B^2 \mathscr{W}\left[\psi_{\text{ion}}, \psi_{\text{cov}}\right]\right\} \tag{3.83}$$

It only remains to determine the radius r_B of this sphere. However, its value does not matter. Indeed, the result of the integration does not depend on the radius, as long as the approximations stated in the remainder of the text are valid. The reason for the validity of this choice is given below.

3.2.4 One-electron exchange approximation

The surface integral applies to the entirety of the molecular wavefunctions of the ionic state and of the covalent state. Solving for the entirety of each of the wavefunctions is a complex operation. It requires: taking into account all the electrons – located around each atom in each of the possible configurations –, calculating the total electron wavefunction, obtaining the potential energy curve of each possible molecular state as well that the interaction potential between each state at each interatomic distance up to large distances. This operation must be repeated for each molecular symmetry Λ, S of the molecule (the quantum numbers that describe the state of a molecule). Thus, even if this calculation is theoretically possible, it is only possible in practice for simple systems (such as Li-H [51]).

To get around this problem, the idea is to consider that the interaction between the two wavefunctions occurs only through the exchange of a single electron. This electron is a valence electron whose configuration is well determined [17]. This approximation makes it possible to rewrite the reaction

$$[A^+ + B^-]_{\Lambda,S} \rightarrow [A^0 + B^0]_{\Lambda,S} \tag{3.84}$$

[17] Although this approximation is not fully valid, it makes it possible to obtain a first quali-

as

$$[A^+_{L,S} + (B^0_{L',S'} + e^-_{l,s})_{L'',S''}]_{\Lambda,S} \rightarrow [(A^+_{L,S} + e^-_{l,s})_{L''',S'''} + B^0_{L',S'}]_{\Lambda,S} \tag{3.85}$$

where the quantum numbers indicated in subscript are the quantum numbers describing each component of the reaction. As the pair of atoms forms a diatomic molecule, a projection axis is formed for each angular momentum in the molecule. This axis defines the projection axis of each projection m_L, m_l, m_S and m_s associated with the orbital quantum numbers L and l as well as the spin quantum numbers S and $s = 1/2$.

These quantum numbers are defined as follows for each component (for open-shell systems):

$$A^+ : (n_{A+}l_{A+})^{N_{A+}\ \ 2S_{A+}+1}L_{A+} \tag{3.86}$$

$$B^- : (n_{B-}l_{B-})^{N_{B-}\ \ 2S_{B-}+1}L_{B-} \tag{3.87}$$

$$A^0 : (n_{A0}l_{A0})^{N_{A0}\ \ 2S_{A0}+1}L_{A0} \tag{3.88}$$

$$B^0 : (n_{B0}l_{B0})^{N_{B0}\ \ 2S_{B0}+1}L_{B0} \tag{3.89}$$

$$AB :\ ^{2S_{mo}+1}\Lambda \tag{3.90}$$

where $\Lambda = |m_{Lmo}| = |\tilde{\Lambda}|$, $(n_i l_i)^{N_i}$ is the electronic configuration of the outer shell of the atom i. If $N_{A0} > 0$, then $N_{A+} = N_{A0} - 1$, $l_{A+} = l_{A0}$ and $n_{A+} = n_{A0}$. If $N_{B-} > 0$, then $N_{B0} = N_{B-} - 1$, $l_{B0} = l_{B-}$ and $n_{B0} = n_{B-}$.

Likewise, the electron e^-_A attached to A^+ and the one e^-_B attached to B^0 have their quantum numbers defined as:

$$e^-_A : (n_{A0}; l_{A0}, m_{lA0}; 1/2, m_{sA0}) \tag{3.91}$$

$$e^-_B : (n_{B-}; l_{B-}, m_{lB-}; 1/2, m_{sB-}) \tag{3.92}$$

Their binding energies $\gamma^2_{A0}/2$ and $\gamma^2_{B-}/2$ are defined as (figure 5.1):

$$\frac{\gamma^2_{A0}}{2} = IP(A^0) + E_{\text{lev}}(A^+) - E_{\text{lev}}(A^0) \tag{3.93}$$

$$\frac{\gamma^2_{B-}}{2} = EA(B^0) + E_{\text{lev}}(B^0) - E_{\text{lev}}(B^-) \tag{3.94}$$

where IP is the ionization potential, $EA > 0$ is the electron affinity and E_{lev} is the level energy.

The remainder of the discussion sets out to isolate the wavefunctions of the exchanged electron ϕ_{ion} and ϕ_{cov} within the complete wavefunctions of the molecule ψ_{ion} and ψ_{cov}.

tative result of the branching ratios. Possible extensions of the model are described in sections 5.4.1 and 5.2.3.

Total wavefunction of the ionic state

The wavefunction of the ionic state is characterized by

$$|\psi_{ion}(\Lambda,S)\rangle = |\bar{\eta}_{A+},L_{A+},S_{A+};\bar{\eta}_{B-},L_{B-},S_{B-};\Lambda_{ion},S_{ion}\rangle \tag{3.95}$$

with $\bar{\eta}_{A+}$ and $\bar{\eta}_{B-}$ the set of other quantum numbers which characterize the ions A^+ and B^-.

However, even though L_{ion} and m_{Sion} are not quantum numbers that define the energy associated with the wavefunction, they form degenerate states of the system. Likewise, it is easier to work with the signed projection of the orbital angular momentum $\tilde{\Lambda}_{ion} = m_{Lion} = \pm\Lambda_{ion}$. It is always possible to sum over these states (omitting to $\bar{\eta}_{A+}$ and $\bar{\eta}_{B-}$ for better readability):

$$\begin{aligned}|\psi_{ion}(\Lambda_{ion},S_{ion})\rangle =& \frac{1}{\sqrt{\#m_{Sion}}}\sum_{m_{Sion}=-S_{ion}}^{S_{ion}}\frac{1}{\sqrt{\#\tilde{\Lambda}_{ion}}}\sum_{\tilde{\Lambda}_{ion}}\frac{1}{\sqrt{\#L_{ion}}}\sum_{L_{ion}}\times \\ &\times\left|L_{A+},S_{A+};L_{B-},S_{B-};L_{ion},\tilde{\Lambda}_{ion},S_{ion},m_{Sion}\right\rangle\end{aligned} \tag{3.96}$$

where $\#m_{Sion} = 2S_{ion}+1$ is the number of m_{Sion} leading to S_{ion}, $\#\tilde{\Lambda}_{ion} = 1,2$ is the number of $\tilde{\Lambda}_{ion}$ leading to Λ_{ion} and $\#L_{ion}$ is the number L_{ion} leading to Λ_{ion} which is given by the Wigner-Witmer rule (appendix C.2.3).

The diatomic wavefunction of the ionic state, when the interatomic distance is large, is then expressed as [153, Eq. 3.22]:

$$\begin{aligned}&\left|L_{A+},S_{A+};L_{B-},S_{B-};L_{ion},\tilde{\Lambda}_{ion},S_{ion},m_{Sion}\right\rangle \\ &=\hat{A}_{ion}\sum_{m_{LA+},m_{LB-}}\sum_{m_{SA+},m_{SB-}}\begin{bmatrix}L_{A+} & L_{B-} & L_{ion}\\ m_{LA+} & m_{LB-} & \tilde{\Lambda}_{ion}\end{bmatrix}\begin{bmatrix}S_{A+} & S_{B-} & S_{ion}\\ m_{SA+} & m_{SB-} & m_{Sion}\end{bmatrix} \\ &\left|(n_{A+}l_{A+})^{N_{A+}};S_{A+},m_{SA+},L_{A+},m_{LA+}\right\rangle\left|(n_{B-}l_{B-})^{N_{B-}};S_{B-},m_{SB-},L_{B-},m_{LB-}\right\rangle\end{aligned} \tag{3.97}$$

where $\begin{bmatrix}j_1 & j_2 & j_3\\ m_1 & m_2 & m_3\end{bmatrix}$ are the Clebsch-Gordan coefficients and $\hat{A}$ is the antisymmetrization operator, the processing of which is described in detail in the subsection C.2.4.

As the exchanged electron is attached to the negative ion, the ion wavefunction is decomposed, according to [153, eq3.9]:

$$\begin{aligned}&\left|(n_{B-}l_{B-})^{N_{B-}};S_{B-},m_{SB-},L_{B-},m_{LB-}\right\rangle = \sum_{S_{B0},L_{B0}}(-1)^{N_{B0}}G^{S_{B-},L_{B-}}_{S_{B0},L_{B0}} \\ &\sum_{m_{SB0},m_{sB-}}\sum_{m_{LB0},m_{lB-}}\begin{bmatrix}S_{B0} & s_{B-} & S_{B-}\\ m_{SB0} & m_{sB-} & m_{SB-}\end{bmatrix}\begin{bmatrix}L_{B0} & l_{B-} & L_{B-}\\ m_{LB0} & m_{lB-} & m_{LB-}\end{bmatrix} \\ &\left|(n_{B0}l_{B0})^{N_{B0}};S_{B0},m_{SB0},L_{B0},m_{LB0}\right\rangle\left|\phi^{l_{B-},m_{lB-}}_{ion}(\vec{r}_B)\right\rangle\left|\chi^{s_{B-}=1/2}_{m_{sB-}}(\vec{\sigma}_B)\right\rangle\end{aligned} \tag{3.98}$$

where $G^{S_k L_k}_{\sigma_k \lambda_k}$ are the coefficients of fractional parentage. These have been defined in [172–175] and tabulated - for example - in [176].

Total wavefunction of the covalent state

In the same way as above, the wavefunction of the covalent state is characterized by:

$$|\psi_{cov}(\Lambda, S)\rangle = |\bar{\eta}_{A0}, L_{A0}, S_{A0}; \bar{\eta}_{B0}, L_{B0}, S_{B0}; \Lambda_{cov}, S_{cov}\rangle \tag{3.99}$$

with $\bar{\eta}_{A0}$ and $\bar{\eta}_{B0}$ the set of all the other quantum numbers which characterize the ions A^0 and B^0.

However, even though L_{cov} and m_{Scov} are not quantum numbers that define the energy associated with the wavefunction, they form degenerate states of the system. Likewise, it is easier to work with the signed projection of the orbital angular momentum $\tilde{\Lambda}_{cov} = m_{Lcov} = \pm\Lambda_{cov}$. Therefore, to facilitate the development, it is possible to sum over these states (omitting to $\bar{\eta}_{A0}$ and $\bar{\eta}_{B0}$ for better readability):

$$\begin{aligned}|\psi_{cov}(\Lambda_{cov}, S_{cov})\rangle = &\frac{1}{\sqrt{\#m_{Scov}}} \sum_{m_{Scov}=-S_{cov}}^{S_{cov}} \frac{1}{\sqrt{\#\tilde{\Lambda}_{cov}}} \sum_{\tilde{\Lambda}_{cov}} \frac{1}{\sqrt{\#L_{cov}}} \sum_{L_{cov}} \times \\ &\times \left|L_{A0}, S_{A0}; L_{B0}, S_{B0}; L_{cov}, \tilde{\Lambda}_{cov}, S_{cov}, m_{Scov}\right\rangle \end{aligned} \tag{3.100}$$

where $\#m_{Scov} = 2S_{cov} + 1$ is the number of m_{Scov} leading to S_{cov}, $\#\tilde{\Lambda} = 1, 2$ is the number of $\tilde{\Lambda}_{cov}$ leading to Λ_{cov}, and $\#L_{cov}$ is the number L_{cov} leading to Λ_{cov} which is given by the Wigner-Witmer rule (appendix C.2.3).

The diatomic wavefunction of a covalent state, when the interatomic distance is large, is then expressed as [153, eq3.22]:

$$\begin{aligned}&\left|L_{A0}, S_{A0}; L_{B0}, S_{B0}; L_{cov}, \tilde{\Lambda}_{cov}, S_{cov}, m_{Scov}\right\rangle \\ &= \hat{A}_{cov} \sum_{m_{LA0}, m_{LB0}} \sum_{m_{SA0}, m_{SB0}} \begin{bmatrix} L_{A0} & L_{B0} & L_{cov} \\ m_{LA0} & m_{LB0} & \tilde{\Lambda}_{cov} \end{bmatrix} \begin{bmatrix} S_{A0} & S_{B0} & S_{cov} \\ m_{SA0} & m_{SB0} & m_{Scov} \end{bmatrix} \\ &\left|(n_{A0} l_{A0})^{N_{A0}}; S_{A0}, m_{SA0}, L_{A0}, m_{LA0}\right\rangle \left|(n_{B0} l_{B0})^{N_{B0}}; S_{B0}, m_{SB0}, L_{B0}, m_{LB0}\right\rangle \end{aligned} \tag{3.101}$$

As the exchanged electron is attached to the atom A^0, the wavefunction of this atom is decomposed, according to [153, eq3.9]:

$$\begin{aligned}&\left|(n_{A0} l_{A0})^{N_{A0}}; S_{A0}, m_{SA0}, L_{A0}, m_{LA0}\right\rangle = \sum_{S_{A+}, L_{A+}} (-1)^{N_{A+}} G^{S_{A0}, L_{A0}}_{S_{A+}, L_{A+}} \\ &\sum_{m_{SA+}, m_{sA0}} \sum_{m_{LA+}, m_{lA0}} \begin{bmatrix} S_{A+} & s_{A0} & S_{A0} \\ m_{SA+} & m_{sA0} & m_{SA0} \end{bmatrix} \begin{bmatrix} L_{A+} & l_{A0} & L_{A0} \\ m_{LA+} & m_{lA0} & m_{LA0} \end{bmatrix}\end{aligned}$$

$$\left|(n_{A+}l_{A+})^{N_{A+}};S_{A+},m_{SA+},L_{A+},m_{LA+}\right\rangle \left|\varphi_{cov}^{l_{A0},m_{lA0}}(\vec{r}_A)\right\rangle \left|\chi_{m_{sA0}}^{s_{A0}=1/2}(\vec{\sigma}_A)\right\rangle \tag{3.102}$$

Combination of the two wavefunctions

Thus, the wavefunction of the ionic state (for a given symmetry) is obtained by inserting equation 3.98 in equation 3.97. Similarly, the wavefunction of the covalent state is obtained by inserting equation 3.102 into equation 3.101.

Therefore, it is possible to combine these two results in the Firsov integral 3.80 and re-express the interaction potential for a given symmetry:

$$E_{ic}(\Lambda_{mo},S_{mo}) = -\frac{1}{2}\oint\left(\psi_{ion}\vec{\nabla}\psi_{cov} - \psi_{cov}\vec{\nabla}\psi_{ion}\right)\cdot\mathrm{d}\vec{S} \tag{3.103}$$

Before continuing, it is useful to detail the action of this integral on the two wavefunctions: This integral applies to a spherical surface centered around the atom B. This sphere is large enough that the wavefunction of the exchanged electron is exponentially decreasing. This means that the core electrons – better localized around each atom – have an almost zero (therefore constant) wavefunction around the integrated surface. Thus the gradient of the wavefunction only applies to the exchanged electron:

$$\vec{\nabla}\psi_{ion}(\Lambda,S) = \vec{\nabla}\left(\sum_i A_i\phi_{ion,i}^{l_B,m_B}\right) = \sum_i A_i\vec{\nabla}\phi_{ion,i}^{l_B,m_B} \tag{3.104}$$

where the index i designates the set of combinations of quantum numbers presented above and the factor A_i which combines all the factors linked to this combination (other wavefunctions included).

A similar reasoning also applies for the wavefunction of the covalent state:

$$\vec{\nabla}\psi_{cov}(\Lambda,S) = \vec{\nabla}\left(\sum_i A_i'\phi_{cov,i}^{l_A,m_A}\right) = \sum_i A_i'\vec{\nabla}\phi_{cov,i}^{l_A,m_A} \tag{3.105}$$

Thus, all the other wavefunctions can be taken out of the integral and make it possible to define a reduced interaction potential:

$$\tilde{E}_{ic}(l_A,l_B,m_A,m_B) = -\frac{1}{2}\oint\left(\phi_{ion}^{l_B,m_B}\vec{\nabla}\phi_{cov}^{l_A,m_A} - \phi_{cov}^{l_A,m_A}\vec{\nabla}\phi_{ion}^{l_B,m_B}\right)\cdot\mathrm{d}\vec{S} \tag{3.106}$$

with $l_A = l_{A0}$, $l_B = l_{B-}$, $m_A = m_{lA0}$ and $m_B = m_{lB-}$.

Moreover, by application of the antisymmetrization operators:

$$\left\langle(S_{A+},m_{SA+},L_{A+},m_{LA+})\,(S_{B0},m_{SB0},L_{B0},m_{B0})\left(\chi_{m_{sA0}}^{s_{A0}=1/2}\phi_{ion}^{l_B,m_B}\right)\right| \times$$
$$\times\hat{A}_{ion}\times H\times\hat{A}_{cov}\times$$

$$\times \left| \left(S'_{A+}, m'_{SA+}, L'_{A+}, m'_{LA+}\right) \left(S'_{B0}, m'_{SB0}, L'_{B0}, m'_{LB0}\right) \left(\chi^{s_{B-}=1/2}_{m_{sB-}} \phi^{l_A, m_A}_{cov}\right) \right\rangle$$

$$=$$

$$A_{antisym} \times$$

$$\left\langle \left(S_{A+}, m_{SA+}, L_{A+}, m_{LA+}\right) \left(S_{B0}, m_{SB0}, L_{B0}, m_{B0}\right) \left(\chi^{s_{A0}=1/2}_{m_{sA0}} \phi^{l_B, m_B}_{ion}\right) \right| \times$$

$$\times H \times$$

$$\times \left| \left(S'_{A+}, m'_{SA+}, L'_{A+}, m'_{LA+}\right) \left(S'_{B0}, m'_{SB0}, L'_{B0}, m'_{LB0}\right) \left(\chi^{s_{B-}=1/2}_{m_{sB-}} \phi^{l_A, m_A}_{cov}\right) \right\rangle \tag{3.107}$$

where

$$A_{antisym} = \sqrt{N_{A0} N_{B-}} \tag{3.108}$$

is a factor given by the antisymmetrization. This factor is established in section C.2.4.

It is then easy to apply the following orthogonality rules:

$$\begin{aligned} &\left\langle \bar{\eta}_{A+}; S_{A+}, m_{SA+}, L_{A+}, m_{LA+} | \bar{\eta}'_{A+}; S'_{A+}, m'_{SA+}, L'_{A+}, m'_{LA+} \right\rangle \\ &\quad = \delta_{\bar{\eta}_{A+}, \bar{\eta}'_{A+}} \delta_{L_{A+}, L'_{A+}} \delta_{m_{LA+}, m'_{LA+}} \delta_{S_{A+}, S'_{A+}} \delta_{m_{SA+}, m'_{SA+}} \end{aligned} \tag{3.109}$$

$$\begin{aligned} &\left\langle \bar{\eta}_{B0}; S_{B0}, m_{SB0}, L_{B0}, m_{B0} | \bar{\eta}'_{B0}; S'_{B0}, m'_{SB0}, L'_{B0}, m'_{LB0} \right\rangle \\ &\quad = \delta_{\bar{\eta}_{B0}, \bar{\eta}'_{B0}} \delta_{L_{B0}, L'_{B0}} \delta_{m_{LB0}, m'_{LB0}} \delta_{S_{B0}, S'_{B0}} \delta_{m_{SB0}, m'_{SB0}} \end{aligned} \tag{3.110}$$

$$\left\langle \chi^{s_{A0}=1/2}_{m_{sA0}}(\vec{\sigma}_A) | \chi^{s_{B-}=1/2}_{m_{sB-}}(\vec{\sigma}_B) \right\rangle = \delta_{s_{A0}, s_{B-}} \delta_{m_{sA0}, m_{sB-}} \tag{3.111}$$

Therefore, the interaction term is written

$$\begin{aligned} &E_{ic}(\Lambda_{mo}, S_{mo}) \\ &= (-1)^{N_{A+}+N_{B0}} \quad G^{SA0,LA0}_{SA+,LA+} \; G^{SB-,LB-}_{SB0,LB0} A_{antisym} \\ &\times \sum_{\substack{m_{SA+}, m_{SB0} \\ m_{SA0}, m_{SB-} \\ m_s, m_{Smo}}} \begin{bmatrix} S_{A+} & 1/2 & S_{A0} \\ m_{SA+} & m_s & m_{SA0} \end{bmatrix} \begin{bmatrix} S_{A0} & S_{B0} & S_{mo} \\ m_{SA0} & m_{SB0} & m_{Smo} \end{bmatrix} \\ &\quad \frac{1}{2S_{mo}+1} \begin{bmatrix} S_{B0} & 1/2 & S_{B-} \\ m_{SB0} & m_s & m_{SB-} \end{bmatrix} \begin{bmatrix} S_{A+} & S_{B-} & S_{mo} \\ m_{SA+} & m_{SB-} & m_{Smo} \end{bmatrix} \\ &\times \sum_{\tilde{\Lambda}, L_{ion}, L_{cov}} \sum_{\substack{m_{LA+}, m_{LB0} \\ m_{LA0}, m_{lA0} \\ m_{LB-}, m_{lB-}}} \begin{bmatrix} L_{A+} & l_{A0} & L_{A0} \\ m_{LA+} & m_{lA0} & m_{LA0} \end{bmatrix} \begin{bmatrix} L_{B0} & l_{B-} & L_{B-} \\ m_{LB0} & m_{lB-} & m_{LB-} \end{bmatrix} \\ &\quad \frac{1}{\sqrt{\#L_{ion}}\sqrt{\#L_{cov}}} \begin{bmatrix} L_{A0} & L_{B0} & L_{cov} \\ m_{LA0} & m_{LB0} & \tilde{\Lambda} \end{bmatrix} \begin{bmatrix} L_{A+} & L_{B-} & L_{ion} \\ m_{LA+} & m_{LB-} & \tilde{\Lambda} \end{bmatrix} \\ &\times \tilde{E}_{ic}(l_A, l_B, m_A, m_B) \end{aligned} \tag{3.112}$$

It is possible to simplify the spin terms using angular momentum algebra identities (appendix C.2.2), and to isolate the sums on L_{ion} and L_{cov}. This gives [18]:

$$
\begin{aligned}
&E_{ic}(\Lambda_{mo}, S_{mo}) \\
&= (-1)^{N_{A+}+N_{B0}} \quad G^{SA0,LA0}_{SA+,LA+} \; G^{SB-,LB-}_{SB0,LB0} A_{antisym} \\
&\times (-1)^{S_{mo}+S_{A+}+S_{B-}} \left[(2S_{A0}+1)(2S_{B-}+1)\right]^{1/2} \left\{ \begin{array}{ccc} S_{A+} & 1/2 & S_{A0} \\ S_{B0} & S_{mo} & S_{B-} \end{array} \right\} \\
&\times \sum_{\tilde{\Lambda}} \sum_{\substack{m_{LA+},m_{LB0} \\ m_{LA0},m_{lA0} \\ m_{LB-},m_{lB-}}} \left[\begin{array}{ccc} L_{A+} & l_{A0} & L_{A0} \\ m_{LA+} & m_{lA0} & m_{LA0} \end{array} \right] \left[\begin{array}{ccc} L_{B0} & l_{B-} & L_{B-} \\ m_{LB0} & m_{lB-} & m_{LB-} \end{array} \right] \\
&\qquad \times \left(\frac{1}{\sqrt{\#L_{ion}}} \sum_{L_{ion}} \left[\begin{array}{ccc} L_{A+} & L_{B-} & L_{ion} \\ m_{LA+} & m_{LB-} & \tilde{\Lambda} \end{array} \right] \right) \\
&\qquad \times \left(\frac{1}{\sqrt{\#L_{cov}}} \sum_{L_{cov}} \left[\begin{array}{ccc} L_{A0} & L_{B0} & L_{cov} \\ m_{LA0} & m_{LB0} & \tilde{\Lambda} \end{array} \right] \right) \\
&\times \tilde{E}_{ic}(l_A, l_B, m_A, m_B)
\end{aligned}
\tag{3.114}
$$

3.2.5 Electron wavefunction for the covalent state

Now that the wavefunctions of the isolated electron (the exchanged electron) of the ionic state and of the covalent state are extracted from the molecular wavefunctions, it remains to obtain a development of these mono-electronic wavefunctions which are asymptotically "exact".

[18] Janev obtains a similar result, however, since this development is not published it is only possible to make assumptions about his method of resolution. This resolution is cited as "Janev 1973 (unpublished)" [89, 163].

$$
\begin{aligned}
\Delta = A_S \sqrt{N_{A0} N_{B-}} \sqrt{(2L_{A0}+1)(2L_{B-}+1)} \quad & G^{SA0,LA0}_{SA+,LA+} G^{SB-,LB-}_{SB0,LB0} \\
\times \sum_{m_l} (-1)^{(l_{A0}-L_{A+}-m_{LA0})+(l_{B-}-L_{B0}-m_{B0}-m_{lB0})} \quad & \Delta_{m_l} \\
\left(\begin{array}{ccc} l_{A0} & L_{A+} & L_{A0} \\ m_{lA0} & m_{LA0}-m_{lA0} & -m_{LA0} \end{array} \right) & \left(\begin{array}{ccc} l_{B-} & L_{B0} & L_{B-} \\ m_{lB-} & m_{LB0} & -(m_{LB0}+m_{lB-}) \end{array} \right)
\end{aligned}
\tag{3.113}
$$

where

$$
A_S = (-1)^{S_{mo}+S_{A+}+S_{B0}+1/2} \sqrt{(2S_{A0}+1)(2S_{B-}+1)} \left\{ \begin{array}{ccc} S_{A+} & 1/2 & S_{A0} \\ S_{B0} & S_{mo} & S_{B-} \end{array} \right\}
$$

with $\left(\begin{smallmatrix} j_1 & j_2 & j_3 \\ m_1 & m_2 & m_3 \end{smallmatrix}\right)$ the Wigner 3-j symbols and $m_l = m_{lA0} = m_{lB-}$ is due to a selection rule within Δ_{m_l}.

The main difference between the equations 3.114 and 3.113 is that Janev did not take into account the orbital molecular symmetry in its formula.

When the two atoms A^+ and B are far from each other, the wavefunction of the covalent state is approximately the atomic wavefunction of the electron attached to the ion A^+. As this wavefunction will be evaluated on a sphere centered around the atom B, a change of reference frame must be made. Thus, when the two atoms are far from each other, the wavefunction of the covalent state around the atom B is approximately the atomic wavefunction of the atom A in an excited state, disturbed by the potential of the atom B.

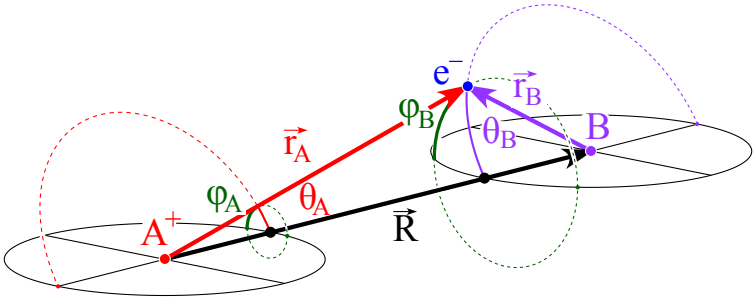

Figure 3.10: Representation of the spherical coordinates used.

Therefore, the first step is to no longer express the covalent wave function according to the coordinate $\vec{r}_A$, but according to $\vec{r}_B$ (see figure 3.10):

$$\vec{r}_A = \vec{R} + \vec{r}_B \tag{3.115}$$

where the position vectors are expressed in spherical coordinates as $\vec{r}_A = (r_A, \theta_A, \varphi_A)$, $\vec{R} \simeq (R, \theta_A, \varphi_A)$ and $\vec{r}_B = (r_B, \theta_B, \varphi_B)$.

Therefore, the wavefunction becomes:

$$\phi_{\text{cov}}(\vec{r}_A) = \phi_{\text{cov}}(\vec{R} + \vec{r}_B) \tag{3.116}$$

The idea is to separate the wavefunction of the covalent state according to a term which depends only on the interatomic distance, and a term which depends only on the distance from the second atom.

Separation of atomic and perturbative components

The first term is, asymptotically, that of the atomic orbital χ_A while the second will be developed in the basis of spherical harmonics.

When $R >> R_B$, the distance of a point from the ion A^+ is approximately [84, 85] (Al Kaschi theorem):

$$r_A = \sqrt{R^2 - 2 r_B R \cos\theta_B + r_B^2} \sim R - r_B \cos\theta_B \tag{3.117}$$

Using reasoning similar to that performed under the Born-Oppenheimer approximation, the variation of the wavefunction as a function of the interatomic distance is much slower than the variation of the wavefunction around the atom B. In this way, for a given interatomic distance, it is possible to estimate the wavefunction around that atom.

Therefore, it is possible to perform a variable separation such as:

$$\phi_{\text{cov}}(\vec{r}_A) = \chi_A(\vec{R})\tilde{\phi}(\vec{r}_B) \simeq \chi_A(R)Y_{l_A,m_A}(\theta_A,\varphi_A)\tilde{\phi}(\vec{r}_B) \tag{3.118}$$

where $Y_{l,m}(\theta,\varphi)$ are the spherical harmonics and $\chi_A(R)$ is the atomic wavefunction whose asymptotic component is given by (appendix C.2.5):

$$\chi_A(R) \simeq \mathscr{N}_A R^{-1+1/\gamma_{A0}} \exp(-\gamma_{A0}R) \tag{3.119}$$

where $\mathscr{N}_A$ is the normalization factor. When the atom A is a highly excited atom, this factor approaches the Coulomb normalization factor

$$\mathscr{N}_A^{\text{Coul}} = \gamma_A(2\gamma_A)^{1/\gamma_A}\left[\Gamma\left(\frac{1}{\gamma_A}+l_A+1\right)\Gamma\left(\frac{1}{\gamma_A}-l_A\right)\right]^{-1/2} \tag{3.120}$$

and

$$\begin{aligned}\tilde{\phi}(\vec{r}_B)Y_{l_A,m_A}(\theta_A,\varphi_A) \simeq{}& \frac{1}{(2\beta R)^{|m_A|}\,|m_A|!}\sqrt{\frac{(2l_A+1)}{2}\frac{(l_A+|m_A|)!}{(l_A-|m_A|)!}} \\ &\times \sum_{l=|m_A|}^{\infty}\left[\mathsf{i}_l^{(2)}(\beta r_B)+\frac{C_l}{\pi}\mathsf{k}_l(\beta r_B)\right]2\sqrt{\frac{(2l+1)}{2}\frac{(l+|m_A|)!}{(l-|m_A|)!}}Y_{l,m_A}(\theta_B,\varphi_B)\end{aligned} \tag{3.121}$$

where $\Gamma(x)$ is the gamma function.

Which leads to:

$$\begin{aligned}\phi_{\text{cov}} \simeq{}& \frac{\gamma_A(2\gamma_A)^{1/\gamma_A}R^{-1+1/\gamma_{A0}}\exp(-\gamma_{A0}R)}{\sqrt{\Gamma\left(\frac{1}{\gamma_A}+l_A+1\right)\Gamma\left(\frac{1}{\gamma_A}-l_A\right)}} \\ &\times \frac{1}{(2\beta R)^{|m_A|}\,|m_A|!}\sqrt{(2l_A+1)\frac{(l_A+|m_A|)!}{(l_A-|m_A|)!}} \\ &\times \sum_{l=|m_A|}^{\infty}\left[\mathsf{i}_l^{(2)}(\beta r_B)+\frac{C_l}{\pi}\mathsf{k}_l(\beta r_B)\right]\sqrt{(2l+1)\frac{(l+|m_A|)!}{(l-|m_A|)!}}Y_{l,m_A}(\theta_B,\varphi_B)\end{aligned} \tag{3.122}$$

where i_l and k_l are modified Bessel functions, the coefficients C_{l_B} vary in the literature (however, these coefficients will vanish when calculating the integral

3.83), and

$$\begin{aligned}\beta &= \gamma_{A0} + \left(\frac{1}{\gamma_{A0}} - 1\right)\left(\frac{1}{r_B\cos\theta_B}\right)\ln\left(1 - \frac{r_B\cos\theta_B}{R}\right) \\ &\simeq \sqrt{\gamma_{A0}^2 - \frac{2}{R}} \quad \text{when } R \simeq R_c. \end{aligned} \tag{3.123}$$

3.2.6 Electron wavefunction for the ionic state

Now that the wavefunction of the covalent state has been established asymptotically around the atom B, it remains to establish the wavefunction of the covalent state asymptotically around this same atom B. This wavefunction is simpler to establish, because the wavefunction of the ionic state is the wavefunction of the anion B^- disturbed by the Coulomb potential of the ion A^+. It is no longer necessary to change the coordinate system.

In order to establish the wavefunction of the ionic state, the first step is to separate the radial component from the angular components similarly to the previous section

$$\phi_{\text{ion}}(\vec{r}_B) = \phi_{\text{ion}}(r_B)Y_{l_B,m_B}(\theta_B,\varphi_B) \tag{3.124}$$

Therefore, the radial component satisfies the radial Schrödinger equation

$$\left(\frac{1}{2}\frac{\partial^2}{\partial r_B^2} - \frac{1}{r_A} + \frac{\gamma_{B^-}^2}{2}\right)(r_B\phi_{\text{ion}}) = 0 \tag{3.125}$$

A solution of this equation is presented by Smirnov [83] (an alternate resolution of this equation is shown in appendix C.2.6) and taken up by Janev & Salin [149]. This method considers the electron to be close to the interatomic axis [19]. Therefore, $r_A = R - r_B$.

If $r_B\gamma_{B^-} >> 1$ and $r_B << R$, the solution of this equation is:

$$\phi_{\text{ion}}(r_B) \simeq \mathscr{N}_{B^-}\left(\frac{R}{R-r_B}\right)^{1/\gamma_B}\frac{\exp\left(-\gamma_B r_B - \frac{1}{\gamma_B}\frac{r_B}{R}\right)}{r_B} \tag{3.126}$$

whose asymptotic solution is (in terms of spherical Bessel functions),

$$\phi_{\text{ion}}(r_B) \simeq \mathscr{N}_{B^-}\frac{2}{\pi}\gamma_B \mathsf{k}_{l_B}(\gamma_B r_B) \tag{3.127}$$

[19] This means that the potential $f(r_B) = 1/r_A$ is linear around B along the interatomic axis, i.e. the Coulomb potential of the cation is viewed as a linear potential for the electron attached to the atom B.

The validity of this approximation is not perfect. However, to my knowledge, there is no resolution whose approximation is less strong.

A more detailed version of this resolution is described by Radtsig [177]. This resolution, which uses elliptical coordinates, finds the same asymptotic behavior for the wavefunction.

where

$$\lim_{\gamma_B r_B \to \infty} \mathsf{k}_{l_B}(\gamma_B r_B) \simeq \frac{\pi}{2} \frac{e^{-\gamma_B r_B}}{\gamma_B r_B}, \tag{3.128}$$

$\mathscr{N}_{B^-} = A_{B^-}$ is the normalization factor and A_{B^-} an adjustment parameter obtained by the fit of the asymptotic wavefunction

$$\lim_{r\gamma >> 1} \phi(nl/r) \simeq A_{B^-} r^{-1+Z_c/\gamma} e^{-r\gamma} \left[1 - \frac{Z_c}{2r\gamma^2} \left(\frac{Z_c}{\gamma} - 1 \right) + \frac{l(l+1)}{2r\gamma} + \mathscr{O}(r^{-2}) \right] \tag{3.129}$$

with the wavefunction obtained using more complex methods – such as the Hartree-Fock method[178, 179] [20].

Finally, the asymptotic form of the wavefunction of the ionic state is

$$\phi_{\text{ion}}(\vec{r}_B) \simeq A_{B^-} \frac{2}{\pi} \gamma_B \mathsf{k}_{l_B}(\gamma_B r_B) Y_{l_B,m_B}(\theta_B, \varphi_B) \tag{3.130}$$

3.2.7 Result of the surface integral

Now that the asymptotic wavefunctions ϕ_{ion} and ϕ_{cov} are known, it is possible to evaluate:

$$\tilde{E}_{\text{i,c}} = -\frac{1}{2} \int_{-1}^{1} \mathrm{d}\cos\theta_B \int_0^{2\pi} \mathrm{d}\varphi_B \; r_B^2 \, \mathscr{W}\left[\phi_{\text{ion}}, \phi_{\text{cov}}\right] \tag{3.131}$$

As the derivatives of the Wronskian are evaluated only according to the component perpendicular to the surface, only the radial terms (according to r_B) are concerned.

$$\begin{aligned}
&\tilde{E}_{\text{i,c}} \\
&= -\frac{1}{2} \int_{-1}^{1} \mathrm{d}\cos\theta_B \int_0^{2\pi} \mathrm{d}\varphi_B \;\; Y_{l_B,m_B}(\theta_B, \varphi_B) Y_{l,m_A}(\theta_B, \varphi_B) \\
&\times \frac{\gamma_A (2\gamma_A)^{1/\gamma_A} R^{-1+1/\gamma_{A0}} \exp(-\gamma_{A0} R)}{\sqrt{\Gamma\left(\gamma_A^{-1} + l_A + 1\right) \Gamma\left(\gamma_A^{-1} - l_A\right)}} \frac{A_{B^-} \gamma_B}{(2\beta R)^{|m_A|} \, |m_A|!} \sqrt{(2l_A+1) \frac{(l_A + |m_A|)!}{(l_A - |m_A|)!}}
\end{aligned}$$

[20] The first descriptions of this method are taken from the 1960s [169]. This uses the values obtained for H^-, $A_{H^-} = 2.63$, from those obtained by Armstrong [168] and Ohmura & Ohmura [180]. The first obtains this value using an adjustment of its calculation to experimental measurements of photodetachment of H^-. This is obtained by performing the calculation for several distances included in the interval of 1 to 3 a_0 and by estimating the convergence of this value at greater distances. It is this value that is still used in recent literature, for example [109]. Note however that this calculation adjusts the value of A_{H^-} to double it afterwards, because H^- includes two electrons [168]. Therefore, as the asymptotic model already takes into account the multiple electrons in the same valence shell (section C.2.4), this value is not doubled and is equal to 1.32 in the simulations performed here.

Values of this parameter have been calculated more recently for the other atoms involved in the reactions studied [178, 179]:

$A_{C^-} = 0.75$, $A_{O^-} = 0.64$, $A_{Si^-} = 1.17$, $A_{P^-} = 0.87$ and $A_{S^-} = 1.14$.

$$\times \sum_{l=|m_A|}^{\infty} \sqrt{(2l+1)\frac{(l+|m_A|)!}{(l-|m_A|)!}} \left(\frac{2r_B^2}{\pi}\right) \mathscr{W}\left(\mathsf{i}_l^{(2)}(\beta r_B) + \frac{C_l}{\pi}\mathsf{k}_l(\beta r_B), \mathsf{k}_{l_B}(\gamma_B r_B)\right) \tag{3.132}$$

Moreover, it is possible to take out all the factors of the integral with the exception of the spherical harmonics [21], whose integral gives the condition [22]:

$$l = l_B \text{ and } m_A = m_B \equiv m_l. \tag{3.133}$$

It only remains to deal with the Wronskian of modified spherical Bessel functions. On the one hand, given the definition of the Wronskian, when it is applied to two identical functions, it is zero:

$$\mathscr{W}(f(x), f(x)) = 0 \tag{3.134}$$

on the other hand, the Wronskian applied to first and second order modified Bessel spherical functions is given in the DLMF [171, §10.50.2]

$$\mathscr{W}[\mathsf{i}_l(x), \mathsf{k}_l(x)] = -\frac{\pi}{2}\frac{1}{x^2} \tag{3.135}$$

However, this formula does not apply directly: i_l and k_l do not seem to depend on the same variable. However, if we remember the definition of β given by the equation 3.123:

$$\frac{\beta^2}{2} = \frac{\gamma_A^2}{2} - \frac{1}{R}, \tag{3.136}$$

that the critical distance R_c of crossing of the curves of ionic and covalent potential is given by

$$\begin{aligned} \frac{1}{R_c} &= E_{ion} - E_{cov} \\ &= -\frac{\gamma_A^2}{2} - \left(-\frac{\gamma_B^2}{2}\right) \end{aligned} \tag{3.137}$$

Then

$$\beta(R_c) = \gamma_B \tag{3.138}$$

and therefore, this concern is not justified. One should note that the relation above is valid only at $R = R_c$. Which means that this asymptotic model can compute the interaction potential only at the crossing point, nowhere else.

[21] NIST-DLMF [171, §14.30.8]:

$$\int_{-1}^{1} \mathrm{d}\cos\theta_B \int_0^{2\pi} \mathrm{d}\varphi_B \bar{Y}_l^m(\theta_B, \varphi_B) Y_{l''}^{m'}(\theta_B, \varphi_B) = (-1)^m \delta_{l'l}\delta_{m'm}$$

[22] See appendix C.2.7 for a comment on the validity of equation 3.133.

The second problem to be fixed is that the derivative of the Wronskian is taken relative to r_B instead of $\gamma_B r_B$, which modifies the result of the Wronskian [23]

$$\mathscr{W}_{r_B}\left[\mathsf{i}_l(\gamma_B r_B), \mathsf{k}_l(\gamma_B r_B)\right] = \gamma_B \mathscr{W}_{\gamma_B r_B}\left[\mathsf{i}_l(\gamma_B r_B), \mathsf{k}_l(\gamma_B r_B)\right] = -\frac{\pi}{2}\frac{1}{\gamma_B r_B^2} \tag{3.139}$$

therefore

$$\begin{aligned}\tilde{E}_{\mathrm{i,c}} =& \frac{\gamma_A (2\gamma_A)^{1/\gamma_A} R_c^{-1+1/\gamma_{A0}} e^{-\gamma_{A0} R_c}}{\sqrt{\Gamma\left(\gamma_A^{-1} + l_A + 1\right)\Gamma\left(\gamma_A^{-1} - l_A\right)}} \\ &\times \frac{A_{B^-}}{(2\gamma_B R_c)^{|m_l|}\ |m_l|!}\sqrt{\frac{(2l_A+1)}{2}\frac{(l_A+|m_l|)!}{(l_A-|m_l|)!}}\sqrt{\frac{(2l_B+1)}{2}\frac{(l_B+|m_l|)!}{(l_B-|m_l|)!}}\end{aligned} \tag{3.140}$$

While it is tempting to expand this formula in order to adiabatize the potential energy curves (as done by Zhou and Dickinson [137]), one should recall that this equation is valid only at $R = R_c$. Then, apart from the crossing itself, it is not possible to use this formula for the adiabatization of the potential energy curves. This explains why there is no potential energy curves shown in chapter 5, as those would not make sense.

3.2.8 Diabatic basis of antisymmetrized wavefunctions

Before closing this section on the asymptotic model, it is important to discuss the overlap of diabatic wavefunctions, which appears during the antisymmetrization and the normalization of the wavefunction (appendix C.2.4 – also briefly mentioned in section 1.4.4 of the introduction).

This equation assumes that the atomic wavefunctions after antisymmetrization still form a diabatic basis. As a reminder, the basis of the wavefunctions is said to be adiabatic if:

$$\left\langle \phi_i^{diab} \middle| \partial/\partial R \middle| \phi_j^{diab} \right\rangle = 0 \tag{3.141}$$

[23]

$$\begin{aligned}\mathscr{W}_x[f_1(g(x)), f_2(g(x))] &= \frac{\mathrm{d}f_1(g(x))}{\mathrm{d}x} f_2(g(x)) - f_1(g(x))\frac{\mathrm{d}f_2(g(x))}{\mathrm{d}x} \\ &= \frac{\mathrm{d}g(x)}{\mathrm{d}x}\frac{\mathrm{d}f_1(g)}{\mathrm{d}g} f_2(g) - f_1(g)\frac{\mathrm{d}g(x)}{\mathrm{d}x}\frac{\mathrm{d}f_2(g)}{\mathrm{d}g} \\ &= \frac{\mathrm{d}g(x)}{\mathrm{d}x}\mathscr{W}_g[f_1(g(x)), f_2(g(x))]\end{aligned}$$

Similarly, the antisymmetrized wavefunctions χ_i obtained from the atomic wavefunctions χ_i basis set follow the relation:

$$\hat{A}\,|\phi_i\rangle \sim \left(1-\sum_j S_{ij}^2\right)^{-1/2} \left|\chi_i^{at}\right\rangle \tag{3.142}$$

where $S_{ij} = \langle \phi_i | \phi_j \rangle$ is the overlap matrix of the wavefunctions. The atomic wavefunctions are independent of the interatomic distance. Meaning :

$$\left\langle \chi_i^{at} \right| \partial/\partial R \left| \chi_j^{at} \right\rangle = 0 \tag{3.143}$$

However, the atomic wavefunctions, once antisymmetrized, no longer respect this rule! Indeed, the antisymmetrization adds the term of overlap of the wavefunctions which depends on the interatomic distance as:

$$\left\langle \hat{A}\chi_i^{at} \right| \partial/\partial R \left| \hat{A}\chi_j^{at} \right\rangle \neq 0 \tag{3.144}$$

Thus, when the overlap of the wavefunctions can no longer be neglected (small interatomic distances), the basis set of the antisymmetrized atomic wavefunctions is no longer a diabatic basis (neither an adiabatic basis set).

Even if, within the scope of this thesis, the interatomic distance is supposed to be sufficiently large, it is interesting to evoke a method to diabatize the functions of antisymmetrized atomic wavefunctions (while preserving the antisymmetric character of the wavefunctions). This issue was explored by [70, 71], whose reasoning is repeated here.

The idea is to build new wavefunctions $\tilde{\phi}_i$ which preserve the ionic or covalent character of the system, while ensuring that the associated overlap $\tilde{S}_{ij}$ is zero if $i \neq j$.

Sidis *et al* [70] propose three orthogonalizations: one preserves the purely ionic character of the ionic wavefunction (OI):

$$\begin{aligned} \left|\tilde{\phi}_c^I\right\rangle &= N_{ic}\left[|\chi_{A0}\rangle - S_{ic}\,|\chi_{B-}\rangle\right] \\ \left|\tilde{\phi}_i^I\right\rangle &= |\chi_{B-}\rangle \end{aligned} \tag{3.145}$$

Another preserves the strictly covalent character of covalent states (OII):

$$\begin{aligned} \left|\tilde{\phi}_c^{II}\right\rangle &= |\chi_{A0}\rangle \\ \left|\tilde{\phi}_i^{II}\right\rangle &= N_{ic}\left[|\chi_{B-}\rangle - S_{ic}\,|\chi_{A0}\rangle\right] \end{aligned} \tag{3.146}$$

and the last transformation symmetrically modifies the purely ionic and purely covalent states (Löwdin symmetric orthogonalization — OIII):

$$\left|\tilde{\phi}_i^{III}\right\rangle = N_{ic}\left[a_+\,|\chi_{A0}\rangle + a_-\,|\chi_{B-}\rangle\right]$$

$$\left|\tilde{\phi}_i^{III}\right\rangle = N_{ic}\left[a_- \left|\chi_{A0}\right\rangle + a_+ \left|\chi_{B-}\right\rangle\right] \tag{3.147}$$

with $a_\pm = \frac{1}{2}\left[\sqrt{1-S_{ic}} \pm \sqrt{1+S_{ic}}\right]$, $N_{ic} = (1-S_{ic}^2)^{-1/2}$ and $S_{ic} = \langle\chi_{A0}|\chi_{B-}\rangle$ [24].

If we observe the three relationships above, we see that: the orthogonalization OI generates a diabatic basis around the center B, the orthogonalization OII generates a diabatic basis around the center A and the orthogonalization OIII generates a diabatic basis at the midpoint plane between the two atoms.

In order to model the adiabatic behavior of the wavefunctions at low interatomic distances, it is necessary to choose an orthogonalization method. To achieve this, we can look at the few arguments in favor or against these different methods:

- Piacentini & Salin [181] prescribe to place the frame of reference on the center of the donor so that the spurious couplings are only on acceptor centers (and not on the two centers). This would give a good approximation of the total cross section of mutual neutralization (to the detriment of branching ratios). This argument was justified by the experimental measurements of the time. These mainly focused on total cross sections, while more recent calculations focus on partial cross sections.

- The orthogonalization method presented by Janev [163] for his asymptotic method uses OIII orthogonalization, but then uses $S_{ic} = 0$. Thus, as no orthogonalization is presented, it is possible to choose another.

- The OI and OIII orthogonalizations are suitable for processing by the Landau-Zener model while the OII orthogonalization is suitable for processing by the Demkov model. The latter being suitable for large collision energies, it is therefore not suitable for describing measurements at low collision energy.

- The main difference between the orthogonalization given by Janev ([163]) and Smirnov ([83]) comes from the surface integral used in order to obtain the interaction term. The first estimates this interaction term in the vicinity of the atom B (while remaining in the asymptotic zone of its wavefunction) while the second estimates the asymptotic term using a midplane between the two atoms. Thus, Janev's asymptotic method should use OI type orthogonalization while Sminov's method should use OIII method. This in order to remain consistent.

- Orthogonalization problems appear mainly at small interatomic distances. As these interatomic distances are hardly reached at low collision energy, these effects are weak in most cases. However, if the

[24] Note that if the interatomic distance is huge, the overlap of the wavefunctions is zero ($S_{ic} = 0$). In this case, the three orthogonalizations are equivalent.

cation is initially in an excited state, some states associated with the neutralized ion have a much more diffuse wavefunction than expected. Consequently, the orthogonalization seems critical in those cases (see section 5.4.4). Indeed, figure 5.14 clearly shows a significant overlap of the wavefunctions.

3.2.9 Limitations of the Anion Centered Asymptotic Model

This long development provides the asymptotic interaction term between an ionic state ($A^+ + B^-$) and a covalent state ($A^0 + B^0$). It is obtained by combining the equations 3.114, 3.140 and 3.108:

$$
\begin{aligned}
&E_{ic}(\Lambda, S) \\
&= (-1)^{N_{A+}+N_{B0}} \quad G^{SA0,LA0}_{SA+,LA+} \; G^{SB-,LB-}_{SB0,LB0} \sqrt{N_{A0} N_{B-}} \\
&\times (-1)^{S_{mo}+S_{A+}+S_{B-}} \left[(2S_{A0}+1)(2S_{B-}+1)\right]^{1/2} \left\{ \begin{array}{ccc} S_{A+} & 1/2 & S_{A0} \\ S_{B0} & S_{mo} & S_{B-} \end{array} \right\} \\
&\times \sum_{\tilde{\Lambda}} \sum_{\substack{m_{LA+},m_{LB0} \\ m_{LA0},m_{LB-} \\ m_l}} \left[\begin{array}{ccc} L_{A+} & l_{A0} & L_{A0} \\ m_{LA+} & m_l & m_{LA0} \end{array} \right] \left[\begin{array}{ccc} L_{B0} & l_{B-} & L_{B-} \\ m_{LB0} & m_l & m_{LB-} \end{array} \right] \\
&\quad \times \left(\frac{1}{\sqrt{\#L_{ion}}} \sum_{L_{ion}} \left[\begin{array}{ccc} L_{A+} & L_{B-} & L_{ion} \\ m_{LA+} & m_{LB-} & \tilde{\Lambda} \end{array} \right] \right) \\
&\quad \times \left(\frac{1}{\sqrt{\#L_{cov}}} \sum_{L_{cov}} \left[\begin{array}{ccc} L_{A0} & L_{B0} & L_{cov} \\ m_{LA0} & m_{LB0} & \tilde{\Lambda} \end{array} \right] \right) \\
&\quad \times \frac{\gamma_A (2\gamma_A)^{1/\gamma_A} R^{-1+1/\gamma_{A0}} e^{-\gamma_{A0} R}}{\sqrt{\Gamma\left(\gamma_A^{-1} + l_A + 1\right) \Gamma\left(\gamma_A^{-1} - l_A\right)}} \\
&\quad \times \frac{A_{B^-}}{(2\gamma_B R)^{|m_l|} \; |m_l|!} \sqrt{\frac{(2l_A+1)}{2} \frac{(l_A+|m_l|)!}{(l_A-|m_l|)!}} \sqrt{\frac{(2l_B+1)}{2} \frac{(l_B+|m_l|)!}{(l_B-|m_l|)!}}
\end{aligned}
\tag{3.148}
$$

This has necessitated a number of assumptions which are related to the nature of the method used: The asymptotic method.

First, we must find a distance r_B such that the integral is possible to evaluate. This hypothesis is more complicated to satisfy than it seems at first glance. First, it is necessary to be able to split the wavefunction of the covalent state according to the internuclear component and the component located around the atom B. It is then necessary to be able to evaluate the wavefunction of the ionic state: To obtain the asymptotic ionic wavefunction, equation 3.126 must take the form of spherical Bessel functions. To do this, the following conditions

must be met:

$$\left(\frac{R}{R-r_B}\right)^{1/\gamma_B} \simeq 1 \quad \text{and} \quad \exp\left(-\frac{1}{\gamma_B}\frac{r_B}{R}\right) \simeq 1 \tag{3.149}$$

The first order development of each of both conditions implies::

$$\gamma_B R >> r_B. \tag{3.150}$$

This condition is combined with the following: that the distance r_B is sufficiently large so that the wavefunction of B^-, undisturbed by A^+, can also be considered as asymptotic. This is more difficult to estimate. There is no standard method which allows verifying it. One must find in the paper which the asymptotic anion wavefunction normalization N_{B^-} is estimated then find, in the same paper, the r_B range in which the approximation is valid [25].

Then, you have to be able to express the Wronskian easily: The Wronskian property used in the equation 3.135 requires that $\beta \simeq \gamma_B$, this assumption comes from the equation 3.123:

$$\beta^2 = \left(\gamma_A - \frac{1}{\gamma_A R}\right)^2 \simeq \gamma_A^2 - \frac{2}{R} \tag{3.151}$$

This approximation is only valid if $2\gamma_A R >> 1$.

Now that the conditions of validity are established, it is possible to verify them in practice. To get there, we must remember the definition of interatomic crossing distance:

$$\frac{1}{R_c} = \frac{\gamma_A^2}{2} - \frac{\gamma_B^2}{2}. \tag{3.152}$$

Since the binding energy for the atom A is about 2 to 4 eV (0.07 to 0.15 Hartree) and the binding energy for the anion B^- is about 1 eV

[25] The estimation of this normalization is carried out for an expansion of the Whittaker function to order 0. In this situation, it is necessary to be able to neglect the first order (and the higher orders):

$$\frac{l(l+1)}{2\gamma_B r_B} << 1$$

or, if $l = 1$ (which is often the case for the reactions studied):

$$\gamma_B r_B >> 1.$$

However, the wavefunction used in this development takes into account the whole development of Whittaker's function. Therefore, the approximation of the asymptotic development is valid for distances r_B shorter. Thus, it is more complex to estimate the minimum possible value of r_B, the only constraint is that the approximation of the mean field of the core electrons must be valid. This is valid as long as the distance r_B is greater than the average distance of the electrons from the outermost core shell. This is "zero" for hydrogen, less than 1 a_0 for carbon and oxygen, and of the order of 1 a_0 for sulfur and phosphorus.

(0.03 Hartree), the critical interatomic distance is between 30 and 10 a_0, respectively. This gives on the one hand that $2\gamma_A R$ varies between 10 and 20, which is almost sufficient. On the other hand, $\gamma_B R_c$ varies between 8.1 and 2.7 a_0, thus assuming that the minimum possible value for r_B is less than 1 a_0 (see footnote), it is possible to find a value of r_B satisfying the condition $\gamma_B R_c >> r_B$.

However, the second critical radius value ($R_c = 10$ a_0) undermines the validity conditions of the model (as much $2\gamma_A R >> 1$ as $\gamma_B R_c >> r_B > r_{B,min}$). Thus, this asymptotic development model is valid only when the charge exchange occurs at a large distance (from about 10 a_0). Luckily, it is at these interatomic distances that most of the reaction channels are found.

3.3 Validity of the Landau-Zener model for the mutual neutralization reaction

The validity domain of the Landau-Zener model has been studied for an alternative demonstration of the Landau-Zener formula [153, 182]. The validity domain could be estimated using the following adimensional variables:

$$\varepsilon = \frac{(E_{r,i} - V(R_c))}{2E_{ic}} \frac{|\Delta F|}{F} \tag{3.153}$$

and

$$\beta = 4E_{ic}\sqrt{\frac{\mu E_{ic}}{F|\Delta F|}} \tag{3.154}$$

where E_{ic} is the interaction potential, $E_{r,i}$ is the collision energy and $V(R_c) = V_{ion}(R_c) = V_{cov}(R_c) = -KER \simeq -1/R_c$ is the potential energy at the crossing point i.e., $(E_{r,i} - V(R_c))$ corresponds to the kinetic energy of the pseudo-particle of reduced mass μ at the crossing point, $F_{ion,cov} = \frac{\partial V_{ion,cov}}{\partial R}|_{R=R_c}$, $\Delta F = V_{ion} - V_{cov}$ and $F = \sqrt{F_{ion}F_{cov}}$.

The Landau-Zener model is valid when:

$$\varepsilon >> 1 \text{ and } \beta\varepsilon^{3/2} >> 1. \tag{3.155}$$

For the mutual neutralization asymptotic case, $R_c > 10$ a_0, $(E_{r,i} - V(R_c)) > 2E_{ic}$, $F_{ion} \simeq 1/R^2$ and $F_{cov} \simeq a/R^7$ with $a \sim 300$ a.u. using the van der Waals

interaction [26]. Then $\Delta F \simeq 1/R_c^2$ and $F \simeq a^{1/2} R_c^{-9/2}$ and one finds that:

$$\varepsilon \simeq \underbrace{\frac{(E_{r,i} - V(R_c))}{2E_{ic}}}_{>1} \underbrace{a^{-1/2}}_{\simeq 1/20} \underbrace{R_c^{7/2}}_{>3000} \gg 1 \tag{3.156}$$

and

$$\beta \varepsilon^{3/2} = 4\,(E_{r,i} + 1/R_c)\,\frac{\Delta F}{F^2} \simeq 4\,\underbrace{R_c^4}_{>10000}\,\underbrace{a^{-1}}_{\simeq 1/300} \gg 1 \tag{3.157}$$

Which means that the validity conditions for the Landau-Zener model are satisfied for the low collision energies. This validity comes from the strongly attractive Coulomb potential and the nearly flat covalent potential energy curves combined with the fact that the neutral products are excited states, which means that the interaction potential is small. One should note that the Landau-Zener model was successfully used for even smaller collision energies (mK) for the collision between a Rydberg rubidium atom and a magnetically trapped spin polarized ground state rubidium atom [184].

3.4 MN at low collision energy

The discussion in chapter 5 and the results given in appendix F do not put a strong emphasis on the collision energy: those chapters simply assume that the collision energy is small.

This section details what "small collision energy" means, and use the two-channel Landau-Zener model (section 3.1.5 – whose validity for the MN is given in section 3.3) in order to explain why the branching ratios do not depend on the collision energy in the low collision energy range and why the collision energy should be used instead of the collision velocity in order to describe the cross section [27]. This section also explains why the isotopic effect on the MN reaction is not trivial and therefore why the reduced collision energy ($E_{r,i}/\mu$) is not adapted to describe this collision.

In order to proceed, let us recall the Landau-Zener partial cross section formula (equation 3.62):

$$\sigma_{LZ} = 4\pi R_c^2 \left(1 - \frac{V(R_c)}{E_{r,i}}\right) G(\zeta) \tag{3.158}$$

[26] The van der Waals potential is used here, it follows $V_{cov} = C_6/R^6$, where the C_6 coefficients are estimated using values from Gould and Bučko [183]. Those values are always of a few dozen, except for $C_6(\mathrm{N}-\mathrm{S}) = 324$. Those C_6 values need to be multiplied by 6 due to the derivative.

[27] The multi-channel Landau-Zener model could also be used, but it would complexify the discussion without modifying the conclusions.

where $G(\zeta)$ is a highly non-linear function of the collision energy (see figure 3.11) and

$$\zeta = \frac{2\pi E_{ic}^2}{\hbar\Delta F v_0 \sqrt{1 - V(R_c)/E_{r,i}}}. \tag{3.159}$$

When the collision energy is small, i.e. $E_{r,i} \ll KER = -V(R_c)$ then the two equations above become:

$$\sigma_{LZ} \simeq 4\pi R_c^2 \frac{KER}{E_{r,i}} G(\zeta) \tag{3.160}$$

and

$$\zeta \simeq \frac{2\pi E_{ic}^2}{\hbar\Delta F v_{r,i} \sqrt{2KER/\mu} v_{r,i}} = \frac{2\pi E_{ic}^2}{\hbar\Delta F} \sqrt{\frac{\mu}{2KER}} \tag{3.161}$$

As shown in equation 3.161, there is no collision energy dependency on ζ, which means (as stated in equation 3.160) that the partial cross section is inversely proportional to the collision energy. This also means that the branching ratios remain constant for such small collision energies, i.e. below 100 meV for the MN reaction.

It remains to describe the isotopic effect on the reaction, which is given by the $\sqrt{\mu}$ factor in equation 3.161. But before discussing the effects of this factor on the total cross section, one should remind that this discussion is about all possible output channels of the reaction. One cannot make the analysis for a given value of $\{E_{ic}, \Delta F\}$ but must take into account all the possible values of $\{E_{ic}, \Delta F\}$.

For a given MN reaction between two ions whose reduced mass is μ and with N output channels i, there are N values of ζ_i. Let us now evaluate $G(\zeta_i)$ as a function of the interatomic distance using $E_{ic} \propto \exp\{-\gamma_A R_c\}/R_c$ (equation 3.148) and $\Delta F \simeq 1/R_c^2$ (equation 3.27 with a $1/R$ potential): For small interatomic distance, $\zeta_i > 0.424$ (above $G(\zeta)$ maximum) and for larger interatomic distance $\zeta < 0.424$ (below $G(\zeta)$ maximum), i.e. there are states above and below the maximum of $G(\zeta)$.

If one studies the same MN reaction with other isotopes whose reduced mass is μ', then for each channel $\zeta_i' = \sqrt{\mu/\mu'}\zeta_i$. This means that all channels are shifted by the same factor. But as some channels are above and others are below the maximum, then the partial cross section of some channels decreases, while the partial cross section of the other channels increases. As a result, there is no clear dependency on μ for the total cross section (neither for the partial cross section as one should find first on which side of the maximum this channel is).

As all the branching ratios displayed in this manuscript were measured at a collision energy below 25 meV, the small collision energy condition is satisfied, which means that the branching ratio remains constant as long as the small

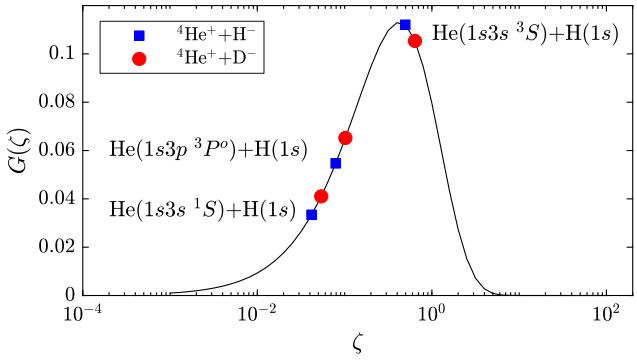

Figure 3.11: Isotope effect on the branching ratios of the He^++H^- MN reaction illustrated by the $G(\zeta)$ function (equation 3.62). The values for E_{ic} are given by the anion centered asymptotic model.

collision energy condition is satisfied (and remains valid for reaction rates below 1000 K). The partial cross section is inversely proportional to the collision energy with a non-linear effect of the isotope on the cross section. Hence, the best way to show the cross sections for small collision energy is to show them as a function of the collision energy (without a factor μ which would complexify the analysis), while the collision energy does not affect much the branching ratios [28].

In order to be convinced, one could look at the calculations done by Larson *et al.* [101] for the ^{3,4}He$^+$+H/D$^-$ MN reaction (figure 3.12). This example clearly shows, at low collision energies, that a reduced collision energy $E_R = E_{r,i}/\mu$ does not apply here. Also, one should note that the branching ratios remain constant at low collision energies. At last, the isotopic effect on the branching ratios could be explained in a similar way (figure 3.11): The increase of μ for He^++D^- (1.33) compared to the one for He^++H^- (0.8) leads to an increase of ζ for He^++D^-, which favors the higher excited states of helium ($1s3s$ ^1S, $1s3p$ $^3P^o$) compared to the lesser excited state ($1s3s$ ^3S) situated above the $G(\zeta)$ maximum. This leads to a non-trivial change in the total cross section.

[28] It should be noted that the apparent collision energy dependency for the branching ratio in the Li^++D^- MN reaction (table 4.2) should come mostly from a bad estimation of the differential cross section than a real change in the branching ratio.

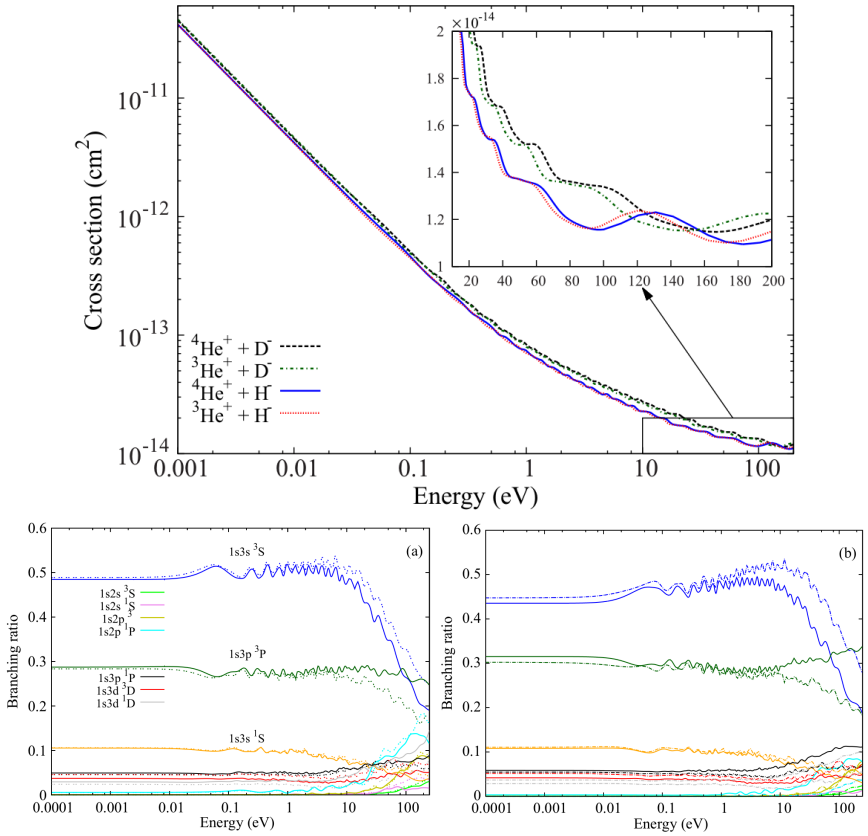

Figure 3.12: Top (reproduced from Larson *et al.* [101, Fig.9]): Calculated cross section of mutual neutralization in collisions of different isotopes of hydrogen and helium ions. Bottom (reproduced from Larson *et al.* [101, Fig.11]): Calculated final-state distributions in mutual neutralization in (a) ^{4}He$^+$+H$^-$ and (b) ^{4}He$^+$+D$^-$ collisions with (dashed lines) and without (solid lines) inclusion of rotational couplings.

Chapter 4

Differential cross section and kinetic energy release

The experimental study of mutual neutralization reactions is fraught with pitfalls. For a given reaction, once the experimental measurement has been carried out, once all the events have been correctly analyzed, once the background has been removed, it is not yet possible to compare the data obtained with the theoretical predictions. Events which cannot be detected are not taken into account. These must be.

Consequently, this chapter aims to detail the consideration of unmeasured events:

It begins with the modeling of the detection system in order to obtain the geometric probability of detecting each event. The modeling of an angular acceptance map. However, this map is not sufficient to estimate the proportion of lost events. To achieve this, it is necessary to estimate the angular distribution of the collisions (section 4.2), the differential cross-section (section 4.3) to finally convolve the two (section 4.4). This convolution makes it possible to estimate the differential cross section at the same time, to explain why the measured branching ratios are correct – once corrected –, to explain in which cases - because of the geometry of the detection system – it is no longer possible to correct these branching ratios, and finally to determine the limiting factor in the energy resolution of the relative kinetic energy spectra after collision.

4.1 Geometric detection probability

This section develops the method used to estimate the geometric probability of detection when the pair of neutral products of the mutual neutralization reaction arrives on different detectors. The reasoning to get there is the following: An event is generated in the center-of-mass reference frame, the pseudo-

particle of reduced mass μ acquires a kinetic energy $E_{r,f}$ and a given direction (θ_f, φ_f). This pseudo-particle trajectory is obtained using the two particles (atoms/ions) trajectories in the laboratory fixed frame (the frame where the detection system is static). Therefore, it is also possible to obtain the trajectory of the two particules in the laboratory fixed frame using the pseudo-particle trajectory in the center-of-mass frame (aligned along the beam axis) and the center-of-mass trajectory. Using these trajectories, it is easy to check whether the neutral atoms are each impacting a detector. So – for each combination $(E_{r,f}, \theta_f)$ – the average over φ_f gives the probability of detecting that combination.

This method, while effective, is converging slowly. This section describes a faster and evenly accurate method (if not more). It also takes into account the different elements (diaphragms, ...) which could block the path of the atoms before they reach the plane of the detectors.

4.1.1 Trajectories of neutralized ions

The first step in estimating whether an event is detectable consists in properly describing the kinematics of reactions in the center-of-mass frame to convert it to that of the laboratory frame.

Before the reaction, the two beams, composed of ions A^+ and B^-, respectively have an average kinetic energy E_A and E_B, and a speed $\vec{v}_{A,l,i}$ and $\vec{v}_{B,l,i}$ in the laboratory fixed frame.

The velocity of the center-of-mass differs only from zero in the laboratory frame. This velocity is conserved during the reaction. It is given by:

$$\vec{v}_{cm} = \frac{1}{m_A + m_B} \left(m_A \vec{v}_A + m_B \vec{v}_B \right) \tag{4.1}$$

where m_A and m_B are the masses of the ions A^+ and B^- respectively.

The relative velocity before collision is independent of the reference frame, it is given by:

$$\vec{v}_{r,i} = \vec{v}_{A,l,i} - \vec{v}_{B,l,i} \tag{4.2}$$

From which the kinetic energy of collision derives directly:

$$\begin{aligned} E_{col} = E_{r,i} &= \frac{\mu \vec{v}_{r,i}^2}{2} \\ &= \mu \left(\frac{E_A}{m_A} + \frac{E_B}{m_B} - 2\sqrt{\frac{E_A}{m_A}\frac{E_B}{m_B}} \cos\theta_{AB,i} \right) \end{aligned} \tag{4.3}$$

where μ is the reduced mass and $\theta_{AB,i}$ is the angle between the trajectory of the ions A^+ and B^- in the laboratory fixed frame before the collision.

After the reaction, the A^+ and B^- ions are respectively neutralized to $A^{(*)}$ and $B^{(*)}$, with a velocity $\vec{v}_{A,l,m}$ and $\vec{v}_{B,l,m}$ in the laboratory fixed frame. In the center-of-mass frame, these are

$$\vec{v}_{A,f} = \vec{v}_{A,l,f} - \vec{v}_{cm} \tag{4.4}$$

$$\vec{v}_{B,f} = \vec{v}_{B,l,f} - \vec{v}_{cm} \tag{4.5}$$

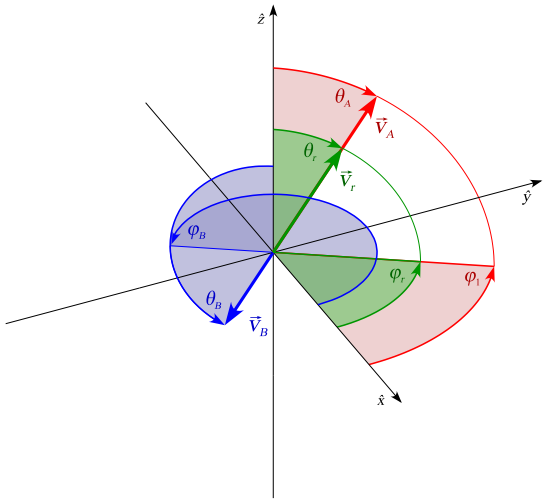

Figure 4.1: Representation of the alignment of the relative velocity $\vec{v}_{f,r}$ with respect to the velocity of the particle A and of the particle B, in the coordinate system of the center-of-mass. The $\hat{z}$ axis corresponds to the main propagation axis of the beams.

The relative velocity after the reaction is

$$\vec{v}_{r,f} = \vec{v}_{A,l,f} - \vec{v}_{B,l,f} = \vec{v}_{A,f} - \vec{v}_{B,f} \tag{4.6}$$

It is parallel with $\vec{v}_{A,f}$ and $\vec{v}_{B,f}$, but not necessarily in the same direction (figure 4.1). Thus, from the relative velocity between the neutralized ions, it is easy to find the velocity of each of the atoms:

$$\mu\vec{v}_{r,f} = m_A\vec{v}_{A,f} = -m_B\vec{v}_{B,f} \tag{4.7}$$

The relative kinetic energy between atoms after reaction $E_{r,f}$ is the sum of the initial kinetic energy of collision $E_{r,i}$ and the kinetic energy release (KER) of the reaction

$$E_{r,f} = \frac{\mu v_{r,f}^2}{2} = E_{r,i} + KER \tag{4.8}$$

The method used to theoretically deduce the relative velocity after reaction $\vec{v}_{r,f}$ as a function of the initial relative velocity from the differential cross section is described in the section 4.3.3.

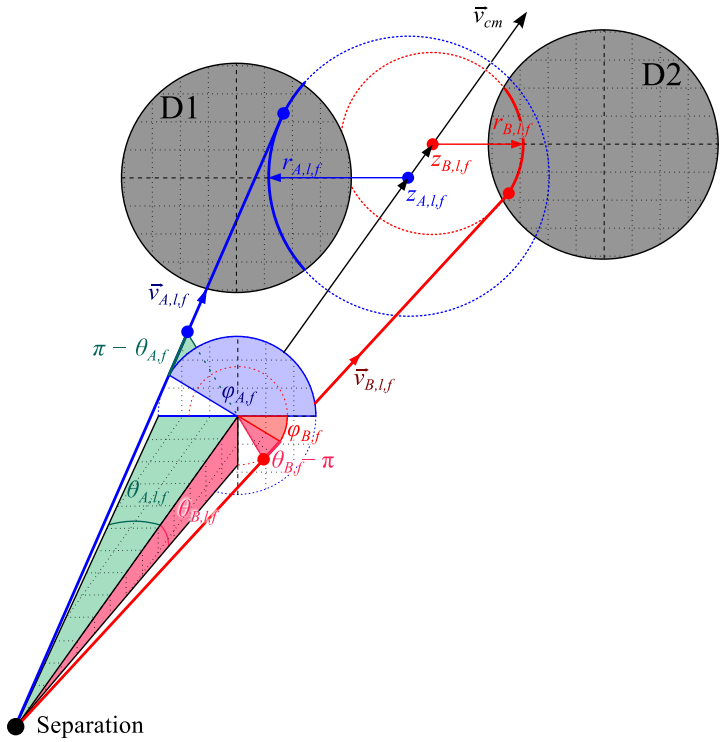

Figure 4.2: Representation of the trajectory of the ions in the laboratory frame, and in the center-of-mass frame.

Within the experimental setup, the propagation axis of the beams is horizontal. Now that the main axes of the reaction are defined, it is possible to correctly define the choice of reference marks used.

Cartesian coordinates are chosen as follows: The $\hat{z}$ axis corresponds to the main direction of the centers of mass, the $\hat{x}$ axis corresponds to the vertical axis and the axis $\hat{y}$ corresponds to the horizontal axis perpendicular to $\hat{z}$.

The spherical coordinates are also defined according to the main axis of propagation of the centers of mass. The angle θ is the zenith angle (the angle between the vector and the principal axis) while the angle φ is the azimuthal angle (angle between the projection of the vector on the plane perpendicular to the main axis and the horizontal).

In order to link the modeling of the reaction at the nanoscopic scale with the experimental measurements, determining the kinematics of the reaction is an important first step. It is nevertheless necessary to re-express this kinematics in the form of a trajectory in the laboratory frame.

Using these coordinates, the distance $r = \sqrt{x^2 + y^2}$ from the main axis as

a function of the length z traveled by the atom since its neutralization is

$$r_{X,l,f} = z_{X,l,f} \tan \theta_{X,l,f} \tag{4.9}$$

where $X = A, B$.

However, $\theta_{X,l,f}$ is not directly known. However, this angle is expressed as a function of the spherical coordinates of the center-of-mass frame according to:

$$\tan \theta_{X,l,f} = \frac{r_{X,l,f}}{z_{X,l,f}} = \frac{\frac{\mu}{m_X} v_{\mathrm{r,f}} \sin(\theta_{r,f})}{v_{cm} \pm \frac{\mu}{m_X} v_{r,f} \cos(\theta_{r,f})} \tag{4.10}$$

Which gives

$$r_{A,l,f} = z_{A,l,f} \frac{\frac{\mu}{m_A} v_{\mathrm{rf}} \sin(\theta_{r,f})}{v_{cm} + \frac{\mu}{m_A} v_{r,f} \cos(\theta_{r,f})} \tag{4.11}$$

$$r_{B,l,f} = z_{B,l,f} \frac{\frac{\mu}{m_B} v_{r,f} \sin(\theta_{r,f})}{v_{cm} - \frac{\mu}{m_B} v_{r,f} \cos(\theta_{r,f})} \tag{4.12}$$

These trajectories depend only on the parameters of the reaction obtained below in section 4.3.3.

Once neutralized, the atoms propagate in straight line to the detection system described in section B.1. The latter is composed of two detectors $D1$ and $D2$ sensitive to position and time, located at a distance z_{D1} and $z_{D2} > z_{D1}$ from the observation cell. These circular detectors have respectively a radius r_{D1} and a radius r_{D2}, whose center is located at a distance $L_{D1} = x_{D1}$ and $L_{D2} = -x_{D2}$ vertically with respect to the principal axis of the centers of mass, respectively.

The detection of a mutual neutralization event is triggered when particle A arrives at detector $D1$ and particle B arrives at detector $D2$, or vice versa. The analysis method described in the section 2.8 then makes it possible to obtain on the one hand the position of the center-of-mass of the system in the plane of the detectors in the laboratory frame (x_{cm}, y_{cm}) and on the other hand the final vector velocity of the pseudo-particle in the center-of-mass frame $(E_{r,f}, \theta_{r,f})$.

Despite its advantages, this detection system is subject to a major flaw: its angular opening. Indeed, due to its geometry, only certain events linked to a given combination $(E_{r,f}, \theta_{r,f})$ are detectable experimentally.

However, as each combination $(E_{r,f}, \theta_{r,f})$ is now linked to a set of trajectories, it is possible to determine the proportion of detectable events for each of these combinations [1]. This proportion is called *acceptance*.

[1] This assertion assumes that the distribution of the events according to the angle $\varphi_{r,f}$ is uniform (or, at least, known exactly). This hypothesis is verified in section 4.2.

4.1.2 Derivation of the acceptance

In order to obtain the acceptance for a combination $(E_{r,f}, \theta_{r,f})$, i.e. the geometrical detection probability of the system for this $(E_{r,f}, \theta_{r,f})$ combination, it is necessary to take into account all trajectories associated with this combination. Let us associate a weight $\mathscr{P}$ at each trajectory [2] , determine if this trajectory is detectable $\mathscr{S} = \{0, 1\}$, then integrate this weight according to the set of variables that generate these trajectories:

$$Acc(E_{r,f}, \theta_{r,f}) = \iiint \mathscr{P}(x_{cm}, y_{cm}; \varphi_{r,f}) \mathscr{S}(x_{cm}, y_{cm}; \varphi_{r,f}; E_{r,f}, \theta_{r,f}) \quad (4.13)$$

The center-of-mass distribution is independent of the azimuthal angular distribution. It will be derived in section 4.2.1. As for the azimuthal distribution, it is uniform, as a result of the cylindrical symmetry of the collision directions.

Finally, all what remains is to find a method to determine whether each pair of trajectories of the neutralized ions does indeed each meet a detector. The easiest is to simply check each trajectory. This method is unfortunately prohibitively slow [3].

The method of choice takes into account the entire azimuthal distribution at once. It allows to calculate, for a given center-of-mass position, what proportion of the azimuthal distribution can be detected by the detection system.

Intersecting circles method

If the collision takes place on the main center-of-mass axis, for a given combination $(E_{r,f}, \theta_{r,f})$, the distribution according to the angle $\varphi_{r,f}$ of the atoms A and B form two cones of revolution [4], whose radii as a function of the neutralization distance are given by the equation 4.12.

---

[2] This probability $\mathscr{P}$ depend on the process to study. It corresponds to the differential cross section averaged by the collision distribution. But since the atoms are not oriented before the collision, and the collision distribution is uniform along $\varphi_{r,i}$ (figure 4.13), then the probability $\mathscr{P}$ is uniform along $\varphi_{r,f}$.

[3] It generally takes about ten minutes to generate a complete acceptance map with sufficient precision. Since it is regularly necessary to finely adjust the position and the width of the distribution of the center-of-mass in order to obtain an acceptance map as close as possible to the experimental distribution, an acceleration of the calculation without loss of precision is greatly appreciated. The time saving of the second method is about a factor of 100.

[4] The beam propagation axis is always assumed to point in the same direction (perfectly parallel to the propagation axis), even if it points to a different location (not exactly between the two detectors). This approximation is valid as long as the angle between the propagation of the center-of-mass and the main axis of propagation of the centers of mass is small.

Otherwise, the cone of revolution formed by $(E_{r,f}, \theta_{r,f})$ forms an ellipse instead of a circle once the cone is projected onto the plane of the detectors.

Consequently, the proportion of atoms A detectable by the detector $D1$ is the proportion of the circle A of radius $r_A = r_{A,l,f}(z_1)$ inscribed in the circle of the detector.

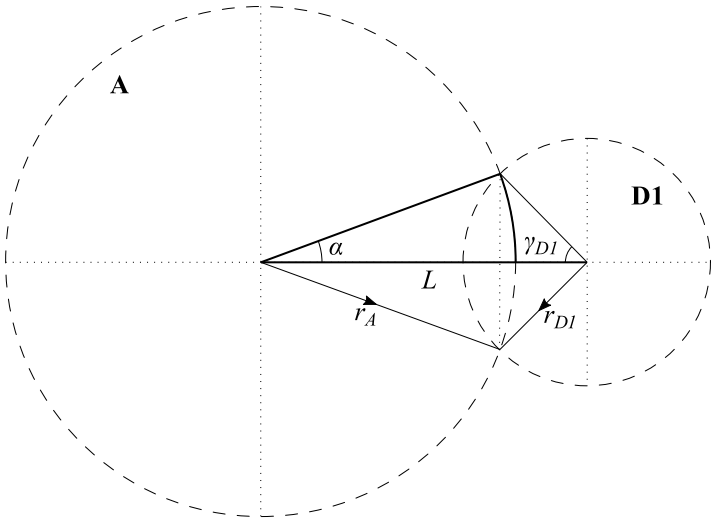

Figure 4.3: Representation of the initial arc.

In other words, the arc $[-\alpha, \alpha]$ of the circle A of radius r_A which is inscribed in a circle $D1$ of radius r_{D1} separated by a distance L_{D1} is obtained using the following trigonometric relations (see figure 4.3):

$$r_A \sin\alpha = +r_{D1} \sin\gamma_{D1} \tag{4.14}$$

$$r_A \cos\alpha = -r_{D1} \cos\gamma_{D1} + L_{D1} \tag{4.15}$$

where γ_{D1} is the angle between the axis which connects the two circles and the axis which starts from the center of the circle $D1$ until the intersection of the two circles.

The combination of these equations eliminates γ_{D1}, which gives

$$r_{\mathrm{A}} \cos\alpha + \sqrt{r_{\mathrm{D1}}^2 - r_{\mathrm{A}}^2 \sin\alpha} = L_1 \tag{4.16}$$

or again, by isolating α,

$$\alpha = \pm \arctan \sqrt{\frac{-r_A^2 + r_{D1}^2 + 2r_A L_{D1} - L_{D1}^2}{r_A^2 - r_{D1}^2 + 2r_A L_{D1} + L_{D1}^2}} \tag{4.17}$$

Therefore, the proportion Acc_1 of the neutral particle beam A detectable by the detector $D1$ is:

$$Acc_1 = 2\alpha/2\pi. \tag{4.18}$$

The same reasoning allows to find the arc $[-\beta,\beta]$ of the circle of the particle beam B of radius r_B inscribed in a circle of the detector $D2$ of radius r_{D2} separated by a distance L_{D2}. Which give:

$$\beta = \pm \arctan \sqrt{\frac{-r_B^2 + r_{D2}^2 + 2r_B L_{D2} - L_{D2}^2}{r_B^2 - r_{D2}^2 + 2r_B L_{D2} + L_{D2}^2}} \tag{4.19}$$

and the proportion Acc_2 of the beam of neutral particles B detectable by the detector $D2$ is:

$$Acc_2 = 2\beta/2\pi. \tag{4.20}$$

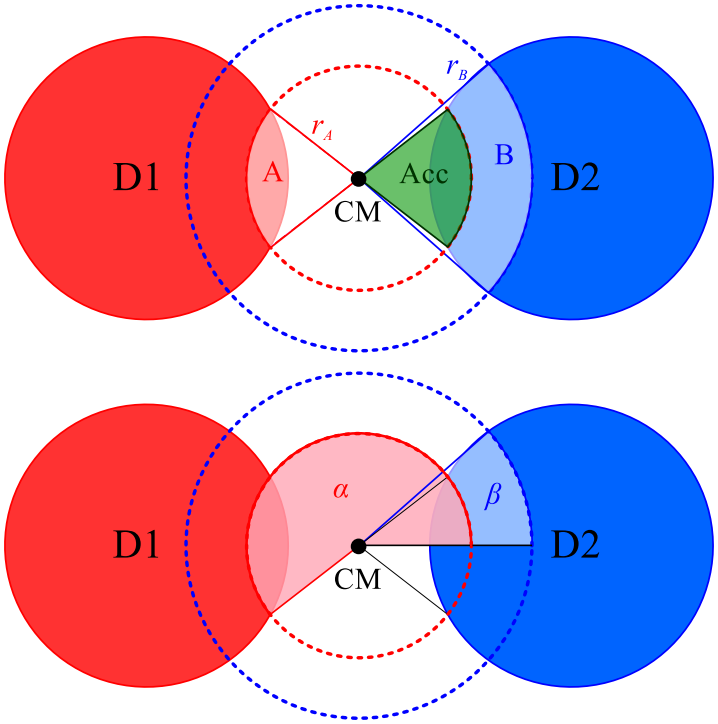

Figure 4.4: Acceptance in a simple case. Top: Detection probability for atom A and B on detector $D1$ and $D2$ respectively. Bottom: Angles α and β definition.

Moreover, for the products of the reaction to generate an event, A must arrive on D1 (assumed above the beam) and B on D2 (assumed below the beam). Thus the acceptance of the detection system is not a simple combination of Acc_1 and Acc_2. Fortunately, the atoms A and B go in the opposite direction in the center-of-mass frame (equation 4.7 – i.e. $\varphi_{A,f} - \varphi_{B,f} = \pi$ and $\theta_{A,f} - \theta_{B,f} = \pi$). This needs to be taken into account in the definition of α (see

figure 4.4). Consequently, the total acceptance Acc of the system is

$$Acc(E_{r,f}, \theta_{r,f}) = \frac{2\min(\alpha - \pi, \beta)}{2\pi}. \tag{4.21}$$

Center-of-mass offset

The case presented above only applies when the center-of-mass of the two particles lies exactly between the two detectors. However, the center-of-mass follows a spatial distribution [5]. The center-of-mass of an event is (x_{cm}, y_{cm}). It does not depend on z as the trajectory of the center-of-mass remains parallel to this axis.

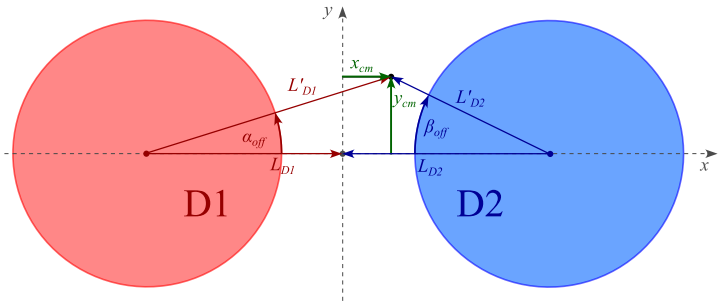

Figure 4.5: Graphical representation of obtaining the new distances and angles, taking into account the center-of-mass offset (x_{cm}, y_{cm}).

As the center-of-mass is no longer centered between the two detectors, the distance between the center-of-mass and the center of each detector changes. It means that, while the radii r_A and r_B remain the same, the circles A and B are shifted by (x_{cm}, y_{cm}). Then, the new distance L'_{D1} between the center of the detector $D1$ and the center-of-mass is

$$L'_{D1} = \sqrt{(L_{D1} + x_{cm})^2 + y_{cm}^2} \tag{4.22}$$

Likewise, the distance L'_{D2} between the center of detector $D2$ and the center-of-mass is

$$L'_{D2} = \sqrt{(L_{D2} - x_{cm})^2 + y_{cm}^2} \tag{4.23}$$

The arcs $[-\alpha, \alpha]$ and $[-\beta, \beta]$ are obtained as in the previous subsection, by modifying the distance between the circles.

[5] When the mass difference between the atoms A and B is large, the radii r_A and r_B also differ significantly. In that case, the acceptance is larger when the heavy beam is closer to one detector than the other.

In such a situation, the average position of the center-of-mass is volontarily shifted towards one of the two detectors (either by adjusting the main axis of the beams, or by moving the detection system).

However, as the center-of-mass with respect to the axis of the detectors is offset, the circles of radii r_A and r_B will no longer be centered around the horizontal axis, there is an offset angle with respect to the axis α_{off} (see figure 4.5). This angle is

$$\alpha_{off} = \tan^{-1}\left(\frac{y_{cm}}{x_{cm}+L_{D1}}\right) \tag{4.24}$$

Likewise, for the detector $D2$,

$$\beta_{off} = \tan^{-1}\left(\frac{y_{cm}}{x_{cm}-L_{D2}}\right) \tag{4.25}$$

This gives the two arcs A and B inscribed in the detectors $D1$ and $D2$ respectively

$$[\alpha_-,\alpha_+] = [-\alpha+\alpha_{off},\alpha+\alpha_{off}] \tag{4.26}$$
$$[\beta_-,\beta_+] = [-\beta+\beta_{off},\beta+\beta_{off}] \tag{4.27}$$

with $\alpha_\pm \in [\pi/2, 3\pi/2]$ and $\beta_\pm \in [-\pi/2, \pi/2]$.

A slight modification is necessary to replace the angles within the same quadrant, in oreder to be able to compare them easily (similarly to equation 4.21).

$$\beta'_\pm = \mod\left(\beta_\pm + \frac{\pi}{2}, 2\pi\right) - \frac{\pi}{2} \tag{4.28}$$
$$\alpha'_\pm = \mod\left(\alpha_\pm + \frac{3\pi}{2}, 2\pi\right) - \frac{\pi}{2} \tag{4.29}$$

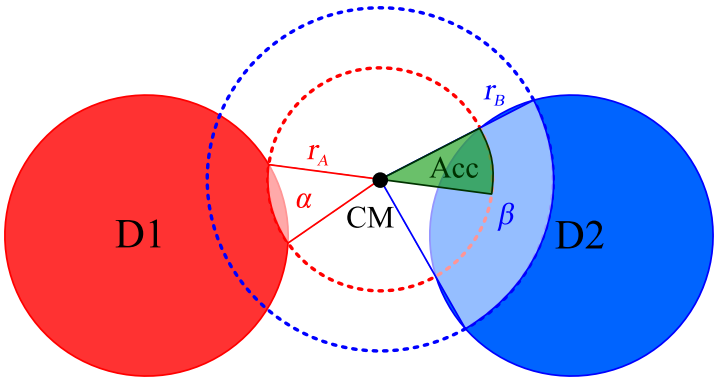

Figure 4.6: Acceptance when the center-of-mass is off-center.

By paying attention to the definition of the angles, the acceptance becomes:

$$Acc(E_{rf},\theta_{r,f}) = \frac{1}{2\pi}\max\Big(\ \min(\alpha_+,\beta_+) - \max(\alpha_-,\beta_-)\ ;\ \ 0\ \Big) \tag{4.30}$$

Changes in the shape of detectors

The acceptance modeling is almost complete. However, there remain two experimental imperfections, independent of the design of the detection system:

The first comes from a large vertical slit originally present beyond the observation cell (7.6 mm wide, located 350 mm and 700 mm after the observation cell for the purpose of differential pumping). This stops the trajectories whose horizontal component is too large. Which means that those events are lost, they cannot be measured by the setup.

The second depends on the aging of the ADCs which measure the position of the impacts on the detectors. The minimum value along the x axis encoded by the ADC of the $D1$ detector is greater than what the ADC should provide when detecting a particle close to the main axis. The position x encoded for these impacts in such case is the lowest possible x position and some pile-up occurs. As the impact positions related to these events are non-physical, these events are discarded during the analysis. Which should also be taken into account by the acceptance map.

These two cases have one thing in common: Both form a horizontal straight line perpendicular to the axis linking the two detectors. In the first case, only the events whose trajectories do not exceed the line are preserved. The second case requires that the events kept are those whose trajectory exceeds the line.

Therefore, for each particle, there are two sets of arcs. The first set of arcs $(\alpha_{ACD,\pm}, \beta_{ACD,\pm})$ is linked to ADCs, it indicates detectable events. The other set $(\alpha_{slit,\pm}, \beta_{slit,\pm})$ is linked to the slot, it indicates undetectable events.

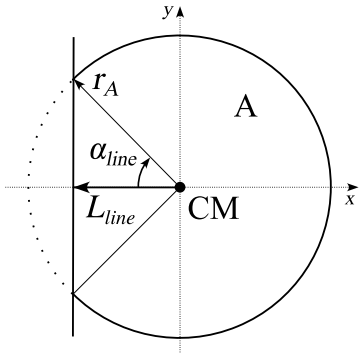

Figure 4.7: Opening angle of the acceptance linked to a line.

If the distance $L_{1,ADC}$ (or $L_{2,ADC}$) is the distance of a vertical line crossing the detector $D1$ (or $D2$) with the center-of-mass, then the arc $[-\alpha_{ADC}, \alpha_{ADC}]$ centered on the center-of-mass which starts from an intersection between the edge of the detector to the other intersection (or $[-\beta_{ADC}, \beta_{ADC}]$) is given by

(see figure 4.7):

$$\alpha_{ADC,\pm} = \pm \arcsin \frac{r_A}{L_{1,ADC}} \tag{4.31}$$

$$\beta_{ADC,\pm} = \pm \arcsin \frac{r_B}{L_{2,ADC}} \tag{4.32}$$

Obtaining the arc of a circle linked to the slit is identical.

These arcs – previously transposed into the same quadrant using the relation 4.29 – must then be combined with the arc obtained by the equation 4.27. Which gives for the ADC limit:

$$\alpha''_{slit,\pm} = \min\left(\alpha'_{\pm}, \alpha'_{slit,\pm}\right) \tag{4.33}$$

$$\beta''_{slit,\pm} = \max\left(\alpha'_{\pm}, \alpha'_{slit,\mp}\right) \tag{4.34}$$

The same applies to the slit.

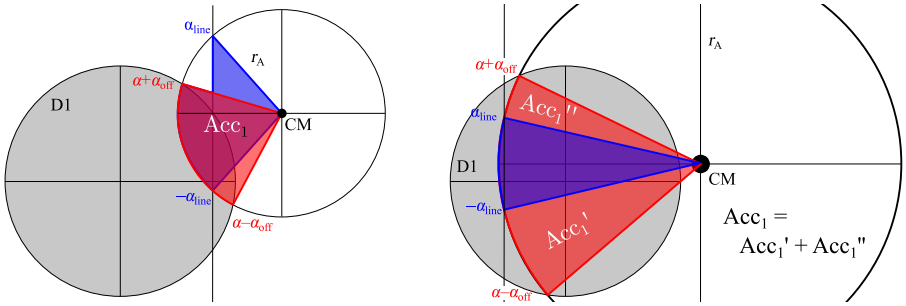

Figure 4.8: The figure on the left indicates a combination of acceptances that takes into account the addition of an internal cut-off. The figure on the right indicates a combination of acceptances which takes into account the addition of an external cut-off.

The acceptance given by the combination of circles inscribed with the ADC Acc_{ADC} and that given by the slit Acc_{slit} are given by:

$$Acc_{slit}(E_{rf}, \theta_{r,f}) = \frac{1}{2\pi} \max\left(\min(\alpha''_{slit,+}, \beta''_{slit,+}) - \max(\alpha''_{slit,-}, \beta''_{slit,-});\ 0 \right) \tag{4.35}$$

$$Acc_{ADC}(E_{rf}, \theta_{r,f}) = \frac{1}{2\pi} \max\left(\min(\alpha''_{ADC,+}, \beta''_{ADC,+}) - \max(\alpha''_{ADC,-}, \beta''_{ADC,-});\ 0 \right) \tag{4.36}$$

The total acceptance is then the subtraction of these two terms. That is to say the subtraction between the acceptance linked to the accepted events and the acceptance linked to the discarded events within the set of initially accepted events:

$$Acc(E_{rf}, \theta_{r,f}) = Acc_{ADC}(E_{rf}, \theta_{r,f}) - Acc_{slit}(E_{rf}, \theta_{r,f}) \tag{4.37}$$

4.1.3 Acceptance map

The above development made it possible to determine an acceptance Acc for each combination $(E_{r,f}, \theta_{r,f})$.

The acceptance map is generated as follows: An experimental distribution of the center-of-mass (x_{cm}, y_{cm}) is generated numerically [6] Then a uniform grid is generated according to the parameters $E_{r,f}$ and $\cos\theta_{r,f}$ [7]. The acceptance is finally calculated for each value of the grid.

This grid is uniform according to $\cos\theta_{r,f}$ instead of $\theta_{r,f}$. This grid format makes it easy to compare the shape of the acceptance with actual mutual neutralization measurements where the collision energy is dominated by the angular distribution of the beams. Under these conditions, the angular distribution of the events produced during the reaction is uniform (see section 4.3.3). It follows that the angular distribution measured experimentally is identical to the angular distribution of acceptance.

Once the acceptance map is obtained, it is possible to compare it with the experimental data [8].

During each measurement day, the experimental setup is adjusted to maximize the measured signal. This method of adjusting the device makes it possible to minimize the collision energy. Indeed, as the reaction is exothermic, the total cross section of the reaction is inversely proportionnal to the collision energy (section 3.4) when this collision energy tends to zero and maximizes the number of events detected. On the other hand - once the beams of the device have been optimized in order to maximize the signal - the only element to be adjusted is the voltage of the observation cell. This modifies the collision energy without modifying the other optical properties of the beams (see section 2.5).

A first measurement is always carried out at minimum energy, before modifying the observation voltage.

---

[6] This simulated distribution contains about 200 events. This number gives the best ratio between the necessary resources (calculation time and random access memory) and the precision of the calculation.

Since the distribution of the center-of-mass is assumed to be independent of the combination $(E_{r,f}, \theta_{r,f})$, this distribution is generated only once. It is kept in memory during the entire execution of the program.

This simulated distribution of events is systematically compared with the experimental distribution of the center-of-mass, which contains about 20,000 events per measurement.

[7] The typical step of the acceptance grid is 0.005 eV in energy, and 0.01 according to $\cos\theta_{r,f}$. These step values give sufficient precision, while limiting the computation time.

[8] The value $E_{r,exp}$ obtained during the analysis of the experimental data has a systematic error. This error is linked to a slight imprecision in the measurement of distances (interaction cell / detectors, detector / detector) or time (slow drift of the reference time). This systematic error is obtained during the analysis of the distance energy spectra. It changes the energy scale by about 1%. This change of scale must be applied to the events before comparing them with the acceptance.

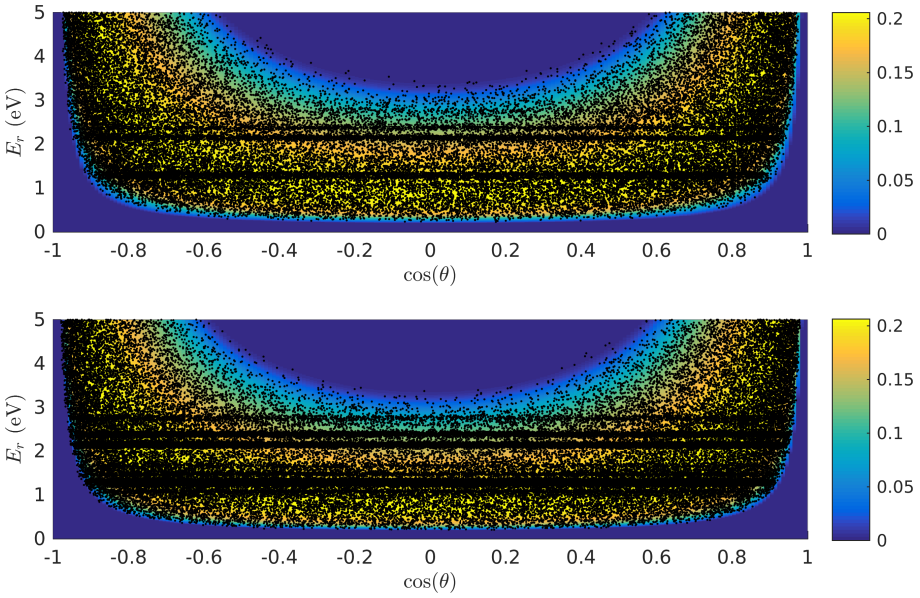

Figure 4.9: Acceptance map for the mutual neutralization reaction of N^+ with O^-. The acceptance map is represented by the colormap, while the actually measured events (minimum collision energy) are represented by black dots on the map. The top figure shows the result obtained when N hits $D1$ and O hits $D2$, the bottom figure shows the other mass combination (section 2.8).

In order to ensure that the acceptance corresponds to the configuration of the experimental setup, two verification methods are possible.

The first method is only qualitative, but it helps to understand the overall behavior of acceptance. It consists in representing the events distribution measured experimentally on the acceptance map (see figure 4.9). When the beam parameters have been correctly evaluated, the experimental points are located on the acceptance map only within the zones where the value of the acceptance is not zero. The higher the acceptance of this zone of the map, the greater the density of points.

Figure 4.9 shows an acceptance map and the events related to this measurement of mutual neutralization of N^+ with O^-. It is evident that the measured events cluster in the areas where the acceptance is maximum.

The acceptance map has a typical shape. When the relative energy after collision is low, the acceptance is zero. This is imposed by the space between the two detectors. The recoil speed is too low for the neutralized ions to reach them. As the recoil energy increases, the acceptance increases for $\cos\theta = 0$, but remains zero for $\cos\theta = \pm 1$. Indeed, if $\cos\theta = 0$, then the atoms are emitted perpendicular to the axis of propagation (in the reference of the center-

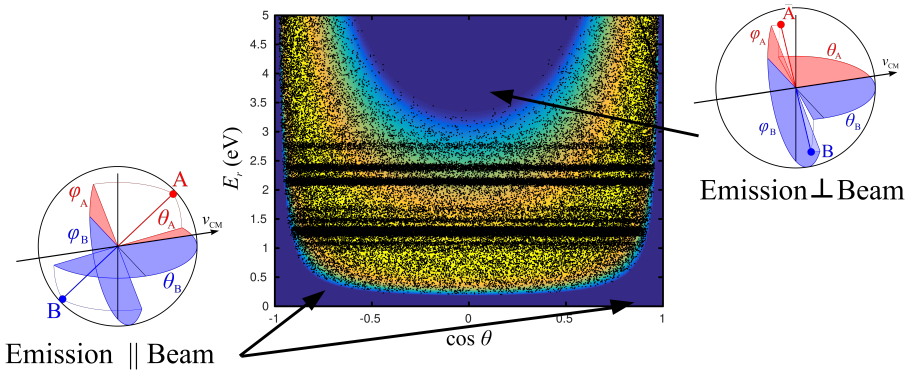

Figure 4.10: Acceptance map for the mutual neutralization reaction of N^+ with O^-. This figure is the same as the lower part of the figure 4.9, to which has been added a representation of the direction of propagation of the particles after collision, as in the figures 4.2 and 4.1.

of-mass). These events require the lowest recoil energy to be detected. [9]. In contrast, if $\cos\theta = \pm 1$, then the atoms are emitted in the direction parallel to the beam propagation axis. They can therefore never be detected (because they will always pass between the detectors - figure 4.10).

When the relative energy after collision is higher, a minimum forms around $\cos\theta = 0$. As the atoms are emitted perpendicular to the axis of propagation, the recoil of the atoms is sufficiently important for them to propagate beyond the detectors [10] (figure 4.10). This hollow widens as the relative energy after collision increases, until it forms two fine bands of acceptance located around $\cos\theta = \pm\ 0.75$. The position of these bands varies depending on the system studied and the distance between the observation cell and the detectors.

For this reaction, the mass ratio between the two ions is relatively balanced. The direction of the main axis of mass centers was directed between the two detectors. Therefore, the acceptance changes little when the nitrogen atom is assigned to detector 2 instead of detector 1 and the oxygen atom to detector 1 instead of detector 2.

Figure 4.11 shows the acceptance map and events related to a mutual neutralization measure of $Li^+ + D^-$. As before, the measured events are grouped together in the zones where the acceptance is maximum. The shape of the acceptance map of a certain mass combination is similar to that of figure 4.9. In contrast, the acceptance map of the other mass combination is empty.

Since the mass ratio between lithium and deuterium is large, while the re-

[9] The detector dead zone linked to ADCs will change the minimum relative energy at which events can be detected as it increases the position for which the acceptance begins to be non-zero.

[10] When the slit after the observation cell is in place, events do not propagate to the detectors. They are stopped by the slit.

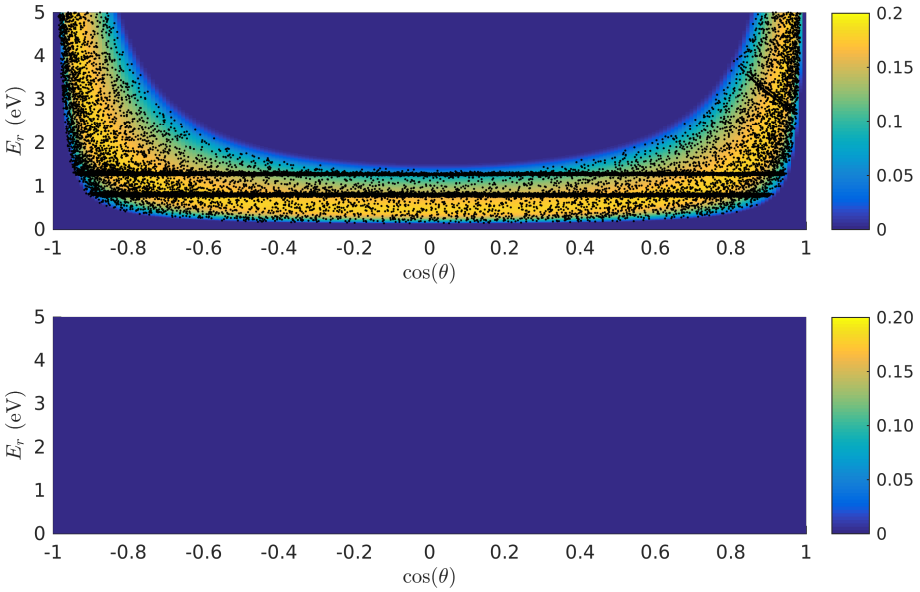

Figure 4.11: Acceptance map for the mutual neutralization reaction of Li^+ with D^-. The acceptance map is represented by the colormap, while the events actually measured (minimum collision energy) are represented by black dots on the map.

coil of the lithium atom is still small, the deuterium atom already has a large recoil. If the center-of-mass of the particles is directed right between the two detectors, the lithium atom would remain between the detectors, while the isotope of hydrogen is already leaving beyond the detectors.

In order to avoid this problem, the average center-of-mass of the combination of the beams is not directed exactly between the two beams, but shifted towards the detector $D1$. Consequently, the lithium atom, despite its low recoil speed, is detectable by the $D1$ detector which is located nearby and the deuterium is detectable by the $D2$ detector located further away. However, it is therefore no longer possible for the detector $D2$ to detect Li when the detector $D1$ detects Li (the deuterium atom is further away from the outer part of the detector when the lithium atom reaches the inner part of the other detector). Hence an empty acceptance map for a combination of masses.

This center-of-mass shift – even if it negates the possibility of detection for a combination of masses – increases the overall acceptance of the system.

4.2 Beam modeling

As said previously, the distribution of the impact position of the center-of-mass on the "plane" of the detectors influences the probability of detecting an event $(E_{r,f}, \theta_{r,f})$. To estimate its influence on the probability of detection, it is

necessary to model the collision between the initial ions, i.e. to model the ion beams brought into confluence.

4.2.1 Collisions distribution

The objective of this section is to numerically estimate the angular and spatial distribution of collisions within the observation cell. To achieve this, we must initially know the emittance of each of the beams within the interaction zone. By making these beams interact, it is possible to obtain the angular distribution of collisions, as well as the distribution perpendicular to the beam of the center-of-mass of the collision.

The first step is to characterize the distribution of each of the two beams which enter the observation cell. If the emittance of the source is known, it suffices to apply the transformation matrix of each of the optical elements that each of the beams crosses before reaching the interaction cell. However, the emittance of the beam is not known, moreover the position of each optical element is not known neither with sufficient precision. It is therefore necessary to use another method.

This other method requires several assumptions. First, the initial emittance of each of the beams is large compared to the emittance determined by the set of diaphragms through which each beam passes. Then, the space charge of each of the beams is negligible (fast beams of low density). Finally, the planar deflectors and the observation cell do not modify the emittance of a beam (absence of focusing linked to deflection and acceleration). Therefore, given that the focusing is done before passing through the diaphragms, the emittance of the beam within the observation cell is made up of all the trajectories which arrive in the cell while passing through the diaphragms.

Once these hypotheses have been verified, a set of trajectories are uniformly generated within the observation cell (cylinder 8 cm long and 1.9 mm in diameter, with a uniform direction of propagation [11]. They must pass through a first diaphragm located 47.0 cm before 0.95 mm in diameter, then a second located 78.1 cm from the cell, with a diameter of 1.45 mm of diameter. At last, they pass through a 1.45 mm of diameter diaphragm before the cell [12].

The position of the path starting from the cell (index c) at the level of the diaphragm (index d) in the plane perpendicular (x,y) to the direction of the mean path z, is

$$x_d = (z_d + z_c)\tan\theta_c \cos\varphi_c + x_c \tag{4.38}$$

[11] In order to limit the size of the event distribution, it is limited to a maximum angle of 5 mrad with the main propagation axis, this angle is large enough so that no path with a higher propagation direction can pass through all the diaphragms.

[12] These parameters were finely adjusted, from the distances measured approximately on the device, in order to reproduce the experimental measurement of the emittance of each beam.

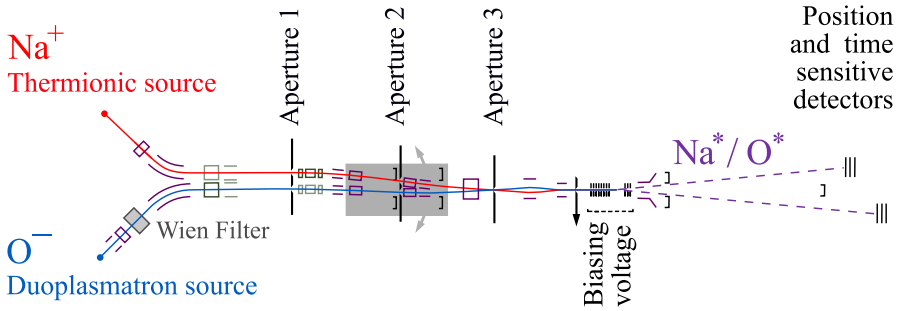

Figure 4.12: Diaphragms position in the experimental setup.

$$y_d = (z_d + z_c)\tan\theta_c \sin\varphi_c + y_c \tag{4.39}$$

This path passes through the diaphragm if:

$$(x_d^2 + y_d^2) < r_d^2 \tag{4.40}$$

where r_d is the radius of the diaphragm (figure 4.12 and table 4.1).

The set of trajectories which satisfy this condition form the distribution of the beam within the observation cell. This distribution being entirely geometric, it is independent of the speed of the beam (figure 4.13). It is obtained using a Monte-Carlo method.

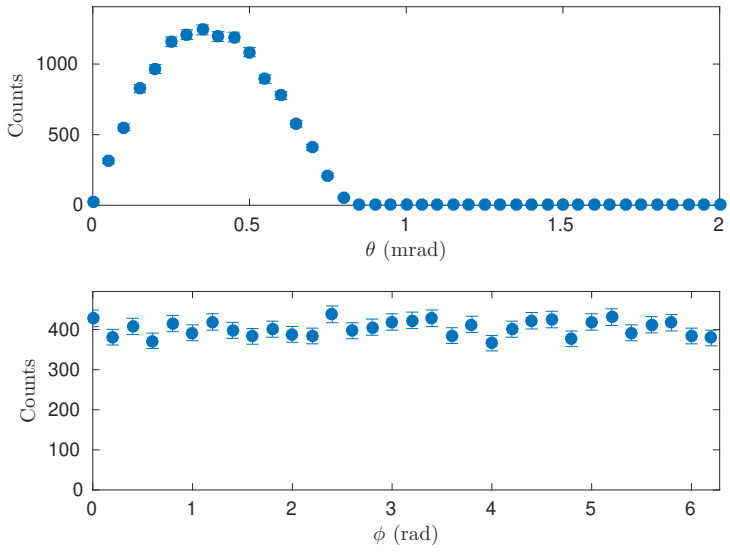

Figure 4.13: Simulated angular distribution of the beams passing the diaphragms (table 4.1) of the experimental setup using a Monte-Carlo method.

Optical element	Diameter (mm)	Position (mm)
Aperture 1	2.90	−781
Aperture 2	1.90	−470
Aperture 3	1.45	−125
Interaction region	–	$0 \rightarrow +80$

Table 4.1: Position of the apertures defining the beam emittance.

The only remaining component of the beams to be modeled is its speed distribution. This depends on the type of sources used. For a duoplasmatron source or an ECR source, at the source output, the energy distribution of the beam follows an approximately Gaussian curve, the full width at half maximum (FWHM) is 5 eV (a more detailed description of this distribution is presented in section 4.4.3). The average energy of each of the beams is for its part obtained using the characteristics of the experimental device: The difference in speed between the beams before entering the observation cell is relatively large. Upon entering the cell, a bias voltage will accelerate the slower beam and slow down the faster beam. This polarization voltage does not modify the sum of beam energies E_0. To adjust the relative kinetic energy $E_{r,i}$ between the beams, it suffices to adjust the bias voltage. The energy of each beam E_1, E_2 then becomes:

$$E_1 = \frac{m_1}{m_1 + m_2} \left(\sqrt{E_0 - E_{r,i}} + \sqrt{\frac{m_2}{m_1} E_{r,i}} \right)^2 \tag{4.41}$$

$$E_2 = E_0 - E_1 \tag{4.42}$$

where m_1 is the mass of the ions in beam 1 and m_2 is the mass of the ions in beam 2.

Once the distribution of trajectories of each beam is known, it remains to determine the direction of impact in the center-of-mass reference frame (collision axis in the center-of-mass frame aligned with the beams propagation axis), as well as the direction of the center-of-mass in the reference frame of the laboratory.

In the coordinate system of the center-of-mass, the distribution of the direction of collisions is the distribution of the relative velocity between the beams, thus

$$\vec{v}_{\text{coll}} = \vec{v}_1 - \vec{v}_2 \tag{4.43}$$

where care must be taken to invert the masses according to the type of event analysis desired [13].

[13] Since all beam distributions are performed in polar coordinates, the sum of two vectors is

When $E_1/m_1 = E_2/m_2$, the collision velocity is globally zero, while the collision energy is given by the relation 4.3. If the two beams are perfectly aligned within the observation cell, the average collision energy is given by the angular distribution of each beam. This configuration has two properties. On the one hand, it controls the minimum collision energy attainable by the experimental set-up. For the Louvain-la-Neuve setup, this angular distribution gives a minimum collision energy for the mutual neutralization reaction of about 10 meV [14]. On the other hand, when the collision energy is minimal [15], the angular distribution of the collision axis is approximately uniform (according to $\cos\theta_c$ and φ_c). Consequently, as no axis is privileged within the center-of-mass frame, the angular distribution - along the axis separating the atoms after collision (neutralization) – is also uniform.

An example of a randomly generated distribution is shown in figure 4.14.

---

performed from the Cartesian reconstruction of the vectors:

$$\begin{aligned} x_i &= r_i \sin(\theta_i)\sin(\varphi_i) \\ y_i &= r_i \sin(\theta_i)\cos(\varphi_i) \\ z_i &= r_i \cos(\theta_i) \end{aligned}$$

where $i = 1,2$.

The sum of vectors is then direct:

$$\begin{aligned} x_3 &= x_1 + x_2 \\ y_3 &= y_1 + y_2 \\ z_3 &= z_1 + z_2 \end{aligned}$$

It only remains to reconstruct the vector obtained in the polar coordinates:

$$\begin{aligned} r_3 &= \sqrt{x_3^2 + y_3^2 + z_3^2} \\ \tan\theta_3 &= z_3/\sqrt{x_3^2 + y_3^2} \\ \tan\varphi_3 &= (y_3/x_3) \end{aligned}$$

It should be noted that a sum of vector in polar coordinate is also possible without going to Cartesian coordinates, but it is more complex to implement, and therefore more difficult to verify.

[14] The energy distribution of the collision happens to be a thermal distribution of a temperature close to 50 K. Hence the name: subthermal reactions.

[15] The minimum collision energy condition assumes two things: On the one hand, the distribution of longitudinal collision energies is given by the energy dispersion of the beams. This energy dispersion varies between 5 and 10 eV depending on the source conditions. Thus, the relative energy distribution changes according to the energy of the beams and the source conditions (and is independant of the beam energy – section 4.4.3). On the other hand, the distribution of energies of transverse collisions is given by the angular distribution of the beams within the observation cell. This distribution is given by the geometry of the device. Thus, the two distributions are not identical, but remain substantially similar. A detailed discussion of the effect of beam energy distribution is given later in this chapter (section 4.4.2).

These two figures represent the histogram of these distributions composed of 10^6 events per collision energy.

The distribution according to the polar angle with respect to the axis of propagation of the beams is uniform, independent of the relative energy between the beams ensuring the cylindrical symmetry of the system.

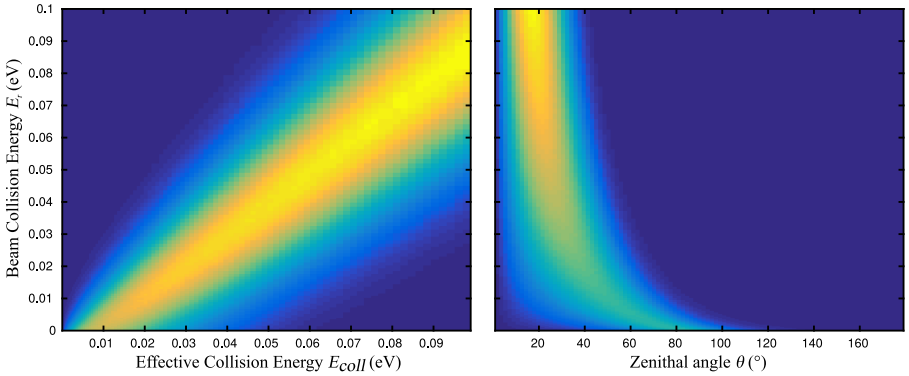

Figure 4.14: Effects of the beams energies and angular distributions for the $N^+ + O^-$ mutual neutralization reaction as a function of the unspread collision energy. The combined kinetic energy of the two beams is fixed at 14,000 eV. Left: effective collision energy distribution. Right: distribution of the zenith angle of collision θ in the center-of-mass frame with respect to the principal axis of the beams. In order to compare this figure with the following ones, one should note that $f(\cos\theta)\,\mathrm{d}\cos\theta = f(\cos(\theta))(\mathrm{d}\theta/\sin\theta)$.

The left part of the figure 4.14 indicates the effective collision energy distribution as a function of the detuning energy (unspread collision energy) between the two merged beams defined as $\frac{\mu}{m_A+m_B}(v_A^2 - v_B^2)$. If the relative energy is large enough ($E_r > 0.3$ eV), the collision energy follows a distribution centered around the collision energy. The width of this distribution is fixed. On the other hand, when the relative energy is low, the collision energy no longer varies linearly with the relative energy between the beams. The distribution of the collision energy becomes independent of the relative energy. The maximum of this distribution is about 8 meV.

The maximum collision energy shown here is greater than that shown above. In order to explain this difference, it is necessary to take into account the behavior of the cross section of mutual neutralization (section 3.1.5): When the reactants are ions of opposite charges, this diverges as $1/E_{r,i}$ when the collision energy tends to zero.

The reaction rate that depends on the distribution of relative velocities between anions and cations in the interaction region [16]. Thus, the received signal

[16] The ions travel through the observation cell of length l at a speed v_{cm}: This limits a possible interaction time to $t_{int} = l/v_{cm}$.

If we assume that anions and cations have a uniform relative velocity $v_{r,i}$, then the distance

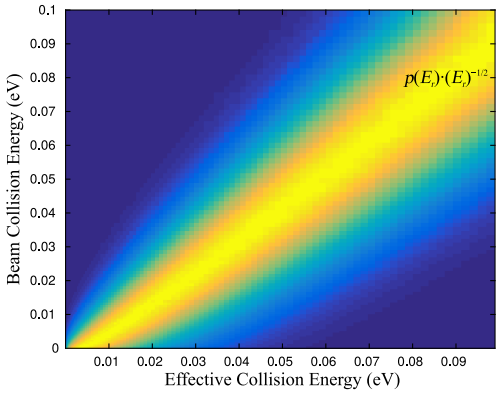

Figure 4.15: Simulated distribution of the collision energy when taking into account the $E^-1/2$ dependence of the rate coefficient $\sigma \times v_r$ between the atoms under the same conditions as in figure 4.14.

is given by

$$Signal \sim \langle \sigma v_{r,i} \rangle \sim \left\langle 1/\sqrt{E_{r,i}} \right\rangle \tag{4.44}$$

As a result, the collision energy distribution of mutually neutralized ions $\mathscr{P}_{MN}(\vec{v})$ differs from the collision independent ion distribution $\mathscr{P}_{coll}(\vec{v}_{r,i})$ by the relation

$$\mathscr{P}_{MN}(\vec{v}_{r,i}) = \frac{\mathscr{P}_{coll}(\vec{v}_{r,i})\sigma_{MN}(\vec{v}_{r,i})v_{r,i}}{\int \mathscr{P}_{coll}(\vec{v}_{r,i})\sigma_{MN}(\vec{v}_{r,i})v_{r,i}\,\mathrm{d}\vec{v}_{r,i}} \tag{4.45}$$

Therefore $\mathscr{P}_{MN}(\vec{v})$ is shifted towards small collision energies compared to $\mathscr{P}_{coll}(\vec{v})$ (figure 4.15).

The right part of the figure 4.14 shows the angular component of the collision velocity distribution [17]. When the speed difference is large, the collisions

---

that a cation travels in the anion beam d during this interaction time is given by: $d = v_{r,i}t_{int}$.

If the ions are uniformly distributed within their respective beams (linear density ρ), the number of anions n that a cation encounters within the interaction cell is

$$n = \rho d = \rho v_{r,i} l / v_{cm}$$

This reasoning extends easily by taking into account the cross section (it is necessary to replace the linear density by the volume density, then to multiply by the cross section) which gives

$$Signal \sim \sigma v_{r,i}$$

[17] This distribution is carried out according to the angle θ_{coll} instead of the angle $\cos\theta_{coll}$. This allows to better visualize the angular distribution, by avoiding the compression of the distribution along the vertical axis $\theta_{coll} = 0$.

The distribution according to the angle $\cos\theta_{col}$ is advantageous when this distribution is approximately uniform on the sphere.

occur along the main beam axis [18]. Then, the collision energy is nearly equal to the detuning energy. When the speeds of the beams are the same, the direction of collision is perpendicular to the axis of propagation of the beams. The parallel component being zero, there is no collision in that direction. Therefore, the distribution of the collision energy at zero relative energy is given by the angular distribution of each of the beams. If the beams are well defined – have low emittance – then the minimum collision energy is low. This explains the presence of diaphragms within the experimental setup. These are placed within the device in order to optimize the quality and quantity of the signal [19][20].

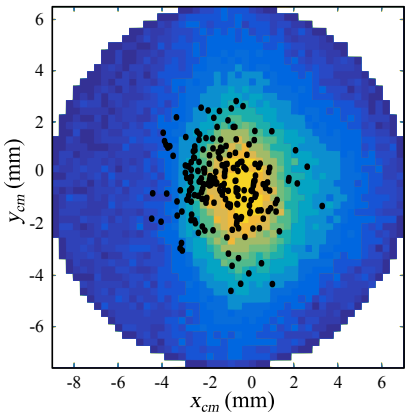

Figure 4.16: Distribution of the center-of-mass. The false color diagram is the two-dimensional histogram of events for the reaction depicted in figure 4.9. The black dots correspond to the simulated distribution, as described in this section.

The distribution of the center-of-mass of the collision is given by the sum of the momentum of a particle of each beam:

$$\vec{v}_{\mathrm{cm}} = \frac{1}{m_1 + m_2}\left(m_1\vec{v}_1 + m_2\vec{v}_2\right) \tag{4.46}$$

This last distribution is not essential for the analysis of the events themselves, but it allows to reproduce the experimental distribution of the center-

[18] The distribution generated when the masses are reversed is the same as this one with axial symmetry applied around 90^o.

[19] However, it is not possible to optimize these two parameters simultaneously. A thinner diaphragm improves the definition of a beam, but decreases the number of particles that pass through. A larger or closer diaphragm has the opposite effect. Thus, the position and size of the diaphragms are critical parameters.

[20] The effect of the beams distributions ΔE_1, ΔE_2 and $\Delta\theta$ is given by [185]:

$$\frac{\Delta E_{r,i}}{E_{r,i}} = 2\sqrt{\frac{\mu}{m_1+m_2}}\frac{\Delta E_1 + \Delta E_2}{\sqrt{E_r E_0}} + \frac{\mu}{m_1+m_2}\frac{E_0}{E_{r,i}}(\Delta\theta)^2.$$

of-mass. $(x_{\mathrm{cm}}, y_{\mathrm{cm}})$:

$$x_{\mathrm{cm}} = z_{\mathrm{det}} \sin(\theta_{\mathrm{cm}}) \sin(\varphi_{\mathrm{cm}}) \tag{4.47}$$

$$y_{\mathrm{cm}} = z_{\mathrm{det}} \sin(\theta_{\mathrm{cm}}) \cos(\varphi_{\mathrm{cm}}) \tag{4.48}$$

where z_{det} is the distance between the observation cell and the detectors (figure 4.16).

4.3 Modeling of the differential cross section

The treatment of the beam distribution has shown its importance in obtaining the average collision energy. Moreover, this processing shows that to obtain the energy distribution of the signal, it is necessary on the one hand to estimate the collision energy, but also to know (at least in a simplified manner) the effective section of the reaction studied.

The above reasoning also applies to the shape of the experimental angular distribution (according to $\cos\theta_{r,f}$): To estimate the signal lost by the detection system, it is necessary to estimate both the angular distribution of collisions, but also the differential cross section of the reaction (the probability that the particles will be deflected by a given angle during the reaction). This section sets out to develop simple methods to estimate the differential cross section.

4.3.1 Methodology

The differential cross section of a reaction is best obtained by propagation of the wave packet through the potential energy surfaces. To describe the processes that come into play, it is then necessary to follow the propagation of the wave packet and to describe its behavior.

The development presented here follows a radically different approach: Building models of increasing complexity starting with a classical picture of the scattering event, until obtaining a differential cross section which satisfactorily reproduces the measured differential cross section. This method - even if it does not lead to exact results - nevertheless makes it possible to highlight the importance and the effect of the various simplifying assumptions linked to each model. Thus the appearance of an important effect for a slightly more complex model makes it possible to explain what these emerging properties in the differential cross section are due to.

Moreover, as the assumptions set up here can be put in parallel with the assumptions set up during the calculation of the total cross section (chapter 3), it is then possible to evaluate independently the validity of the assumptions made in that chapter.

4.3.2 Interrupted Rutherford scattering

To begin with, let us take the simplest model which allows the estimation of the differential cross section, i.e. Rutherford scattering interrupted when the critical radius is intersected. This model is comparable to the asymptotic model for the following reasons:

This model describes the trajectory of a cation A^+ approaching an anion B^- assumed to be fixed – if the anion is not fixed, the development is similar if it is performed in the the center-of-mass frame. This change of reference frame does not affect the change in direction. – The trajectory of the cation is determined by the attractive Coulomb force. This is similar to Rutherford scattering.

However, this trajectory may change when the distance between the two ions reaches a critical distance R_c. At this distance, the two ions can neutralize each other. The cation A^+ then becomes the excited atom A^*, its trajectory becomes rectilinear. The probability of this neutralization is assumed to be either constant or given by the Landau-Zener model.

Using these few assumptions, it is possible to evaluate the semi-classical differential cross section of the mutual neutralization reaction.

Kinematics in a Coulomb potential: conical trajectory

To begin with, it is important to remember why the trajectory of the pseudo-particle of reduced mass μ in the coordinate system of the center-of-mass [21] follows a conical (elliptic or hyperbolic) trajectory when subjected to a central potential and to obtain the parameters of this trajectory:

Lets define two particles (1 and 2), then the center-of-mass frame such as

$$m_1\vec{r}_1 + m_2\vec{r}_2 = 0 \Rightarrow m_1\vec{v}_1 + m_2\vec{v}_2 = 0 \tag{4.49}$$

where m_1 and m_2 are the masses of the particles, $\vec{r}_1$ and $\vec{r}_2$ their position and $\vec{v}_1$ and $\vec{v}_2$ their velocity.

Suppose that those particules are attracted by a force which derives from a potential whose depends only on the distance between the two particles $V_{12} = -k/r$ where $r = |\vec{r}| = \|\vec{r}_1 - \vec{r}_2\|$ is the distance between the two particles and $k = e^2/(4\pi\varepsilon_0)$. The energy of the system in the center-of-mass frame is given by:

$$E_{\text{tot}} = \frac{m_1 v_1^2}{2} + \frac{m_2 v_2^2}{2} - \frac{k}{r} \tag{4.50}$$

The Newton's second law applied to this system is:

$$m_i\dot{\vec{v}}_i = (-1)^i k\frac{\hat{r}}{r^2} \tag{4.51}$$

[21] The name "pseudo-particle" comes from the idea that it is neither atom 1 or atom 2, but the trajectory of both atoms can be derived from the trajectory of this pseudo-particle.

where $\hat{r} = \vec{r}/r$ is the nomalized direction of the vector $\vec{r}$.

The relative velocity between the two atoms is by definition:

$$\vec{v}_r = \vec{v}_1 - \vec{v}_2 \tag{4.52}$$

or, using the center-of-mass frame definition:

$$\vec{v}_r = \vec{v}_1 + \frac{m_1}{m_2}\vec{v}_1 = \frac{m_1}{\mu}\vec{v}_1 \tag{4.53}$$

similarly $\mu\vec{v}_r = -m_2\vec{v}_2$, with μ the reduced mass [22].

The kinetic energy term becomes, in terms of relative velocities:

$$\frac{m_1 v_1^2}{2} + \frac{m_2 v_2^2}{2} = \frac{m_1}{2}\frac{\mu^2}{m_1^2}v_r^2 + \frac{m_2}{2}\frac{\mu^2}{m_2^2}v_r^2 = \frac{\mu^2 v_r^2}{2}\left(\frac{1}{m_1} + \frac{1}{m_2}\right) = \frac{\mu v_r^2}{2} \tag{4.54}$$

thus

$$E_{\text{tot}} = \frac{\mu v_r^2}{2} - \frac{k}{r} \tag{4.55}$$

Therefore, the equations of motion of the system become:

$$\mu\ddot{\vec{r}} = -\frac{k}{r^2}\hat{r} \tag{4.56}$$

In this system, since there is no external force, the angular momentum $\vec{L} = \mu\vec{v}\times\vec{r}$ is preserved. Likewise, the Runge-Lenz vector $\vec{a} = \vec{p}\times\vec{L} - \mu k\hat{r}$ is also conserved, with which is associated the vector of eccentricity $\vec{e} = \vec{a}/\mu k$.

The eccentricity vector being preserved, the trajectory of the pseudo-particle in the frame of the center-of-mass is a conic. If $E_{tot} > 0$, $e > 1$ and the trajectory is a hyperbola (if $E_{tot} < 0$, $e < 1$ and the trajectory is an ellipse). Then E_{tot} can be identified as the initial kinetic relative energy $E_{r,i} = E_{tot}$.

This is expressed in the Cartesian plane as

$$x^2(1-e^2) + y^2 = \frac{\mathtt{p}^2}{1-e^2} \tag{4.57}$$

where $\mathtt{p}$ is the orbit parameter:

$$\mathtt{p} = \frac{L^2}{\mu k}. \tag{4.58}$$

[22] It is useful to notice that the velocity of particle 1 has the same direction and the same sense as the pseudo-particle related to the relative velocity. Same thing for particle 2, its direction is the same, but in the opposite direction.

The proportionality between the relative velocity and the velocity of the particles in the center-of-mass frame of reference implies an equivalence between the trajectory of the pseudo-particle with respect to the center-of-mass and the trajectory of one particle with respect to the other. The only difference between these trajectories is a scale factor. This second representation has the advantage of being more intuitive, while remaining rigorous.

If $v_{r,i}$ is the initial relative speed, and b the impact parameter, then

$$L^2 = (\mu v_{r,i} b)^2 = 2E_{r,i} b^2 \tag{4.59}$$

Therefore

$$e^2 - 1 = \frac{2L^2 E_{r,i}}{k^2 \mu} = \frac{4E_{r,i}^2 b^2}{k^2} \tag{4.60}$$

and

$$\mathtt{p} = \frac{2E_{r,i} b^2}{k} \tag{4.61}$$

In order to simplify the development, the equation of the hyperbola may also be written as

$$\frac{x^2}{a^2} - \frac{y^2}{\tilde{b}^2} = 1 \tag{4.62}$$

whose parameters a and $\tilde{b}$ are obtained by identification:

$$|a| = \frac{\mathtt{p}}{e^2 - 1} = \frac{k}{2E_{r,i}} \tag{4.63}$$

and

$$\tilde{b} = \frac{\mathtt{p}}{\sqrt{e^2 - 1}} = b \tag{4.64}$$

This representation is easier, because the parameter $\tilde{b}$ is the impact parameter b, while the parameter a depends only on the total energy of the system. In atomic units $a = (2E_{\mathrm{r,i}})^{-1}$.

The hyperbola equation can also be written in polar coordinates in the form

$$r(\theta) = \frac{\mathtt{p}}{e - \cos\theta} \tag{4.65}$$

therefore, the minimum distance of the pseudo-particle from the center-of-mass is

$$r_{\min} = \frac{\mathtt{p}}{e + 1} \tag{4.66}$$

with $e = \sqrt{1 + b^2/a^2}$ and $\mathtt{p} = b^2/a$.

Differential cross section

Thus, when subjected to an attractive Coulomb potential, the trajectory of an incident cation A^+ with initial velocity $\vec{v}_{r,i}$ on an anion B^- at rest can be written in the form of a hyperbola in the Cartesian plane $\{x, y\}$ as follows

$$\frac{x^2}{a^2} - \frac{y^2}{b^2} = 1 \tag{4.67}$$

with $a = -k/(2E_{r,i}) < 0$, $k = e^2/(4\pi\varepsilon_0)$, $E_{r,i} = mv_{r,i}^2/2$ the initial energy of the incident particle and b the impact parameter. The two focus points of this hyperbola are at $\{\pm\sqrt{a^2+b^2}, 0\}$. Then, the nearest of the two curves correspond to the attractive trajectory (the other one is the repuslive trajectory).

Let's arbitrarily choose le left focus point $\{\sqrt{a^2+b^2}, 0\}$ and a trajectory coming from $y = -\infty$. According to this representation, the distance between the pseudo-particles and the focus point is

$$R = \sqrt{\left(x + \sqrt{a^2+b^2}\right)^2 + y^2} \tag{4.68}$$

This distance is also the interatomic distance.

The direction angle θ of the pseudo-particle when it is at a distance R_c from the focus point is

$$\tan\theta = \frac{\mathrm{d}y}{\mathrm{d}x} = \pm\frac{b}{a}\frac{x}{\sqrt{x^2-a^2}} \tag{4.69}$$

which gives at $r = R_c$:

$$\tan\theta_c = \mp\frac{b}{a}\frac{R_\mathrm{c} - a}{\sqrt{R_\mathrm{c}^2 - 2aR_\mathrm{c} - b^2}} \tag{4.70}$$

The angles of deviation of the particle from its initial direction after the first pass Θ and after the second pass Θ' through the critical radius are given by $\Theta = \theta - \theta_0$ and $\Theta' = \pi - \theta - \theta_0$, with the initial direction of the particle A^+ defined as (see figure 4.17):

$$\theta_0 = \theta(r \to \infty) = \mathrm{atan}\left(-\frac{b}{a}\right) \tag{4.71}$$

By using the addition formula for the tangentand by introducing the above expression of the initial direction of the pseudo-particle, the direction of propagation is expressed as

$$\tan\theta = \tan(\Theta + \theta_0) = \pm\frac{b}{a} \times \frac{1 + \frac{a}{b}\tan\Theta}{1 - \frac{b}{a}\tan\Theta} \tag{4.72}$$

This equation can be equaled to equation 4.70, which gives

$$\frac{1 - \frac{a}{b}\tan\Theta}{1 + \frac{b}{a}\tan\Theta} = \mp\frac{R_\mathrm{c} - a}{\sqrt{R_\mathrm{c}^2 - 2aR_\mathrm{c} - b^2}} \tag{4.73}$$

The minus term corresponds to the first crossing while the plus term corresponds to the second one.

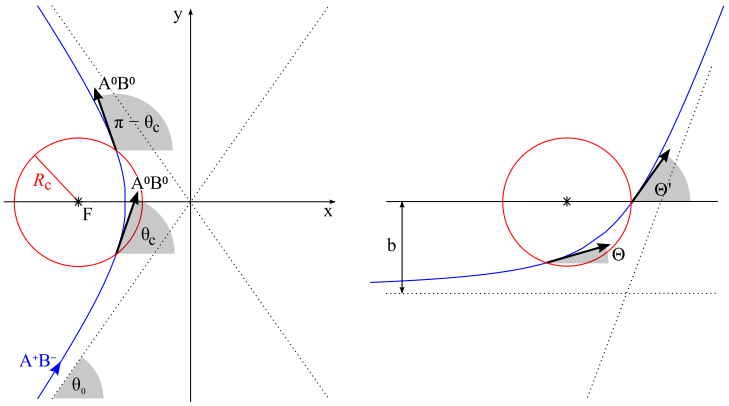

Figure 4.17: Scattering angles in the interrupted Rutherford model. The focus point is noted F, the trajectory of the ionic pseudo-particle A^+B^- is indicated in blue, the critical radius in red, the trajectories of the particle neutralized A^0B^0 by the black arrows. The left figure represents the trajectory in the initial frame $\{x,y\}$, while in the left figure, this trajectory is rotated in order to have a better representation of the angles of diffusion and the impact parameter b.

By isolating the impact parameter as a function of the distance and the scattering angle of the pseudo-particle, one finds that both solutions are identical with complementary solution domains and finally obtains:

$$b = a\left(\frac{\sin\Theta\cos\Theta + c\sin\Theta}{d+\sin^2\Theta}\right) \tag{4.74}$$

with the dimensionless parameters c and d defined as follows:

$$c = \frac{R_c - a}{\sqrt{R_c^2 - 2aR_c}} \tag{4.75}$$

$$d = \frac{a^2}{R_c^2 - 2aR_c} \tag{4.76}$$

It is therefore possible to express the angular derivatives of the impact parameter:

$$\frac{db}{d\Theta} = a\left[\frac{2\cos^2\Theta - 1 + c\cos\Theta}{d+\sin^2\Theta} - \frac{2\sin^2\Theta\cos\Theta(\cos\Theta + c)}{\left(d+\sin^2\Theta\right)^2}\right] \tag{4.77}$$

The differential cross section, by definition, is given by:

$$\frac{d\sigma}{d\Omega} = \frac{b}{\sin\Theta}\left|\frac{db}{d\Theta}\right| \cdot p(b) \tag{4.78}$$

Or, assuming $p(b) = 1$, and expressing the impact parameter, as well as its derivative in terms of the scattering angle:

$$\frac{\mathrm{d}\sigma}{\mathrm{d}\Omega} = \frac{a^2}{\sin\Theta}\left[\frac{\sin\Theta\cos\Theta + c\sin\Theta}{d+\sin^2\Theta}\right] \times \left[\frac{2\cos^2\Theta - 1 + c\cos\Theta}{d+\sin^2\Theta} - \frac{2\sin^2\Theta\cos\Theta(\cos\Theta + c)}{\left(d+\sin^2\Theta\right)^2}\right] \tag{4.79}$$

It is therefore possible to obtain the differential cross section section as a function of the critical (crossing) radius, because the latter is directly related to the kinetic energy release (see section 1.2). This method makes it possible to approach the angular scattering of mutual neutralization to the first order, in order to obtain a realistic acceptance map.

In order to examine this expression, it is important to note that the differential cross section depends on the parameters c and d which themselves depend on the critical distance R_c between the two interacting particles in the Landau-Zener model.

Case of interaction to infinity: Rutherford scattering

To assess the validity of this analytical expression, one method consists in studying the limiting case where the critical distance tends to infinity ($c = 1$ and $d = 0$). One must verify the following conditions:

- At the first passage through the critical radius, the differential cross section is that of an absence of scattering (the particle A is always neutral),
- the second passage through the critical radius gives the Rutherford scattering (the particle A is always charged, there is no charge exchange), whose differential cross section is

$$\frac{\mathrm{d}\sigma}{\mathrm{d}\Omega} = \frac{a^2}{4}\sec^4\frac{\Theta}{2} \tag{4.80}$$

Let's start by describing this second passage, the impact parameter (Eq. 4.74) is then:

$$b = a\frac{\cos\Theta + 1}{\sin\Theta} = a\frac{2\cos^2\frac{\Theta}{2}}{2\sin\frac{\Theta}{2}\cos\frac{\Theta}{2}} = a\cot\frac{\Theta}{2} \tag{4.81}$$

whose derivative according to the zenith angle is:

$$\frac{\mathrm{d}b}{\mathrm{d}\Theta} = a\left[\frac{2\cos^2\Theta - 1 + \cos\Theta}{\sin^2\Theta} - \frac{2\sin^2\Theta\cos\Theta(\cos\Theta + 1)}{\sin^4\Theta}\right]$$

$$
\begin{aligned}
&= \frac{a}{\sin^2\Theta}\left(2\cos^2\Theta - 1 + \cos\Theta - 2\cos^2\Theta - 2\cos\Theta\right) \\
&= a\frac{\cos\Theta + 1}{\sin^2\Theta} = a\frac{-2\cos^2\frac{\Theta}{2}}{4\sin^2\frac{\Theta}{2}\cos^2\frac{\Theta}{2}} \\
&= \frac{-a}{2\sin^2\frac{\Theta}{2}}
\end{aligned} \tag{4.82}
$$

and which can be replaced in the expression of the differential cross section

$$
\begin{aligned}
\frac{\mathrm{d}\sigma}{\mathrm{d}\Omega} &= \frac{1}{\sin\Theta} \times b \times \left|\frac{\mathrm{d}b}{\mathrm{d}\Theta}\right| = \frac{1}{2\sin\frac{\Theta}{2}\cos\frac{\Theta}{2}} \times \frac{\cos\frac{\Theta}{2}}{\sin\frac{\Theta}{2}} \times \frac{a}{2\sin^2\frac{\Theta}{2}} \\
&= \frac{a^2}{4\sin^4\frac{\Theta}{2}}
\end{aligned} \tag{4.83}
$$

This expression is indeed that of the Rutherford scattering [186].

All what remains is to obtain the differential cross section during the first passage through the critical distance. To achieve this, we must use an alternate expression of the impact parameter (Eq. 4.74):

$$
b = -a\left(\frac{\sin\Theta'\cos\Theta' - c\sin\Theta'}{d + \sin^2\Theta'}\right) \tag{4.84}
$$

which is identical to the equation 4.74, using $\Theta' = \pi - \Theta$. In the asymptotic case ($c = 1$ and $d = 0$), this equation becomes:

$$
b = a\left(\frac{\cos\Theta - 1}{\sin\Theta}\right) \tag{4.85}
$$

Using the trigonometric identity

$$
\cos\Theta - 1 = 2\cos^2\frac{\Theta}{2}, \tag{4.86}
$$

the differential cross section is then deduced in a similar way and gives

$$
\frac{\mathrm{d}\sigma}{\mathrm{d}\Omega} = \frac{a^2}{4\cos^2\frac{\Theta}{2}\sin^2\frac{\Theta}{2}} = \frac{a^2}{\sin^2\Theta} \tag{4.87}
$$

This expression corresponds to the case where there is no scattering. Indeed, the solid angle element is rewritten as $\mathrm{d}\Omega' \sin\Theta \mathrm{d}\Theta \mathrm{d}\phi$ in spherical coordinates. Thus, since the cross section is monotonic along the azimuthal angle, it is easily integrated along this coordinate, which gives:

$$
\frac{\mathrm{d}\sigma}{\mathrm{d}\Theta} = \frac{2\pi a^2}{\sin\Theta} \tag{4.88}
$$

This equation is that of a horizontal line which passes at a distance $2\pi a^2$ from the origin. The initial particle is therefore never deflected.

4.3.3 Impact parameter model

The following model takes into account the true potential energy curves.

Indeed, Rutherford scattering assumes that the attractive potential between the two ions is a Coulomb potential, while the potential of the covalent state is constant. This assumption is indeed valid when the interatomic distance is large (beyond 20 a_0).

However, while the trajectory of the atoms is assumed to be classical, the minimum interatomic distance lies outside this domain of validity for a large number of impact parameters.

In addition, the probability of transition from one state to another is given by 3.28

$$P_{\mathrm{i,c}} = 1 - \exp\left(-\frac{2\pi E_{\mathrm{ic}}^2}{\hbar v_R \Delta F}\right) \tag{4.89}$$

This depends on the radial velocity at the critical interatomic distance. As this speed depends on the impact parameter, the differential cross section becomes

$$\frac{\mathrm{d}\sigma}{\mathrm{d}\Omega} = P_{\mathrm{i,c}}\left(v_R(\theta)\right)\left(1 - P_{\mathrm{i,c}}\left(v_R(\theta)\right)\right)\left|\frac{b}{\sin\theta}\frac{\mathrm{d}b}{\mathrm{d}\theta}\right| \tag{4.90}$$

This section describes different models that improve the calculation of the differential cross section.

Classical trajectories in any potential

As the potentials are generally not analytical, it is no longer possible to obtain an analytical expression of the cross section.

This semi-classical method is not as accurate as quantum models for calculating cross-sections. It nevertheless retains several advantages. The first, and most obvious, is to be much faster to integrate numerically. The other advantage, which is more important, comes from the simplicity of the model, its sensitivity to potential energy curves and the possibility of extracting intermediate results from the simulation. It makes it possible to highlight the different components of the cross section and thus to check the validity of the approximations made within the framework of the anion centered asymptotic model for the interaction term (see section 3.2).

Note however that this model does not allow for any interference phenomenon. Indeed, the multiple trajectories are always treated in an independent pathways and hence they cannot interfere. This model is nevertheless sufficient for a comparison with the experimental data: the resolution obtained in the measurement of differential cross section is lower than the period of oscillation of the inter-path interference.

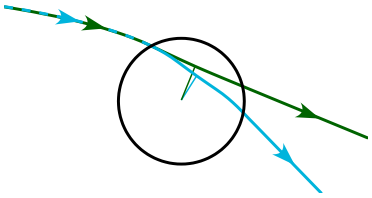

Figure 4.18: Example of modeled trajectories of a pseudo-particle in the coordinate system of the center-of-mass. The green (blue) curve shows the trajectory when the neutralization takes place during the first (second) passage through the avoided crossing.

In practice, the deflection angle is obtained by integrating the trajectory in spherical coordinates for each impact parameter (i.e. an impact parameter model or IPM). This function is then inverted and differentiated to obtain the differential cross section.

Path calculation method

By assuming the conservation of energy

$$E_{r,i} = \frac{\mu v_{r,i}^2}{2} = \frac{\mu v^2(t)}{2} + V\big(R(t)\big) \tag{4.91}$$

and the conservation of angular momentum

$$L = \mu v_{r,i} b = \mu v_\theta(t) R(t) \tag{4.92}$$

the angular velocity is

$$|\dot{\theta}|(t) = \frac{v_\theta(t)}{R(t)} = \frac{v_0 b}{R^2(t)} \tag{4.93}$$

while the radial velocity is

$$|\dot{R}|(t) = v_R(t) = \sqrt{v^2(t) - v_\theta^2(t)} = v_0 \sqrt{1 - \frac{V\big(R(t)\big)}{E_0} - \frac{b^2}{R^2}} \tag{4.94}$$

The minimum interatomic distance, at which the above square root cancels out, is obtained from:

$$1 - \frac{V(R_{\min})}{E_0} - \frac{b^2}{R_{\min}^2} = 0 \tag{4.95}$$

In the framework of the Landau-Zener model applied to mutual neutralization, the exchange of an electron is possible only when the ionic potential energy curve crosses the covalent potential energy curve. These intersect at an interatomic distance R_c.

If the impact parameter satisfies $R_{\min} > R_c$, then the trajectory does not reach the intersection between the potential curves. It follows that there is a

maximum impact parameter $b_{\max}$ beyond which charge exchange is impossible:

$$b_{\max} = R_c \sqrt{1 - \frac{V(R_x)}{E_0}} \tag{4.96}$$

Equations 4.93 and 4.94 do not allow to determine the sign of the angular and radial velocity components. This is not really a problem. The trajectory has two segments: An incoming trajectory (in) and an outgoing trajectory (out). The sign of $\dot{R}$ and $\dot{\theta}$ is conserved along each of the trajectories. The angular velocity has the same sign for both segments, while the radial velocity is negative when approaching and positive when moving away.

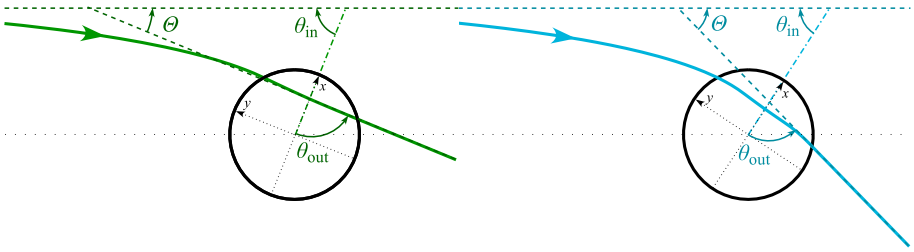

Figure 4.19: Semi-classical trajectory of the pseudo-particle in the coordinate system of the center-of-mass for the reaction $Li^+ + D^- \rightarrow Li(1s^2 3p) + D$ having a collision energy of 0.02 eV and an impact parameter of 3/5 of the maximum impact parameter which contributes to the reaction. The figure on the left shows the trajectory when the neutralization takes place during the first passage through the avoided crossing. The figure on the right corresponds to the neutralization during the second passage.

In order to speed up the integration of the trajectory, two modifications are applied [23]. The first is to integrate from the minimum interatomic distance with a positive radial velocity (with $\theta(r_{\min}) = 0$ set arbitrarily). As the angular velocity decreases when the interatomic distance increases, it thus decreases as the integration progresses. It is then possible to determine a threshold beyond which the angular velocity is sufficiently low as to no longer influence the angular deviation of the trajectory. This gives an angle of deviation:

$$\Theta = \theta_{\text{in}}(t \rightarrow \infty) + \theta_{\text{out}}(t \rightarrow \infty) - \pi; \tag{4.97}$$

The second optimization follows from the behavior of the asymptotic trajectory. As this does not pass through the center of the reference frame, the angular position of the path continues to evolve. If the iteration is long enough,

[23] Added to this is the choice of the integration method. This must be fast enough, and converge correctly. The selected method is the `ode113` method from MATLAB. This method is the fastest method which converges correctly.

the angular position tends towards the direction of the path. These two quantities each indicate the angle of deviation for a given impact parameter [24].

The direction of the trajectory converges faster than the angular position. Therefore, it is more advantageous to define the deflection angle as:

$$\theta_f = \tan^{-1}\left(\frac{\mathrm{d}(R\sin\theta)/\mathrm{d}t}{\mathrm{d}(R\cos\theta)/\mathrm{d}t}\right) = \tan^{-1}\left(\frac{\mathrm{d}y}{\mathrm{d}x}\right) \tag{4.99}$$

Definition of potentials

It remains to determine the potential $V(R)$ used for the trajectory calculation. This can be constructed from the adiabatic potential energy curves. In many systems (for example $C^+ + O^-$) such curves are always a real challenge to model. They can nevertheless be obtained for simple systems ($Li^+ + H^-$, $He^+ + H^-$ – figure 4.20).

The potential beyond the crossing distance corresponds, in the case of the approach, to the potential energy curve associated with the ionic state. Conversely, when the particles move away, it corresponds to the potential energy curve associated with the covalent state.

As described in section 3.1.3, the multichannel Landau-Zener model indicates that there are several possible trajectories once the system reaches interatomic distances less than R_c. For each impact parameter, it is necessary to calculate the deviation due to each of the trajectories. Each trajectory is associated to the diabatic state reached at low interatomic distance (figure 4.21). The first corresponds to the crossing avoided on approach, then crossed during the departure. The other corresponds to crossing traversed during the approach then avoided when the atoms move away.

The potential energy curves away from the avoided crossings are easily constructed from the adiabatic potential curves. However, a proper description of the crossing region requires a diabatization of the curves.

If the interaction terms are unknown, they can be easily estimated near the crossing (half of the minimum distance between the two adiabatic curves).

[24] It is also possible to solve those differential equations directly. In order to do so, let us redefine the radial speed as $\dot{R}(t) = v_R(t)$. Then $R(t) = R_{min} + \int_0^t v_R(t')\,\mathrm{d}t'$, which could easily be inserted in the angular part of the differential equation, substituting $\mathrm{d}t$ with $\mathrm{d}R/v_R$, which gives:

$$\theta(t\to\infty) = \int_{R_{min}}^{\infty} \frac{b}{R^2\sqrt{1 - V(R)/E_{r,i} - b^2/R^2}}\,\mathrm{d}R. \tag{4.98}$$

While this method does not give any information on the trajectory, it is a hundred times faster to integrate than the other method. It should also be noted that the integral could give a negative angle. One then needs to take the absolute value in order to get the right deflection angle.

One should also not that, as in the interrupted Rutherford scattering model, the scattering does not depend on the mass.

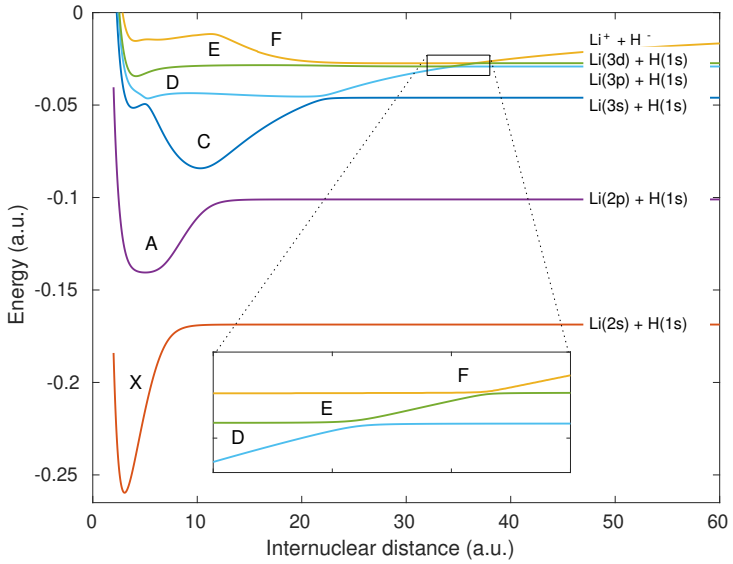

Figure 4.20: Adiabatic potential energy curves for LiH ($^1\Sigma^+$ symmetry, which applies also for LiD) [51].

Assuming a constant interaction term between the curves, the potential at the crossings is obtained thanks to the information contained in section 3.1.1:

$$V_{\text{ion}} = \frac{1}{2}\left((V_1+V_2) \mp \sqrt{(V_1-V_2)^2 - 4E_{\text{ic}}^2}\right) \tag{4.100}$$

$$V_{\text{cov}} = \frac{1}{2}\left((V_1+V_2) \pm \sqrt{(V_1-V_2)^2 - 4E_{\text{ic}}^2}\right) \tag{4.101}$$

where the sign changes on either side of the crossing point.

Unfortunately, this simple diabatization technique is not effective when several avoided crossings overlap.

Obtaining the differential cross section from the trajectories

If the potential curves are available, with isolated avoided crossings, it is possible to obtain the trajectory of the pseudo-particle in the center-of-mass frame for each allowed impact parameter.

$$b \leq b_{max} \tag{4.102}$$

An example of this set of trajectories for the reaction:

$$\text{Li}^+(^1S) + \text{D}^-(^1S) \rightarrow \text{Li}(1s^2 3p\ ^2P) + \text{D}(1s\ ^2S) \tag{4.103}$$

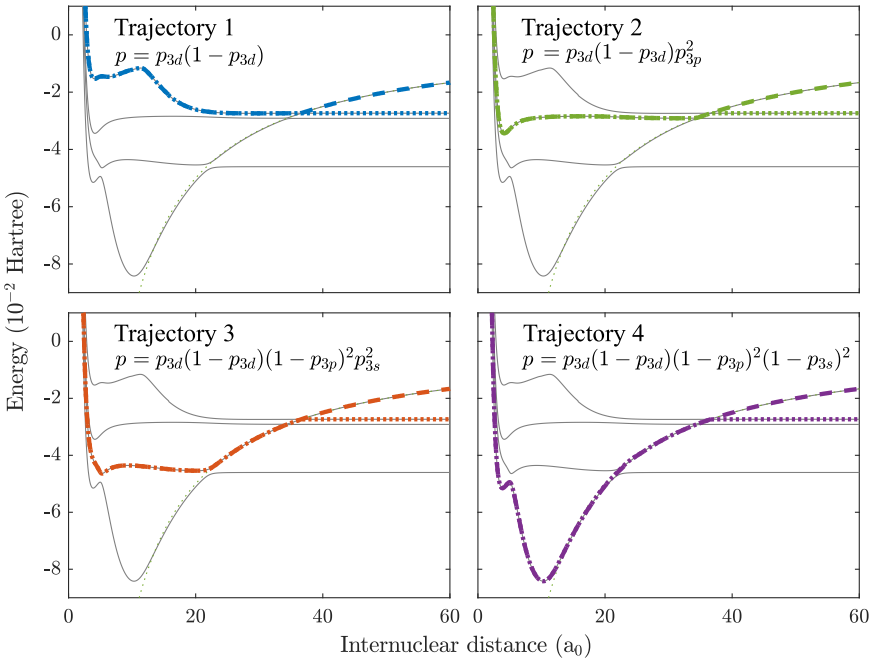

Figure 4.21: Potential energy curves corresponding to the different paths which lead to the mutual neutralization of Li^+ with D^- towards the state $Li(1s^2 3d\ ^2D)$ + $D(1s^2\ ^1S)$. The solid curves correspond to the adiabatic curves of LiD (see figure 4.20). The dashed lines correspond to the potential energy curve followed during the approach while the dotted lines correspond to the potential energy curve followed during the departure. For each of the curve combinations, the exchange probability is given (see text).

is given in figure 4.22. The total deflection angle induced for each of these impact parameters is given in figure 4.23. These two figures make it possible to understand different components of the differential cross section.

When the impact parameter is maximum, the trajectory of closest approach is tangent to the circle of the avoided crossing. For this impact parameter, the first passage through the crossing occurs at the same time as the second passage (figure 4.22). The deflection angle is thus identical for all trajectories (figure 4.23). Consequently, the curve of the impact parameter as a function of the deflection angle is continuous and differentiable around the maximum impact parameter. This corresponds to the behavior obtained by the interrupted Rutherford scattering model.

When the impact parameter is close to the maximum impact parameter, the trajectory smoothly evolves as a function of the impact parameter (figure 4.22 – these trajectories correspond to those indicated by the first arrow starting from the darkest path [25]). The deflection angle is close to that given by

[25] Note that the first arrow on the left side of figure 4.22 points in the opposite direction from

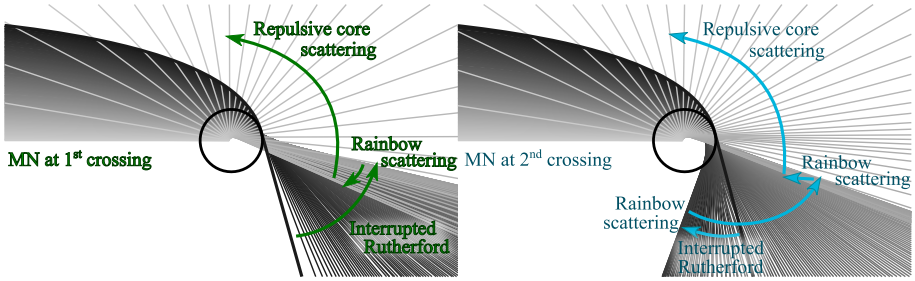

Figure 4.22: Set of semi-classical trajectories of the pseudo-particle in the coordinate system of the center-of-mass for the reaction $Li^+ + D^- \rightarrow Li(1s^2 3p\ ^2P) + D$, at a collision energy of 0.02 eV. The figure on the left shows the trajectory when the neutralization takes place during the first passage through the avoided crossing. The figure on the right corresponds to the neutralization during the second passage. The black circle indicates the position of the avoided crossing. The full gray curves each correspond to a trajectory. The brighter the curve, the lower the impact parameter. The thick black line is the trajectory linked to the impact parameter b_{max}. This curve is identical in the figure on the left and on the right. The colored arrows indicate the evolution of the deflection when the impact parameter decreases.

the interrupted Rutherford scattering model. Indeed, as the minimum interatomic distance for these trajectories is large (greater than 30 a_0), the potential curves are approximately those assumed in the interrupted Rutherford scattering model.

When the impact parameter decreases, there is a value for which the direction of propagation returns to the same deviation angle as the previous impact parameters. This inversion in the evolution of the direction of propagation generates an accumulation of identical trajectories for different impact parameters [26]. This set of different paths leading to the same deflection angle is called *rainbow scattering*. This scattering is characterized by an extremum of the scattering angle as a function of the impact parameter, which means that the derivative of the impact parameter as a function of the scattering angle diverges.

For smaller impact parameters, the interrupted Rutherford scattering model is no longer valid. The minimum interatomic distance is also smaller, meaning that the potential energy curves are no longer only Coulomb or constant. It is necessary to take into account the real electronic states of the molecule. It is also possible that the generated trajectories lead to multiple rainbow scattering.

Once the impact parameter is small enough, the minimum interatomic distance is dictated by the repulsive part of the interatomic potential. Once this

the first arrow on the right side of the figure. This argument reinforces the hypothesis of the continuous and derivable evolution of the deflection angle as a function of the impact parameter, around the maximum impact parameter.

[26] This stagnation in the deviation corresponds to the trajectories for which the distance of closest approach corresponds to an inflection point in the potential curve.

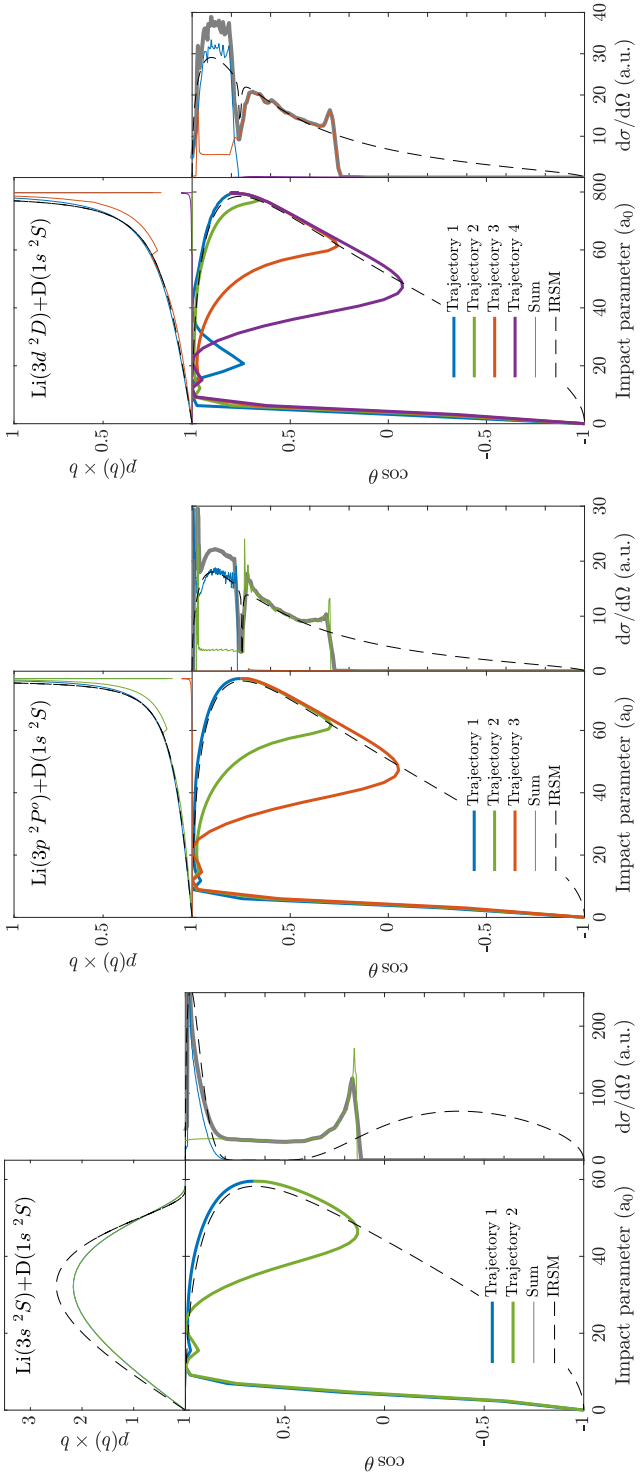

Figure 4.23: Differential cross section for the Li^++D^- mutual neutralization reaction for an collision energy of 200 meV.

impact parameter is reached, the scattering angle will quickly rise to 180^o (last arrow in figure 4.22 – impact parameter less than 25 a_0 in figure 4.23). The contribution linked to this last component of the angular distribution is small: the angle variation as a function of the impact parameter is rapid, therefore the density of the trajectories is low.

The differential cross section is obtained in the same way as in the interrupted Rutherford scattering model (equation 4.90)

$$\frac{\mathrm{d}\sigma}{\mathrm{d}\Omega} = p(\theta)\frac{b}{\sin\theta}\left|\frac{\mathrm{d}b}{\mathrm{d}\theta}\right| \tag{4.104}$$

where $p(b)$ is obtained using the multi-channel Landau-Zener model (section 3.1.5 detailed in figure 4.21).

In order to obtain the differential cross section, it is necessary to invert the function $\theta(b)$. This function is not uniform over the interval $[0, b_{max}]$. However, it is locally uniform over n subsegments. Therfore:

$$b(\theta) = \sum_{i=1}^{n} b_i(\theta) \tag{4.105}$$

where $b_i(\Theta)$ is the inverse function of the ith uniform part of $\Theta(b)$.

Nevertheless, obtaining the derivative of the impact parameter is not direct, but must be done within the sum.

$$\frac{\mathrm{d}b}{\mathrm{d}\theta} = \sum_{i=1}^{n} \frac{\mathrm{d}b_i}{\mathrm{d}\theta} \tag{4.106}$$

The same goes for all the variables that result from the inverse of this function,

$$f(b) = \sum_{i=1}^{n} f(b_i) \tag{4.107}$$

Thus, the differential cross section is written:

$$\frac{\mathrm{d}\sigma}{\mathrm{d}\Omega} = \sum_{i=1}^{n} p(b_i)\, b_i \left|\frac{\mathrm{d}b_i}{\mathrm{d}\cos\theta}\right| \tag{4.108}$$

The result obtained – as well as the intermediate results – for the mutual neutralization reaction $\mathrm{Li}^+ + \mathrm{D}^- \rightarrow \mathrm{Li}(1s^2 3p\ ^2P) + \mathrm{D}$ is given in figure 4.23.

The upper part of this figure represents:

$$b\left|\frac{\mathrm{d}b}{\mathrm{d}\cos\theta}\right| = \sum_{i=1}^{n} b_i \left|\frac{\mathrm{d}b_i}{\mathrm{d}\cos\theta}\right| \tag{4.109}$$

This allows to compare the result obtained by integration of trajectory with that of the interrupted Rutherford scattering model[27]. The first visible element is the presence in both cases of a minimum in the differential cross section. This minimum is given by the deflection at maximum impact parameter. Indeed, for this maximum impact parameter the derivative of the impact parameter is zero.

$$\left|\frac{\mathrm{d}b}{\mathrm{d}\cos\theta}\right|_{b_{max}} = 0. \tag{4.110}$$

The second element visible in this differential cross section is the presence of a maximum deflection angle. This angle is one of the rainbow scattering angles. This maximum angle is not visible for the interrupted Rutherford scattering model. Indeed, given the exclusively attractive character of the Coulomb potential, there is no rainbow scattering. This maximum in the distribution of the scattering angle is visible experimentally (figure 4.29).

The last part to be taken into account is the difference in behavior of the partial cross section depending on whether the mutual neutralization takes place during the first passage through the avoided crossing, or during the second passage. This difference is explained by the drastically different shape of the trajectories for the dominant impact parameters. Even if the trajectories are similar for small impact parameters, these contribute very little to the cross section. In addition, since the deflection angle varies a lot depending on the impact parameter, the transition pobability for small impact parameters is also small.

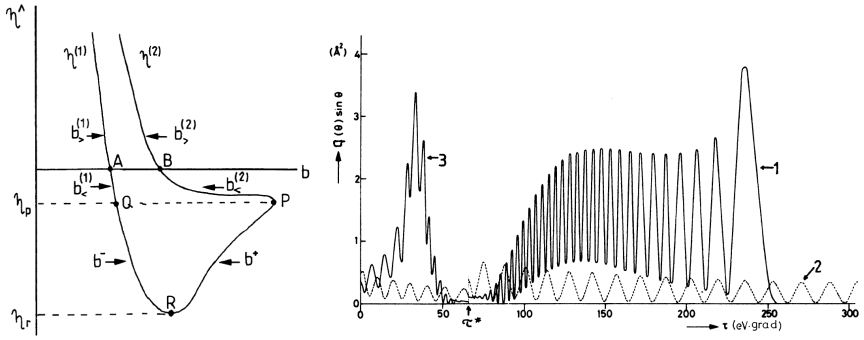

Figure 4.24: Differential cross section of the reaction $\mathrm{Na}+\mathrm{I}\rightarrow\mathrm{Na}^{+}+\mathrm{I}^{-}$ [153]. Left: Deflection angle η according to the impact parameter b. Right: Differential cross section.

It should be noted that the differential cross section of the mutual neutral-

[27] The oscillations visible in the differential cross sections are due to numerical inaccuracies in the calculated potential energy curves. These numerical oscillations do not pose a concern for the comparison with the experimental data, because the differential cross section is to be convolved with the experimental distribution of the collisions (section 4.4.1).

ization is similar to that obtained for the reverse reaction (chem-ionization – figure 4.24). This is because the potential curves are identical, but followed in the opposite direction.

Figure 4.23 also displays the partial differential cross section for each state. It makes it possible to estimate the influence of each path on the differential cross section. This is particularly visible for the partial cross section of the state $3d$: The deviation linked to the covalent state (curve $3d$) leads to the peak of the differential cross section near $\cos\theta = 1$. The following peaks each contribute to a maximum in the differential cross section (related to rainbow scattering). However, as each peak is linked to the probability of following this curve (given in the figure 4.21), the probability of following each curve decreases with the number of crossings to pass. Thus, the rainbow scattering linked to the state $3p$ is important, decreases for the contribution of the state $3s$ and becomes negligible for the ionic state.

The fact that the ionic state contributes so little is related to the greater interaction potential between the $3s$ state and the ionic state. Consequently, the probability that the collision continues on the ionic potential curve is much lower (because it is entirely transferred to the curve $3s$). It explains why lower potential energy curves are not included here, as they are never populated.

To assess the effect of collision energy, it is useful to look at figure 4.25. This figure represents the dependency of the differential cross section on the collision energy. The effect of the collision energy is the same as the one obtained using the simpler interrupted Rutherford scattering model, which assumes that the trajectory is a hyperbola:

$$\frac{x^2}{a^2} - \frac{y^2}{b^2} = 1 \tag{4.111}$$

where b is the impact parameter, $a = C/(2E_{r,i})$ and C is a parameter which depends only on the Coulomb force of attraction.

When $E_{r,i}$ decreases, an identical trajectory is obtained with a larger impact parameter. This increase in the impact parameter is clearly visible when comparing the two figures. It induces a greater reduction of the radial speed compared to the total speed. This results in an increase in transverse speed which increases the general deflection: The differential cross section widens when the collision speed decreases. In other words, the greater the collision energy, the more the differential cross section is concentrated around $\cos\theta = 1$.

4.4 Signal modeling

Now that the differential cross section has been modeled and the angular acceptance of the detectors is known, it is possible to compare it to experiment

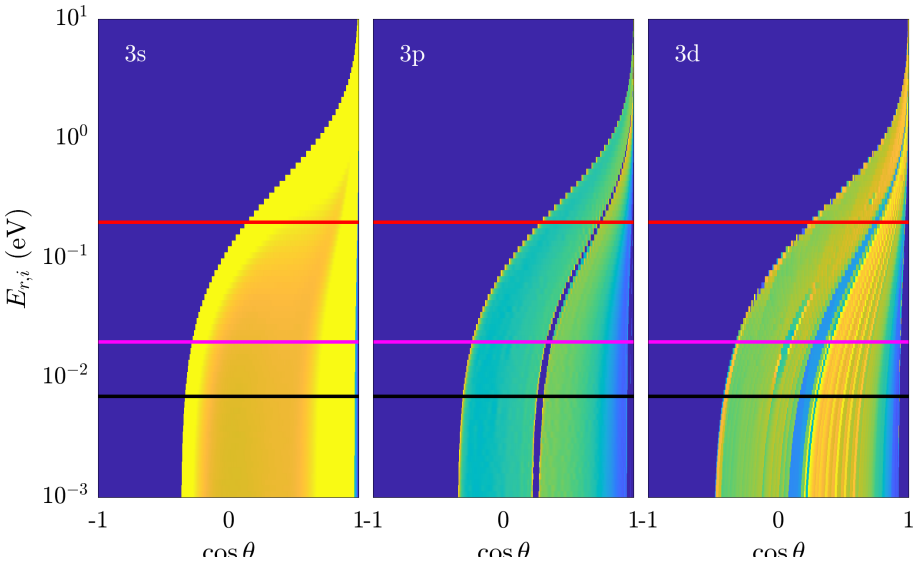

Figure 4.25: Normalized partial differential cross section for the Li^++D^- MN reaction, computed modeled using the impact parameter model. The horizontal lines correspond to the collision energies in figure 4.26 (black: 7 meV; purple: 20 meV; red: 200 meV).

(figures 4.25 and 4.26). From these figures, several elements are to be observed. First, when the collision energy is greater than 10 meV, the angular distribution in no longer uniform. It appears that the cut in the experimental angular distributions corresponds to the rainbow scattering in the differential cross sections.

However, when the collision energy is minimal, there is an important difference between the differential cross section and the experimental angular distribution. This difference arises from the uniformity of the initial distribution of the collisions. So how does the transition go from a uniform angular distribution to a distribution that follows the differential cross section take place?

The answer to this question can be found in figure 4.14. This shows how the collision distribution changes from a uniform distribution to a sharp distribution around 0°, i.e. $\cos\theta = 1$. Therefore, it is necessary to combine the initial distribution of collisions with the differential cross section in order to obtain the experimental angular distribution.

Other phenomena are interesting to point out in the figure 4.26: By observing the distribution of events more carefully, we note that the background seems more important on the right side of the figure. These events appear to have the same distribution regardless of the collision energy: a distribution that resembles the differential cross section. These events come from the edges of observation cell. Indeed, during their entry in (and exit of) the observation cell, the ions cross a potential gradient. As the beams are aligned, these events are

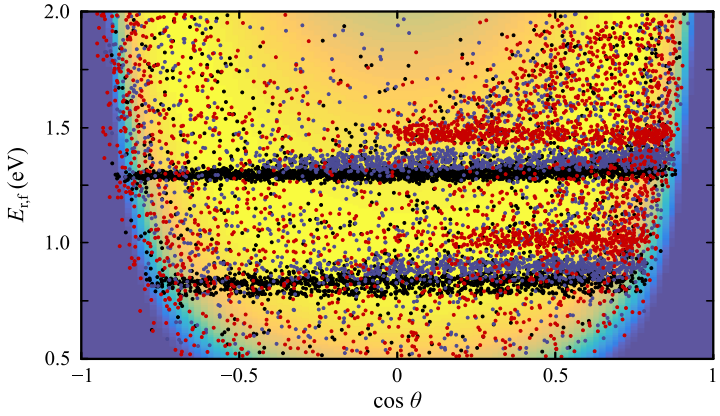

Figure 4.26: Representation of measured events of mutual neutralization reaction between Li^+ and D^- (black: 7 meV; purple: 20 meV; red: 200 meV average reaction energy) placed on the acceptance map. The upper stripe series corresponds to the reaction products $Li(1s^2 3s\ ^2S) + D(1s^2\ ^1S)$ while the lower stripe series corresponds to $Li(1s^2 3p\ ^2P) + D(1s^2\ ^1S)$ and $Li(1s^2 3d\ ^2D) + D(1s^2\ ^1S)$. The lowest collision energy is obtained using an observation cell of reduced length (about 2 cm), while the other two measurements were performed using an observation cell of about 8 cm.

recorded, but at higher collision energy than within the observation cell [28].

The last phenomenon to observe is the width of the peaks between the different measurements: During the measurement carried out at minimal collision energy, the events associated with each state have a narrower energy distribution compared to the other measurements. This difference also comes from the observation cell. Its length is the main broadening factor in the measurement of the relative energy after collision, i.e. the width of the peaks is directly related to the length of the cell. The solution would therefore seem to always use a reduced observation length. A longer observation cell however allows to better discriminate events occuring at the desired relative energy against those occuring in the electric potential gradients.

It is now possible to account for the entire collision process by combining the distribution of the beams, the differential cross section and the geometry of the observation cell.

4.4.1 Convolution with the angular distribution of collisions

In order to compare the differential section obtained using the model above with the experimental angular distribution, it is necessary to convolve it with the experimental distribution of the beam. The method used here is, first, to

[28] The fact that these events do not dominate comes from the fact that the cross-section of mutual neutralization drops as E^{-1} up to ~ 1 eV.

generate an event distribution that matches the experimental collision distribution (θ_v, φ_v). Next, to generate a random distribution of events that matches the differential cross section θ. Finally, to rotate each event of the first distribution by an angle corresponding to the second distribution.

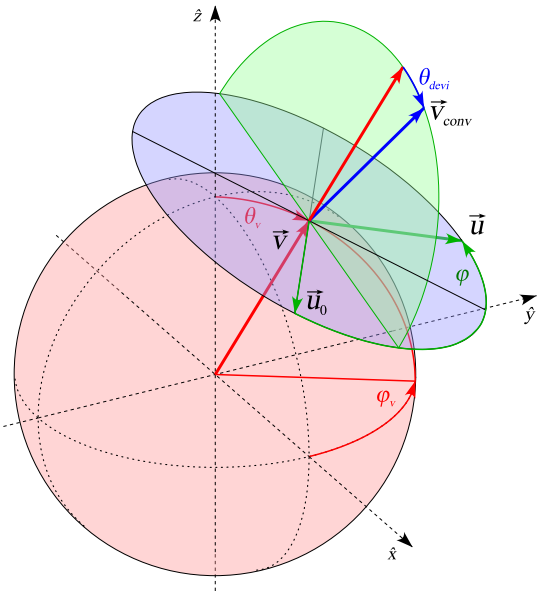

Figure 4.27: Coordinate system and representation of the vectors useful for the convolution of the differential cross section by the angular distribution of the beams.

The angular distribution of collision between the beams is obtained within the section 4.2.1. It consists of a set of vectors $\vec{v} = (v_x, v_y, v_y)$, where the axis $\hat{z}$ is the propagation axis of the beam. The components are written as a function of the angles as:

$$v_x = \rho \sin\theta_v \cos\varphi_v \tag{4.112}$$

$$v_y = \rho \sin\theta_v \sin\varphi_v \tag{4.113}$$

$$v_z = \rho \cos\theta_v \tag{4.114}$$

Each of these events is rotated around an axis randomly chosen in the plane perpendicular to its direction of propagation [29]. This rotation takes place at an angle chosen within the angular distribution linked to the differential cross section. The distribution of events thus obtained can be compared with an experimental angular distribution.

The rotation matrix around a unit vector $\vec{w}$ of an angle ϕ is:

$\mathscr{R}_{\vec{w},\phi}$

[29] It is not possible to determine, a priori, the axis around which the deflection induced by the differential cross section is to be applied.

$$= \begin{pmatrix} w_x^2(1-c_\phi)+c_\phi & w_x w_y(1-c_\phi)-w_z s_\phi & w_x w_z(1-c_\phi)+w_y s_\phi \\ w_x w_y(1-c_\phi)+w_z s_\phi & w_y^2(1-c_\phi)+c_\phi & w_y w_z(1-c_\phi)-w_x s_\phi \\ w_x w_z(1-c_\phi)-w_y s_\phi & w_y w_z(1-c_\phi)+w_x s_\phi & w_z^2(1-c_\phi)+c_\phi \end{pmatrix} \tag{4.115}$$

where $c_\phi = \cos\phi$ and $s_\phi = \sin\phi$, $w_x^2 + w_y^2 + w_z^2 = 1$.

To choose a vector $\vec{u}$ randomly in the plane perpendicular to the vector $\vec{v}$, we must find a vector which satisfies the conditions $(\vec{u}|\vec{v}) = 0$ and $(\vec{v}|\vec{v}) = 1$.

One solution is to find a vector $\vec{u}_0$ which belongs to this plane. For example $\vec{u}_0 = (v_y, -v_x, 0)/\sqrt{v_x^2 + v_y^2}$. Then rotate this vector by a uniformly random angle φ around the axis $\vec{v}$. Thus the set of vectors

$$\vec{u}\,(\vec{v}, \varphi) = \mathscr{R}_{\vec{v},\varphi}\vec{u}_0(\vec{v}) \tag{4.116}$$

lie in the plane perpendicular to $\vec{v}$.

The convolved distribution $\vec{v}_{\text{conv}}$ is the rotation of the vector $\vec{v}$ around the axis $\vec{u}$ from an angle Θ

$$\vec{v}_{\text{conv}} = \mathscr{R}_{\vec{u},\Theta}\vec{v} \tag{4.117}$$

Finally, the convolved angular distribution is given by:

$$\cos\theta_{\text{conv}} = \frac{v_{z,\text{conv}}}{v_{\text{conv}}} \tag{4.118}$$

with $v = \sqrt{v_x^2 + v_y^2 + v_z^2}$.

It has several properties: On the one hand, when the collision distribution of the beams is isotropic, the convolved angular distribution indeed gives a uniform angular distribution according to $\cos\theta_{\text{conv}}$ and φ_{conv} regardless of the differential cross section. On the other hand, the distribution according to the azimuthal angle φ_{conv} is always uniform.

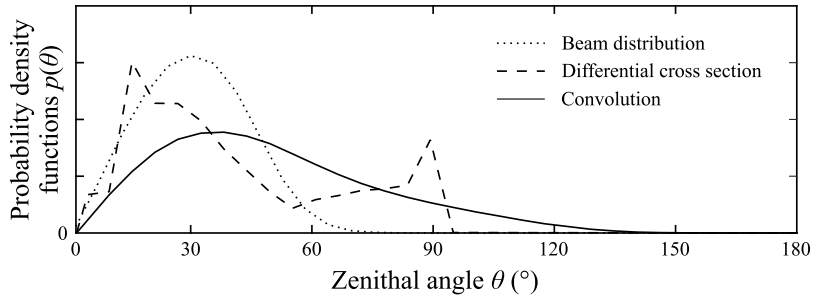

Figure 4.28: Convolution (solid curve) of the differential cross section (dashed lines) with the angular distribution of collisions (dotted curve) for the mutual neutralization reaction of Li^+ with D^- for a collision energy of 20 meV leading to Li($3s$).

An example of the differential cross section convolved with the collision distribution is given by the figure 4.28 [30]. This shows the smoothing and widening of the differential cross section by the angular distribution of collisions, as well as the attenuation of the peaks linked, among other things, to the rainbow scattering.

The last step before comparing the angular distribution of events with the differential cross section is to multiply the latter by the angular acceptance at the kinetic energy release coresponding to each final state. An example of comparison is given in figure 4.29 [31]. Their similarity suggests that the acceptance map and the differential cross section are correctly generated. They make it possible to correct the experimental cross section in order to obtain the branching ratio as well as the total cross section.

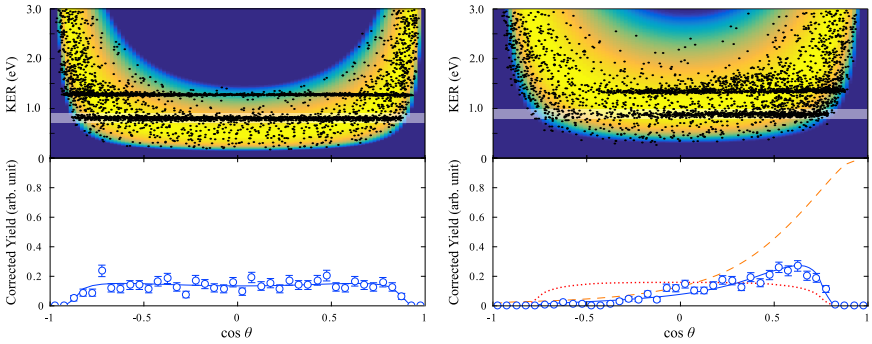

Figure 4.29: Top: Acceptance maps for the mutual neutralization reaction of Li^+ with D^-. The area used for the angular histogram is delimited by the light box. Bottom: Angular histograms associated within the frames. The figure on the left corresponds to minimum collision energy. The figure on the right corresponds to a collision energy of approximately 22 meV. Dashed line: convolved angular distribution; dotted line: angular acceptance.

4.4.2 Effects of the geometry of the observation cell

So far, the variation in bias potential at the entry and exit of the observation cell was assumed to be instantaneous. However, this is not the case. This sec-

[30] The convolved differential cross section here is that of the figure 4.23 (taken with a coarser discretization). Note that the distribution is given according to θ instead of $\cos\theta$.

[31] The experimental differential cross section of a given state is obtained by the following method: First, the events related to this state are selected. These satisfy:

$$E_{r,f,event} \in]KER + E_{col} - \Delta E_{cell}, KER + E_{col} + \Delta E_{cell}[$$

Then, an angular histogram is generated from these experimental events, from this histogram is subtracted the background histogram (see section 2.10). The events in the background histogram satisfy the same conditions as those in the signal histogram. The final histogram is subsequently normalized.

tion describes how the geometry of the observation cell influences the gradual variation of the observation potential and modifies the collision energy distribution.

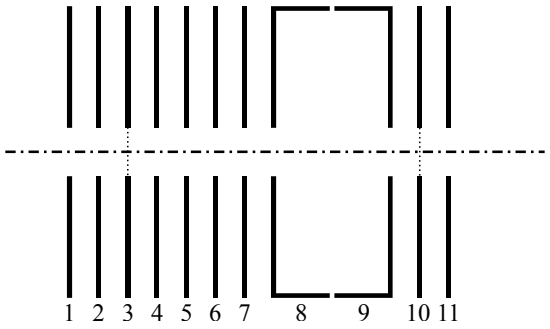

Figure 4.30: Scale diagram of the observation cell. This is 8 cm long (plates 3 to 10). The holes along the axis are 1 cm in diameter. Plates 1,2 and 10 are grounded. Some holes (3 and 10) can be reduced (up to 1 mm in diameter) using a movable diaphragm, shown by dotted lines. This observation cell is called "reduced observation" when only the plates 3, 4 and 5 are at the bias potential.

Indeed, the observation cell is composed of a set of perforated plates through which the beams pass (figure 4.30). The width of the holes drilled through the plates is relatively wide in order to ensure that the entire two beams pass through the cell and to minimize the lensing effect due to the acceleration or deceleration of the beam. However, the use of large holes has a drawback: the electrostatic potential along the axis is less constrained by the plates (these plates are farther from the axis). Consequently, the jump in potential from the ground to the bias potential is less abrupt. There are then two zones – on the edges of the observation cell – where the beams are already brought into confluence, but with a relative kinetic energy different from that in the cell itself. The ions in the beams neutralize each other in these areas and contribute to the signal. These events are real events, as opposed to the background generated by the residual gas (section 2.10). They modify the collision energy distribution and the apparent cross section of the reaction. The modeling of these effects makes it possible to correct the apparent cross section in order to obtain the real cross section.

The first step in this modeling consists in estimating the bias potential within the observation cell. To do this, the observation cell can be modeled in 3D using the SIMION software to extract the electrostatic potential along the axis [32]. The figure 4.31 shows the potential gradient along the axis at the edges of the cell. This gradient is identical when the length of the observation

[32] The potential is assumed to have no radial variation. Even if this assumption is not completely true, the radial variation of the electrostatic potential is sufficiently weak not to have to

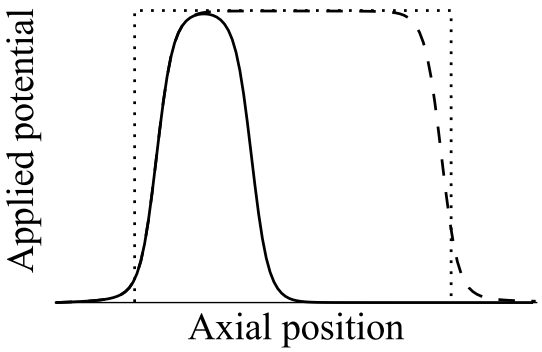

Figure 4.31: Bias potential applied to a beam along the axis for: an idealized cell (dotted curve), a cell in normal configuration (solid curve), and when only plates 3, 4 and 5 (defined in figure 4.30) are at the potential for bias (dashed curve).

cell is reduced. But since the length for which the observation is at the nominal bias potential is smaller, the edge effect is greater for the reduced observation.

The next step in the modeling requires the estimation of the cross section as a function of the bias potential. As seen previously (section 2.5), the bias voltage applied to the observation cell determines the collision energy by slowing down the fastest beam, and accelerating the slowest beam. If the positive ion beam initially has a kinetic energy E_A and the negative ion beam has an energy E_B, then the collision energy for mutual neutralization is given by the equation 4.3. When the bias voltage is applied to the two collinear beams, the kinetic energy of the positive beam becomes $E_A - V_{obs}$ and that of the negative beam becomes $E_B + V_{obs}$, which gives as relative energy:

$$E_{r,i} = \mu \left(\frac{E_A - V_{obs}}{m_A} + \frac{E_B + V_{obs}}{m_B} - 2\sqrt{\frac{E_A - V_{obs}}{m_A} \cdot \frac{E_B + V_{obs}}{m_B}} \cos\theta_{AB,i} \right) \tag{4.119}$$

Therefore, as the cross section is inversely proportional to the collision energy when this collision energy is low (section 3.1.5), the cross section is easily calculated by combining the angular and energy distribution of the two beams (section 4.2.1) with the bias potential for each spatial position along the axis of the observation cell.

The edge effect (of the bias potential) is shown in figures 4.32 and 4.32. This effect is much more marked when the cross section of mutual neutraliza-

be taken into account. Indeed, on the one hand, the observation cell is designed to minimize the lens effect – the diameter of the holes (1 cm) is an order of magnitude greater than the diameter of the beams passing through (1 mm), on the other hand the simulation of the angular distribution of collisions of the section 4.2.1 closely reproduces the collision distribution obtained experimentally.

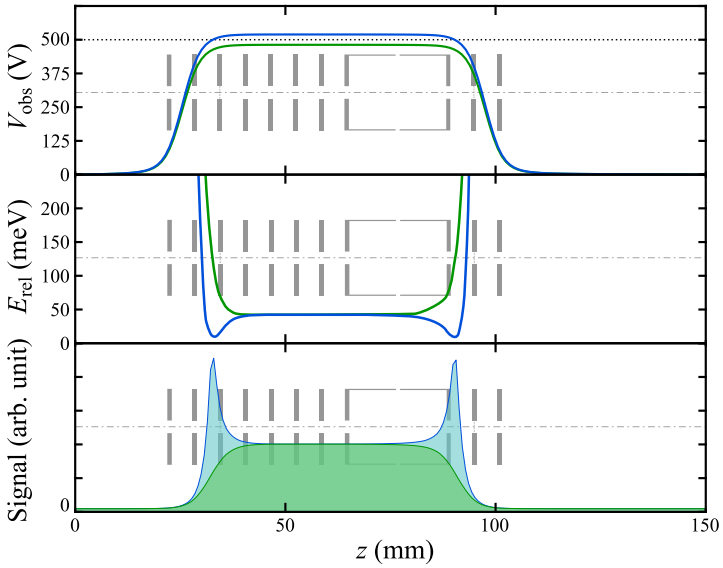

Figure 4.32: Representation of the edge effects of the bias potential of the observation cell for an ideal bias potential of 500 V when the potential is applied to the entire cell. The green curves correspond to a bias potential shifted 20 V below the optimal potential (480 V). The blue curves correspond to a bias potential shifted by 20 V above the optimal potential (520 V). Both potentials set a collision energy of 50 meV. The upper figure shows the bias potential as a function of the axial position within the cell. The central figure shows the collision energy as a function of the axial position within the cell. The lower figure shows the signal recorded for each axial position within the cell.

tion is not measured at the minimum collision energy, but shifted from the minimum. This method is the one used to measure the cross section as a function of the collision energy. The figure shows the case of a cross section measurement for the reaction of Li^+ with D^- for a collision energy fixed at 50 meV (the summed kinetic energy of the two beams is 15740 eV). This collision energy can be obtained in two different ways. By lowering the bias potential applied to the cell (low potential) or increasing it (high potential). Even though these two methods seem similar, the edge effect changes the apparent cross section.

Indeed, on the edges of the observation cell, the bias potential decreases. This drop to low potential simply decreases the collision energy at the edges of the cell. As the cross section is inversely proportional to the collision energy, the signal produced at the edges of the cell is much weaker than that received by the cell itself. The edge effect for the low potential is, therefore, almost negligible. On the other hand, this edge effect differs for the high potential. In this case, the drop in potential at the edges first decreases the collision energy. Thus, the minimum collision energy (section 4.2.1) is actually reached at the

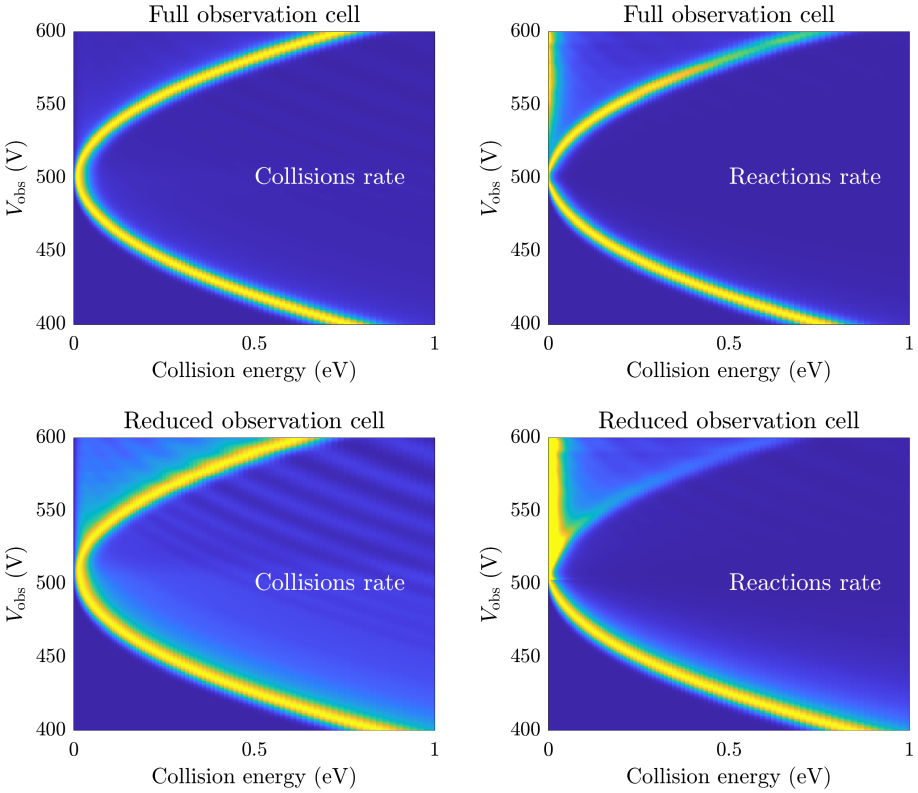

Figure 4.33: Collision behavior for a full (top) and reduced (bottom) observation cell. Left, collision rate as a function of collision energy and bias voltage. This collision density is normalized at each bias voltage. Right, reaction rate as a function of collision energy and bias voltage. This collision density is normalized at each bias voltage. The oscillations visible in the figure at the bottom left are due to the discretization of the bias potential along the axis of propagation.

edges. Again, since the cross section is inversely proportional to the collision energy, the signal density produced at the edges is greater than that produced in the cell itself. As the length of the edges is not negligible compared to the length of the cell, the component of the signal produced at the edges is no longer negligible.

The measured cross section is then greater for the high potential than for the low potential (figure 4.34). The signal maximum is also shifted to a slightly higher bias potential value (2 or 3 V) for the entire observation cell. This slight offset is corrected when converting the signal to a total cross section. This shift is much larger for the small observation cell. In addition, the measured signal decreases more slowly for high potential values. In fact, when the high potential increases, the signal linked to the central section observation cell decreases,

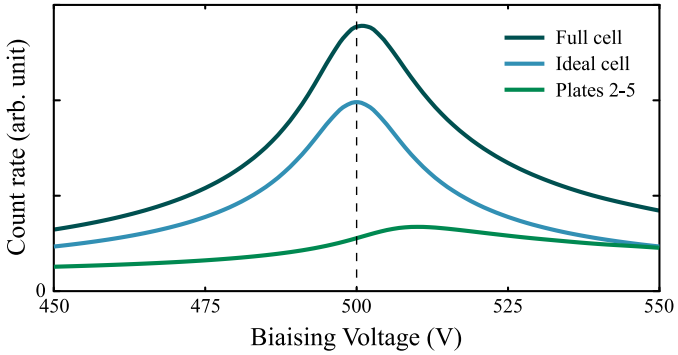

Figure 4.34: Cross section simulated as a function of the observation potential for an idealized observation cell (dark blue), the complete observation cell (light blue) and the reduced observation cell (green). The vertical scale is not kept between the curves.

while the signal linked to the edges of the cell remains nearly constant. The cross section measured for the high potential values is therefore overestimated. The total cross section must therefore be measured for potential values lower than that matching the beam velocities and producing the minimal collision energy. Likewise, the reduced observation cell cannot be used for absolute cross section measurements (which is never the case anyway, given that the signal produced in the reduced observation cell is always weaker than the signal originating from the full observation cell). This reduced observation cell, however, allows for much more precise spectra of relative kinetic energy after collision (section 4.4.3). Furthermore, to analyze the experimental differential cross section spectra, the collision energy distribution of the reaction must take into account the effects of the geometry of the observation cell (figure 4.33).

4.4.3 Peak width of experimental spectra

Previous descriptions of the acquisition system [63, 187] indicate that the imprecision according to $E_{r,f}$ is not related to the acquisition system itself, but to imprecisions related to the way the process itself takes place. In Fabre's thesis [187], this imprecision was linked to the lifetime of the excited hydrogen molecule before dissociation. In the case of mutual neutralization, this imprecision comes on the one hand from the potential gradient (see previous subsection), but also from the length of this observation cell. As this is known, it is possible from approximate kinematics equations to estimate the uncertainty on $E_{r,f}$.

The time T traveled by the center-of-mass to reach the detectors is given by $v_{cm}T = L$. During the same time interval, the distance traveled by the pseudo particle Δx is $v_r T = \Delta x$. Thus, by combining these two relations squared, the

relative kinetic energy after collision can be written as:

$$E_{r,f} = \frac{\mu}{m_{tot}} \left(\frac{\Delta x}{L} \right)^2 E_0 \tag{4.120}$$

The distance traveled is the combination of the distance traveled in the plane of the detectors R_r and that traveled along the propagation axis z_r.

Since the distance along the axis z_r is not measured directly, but rather the time separating the impact of the first particle from the impact of the second. The slower particle – of speed v_0 – takes a time τ to travel the distance z_r that separates it from the detectors.

Thus, the relative kinetic energy after collision can be expressed in a simple (but approximate) way using different experimental observables as:

$$E_{r,f} = \frac{\mu}{m_{tot}} \frac{E_0}{L^2} \left(R_r^2 + v_0^2 \tau^2 \right) \tag{4.121}$$

The characterization of the uncertainties on the energy definition of the beam ΔE_0, the interaction length ΔL, the precision of the position measurements ΔR_r and the time measurement $\Delta \tau$ makes it possible to characterize the broadening of the peaks in the relative kinetic energy spectra.

Taking into account the energy definition of the beam is not trivial. This was discussed in sections 4.2.1 and 4.4.2.

The precision on the spatial position is about 100 μm for distances of about 4 cm. The precision on time is about 50 ps for time differences of about 500 ns [33]. The accuracy related to time and position measurements is thus less than a percent.

The precision on the distance traveled is given by the length of the interaction cell. This is approximately 8 cm for a distance of travel after reaction ranging from 3 m to 4.5 m. This gives a relative uncertainty of just over 2% on average. This corresponds to a peak width on the relative kinetic energy histograms of approximately 20 meV for a relative energy of 1 eV, in agreement with the measured width of the peaks.

The spread of the peaks of the relative kinetic energy histograms is thus due to the length of the observation cell. In order to improve the energy resolution of the relative kinetic energy spectra, it is possible to reduce the length of the observation cell to resolved states whose binding energy difference is about 5 meV (e.g. mutual neutralization of Li^+ with D^-). In these conditions, the effect of the energy distribution of the beams is no longer negligible (section 4.4.2).

[33] The temporal precision given in [187] is estimated to be 250 ps. However, the theoretical accuracy of the detectors is 50 ps.

Full observation cell

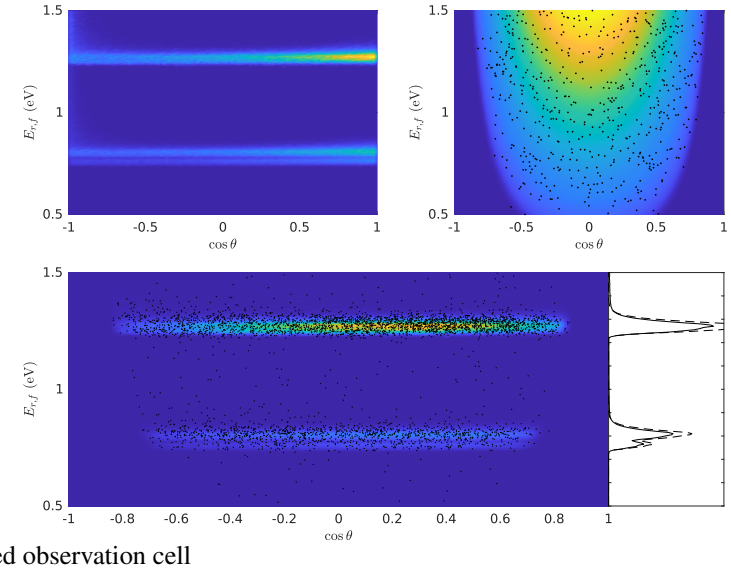

Reduced observation cell

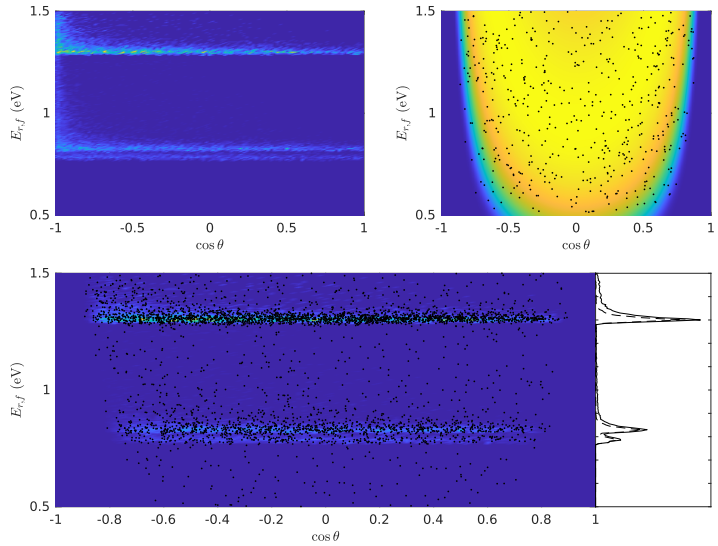

Figure 4.35: Comparison between the experimental distribution of events according to $\cos\theta$ and $E_{r,f}$ for the complete (top) and reduced (bottom) observation cell. The simulated distribution of full-acceptance events is on the top left, the acceptance map combined with the distribution of background events (points) is on the top right, the product map of the simulated distribution with the acceptance combined with the experimental distribution (points) is given at the bottom.

To be convinced of this effect, it is possible to run a full simulation. This simulation requires (i) taking into account, for each position within the observation cell, of speed distribution of each of the beams (section 4.2.1), (ii) to combine this beam distribution in the frame of the center-of-mass (continuation of section 4.2.1) to obtain the angular and energy distribution of collisions within the observation cell (this depends on the position within the cell of observation – section 4.4.2), (iii) to deflect each collision vector using the differential cross section (section 4.3.3), (iv) to compute the reaction probability (section 3.1.5) to deduce the probability of obtaining a signal from the cross section (equation 4.44) and finally (v) to deduce the relative energy after reaction (the sum of the initial kinetic energy, the released kinetic energy KER and an offset given by actual position at which the reaction took place, $\Delta E_{r,f} = E_{r,f} \times 2(L - L_0)/L_0$).

The combination of all these elements allows us to visualize the dispersion in kinetic energy after reaction (figure 4.35). The upper part shows the result of the simulation when the observation cell is complete, combined with the event distribution of an experimental measurement. The lower part shows the situation when the observation cell is reduced. In this figure, it is clear that the width of relative energy distribution after reaction is effectively controled by length of the interaction cell. This simulated reduction in peak width corresponds exactly to the reduction in experimental width.

Note also that the distribution simulated before application of the acceptance is neither uniform nor centered. This effect is the consequence of two experimental phenomena.

The first is relatively easy to explain: the maximum signal is not obtained when the two beams have a minimum collision energy within the observation cell (see figure 4.34). Thus, on the edges of the observation, if the particle A is faster than the particle B, the direction of the collision velocity $\vec{v}_A - \vec{v}_B$ points toward the detector. Within the observation cell, as the cell voltage exceeds the optimum voltage, the B particle becomes faster than the A particle. The direction of the collision velocity is reversed. Therefore, the measured differential cross section is reversed: There is a widening of the peaks on the left of the map, combined with a piling up of events on the right of the map. These events correspond to a non-zero collision energy within the observation cell.

The second phenomenon is linked to the kinetic energy distribution of each beam, which depends on the type of source used: As the ions are extracted from a certain volume within this source (section A.1.3), these ions are extracted with a certain distribution in kinetic energy. This energy distribution depends on two parameters: The kinetic energy distribution of the ions within the source as well as the variation of the electrostatic potential within the extracted volume. These two parameters depend on the operating principle and

the geometry of each source.

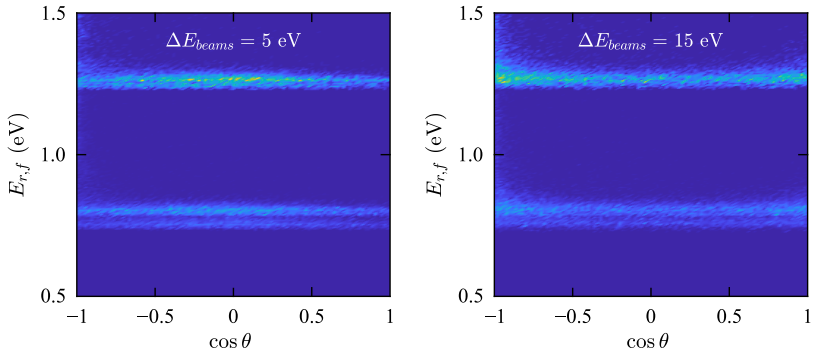

Figure 4.36: Comparison between the distribution simulated according to $\cos\theta$ as a function of the dispersion in longitudinal energy of the beams placed in confluence. The observation potential is chosen to minimize the kinetic energy of collision. The figure on the left corresponds to an initial kinetic energy distribution for the two beams of 5 eV and the figure on the right to a distribution of 15 eV.

It is however reasonable to assume that this energy distribution is between 5 and 10 eV at the extraction [34]. This variation in kinetic energy may appear small. However, it has a significant effect on the angular distribution of collisions. Indeed, if we observe figure 4.36, we see that this variation of the initial kinetic energy distribution has a visible effect on the angular distribution of events.

Indeed, the transverse energy distribution of each of the beams is given by the emittance of these (linked to the geometry of the system). This transverse distribution equals the longitudinal distribution when the energy distribution of the two beams is about 10 eV. Thus, if the longitudinal distribution is reduced (figure above), the transverse distribution is larger, the particles meet perpendicularly to the direction of the center-of-mass and – as the differential cross section is maximum for 0° deflection – particles mainly separate perpendicu-

[34] Note that this energy distribution is constant, regardless of the kinetic energy of the beam. Indeed, the application of an electrostatic potential adds a longitudinal energy to all the particles in a uniform manner. Therefore, if a particle has an initial kinetic energy

$$E_i = E_{0,i} + \Delta E_i$$

where $E_{0,i}$ is the mean kinetic energy of the beam and ΔE_i is the term given by the kinetic energy distribution, then the kinetic energy of the particle E_f after application of a electrostatic potential $-V_{i,f}$ is given by:

$$E_f = E_i + V_{i,f} = E_{0,i} + V_{i,f} + \Delta E_i = E_{0,f} + \Delta E_f$$

where $E_{0,f} = E_{0,i} + V_{i,f}$ is the average kinetic energy of the beam after acceleration is $\Delta E_f = \Delta E_i$ is the kinetic energy distribution of the beam after acceleration.

larly to the beam axis, hence the maximum signal at $\cos\theta = 0$. In contrast, when the longitudinal distribution is larger than the transverse distribution, the particles meet parallel to the beam and, by the previous reasoning, the angular distribution measured is maximum at $\cos\theta = \pm 1$ [35].

4.4.4 Correction of the branching ratios

This approach which uses the differential cross section is not always tractable as it requires some knowledge of the the potential energy curves of the system. However, when the collision energy is minimal (section 4.2.1), there is no preferred direction for collisions. Therefore, the normalized convolution of the differential cross section with an isotropic distribution of the collisions is independent of the differential cross section and the product between the acceptance and the convolved differential section reduces to the acceptance. Therefore, it is possible to correct experimental branching ratios for any mutual neutralization reaction, as long as these reactions are measured for minimal collision energy, provided the assumption of an isotropic collision distribution is valid.

These branching ratios are corrected by the following method: A weight $w(E_{r,f}, \theta_{r,f})$ is associated with each measured event. This weight $w_1(E_{r,f}, \theta_{r,f})$ indicates the number of events that should have been measured for each combination of $E_{r,f}$ and $\theta_{r,f}$ if the device had full angular acceptance. In other words, this weight represents the proportion of all geometrically undetectable events of the same combination $(E_{r,f}, \theta_{r,f})$. Therefore, the histogram of kinetic energy after collision becomes a weighted histogram.

The weight w_1 is inversely proportional to the acceptance $Acc(E_{r,f}, \theta_{r,f})$ calculated in the section 4.1. In practice, the acceptance linked to a particular event is obtained by bilinear interpolation of the acceptance map. This is why this acceptance map is built on a constant double grid. If the grid is not constant, the interpolation algorithm has instabilities. Likewise, the interpolation is chosen to be bilinear in order to minimize numerical instabilities.

However, the number of events measured experimentally is not infinite. So when the acceptance is low – $Acc(E_{r,f}, \theta_{r,f}) < Acc_{\min}$ where $Acc_{\min} = 0.01$ is the acceptance threshold – the number of events detected in this area is small, meaning the uncertainty on this number is large. The weighting of this zone induces a great imprecision on the number of events.

For a measurement made up of 20,000 events, the number of events detected in this low acceptance zone is of the order of ten at maximum. Once

[35] Note that unlike the figure 4.35, the collision distribution is not aligned along the propagation axis (neither backward of forward). Therefore, the differential cross section is symmetrical for the "zero" collision energies. The asymmetry visible in the figure 4.36 comes from the edges of the observation cell.

corrected, these few events would correspond to tens of thousands of events. But since these events follows a Poisson distribution, the relative uncertainty associated with these tens of thousands of events is 30%. To take these events into account would propagate an error which is far too important. Therefore, events related to areas of low acceptance are rejected.

This argument is confirmed experimentally. The distribution of events in areas of low acceptance is identical to the background distribution of noise (with a margin of error smaller than that of statistical uncertainty).

To mitigate that numerical imprecision, the weight associated with these events is set to zero, i.e. the weight w is

$$w_1(E_{r,f},\theta_{r,f}) = \begin{cases} 1/Acc(E_{r,f},\theta_{r,f}) & \text{if } Acc(E_{r,f},\theta_{r,f}) > Acc_{\min} \\ 0 & \text{otherwise.} \end{cases} \tag{4.122}$$

While this correction is valid at a given $E_{r,f}$, it does not allow to evaluate the energy dependent contribution of undetectable events to the branching ratio. A second correction must be applied to account for gaps in the angular distribution created by zero or negligible acceptance.

By setting $Q(E_r,\theta)$ such that:

$$Q(E_r,\theta) = \begin{cases} 1 & \text{if } Acc(E_r,\theta) > Acc_{\min} \\ 0 & \text{otherwise,} \end{cases} \tag{4.123}$$

the overall correction factor to aply to the histogram of events vs. energy is

$$w_2(E_{r,f}) = \frac{\int_{-1}^{1} \frac{\mathrm{d}\tilde{\sigma}}{\mathrm{d}\Omega}(E_r,\theta)\mathrm{d}\cos\theta}{\int_{-1}^{1} Q(E_r,\theta)\frac{\mathrm{d}\tilde{\sigma}}{\mathrm{d}\Omega}(E_r,\theta)\mathrm{d}\cos\theta} \tag{4.124}$$

where $\mathrm{d}\tilde{\sigma}/\mathrm{d}\Omega$ is the differential cross section convolved by the distribution of collisions.

This data correction however requires prior knowledge of the differential cross section of each produced state. This is not applicable when the peaks associated with different states overlap, in which case the choice of weight applied to that event is arbitrary.

That said, if the reaction occurs at the minimum collision energy, this differential cross section (normalized in energy), once convolved with the collision distribution, is nearly constant. The second component of the weight factor becomes:

$$w_2(E_{r,f}) = \frac{2}{\int_{-1}^{1} Q(E_{r,f},\theta)\mathrm{d}\cos\theta.} \tag{4.125}$$

Using this method, the branching ratio is no longer calculated using the histogram of the events as a function of $E_{r,f}$, but according to the histogram

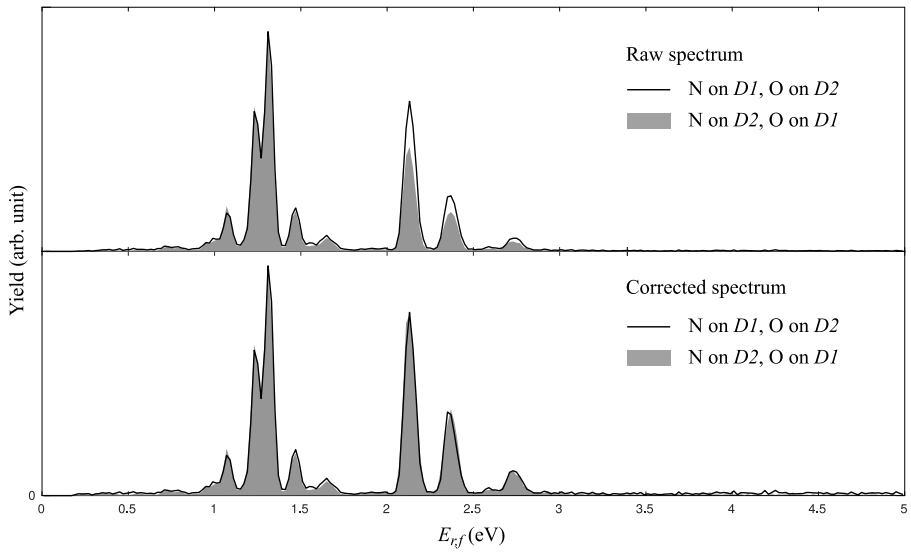

Figure 4.37: Experimental kinetic energy release histograms for the mutual neutralization reaction of N^+ with O^- at minimal collision energy. The top figure shows the histogram of events not corrected for acceptance. The branching ratio differs depending on whether the analysis of the events assigns the atom N to the detector $D1$ or $D2$. The figure below shows the weighted histogram of events using the acceptance map. After weighting, the branching ratios given by the analysis of this histogram no longer differ according to the assignment of a particle to one detector or to the other.

weighted by the two weight factors discussed above. This new histogram takes into account all the undetectable events [36].

Let us note before concluding that when the angular distribution of the events is (slightly) asymmetrical, there are several combinations {energy distributions of the beams, maximum voltage of the observation cell} which lead

[36] Note that a second method is possible. The second method differs in the order in which the correction is applied. It requires first to generate the histogram of kinetic energy of separation, this histogram is then to correct it for each relative energy. This method requires determining the collision energy and the uncorrected branching ratios using a prior analysis. It is then necessary, for each state produced, to correct the branching ratio by a factor

$$w_{\text{state}} = \frac{\int_{-1}^{1} \frac{\mathrm{d}\tilde{\sigma}}{\mathrm{d}\Omega}(E_{r,f},\theta_{r,f})\mathrm{d}\cos\theta_{r,f}}{\int_{-1}^{1} Acc(E_{r,f},\theta)\frac{\mathrm{d}\tilde{\sigma}}{\mathrm{d}\Omega}(E_{r,f},\theta_{r,f})\mathrm{d}\cos\theta_{r,f}}$$

where $E_{r,f} = E_{col} + KER$ depends only on the produced state, to normalize these branching ratios again to finally obtain the corrected ing ratios.

A simplified version of this method (uniform angular distribution) is written:

$$w(E_{r,f}) = \frac{2}{\int_{-1}^{1} Acc(E_{r,f},\theta)\mathrm{d}\cos\theta.}$$

to the same experimental angular distribution. When measuring branching ratios of the mutual neutralization of $Li^+ + D^-$ (table 4.2), the widening of the error bar is generated by the uncertainty in the estimation of events located outside the acceptance of detectors. Likewise, no value has been deduced from the higher collision energies, because – as shown in figure 4.25 – the differential section is much too concentrated off the acceptance window. As the majority of the signal is outside the acceptance window for collision energies of about 1 eV, the slightest error in the measured signal produces a large error in the corrected branching ratio.

$\langle E_{r,i} \rangle$	Li($3s$)	Li($3p$)	Li($3d$)
3.9 meV	$63.4 \pm 2.1\%$	$26.6 \pm 1.2\%$	$10.0 \pm 0.7\%$
20 meV	$60.0 \pm 2.0\%$	$32.0 \pm 1.0\%$	$8.0 \pm 1.0\%$
200 meV	$59.9 \pm 4.0\%$	$33.7 \pm 7.0\%$	$6.5 \pm 2.0\%$

Table 4.2: Experimental branching ratios obtained for the Li^++D^- mutual neutralization reaction [51]. The error bars are a combination of the statistical error and the estimated error on the differential cross section. The statistical error is mostly constant and largely dominates for the lowest collision energy while the error due to uncertainty of the differential cross section increases with the collision energy, due to the combined effect of the alignment of the collision distribution along the beam axis and the decrease of the scattering angle when the collision energy increases. These effects increase the proportion of atoms going between the detectors and remaining undetected.

The last set of measurements to be discussed concerns measurements for which the collision energy is minimal. This situation makes it possible to effectively correct the experimental branching ratios, for several reasons: When the collision energy is low, the collision distribution is roughly uniform, while the differential cross section is broad. The experimental angular distribution is then dominated by the collision distribution, and hence is similar for all the produced states. Thus, if the angular distribution is known for one state – once the acceptance correction has been applied – it is possible to apply this angular distribution to the other states in combination with the energy-dependent acceptance map.

Note that the angular distribution of the initial collisions need not be uniform. Likewise, the differential cross section should not follow exactly the shape given above. It is enough that the differential section is sufficiently similar so that its convolution by the initial distribution of the collisions gives a similar distribution for all the produced states.

This condition is easily verified when observing the angular distribution of each produced state, once the acceptance correction has been performed. Hence, the branching ratio is simply the branching ratio of the corrected signal

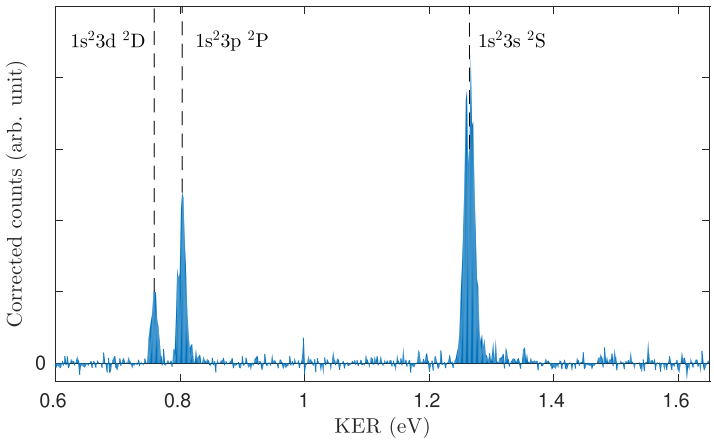

Figure 4.38: Relative kinetic energy spectrum after reaction for the mutual neutralization reaction of $Li^+ + D^-$ for an average collision energy of 3.9 meV [51].

taken in an angular region where all states give a measurable signal.

Note that this method makes it possible to choose the angular band for which the branching ratios are obtained, e.g. by taking the weighted histogram (at $E_{r,f} = E_{r,i} + KER$) of the events which satisfy $\cos\theta \in [0;0.8]$. This selection makes it possible to eliminate the events for which the collision energy $E_{r,i}$ is greater than the nominal value, while preserving the branching ratios. The reduction of the width of the peaks is visible both in figure 4.35 of this section (simulation) and in figure 4.26 (experiment). Indeed, when the observation cell has a reduced length, the width of the peaks linked to this interaction length decreases greatly. In addition, by taking only the events on the right in the figure, one further reduces the energy distribution of the measured events. This explains the narrowness of the peaks obtained by Launoy *et al.* [51] for the measurement of mutual neutralization of $Li^+ + D^-$ (figure 4.38).

Chapter 5

Results and interpretation

5.1 Preamble

During this thesis, a large number of mutual neutralization reactions were studied (table 5.1).

	H^-/D^-	C^-	O^-	Si^-	P^-	S^-
He^+	E.1, F.1.1					
Li^+	E.2, F.2.2					
C^+	F.4.2	E.4, F.4.4	E.5, F.4.5	F.4.3	F.4.1	F.4.6
N^+	F.5.2	F.5.4	E.6,F.5.5	F.4.3	F.5.1	F.5.6
O^+	F.6.2	F.6.4	E.7,F.6.5	F.6.3	F.6.1	F.6.6
Na^+			E.3, F.3.2			F.3.3
Ne^+		E.8, F.7.1	F.7.2			F.7.3

Table 5.1: Summary of reactants used in mutual neutralization measurements. Labels redirect to the appendices.

As this list of reactions would be too long to be treated on a case-by-case basis. Instead, this chapter gives a general description of the processes involved. Each process will be discussed for one or more reactions which illustrate the point.

Incidentally, the initial state of the ion is not mentioned here. This lack of specification is explained as follows: it is impossible to know a priori the state in which the ions are produced once extracted from the source, because the sources used can produce excited states in minor quantities (section A.2). This mixture of states can only be determined from the different spectra of relative kinetic energy after collision. These make it possible to estimate the branching ratio between the different states produced by the ion beams (which should normally be combined with the partial section of each collision).

Thus, after analysis, it is possible to conclude that the ions that make up these beams are in a state H/D$^-$(^1S), C$^-$($^4S^o$), O$^-$($^2P^o$), Si$^-$($^4S^o$), P$^-$(^3P), S$^-$($^2P^o$), He$^+$(^1S), Li$^+$(^1S), C$^+$($^2P^o$), Na$^+$(^1S) and Ne$^+$($^2P^o$) with a statistical population according to J. The beams of N$^+$ and O$^+$ contain a non-negligible proportion of excited states (about 5 to 15 %). So these beams have the following composition : N$^+$(^3P,^1D) and O$^+$($^4S^o$,$^2P^o$).

Nevertheless, for the sake of completeness, all the results – detailed for each reaction (corrected raw spectra, their analysis (fit) and their simulations) – are included within appendices E (differential cross sections) and F (branching ratios). The parameters used in the model (energy levels list, wavefunction normalization,...) are listed in appendix D.

As a reminder, the kinetic energy release is the difference between the binding energy of the electron attached to the anion (equation 3.94) and the binding energy of the electron attached to the neutralized cation (equation 3.93), i.e. (figure 5.1)

$$KER = \left[IP(A^0) + E_{\text{lev}}(A^+) - E_{\text{lev}}(A^0)\right] - \left[EA(B^0) + E_{\text{lev}}(B^0) - E_{\text{lev}}(B^-)\right] \tag{5.1}$$

where IP is the ionization potential, $EA > 0$ is the electron affinity and E_{lev} is the level energy.

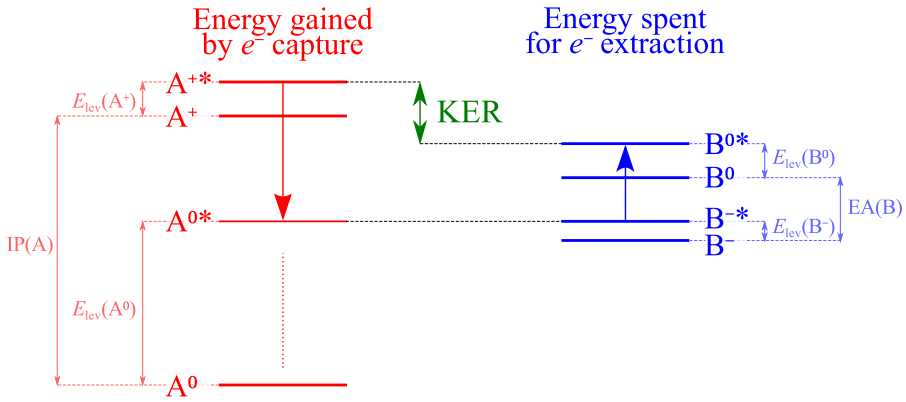

Figure 5.1: Kinetic energy release definition as a function of the energy levels of the initial ions and the final (neutral) products.

But before starting the discussion of the model validity, let us take a look at a subset of the spectra providing an overview of the process (figures 5.2, 5.3 and 5.4). This should give hints on how the process works and will help to determine the parameters that control the reaction: First, the products of the reaction depend on the electron affinity of the anion, while all these products have a kinetic energy release contained in the 0.5 to 3 eV range. Second, the term of the anion plays an important role in the process, it is clearly visible

when we compare the reaction involving C^- and O^- whose electron affinities are similar, while the latter allows more products. Those effects need to be rationalized with the help of a model.

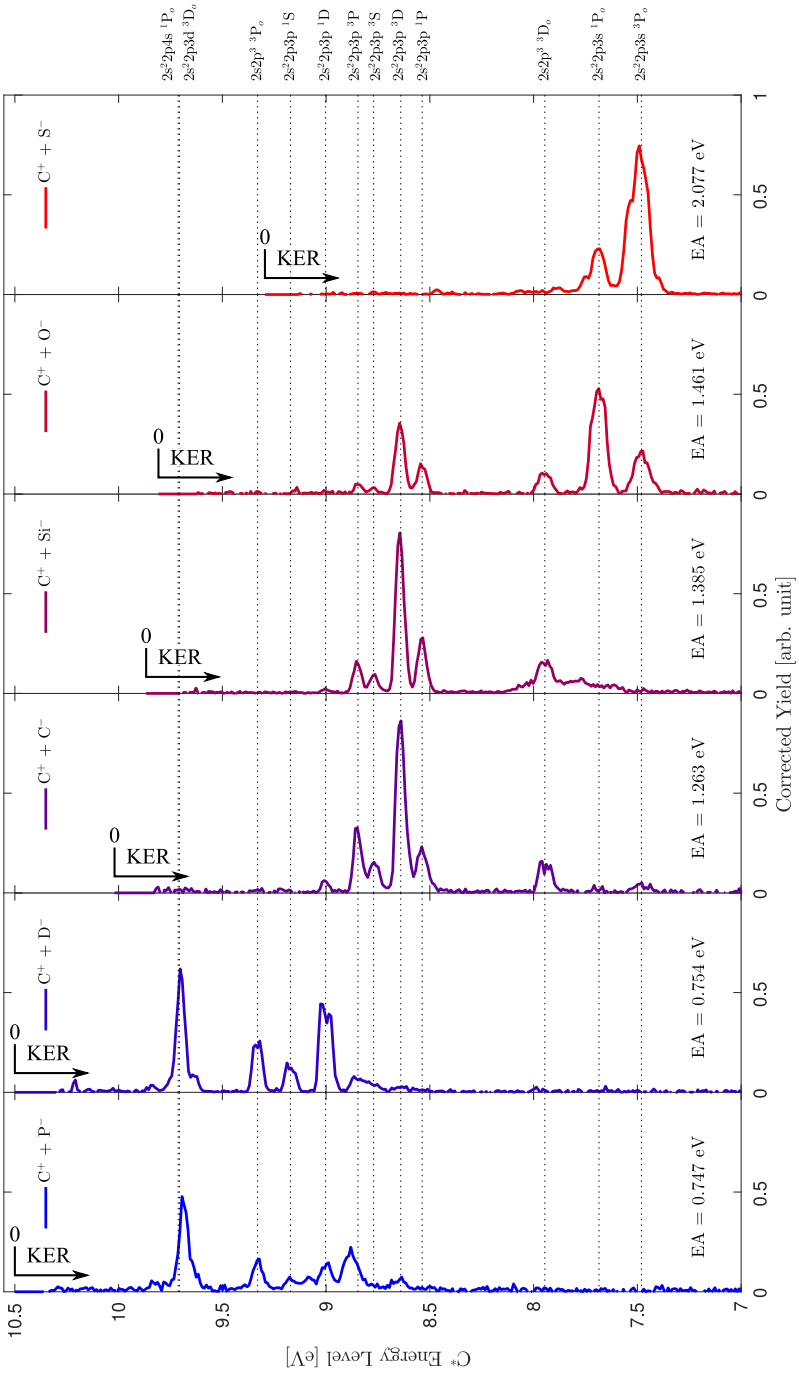

Figure 5.2: Combined experiments : $C^+ + X^-$ (peak assignments). The neutralized cation energy spectra are obtained using equation 5.1, under the assumption that both ions and the neutralized anion are in their ground states, i.e. $E_{\text{lev}}(\text{C}) = IP(\text{C}) - EA(X) - KER$, where $IP(\text{C}) = 11.266$ eV. The $1s^2$ component of the configuration is omitted for clarity.

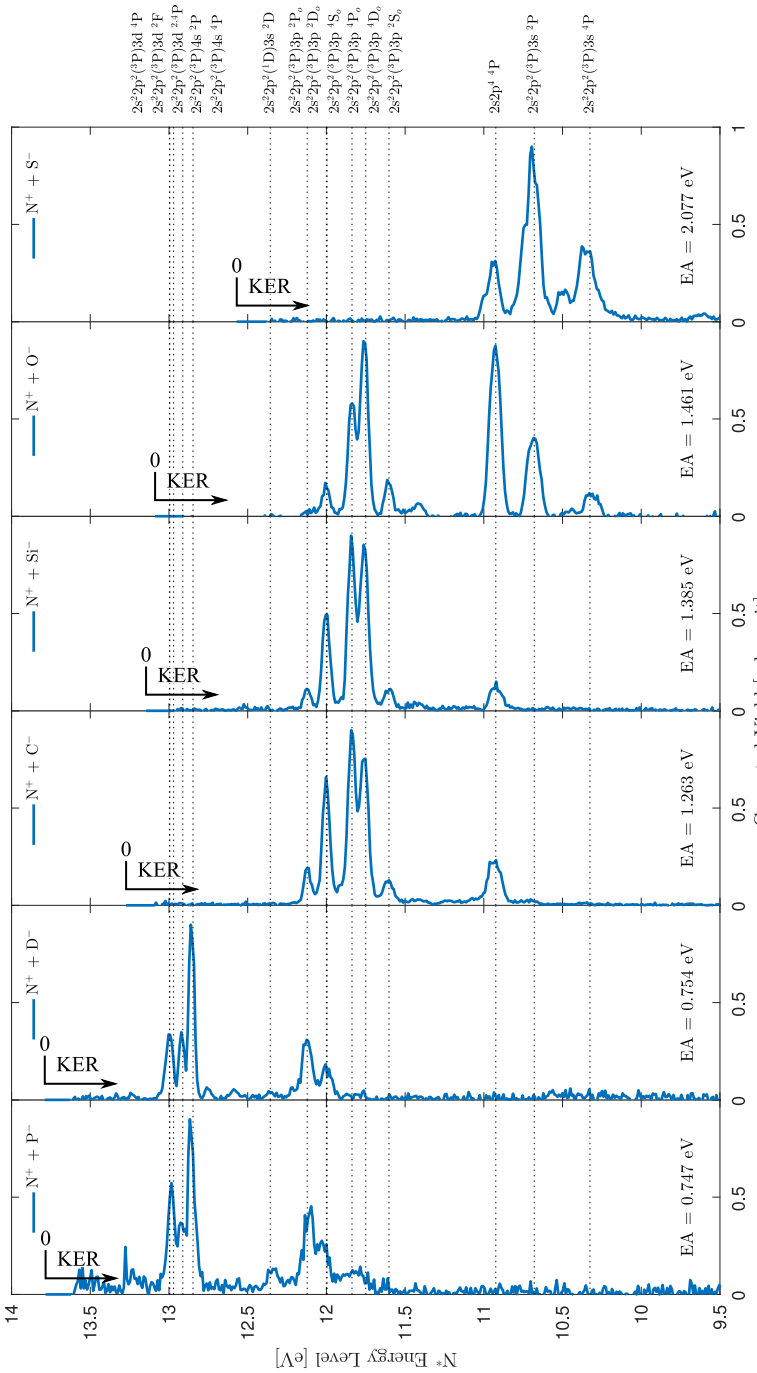

Figure 5.3: Combined experiments : $N^+ + X^-$ (peak assignments). The neutralized cation energy spectra are obtained using equation 5.1, under the assumption that both ions and the neutralized anion are in their ground states, i.e. $E_{\text{lev}}(\text{N}) = IP(\text{N}) - EA(X) - KER$ where $IP(\text{N}) = 14.545$ eV. The $1s^2$ component of the configuration is omitted for clarity.

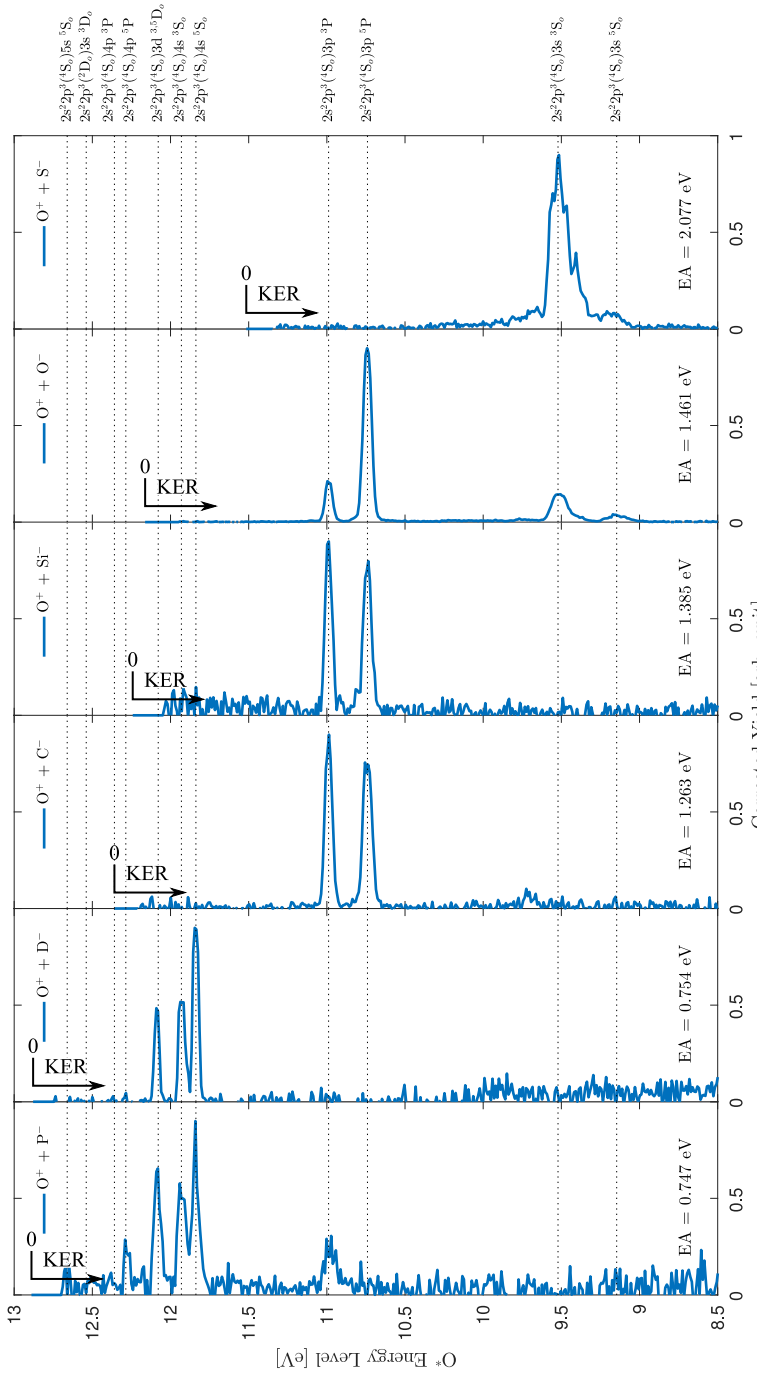

Figure 5.4: Combined experiments : $O^+ + X^-$ (peak assignments). The neutralized cation energy spectra are obtained using equation 5.1, under the assumption that both ions and the neutralized anion are in their ground states, i.e. $E_{\text{lev}}(O) = IP(O) - EA(X) - KER$ where $IP(O) = 13.596$ eV. The $1s^2$ component of the configuration is omitted for clarity.

5.2 Checking the model validity

5.2.1 Asymptotic extent of the anion wavefunction

The Anion-Centered Asymptotic Model (ACAM) predicts the partial cross sections of the various states produced. However, since this model assumes that the electrons are arranged in a single given configuration, it is possible that a asymptotic extent error ensues. Thus, the first step in validating the model consists in verifying that the asymptotic model works for simple reactions for which there are more complete simulations available that agree with the experimental measurements.

A first series of simulations for reactions involving D^- showed that the Landau-Zener window was shifted so that the states with a low kinetic energy release were overrepresented (figure 5.5). A similar shift was observed for the various anions considered individually. It thus seemed necessary to adapt the description of the anion in the calculation of the interaction term.

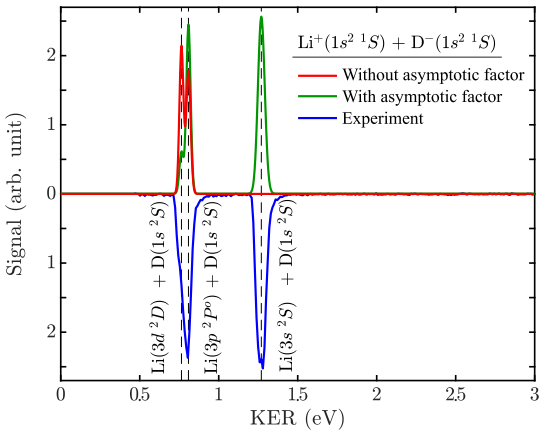

Figure 5.5: Simulated kinetic energy release spectra – with (green) and without (red) the asymptotic factor of the D^- wavefunction – compared to the experimental spectra (blue) for the Li^+ + D^- mutual neutralization reaction.

The dependence of the interaction term (equation 3.148) on the wavefunction of the anion is:

$$E_{ic} \propto \frac{A_{B^-}}{(2\gamma_{B^-}R)^{|m_l|}} \sqrt{N_{B-}} \times a(L,S) \tag{5.2}$$

where $A(L,S)$ takes into account the LS term of the anion (contracted notation):

$$A(L,S) = G^{SB-,LB-}_{SB0,LB0} \begin{bmatrix} L_{B0} & l_{B-} & L_{B-} \\ m_{LB0} & m_l & m_{LB-} \end{bmatrix} \sqrt{2S_{B-}+1} \begin{Bmatrix} S_{A+} & 1/2 & S_{A0} \\ S_{B0} & S_{mo} & S_{B-} \end{Bmatrix} \tag{5.3}$$

In the following, we will focus on the deuterium anion case and then extend the reasoning to the other anions [1].

The different factors in the equation for $A(L,S)$ all assume that the anion D^- is in the $1s^2$ configuration, which is not the case. D^- is a mixture of configurations. It is necessary to describe this anion differently for this description to be satisfactory. Consider, for example, that this wavefunction is of the form [71, 189]:

$$\psi(\vec{r}_1,\vec{r}_2) = K\left[u_1(\vec{r}_1)u_2(\vec{r}_2) + u_2(\vec{r}_1)u_1(\vec{r}_2)\right] \tag{5.4}$$

with $u_1(r) = e^{-ar}$, $u_2(r) = e^{-br}$. Where a and b are parameters to be optimized in order to minimize the energy of the system. Applying this minimization, we find $a = 1.039$ and $b = 0.283$. This means that the wavefunction of D^- is of the form $1s1s'$: one electron is close, while the other is on a much more diffuse orbital (before antisymmetrization). So, the wavefunction of the anion is the combination of an electron in state $1s$ and an electron which is in a linear combination of atomic orbitals.

This combination of orbitals is obtained, for example, by the method of configuration interaction [190] which adds terms related to orbitals $2p$ ($Z_{2p} = 1.95$).

Thus, the normalization of the wavefunction given in the section 3.2.6 is not directly applicable. An asymptotic factor, added "by hand", modifies the apparent normalization term in order to obtain the part of the wavefunction effectively in the state $1s^2$ and thus compensate for the incorrect description of the term $A(L,S)$ quoted above [2].

This factor is adjusted so that the interaction terms coincide approximately with those obtained by Launoy *et al.* [51] for the reaction of Li^+ with D^- (the interaction terms is obtained from the adiabatic curves by estimating the minimal distances between two potential energy curves, then using equation 3.18). Which leads to $A_{B^-} \simeq 0,66$ (table D.1) [3].

Figure 5.6 and Table 5.2 show the ACAM results, compared to the experimental measurement. As the theoretical predictions are uniformly in agreement with experiment, it is possible to argue that changing the normalization of the anion wavefunction provides a empirical solution to the Landau-Zener window mismatch.

---

[1] One should note that this asymmetry of the wavefunction between the two electrons is non-physical. More rigorous calculations show that the wavefunction of the two electrons is symmetric [188], i.e. the two electrons are equivalent. Nonetheless, the use of the asymmetric wavefunction greatly simplifies this discussion as it drastically reduces the number of parameters involved.

[2] It should be noted that this change in the norm of the asymptotic component of the wavefunction precludes any correct prediction of a partial cross section involving other states of D^0.

[3] Similar normalization issues were found by P. Barklem [90, 191].

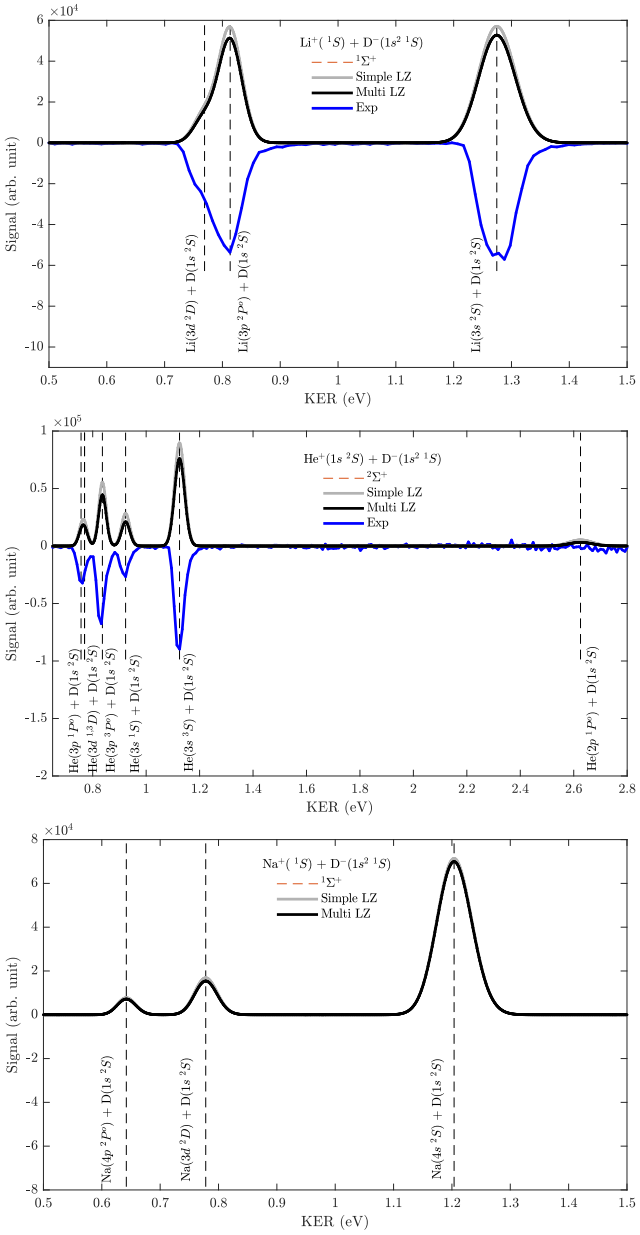

Figure 5.6: Branching ratio simulation for the reactions : $Li^+ + D^- \rightarrow Li + D$ (top); $He^+ + D^- \rightarrow He + D$ (middle); $Na^+ + D^- \rightarrow Na + D$ (bottom).

$Li^+ + D^-$ MN branching ratios

Li + D($1s^2S$)	Theories		Experiments	
	[51]	ACAM	[51]	[192]
$E_{r,i}$ (meV)	3.9	20	3.9	78
$3s\ ^2S$	0.601	0.5151	0.522(5)	0.578(7)
$3p\ ^2P^o$	0.305	0.3912	0.341(1)	
$3d\ ^2D$	0.089	0.0936	0.136(3)	

$Na^+ + D^-$ MN branching ratios

Na + D($1s^2S$)	ACAM	Experiment[5]
$E_{r,i}$ (meV)	20	80
$3p\ ^2P^o$	0.0002	0.000(0)
$4s\ ^2S$	0.7991	0.768(7)
$3d\ ^2D$	0.1411	0.177(9)
$4p\ ^2P^o$	0.0596	0.056(8)

$He^+ + D^-$ MN branching ratios

He + D($1s^2S$)	ACAM	Experiment
$E_{r,i}$ (meV)	20	24
$1s2p\ ^1P^o$	0.0312	0.016(3)
$1s3s\ ^3S$	0.4896	0.428(8)
$1s3s\ ^1S$	0.1226	0.114(4)
$1s3p\ ^3P^o$	0.2466	0.271(5)
$1s3d\ ^{3,1}D$	0.0667	0.090(3)
$1s3p\ ^1P^o$	0.0434	0.043(2)

Table 5.2: Branching ratio simulation for the reactions : $Li^+ + D^- \rightarrow Li + D$ (top); $He^+ + D^- \rightarrow He + D$ (middle); $Na^+ + D^- \rightarrow Na + D$ (bottom).

Thus, by the same argument given above, the normalization of the wavefunctions of the different anions has also been adjusted (by the multiplication of an asymptotic factor) to better reproduce the measured branching ratios (each anion has a unique asymptotic factor, applied to all the reactions involving this anion [4]).

Once these parameters are properly adjusted, the majority of systems are reproduced satisfactorily, with the exception of systems which involve the O^+ ion.

To understand this difference, it is necessary to observe the detail of the

[4] The asymptotic factor of the wavefunction of the different anions nevertheless follows some systematics: it is similar for similar configurations ($O^-/S^-(np^5\ ^2P^o)$ et $C^-/Si^-(np^3\ ^4S^o)$).

spectrum of $O^+(^2D^o)$ + $O^-(^2P^o)$ whose description is given in section 5.4.3. This spectrum highlights the poor attribution of fractional parentage of the configuration terms $2p^3n\ell$ with respect to the configuration terms $2p^3$. To overcome this global error, a renormalization factor was applied to the wavefunction associated with the cation. A common factor is applied to all reaction products. This induces an error in the various branching ratios. However, this global parameter makes it possible to consider an average effect on all the produced states, because this effect cannot be evaluated for each state in isolation without performing the configuration interaction to each state.

5.2.2 Comparison with experimental spectra

Once the correct asymptotic wavefunction of the anion is taken into account, it is possible to compare the prediction given by the ACAM with the experimental spectra (figure 5.7). The first observation is that the overall description of the branching ratios seems accurate.

This model seems also to explain the differences between the channels:

$$A^+(^{2S+1}L) + C^-(^4S^o)/O^-(^2P^o) \rightarrow A((^{2S+1}L)3s\,^{2S'+1}L) + C(^3P)/O(^3P) \tag{5.5}$$

where A corresponds to C, N and O. Those channels seem to be favored when the O^- is involved instead of C^-, while this propensity cannot be explained by the binding energy of the anion. The main difference between them is their term.

In such a case, the $3s$ orbital imposes $m_l = 0$, which implies $m_{LA0} = m_{LA+}$ and $m_{LB0} = m_{LB-}$. It leads to an identical $\tilde{E}_{ic}$ (equation 3.140) for both (C^- and O^-) reactions, the same applies for the factor

$$\begin{bmatrix} L_{A+} & l_{A0} & L_{A0} \\ m_{LA+} & m_{lA0} & m_{LA0} \end{bmatrix} \begin{bmatrix} L_{B0} & l_{B-} & L_{B-} \\ m_{LB0} & m_{lB-} & m_{LB-} \end{bmatrix} \tag{5.6}$$

of the interaction potential (equation 3.114). The only remaining factors which could play a role are:

$$\left(\frac{1}{\sqrt{\#L_{ion}}} \sum_{L_{ion}} \begin{bmatrix} L_{A+} & L_{B-} & L_{ion} \\ m_{LA+} & m_{LB-} & \tilde{\Lambda} \end{bmatrix} \right) \tag{5.7}$$

and

$$\left(\frac{1}{\sqrt{\#L_{cov}}} \sum_{L_{cov}} \begin{bmatrix} L_{A0} & L_{B0} & L_{cov} \\ m_{LA0} & m_{LB0} & \tilde{\Lambda} \end{bmatrix} \right) \tag{5.8}$$

which are smaller for $\tilde{\Lambda} = L_{A+} + L_{B-}$ than for $\tilde{\Lambda} = 0$.

The reduction of the interaction terms leads to an increased partial cross section for the states whose kinetic energy release is higher (see the discussion

in section 3.4 and in particular figure 3.11). Also, the decrease of the interaction term decreases the partial cross section for the states whose kinetic energy release is lower, which favors even more the partial cross section of the higher KER states.

The analysis above predicts that the partial cross section for the $(^{2S_{A+}+1}L_{A+})3s\ ^{2S_{A0}+1}L_{A+}$ states is dominated by the $^{2S_{mo}+1}\Delta$ symmetries for the $N^+C^+ + O^-$ mutual neutralization reaction and the $^{2S_{mo}+1}\Pi$ symmetries for the $O^+ + O^-$ reaction. Which is effectively the case (figures F.39, F.72 and F.102). One should note that those symmetries do not exist for the $A^+ + C^-$ equivalents as shown on table 5.3 (and figures F.36, F.67 and F.96).

	$C^-(^4S^o)$	$O^-(^2P^o)$
$C^+(^2P^o)$	Π	Δ
$N^+(^3P)$	Π	Δ
$O^+(^4S^o)$	Σ	Π

Table 5.3: Highest Λ symmetry for a given mutual neutralization reaction.

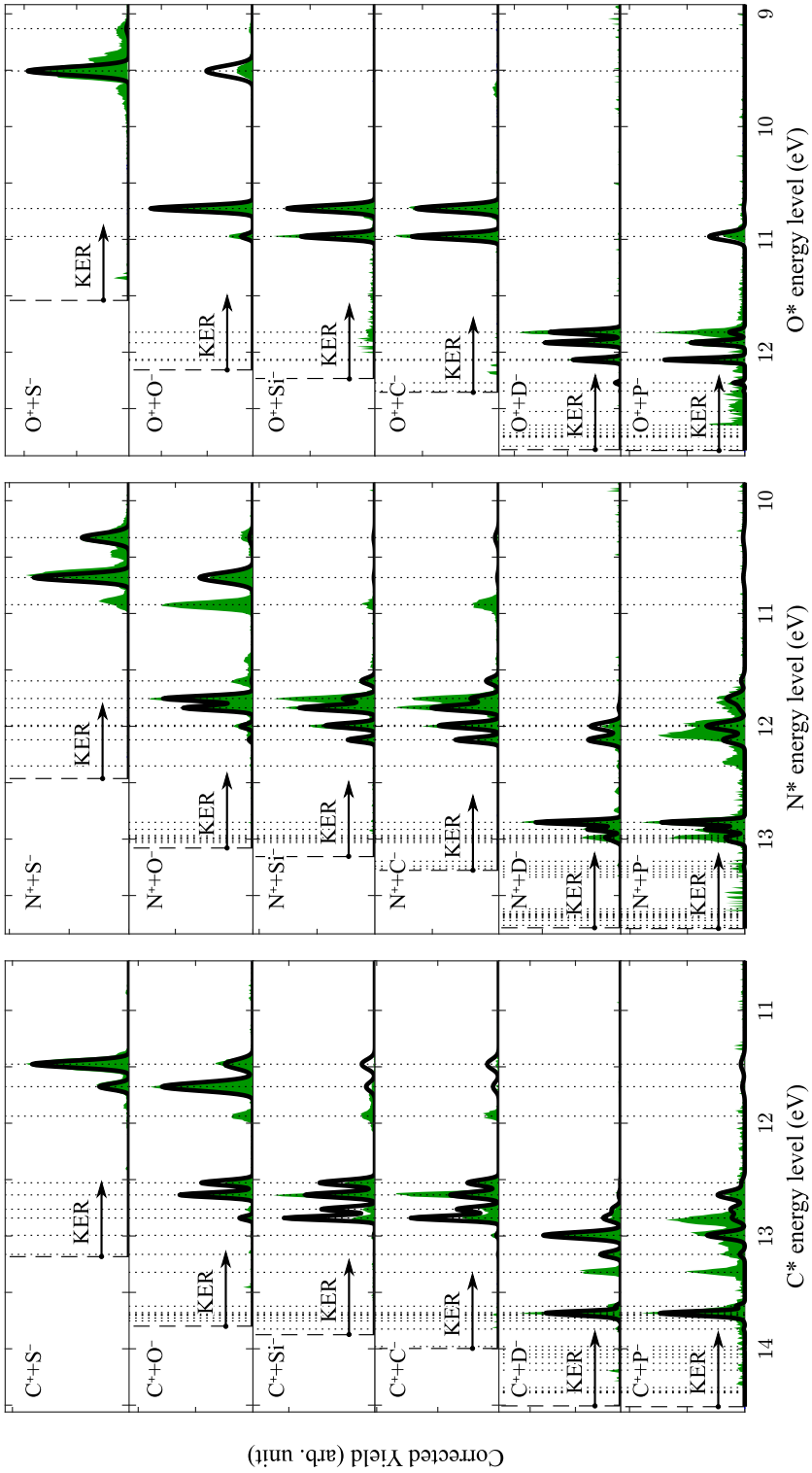

Figure 5.7: Comparison between experimental spectra (shaded areas) and theoretical prediction (black curves) for the $C^+/N^+/O^+ + S^-/O^-/Si^-/C^-/D^-/P^-$ mutual neutralisation reaction at low collision energies (5-25 meV). Only the excited states of the neutralized cation were put into the model (dotted lines). Tghose correspond to the ones shown in figures 5.2, 5.3 and 5.2.

5.2.3 Comparison with other theoretical predictions

Now that the anion-centered asymptotic model (ACAM — chapter 3) is adjusted, it is possible to compare its results to other theoretical predictions. Three systems have been the subject of recent studies: $O^+ + H^-$ [6, 8, 111], $C^+ + H^-$ [7], $N^+ + H^-$ [7] and $Mg^+ + D^-$ [62]. It is therefore possible to compare these theoretical calculations with the simple ACAM model and the experiment (whose experimental branching ratios are taken from Tables 5.4, 5.7, 5.5 and [62]).

The methods used are (see section 1.4 for more details):

- Ab initio methods: One takes into account "all" of the configuration interactions (FCI) for an MCSCF-IC-MRCI calculation [6]. The other method modifies the FCI approach following an Efficient Configuration Interaction (ECI) approach [111].
- Another ab initio method: A numerical method based on a linear combination of atomic orbitals (LCAO) [7, 8].

O	H/D	Theory					Experiment$_D$
		Full CI$_H$ [6]	ECI$_H$ [111]	LCAO$_H$ [8]	ACAM$_H$	ACAM$_D$	
$(^4S^o)3s\ ^5S^o$	$1s$	0.0000	0.0000	0.0000	0.0000	0.0000	0.003(3)
$(^4S^o)3s\ ^3S^o$	$1s$	0.0000	0.0053	0.0000	0.0000	0.0000	0.003(3)
$2s2p^4\ ^3P$	2ℓ	0.0000	0.0326	0.0000	-	-	0.000(0)
$2s2p^4\ ^1D$	2ℓ	0.0000	0.0000	0.0000	-	-	0.004(1)
$(^4S^o)3p\ ^5P$	$1s$	0.0300	0.0188	0.0000	0.0000	0.0000	0.002(1)
$(^4S^o)3p\ ^3P$	$1s$	0.3719	0.2813	0.0000	0.0027	0.0003	0.013(2)
$(^4S^o)4s\ ^5S^o$	$1s$	0.4931	0.5184	0.1802	0.4501	0.3701	0.466(9)
$(^4S^o)4s\ ^3S^o$	$1s$	0.1050	0.1436	0.3657	0.3428	0.3771	0.280(7)
$(^4S^o)3d\ ^{3,5}D^o$	$1s$	-	-	0.2567	0.1853	0.2279	0.216(7)
$(^4S^o)4p\ ^5P$	$1s$	-	-	0.1519	0.0176	0.0226	0.005(1)
$(^4S^o)4p\ ^3P$	$1s$	-	-	0.0455	0.0016	0.0020	0.002(2)

Table 5.4: Branching ratio for the $O^+ + H/D^-$ mutual neutralization reaction. The branching ratio from Full CI$_H$, ECI$_H$, LCAO$_H$ and LCAO$_D$ are extracted from the reaction rates at 1000 K. The collision energy for the ACAM$_H$ and ACAM$_D$ is 20 meV. The means collision energy for the experiment is around 12 meV.

The first thing to note is that ab initio methods require a very large number of configurations to estimate the potential energy curves. Therefore, these cannot include the highly excited states of neutral atoms in their model. This technical limitation (numerical convergence and computation time) forbid to take into account the $3d$ and $4p$ orbitals of oxygen, which prevents these methods from obtaining these branching ratios, even if they are dominant in the experiment. (25% of the signal).

The LCAO method seems to take into account most of the states present in the experiment. However, a shift remains between the states predicted to be

dominant, and those observed experimentally. This is strange, as it has been recently shown that the LCAO and the ACAM should asymptotically predict the same results [193] (for the $Li^+/Na^+/Mg^+ + D^-$ MN reactions), and as the normalization of the D^- wavefunction is similar (the asymptotic factor applied to the ACAM leads to an asymptotic wavefunction identical to the one used by the LCAO model), the source of the discrepancy between the two models remains unknown.

		Theory			Experiment	
N	H/D	$LCAO_H$	$ACAM_H$	$ACAM_D$	All	only H($1s$)
$2p^2(^3P)3s\ ^4P$	$1s$	0.0000	0.0000	0.0000	0.006(3)	0.007(3)
$2p^2(^3P)3s\ ^2P$	$1s$	0.0000	0.0006	0.0000	0.002(1)	0.002(1)
$2s2p^4\ ^4P$	$1s$	0.0000	-	-	0.000(0)	0.000(0)
$2p^2(^3P)3p\ ^2S^o$	$1s$	0.0000	0.0017	0.0004	0.011(2)	0.012(2)
$2p^2(^3P)3p\ ^4D^o$	$1s$	0.0000	0.0119	0.0028	0.010(1)	0.011(1)
$2p^2(^3P)3p\ ^4P^o$	$1s$	0.0000	0.0338	0.0138	0.014(2)	0.016(2)
$2p^2(^3P)3p\ ^4S^o$	$1s$	0.0000	0.0400	0.0237	0.066(3)	0.075(3)
$2p^2(^3P)3p\ ^2D^o$	$1s$	0.0000	0.2068	0.1574	0.017(2)	0.019(2)
$2p^2(^3P)3p\ ^2P^o$	$1s$	0.0000	0.2048	0.1883	0.110(4)	0.125(5)
$2p^2(^1D)3s\ ^2D$	$1s$	0.0000	-	-	0.019(1)	0.022(1)
$2p^2(^3P)4s\ ^4P$	$1s$	0.0711	0.3056	0.3667	0.328(5)	0.372(6)
$2p^2(^3P)4s\ ^2P$	$1s$	0.1015	0.1113	0.1395	0.117(3)	0.133(3)
$2p^2(^3P)3d$						
$^{2,4}P,D,F$	$1s$	0.7310	0.0812	0.1044	0.158(4)	0.179(5)
$2p^2(^3P)4p\ ^2S^o$	$1s$	0.0424	0.0004	0.0005	0.003(1)	0.003(1)
$2p^2(^3P)4p\ ^4D^o$	$1s$	0.0238	0.0014	0.0018	0.010(1)	0.011(1)
$2p^2(^3P)4p\ ^4P^o$	$1s$	0.0148	0.0004	0.0005	0.000	0.000(0)
$2p^2(^3P)4p\ ^2D^o$	$1s$	0.0087	0.0001	0.0002	0.003(1)	0.003(1)
$2p^2(^3P)4p\ ^4S^o$	$1s$	0.0045	0.0000	0.0000	0.000	0.000(0)
$2p^2(^3P)4p\ ^2P^o$	$1s$	0.0023	0.0000	0.0000	0.006(1)	0.007(1)
$2p^3\ ^4S^o$	2ℓ	0.0000	-	-	0.007(3)	
$2p^3\ ^4S^o$	3ℓ	0.0000	-	-	0.054(3)	
$2p^3\ ^4S^o$	4ℓ		-	-	0.025(1)	
$2p^3\ ^4S^o$	5ℓ		-	-	0.008(1)	
$2p^3\ ^2D^o$	2ℓ		-	-	0.024(1)	

Table 5.5: Branching ratio for the $N^+ + H/D^-$ mutual neutralization reaction. The branching ratio from $LCAO_H$ [7] are extracted from the reaction rates at 1000 K. The collision energy for the $ACAM_H$ and $ACAM_D$ is 20 meV. The means collision energy for the experiment is around 16 meV.

	Theory				Experiment
Mg*+H(1s)	FQ$_H$	LCAO$_H$	LCAO$_D$	ACAM$_D$	DESIREE$_D$
$3s3p\ ^3P^o$	0.001	0.000	0.000	0.000	
$3s3p\ ^1P^o$	0.007	0.032	0.011	0.001	
$3s4s\ ^3S$	0.046	0.138	0.085	0.013	0.031(11)
$3s4s\ ^1S$	0.622	0.169	0.179	0.272	0.218(13)
$3s3d\ ^1D$	0.254	0.097	0.110	0.100	0.075(36)
$3s4p\ ^3P^o$	0.070	0.336	0.337	0.394	0.603(26)
$3s3d\ ^3D$	-	0.200	0.244	0.163	
$3s4p\ ^1P^o$	-	0.027	0.034	0.057	0.073(11)

Table 5.6: Branching ratio for the Mg^+ + H/D^- mutual neutralization reaction. The data from FQ$_H$, LCAO$_H$, LCAO$_D$ and DESIREE$_D$ comes from [62]. The collision energy for the ACAM$_H$ and ACAM$_D$ is 20 meV. The collision energy is 59$\pm$12 meV.

	Theory			Experiment	
C* + H/D(1s)	LCAO$_H$	ACAM$_H$	ACAM$_D$	All	no $2s2p^3$
$2s^22p3s\ ^3P$	0.0000	0.0000	0.0000	0.001(1)	0.001(1)
$2s^22p3s\ ^1P$	0.0000	0.0035	0.0005	0.003(1)	0.004(1)
$2s2p^3\ ^3D^o$	0.0000	-	-	0.005(1)	
$2s^22p3p\ ^1P$	0.0000	0.0091	0.0031	0.007(1)	0.008(1)
$2s^22p3p\ ^3D$	0.0000	0.0341	0.0119	0.017(1)	0.020(1)
$2s^22p3p\ ^3S$	0.0000	0.0677	0.0453	0.026(1)	0.030(1)
$2s^22p3p\ ^3P$	0.0000	0.1376	0.0888	0.049(2)	0.057(2)
$2s^22p3p\ ^1D$	0.0006	0.3617	0.3759	0.284(4)	0.333(5)
$2s^22p3p\ ^1S$	0.0039	0.0808	0.0935	0.081(2)	0.095(2)
$2s2p^3\ ^3P^o$	0.0000	-	-	0.141(3)	
$2s^22p3d\ ^1Do$	0.0481	0.0151	0.0190	0.035(1)	0.041(1)
$2s^22p4s\ ^{1,3}P^o$					
$+2s^22p3d\ ^{1,3}F^o$	0.7703	0.2838	0.3532	0.284(4)	0.333(5)
$+2s^22p3d\ ^3D^o$					
$2s^22p3d\ ^1P^o$	0.0648	0.0028	0.0037	0.016(1)	0.019(1)
$2s^22p3d\ ^3P^o$	0.0546	0.0033	0.0043	0.015(1)	0.018(1)
$2s^22p4p\ ^1P$	0.0320	0.0002	0.0002	0.002(1)	0.002(1)
$2s^22p4p\ ^3D$	0.0167	0.0003	0.0004	0.005(1)	0.006(1)
$2s^22p4p\ ^3S$	0.0064	0.0000	0.0000	0.002(2)	0.002(2)
$2s^22p4p\ ^3P$	0.0025	0.0000	0.0000	0.003(1)	0.003(1)
$2s^22p4p\ ^1D$	0.0002	0.0000	0.0000	0.005(1)	0.006(1)

Table 5.7: Branching ratio for the C^+ + H/D^- mutual neutralization reaction. The branching ratio from LCAO$_H$ [7] are extracted from the reaction rates at 1000 K. The means collision energy for the experiment is around 5 meV.

5.3 Strongly interacting states and differential cross section

As shown in the case of Li-D, the differential cross section can be reproduced using a trajectory model. Likewise, when the partial differential cross section is known (for example the He-D system [101, 194]), it is also possible to reproduce the angular distribution of events by convolving this cross section with the distribution of the beams (figures E.2, E.3 and E.4) [5]. The only notable difference is in the partial differential cross section of the reaction $He^+(^2S) + D^-(^1S) \rightarrow He(1s3s\ ^3S) + D(1s)$. Indeed, the angular distribution of events seems to remain uniform much longer than for the other products of the reaction.

This section therefore aims at demonstrating the effect of weakly excited levels of neutralized atoms on the mutual neutralization reaction. It describes how these states act on the differential cross section without affecting the partial cross section.

This explanation will take as an example the mutual neutralization reaction of $Na^+(^1S)$ with O^- $(2p^5\ ^2P^o)$ towards its main reaction products (95%): $Na(3p^2P)$ + $O(2p^4\ ^3P)$. This reaction is chosen because it presents a spectrum that is easy to analyze, while significantly demonstrating the effect of the fundamental levels of the atoms neutralized. This will allow to discuss the statement of Mitrushchenkov *et al.* [6]: "The asymptotic model does not allow to correctly characterize weak partial cross sections as well as to take into account strongly bound states." This statement is based on the following consideration: the asymptotic model does not properly take into account crossings located at a small interatomic distance.

The experimental angular distribution, as well as two simple models (interrupted Rutherford scattering and the impact parameter model [6]) are illustrated

[5] Note that the difference between theory and experiment can be explained in different ways. The first explanation is given by the choice of isotope, the theoretical differential section being that of He-H instead of He-D in our experiment (figure E.1). These two differential cross sections differ slightly. The second explanation might be a too short integration time of the "trajectory" for the theoretical differential cross section (however, this integration time does not influence the partial cross sections). The last explanation could come from a poor estimation of the collision angular distribution of the beams. This last explanation seems less likely: the distribution of the beams is correct for other reactions. However, if the beams were not perfectly aligned (as in the simulation), then the angular distribution of the events would widen, as in the experiment.

Note also that in the figures, the distribution of events is centered around $\cos\theta = -1$. This is simply due to the assignment of masses during data analysis (more details of this effect are given later in this section).

[6] This trajectory model is generated using the simplified potential curves (constant for the covalent states and in $1/R$ for the ionic state). From these diabatic curves, adiabatic curves are extracted using the definition of the interaction term given in the section 3.1.1 and considering that the interaction potential decreases exponentially as a function of the distance interaction:

in figure 5.8 for different collision energies. Let's start by observing the behavior of the different experimental angular distributions: The left part of the figure shows the passage from a uniform angular distribution at low collision energies to an angular distribution similar to a differential cross section (right part of the figure). This second part of the figure shows the appearance of different structures in the differential cross section: a grouping of events at small angle (low angular scattering), a moving peak around 90° and another group of events around 180° (U-turn).

The event concentration at small scattering angles is easily explained with the interrupted Rutherford scattering model. This can be explained as follows: half of the events pass the avoided crossing on the way in and avoid it on the way out, while the other half avoid it on the way in and pass it on the way out. These two halves of events are distributed on either side of the deflection linked to the single passage through the crossing (the trajectory is tangent to the circle of radius R_c. Thus, as this deflection angle is less than 90° there is an event concentration at small deflection angles.

The concentration of events around $\cos\theta \simeq 0$ is not reproducible by the interrupted Rutherford scattering model. To explain it, it is necessary to use at least the classical trajectory model [7]. This method has the advantage of identifying the contribution of the various trajectories to the differential cross section. These are four in number, characterized by their diabatic curve at short distance (figure 5.10): Those that follow through the state Na($3p\ ^2P^o$) + O($2p^4\ ^3P$) called $3p-^3P$ at short range, the state Na($3s\ ^2S^o$) + O($2p^4\ ^1D$) called $3s-^1D$, the state Na($3s\ ^2S^o$) + O($2p^4\ ^3P$) called $3s-^3P$ and in the ionic state $Na^+(^1S)$ + $O^-(^2P^o)$ called *ion*. These trajectories are simulated for the two possible initial symmetries: $^2\Sigma^+$ and $^2\Pi$ (the interaction terms are given in table F.15). A detail of this simulation is shown in figure 5.9. This illustrates the effect of each of these paths:

On the one hand, the differential cross section due to the $^2\Sigma^+$ symmetry is very similar to the one given by the interrupted Rutherford scattering model.

$E_{ic}(R) = E_{ic}(R_c)(R/R_c)^{1/\gamma_A - 1} e^{-\gamma_A(R-Rc)}$. This decrease corresponds approximately to the evolution of E_{ic} following R (equation 3.148) neglecting terms other than $m_l = 0$.

The diabatic curve is used when the crossing is crossed, while the adiabatic potential curve is used when the crossing is avoided. The probability of following through one or the other curve is given, for each impact parameter, by the multiple Landau-Zener probability.

It should be noted that the interaction potential used for the adiabatization of the curves (proposed by Zhou & Dickinson [137]) does not make sense outside the crossing point. This is explained as follows: The evaluation of the interaction term requires to compute the Wronskian $\mathscr{W}(\mathrm{i}_l(\beta r), \mathrm{i}_l(\gamma_B r))$ (section 3.2.7), where $\beta^2/2 \simeq \gamma_A^2/2 - 1/R$ (equation 3.123). This Wronskian can be easily evaluated only when $\beta = \gamma_B$ (equation 3.139). This happens only at $R = R_c$. Thus the asymptotic formula for the interaction term makes sense only for $R = R_c$.

[7] This model makes it possible to classically process the multiple Landau-Zener model, while the interrupted Rutherford scattering model takes into account only the single-channel Landau-Zener model.

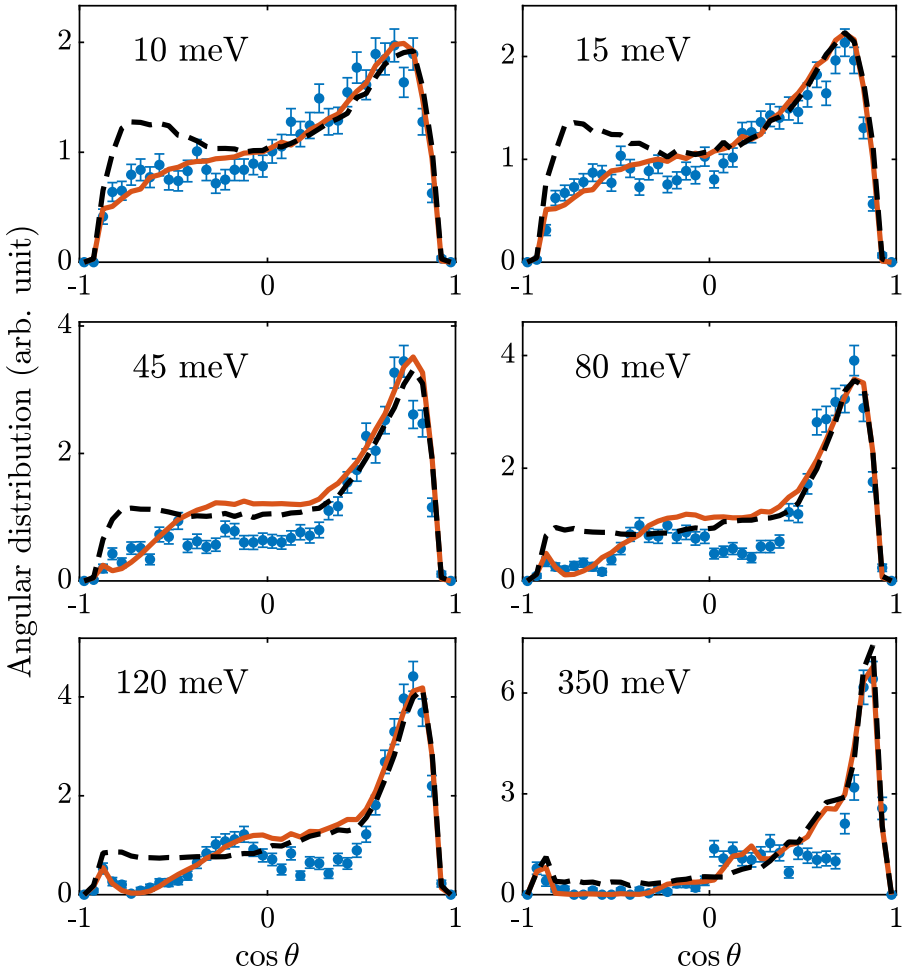

Figure 5.8: Convolved partial differential cross section of the reaction $Na^+(^1S) + O^-(2p^5\ ^2P^o)$ $\rightarrow$ $Na(3p\ ^2P) + O(2p^4\ ^3P)$ given for several collision energies (written on the top left of each panel). The blue circles correspond to the experimental data, the plain red curve corresponds to the impact parameter model, and the black dashed curve corresponds to the interrupted Rutherford scattering model.

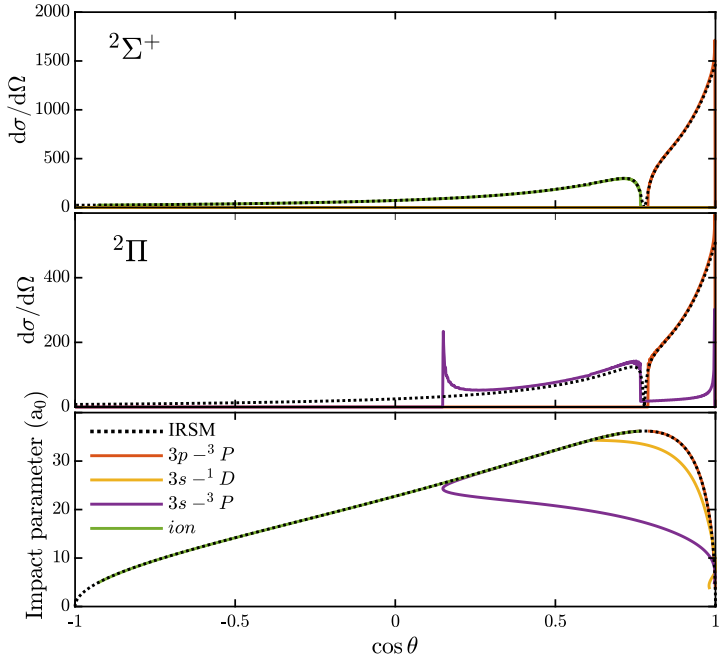

Figure 5.9: Differential cross section simulation details using the classical trajectories method for $Na^+(^1S)$ + $O^-(2p^5\ ^2P^o) \rightarrow Na(3p^2P)$ + $O(2p^4\ ^3P)$ at a collision energy of 465 meV. Top: differential cross section in symmetry $^2\Sigma^+$; middle: differential cross section in symmetry $^2\Pi$; bottom: impact parameter as function of the deflection angle.

Indeed, the curve $3s\ ^{-1}D$ has little influence (because very sparsely populated). Thus, the only useful curves are the $3p\ ^{-3}P$ and *ion* curves. As in the interrupted model [8].

However, the differential cross section due to the $^2\Pi$ symmetry differs for large deflection angles. Those events are missing! This can be explained as follows: unlike the $^2\Sigma^+$ symmetry, the potential for interaction between the states $3s\ ^{-3}P$ and *ion* is very large (10^{-3} Hartree). Thus, the crossing is (almost) always avoided both on the way out and back [9]. The avoidance of the crossing leads to a rainbow scattering, visible on the experimental spectra. However, it should be noted that this model — even if it predicts the correct position for the rainbow scattering — does not reproduce its shape well. This is linked to the model used. As the trajectory is given by a classical model, it is not possible

[8] We find ourselves in a situation comparable to the simple Landau-Zener model. This explains the validity of the interrupted Rutherford model.

[9] This explains the low proportion of the state in the branching ratio spectra. Note however that this branching ratio is underestimated (0.3 % instead of 1 %). This branching ratio can easily be corrected by changing the interaction term by a factor of 0.85. This state is therefore just at the edge of the Landau-Zener window.

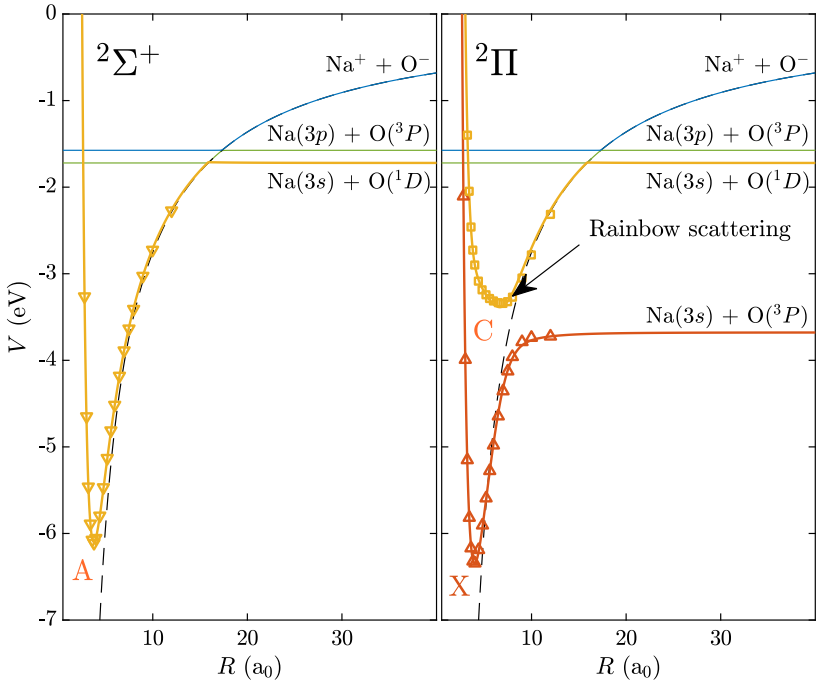

Figure 5.10: Potential energy curves (PEC) of the $^2\Sigma^+$ symmetry (left) and the $^2\Pi$ symmetry (right). The PEC of the $X^2\Pi$ (upward triangles), $A^2\Sigma^+$ (downward triangles) and the $C^2\Pi$ (squares) are fitted from [195] for the low interatomic distances. The plain curves are the diabatic curves, the dashed curve is the diabatic ionic curve with the dipole-dipole interaction $V(R) = -1/R - (\alpha_{Na^+} + \alpha_{O^-})/(2R^4)$, with $\alpha_{Na^+} = 1.00$ a.u. and $\alpha_{O^-} = 21.59$ a.u. [196, 197]. The component of the potential which leads to the rainbow scattering is indicated by the arrow.

to reproduce the width of the rainbow scattering. It is nevertheless impressive that such a simple model can predict this kind of phenomenon and correctly explain the peak displacement according to the collision energy.

The last peak to be discussed is the one associated with a U-turn in the trajectory. This peak cannot be reproduced using the asymptotic model. If it were true, it would be an indisputable signature of effects induced by interactions at short distances. Unfortunately, this peak is simply an artifact related to the analysis of experimental events (appendix B.2).

Thus, the asymptotic model makes it possible to explain, in this special case, all the phenomena observable experimentally. Moreover, it allows us to detect, from the raw experimental spectra, the contribution of the (temporary) population of states close to the ground state of each atom (without going through a simulation).

For example, the rainbow scattering seems important for the mutual neutralization of $C^+ + O^-$ (figure E.11), $C^+ + C^-$ (figure E.10) and possibly $O^+ + O^-$ (figure E.13). Doubt hangs over the latter case because of the low collision

energies measured. At least, the analysis seems more nuanced: the figure E.14 indicates that the differential cross section of the states ^3P, ^5P and ^5S seems to remain uniform, while the differential cross section of state ^3S quickly focuses around $\cos\theta = 1$, combined with a rainbow scattering around $\cos\theta = \pm 1/2$. Thus, as in the case of Na-O, the rainbow scattering depends on the symmetry of the collision studied.

On the other hand, this rainbow scattering is absent from the mutual neutralization of $Ne^+ + C^-$ (figure E.15). Indeed, the only state located below that which can lead to a rainbow scattering is the ground state $Ne(2s^2 2p^6\ ^1S)$ located 16 eV lower. Therefore, if the rainbow scattering is present, it is given by an avoided crossing located at a very small interatomic distance (the crossing radius with the ionic state is located at 1.34 a_0). Only the very low impact parameters make it possible to go so deep in the potential well. As the differential section is given by:

$$\frac{d\sigma}{d\Omega} = \frac{p(b)}{\sin\theta} \times b\frac{db}{d\theta} \tag{5.9}$$

The low impact parameter compensates for the divergence of its derivative and strongly reduces the importance of the rainbow scattering.

5.4 States not predicted by the model

Although the one-electron exchange model seems to reproduce the experimental branching ratios satisfactorily, some levels seem to escape predictions. This section aims at listing these and explaining this shortcoming.

5.4.1 $2s2p^{N_{A+}+2}$ configurations

The first series of levels that the simulations fail to reproduce are the states associated with the neutralized cation in a $2s2p^{N_{A+}+2}$ configuration, i.e. with a $2s$ hole. Both carbon and nitrogen atoms have states with this configuration: N($2s2p^4\ ^4P$), C($2s2p^3\ ^5S^o$) and C($2s2p^3\ ^3P^o$). These are particularly present in the following reactions (branching ratios $\geq$5%):

- C($2s2p^3\ ^3P^o$):
  - $C^+ + D^-$ (14 % – section F.4.2),
  - $C^+ + P^-$ (10 % – section F.4.1);
- C($2s2p^3\ ^3D^o$):
  - $C^+ + C^-$ (10 % – section F.4.4),
  - $C^+ + Si^-$ (8 % – section F.4.3),
  - $C^+ + O^-$ (8 % – section F.4.5);
- N($2s2p^4\ ^4P$):
  - $N^+ + C^-$ (11 % – section F.5.4),
  - $N^+ + Si^-$ (5 % – section F.5.3),
  - $N^+ + O^-$ (27 % – section F.5.5),
  - $N^+ + S^-$ (14 % – section F.5.6).

These states being much populated, it seems necessary to find an explanation to their contribution, since these states cannot be predicted using the asymptotic one electron model (ACAM). Two explanations are plausible: Either these states are not produced by the exchange of a single electron, or it is the configuration of the state which is not well described. These two explanations are discussed here.

The first explanation assumes that the process does not involve the exchange of one electron, but two. So, if we assume that the description of the states using only a single configuration is correct, then the states of interest are produced by the following process: the cation A^+ is initially in a $2s^2 2^{N_{A+}}$ configuration. Thus, to produce the configuration $2s2p^{N_{A+}+2}$, it is first necessary that the capture of an electron from the cation leads to a configuration

$2s^2 2^{N_{A+}+1}$, then that a process of reorganization of the configuration occurs during the reaction so that an electron $2s$ passes to the orbital $2p$.

The LCAO method presented by Amarsi & Barklem [7] follows this line of thought, using the two-electron process given by [78, 122] :

$$H_{i,c}^{2e} = \left\{H_{i,c}^{1e}\right\}^2 \times R, \tag{5.10}$$

but also adjusting the coupling as follows: the angular momentum coupling term is assumed to be unitary (see equation 3.114), the binding energy is that of the nucleus which leads to the largest fractional parentage coefficient, the fractional parentage coefficient is set to unity [7]. This method seems nevertheless not to lead to convincing results (tables 5.7 and 5.5).

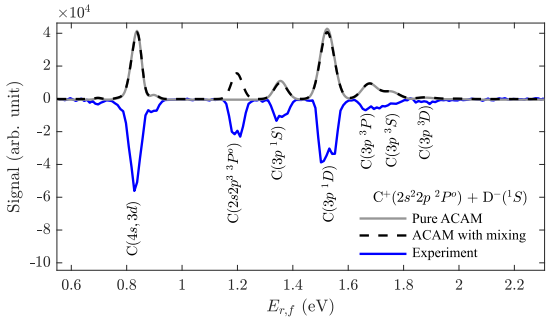

Figure 5.11: Experimental and simulated $E_{r,f}$ spectra using the configuration mixing given by the NIST for the C($2s2p^3\ ^3P^o$) state (see text).

The other possible method consists in taking into account the multiple configurations which can lead to the desired term. Indeed, the NIST tables for carbon (which takes its recommended values from [198]) indicate that only 79% of the level comes from the $2s2p^3$ configuration and that 15% comes from the $2s2p3d$ configuration[10]. Using this configuration mixing, the branching ratios given by this model correspond to the experimental branching ratios (figure 5.11).

This method was successfully applied to the $N^+ + O^-$ reaction [4, 156], using the MCHF (Multi-Configuration Hartree-Fock) method. However, this method is not implemented in this thesis (neither in the appendix) as it requires atomic configuration mixing calculations which does not remains strictly within the ACAM.

[10] About 7% remain to be allocated, which were supposed to not play a role in the mutual neutralization process

5.4.2 Excited states of the neutralized anion

Excited states of the neutralized anion are present in a number of reactions. These can be classified into two categories depending on whether the anion is neutralized in its ground configuration (not necessarily its ground term) or in some excited configuration.

In the first category are the following reactions:

- $Na^+ + O^-$ (4% of Na($3s\ ^2S$)+O(^1D) – section F.3.2),
- $Na^+ + S^-$ (94% of Na($3s\ ^2S$)+S(^1D) – section F.3.3),
- $C^+ + P^-$ (21% of C($3s\ ^{1,3}P^o$)+P($^2D^o$) – section F.4.1) : the state C($2s2p^3\ ^3D^o$)-P($^2D^o$) is not reproduced due to the carbon configuration $2s2p^3\ ^3D^o$.
- $N^+ + P^-$ (21% – section F.5.1) : the state N($2s2p^4\ ^4P$)-P($^2D^o$) is not reproduced due to the nitrogen configuration $2s2p^4\ ^4P$. Also the state, a priori forbidden, N($2s^22p^2(^1D)3s\ ^2D$) is certainly a mixture with the configuration $2s^22p^2(^3P)3d\ ^2D$.
- $Ne^+ + S^-$ (79% of Ne($3s$)+S(^1D) – section F.7.3) : As this system is not described in the *LS* coupling scheme, it is not tractable by the current version of the ACAM model.

For these reactions, the asymptotic one-electron model easily reproduces the excited states. This anion is explained as follows, taking the oxygen anion as an example. This is initially in state $2p^5\ ^2P^o$. These five electrons are indistinguishable. It is not possible to isolate an electron from the others in order to be able to write this state as $2p^4(^{2S+1}L)2p\ ^2P^o$. The $2p^4(^{2S+1}L)$ substate does not exist but rather is a linear combination of the possible substates. Therefore, when an electron is extracted from the anion, it is only possible to predict the probability that each of these substates is produced (given by the fractional parentage coefficients). This way of looking at the reaction agrees with the one-electron model. Therefore, it allows these behaviors to be reproduced.

The second category includes the states of the neutralized anion whose configuration is not the ground configuration (it should be noted that in such case the states of the neutralized cation are systematically found in its ground configuration). Nevertheless, the asymptotic method with one electron still makes it possible to explain the presence of these states, it however requires to re-express differently the development of the multiple Landau-Zener model given in section 3.1.5. To see more clearly, let us take an example: the mutual neutralization of C^+ with S^- whose relevant potential curves are represented in figure 5.12. In this figure, two sets of curves are represented: The set of

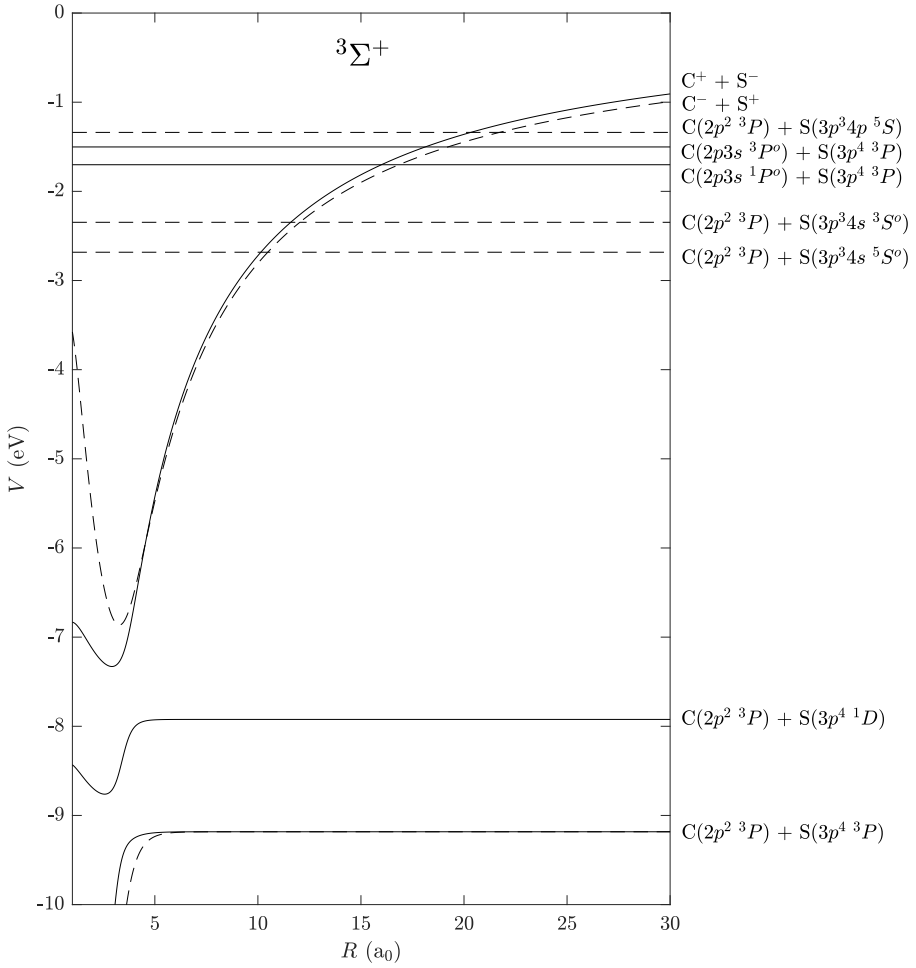

Figure 5.12: Potential diagram for the $^3\Sigma^+$ symmetry of C–S. The states shown are those associated with the mutual neutralization reaction of C^+–S^-. The solid curves represent the curves interacting with the ionic curve C^+–S^- while the dashes represent the curves interacting with C^-–S^+. The adiabatization of the potential energy curves are done two by two, each time between the (modified) ionic curves and a new covalent curve. The adiabatization is done using equations 3.12, 3.14 and 3.15. The adiabatization is done only for the covalent states whose atomic configurations follow C($2p^2$)–S($3p^4$). The interaction terms used at the crossing radii are given in the table F.46 and follows an $R^{1/\gamma_A - 1} \exp -\gamma_A R$ interatomic dependency (the validity of this formula is discussed in section 3.2.7). Therefore the adiabatic potential energy curves given in this figure are only qualitative.

curves correlating with C^+–S^- ($H_{ic} \geq 10^{-6}$ a.u. – solid lines) and the set of curves correlating with S^+-C^- ($H_{ic} \geq 10^{-6}$ a.u. – dashes).

Let us note first that the two ionic curves are very close to each other (shifted by only $IP_C + EA_C - IP_S - EA_S = 86$ meV) – The curve of S^+–C^- is located slightly below – and, that the related interaction potentials – between these two curves and the ground state of the two neutralized ions C(^3P)–S(^3P) – are quite big.

Therefore, if C^+ approaches S^- enough to reach this crossing, a first electron transfer occurs. However, the state C(^3P)-S(^3P) interacting with C^+–S^- is also the state C(^3P)–S(^3P) interacting with the state S^+–C^- (when molecular symmetry allows it). Thus, during the splitting phase, it is possible that the crossing between C(^3P)–S(^3P) and C^+–S^- is avoided to reach the curve S^+–C^-. The neutralized states will then be a Rydberg series associated with S^+, produced by the exchange of a single electron (taken into account by the asymptotic method) or to a double charge exchange process.

However, this phenomenon is accentuated by the proximity of the two curves: It is no longer possible to formulate the Landau-Zener hypothesis according to which the avoided crossings are occuring two by two. There is then a mixture of ionic curves, the description of which goes beyond both the Landau-Zener model and the asymptotic model centered around the anion. A correct description of the reaction would require rigorous quantum processing.

This phenomenon is present in the following reactions:

- C^+ + S^- (10 %, mostly represented by the C(^3P)+S($4s\ ^{3,5}S^o$) states – section F.4.6),
- O^+ + S^- (18% of O(^1D)+S($4s, 4p$) – section F.6.6) : This proportion is probably overestimated, due to the presence of states related to O* in the same area on the $E_{r,f}$ spectrum,
- C^+ + Si^- ($\sim$22 % – section F.4.3) : These states are represented by two Rydberg series converging to the states C(^3P)+Si^+($2P^o$) and C(^1D)+Si^+($2P^o$).

All these reactions are characterized by an ionization potential of the neutralized anion lower than that of the cation, which makes it possible to have the ionic curve of inverted charges located below the initial ionic curve. This condition is necessary to obtain these excited states associated with the anion [11].

[11] Other reactions could also give rise to such reactions (O–C system). Nevertheless, it is necessary to have states within the Landau-Zener window to observe a mutual neutralization reaction. On the other hand, if no state is present within this window, it is possible that the double charge exchange cross section increases.

In order to end this section, it is important to note that some reactions do not fit into any of these two categories:

- $C^+ + D^-$ (2% – section F.4.2) : However, the detected state – C(^3P)-D(2ℓ) – is at the lower limit of $E_{r,f}$ detectable by the system (0.27 eV). In addition, this state overlaps with the state C($4p\ ^1S$) + D($1s\ ^2S$).

- $N^+ + D^-$ (12% of N($2p^3\ ^4S^o, ^2P^o$)+D($n = 2,3,4$) – section F.4.2) : This case cannot be attributed to a curve D^+-N^- (because there is no inverted ionic curve below the initial ionic curve. Nevertheless, the excited states of deuterium are part of the list of states associated with the anion D^- (see section 5.2). The definition of the fractional parentage coefficient is not applicable in this case. [12].

- $N^+ + S^-$ (<1% – section F.4.2) : This reaction seems to produce several excited states of sulfur: $4p\ ^3P$ in the peak at 2.1 eV, $4p\ ^5P$ in the tail of this peak at 2.25 eV, but also $4s\ ^3S^o$ isolated at 3.3 eV and $4s\ ^5S^o$ at 3.65 eV. The ends of the peak at 2.1 eV (2.05 and 2.40 eV) carry the possible traces of the state N(^3P)–S($4s\ ^{3,5}S^o$). Nevertheless, the low proportion of the produced states, combined with the small crossing distance of those states, makes us conclude that the production of these states exceeds the framework of an asymptotic model. A more rigourous treatment is necessary to reproduce these states.

The cases listed above can either be classified in the first category, or they produce a weak branching ratio which implies an interaction at short distance (impossible to predict with the asymptotic model).

5.4.3 Fractional parentage coefficients of Rydberg states

Another set of product states which is not predicted by the model is found in the measurement of the reaction of $O^+(^2D^o)$ with $O^-(^2P^o)$. In the spectrum of released kinetic energy (see figure 5.13) there is the following Rydberg series O($2s^2 2p^3(^4S^o)n'p\ ^3P$)–O($2s^2 2p^4\ ^3P$).

[12] Moreover, for the fundamental configuration of nitrogen, the Coulomb normalization (equation 3.120):

$$N_A^{\text{Coul}} = \gamma_A (2\gamma_A)^{1/\gamma_A} \left[\Gamma\left(\frac{1}{\gamma_A} + l_A + 1\right) \Gamma\left(\frac{1}{\gamma_A} - l_A\right) \right]^{-1/2}$$

is no longer valid. As $\frac{1}{\gamma_A} - l_A < 1$, the Γ function returns an imaginary number. This is explained by the domain of validity of the Coulomb normalization which is valid only for strongly excited states. It cannot therefore be applied to the fundamental configuration.

Note however that for Li, He and Na atoms, the fundamental configuration is already part of the Rydberg series. This explains the concordance between theory and experiment for the associated reactions.

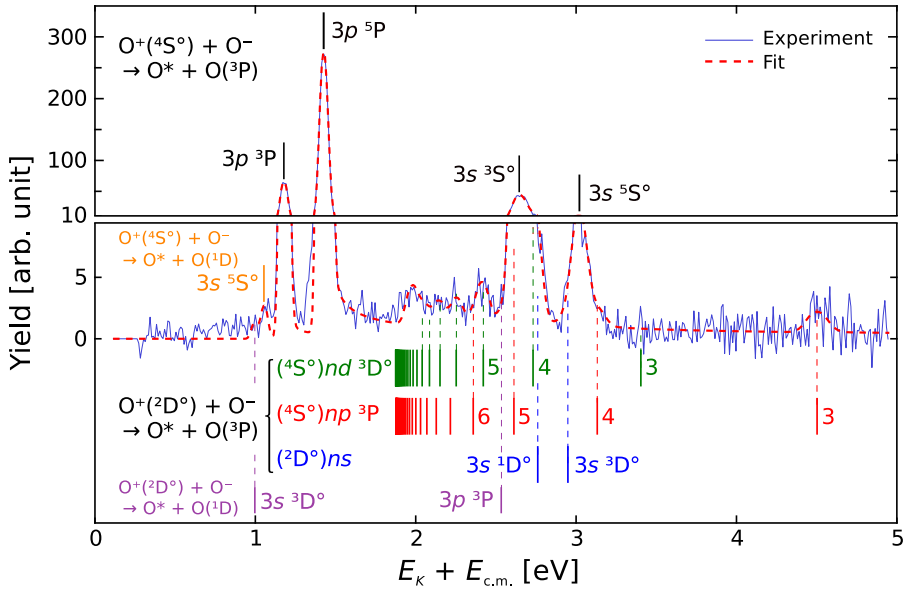

Figure 5.13: Relative kinetic energy spectrum after collisions for the $O^+ + O^-$ mutual neutralization reaction. The peaks assigned in black correspond to $O^+(^4S^o) + O^-(^2P^o)$, those assigned in red/blue/green correspond to the $O^+(^2D^o) + O^-(^2P^o)$ reaction.

In principle, the O $(2s^2 2p^3 (^4S^o) n'p\ ^3P)$ states are Rydberg states associated with an $O^+(2s^2 2p^3\ ^4S^o)$ core, inaccessible by capture of an electron by the ion $O^+(2s^2 2p^3\ ^2D^o)$. Fractional parentage coefficients should forbid it.

However, looking at Table 5.8, we see the presence of three states $np^3 n'p\ ^3P$, each associated with a different core.

np^3	$np^3 n'p$															
	^5P	^5S	^3F	^3D		^3P			^3S		^1F	^1D		^1P		^1S
				1	2	1	2	3	1	2		1	2	1	2	
$^4S^o$	1	1	0	0	0	1	0	0	1	0	0	0	0	0	0	0
$^2D^o$	0	0	1	1	0	0	1	0	0	0	1	1	0	1	0	0
$^2P^o$	0	0	0	0	1	0	0	1	0	1	0	0	1	0	1	1

Table 5.8: Fractional parentage coefficients between $np^3 n'p$ and np^3 (as described in section C.2.3).

However, the manual building of the wavefunctions [13] gives a more ambiguous result. The three terms $np^3 n'p\ ^3P$ are each a linear combination of the core terms np^3. Fractional parentage coefficients allow you to choose a core

[13] The construction of the different wavefunctions from different m_l and m_s, by application of the operators L_+ and L_-.

term. However, this choice, while not arbitrary, is wrong.

Indeed, the choice of the combination of core terms is more complex. It requires to maximize the binding energy of the most bound term, to the expense of the least bound ones [14].

Therefore, the $2p^3n'p$ states should be written in the form

$$2s^2 2p^3(a_1 \times {}^4S^o + a_2 \times {}^2D^o + a_3 \times {}^2P^o)n'p\ {}^3P \tag{5.11}$$

where a_1, a_2 and a_3 are the mixing coefficients. However, in order to simplify the notations, only the most represented term is noted. This plays the main role in the behavior of the state.

5.4.4 Rydberg series

Finally, let us also note the presence of several Rydberg series:

- $O^+(^2D^o) + O^-(^2P^o) \rightarrow O(^4S^o n\ell) + O(^3P)$ – section F.6.5 and figure 5.13,
- $O^+(^2D^o) + P^-(^3P) \rightarrow O(^4S^o n\ell) + P(^4S^o)$ – section F.6.1,
- $C^+(^2P^o) + Si^-(^4S^o) \rightarrow C(^3P) + Si(^2P^o n\ell)$ and $C^+(^2P^o) + Si^-(^4S^o) \rightarrow C(^1D) + Si(^2P^o n\ell)$ – section F.4.3,
- $O^+(^4S^o) + C^-(^4S^o) \rightarrow O(^3P) + C(^2P^o n\ell)$ – section F.6.4

each of which appears to produce an approximately constant density of events which converge to either a collisional detachment or a transfer ionization process, suggesting that those processes might happen (at a lesser order of magnitude that the mutual neutralization process as the signal associated with individual Rydberg channel is two orders of magnitude smaller than the main ones – appendix F.6.4).

One should note that these patterns stop slightly before the end of the Rydberg series. This effect comes from the (diabatic) electric field-induced ionization of the Rydberg atoms, which ionizes all the states whose binding energy $IP - E_{lev}(\mathrm{cm}^{-1}) \leq 4\sqrt{F_l(\mathrm{V/cm})}$ [200]. The two sources of strong electric field F_l in the setup are the exit of the observation cell (500 V/cm – figure 4.30) and the separating electrodes (2000 V/cm – section 2.6), which leads to a lowering of the ionization limit by 22 meV (which should be compared to the individual peak width, which is around 20 meV), i.e., using the $1/n^2$ approximation for the binding energy of the Rydberg atoms, all Rydberg states whose principal quantum number n is higher than 24 is ionized by the electric field.

[14] An argument in favor of this reasoning is that the $2s^2 2p^3(^2D^o)n'p\ {}^3P$ and $2s^2 2p^3(^2P^o)n'p\ {}^3P$ states are not in the NIST tables [199] because they are beyond their respective ionization limits ($2s^2 2p^3\ {}^2D^o$ and $2s^2 2p^3\ {}^2P^o$ respectively).

Those re-ionized atoms are deflected, they cannot reach the detection system and are absent from the $E_{r,f}$ spectra.

For this experimental finding to be reproduced by the model, the product of the partial cross section and the density of states must be approximately constant.

The density of states is the reciprocal of the spacing between two consecutive levels. This is approximately:

$$\left(\frac{1}{n^2}-\frac{1}{(n+1)^2}\right)^{-1} \simeq \frac{n^3}{2} \tag{5.12}$$

Assuming that there is only one state per principal quantum number[15].

The partial cross section of the Rydberg series is obtained by the following reasoning: Since the Rydberg series leads a kinetic energy release of ~ 1 eV, most terms in the equations 3.62 and 3.63 are approximately constant. Only the interaction term varies depending on the principal quantum number. Moreover, since the interaction term is small, $G(\zeta)$ varies linearly with ζ. Thus partial cross sections evolve proportionally to the square of the interaction potential:

$$\sigma_n \sim H_{ic}^2(n) \tag{5.13}$$

This equation gives a constraint on the interaction term that it should be possible to verify using the asymptotic model. This interaction term for γ_A small — given by the equation 3.148 — follows approximately:

$$H_{ic} \sim \frac{\gamma_A(2\gamma_A R)^{1/\gamma_A}e^{-\gamma_A R}}{\Gamma(1/\gamma_A+1)/\sqrt{1/\gamma_A}} \tag{5.14}$$

By replacing γ_A with its approximate value $\gamma_A \simeq 1/n$, the previous equation becomes (assuming R constant) [16]:

$$H_{ic} \sim \frac{1}{n}\frac{(2R/n)^n}{n!/\sqrt{n}}e^{-R/n} \sim \frac{1}{n}\frac{(2R/n)^n}{e^{-n}n^n}e^{-R/n} \sim \frac{1}{n}\left(\frac{2R}{n^2}\right)^n e^{n-R/n} \sim \frac{1}{n}\left(\frac{2Re}{n^2}\right)^n \tag{5.15}$$

which decreases faster than $1/n^3$ as n increases. Thus, the asymptotic model does not allow to reproduce the partial cross section of mutual neutralization towards Rydberg states.

This is explained by the invalidity of the assumptions put in place when establishing the asymptotic interaction potential. The first invalidated hypothesis

[15] The same result is obtained under the assumption that, for each principal quantum number there are $2\sum_{l=0}^{n-1}(2l+1) = 2n^2$ states, assuming all of these states are equivalent. Both cases produce a power law for the states density.

[16] As a reminder: $n! \simeq n^n e^{-n}\sqrt{2\pi n}[1+\mathcal{O}(1/n)]$ and $\sqrt{\Gamma(1/\gamma_A+l+1)\Gamma(1/\gamma_A-l+1} \geq \Gamma(1/\gamma_A+1)$.

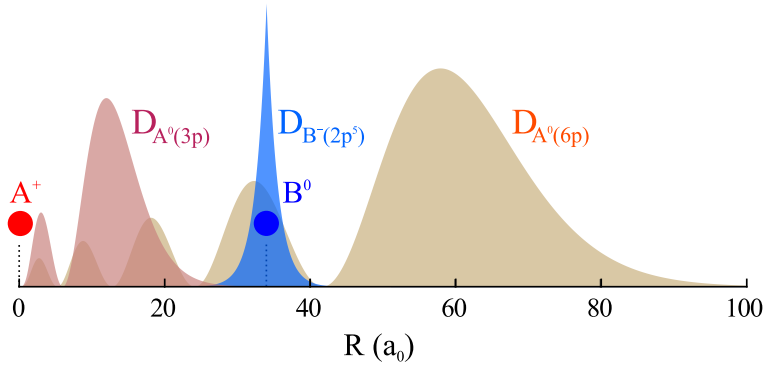

Figure 5.14: Squared radial wavefunctions $D = r^2|\phi(r)|^2$ of the $3p$ (red) and $6p$ (orange) hydrogenic states (shaded areas) centered around A^+ which form the covalent state $A^0(np)$. The atom B^0 (blue) is positioned such that the kinetic energy release is 0.8 eV. The associated squared radial wavefunction of the anion is given by the blue shaded area.

is in the initial step: the Firsov integral (sections 3.2.3 and 3.2.2). Indeed, this integral requires the definition of a surface which entirely contains the wavefunction of the ionic state (the electron attached to the atom B^0) — with the exception of an exponentially decreasing term — while entirely excluding the wavefunction of the covalent state (the electron attached to the A^+ ion) — with the exception of an exponentially decreasing term. If this is not the case, the simplifications made to the equation 3.78 become invalid.

To determine the possibility of defining this surface, let us observe for a moment figure 5.14. This illustrates two (squared) hydrogenic wavefunctions atom centered around the A^+ ion. The position of the atom B^0 is located at an interatomic distance R such that the kinetic energy released during the reaction is 0.8 eV. We then see that the wavefunction associated with the state $3p$ makes it possible to define a surface centered around B^0 which includes the wavefunction of B^-, while excluding the wavefunction $A^0(3p)$ — except for exponentially decreasing components.

On the other hand, it is impossible to determine such a surface for the $6p$ state! In this case, the atom B^0 is located inside the wavefunction. It is not possible to perform the asymptotic development of the wavefunctions, i.e. to assume that the interatomic distance is greater than the size of the two isolated atoms. This type of electron exchange requires an entirely different treatment. Because the exchanged electron becomes a "spectator" of the collision which involves its own exchange [17]!

Then, why does the asymptotic model function for the $O^+(^4S^o) + O^-(^2P^o)$

[17] This observation also allows the use of a beam of atoms in a Rydberg state instead of an ion beam to measure a cross section. For example $H_2^+ + H_2 \rightarrow H_3^+ + H$ [201].

reaction and all the other reactions involving the ions in their ground term? Simply because the Firsov hypothesis is also valid in those cases. This hypothesis could be expressed as follows: The crossing radius R_c must be greater than the mean radius R_n of the Rydberg electron on a level n:

$$\frac{1}{R_c} < \frac{1}{R_n} \tag{5.16}$$

In order to check whether this condition is satisfied or not, one should remember the definition of the kinetic energy release based on the reactants and products energy levels:

$$KER = (IP^{A0} + E_{lev}^{A+} - E_{lev}^{A0}) - (EA^{B0} + E_{lev}^{B0} - E_{lev}^{B-}). \tag{5.17}$$

where all the energies used are chosen positive. Also, as the ionic potential follows a $-1/R$ curve and the covalent potentials are approximately flat[18], the crossing radius is $R_c = 1/KER$.

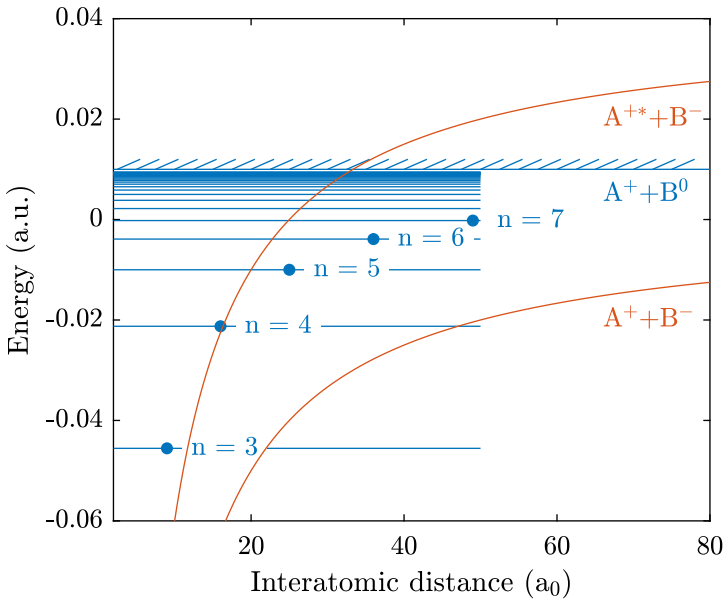

Figure 5.15: Schematic for representation of the validity domain. Blue curves: covalent potential energy whose ionization limit is given by the stripped band, red curves: the ionic potential energy, blue dots: electron mean radius around the cation. The Firsov integral is valid for the covalent states whose blue dots are above the ionic potential energy curve.

Then, in order to get a qualitative description of the system, one could use the hydrogenic approximation:

[18] This is valid only within the $1/R$ potential hypothesis. But the addition of the polarization term will not change the conclusion obtained here.

- The mean radius is $R_n \simeq n^2$,
- and the binding energy of the electron attached to the cation is $IP^{A0} - E_{lev}^{A0} \simeq 1/2n^2$.

Let's now study two cases (figure 5.15): The first one corresponds to the neutralization of two ions in their ground states ($A^+ + B^- \rightarrow A^* + B$), which means that $E_{lev}^{B-} = 0$ and $E_{lev}^{A+} = 0$. And the second case to the neutralization of the two ions, but with the cation in an excited state ($A^{+*} + B^- \rightarrow A^* + B$), which means that $E_{lev}^{B-} = 0$ and $E_{lev}^{A+} > 0$. Both reactions would produce a neutralized anion in its ground state $E_{lev}^{B0} = 0$[19].

The first case applied to equation 5.16 leads to:

$$\frac{1}{2n^2} - EA^{B0} < \frac{1}{n^2} \tag{5.18}$$

or

$$\frac{1}{2n^2} + EA^{B0} > 0 \tag{5.19}$$

which is always satisfied. It means that, when both ions are in their ground states, the Firsov integral method is always valid.

But, when the cation is in an excited state (case two), equation 5.16 becomes:

$$\frac{1}{2n^2} + EA^{B0} - E_{lev}^{A+} > 0 \tag{5.20}$$

which means that, if $EA^{B0} < E_{lev}^{A+}$ – which is the case for the $O^+(^2D^o)$ + $O^-(^2P^o)$ reaction – there is an upper limit to n for the validity of the Firsov integral. In such a case, the asymptotic model is not valid anymore. The ACAM cannot describe the Rydberg series.

5.4.5 Mutual neutralization into autoionizing states

Detailed observation of the $O^+ + O^-$ reaction spectrum revealed the significant presence of excited states within the positive beam.

The statistics of this measurement allowed a partial estimation of the excited states produced by the reaction $O^+(2p^3\ ^2D^o) + O^-(2p^5\ ^2P^o)$ – see section 5.4.3 and [202]. All the states produced during this reaction were below the ionization limit of $O^+(2p^3\ ^4S^o)$-$O(2p^4\ ^3P)$. However, it is not excluded that states above this ionization limit are produced. Indeed, the most probable states predicted by the asymptotic model (e.g. $O(2p^3(^2D^o)3p)$) overlap with the main peak of the reaction $O^+(2p^3\ ^4S^o) + O^-(2p^5\ ^2P^o)$ (see figure 5.16), it is therefore not possible to estimate whether or not they are produced during

[19] One could also study the cases where $E_{lev}^{B-} \neq 0$ and $E_{lev}^{B0} \neq 0$, but those cases wouldn't add anything.

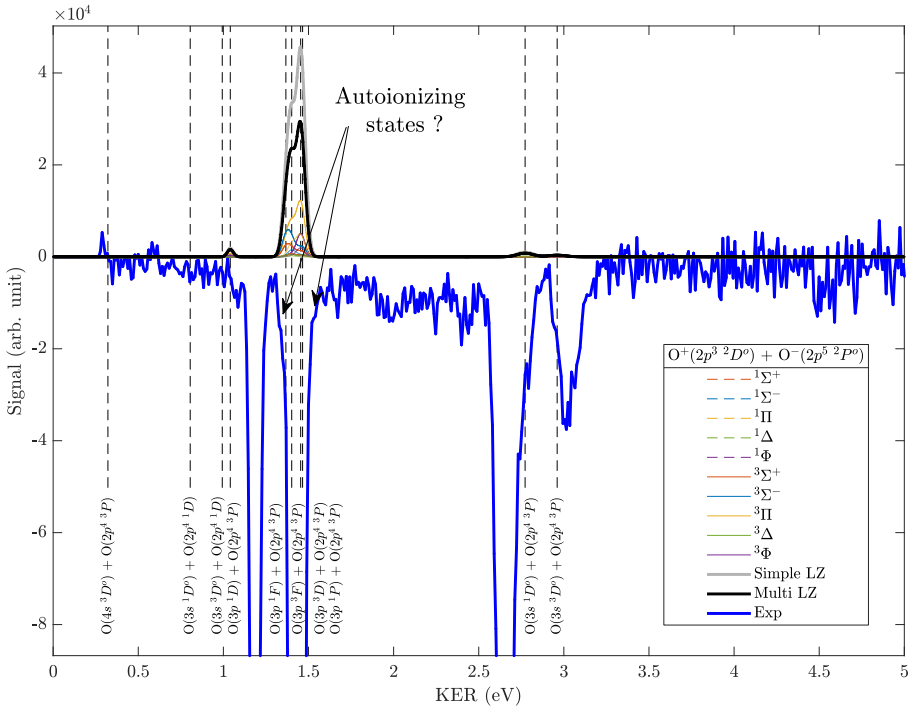

Figure 5.16: Simulation of the presence of autoionizing states lead by the $O^+(^2D^o)$+$O^-(^2P^o)$ mutual neutralisation reaction.

the reaction. Even if shoulders at the base of this peak suggest their presence, their low intensity and the overlap of the peaks make it difficult to estimate their extent.

The question then is, what happens when these doubly excited states are produced?

These are auto-ionizing states, but also radiating states (observed experimentally and integrated into the NIST-ASD database). Thus, one part radiatively decays (with a lifetime of a few tens of nanoseconds – this negligibly modifies the kinetic energy of the atoms), while another part autoionizes (which prevents their detection).

Such a process is analogous to the so-called capture into the continuum of the projectile, as it concerns electron capture into autoionizing states of the projectile. Such processes have been extensively documented for fast and slow collisions involving multiply charged ions, and usually result from double electron capture [203].

5.4.6 The unidentified peak

Before concluding, we note that only one peak among all our measured branching ratios defies our analysis. This peak is present on the O^+ + Si^- mutual neutralization spectrum, where a peak at $E_{r,f} = 1.4$ eV remains unexplained.

Chapter 6

Conclusion and perspectives

With the help of a merged beam apparatus and an asymptotic model, we were able to conduct a systematic study of the mutual neutralization reaction between atomic reactants. General phenomena and basic mechanisms were identified, modeled and explained in light of the observed branching ratios.

The role of the asymptotic expansion of the anion wavefunction has been highlighted. It was shown that the previous calculations of the mutual neutralization using asymptotic model were inherently flawed by a wrong normalization of this asymptotic wavefunction. The same applies to the orbital momentum dependency of the interaction term, which was updated, and now the asymptotic model matches the experimental branching ratios.

A classical deflection model was set up in order to be able to correct those branching ratios for detection losses. Angular distributions were shown to closely follow the state-specific differential cross sections, providing unvaluable insight into the potential energy landscape of the transient molecular system.

Detailed information about the electronic states of both atoms populated by single-electron transfer guided the improvement of the asymptotic one-electron model, and revealed the unexpected role played by Rydberg series and core-excited states.

To conclude this thesis, we would like to discuss an application of the Louvain-la-Neuve measurement, some ongoing projects and some upcoming projects in order to improve the understanding of mutual neutralization.

6.1 Ongoing improvements

6.1.1 Experimental setup

As seen throughout the previous chapter and the numerous appendices, the experimental setup made it possible to perform numerous branching ratio mea-

surements. However, the limited angular acceptance of the detection system complicates the measurements. In addition, this system is limited to the detection of only two particles in coincidence. A detection system able to measure a larger number of particles in coincidence, with a much better angular acceptance is available at the Louvain-la-Neuve laboratory [148] and is already used for various other measurements [65, 66]. However, the insufficient vacuum within the interaction cell (2 10^{-10} mbar) combined with the alignment of the beam on the axis of the detectors generates too many events due to neutralization with residual gas (section 2.9). Placing such a detector on axis would destroy it. To avoid this problem, all the chambers of the device are being replaced (vacuum chambers and pumping systems) in order to achieve a pressure one to two orders of magnitude lower. This will greatly reduce the background associated with the residual gas and allow the detection system to be changed. This system, combined with a real-time measurement technique for measuring the detection efficiency of detectors, recently developed in Louvain-la-Neuve [66], would then make it possible to carry out absolute cross section measurements without resorting to the renormalization procedure requiring the simultaneous measurement of the associative ionization cross section [4].

This upgrade of the device would make it possible to easily measure smaller cross sections, such as those that involve halogen anions. Such measurements would allow us to compare the confluent beam method with the method for measuring reactions in a plasma (section 1.3.1).

6.1.2 Theoretical model

The theoretical model used – the asymptotic model centered around the anion (appendix 3.2) – satisfactorily reproduces the branching ratios in most of the systems studied. Its main advantage lies in its analytical simplicity (and therefore its speed of execution). Nevertheless, among its flaws, one can cite: the asymptotic amplitude parameter of the wavefunction of the anion which seems – a priori – arbitrary, as well as the failure to take into account the mixing of the atomic configurations of the excited states of the neutralized cation, only described by the angular momentum algebra.

This poor description of the mixture of atomic configurations prevents the prediction of certain states observed experimentally (see section 5.4.1). The model is being improved on this last point: account of different atomic configurations of the same atomic term using a configuration interaction method (e.g. CIV3 [204]).

Another item that limits this model is its description given only by the coupling *LS* which does not take into account the total angular momentum *J* of the atoms (see section 3.2.4). However, the splitting according to *J* of some atoms is large enough to be distinguished during measurements. To predict

the ratio between these components, it is essential to include, in the derivation done in the section 3.2.4, the total angular momentum. This is not yet the case.

These two paths of improvement should improve the accuracy and validity of the asymptotic model.

The next steps for improving the model will be: taking into account the overlap matrix of atomic wavefunctions (sections C.2.4 and 3.2.8), which should not pose any fundamental problems, then modifying the asymptotic wavefunctions by taking into account the polarization potential (thereby improving the prediction of states produced at short interatomic distance).

6.1.3 Calibration of another setup

It seems obvious that our experimental measurements make it possible to estimate the validity of different theoretical models which describe the mutual neutralization reaction (see section 5.2.3). But it would be even better if two independent measurements lead two the same results.

From this point of view, the mutual neutralization measurements done in Louvain-la-Neuve are also used as reference measurements for another device: DESIREE [47]. This device is a double asymmetric storage ring. It also makes it possible to carry out mutual neutralization measurements by the confluent beam method. As this device has two storage rings, it allows to wait for the radiative de-excitation of the ions of each beam before measuring the reaction (which the Louvain-la-Neuve setup does not allow). However, before producing new measurements that involve cold molecular ions, it is necessary to ensure that DESIREE is functioning properly. Thus, the measurements taken in Louvain-la-Neuve serve as reference measurements for DESIREE. This took place for the reaction Li^++D^- and is in progress for the reactions O^++O^- [202] and N^++O^- (Poline, Dochain *et al.*, in preparation), the latter shows a perfect agreement between the two measurements.

6.2 Areas for improvement

6.2.1 Measuring differential cross section at minimum collision energy

As indicated in the section 5.3, the device allows to indirectly measure the partial differential section of the mutual neutralization by deconvolving the observed angular distribution of the products. However, at low collision energies, since the angular distribution of collisions is approximately uniform, it is impossible to measure the differential section. To counter this technical limitation, it is necessary to directly act on the angular distribution of the collisions.

This uniform angular distribution comes from the equality of the transverse distribution (due to the size of the apertures along the beam path) and the longitudinal distribution (related to the energy distribution of each beam). Thus, if it were possible to reduce the latter distribution, it would orient the collisions in the laboratory frame perpendicularly to the beam axis and allow to observe the differential section at lower collision energies.

This reduction of the beam longutudinal energy spread was recently achieved in the laboratory as part of another experiment [1]. This showed that the cylindrical deflector (section A.1.6) also acts as an energy selector, whose energy selection is slightly greater than 0.2%. This filter is insufficient for a beam of several keV of kinetic energy. However, when the beam has a kinetic energy in the order of a hundred eV, this energy filter has tremendous efficiency, and has reduced the kinetic energy distribution to 0.3 eV. Thus, if each beam is initially produced at low energy, filtered in energy, then accelerated, since the energy distribution of the beam is independent of its kinetic energy, we would obtain a beam of low kinetic energy dispersion [2].

As the longitudinal collision distribution is greatly reduced, only transverse collisions would remain (the collision axis lying in the detection plane) and it would become possible to measure the differential cross section at lower energy. This would make it possible to decouple the tightening of the differential cross section which takes place around 100 meV from the narrowing of the angular distribution of the collisions which takes place between 50 and 100 meV, which greatly complicates the current experimental analysis.

6.2.2 Another method for measuring branching ratios

The reactions $Ne^+ + C^-$ and $Ne^+ + O^-$ mainly produce neon atoms in the configuration $2p^5(^2P^o_{J'})3p$ (see section F.7). However, the device does not have the energy resolution to more precisely determine the states of the neon thus produced (the splitting in J is sufficiently important for the states to be distinguishable, but the huge number of states in this zone of the KER spectra make these peaks indistinguishable – it sould be noted that the splitting in J of the cation also plays a role in this congested spectrum).

This measurement is important, in fact, as the excited states of neon are not characterized by a LS coupling but by a J_1L_2 coupling [3]. This requires

[1] Transmission of slow H^0 through a graphene monolayer. The beam was produced from the negative ion line of the setup described in this thesis, neutralized by photodetachment within the interaction cell.

[2] However, a technical difficulty that should not be forgotten comes from the fact that extracting a large current from a source (several hundred nanoamperes) when the acceleration of the ions is weak is an eminently complex task.

[3] Unlike the LS coupling, whose terms are given by ^{2S+1}L, the J_1L_2 coupling (in the case of neon) is characterized as follows: The excited states of this atom are characterized by a valence

a complete rewrite of section 3.2.4, taking care that the characterization of molecular symmetry may differ. Thus, the comparison between the theoretical predictions thus obtained with experimental branching ratios is very important.

There is nevertheless a method which makes it possible to experimentally determine these branching ratios: measuring the photons emitted during the de-excitation of the neon after neutralization. These transitions are the $3p \rightarrow 3s$ transitions known to give this orange color to the neon tubes.

If we assume that the neon beam has a kinetic energy of 12,000 eV, then it is traveling at about 3.4 10^5 m/s. Thus, if the radiative lifetime of the neon state is in the order of 100 ns, the states produced will have decayed in the first 3 cm after being produced. This position corresponds to the center of the observation cell. It is then possible to collect the emitted photons. Then, using a monochromator, to measure the wavelength of this photon and thus obtain a spectrum.

As the lifetime of each state is known, it is possible to obtain branching ratios from the emission spectrum.

A question can then arise about the possibility of measuring such a spectrum: is it sufficiently intense? Possibly not. However, since this measurement is not performed using the position-sensitive detection system, there is no real limit to the intensity of the beams that could kill the detectors. It is then possible to increase the intensity of the beams, which is possible for neon (ECR source) and oxygen (any oxide in the sputter ion source produces a negative oxygen beam against which we fight so that it disappears. Similarly, this beam is easy to produce using the duoplasmatron source). It will nevertheless be necessary to ensure that the collision angular distribution is indeed approximately uniform to avoid any angular effect during detection due to orbital alignment.

6.2.3 Comparison with plasma measurements

Once the Louvain-la-Neuve setup is upgraded, it would be possible to measure the mutual neutralization between atomic ions already measured with the VENDAMS method: $H^+/D^+/He^+/C^+/N^+/O^+/Ne^+/Ar^+/Kr^+/Xe^+$ + $Cl^-/Br^-/I^-$ [23–27]. In order to facilitate the cross section measurement, one should select a system whose total cross section is quite high. Using a rapid calculation made with the ACAM helps in such a case. Table 6.1 shows such calculations. In this table, one can see that all the mutual neutralization re-

configuration $2p^5$ – characterized by an orbital angular momentum $\vec{L}_1$ a spin $\vec{S}_1$ and a total angular momentum $\vec{J}_1 = \vec{L}_1 + \vec{S}_1$ – and an electron in another configuration – characterized by an angular orbital momentum $\vec{L}_2$ a spin $\vec{S}_2$ and a total angular momentum $\vec{J}_2 = \vec{L}_2 + \vec{S}_2$.

These excited states are then characterized by the quantum number $\vec{K} = \vec{J}_1 + \vec{L}_2$, hence the name "coupling J_1L_2". These states are noted as (in the neon case): $2p^5(^2P^o_{J_1})n\ell\ ^{2S_2+1}[K]_{J_2}$ where $2S_2+1$ is the multiplicity of state K (the number of possible J_2) [205, 206].

actions measured with the VENDAMS apparatus have a much smaller cross section than the other mutual neutralization reactions.

A theoretical explanation for such small cross sections is already given in section 3.1.6: As the electron affinity of chlorine, bromine and iodine is high (> 3 eV) and no excited state below 7 eV for the neutralized anion, the binding energy of the neutralized cation must be higher than 3 eV (4 eV in order to be in the maximum of the Landau-Zener window). This condition forces the cation to be formed in its ground configuration state with a kinetic energy release higher than 4 eV, i.e. outside the Landau-Zener window. This leads to a small cross section (orders of magnitude lower than the other mutual neutralization reactions).

An exception seems to appear in the alkali metals. The explanation is simple: Their ionization potential is much lower and the ground configuration of such atoms appears to be within the Landau-Zener window.

	D^+	He^+	Li^+	Na^+	Mg^+	C^+	N^+	O^+
D^-	2.9e-12	9.1e-12	6.4e-12	5.3e-12	9.6e-12	7.8e-12	8.0e-12	1.0e-11
C^-	1.9e-12	6.2e-13	6.1e-13	2.8e-12	4.7e-12	6.1e-12	5.4e-12	3.8e-12
O^-	2.8e-12	2.5e-12	1.4e-12	4.7e-13	1.8e-12	2.1e-12	2.4e-12	6.4e-13
Si^-	1.7e-12	3.2e-13	2.2e-13	2.8e-12	5.2e-12	5.3e-12	5.5e-12	4.1e-12
P^-	2.1e-12	5.4e-12	3.2e-12	2.3e-12	4.9e-12	6.6e-12	7.0e-12	5.2e-12
S^-	3.1e-13	1.4e-12	7.4e-13	4.3e-13	1.8e-12	2.7e-12	2.2e-12	1.6e-12
Cl^-	**< 1e-25**	**2.5e-14**	3.3e-12	2.0e-12	8.1e-15	**4.6e-14**	**5.4e-23**	**9.0e-17**

Table 6.1: Various total cross sections (in cm^2) computed with the ACAM-MLZ at $E_{r,i}$ = 20 meV. REactions measures by VENDAMS are in bold font.

From the considerations above, one could consider that the plasma measurement requires that the anions are not destructed too rapidly in the plasma. Therefore, as the mutual neutralization is usually the main anion destruction mechanism when the electrons have recombined, the VENDAMS setup requires a small mutual neutralization rate in order to be able to measure it. Otherwise, the mutual neutralization could already be non-negligible before the end of the electron recombination phase. It would forbid an accurate measurement of the mutual neutralization process. This could explain the choice of the reactants.

6.3 Conclusion

This work manages to significantly improve the understanding of the mutual neutralization process for collision energies below 1 eV: The measurement of the branching ratios and the differential cross section for a wide range of reactants allowed us to build a realistic model of how the charge exchange

happens.

This reaction can be characterized by the interaction between the asymptotic component of the neutralized cation wavefunction with the asymptotic component of the anion wavefunction. As the anion ground state wavefunction is more localized than the neutralized cation wavefunction, it is a good choice to express those wavefunctions around the anion core. It remains to carefully take into account the antisymmetrization of the quasi-molecular wavefunction as well as the symmetries of the system.

Once this is done, it is possible to follow the collision through all the crossings occuring at some internuclear distance R_c using the Landau-Zener collision model. This model shows that the partial cross section (at low collision energy $E_{r,i}$) is proportional to $R_c/E_{r,i}$ multiplied by a non-linear function of H_{ic}^2, meaning that there is an optimum for the interaction term H_{ic}, i.e., a window in kinetic energy release for the output channel to be significantly populated. This window must be estimated for each molecular symmetry. An analysis of the Λ dependency of the reaction shows that higher Λ leads to a LZ window with higher KER, explaining the difference between the $A^+ + C^-$ and $A^+ + O^-$ mutual neutralization. This model also explains the production of excited neutralized anions, as long as they remain in their ground configurations.

This understanding of the process is provided by an analytical model (developed or improved during this work) whose simplicity allows dissecting the process, i.e. determining the role of each atomic and molecular quantum number involved, and obtaining the collision energy dependency (for both the branching ratios and the differential cross section). It also allows to acquire a better insight into the collision dynamics, e.g., the importance for the process of the (only) temporarily populated channels. However, this simple model cannot reproduce the experimental data completely. But, as the validity domain of the model was extensively documented, the discrepancy between theory and experiment allows once again to better understand the reaction, e.g., how and why a Rydberg series happens to contribute.

Despite the good understanding of the mutual neutralization between two ions in their ground states, other phenomena appear when (at least) one of the ions is in an excited state. Are new data still needed in order to get a complete understanding of those phenomena? There is a need for measuring branching ratios for the mutual neutralization between excited ions only (or repeating the experiment while varying the electronic populations of the ions). As there are hints that those reactions would reveal a higher lever of complexity in the mutual neutralization process, this would allow to further improve our theoretical approach of the process.

This understanding of the microscopic process is needed in order to explain the phenomena one observes from a distance. As it is really difficult to measure the abundance and degree of ionization of each species in a gas/plasma, be it an

industrial one, the only way to determine the density of the cation/anion/atoms in such plasma is by measuring the radiation it emits or absorbs. However, as the anions do not emit light (as most of them have only one stable state), the only way to determine their presence in plasma is by their destruction mechanism. Thus, knowing the excited states formed by the mutual neutralization process allows to reveal their presence (and their destruction) by measuring the radiative cascade of the neutralized ions, provided there is no other mechanism which could produce those excited states.

Understanding the mutual neutralization process may ultimately help us to address more general questions: why are there anions in space? What is the elemental composition of celestial bodies?Does mutual neutralization affect industrial plasmas? How do anions react with the other components of the gas? How does it affect the radiation of this gas?

Ultimately, mutual neutralization is just one reaction among the complicated chemical network of astrochemistry and plasma chemistry. But that is another story.

Appendices

Appendix A

Experimental setup: Ion beams and plasma physics

A.1 Elements of corpuscular optics

A.1.1 Characteristics of ion beams

The experimental set-up described in chapter 2 requires the use of an ion beam. An ion beam is a collection of charged particles that move in vacuum in a given direction. Its overall charge is non-zero, unlike that of a plasma. A beam is characterized by its chemical composition, its spatial distribution and its velocity distribution (similar to an angular distribution). These last two distributions form a six-dimensional distribution in phase space, called emittance.

As these ions move, there is an axis along which the average speed of the ions is maximum, while the average speed along the other axes is zero. This is the beam propagation axis.

Since an ion beam is made up of charged particles, their trajectories are modified by the electric and magnetic field they pass through. If we assume that the density of the ions that make up the beam is sufficiently low [1], then the trajectory of the ions is modified only by the nonrelativistic Lorentz force. [2].

$$\vec{F} = q\left(\vec{E} + \vec{v} \times \vec{B}\right) \tag{A.1}$$

[1] The particles that make up the beam are separated on average by 0.1 mm (a density of 10^6 cm^{-3} – see section 2.9). As these ions travel through the device in a few tens of microseconds, the repulsion between the particles does not have time to modify the spatial and angular distribution of the beam. The distribution of it is much wider.

This effect of charge density of a beam – called space charge – is however not negligible when the ion current is greater, or when the ions have a longer travel time.

[2] The ion beams used have a kinetic energy of a few keV, that is to say a speed of several hundreds of kilometers per second, much lower than the speed of light.

where the electric $\vec{E}$ and magnetic $\vec{B}$ fields are applied to the trajectory of the ions (of charge q and velocity $\vec{v}$) using electrodes and (electro) magnets.

Thus, since this particle beam propagates along an axis, and the shape and direction of this beam can be modified by elements external to the beam, the characterization of the beam can be done using a method similar to that of light optics. This method is called corpuscular optics.

The different electrodes and the magnetic sectors then form different optical elements: lenses, deflectors, sources and probes. This section aims at briefly describing these optical elements.

A.1.2 Emittance of the beams

Each of the ions in a beam has a position (x, y, z) and a velocity (v_x, v_y, v_z). The set of particles then fill a volume in the space of the six-dimensional phases thus created. If the Hamiltonian associated with the different elements of the experimental set-up is independent of time (electrostatic and magnetostatic), then the volume occupied by this set of particles in phase space is constant (Liouville's theorem [207, 208]). The transverse emittance of a beam is the characterization of the volume occupied within the phase space perpendicular to the axis of propagation of the beam. This theorem leads to several consequences.

When the beam propagates at constant speed, the emittance deforms at constant volume. Therefore if an optical element reduces the spatial distribution of the beam, then this spatial reduction is done to the detriment of the angular distribution of the beam. Thus, in order to reduce the angular and spatial distribution of an ion beam, one method consists in reducing the angular distribution of the beam, then removing the ions from the beam whose spatial difference is too great. In all cases, reducing the emittance of a beam at constant speed implies a reduction in the particle flux of the beam. This is why the current at the output of the source is always greater (by orders of magnitude) than the current within the interaction cell.

When the beam is accelerated, the transverse emittance of the beam decreases as a result of an increase of the longitudinal momentum. Therefore, for the same ion source, the faster a beam, the better it is defined. As the experimental device uses beams of low kinetic energy (compared to those of the beams used in particle accelerators), emittance plays a non-negligible role in the behavior of the device. This is why each of the beams travels several meters before interacting. This course together with the placement of limiting apertures, improves the definition of emittance. However, this path is not too long in order to avoid losing too much of the current between the output of the source and the interaction cell.

Another interesting property of ion beams occurs when they are subjected

to electric fields only (no magnetic fields). In this case, as the force exerted on the beam ions depends only on the position of the particles, the trajectory of the ions does not depend on their mass. Only their kinetic energy. Therefore, the modification of the composition of a beam requires only the modification of the magnetic optical elements.

A.1.3 Extracting a beam from an ion source

Once a source has generated ions, they must be extracted from the source and accelerated to form a beam.

In order to extract these ions, several methods are possible. The simplest applies an electric field within the source using different electrodes (usually a cathode and an anode). The electrode which attracts the ions is pierced in its center to allow part of it to pass.

However, in most cases the ions do not leave the source because of the potential difference between a cathode and an anode, but rather by the application of an extraction voltage applied to an electrode (usually of conical shape) placed behind one of the source electrodes (the anode for a duoplasmatron type source). The electric field penetrates into the volume of the source through the orifice made in the electrode of the source.

The average kinetic energy of the ions at the output of the source is fixed by polarizing all the components linked to the source with respect to the earth (ground) [3]. The entire source is then at a voltage V_{acc} called the acceleration voltage.

When the ions leave the source, the electrostatic potential to which the ions are subjected will vary until it reaches the potential of the earth. Thus, if the source is at a voltage of $+1000$ V then the kinetic energy of the singly chragred ions of a positive beam will be 1000 eV when they circulate in the rest of the device at the potential of the earth.

Let us assume initially that the ions are accelerated only along the beam propagation axis. Therefore, according to Liouville's theorem, the angular distribution of the beam contracts along the axis of propagation. The greater the kinetic energy of the beam, the more the angular distribution is reduced by the acceleration of the ions. This makes it possible to switch from a uniform angular distribution of the ions within the source (outside the extraction electric field) to a distribution centered along beam propagation axis. It is therefore interesting to have a maximum extraction voltage in order to maximize the

[3] More precisely, it is conditioned by the potential at which the plasma is established, generally that of the anode and/or of the enclosure in which the ionized gas is contained. In the case of solid emitters (thermionic emitter, sputtering cathode), it is the potential applied to them which determines the energy of the ions.

intensity of the beam [4].

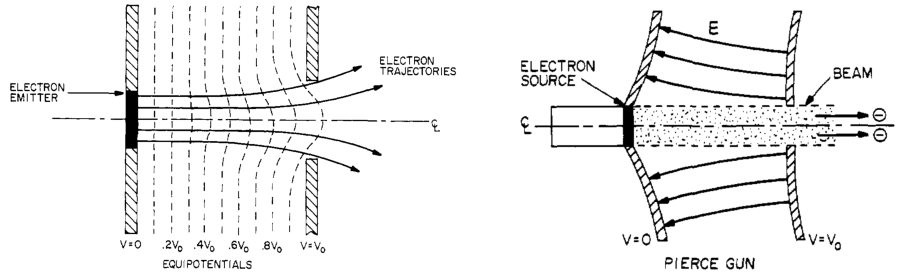

Figure A.1: Illustration of the utility of Pierce geometry. Left: Accelerated ion trajectories in the case of two parallel plates, the equipotential curves are represented by dashes, the trajectories (represented by solid lines) are divergent. Right: Trajectories of the ions (shaded area) when the extraction follows a Pierce geometry [209].

However, at the source output, the beam has a certain space charge: As each ion has an electric charge, they repel each other and cause the beam to diverge. Moreover, given the low initial kinetic energy of the ions, the effect of divergence due to the space charge is important. As the beam density is high enough, the intensity of the extracted beam is limited by this space charge (space-charge-limited current). A method used to correct the divergence of a beam limited by the space charge is that developed by Pierce [210]: Modifying the geometry of the electrodes (for electrons, the anode is on the extraction side and the cathode is on the source side) so that the electric field exactly compensates for the divergence of the beam when it is extracted from the source. This geometric configuration of the electrodes, called *Pierce geometry*, applies when the ion source is a perfectly defined plane surface (for example the thermionic emission source).

When the ions come from a plasma, the source surface is not, on the one hand, perfectly flat, and on the other hand, perfectly defined. This surface has a thickness out of which it is possible to extract ions. To overcome this imprecision, an electrode is added. The system is then composed of the source, placed at the acceleration voltage, the extraction electrode, the voltage of which is chosen independently (unlike the case of Pierce geometry where the extraction electrode is grounded) , and a third electrode placed at ground. This additional degree of freedom makes it possible to adjust the extraction according to the operation of the source, to then select the point of the source (the position in front of or behind the source electrode) where the plasma is extracted. The

[4] The upper limit of the kinetic energy of the beam is constrained by electrical insulation devices, generally limited to a few hundred kV in air, more typically to a few tens of kV as here.

In addition, since the objective of this device is to bring two beams at the same speed within a precise zone, the absolute precision of voltage sources must remain the same, which increases the constraint on the relative precision of the voltage applied to the source.

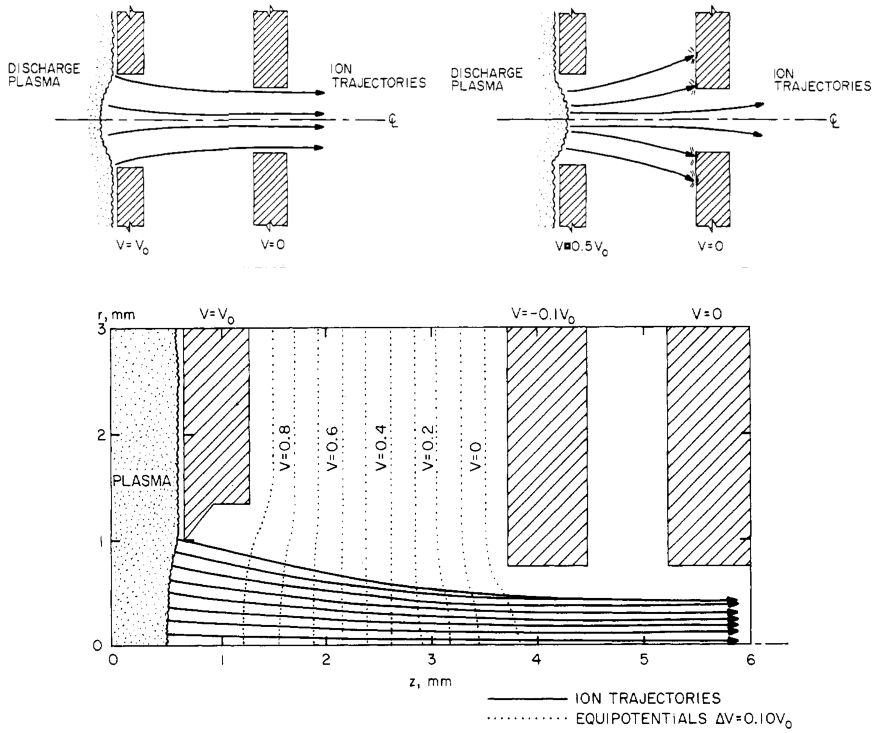

Figure A.2: Top: Trajectories of the extracted ions (solid lines) as a function of the geometry of the plasma. The focus depends on the geometry [209]. Bottom: Three-electrode extraction system (acceleration-deceleration type) [211].

second lens serves as post-focusing of the beam (see next subsection). Indeed, depending on the operating mode of the source, the distributions of the ions may vary. The ions that you want to extract can be found elsewhere in the source.

A.1.4 Electrostatic lens

To begin the description of the different optical elements used, it is useful to understand how one of the simplest elements acts on the beam: the simple lens (or Einzel lens).

The simple lens (Einzel lens) is made up of three elements (figure A.3): two cylindrical electrodes whose voltage V_0 is at the same potential as the vacuum chamber. Between these is placed a third polarized electrode, the potential of which is adjustable.

If V_1 is of opposite sign to the charge of the ions, when they approach the central electrode, the electric field due to the potential difference between the

electrodes accelerates the ions. Then, they are slowed down at the exit of the central electrode, to regain their initial speed. Such a lens does not modify the kinetic energy of the beam.

The focusing effect of these lenses is due to the geometry of the equipotential surfaces between the electrodes. This effect is inversely proportional to the distance from the charge which generates it (the electrode). Close to the electrodes, the field associated with them is very strong. The equipotential surfaces are very tight. Far from the electrodes, at the level of the beam propagation axis, the field is lower. The equipotential surfaces move away. Therefore, on the one hand the distance between the equipotentials decreases with the deviation from the beam axis, on the other hand - due to the cylindrical symmetry of the lens, the distance between the equipotentials remains constant in the vicinity of the beam axis. Thus, the perpendicular component of the generated electric field is zero along the axis of propagation to increase when the distance to the axis increases (see figure A.3).

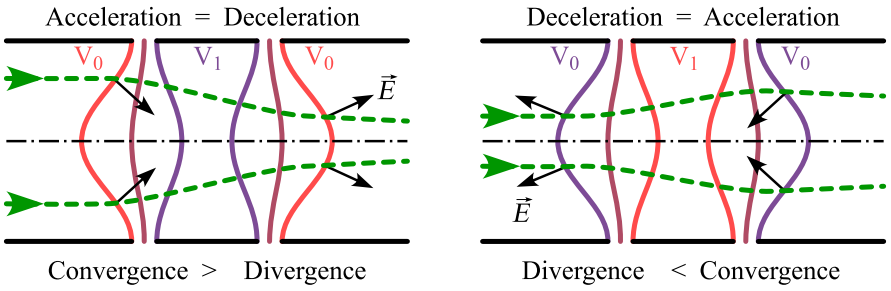

Figure A.3: Representation of ion trajectories (green lines) within a Einzel lens. The equipotential curves are given by the continuous lines while the direction of the electric field within the lens is given by the black arrows. The diagram on the left represents a lens whose potential first accelerates and then slows down the ion passing through it, while the diagram on the right represents a lens which first slows down and then accelerates the ion.

If the polarized electrode has the opposite polarity of the ions, the electric field focuses the beam at the entrance to the electrode – the further the ions are from the axis, the greater the force exerted by the perpendicular electric field – while the electric field tends to defocus the output beam. However, since the spatial distribution of the beam is wider at the entrance than at the exit, the focussing is more important than the defocussing.

If the polarized electrode has the same polarity as the beam, the beam is initially defocused and then focused. As it is wider at the exit than at the entrance, the focussing is again more important than the defocussing.

Although the two polarities of the electrode allow a focusing of the beam, the second widens the beam before reducing it, therefore, it is no longer possible to consider that the ions that make up the beam are close to the axis of

propagation. The focal length depends on the distance of the particle from the axis. This side effect is called a spherical aberration.

It would seem logical to adopt the opposite polarity. However, this focusing effect is proportional to the ratio between the kinetic energy of the ions inside the lens and that outside the lens (e.g. [212]). Doubling the kinetic energy within the lens requires applying a voltage four times greater than that required to reduce this kinetic energy by half. Thus, for both budgetary and technical reasons – voltages that are too high can create arcs – it is simple lenses of the same polarity as the beam which are used in the apparatus.

The properties stated here are applicable to all electrostatic elements. Each element present within the apparatus focuses the beam. If the beam is focused too early, it will be necessary to introduce other focusing elements to refocus the beam.

This effect is also present for the source extraction and acceleration electrodes. This is why a third electrode with a particular geometry is used, the geometry of which is described in [213].

A.1.5 Planar deflector

A planar deflector is made up of two electrodes of opposite polarity parallel to the axis of the beam and forms a planar capacitor. The electric field between the plates is uniform, perpendicular to the plane of the latter. The ions that compose the beam are deflected at an angle proportional to the electric field. The beam deflection angle is determined by the geometry of the deflectors:

$$\theta \simeq \frac{q_e V}{2E_k}\frac{l}{d} \tag{A.2}$$

where V is the potential difference between electrodes, E_k the kinetic energy of the ions (charge q_e), l the length of the deflector and d the distance between electrodes [5].

[5] The force applied by the deflector on the particle is:

$$\vec{F}_{el} = q\vec{E} = q\frac{V}{d}\hat{E}$$

This force is applied as long as the ion is within the deflector. If the ion has an initial velocity parallel to the axis $v_{\parallel} = \sqrt{2E_k/m} = l/t$ – where t is the time spent by the ion inside the deflector – then its velocity perpendicular to the exit of the deflector is:

$$v_{\perp} = \frac{F}{m}t = \frac{q}{m}\frac{V}{d}l\sqrt{\frac{m}{2E_k}}$$

If the angle of deviation θ is small, it is given by

$$\theta \simeq \tan\theta = \frac{v_{\perp}}{v_{\parallel}} = \frac{q}{m}\frac{V}{d}l\sqrt{\frac{m}{2E_k}}\cdot\sqrt{\frac{m}{2E_k}} = \frac{qV}{2E_k}\frac{l}{d}$$

The electrostatic potential along the axis is identical to that of the chamber. When the ions enter the deflector, they keep a constant speed. Within the deflector, as they are no longer maintained along the initial propagation axis, the ions are slightly accelerated and then slowed down at the exit of the deflector. This results in a parasitic focusing effect which accompanies the deflection, stronger for a larger angle of deflection [6].

A.1.6 Cylindrical deflector

In order to obtain a higher deflection angle, one solution is to use a cylindrical deflector (see figure A.4).

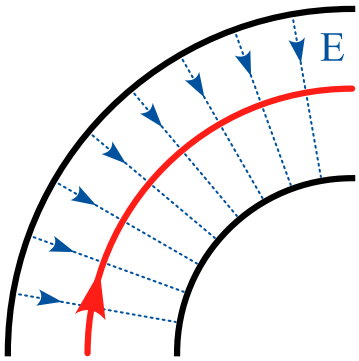

Figure A.4: Diagram of deflection by a cylindrical deflector. The path of the ion is the red line and the electric field is indicated by the blue arrows.

This consists of two cylindrical electrodes with the same center of curvature. The voltage applied to the inner plate is the opposite of that applied to the outer plate. The electric field is perpendicular to the plates (without being uniform).

[6] If an ion enters the deflector at a position slightly offset from the axis of propagation, then its kinetic energy is modified.

If it enters the side of the plate of the same polarity, its kinetic energy decreases $E_k' < E_k$, then the deflection brought to the ion is:

$$\theta' \simeq \frac{qV}{2E_k'}\frac{l}{d} > \frac{qV}{2E_k}\frac{l}{d}$$

In other words, the deflection is more important. This trajectory brings the ion back to the axis of propagation (deflection).

Otherwise (ion closer to the plate of opposite polarity), the kinetic energy of the ion increases. This ion is less deflected. This trajectory brings the ion back to the axis of propagation (deflection).

Consequently, there is indeed a focusing of the beam within the plane deflector. To first order, the focal length is obtained by the location of the intersection of trajectories coming from different heights in the deflector.

If an ion enters the deflector at the right speed, the electric field is always perpendicular to the path of the ion [7]. Its trajectory is circular (no acceleration).

If the ion has a slightly different speed, then the electric field acquires a component tangent to its trajectory which grows along it. The cylindrical deflector is thus a kinetic energy analyser.

If the ion arrives within the deflector slightly closer to the inner (outer) electrode then it is faster (slower) within it. The effect of the electric field is therefore weaker (important), the ion being less (more) deflected. The deflector is therefore an electrostatic lens. This effect combines with the effect of the length of trajectories immersed in the electric field (figure A.5).

A.1.7 Spherical deflector

The cylindrical deflector deflects particles only in the horizontal plane. Therefore, there is no vertical focusing.

This double focusing is obtained using a spherical deflector. This consists of two electrodes in spherical caps with the same center of curvature. Its operating principle is identical to that of the cylindrical deflector.

A.1.8 Magnetic deflector

The magnetic deflector – also called magnetic sector – works by circulating charged particles in the air gap of an electromagnet (the use of permanent magnets is common). This generates a uniform vertical magnetic field across the vacuum chamber placed inside it. In order to ensure the uniformity of the magnetic field, it is guided by a soft iron circuit towards an air gap, the geometry of which ensures on the one hand the uniformity of the field within the desired zone within the chamber, on the other hand, that the magnetic field is zero beyond this zone. Once immersed in the magnetic field B of the deflector, the ions follow a circular trajectory whose radius of curvature R is equal to [8]:

$$R = \frac{mv}{qB} \tag{A.3}$$

[7] This speed is obtained by equaling the centripetal force of a circular path with the force linked to the electric field

$$\frac{mv^2}{R} = \frac{2E_k}{R} = \frac{qV}{d}$$

where V is the potential difference between the electrodes, d their interdistance, and R the radius of curvature of the path.

[8] This radius of curvature is obtained by equaling the centripetal force and the magnetic component of the Lorentz force

$$m\frac{v^2}{R} = qvB$$

If we look at the trajectory of the ions with a constant radius of curvature within the deflector, depending on the distance from the axis of the beam we notice that they are also focused (see figureA.5)

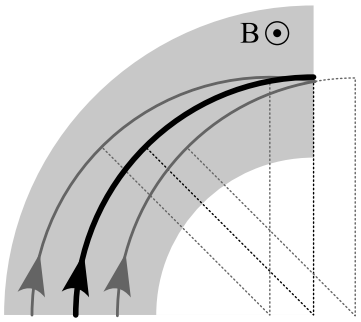

Figure A.5: Focusing effect of a magnetic deflector. All trajectories (solid line) have the same radius of curvature (dotted lines) when they are immersed in the magnetic field (gray area). The trajectories are focused at the exit of the deflector while they are parallel at the entry.

Unlike electrostatic optical elements, the deflection of ions in a magnetic sector, having a given kinetic energy, depends on their ratio between mass and charge. Therefore, this deflector serves as a mass selector. To simplify the machine layout, only one magnetic sector is placed at the start of the line, in order to select the ion which will make up the beam.

A.1.9 Wien filter

This mass filter is composed of a magnetic sector and a planar electrostatic deflector. These generate electric and magnetic fields that are oriented perpendicular to each other and to the beam velocity, so that the Lorentz force $F = q(\vec{E} + \vec{v} \times \vec{B})$ vanishes for particles of selected speed [9].

Thus, depending on the potential applied to the electrodes and on the magnetic field, the selected mass-to-charge ratio is given by:

$$\frac{m}{q} = 2E_k d^2 \left(\frac{B}{V}\right)^2 \tag{A.4}$$

where d is the distance between the electrodes.

An example of a mass spectrum is given by the figure A.6. Several elements are to be noted on this spectrum. On the one hand, the dispersion of each mass component of the beam is constant according to the voltage scale (10 V in the case of the figure). Therefore, as the mass scale is not linear, there

[9] It should be noted that in the absence of path curvature within this optical element, only the electrostatic component gives rise to focusing.

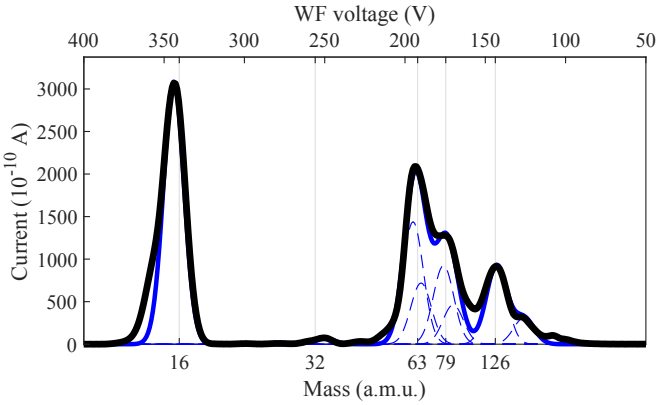

Figure A.6: Mass spectrum produced using a Wien filter. Beam generated by the sputtering source (section A.2.2) with a copper cathode. The black curve is the experimental spectrum. The solid blue curve is a fit of the beam composition produced using a sum of Gaussians (blue lines).

is a maximum mass beyond which it is no longer possible to perform a mass selection for the beam.

Thus, for a given beam dispersion, the mass resolution limit can be adjusted using the magnetic field. The higher the magnetic field, the better the resolution. However, the increased magnetic field requires the use of higher voltages. Too strong a magnetic field prevents the selection of low beam masses.

A.1.10 Faraday Cup

In order to measure the density of ions that make up a beam, the easiest method is to use a Faraday cup. This is made up of a metal cage (probe) connected to an ammeter, itself connected to earth.

If a charged particle comes into contact with the cup, it deposits its charge there. The plate then has an excess of electric charge which is discharged through the ammeter:

$$\frac{\mathrm{d}n}{\mathrm{d}t} = \frac{I}{q} \tag{A.5}$$

If the particle has sufficient kinetic energy, it does not settle on the surface, but collides with it. This collision leads to the extraction of electrons from the surface. Consequently, the measured current no longer indicates the number of charges deposited on the surface, but this current remains proportional to the impact rate on the surface and makes it even possible to measure the density of a beam made up of neutral particles.

To measure the actual current of a beam, a guard electrode is placed in front of the Faraday cup (usually a ring electrode which surrounds the incident beam). This electrode is negatively polarized (cathode) with a voltage low enough not to influence the trajectory of the beam, but large enough to repel the electrons emitted by the surface during the collision of the incident ion.

The verification of this hypothesis is carried out by measuring the current delivered by the probe while increasing the voltage applied to the guard electrode. The voltage is considered sufficient when the current reaches a plateau, that is to say when the measured current no longer depends on the voltage applied to the guard electrode. This voltage varies from -100 V to -200 V depending on the geometry of the Faraday cup [214].

A.1.11 Position sensitive detector

In order to measure the position and the time traveled by the particles after neutralization, a position sensitive detection system is used.

The detection system is composed of a stack of microchannel plates (electron multipliers) placed in front of a resistive anode.

The Micro Channel Plates (MCP) are ceramic wafers with a thickness of 0.5 to 2 mm, pierced with microscopic holes (microchannels - with a diameter of about 10 μm) distributed in a honeycomb structure of $\sim 60\%$ transparency. The orientation of these through channels is inclined a few degrees (5 to 20) relative to the normal to the wafer. The faces are metallized, while the material highly resistive. A potential difference of 800 V maximum per wafer is applied between the faces, that is to say a little less than 2400 V for a stack of three plates in Z (in practice approximately 2100 V).

When a particle with sufficient kinetic energy comes into contact with the surface of the wafer, this particle can eject one or more electrons [10]. If the particle comes into contact with the wafer inside one of the microchannels, because of the polarization of the wafer, the emitted electrons are accelerated towards the rear face of the wafer. Due to the inclination of the microchannels, they in turn collide with the interior of the microchannel with sufficient energy to scavenge other electrons. These new electrons eject others to obtain up to 10 000 electrons at the output of the microchannel.

In order to improve the emission probability and the number of emitted electrons, three wafers are stacked with an alternating microchannel orientation (Z Stack MCP). This makes it possible to prevent incident particles from passing through a microchannel without coming into contact with its walls, and to suppress any ion backstreaming due to residual gas ionization within

[10] The probability of electron extraction from the surface depends on the type of incident particle, as well as its momentum. For neutral atoms, whose kinetic energy is several keV, this probability approaches 100 %.

the channels. The maximum detection efficiency is the ratio between the area covered by the holes in the microchannels and the total area of the wafer while the initial electron ejection obeys Poisson statistics. This arrangement also makes it possible to increase the number of electrons emitted for each incident particle to approximately 10^6 electrons. This number is less than the amplification given by each MCP independently, this amplification is intentionally saturated in order to prevent the current given by each electron packet from varying (depending on the speed or the type of incident particle). This makes it possible to simplify the setting of the time triggers (to prevent the tail of the high amplitude time pulses from being of the same order of magnitude as the peak of the weakest pulses).

To measure the instant of impact of the incident particle on the first wafer, the method used here consists in measuring the charge draw caused by the loss of electrons evacuated during the electronic cascade through a high-pass filter connected to a fast preamplifier.

The ultimate spatial resolution of the electron burst - the precision on the position of the center of the electron burst - is of the order of the distance between two microchannels.

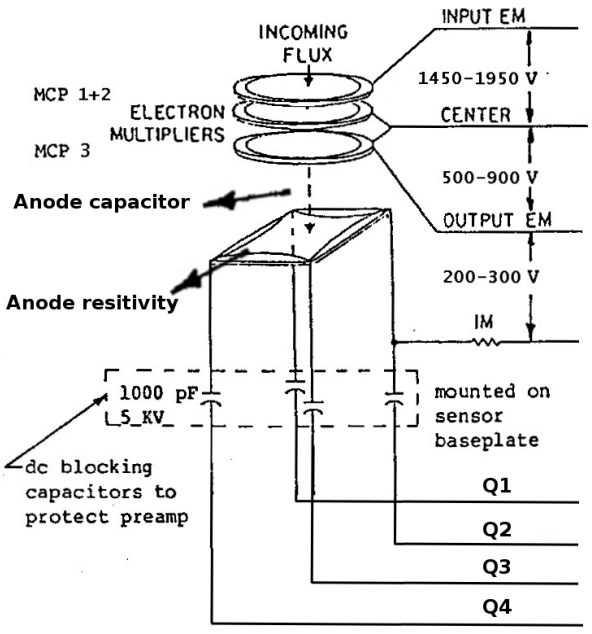

Figure A.7: Simplified diagram of the time and position sensitive detection system [215].

The burst of electrons thus created then arrives on a resistive anode. This is composed of a substrate on which is deposited a thin layer of resistive material. This thin layer is grounded through a resistor (IM - figure A.7), that forms a

capacitor with the nearest wafer. On the edges of this layer are placed four current collectors.

This short electron pulse (< 1 ns) then propagates on the resistive film like an electric current in a *RC* circuit (each thin-film element has a constant infinitesimal capacitance and resistance). This electric wave propagates uniformly isotropically until it reaches the edges of the thin layer. If this edge is not a collector, the wave is reflected. The distribution of electrons on the resistive surface gradually reaches a stationary state, which is discharged through the collectors. Thus, the current which arrives on these collectors varies over time [216]. In addition, the time taken for the electrons to discharge through the collectors is – by several orders of magnitude – greater than the time distribution of the pulse. Therefore, it is not possible to obtain precise temporal information from the currents measured on the resistive anode [217]. This is why the time information is measured on the wafers themselves. Moreover, since it is necessary to integrate the current over time, the anode cannot measure the position of two simultaneous impacts.

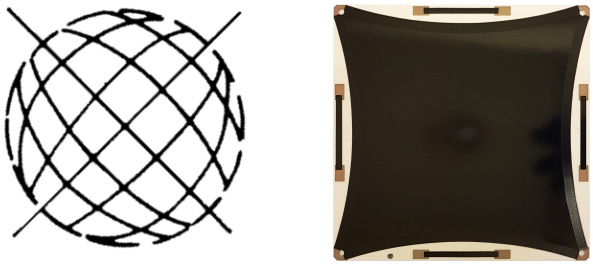

Figure A.8: Resitive anode geometry explanation: The figure on the left shows the shape of a square grid for a circular anode, assuming that the current received is linear [218]. This deformation depends on the geometry of the anode, this explains the shape of the anode used on the experimental device photographed in the figure on the right. This allows you to straighten the curvature of the grid drawn on the left.

However, the total amount of charge collected on each collector is approximately linear with its distance from the impact position of the electrons. The deviation from linearity is given by the geometry of the layer deposition. The chosen geometry optimizes the linearity of the total load received by the collector as a function of the impact distance (see figure A.8).

A.2 Ion sources

This section describes the ion sources used in the experimental setup. Each description includes the production processes of the extracted ions applied to the geometry of the sources used at UCLouvain. These descriptions include elements of [219, 220].

A.2.1 Thermionic emission source

Thermionic sources are relatively simple ion sources [11]. They consist of a surface with a carefully chosen composition placed under vacuum. Once this surface is heated, some of the atoms that compose it escape. However, because the surface is highly electronegative (it tends to capture electrons) atoms lose an electron as they escape from the surface. This effect is all the more important as the mobility of the electrons is large (and increases with temperature).

If an atom is on a conductive surface, the probability of ionization of this atom is given by the Langmuir-Kingdon formula

$$\frac{N^+(ions)}{N_0(neutrals)} = e^{-11600\frac{IP-\Phi}{kT}} \tag{A.6}$$

where IP is the ionization potential (eV), Φ is the minimum binding energy of the conduction band (4.52 eV for tungsten) - this corresponds to the electronegativity of the surface - kT the temperature (K).

Therefore, an alkali with a low ionization potential ($\Phi > IP$) can be incorporated within a matrix of porous tungsten. When the matrix is indirectly heated, the surface emits ions, mainly the alkali incorporated in the matrix.

However, the ionization potential of lithium is greater than the conduction band of tungsten. It would be possible to use tungsten oxide ($\Phi = 5.9$ eV), but the solution used by the source manufacturer is to use – instead of lithium and tungsten – a isotopically enriched lithium aluminosilicate [12]. Thus, the only ion emitted is the lithium ion of the isotope chosen [13].

Once these ions are formed, they are accelerated by mounting the emitter between two electrodes (Pierce geometry). As the emission of the ions takes place in a plane, the initial kinetic energy of the ions is simply given by the thermal energy distribution of the surface (approximately 0.24 eV at 1400 K).

A.2.2 Sputter ion source

Sputter ion sources (or sputter cathode sources) are negative ion sources. These emit anions when an incident particle collides with the surface.

To understand this effect, it is useful to start from the emission rate of a heated surface without an incident particle collision. In this case, the rate of negative ions emitted is given by the Langmuir-Saha relation which gives the

[11] The one used at UCLouvain is the "Heatwave labs lithium-ion emitter".

[12] $Li_2O-Al_2O_3-2SiO_2$ (β-eucryptite) and Li_2O-$Al_2O_3-4SiO_2$ (spodumene)

[13] By changing the composition of the surface, it is possible with this type of source to produce intense alkali beams (low ionization potential). This source, however, is not suitable for producing other beam compositions. It is this inefficiency in the production of other elements which makes it possible to obtain ion beams of great purity.

A similar source was also used to produce a positive sodium beam.

probability of formation of a negative ion from its neutral particle when the system is in thermodynamic equilibrium [221]

$$P_i = \frac{\frac{\omega_-}{\omega_0}\left(\frac{1-r_-}{1-r_0}\right)\exp\left(\frac{E_A-\phi}{kT}\right)}{1+\frac{\omega_-}{\omega_0}\left(\frac{1-r_-}{1-r_0}\right)\exp\left(\frac{E_A-\phi}{kT}\right)} \tag{A.7}$$

where r_- and r_0 are the reflection coefficients of the particle at the surface and ω_- and ω_0 are statistical weights related to the total spin of the negative ion and the neutral atom.

This equation indicates that the negative ion emission rate depends on the work function of an electron output from the surface ϕ. It is linked to the electropositivity of this surface.

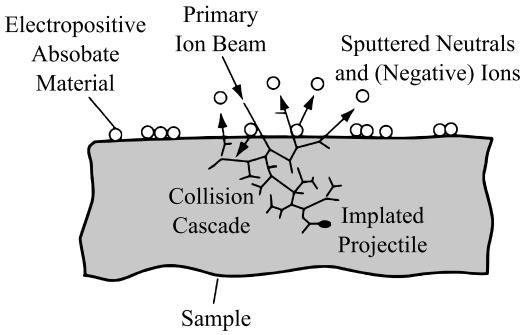

Figure A.9: Process of ejection of a particle from a surface during the impact of another particle on the same surface [221].

When a particle comes into contact with the surface with sufficient incident kinetic energy, it triggers a cascade of collisions within it. These collisions can then extract a particle that makes up this surface (see figure A.9). The probability that the ejected particle is a negative ion depends on the propensity of the surface to donate an electron to this outgoing particle. The lower the extraction function of an electron from the surface the greater the probability of extracting an anion during the collision.

In order to maximize the extraction rate of negative ions from the surface, a commonly used method is to bombard the cathode (from which negative ions are extracted) with cesium ions. The metal vapor from which the ions originate is also deposited on the surface and forms a layer on the surface of the cathode. As cesium is strongly electropositive, it lowers the work of extracting electrons from the cathode (figure A.10), which leads to an increase in the production of extracted negative ions. To maximize the rate of negative ions produced, it is necessary to optimize the kinetic energy of the incident cesium ions and the cesium vapor density.

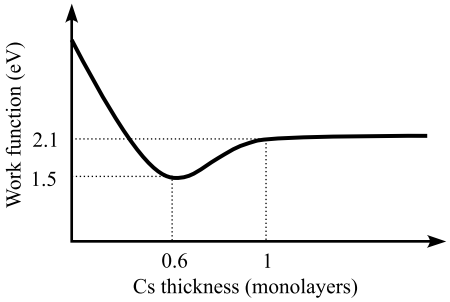

Figure A.10: Extraction function of an electron from a molybdenum surface as a function of the thickness of the cesium layer on this surface (in number of layers) [222].

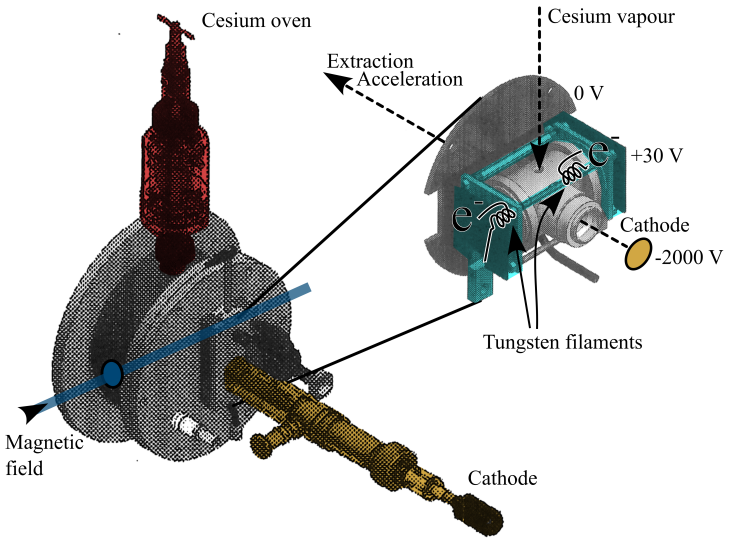

Figure A.11: Diagram of the sputtering source used at UCLouvain.

In practice, the source developed at Aarhus University (DK) and used at UCLouvain is designed as follows (see figure A.11): Following the axis of propagation of the beam, we first find a cathode polarized negatively with respect to the body of the source (between 2 and 3 kV). This cathode is of variable composition [14]. Then, a cell is placed along this axis, at the potential of the source. On either side of this cell are placed tungsten filaments through which a large current passes. These emit electrons. These filaments are brought to a slightly negative voltage (discharge voltage) relative to the cell where cesium vapor is injected. The cesium pressure in the cell is given by the

[14] The composition of the cathode depends on the desired composition of the beam extracted from the source. A list of possible compositions is given by [223].

saturated vapor pressure at the temperature of the reservoir above it [15]. The cell is immersed in a magnetic field perpendicular to the axis of propagation. It is directed along the axis formed by the two filaments. The last elements of the source are the extraction, lens and acceleration electrodes, also placed along the optical axis.

Within the cell, electrons are confined by the magnetic field. They form a cesium plasma within this cell (the cesium pressure is about $5\ 10^{-4}$ mbar). The ions produced within this plasma are accelerated from the center of the cell towards the cathode. The geometry of the cell is such that the two ion beams are focused on the center of the cathode (the distance between the cathode and the cell is adjustable). Cesium cations collide and generate anions by sputtering. The anions are then accelerated towards the cell, pass through it and are then extracted and shaped by the extraction device.

This source has the advantage of being able to produce a wide variety of negative ions. In addition, the kinetic energy distribution of the anions is low, this thermal distribution is dependent on the temperature of the cathode. However, it requires the use of cesium, the handling of which is hazardous. The current extracted from this source can reach 100 μ A at the output, but varies a lot, because the ion current is generated by literally pulverizing the cathode. This has to be replaced regularly (once a day on average).

[15] Below the cell, it is possible to inject gas from outside the source. This makes it possible to perform a mixture between cesium and another gas, which allows to generate a greater variety of negative ions by taking advantage of the production of negative ions by charge exchange with the cesium within the volume of the gas cell. This mode of operation of the source, which is more complicated to describe, has not been used.

A.2.3 ECR Ion Source

The electron cyclotron resonance ion source (ECRIS) is a source that produces ions by heating the electrons in the plasma subjected to an intense magnetic field using an electromagnetic wave whose frequency is resonant with the cyclotron frequency of electrons linked to the magnetic field.

By heating the electrons, their kinetic energy distribution increases ($E_{k,e} \sim kT_e$). These electrons collide with the gas injected into the source vacuum chamber. These collisions ionize the gas, producing ions as well as other electrons. These new electrons are then accelerated by the resonant electromagnetic field, colliding with the gas to produce more ions and electrons. This produces a strongly ionized plasma from which it is possible to extract the ions, and form an ion beam.

To understand how this source works, it is important to understand how charged particles behave in a magnetic field, as well as the process of heating electrons by the phenomenon of electron cyclotron resonance. These elements then make it possible to describe in detail the practical operation of the ECR source used in the merged beam apparatus of UCLouvain.

Electron cyclotron resonance

When a particle is subjected to a magnetic field only, the Lorentz force acts only perpendicular to its velocity. It is then possible to divide the velocity of the particle according to its component parallel to the magnetic field $\vec{v}_{\parallel}$ and its component perpendicular to this same field $\vec{v}_{\perp}$. The component parallel to the magnetic field remains unchanged, this gives the direction of propagation [224]. The perpendicular component of the trajectory follows a circle of radius ρ called radius of gyration (or Larmor radius [16]). This rotation is called

[16] The Larmor radius is the radius of gyration of a particle subjected only to a magnetic field $\vec{B}$. If this particle has an initial velocity component perpendicular to the field $\vec{v}_{\perp}$ then this particle will follow a circular trajectory. It is verified by equaling the magnetic force and the centripetal force,

$$m\frac{v_{\perp}^2}{\rho}\hat{\rho} = q\vec{v}_{\perp} \times \vec{B}$$

where $\hat{\rho}$ is the normalized vector of the radius of curvature $\vec{\rho}$ pointing from the point of trajectory to its center of curvature at this point of the trajectory.

By performing the cross product of this equation with $\vec{B}$ and remembering the vector identity

$$\vec{a} \times \left(\vec{b} \times \vec{c}\right) = \vec{b}\,(\vec{a} \cdot \vec{c}) - \vec{c}\left(\vec{a} \cdot \vec{b}\right)$$

This equation becomes

$$\frac{mv_{\perp}^2}{q\rho^2}\left(\vec{B} \times \vec{\rho}\right) = B^2\vec{v}_{\perp}$$

gyromagnetic rotation, its velocity is

$$\vec{v}_\perp = \frac{q}{m}\vec{B}\times\vec{\rho} \tag{A.8}$$

and the total velocity is

$$\vec{v}_0 = \vec{v}_\parallel + \frac{q}{m}\vec{B}\times\vec{\rho} \tag{A.9}$$

Which is the solution of the homogeneous equation when the electric field is not zero.

If a particle is subjected to a constant magnetic field $\vec{B}$, and an oscillating electric field $\vec{E}$ to an angular frequency ω, then the equation which governs the motion of a ion is

$$m\frac{\mathrm{d}v}{\mathrm{d}t} - q\vec{v}\times\vec{B} = q\vec{E} \tag{A.10}$$

This equation has both a homogeneous solution depending on the velocity (equation A.9), and a particular solution governed by

$$m\frac{\mathrm{d}\vec{v}_1}{\mathrm{d}t} - q\vec{v}_1\times\vec{B} = q\vec{E} \tag{A.11}$$

whose general solution is the combination of these two solutions :

$$\vec{v}_{\mathrm{tot}} = \vec{v}_0 + \vec{v}_1 \tag{A.12}$$

If we assume that we can separate the temporal and the spatial component of the velocity as $\vec{v}_1(x,t) = \vec{v}_1(x)e^{-i\omega t}$ [17], the particular solution becomes

$$-i\omega\vec{v}_1 = \frac{q}{m}\left(\vec{E} + \vec{v}_1\times\vec{B}\right) \tag{A.13}$$

But since the norm of the equation equals the centripetal force with the Lorentz force gives $mv_\perp = q\rho B$, the equation becomes

$$\vec{v}_\perp = \frac{q}{m}\vec{B}\times\vec{\rho}$$

since this trajectory forms a loop and the number of passages of this particle through a point of this trajectory can be considered as a current, this trajectory forms a current loop.

With this current loop is associated a magnetic moment $\mu = \pi\rho^2 I$ which is the product of the surface by the current which crosses it. This magnetic moment can be rewritten as follows:

$$\vec{\mu} = \pi\rho^2 I\hat{e}_B = \pi\rho^2\left(q\frac{v_\perp}{2\pi\rho}\right) = \frac{q}{2}v_\perp\frac{mv_\perp}{qB} = \frac{1}{2}\frac{mv_\perp^2}{B}\hat{e}_B$$

where $\hat{e}_B$ gives the direction of the surface $\pi\rho^2$ which coincides with the magnetic field.

This quantity is invariant, as a first approximation, when the field $\vec{B}$ varies slowly with time and space (adiabatic invariant).

[17] Thus, the total motion of the particle is the combination of a helical motion caused by the static magnetic field $\vec{B}$ and an oscillating motion at the frequency ω caused by the electric field $\vec{E}$.

By defining $\vec{\Omega} = -(q/m)\vec{B}$ and $\overline{\Omega} = -(q/m)B$, the magnetic field along the axis z, and by isolating the speed term on the left side of the equation one gets:

$$\begin{vmatrix} -i\omega & \overline{\Omega} & 0 \\ -\overline{\Omega} & -i\omega & 0 \\ 0 & 0 & -i\omega \end{vmatrix} \cdot \vec{v}_\omega = \frac{q}{m}\vec{E} \tag{A.14}$$

It is then possible to invert the matrix [18] and get

$$\vec{J} = nq\vec{v}_1 = \overline{\overline{\sigma}} \cdot \vec{E} \tag{A.15}$$

where $\overline{\overline{\sigma}}$ is the electrical conductivity tensor. This tensor is written in the rotating coordinates defined as:

$$E_+ = E_x + iE_y \tag{A.16}$$
$$E_- = E_x - iE_y \tag{A.17}$$
$$E_z = E_z \tag{A.18}$$

as follows [19]:

$$\overline{\overline{\sigma}} = \sigma_0 \begin{vmatrix} \frac{\omega}{\omega-\Omega} & 0 & 0 \\ 0 & \frac{\omega}{\omega+\Omega} & 0 \\ 0 & 0 & 1 \end{vmatrix} \text{ where } \sigma_0 = \frac{nq^2}{-i\omega m} \tag{A.19}$$

[18]

$$\vec{v}_1 = \frac{q}{m} \begin{vmatrix} \frac{i\omega}{\omega^2-\overline{\Omega}^2} & \frac{-\overline{\Omega}}{\omega^2-\overline{\Omega}^2} & 0 \\ \frac{\overline{\Omega}}{\omega^2-\overline{\Omega}^2} & \frac{i\omega}{\omega^2-\overline{\Omega}^2} & 0 \\ 0 & 0 & \frac{1}{-i\omega} \end{vmatrix} \cdot \vec{E}$$

and

$$\overline{\overline{\sigma}} = \frac{nq^2}{m(i\omega)} \begin{vmatrix} \frac{\omega^2}{\omega^2-\overline{\Omega}^2} & \frac{i\omega\overline{\Omega}}{\omega^2-\overline{\Omega}^2} & 0 \\ \frac{-i\omega\overline{\Omega}}{\omega^2-\overline{\Omega}^2} & \frac{\omega^2}{\omega^2-\overline{\Omega}^2} & 0 \\ 0 & 0 & 1 \end{vmatrix}.$$

[19] The reverse transformation is

$$E_x = \frac{1}{2}(E_+ + E_-)$$
$$E_y = \frac{1}{2i}(E_+ - E_-)$$

Hence

$$\begin{vmatrix} 1 & i & 0 \\ 1 & -i & 0 \\ 0 & 0 & 1 \end{vmatrix} \cdot \begin{bmatrix} J_x \\ J_y \\ J_z \end{bmatrix}$$

$$= \sigma_0 \begin{vmatrix} 1 & i & 0 \\ 1 & -i & 0 \\ 0 & 0 & 1 \end{vmatrix} \cdot \begin{vmatrix} \frac{\omega^2}{\omega^2-\overline{\Omega}^2} & \frac{i\omega\overline{\Omega}}{\omega^2-\overline{\Omega}^2} & 0 \\ \frac{-i\omega\overline{\Omega}}{\omega^2-\overline{\Omega}^2} & \frac{\omega^2}{\omega^2-\overline{\Omega}^2} & 0 \\ 0 & 0 & 1 \end{vmatrix} \cdot \begin{vmatrix} 1/2 & 1/2 & 0 \\ -i/2 & i/2 & 0 \\ 0 & 0 & 1 \end{vmatrix} \cdot \begin{vmatrix} 1 & i & 0 \\ 1 & -i & 0 \\ 0 & 0 & 1 \end{vmatrix} \cdot \begin{bmatrix} E_x \\ E_y \\ E_z \end{bmatrix}$$

If the oscillation frequency of the electric field corresponds to the electron cyclotron frequency linked to the magnetic field, i.e. $\omega \simeq \Omega_e = (q_e/m_e)B$, a resonance phenomenon along to $\vec{E}_+$ appears. This component accompanies the gyromagnetic rotation of the electrons (same angular frequency). Therefore, the relative phase between $\vec{E}_+$ and the speed of the electrons is constant, the interaction of these two components is cumulative. The particular solution of the differential equation [20] is then:

$$\vec{v}_{1,+} = \frac{q_e}{m_e}\vec{E}_+ t \tag{A.20}$$

By applying the transformation matrices,

$$\begin{bmatrix} J_+ \\ J_- \\ J_z \end{bmatrix} = \sigma_0 \begin{vmatrix} \frac{\omega^2}{\omega^2-\overline{\Omega}^2} + \frac{\omega\Omega}{\omega^2-\overline{\Omega}^2} & 0 & 0 \\ 0 & \frac{\omega^2}{\omega^2-\overline{\Omega}^2} - \frac{\omega\Omega}{\omega^2-\overline{\Omega}^2} & 0 \\ 0 & 0 & 1 \end{vmatrix} \cdot \begin{bmatrix} E_+ \\ E_- \\ E_z \end{bmatrix}$$

or

$$\begin{bmatrix} J_+ \\ J_- \\ J_z \end{bmatrix} = \sigma_0 \begin{vmatrix} \frac{\omega}{\omega-\Omega} & 0 & 0 \\ 0 & \frac{\omega}{\omega+\Omega} & 0 \\ 0 & 0 & 1 \end{vmatrix} \cdot \begin{bmatrix} E_+ \\ E_- \\ E_z \end{bmatrix}$$

[20] As the term σ_+ becomes infinite, it is no longer possible to express the equations of motion of electrons using electrical conductivity. It is necessary to restart the resolution from the initial equations of motion.

If the assumption that $\dot{\vec{v}}_1 = -i\omega\vec{v}_1$ is no longer made, the equations of motion are

$$\frac{\mathrm{d}}{\mathrm{d}t}\begin{bmatrix} v_{1,x} \\ v_{1,y} \\ v_{1,z} \end{bmatrix} = \begin{vmatrix} 0 & \overline{\Omega} & 0 \\ -\overline{\Omega} & 0 & 0 \\ 0 & 0 & 0 \end{vmatrix} + \frac{q}{m}\begin{bmatrix} E_x \\ E_y \\ E_z \end{bmatrix}$$

This equation is transformed in the rotating frame to give

$$\frac{\mathrm{d}}{\mathrm{d}t}\begin{bmatrix} v_{1,+} \\ v_{1,-} \\ v_{1,z} \end{bmatrix} = \begin{vmatrix} -i\overline{\Omega} & 0 & 0 \\ 0 & i\overline{\Omega} & 0 \\ 0 & 0 & 0 \end{vmatrix} + \frac{q}{m}\begin{bmatrix} E_+ \\ E_- \\ E_z \end{bmatrix}$$

And so, along the component $v_{1,+}$, following the hypothesis $E_+ = E_{+,0}e^{-i\omega t}$ and $\overline{\Omega} = \omega$, this equation becomes

$$\frac{\mathrm{d}v_{1,+}}{\mathrm{d}t} = -i\omega v_{1,+} + \frac{q}{m}E_{+,0}e^{-i\omega t}$$

Whose solution is easily obtained using symbolic calculation software:

$$v_{1,+}(t) = C_1 e^{-i\omega t} + \frac{q}{m}E_+(t)\cdot t$$

with C_1 an integration constant, which is zero if $v_{1,+}(t=0) = 0$.

It should be noted that, according to the same reasoning,

$$v_{1,+}(t) = C_1 e^{i\omega t} - \frac{q}{m}\frac{E_-(t)}{2i\omega}$$

which satisfies the condition $\dot{v}_- = -i\omega v_-$.

This motion is a helical motion ($\vec{E}_+$ is a vector rotating in the positive direction around the field $\vec{B}$) of angular velocity $v_\perp = \omega \cdot \rho$. Therefore, the radius ρ of the trajectory induced by the rotating electric field is

$$\rho = \frac{v_{1,+}}{\Omega_e} = \frac{q_e}{m_e \Omega_e} E_+ t \tag{A.21}$$

This solution is added to the homogeneous solution, which gives

$$\vec{v}_{\text{tot}} = \vec{v}_\parallel + \frac{q_e}{m_e} \vec{B} \times \vec{\rho} + \frac{q_e}{m_e} \vec{E}_+ t \tag{A.22}$$

The velocity perpendicular to the magnetic field then increases until the particle meets another particle or a wall. Assuming the mean free path to be large enough, it is necessary to limit the kinetic energy of the electrons to ensure that they do not come into contact with the walls. This is achieved with the help of magnetic mirrors.

Magnetic mirror

When a particle is subjected to a magnetic field, it has a certain orbital magnetic moment

$$\mu = \frac{1}{2} \frac{m v_\perp^2}{B} \tag{A.23}$$

This magnetic moment is an invariant. Therefore, its Lagrangian derivative is zero $\mathrm{d}\mu/\mathrm{d}s = 0$, hence

$$\frac{\mathrm{d}}{\mathrm{d}s} \left(\frac{m v_\perp^2}{2} \right) = \mu \frac{\partial B}{\partial s} \tag{A.24}$$

Moreover, since the Lorentz force is perpendicular to the particle's propagation axis, this force does not modify its speed (only the velocity). In other words, kinetic energy is conserved. So

$$\mathrm{d} \left(\frac{m v_\parallel^2}{2} \right) = -\mu \frac{\partial B}{\partial s} \mathrm{d}s \tag{A.25}$$

This means that when a particle propagates in a helical path along a magnetic field line whose intensity increases, the transverse kinetic energy of this particle increases. This decreases the longitudinal energy of the particle. If the magnetic field reaches a critical value, this energy becomes zero. The particle turns around.

It should be noted that if the trajectory of the particle initially almost follows the field lines, the latter have a very weak effect on the trajectory. Indeed, according to this situation, the orbital magnetic moment is also very weak. In this case, the magnetic field required for the particle to turn around is much

greater. Thus, a field line concentration constitutes a magnetic mirror for most particles, except those which propagate along the field lines. There is thus a loss cone within which, for a given magnetic configuration, the particles are not reflected. This loss cone is independent of the initial kinetic energy of the particles.

Source description

The ECR source used for this thesis was built in collaboration with Giessen University (DE) and is inspired by that proposed by Liehr [225, 226].

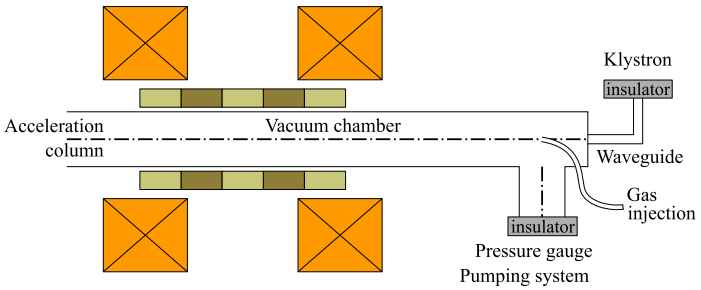

Figure A.12: Diagram of the ECR source.

The ECR source is composed of a cylindrical vacuum chamber (see figure A.12). On one side of this chamber is injected a gas whose composition depends on the composition of the desired beam. The pressure of this gas is controlled using a needle valve and measured using a gauge. The vacuum within the chamber is maintained using a low speed pumping device which maintains the pressure at about 10^{-7} mbar without gas injection. The pressure of the gas injected into the source varies from 10^{-5} to 5 10^{-4} mbar. The pressure determines the average free path of the electrons within the chamber. This chamber is large enough to allow time for the electrons to gain kinetic energy and small enough to maintain an intense production of ions within the chamber.

On the other side of the source chamber is placed a set of electrodes. These make it possible to extract and accelerate the ions produced within the chamber.

Two coils are wound around the chamber. These coils are not in Helmoltz configuration in order to obtain a minimum axial magnetic field between the two coils and two maxima at the level of the coils (figure A.13). These coils generate an axial magnetic field of $\sim$260 mT at each coil and $\sim$190 mT along the axis between the coils. This variation in the intensity of the axial magnetic field makes it possible to reflect the electrons and to maintain them within the

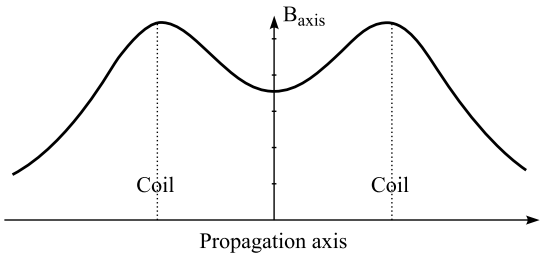

Figure A.13: Axial magnetic field along the axis of propagation within the ECR source.

source along the axis.

Around the chamber, between the two coils is placed a set of permanent magnets (KOERDYM 260). These magnets form a hexapole in the plane perpendicular to the axis of the chamber (no axial component). This magnetic field is much more intense near the walls of the chamber than at the center of the latter and confines the electrons of the plasma within the chamber and minimizes the collisions of electrons with the walls (see figure A.14).

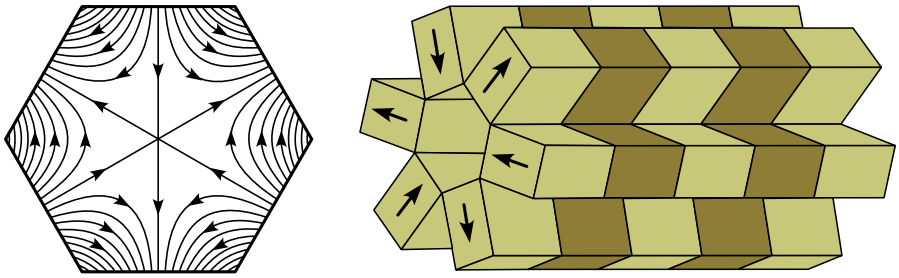

Figure A.14: Configuration of the permanent magnets around the axis of the ECR source. On the left, the hexapolar field in the plane perpendicular to the axis. On the right, the arrangement of the permanent magnets.

An electromagnetic wave (microwave frequency $\sim$ 5 GHz) is injected along the axis of the chamber using a waveguide of suitable geometry. This wave is generated using a klystron [21] with a maximum power of 350 W coupled to a low power oscillator. It propagates along the chamber and generates

[21] A klystron is an amplifier of electromagnetic waves. It consists of an electron gun at a negative potential (about 4500 V), at least two resonators and an electron collector [227].

The electron gun emits a continuous beam of electrons, accelerated around the first resonator. This first resonator is supplied at its resonant frequency by an external source, the oscillator generates an oscillating axial electric field which accelerates some of the electrons and slows down the others, forming electron packets (fast electrons catch up with slow electrons) . It is possible to use several resonators to improve the compression of the electron packets. The last resonator receives packets of compressed electrons at a frequency that corresponds to its resonant frequency. All the electrons which pass through it are then slowed down. The kinetic energy of electrons is converted into an electromagnetic wave. This wave is finally extracted

the rotating electric field. The intensity of this field is controlled using an attenuator placed between the oscillator and the klystron. The magnetic field associated with the frequency of the wave is 178.6 mT. As the axial magnetic field is not uniform, the resonance phenomenon occurs on a surface within the source. The position and size of this surface are controlled using the axial magnetic field, given by the current flowing through the coils (up to 350 A, which is why these coils are cooled with water).

Thus several parameters control the operation of the source: the pressure of the gas within the chamber, the intensity of the electric field and the size of the resonant surface. These three parameters influence the composition of the plasma. Indeed, they influence the electronic density and temperature, but also the mean free path of ions and neutrals within the chamber. These parameters modify the balance of the reactions within the chamber and make it possible to produce more or less atomic or molecular ions, but also to obtain more or less multicharged ions.

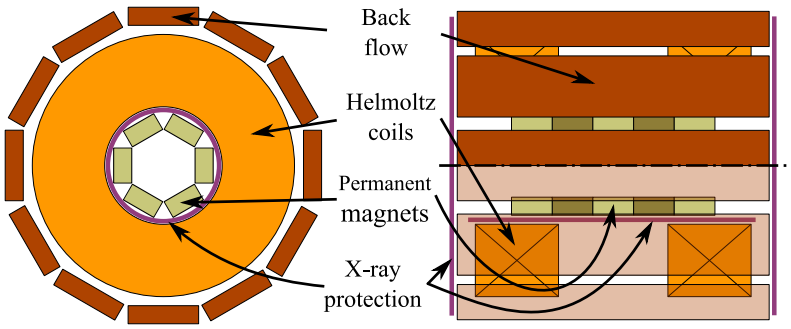

Figure A.15: Diagram of the exterior of the ECR source, with its shielding systems.

Due to the presence of highly energetic electrons, highly ionized gas, as well as strong magnetic fields this source must be shielded. The shielding systems used are shown in the figure A.15.

A.2.4 Duoplasmatron ion source

Duoplasmatron ion sources are sources of positive or negative ions developed in 1956 by von Ardenne [220, 228]. The name duoplasmatron comes from the geometric and magnetic confinement of the plasma before extraction. The following description outlines its operation, during the generation of a negative beam.

This source is composed of an external magnetic field and three electrodes: a hot cathode, an anode and an intermediate electrode. The cathode is usu-

using a waveguide.

ally made of an electron emitting tungsten filament. Gas is injected near the cathode. The anode is a pierced, grounded electrode (acceleration voltage). Between the anode and the cathode, the intermediate electrode is used to confine the electrons emitted by the cathode, then to direct them and accelerate them towards the anode. This electrode has a floating electrostatic potential. Outside the source chamber, a coil generates a magnetic field in the chamber parallel to the axis of the electrodes. This magnetic field is considered negligible between the cathode and the intermediate electrode. In addition, it has a maximum between the intermediate electrode and the anode. This magnetic field focus the primary electrons beam coming from the cathode and confines the secondary electrons generated between the intermediate electrode and the anode. The name duoplasmatron comes from these two electron confinement mechanisms.

However, despite the simplicity of manufacture and operation of the source, its operating principle is way more complex: there are several regions within the source (anode plasma, intermediate plasma and cathode plasma). The plasmas within these regions are generated by electrons whose velocity distributions differ (and may vary depending on the mode of operation of the source). To understand how this source works, it is interesting to analyze each region in detail. This description of the source is largely taken from a combination of articles by C. Lejeune [229–231], but also from [213, 220, 232] for the extraction of a positive beam. The production of negative ions within this source is not trivial either, the production mechanisms of these are also described (the references are in the text).

Debye sheath

Near the wall, if the potential of the latter is identical to that of the adjacent plasma, as electrons have a much greater mobility, the flow of electrons incident to the wall is greater than the flow of ions. Therefore, the metal wall absorb the negative charges.

As the wall is metallic, it accumulates negative charges on its surface only (screening effect). Thus, near the wall, the quasi-neutrality of the plasma is no longer respected. This region is predominantly populated with positive ions, as low kinetic energy electrons are repelled until the flow of electrons $(-)$ entering the wall balances the flow of ions $(+)$ entering.

The thickness of this potential cladding close to the wall is characterized by the Debye length

$$\lambda_D^2 = \frac{\varepsilon_0 k_B T_e}{n_e q_e^2} \tag{A.26}$$

which is the expression of the ratio between the temperature of electrons (and their speed distribution) and the density of these electrons [224].

I. Plasma types

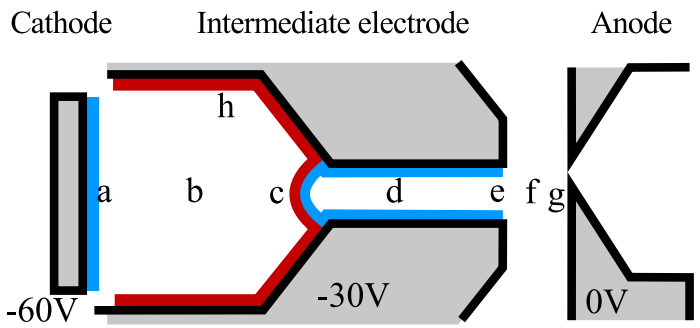

a. Double sheath
(hot cathode)
b. Cathodic plasma
c. Double sheath
(interface between two plasma)
d. Intermediate plasma
e. Potential gradient
f. Anode column
g. Single sheath
(drop in potential
due to primary electrons)
h. Debye sheath
(geometric confinement)

II. Electromagnetic fields

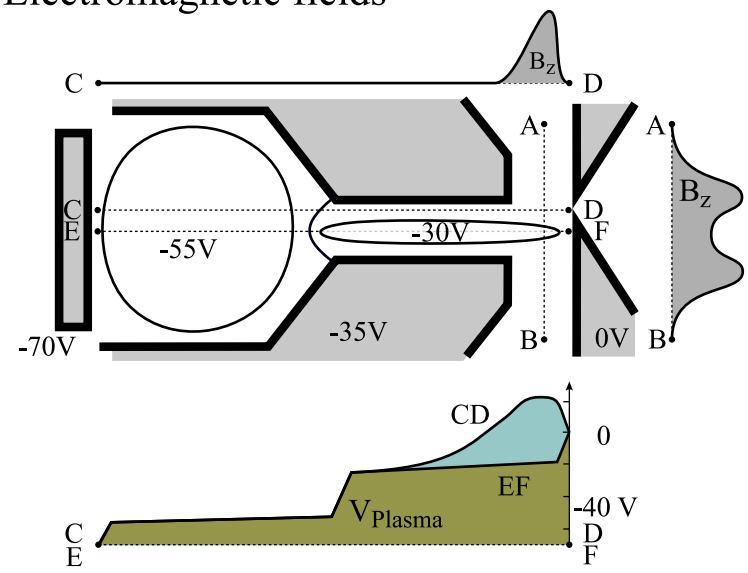

Figure A.16: Schematic profile of a duoplasmatron source used to extract a negative ion beam (compiled from [229]) – Plasma types and electromagnetic fields.

III. Primary electrons

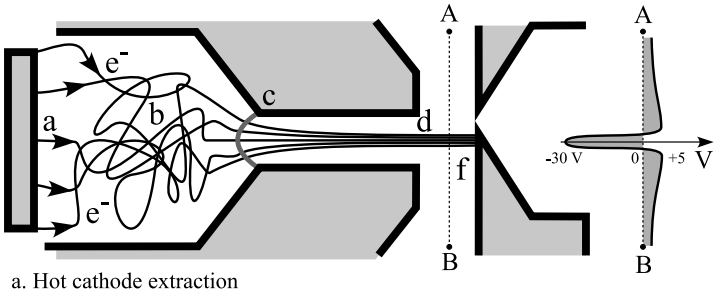

a. Hot cathode extraction
(double extraction duct)
b. Positive column (constant electric field)
thermal electrons.
c. Electrons accelerated and focused
by the double sheath (convex)
alignment of electrons along the axis
d. Arch column
Intense ionization, electronic excitation (radiation)
No magnetic constriction (trajectory too aligned)
f. Generation of an anode sheath
Fix the potential of the double sheath

IV. Secondary electrons

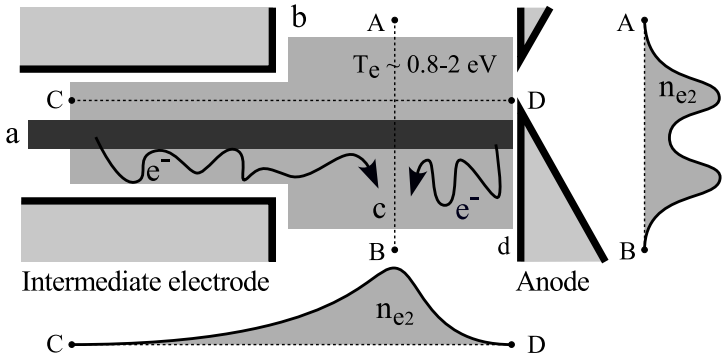

a. Primary electron arc column
Secondary electron generation by Townsend-α
b. Magnetic constriction
c. Excess ions trapped by the magnetic constriction
because the axial mobility of ions is lower
than the mobility of the secondary electrons
d. Negative anode fall (continuity conditions)

Figure A.17: Schematic profile of a duoplasmatron source used to extract a negative ion beam (compiled from [229]) – Electrons density profiles.

This sheathing effect allows the walls to repel the electrons and to confine the plasma in a geometric way.

Cathodic discharge

Cathode plasma is the plasma contained between the intermediate electrode and the hot cathode. The latter generates the primary electrons. These are produced by the cathode filament. A current passes through this filament which heats up by the Joule effect. This hot tungsten filament emits electrons. This electron emission has the following consequence. Plasma remains a good conductor as long as the current carried by the electrons does not exceed the current possibly carried by the ions that make up the plasma. Therefore, a negative sheath is formed around the cathode due to the lack of positive ions, compared to the density of electrons [233] [22]. The electrons emitted by the cathode then move in a zone without an electric field, that is to say an almost constant electrostatic potential, because the cathode voltage is screened by the double sheath near the cathode and by a sheath at the edges, near the intermediate electrode. Ionization of the plasma is due to the thermal population of electrons.

As the Debye length and the mean free path (gas pressure $\sim 10^{-2}$ mbar) are much smaller than the distance between the electrodes, the particles are considered to be independent. This type of plasma is called a free-fall positive column [224, p234].

Since the intermediate electrode is floating, once the plasmas are in equilibrium, the flow of ions entering and leaving the electrode is equal. Therefore,

[22] This lack of positive charge leads to the generation of a double cladding around the cathode. The motion of electrons – emitted by the hot cathode – is governed by a double electrostatic sheath on the surface of the cathode.

Unlike insulating surfaces, whose total current (electrons and ions) is zero, the hot cathode emits electrons. When this cathode is not very hot, the maximum electron emission is given by the Richardson-Dushmann formula [234]. This emission is called thermal emission.

However, the emission of electrons causes an accumulation of electrons close to the cathode, this accumulation generates a cladding in the direct vicinity of the cathode. This accumulation of negative charges causes a drop in potential, and attracts ions close to the cladding, a second cladding is formed [235]. In this case, the space charge – linked to the density of electrons in the direct vicinity of the electrode – limits the emission of electrons. The electron current is then given by the equation A.28. The double sheath is the combination of the electron sheath with the ion sheath bonded to the hot cathode. There is a transition between the two regimes [236].

the potential of the intermediate electrode is given by the cathode plasma [23]:

$$V_{p1} - V_{IE} \simeq \frac{kT_e}{2e} \log\left(\frac{2}{\pi}\frac{M}{m}\right) \tag{A.27}$$

This acts as an ion-emitting anode within the positive column (positive sheath [235]).

Interface with the intermediate electrode

The intermediate electrode separates the plasma from the cathode with the plasma from the anode. The channel of this electrode links these two plasmas. The separation between the cathode plasma and that of the intermediate electrode is caused by a sudden change in diameter between the two chambers. This interface between the two plasmas is an anode sheath (ion source) for the cathode plasma and a cathode sheath for the intermediate plasma. This results in the establishment of a double sheath at this interface. This sheath is convex towards the cathode.

Assuming that the electric field at the boundaries of the intermediate electrode is almost zero, the intensity of these fluxes is limited by the space charge. In order to satisfy the quasi-neutrality of the plasma at equilibrium, these ion flows must satisfy the Langmuir criterion

$$\frac{I_e}{I_{+1}} = \sqrt{\frac{M_{+1}}{m_e}} \tag{A.28}$$

where M_{+1} is the ion mass and m_e is the electron mass. This condition makes it possible to ensure the quasi-neutrality of the plasma during its compression inside the channel of the intermediate electrode. It regulates the potential jump of the double sheath around the intermediate electrode and determines the potential of the cathode and anode plasma [24].

The intermediate electrode is conductive, the geometric constriction sheath connects the plasma of the two discharges: the discharge of the cathode (from

[23] The potential of the plasma of the positive column of the cathode V_{p1} with respect to the anode is not given by the potential applied to the cathode, but depends on the current within the anode plasma I_A, the maximum magnetic field B and the pressure within the anode plasma p_A. Indeed, the drop in potential of the cathode depends on the emission of electrons. This drop in potential then depends on the feedback given by the anode plasma (influenced by the maximum magnetic field B and the pressure), but also within the anode discharge.

[24] These conditions are satisfied by self-regulation of two parameters: The first is the position of the sheath. This determines the flow of electrons extracted from the "quasi-cathodic" plasma, and therefore the flow of ions. The flow of electrons is moreover similar to the arc current I_A within the "quasi anodic" plasma. The second is the magnitude of the potential discontinuity. This jump in potential increases the ionization within the plasma of the "quasi-anode". Therefore, because of the ion transport conditions, this determines the ion current I_{+1} returning within the sheath.

the cathode to the intermediate electrode) with the discharge of the anode (from the intermediate electrode – cathode side – at the anode).

These discharges can vary independently depending on the bias voltage of the intermediate electrode. However, if the intermediate electrode is floating, the currents of each of the discharges are identical [25].

Anodic discharge

The discharge of the anode is generated by the electrons which come from the plasma of the cathode, extracted by the jump of potential of the double sheath.

The electrons are accelerated and are focused by the constriction sheath (concentric plasma sheath which exerts a force towards the center of the sheath) and by the electrostatic forces due to the distribution of the plasma on the other hand. As the angle of incidence of the electrons through the maximum axial magnetic field is small, the rate of reflection of these particles within the mirror is negligible (see section A.2.3). This leads to a channeling of the electron beam [26].

The area of the anode where the discharge occurs is small, compared to the mean free path of the electrons (reduced pressure linked to differential pumping). In other words, the thermalization length is shorter than the interaction length. From then on, the primary electrons continue their way towards the anode and are mainly responsible for the conduction of the plasma arc from the anode. These fast "primary" electrons pass through the anode plasma without collective interaction until they reach the anode. They form an arc within the plasma. This arc begins within the intermediate electrode and then passes through the anode plasma.

Within the arc of the anode column, the current has a high density. This current generates a large rate of charge production (by the Townsend avalanche process – if an electron has sufficient energy, then its collision with a neutral molecule of the gas generates several electrons of lower kinetic energy [27]. These are thermalized – in contrast to primary electrons - and participate in about a third of the total ionization of the medium.

Within the magnetic field, the displacement of charges is greatly reduced (apart from purely axial movements). As the mobility of electrons is more important than the mobility of ions, the leakage of electrons along the axis of

[25] If not, there is a proportionality factor between the cathode and anode currents caused by current leak twoard the resistors which connect the intermediate electrode to the anode and the cathode. There is therefore a modification of the electron and ion currents within the source. However, these modifications do not lead to any modification of the principle of operation.

[26] Beam channeling: generating an electron channel with only one specific direction.

[27] If these secondary electrons are accelerated by the plasma, then they too have enough energy to generate several other electrons in subsequent collisions. The large number of secondary electrons produced generates a large number of collisions related to secondary electrons.

propagation is greater in the direct vicinity of the arc. These electrons, diffused around the arc of the column, then form a "dark" plasma called an anode column. Dark, because electrons do not have sufficient energy to form ions in the excited state (which radiate). Conversely, the more energetic electrons in the arc of the column have sufficient kinetic energy to form excited states.

This plasma differs from the plasma of a conventional positive column (where the conduction of the arc is provided by thermal electrons). Magnetic constriction does not imply the creation of a double layer – present within a classical positive column – because the mobility along the axis of thermal electrons is greatly reduced by the convergence of the magnetic field lines. Consequently, there is an electron density and electric potential gradient between the magnetically confined plasma ("anode column") and the plasma located within the intermediate electrode ("intermediate plasma"). Since ions and secondary electrons have low mobility, only primary electrons come into contact with the anode. In addition, the anode is not an ion source, so the anode sheath of the anode plasma is not positively charged, but negatively.

This leads to an excess of positive charges, these charges increase the electrical potentials until reaching a maximum between the anode and the magnetic constriction [28]. The density of ions is greater near the arc than the density of produced ions.

This potential maximum has two effects. On the one hand, it captures secondary electrons. On the other hand, it accelerates the non-trapped ions towards the anode and the double constriction sheath and maintains the plasma stability criterion given by the equation A.28).

Negative ions generation and extraction

The extraction of negative ions from a duoplasmatron source is carried out through a hole drilled in the anode. This hole is offset about 1 to 3 mm from the axis of the intermediate electrode [237, 238].

This decentring of the extraction improves the extraction of negative ions for several reasons related to the operation of the source.

The first is given by the distribution of electrons within the source. The density of fast electrons which come from the cathode discharge is large ($\sim 10^{15}$ cm^{-3}). Because of the strong non-uniform magnetic field between the intermediate electrode and the anode, the direction of propagation of these electrons is along the axis of the intermediate electrode. These electrons have a narrow radial distribution. Therefore, if the hole in the anode is located along the axis of propagation of the primary electrons, the space charge generated by them would strongly defocus the anion beam extracted from the source. In

[28] This potential maximum is offset from the axial maximum of the magnetic field, in the middle of the plane of the anode column.

addition, these numerous electrons leaving the source tend to neutralize the anions (by detachment), and especially, after acceleration, to produce a large quantity of X-rays.

The decentring of the extraction is also motivated by the mechanism of formation of negative ions within the source. In the case of hydrogen, negative ions are mainly produced by dissociative attachment of the rovibrationally excited hydrogen molecule:

$$H_2(v'' > 0, J > 0) + e^- \rightarrow H^- + H \tag{A.29}$$

The cross section of this reaction strongly depends on the vibrational state of the neutral molecule, it is up to 5 orders of magnitude greater than that of the $v'' = 0$ state of the molecule. Moreover, the cross section of this reaction is maximal when the energy distribution of the electrons is around 1 eV [239]. This distribution corresponds to the energy distribution of secondary electrons, the maximum density of which is slightly off-axis.

However, this vibrationally excited population of hydrogen does not match the thermal population of hydrogen inside the source. This vibrational excitation is partly generated within the arc of the discharge by the primary electrons whose kinetic energy is much greater [29]. The process of vibrational excitation by electronic impact is as follows [30]:

$$H_2(X\ ^1\Sigma_g^+, v'' = 0) + e^- \rightarrow H_2^\star(B\ ^1\Sigma_u, C\ ^1\Pi_u) + e^- \tag{A.30}$$

$$H_2^\star(B\ ^1\Sigma_u, C\ ^1\Pi_u) \rightarrow H_2(X\ ^1\Sigma_g^+, v_f) + h\nu \tag{A.31}$$

The molecules thus excited diffuse out of the region of the arc towards the diffusion region where the density of thermal electrons ($T_e \simeq 0.8 - 2$ eV) is greater [31].

The anions produced must then be extracted from the source. If they are produced in a plasma whose potential is greater than that of the anode, they cannot be extracted. Therefore, only the anions produced within the intermediate plasma are extracted (in accordance with the experimental measurements

[29] Other processes form vibrationally excited hydrogen molecules (among others: Eley-Rideal [240–244]). These reactions take place on the surfaces of the walls of the chamber or around the filament. These processes give a contribution of excited molecules that cannot be overlooked. These components are theoretically predicted, among others, for RF [245] discharges. The effect of the materials used to construct the source on the negative ion current is observed for most types of sources, including pigmatron sources (Penning sources).

The rate of production of vibrationally excited states is not yet fully understood [246].

[30] This process is described in detail for an incident electron beam with a kinetic energy of 50 eV in [247].

[31] This phenomenon is also present in post-discharges [248].

of [249]) [32].

In order to avoid neutralization of anions during their extraction – by process of detachment by electronic collision or by mutual neutralization with H^+, H_2^+ or H_3^+ – the trajectory of anions must avoid the strongly ionized anode plasma region. Therefore, the extracted anion density is greater outside the arc axis of the anodic discharge [237].

[32] However, there are two operating modes of the anode discharge: the normal mode described above and the "starvation" mode. This second mode appears when the primary electron current is much greater. The plasma within the anode discharge is fully ionized, which changes the distribution of electrons. The double layer no longer forms between the cathode plasma and the intermediate electrode, but between the intermediate electrode and the anode plasma. When the discharge propagates according to this mode, the anions are no longer extracted from the intermediate electrode, but at the level of the anode sheath [229, 231].

This last statement could not be measured directly, but is in agreement with our observations of the energy distribution of the beam extracted from the duoplasmatron source. There are indeed two operating modes whose energy distribution varies. This assumes that the ions are extracted from two different places in the source. In addition, one of these modes of operation generates a beam having two components of kinetic energy. This mode is problematic during our measurements, because it duplicates our data.

Appendix B

Data treatement

B.1 Acquisition system

The acquisition system makes it possible to determine the relative kinetic energy between the two particles and their directions of propagation in the coordinate system of the center-of-mass for each coincident event obtained using the pair of position-sensitive detectors (section A.1.11).

The logic in place for the digital conversion of coincident events has already been described on several occasions [187, 250, 251]. It is identical to that given in the references. The remainder of this presentation focuses on the conversion of raw digital data into interpretable data (related to the physics of the reaction studied). This second part of the analysis has been updated.

B.1.1 Scaling

For each event, the acquisition system measures a certain amount of information. Each of this data is stored as provided by the 10-bit ADCs

$$\{X_1, Y_1\}, \{X_2, Y_2\}, \{T_i, T_{i,\text{ref1}}, T_{i,\text{ref2}}\}, \{HAS_{\text{diodesignal}}, IS_{\text{ON/OFF}}\} \qquad \text{(B.1)}$$

where $i = 1, 2, 3$.

The first and second sets of data correspond to the impact position of the events on the first and the second detector.

The following three sets give the time difference between two impacts as well as two reference times shifted by a value $\Delta t_{i,ref}$ given by a finely adjusted delay box [1]. These reference times are acquired identically to T_i [2].

The first of these three time sets indicates the time difference between the impact on the first and the second detector. The other two times are assigned

[1] In practice, this delay is about 500 ns, it is measured using an oscilloscope.

[2] The acquisition system, despite all its qualities, can have failures when taking data, mainly because of a stack of data arriving during the transfer interval to the computer memory. These

for other experiments. They make it possible, for example, to synchronize the acquisition with a pulsed laser. Or to add a third detector to the system of which only the time information is known. This last system makes it possible to make measurements of dissociations to three bodies [252].

The last set of data is a set of conditions to be satisfied when measuring an event [3].

The first step in data processing is to convert positions to meters and times to seconds. Indeed, as ADCs are not immutable, the values they indicate may vary from one measurement campaign to another.

To obtain the time, the raw time data is compared to the reference times as follows

$$t_i = \frac{T_i * \Delta t_{i,\mathrm{ref}}}{T_{i,\mathrm{ref2}} - T_{i,\mathrm{ref1}}} \tag{B.2}$$

using $i = 1,2,3$.

The scaling of the impact positions is carried out from a reference measurement taken at the start of the measurement campaign. This non-coincident measurement is taken with a mask in front of each detector. This mask is composed of holes arranged in a checkerboard pattern on a grid spaced at 5 mm.

Therefore, the numerical position $\{X_{1,g}, Y_{1,g}\}$ and $\{X_{2,g}, Y_{2,g}\}$ of each point of the grid that makes up the mask, is associated with the physical position of these holes on the mask $\{\tilde{x}_{1,g}, \tilde{y}_{1,g}\}$ and $\{\tilde{x}_{2,g}, \tilde{y}_{2,g}\}$.

The physical position of the points of impact of the coincident events is then obtained by interpolating their numerical position linearly using the equation of the plane passing through the three nearest non-aligned points of the

erroneous events are easy to identify because they do not meet the following conditions:

$$\begin{aligned} T1 &\in]0; 8191] \\ X1 &\in [0; 1023] \\ Y1 &\in]0; 1023] \\ X2 &\in]1024; 2047] \\ Y2 &\in [0; 1023] \end{aligned}$$

Each reference time must satisfy the same conditions as the measurement time to which it is associated.

[3] For example if a diode signal was received to synchronize the laser data.

mask [4].

To obtain the position of the impacts in relation to the point where the reaction took place (D1 $\{x_1, y_1, z_1\}$ ou D2 $\{x_2, y_2, z_2\}$), the point of impact on each of the detectors must be offset by the position of the detector D1 $\{x_{D1}, y_{D1}, z_{D1}\}$ ou D2 $\{x_{D2}, y_{D2}, z_{D2}\}$:

$$\{x_i, y_i, z_i\} = \{\tilde{x}_i + x_{Di}, \tilde{y}_i + y_{Di}, z_{D1}\} \tag{B.3}$$

where $i = 1, 2$.

Thus, for each coincident event, the impact position and the time difference are obtained in the laboratory frame:

$$\vec{d_1} = \{x_1, y_1, z_1\}, \vec{d_2} = \{x_2, y_2, z_2\}, \tau \tag{B.4}$$

These are the data which will be used to calculate the kinetic energy released during the reaction (the reference frame used is described in the section 4.1.1).

We can also calculate α_{12}, which is the angle between the two velocities in the laboratory frame. This angle is obtained using the cross product between $\vec{d_1}$ and $\vec{d_2}$:

$$\begin{aligned} \left\| \vec{d_1} \times \vec{d_2} \right\| &= \left\| \vec{d_1} \right\| \left\| \vec{d_2} \right\| \sin(\alpha_{12}) \\ &= \sqrt{(y_1 z_2 - z_1 y_2)^2 + (z_1 x_2 - x_1 z_2)^2 + (x_1 y_2 - y_1 x_2)^2} \end{aligned} \tag{B.5}$$

hence

$$\cos(\alpha_{12}) = \sqrt{1 - \frac{(y_1 z_2 - z_1 y_2)^2 + (z_1 x_2 - x_1 z_2)^2 + (x_1 y_2 - y_1 x_2)^2}{\left(x_1^2 + y_1^2 + z_1^2\right)\left(x_2^2 + y_2^2 + z_2^2\right)}} \tag{B.6}$$

B.2 Mass missattribution due to the center-of-mass distribution

A first index is the asymmetry of the peak following the allocation of masses (present or absent).

[4] A plane defined in three dimensions can be written in the form:

$$f_i(X, Y) = a * X + b * Y + c$$

where a, b and c are parameters to be determined independently for $\tilde{x}$ and $\tilde{y}$:

$$\begin{bmatrix} X_{g,1} & Y_{g,1} & 1 \\ X_{g,2} & Y_{g,2} & 1 \\ X_{g,3} & Y_{g,3} & 1 \end{bmatrix} \cdot \begin{bmatrix} a_{\{x,y\}} \\ b_{\{x,y\}} \\ c_{\{x,y\}} \end{bmatrix} = \begin{bmatrix} \{\tilde{x}, \tilde{y}\}_{g,1} \\ \{\tilde{x}, \tilde{y}\}_{g,2} \\ \{\tilde{x}, \tilde{y}\}_{g,3} \end{bmatrix}$$

Just inverting this, the equation provides the parameters $a_{\{x,y\}}$, $b_{\{x,y\}}$ and $c_{\{x,y\}}$.

These make it possible to obtain the position of impact on the detectors from their digital values.

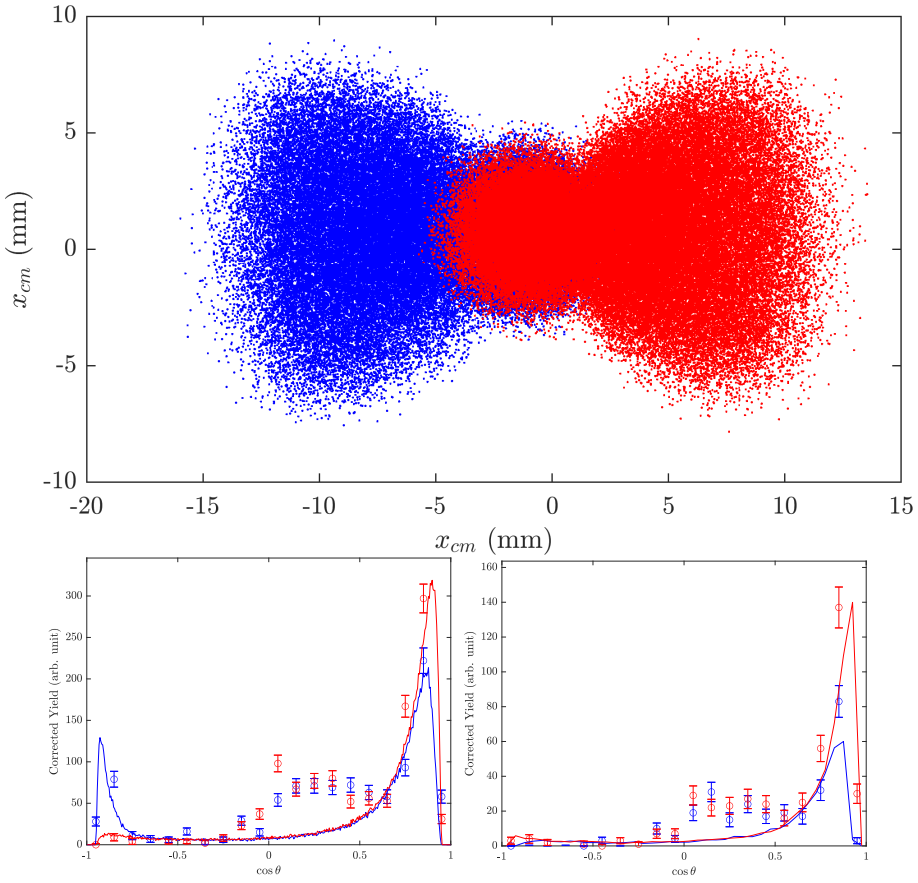

Figure B.1: Explanation of the apparent "backward scattering": The reaction is $Na^+(^1S)$ + $O^-(2p^5\ ^2P^o) \rightarrow Na(3p^2P)$ + $O(2p^4\ ^3P)$ for an average collision energy of 462 meV. The above figure shows the distribution of the center-of-mass given by the analysis of simulated events before selection of the correct mass combination by selection of the center-of-mass closest to the center of the distribution (see section 2.10). Each color shows a combination of masses. The lower figures show a comparison between the simulated partial differential cross sections (solid lines) and the experiment (circles) for each of the mass combinations (red and blue). These results are presented before the correction made by the acceptance of the detectors. The collision distribution is given by the section 4.2.1. The cross section is given by the interrupted Rutherford scattering model (section 4.3.2). The figure on the left shows the result for a fairly large cut of the center-of-mass (showing all the real events). The figure on the right shows the result of the simulation, when the cut-off along the center-of-mass no longer allows missattributions of masses to be occur.

It is easily reproduced by a simulation of the experimental events (time and position on the detectors), then by giving these events to the analysis program (see figure B.1).

The top of the figure represents the position of the center-of-mass after the simulated events are analyzed. It can be seen that if the mass allocation is correct, the center-of-mass is well defined. This center-of-mass coincides for each attribution of mass. However, two lobes are present in the figure, each assigned to a combination of mass given to the analysis program. In order to choose the right combination of mass, the program selects the one whose center-of-mass is closest to the center of the distribution.

The greater the mass ratio, the more these lobes are offset from the actual center-of-mass distribution. Thus, when the difference in mass is significant, this choice of the result makes it possible to obtain the right combination of mass, while avoiding double counting of events. However, in this case, the left lobe overlaps the actual distribution. The mass attribution might be is wrong. And since the angular distribution is inverted during the inversion of masses ($\vec{v}_r = \vec{v}_A - \vec{v}_B$), a peak appears in mirror. If the masses are the same, only one combination of mass is possible, the lobe coincides with the actual distribution. It is no longer possible to distinguish the two atoms: the angular distribution is symmetrical.

Let's note that the more the masses are different, the more these lobes move apart. The case of Na-O is a borderline case where the mass ratio of about 3/2 gives an effect only at the edges of the distribution. If the mass ratio is larger (eg He-D), the lobes are well separated from the actual center-of-mass distribution. Selecting the combination of mass amounts to selecting the events located within the actual center of the mass distribution.

To work around this problem, it is possible to make a selection on the center-of-mass much more radical (bottom right of the figure B.1). This cut effectively (almost) makes the mirror peak disappear. But at the cost of a significant drop in statistics. It was therefore chosen to keep the cut wide in the figure 5.8.

Appendix C

Theory: Derivation details

C.1 Collision dynamics: The Landau-Zener Model

C.1.1 Landau-Zener transition probability

By deriving equations 3.23, replacing the term $\partial C_{\text{ion}}/\partial t$ with equation 3.24 and replacing the term C_{ion} with the first, this system of equations is reduced to the following quadratic equation with only one variable

$$\frac{\partial^2 C_{\text{cov}}}{\partial t^2} + i\frac{E_{\text{cov}} - E_{\text{ion}}}{\hbar}\frac{\partial C_{\text{cov}}}{\partial t} + i\frac{E_{\text{ic}}^2}{\hbar^2}C_{\text{cov}} = 0 \tag{C.1}$$

or, with $f = E_{\text{ic}}/\hbar$:

$$\ddot{C}_{\text{cov}} + i\alpha t\dot{C}_{\text{cov}} + if^2 C_{\text{cov}} = 0 \tag{C.2}$$

This equation is the Sturm-Liouville equation whose solutions are expressed in the form of confluent hypergeometric functions. However, these functions have a node at $t = 0$. In order to take this effect into account, one method consists in expressing this equation in the form of the Weber equation.

One way to do this is to perform the following change of variable:

$$C_{\text{cov}}(t) = e^{-\frac{i}{2}\int_{-\infty}^{t}\alpha t\ \mathrm{d}t}U(t) \tag{C.3}$$

whose first and second derivatives are

$$\dot{C}_{\text{cov}} = e^{-\frac{i}{2}\int_{-\infty}^{t}\alpha t\ \mathrm{d}t}\left[\dot{U} - i\frac{\alpha t}{2}U\right] \tag{C.4}$$

and

$$\ddot{C}_{\text{cov}} = e^{-\frac{i}{2}\int_{-\infty}^{t}\alpha t\ \mathrm{d}t}\left[\ddot{U} - i\alpha t\dot{U} - \left(\frac{i\alpha t}{2} + \frac{\alpha^2 t^2}{4}\right)U\right] \tag{C.5}$$

which, once replaced in the differential equation C.1, gives:

$$\ddot{U}(t) + \left(\frac{\alpha^2 t^2}{4} - \frac{i\alpha t}{2} + f^2\right)U(t) = 0 \tag{C.6}$$

This equation is almost Weber's equation, it only remains to express it as a function of [1]:

$$z = \alpha^{1/2} \exp(-i\pi/4)t \tag{C.7}$$

and remember that $e^{\pm i\pi/2} = \pm i$, therefore:

$$\frac{\partial U}{\partial z} + \left(i\gamma + \frac{1}{2} - \frac{z^2}{4} \right) U = 0 \tag{C.8}$$

using $\gamma = f^2/\alpha$.

This equation is indeed the Weber equation as described by the Digital Library of Mathematical Functions (DLMF) of NIST in chapter §12.2 [171]. The solutions of this differential equation are the parabolic cylinders functions of the form:

$$U(-a, \pm iz) = U\left(i\gamma + \frac{1}{2}, \pm i\, \alpha^{1/2} \exp(-i\pi/4)t \right) \tag{C.9}$$

The asymptotic expansion of this function is given by the Poincarré expansion [171, §12.9], whose phases for which the expansion is valid are indicated by figure C.1,

$$U(a,z) \sim e^{-\frac{1}{4}z^2} z^{-a-\frac{1}{2}} \sum_{s=0}^{\infty} (-1)^s \frac{\left(\frac{1}{2}+a\right)_{2s}}{s!(2z^2)^s}, \tag{C.10}$$

if $|\text{ph } z| < 3\pi/4$ and

$$\begin{aligned} U(a,z) \sim\ & e^{-\frac{1}{4}z^2} z^{-a-\frac{1}{2}} \sum_{s=0}^{\infty} (-1)^s \frac{\left(\frac{1}{2}+a\right)_{2s}}{s!(2z^2)^s} \\ & \pm i \frac{\sqrt{2\pi}}{\Gamma\left(\frac{1}{2}+a\right)} e^{\mp i\pi a} e^{\frac{1}{4}z^2} z^{a-\frac{1}{2}} \sum_{s=0}^{\infty} \frac{\left(\frac{1}{2}-a\right)_{2s}}{s!(2z^2)^s}, \end{aligned} \tag{C.11}$$

if $\pi/4 < \pm\text{ph } z < 5\pi/4$. With $(a)_n$ the Pochhammer symbol [171, §5.2(iii)] which is equal to

$$\begin{aligned} (a)_0 &= 1 \\ (a)_1 &= a \\ &\cdots \\ (a)_n &= a(a+1)(a+2)\ldots(a+n-1) \end{aligned} \tag{C.12}$$

Since the zeroth-order of this asymptotic expansion is sufficient when $z \to \pm\infty$, the equations C.10 and C.11 become:

$$U(a,z) \sim e^{-\frac{z^2}{4}} z^{-a-\frac{1}{2}} \qquad \text{if} \qquad |\text{ph } z| < \frac{3\pi}{4}$$

[1] Otherwise, the second term of equation C.11 would not appears.

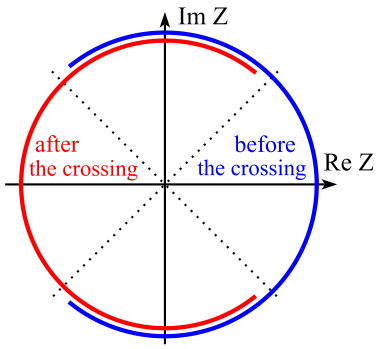

Figure C.1: Representation of the convergence domain of asymptotic development of hypergeometric cylinder functions. In blue, the domain of convergence of the equation C.10 (before the passage through the singularity). In red, the domain of convergence of the equation C.11 (after the passage through the singularity).

$$\sim e^{-\frac{z^2}{4}} z^{-a-\frac{1}{2}} \qquad \pm i \frac{\sqrt{2\pi}}{\Gamma\left(\frac{1}{2}+a\right)} e^{\mp i\pi a} e^{\frac{z^2}{4}} z^{a-\frac{1}{2}} \text{ if } \frac{\pi}{4} < \pm \text{ph } z < \frac{5\pi}{4} \tag{C.13}$$

In order to determine which asymptotic solution to choose, it is necessary to look at ph z according to time. As Weber's equation allows two possible solutions in the form of a parabolic cylinder function, the phase of z for each of these solutions as a function of the time is is determined unsing equation C.7:

$$+iz = +i\alpha^{1/2} e^{-i\pi/4}\, t = \alpha^{1/2} e^{i\pi/4}\, t \tag{C.14}$$

$$-iz = -i\alpha^{1/2} e^{-i\pi/4}\, t = \alpha^{1/2} e^{-i3\pi/4}\, t \tag{C.15}$$

For the second of these solutions (C.15), when $t < 0$ the asymptotic expansion is given by the equation C.10 . Whereas when $t > 0$, the asymptotic expansion is given by the equation C.11. This means that for this solution, the atoms move closer to each other, pass through a node of the function in the complex plane, and then move away.

The first solution (C.14) is traversed along the same axis as the first, but in the opposite direction. The atoms approaching would have already passed through the node, then turn back after it. This solution, even if it has a mathematical sense, does not describe the physics of the problem.

The solution given by the equation (C.15) describes the system. Its time-dependent expression - with a normalization parameter that satisfies the boundary conditions given in 3.20 - is for $t \to -\infty$:

$$A_{-}U(-a, \pm iz) = A_{-}U\left(i\gamma + \frac{1}{2}, i\,\alpha^{\frac{1}{2}} exp^{-i\frac{3\pi}{4}}\, t\right)$$

$$\sim A_- \left[\alpha^{-\frac{i\gamma}{2}} e^{\frac{i\pi}{4}} (-i)^{-i\gamma-1}\right] \left[\alpha^{-\frac{1}{2}} e^{-\frac{\pi\gamma}{4}}\right] \left[e^{-\frac{i\alpha}{4}t^2} t^{-i\gamma-1}\right] \quad \text{(C.16)}$$

The factors between the first brackets are constant normalized factors while the factors between the second brackets are real constant non-normalized factors.

In order to determine the constant A_-, it is necessary to introduce this solution in the equation 3.23 and to take the time derivative of C_{cov} (equation C.4),

$$|A_-|\, \alpha^{-\frac{1}{2}} e^{-\frac{\pi\gamma}{4}} \left| \frac{\mathrm{d}}{\mathrm{d}t} \left(e^{-i\frac{\alpha}{4}t^2} t^{-i\gamma-1} \right) - i\frac{\alpha t}{2} e^{-i\frac{\alpha}{4}t^2} t^{-i\gamma-1} \right| = |-if| \quad \text{(C.17)}$$

or again, once the differentiation is done and while simplifying when $t \to -\infty$,

$$\left| A_- \alpha^{-\frac{1}{2}} e^{-\frac{\pi\gamma}{4}} \left(-i\alpha e^{-i\frac{\alpha}{2}t^2} t^{-i\gamma} \right) \right| = |-if| \quad \text{(C.18)}$$

which gives the norm of the normalization parameter [2]:

$$|A_-| = \gamma^{1/2} e^{-\pi\gamma/4} \quad \text{(C.19)}$$

Now that the function which determines the population coefficient of the covalent state has been obtained, it remains only to determine its value for $t \to \infty$:

$$\begin{aligned} C_{\text{cov}}(t \to \infty) &= e^{-\frac{i}{2}\int_{-\infty}^{t} \alpha t \, \mathrm{d}t} A_- U \left(i\gamma + \frac{1}{2}, i\, \alpha^{\frac{1}{2}} exp^{-i\frac{3\pi}{4}}\, t \right) \\ &= e^{-\frac{i}{2}\int_{-\infty}^{t} \alpha t \, \mathrm{d}t} A_- \\ &\quad \left[\left(\alpha^{-\frac{i\gamma}{2}} e^{\frac{i\pi}{4}} (-i)^{-i\gamma-1} \alpha^{-\frac{1}{2}} e^{-\frac{\pi\gamma}{4}} \right) e^{-\frac{i\alpha}{4}t^2} t^{-i\gamma-1} \right. \\ &\qquad \left. - i\frac{\sqrt{2\pi}}{\Gamma(i\gamma+1)} e^{-\pi\gamma} e^{i\pi/2} e^{i\alpha t^2/4} \alpha^{i\gamma/2} e^{\pi\gamma/4} t^{i\gamma} \right] \end{aligned} \quad \text{(C.20)}$$

The first factor of the part in square brackets tends to 0 when $t \to \infty$. The probability of transition $P_{\text{i,c}}$ from the ionic state to the covalent state through an avoided crossing is given by:

$$P_{\text{i,c}} = \|C_{\text{cov}}(\infty)\|^2 \quad \text{(C.21)}$$

Thereby,

$$\begin{aligned} P_{\text{i,c}} &= \|C_{\text{cov}}(\infty)\|^2 \\ &= \left\| A_- \frac{\sqrt{2\pi}}{\Gamma(i\gamma+1)} e^{-3\pi\gamma/4} \right\|^2 \end{aligned}$$

[2] This solution is the same as that obtained using *WolframAlpha*. However, *WolframAlpha* does not indicate correct results for the asymptotic development of this function.

$$= \frac{2\pi\gamma e^{-\pi\gamma}}{\Gamma(1+i\gamma)\Gamma(1-i\gamma)} \tag{C.22}$$

In order to simplify this equation, it is useful to remember some relations related to the gamma function [171, §5.5]:

$$\text{Recurrence :} \qquad \Gamma(z+1) = z\Gamma(z) \tag{C.23}$$

$$\text{Reflection :} \qquad \Gamma(z)\Gamma(1-z) = \frac{\pi}{\sin\pi z} \tag{C.24}$$

Thereby,

$$\begin{aligned} P_{\text{i,c}} &= 2\pi\gamma e^{-\pi\gamma}\frac{1}{i\gamma}\frac{\sin i\gamma}{\pi} \\ &= 2e^{-\pi\gamma}\frac{1}{i}i\sinh\gamma \\ &= 2e^{-\pi\gamma}\frac{e^{\pi\gamma}-e^{-\pi\gamma}}{2} \\ &= 1-e^{-2\pi\gamma} \end{aligned} \tag{C.25}$$

C.1.2 Two-channel Landau-Zener cross section

The P_{ic} term is equation 3.59 of the cross section has no angular dependence, but depends on the impact parameter. Indeed – even if E_{ic} and ΔF are intrinsic parameters of the system: they are assumed to be independent of time and of the approach dynamics –, the radial speed term of the particle traversing the avoided crossing depends on the impact parameter [3]

$$v_R = v_{r,i}\sqrt{1-\frac{V(R_c)}{E_{r,i}}-\frac{b^2}{R_c^2}} \tag{C.26}$$

[3] Since the angular momentum $\vec{L}$ is conserved before the reaction

$$L = \mu v_{r,i} b = \mu R v_\theta$$

where v_θ is the tangent velocity. Therefore, by conservation of the energy of the system:

$$\begin{aligned} \frac{\mu}{2}v_{r,i}^2 = E_{r,i} &= \frac{\mu}{2}v^2 + V(R) \\ &= \frac{\mu}{2}\left(v_R^2+v_\theta^2\right)+V(R) \\ &= \frac{\mu}{2}\left(v_R^2+\frac{v_{r,i}^2 b^2}{R^2}\right)+V(R) \end{aligned}$$

where the potential energy $V(R)$ is negative, because the reaction is exothermic.

So, isolating v_R, this gives

$$v_R = v_{r,i}\sqrt{1-\frac{V(R_c)}{E_{r,i}}-\frac{b^2}{R_c^2}}$$

This equation shows that not all the trajectories of the incident particle allow it to approach the target particle for the reaction to take place. Indeed, if $b^2 > R_c^2(1-V(R_c)/E_{r,i})$, the minimum distance between the two particles is greater than the critical distance R_c. No reaction is possible. This allows the extent of the surface integral to be reduced depending on the impact parameter:

$$\sigma_{LZ} = 2\pi \int_0^{R_c^2(1-V(R_c)/E_{r,i})} \mathrm{d}b P_{\mathrm{tot}} \tag{C.27}$$

To solve this integral, one method is to perform the following change of variable

$$\frac{1}{x^2} = 1 - \frac{b^2}{R_c^2\,(1-V(R_c)/E_{r,i})} \tag{C.28}$$

thus

$$\frac{\mathrm{d}x}{x^3} = \frac{b\mathrm{d}b}{R_c^2\,(1-V(R_c)/E_{r,i})} \tag{C.29}$$

and the limits of integration are transformed as follows:

$$b \to \begin{cases} 0 \\ R_c^2\,(1-V(R_c)/E_{r,i}) \end{cases} \quad \text{becomes } x \to \begin{cases} 1 \\ 0 \end{cases} \tag{C.30}$$

The radial speed becomes:

$$\begin{aligned} v_R &= v_{r,i}\sqrt{1-\frac{V(R_c)}{E_{r,i}} - \frac{b^2}{R_c}\frac{1-V(R_c)/E_{r,i}}{1-V(R_c)/E_{r,i}}} \\ &= v_{r,i}\sqrt{1-\frac{V(R_c)}{E_{r,i}}}\sqrt{1-\frac{b^2}{R_c\,(1-V(R_c)/E_{r,i})}} \\ &= v_{r,i}\sqrt{1-\frac{V(R_c)}{E_{r,i}}}\cdot\frac{1}{x} \end{aligned} \tag{C.31}$$

Which gives a probability of transition

$$\begin{aligned} P_{\mathrm{i,c}} &= 1 - \exp\left(-\frac{2\pi E_{\mathrm{ic}}^2}{\hbar\Delta F}\frac{x}{v_{r,i}\sqrt{1-V(R_c)/E_{r,i}}}\right) \\ &= 1-\exp(-\zeta x) \end{aligned} \tag{C.32}$$

where

$$\zeta = \frac{2\pi E_{\mathrm{ic}}^2}{\hbar\Delta F v_{r,i}\sqrt{1-V(R_c)/E_{r,i}}} \tag{C.33}$$

Thus, with the assumption that the term

$$\sin^2\left(\frac{\vartheta_{\mathrm{ion}}-\vartheta_{\mathrm{cov}}}{2}\right) \simeq \frac{1}{2} \tag{C.34}$$

is averaged over the set of possible trajectories, the cross section becomes [253]:

$$\begin{aligned}\sigma_{LZ} &= 4\pi R_c^2 \left(1 - \frac{V(R_c)}{E_{r,i}}\right) \int_1^\infty e^{-\zeta x} \left(1 - e^{-\zeta x}\right) \frac{\mathrm{d}x}{x^3} \\ &= 4\pi R_c^2 \left(1 - \frac{V(R_c)}{E_{r,i}}\right) G(\zeta) \end{aligned} \tag{C.35}$$

The last integral $G(\zeta)$ can be solved numerically and is shown in figure 3.2.

To solve this integral, one must remember [254, §3.351.4]:

$$\int_u^\infty \frac{e^{-px}}{x^{n+1}} \mathrm{d}x = (-1)^{n+1} \frac{p^n \mathrm{Ei}(-pu)}{n!} + \frac{e^{-pu}}{u^n} \sum_{k=0}^{n-1} \frac{(-1)^k p^k u^k}{n(n-1)\dots(n-k)}, [p > 0] \tag{C.36}$$

with $\mathrm{Ei}(x) = -\int_{-t}^{\infty} e^{-t}/t$ the exponential integral. This function - non-analytical - is implemented in most scientific calculation software such as the first-order integral exponential $\mathrm{E}_1(x)$, $\mathrm{Ei}(x) = -\mathrm{E}_1(x) - i\pi$. In the case of MATLAB, $\mathrm{E}_1(x)$ matches `expint()`.

Thus, the integral of the equation 3.62 splits into two terms identical to the formula above with the parameters $u = 1$, $n = 2$, $p = \zeta$ or 2ζ, and then becomes

$$\int_1^\infty \frac{e^{-\zeta x}}{x^3} \mathrm{d}x = -\frac{\zeta^2}{2} \mathrm{Ei}(-\zeta) + e^{-\zeta} \left(\frac{1}{2} - \frac{\zeta}{2}\right) \tag{C.37}$$

Which is easy to implement.

C.1.3 Pedestrian approach of the multi-channel Landau-Zener model

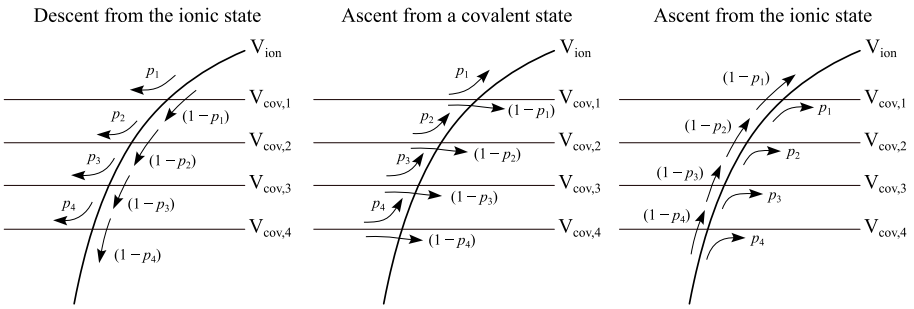

Figure C.2: List of possible paths during a mutual neutralization reaction for a system with four different covalent states.

Before giving a general formulation of this transition probability, it is interesting to tackle a particular case. A representation of the different possible crossings for $N = 4$ is presented in the figure C.2. Let us take in this case the probability that the pseudo-molecule ends in the state $i = 2$.

During the approach phase, it is necessary for the molecule to remain in the ionic state until it crosses the covalent state that we want to produce. Therefore, the total probability has a prefactor $(1 - p_1)$ in front of the rest of the reaction. Then, when crossing with the state 2, several possibilities exist. The first is to avoid the crossing (probability p_2) and then cross this same crossing (probability $1 - p_2$) during the return phase. The other consists of crossing this same crossing (probability $1 - p_2$), carrying out different paths (probability to define $\tilde{p}$) and finally avoiding this crossing during the return. Thus, the total probability of transition is temporarily

$$P_2 = (1 - p_1) \times p_2(1 - p_2) \times (1 + \tilde{p}) \tag{C.38}$$

where it remains to determine $\tilde{p}$ by observing the behavior for $n > 2$.

Thus for the level 3, if the crossing is avoided on the outward journey (probability p_3), it must also be avoided on the return (probability p_3). If the crossing is crossed (probability $1 - p_3$), it must also be crossed on the return (probability $1 - p_3$). Therefore, it is necessary to evaluate the interaction with the fourth level in a similar way: probability p_4^2 added to a probability $(1 - p_4)^2$ which includes that of the lower level. Since this lower level does not exist, the pseudo-molecule remains in the same state between the descent and the ascent (probability 1). Thus, the probability $\tilde{p}$ can be inserted in the preceding relation and gives

$$P_2 = (1 - p_1) \times p_2(1 - p_2) \times \left[1 + p_3^2 + (1 - p_3)^2(p_4^2 + 1)\right] \tag{C.39}$$

This expression can then be generalized for an arbitrary number of covalent states [255]

$$\begin{aligned}
P_i =& (1 - p_1)(1 - p_2) \cdots (1 - p_{i-1}) \\
& \times\ p_i(1 - p_i)\ \times\ \big[1 + \\
& \quad p_{i+1}^2 + (1 - p_{i+1})^2 p_{i+2}^2 + (1 - p_{i+1})^2 (1 - p_{i+2})^2 p_{i+3}^2 + \dots \\
& \quad \dots + (1 - p_{i+1})^2 \cdots (1 - p_{N-1})^2 p_N^2 + (1 - p_{i+1})^2 \cdots (1 - p_N)^2\big] \\
& & \text{if } i < N - 1 \\
=& (1 - p_1)(1 - p_2) \cdots (1 - p_{i-1}) \\
& \times\ p_i(1 - p_i)\ \times\ \left[1 + p_N^2 + (1 - p_N)^2\right] & \text{if } i = N - 1 \\
=& (1 - p_1)(1 - p_2) \cdots (1 - p_{i-1}) \\
& \times\ p_i(1 - p_i)\ \times\ \big[1 + 1\big] & \text{if } i = N
\end{aligned} \tag{C.40}$$

This pedestrian formulation is complex to implement by hand; it is advantageous to implement an expression based on a sum [4] :

$$\begin{aligned} P_i &= \left(\prod_{j=1}^{i}(1-p_j)\right) \times p_i \times \Big[1+p_{i+1}^2 \\ &\quad + \left(\sum_{j=i+1}^{N-1} p_{j+1}^2 \prod_{k=i+1}^{j}(1-p_k)^2\right) + \left(\prod_{j=i+1}^{N}(1-p_j)^2\right)\Big] \quad \text{if } i < N-1 \\ &= \left(\prod_{j=1}^{i}(1-p_j)\right) \times p_i \times \left[1+p_N^2+(1-p_N)^2\right] \quad \text{if } i = N-1 \\ &= \left(\prod_{j=1}^{i}(1-p_j)\right) \times p_i \times 2 \quad \text{if } i = N \end{aligned} \tag{C.42}$$

C.2 Interaction potential model: Anion Centered Asymptotic Model

C.2.1 Firsov surface integral

The first step consists in developing the Hamiltonian applied to adiabatic wavefunctions $H = \nabla^2/2 + V$ by considering on the one hand the kinetic term $\nabla^2/2$ and the set of potential terms, at any point of the integral. For a given interatomic distance, the latter depend only on the position of the electron. Therefore:

$$\psi_2^* V \psi_1 - \psi_1^* V \psi_2 = V\psi_2^*\psi_1 - V\psi_1^*\psi_2 = V\left(\psi_2^*\psi_1 - \psi_1^*\psi_2\right) = 0 \tag{C.43}$$

And so, for the entire Hamiltonian

$$\begin{aligned} &\psi_2^* H \psi_1 - \psi_1^* H \psi_2 \\ &= \psi_2^* \left(\frac{\nabla^2}{2} + V\right)\psi_1 - \psi_1^* \left(\frac{\nabla^2}{2} + V\right)\psi_2 \\ &= \psi_2^* \left(\frac{\nabla^2}{2}\right)\psi_1 - \psi_1^* \left(\frac{\nabla^2}{2}\right)\psi_2 + \psi_2^* V \psi_1 - \psi_1^* V \psi_2 \end{aligned}$$

[4] It is also possible to rewrite this equation as

$$P_i = \left(\prod_{j=1}^{i}(1-\bar{p}_j)\right) \times \bar{p}_i \times \Big[1+\bar{p}_{i+1}^2 + \left(\sum_{j=i+1}^{N} \bar{p}_{j+1}^2 \prod_{k=i+1}^{j}(1-\bar{p}_k)^2\right)\Big] \tag{C.41}$$

with $\bar{p}_j = p_j$ if $j = 1,\ldots N$ and $\bar{p}_{N+1} = 1$ and $\prod_0^{-1} = 1$ (If the product is not feasible, then it is 1). However, this second condition is difficult to implement numerically.

$$= \psi_2^* \left(\frac{\nabla^2}{2} \right) \psi_1 - \psi_1^* \left(\frac{\nabla^2}{2} \right) \psi_2 \tag{C.44}$$

As adiabatic wavefunctions are not easy to calculate, it is easier to re-express this integral in the diabatic basis using equation 3.73:

$$\begin{aligned}
&\psi_2^* \vec{\nabla} \psi_1 - \psi_1^* \vec{\nabla} \psi_2 \\
&= (-a_2 \psi_{\text{cov}}^* + a_1 \psi_{\text{ion}}^*) \vec{\nabla} (a_1 \psi_{\text{cov}} + a_2 \psi_{\text{ion}}) \\
&\quad - (a_1 \psi_{\text{cov}}^* + a_2 \psi_{\text{ion}}^*) \vec{\nabla} (-a_2 \psi_{\text{cov}} + a_1 \psi_{\text{ion}}) \\
&= -a_2 a_1 \psi_{\text{cov}}^* \vec{\nabla} \psi_{\text{cov}} + a_1^2 \psi_{\text{ion}}^* \vec{\nabla} \psi_{\text{cov}} \\
&\quad - a_2^2 \psi_{\text{cov}}^* \vec{\nabla} \psi_{\text{ion}} + a_1 a_2 \psi_{\text{ion}}^* \vec{\nabla} \psi_{\text{ion}} \\
&\quad + a_2 a_1 \psi_{\text{cov}}^* \vec{\nabla} \psi_{\text{cov}} - a_2^2 \psi_{\text{ion}}^* \vec{\nabla} \psi_{\text{cov}} \\
&\quad + a_1^2 \psi_{\text{cov}}^* \vec{\nabla} \psi_{\text{ion}} - a_1 a_2 \psi_{\text{ion}}^* \vec{\nabla} \psi_{\text{ion}} \\
&= (a_1^2 + a_2^2) \psi_{\text{ion}}^* \vec{\nabla} \psi_{\text{cov}} - (a_1^2 + a_2^2) \psi_{\text{cov}}^* \vec{\nabla} \psi_{\text{ion}} \\
&= \psi_{\text{ion}}^* \vec{\nabla} \psi_{\text{cov}} - \psi_{\text{cov}}^* \vec{\nabla} \psi_{\text{ion}}
\end{aligned} \tag{C.45}$$

It is therefore possible to use Green's theorem applied to volumes [171, §1.6E60] on the integral, which gives, including the three previous equations:

$$\begin{aligned}
J &\equiv \int_{\tilde{\mathscr{V}}} \psi_2^* H \psi_1 - \psi_1^* H \psi_2 \, \mathrm{d}\mathscr{V} \\
&= \frac{1}{2} \int_{\tilde{\mathscr{V}}} \psi_2^* \nabla^2 \psi_1 - \psi_1^* \nabla^2 \psi_2 \, \mathrm{d}\mathscr{V} \\
&= \frac{1}{2} \int_{\tilde{\mathscr{V}}} \left[\psi_2^* \nabla^2 \psi_1 + \left(\vec{\nabla} \psi_2^* \right) \cdot \left(\vec{\nabla} \psi_1 \right) \right] - \left[\psi_1^* \nabla^2 \psi_2 + \left(\vec{\nabla} \psi_1^* \right) \cdot \left(\vec{\nabla} \psi_2 \right) \right] \mathrm{d}\mathscr{V} \\
&= \frac{1}{2} \oint_S \left(\psi_2^* \vec{\nabla} \psi_1 - \psi_1^* \vec{\nabla} \psi_2 \right) \cdot \mathrm{d}\vec{S} \\
&= \frac{1}{2} \oint_S \left(\psi_{\text{ion}}^* \vec{\nabla} \psi_{\text{cov}} - \psi_{\text{cov}}^* \vec{\nabla} \psi_{\text{ion}} \right) \cdot \mathrm{d}\vec{S}
\end{aligned} \tag{C.46}$$

where the infinitesimal elements $\mathrm{d}\vec{S}$ are directed towards the interior of the closed surface S.

C.2.2 Angular momentum algebra identities

In order to be able to continue the reasoning, it is important to recall some identities related to the Clebsch-Gordan and to the Wigner $6-j$ symbols. First [153, eq. A.23]

$$\sum_{\substack{m_1, m_3 \\ m_{12}, m_{32} \\ m_2, m_{123}}} \begin{bmatrix} j_1 & j_2 & j_{12} \\ m_1 & m_2 & m_{12} \end{bmatrix} \begin{bmatrix} j_{12} & j_3 & j_{123} \\ m_{12} & m_3 & m_{123} \end{bmatrix}$$

$$\times \begin{bmatrix} j_3 & j_2 & j_{32} \\ m_3 & m_2 & m_{32} \end{bmatrix} \begin{bmatrix} j_{32} & j_1 & j_{123} \\ m_{32} & m_1 & m_{123} \end{bmatrix}$$
$$= (-1)^{2j_{123}}(2j_{123}+1)\left[(2j_{12}+1)(2j_{32}+1)\right]^{1/2} \begin{Bmatrix} j_1 & j_2 & j_{12} \\ j_3 & j_{123} & j_{32} \end{Bmatrix} \tag{C.47}$$

then [153, eq. A.17]

$$\begin{bmatrix} j_1 & j_2 & j_{12} \\ m_1 & m_2 & m_{12} \end{bmatrix} = (-1)^{j_1+j_2-j_{12}} \begin{bmatrix} j_2 & j_1 & j_{12} \\ m_2 & m_1 & m_{12} \end{bmatrix} \tag{C.48}$$

where $\left\{ \begin{smallmatrix} j_1 & j_2 & j_3 \\ j_4 & j_5 & j_6 \end{smallmatrix} \right\}$ are the Wigner $6-j$ symbols.

C.2.3 Coefficients of fractional parentage for excited states

If an atom is in an excited state, the configuration of which is the combination of two open shells

$$\left[(s_1 l_1)^{N_1} \ {}^{2S_1+1}L_1\right] \left[(s_2 l_2)^{N_2} \ {}^{2S_2+1}L_2\right] \ {}^{2S_{12}+1}L_{12}, \tag{C.49}$$

then the coefficients of fractional parentage between this state ${}^{2S_{12}+1}L_{12}$ and the state having one electron less

$$\left[(s_1 l_1)^{N_1} \ {}^{2S_1+1}L_1\right] \left[(s_2 l_2)^{N_2-1} \ {}^{2S'_2+1}L'_2\right] \ {}^{2S'_{12}+1}L'_{12}, \tag{C.50}$$

is given by[256] :

$$\begin{aligned} G^{S_{12},L_{12}}_{S'_{12},L'_{12}} &= (-1)^{l_2+L'_2+L_1+L_{12}} \sqrt{(2L_2+1)(2L'_{12}+1)} \begin{Bmatrix} l_2 & L'_2 & L_2 \\ L_1 & L_{12} & L'_{12} \end{Bmatrix} \\ &\times (-1)^{s_2+S'_2+S_1+S_{12}} \sqrt{(2S_2+1)(2S'_{12}+1)} \begin{Bmatrix} s_2 & S'_2 & S_2 \\ S_1 & S_{12} & S'_{12} \end{Bmatrix} \\ &\times G^{S_2,L_2}_{S'_2,L'_2}(l_2,N_2) \end{aligned} \tag{C.51}$$

Most of the neutralized cations are in a state where $N_2 = 1$ (i.e. $(A^+)n\ell$), therefore the atom is in the state: $\left[(s_1 l_1)^{N_1} \ {}^{2S_1+1}L_1\right] \left[s_2 l_2 \ {}^2 l_2\right] \ {}^{2S_{12}+1}L_{12}$, and the ion in the state: $\left[(s_1 l_1)^{N_1} \ {}^{2S_1+1}L_1\right] \left[\ {}^1S\right] \ {}^{2S'_{12}+1}L'_{12}$. Therefore, the coefficients of fractional parentage become:

$$\begin{aligned} &G^{S_{12},L_{12}}_{S_1,L_1}(l_2,N_2=1) \\ &= (-1)^{l_2+L_1+L_{12}} \sqrt{(2l_2+1)(2L_1+1)} \begin{Bmatrix} l_2 & 0 & l_2 \\ L_1 & L_{12} & L_1 \end{Bmatrix} \\ &\times (-1)^{1/2+S_1+S_{12}} \sqrt{2(2S_1+1)} \begin{Bmatrix} 1/2 & 0 & 1/2 \\ S_1 & S_{12} & S_1 \end{Bmatrix} \end{aligned} \tag{C.52}$$

with $G^{1/2,l_2}_{0,0}(l_2,1)=1$. Or, together with the above notation:

$$\begin{aligned}
&G^{S_{A0},L_{A0}}_{S_{A+},L_{A+}}(l_{A0},N_{A0}=1)\\
&=(-1)^{l_{A0}+L_{A+}+L_{A0}}\sqrt{(2l_{A0}+1)(2L_{A+}+1)}\left\{\begin{array}{ccc} l_{A0} & 0 & l_{A0}\\ L_{A+} & L_{A0} & L_{A+}\end{array}\right\}\\
&\times(-1)^{1/2+S_{A+}+S_{A0}}\sqrt{2(2S_{A+}+1)}\left\{\begin{array}{ccc} 1/2 & 0 & 1/2\\ S_{A+} & S_{A0} & S_{A+}\end{array}\right\}
\end{aligned} \tag{C.53}$$

This expression can be further simplified by using the relations of permutation of the $6-j$ symbols: Its value remains unchanged when two columns are permutated, and when the rows are permutated on two columns.

$$\left\{\begin{array}{ccc} l_{A0} & 0 & l_{A0}\\ L_{A+} & L_{A0} & L_{A+}\end{array}\right\}=\left\{\begin{array}{ccc} l_{A0} & l_{A0} & 0\\ L_{A+} & L_{A+} & L_{A0}\end{array}\right\}=\left\{\begin{array}{ccc} l_{A0} & L_{A+} & L_{A0}\\ L_{A+} & l_{A0} & 0\end{array}\right\} \tag{C.54}$$

Moreover,

$$\left\{\begin{array}{ccc} j_1 & j_2 & j_3\\ j_4 & j_5 & 0\end{array}\right\}=\frac{\delta_{j_2,j_4}\delta_{j_1,j_5}}{\sqrt{(2j_1+1)(2j_2+1)}}(-1)^{j_1+j_2+j_3}\{j_1\ \ j_2\ \ j_3\} \tag{C.55}$$

where $\{j_1\ \ j_2\ \ j_3\}$ is a triangular delta equal to 1 if $|j_1-j_2|\leq j_3\leq|j_1+j_2|$ and 0 otherwise.

Therefore

$$G^{S_{A0},L_{A0}}_{S_{A+},L_{A+}}(l_{A0},N_{A0}=1)=\{L_{A+}\ \ l_{A0}\ \ L_{A0}\}\{S_{A+}\ \ s_{A0}\ \ S_{A0}\} \tag{C.56}$$

Orbital angular momentum processing: Wigner-Witmer rule

During the approach phase between two atoms, the wavefunction is transformed into a molecular wavefunction – if only the multiplicity of states is taken into account – as follows

$$|\psi_A\psi_B\rangle=\sum_{\Lambda,S}\sqrt{\frac{(\#\Lambda)}{(2L_A+1)(2L_B+1)}\ \frac{(\#S)}{(2S_A+1)(2S_B+1)}}\,|\psi(\Lambda,S)\rangle \tag{C.57}$$

where $(\#\Lambda)$ and $(\#S)$ are the multiplicity factors given by Wigner and Witmer [257], more detailed in Mulliken [258] and Herzberg [259].

The spin multiplicity factor is trivial: The sum of the possible m_S. So:

$$(\#S)=(2S+1) \tag{C.58}$$

The orbital angular momentum is more complex to obtain. Indeed, the orbital angular momentum of the molecule in the ionic state L is not a quantum

number which defines the state of the molecule. It is the norm of the projection of this orbital angular momentum which defines the energy level of the molecule: When two atoms A and B – of orbital angular momenta L_A and L_B – approach each other, the interatomic axis forms a quantization axis. Each atom is then in a superposition of states (m_{LA} and m_{LB}) linked to the projection of its orbital angular momentum on this axis. Therefore, the orbital angular momentum of the molecule is given by $\tilde{\Lambda} = m_{LA} + m_{LB}$ and – as the energy of a state is given only by the absolute value of $\tilde{\Lambda}$ – this state is defined by:

$$\Lambda = |m_{LA} + m_{LB}| \tag{C.59}$$

In addition, there is a lifting of degeneracy for $\Lambda = 0$ which remains to be treated. By definition, the Σ states are in odd number. One corresponds to $m_{LA} = m_{LB} = 0$, whose symmetry is Σ^+ if $(-1)^{L_A+L_B+N_A l_A+N_B l_B} = 1$ and Σ^- otherwise. The other Σ states go in pairs. They are a linear combination of Σ^+ and Σ^-.

Thus, the possible set of Λ is obtained by combining all possible values of m_{LA} and m_{LB}. It remains to estimate the multiplicity of each of these states. One method is to go through the orbital angular momenta and estimate their number for each Λ.

The set of total orbital angular momenta is not infinite. Indeed, as the molecule is asymptotically two isolated atoms, the orbital angular momentum of the molecule L_{AB} can only be a combination of the orbital angular momenta of the two atoms L_A and L_B. Therefore:

$$L = |L_A - L_B|, \ldots, (L_A + L_B) \tag{C.60}$$

Moreover, since $\tilde{\Lambda}$ is the projection of L on the interatomic axis, $L \geq |\tilde{\Lambda}|$. So the previous relation becomes, for a given $\tilde{\Lambda}$:

$$L(\tilde{\Lambda}) = \max\left(|L_A - L_B|, |\tilde{\Lambda}|\right), \ldots, (L_A + L_B) \tag{C.61}$$

Using all this information (Wigner-Witmer rules), it is possible to evaluate the multiplicity of a Λ state by permutating the sums on L and Λ,

$$\sum_{L=|L_{A+}-L_{B-}|}^{L_{A+}+L_{B-}} \quad \sum_{\tilde{\Lambda}=-L}^{L} = \sum_{\Lambda=0}^{L_{A+}+L_{B-}} \quad \sum_{\substack{\tilde{\Lambda}=-\Lambda \\ (\Delta\tilde{\Lambda}=2\Lambda)}}^{\Lambda} \quad \sum_{L=\max(\Lambda,|L_{A+}-L_{B-}|)}^{L_{A+}+L_{B-}} \tag{C.62}$$

It remains to estimate the case of symmetries $\sigma = +, -$ (when $\Lambda = 0$). To achieve this, we must replace the term where $\Lambda = 0$ by

$$\sum_{L=|L_A-L_B|}^{L_A+L_B} \mod_2(\sigma' + N_A l_A + N_B l_B + L) \tag{C.63}$$

where $\sigma' = 1$ if $\sigma = +$ and $\sigma' = 0$ if $\sigma = -$ and $\mod_n(x)$ is the remainder of the Euclidean division of x by n.

C.2.4 Antisymmetrization and normalization of the molecular wavefunction

Antisymmetrization operator

To define the normalized and totally anti-symmetrized wavefunction of a molecule ψ in the asymptotic model, the idea is to start by building the wavefunction of the two atoms A and B which constitute the molecule. These wavefunctions ϕ_A and ϕ_B are normalized (and totally anti-symmetrized) separately. Therefore, the wavefunction of the molecule is

$$|\psi\rangle = \mathscr{N}\hat{A}\,|\phi_A\phi_B\rangle \tag{C.64}$$

where $\mathscr{N}$ is the normalization and $\hat{A}$ is the anti-symmetrization operator. This is expressed as

$$\hat{A}\,|\phi_A\phi_B\rangle = \sum_{g\in\mathscr{G}_{A\cup B}} (-1)^{n_g} g\,|\phi_A\phi_B\rangle \tag{C.65}$$

where g is an element of the permutation group $\mathscr{G}_{A\cup B}$ of two electrons (one attached to A, the other attached to B), and n_g is the electron exchange number of the permutation g.

The rest of the development takes into account only the valence electrons of atom A and atom B: The other electrons play a negligible role for normalization (this claim will be substantiated at the end of this section).

Moreover, before continuing, it is useful to detail these permutations: If we number the valence electrons of atom A from 1_A to N_A, and the electrons of atom B from 1_B to N_B, the permutation group of electrons can be written, for example for an atom A of $N_A = 3$ electrons

Atom A	Atom A	Atom A	Atom A	Atom A	Atom A
1_A	2_A	3_A	1_A	3_A	2_A
2_A	3_A	1_A	3_A	2_A	1_A
3_A	1_A	2_A	2_A	1_A	3_A

(C.66)

Therefore, each group of electrons has $N_A!$ possible combinations ($N_A!$ permutations). Likewise, the group of permutations $\mathscr{G}_{A\cup B}$ has $(N_A+N_B)!$ possible permutations. Each of these permutations can be rewritten (uniquely) as [260]:

$$g = P^{(\alpha),i}_{A\leftrightarrow B}\, g_A g_B \tag{C.67}$$

where g_A (g_B) is a permutation of electrons within the atom A (B) and $P^{(\alpha),i}_{A\leftrightarrow B}$ is one of the i possible permutations of α electrons between atom A and atom B.

For example, the permutation

$$\begin{array}{cc} \text{Atom } A & \text{Atom } B \\ 2_A & 3_A \\ 2_B & 1_B \\ 1_A & \end{array} \tag{C.68}$$

is equivalent to rearranging the elementary combination

$$\begin{array}{cc} \text{Atom } A & \text{Atom } B \\ 1_A & 1_B \\ 2_A & 2_B \\ 3_A & \end{array} \tag{C.69}$$

as follows (permutations g_A and g_B):

$$\begin{array}{cc} \text{Atom } A & \text{Atom } B \\ 2_A & 2_B \\ 3_A & 1_B \\ 1_A & \end{array} \tag{C.70}$$

then swap 2_B with 3_A (permutation $P^{(1),i}_{A\leftrightarrow B}$ where i is one of the permutations of a single electron) to get the combination above.

Thus, the equation C.65 becomes

$$\hat{A}_{ion}\,|\phi_A\phi_B\rangle = \sum_{g_A}\sum_{g_B}\sum_{\alpha,i}(-1)^{\alpha+n_{gA}+n_{gB}}P^{(\alpha),i}_{A\leftrightarrow B}g_Ag_B\,|\phi_A\phi_B\rangle \tag{C.71}$$

and since the wavefunctions ϕ_A and ϕ_B are already completely antisymmetric – in other words $g_Ag_B\,|\phi_A\phi_B\rangle = (-1)^{n_{gA}+n_{gB}}\,|\phi_A\phi_B\rangle$ –, the antisymmetrization of the wavefunction is written:

$$\hat{A}\,|\phi_A\phi_B\rangle = N_A!N_B!\sum_{\alpha,i}(-1)^{\alpha}P^{(\alpha),i}_{A\leftrightarrow B}\,|\phi_A\phi_B\rangle \tag{C.72}$$

Once reinjected into the molecular wavefunction (equation C.64), it is written:

$$|\psi\rangle = \mathscr{N}N_A!N_B!\sum_{\alpha,i}(-1)^{\alpha}P^{(\alpha),i}_{A\leftrightarrow B}\,|\phi_A\phi_B\rangle \tag{C.73}$$

Normalization of molecular wavefunction

Now that the antisymmetrization operator is properly defined, it is possible to normalize the molecular wavefunction

$$1 = \langle\psi|\psi\rangle$$

$$= (\mathscr{N} N_A! N_B!)^2 \sum_{\alpha,i} \sum_{\beta,j} (-1)^{\alpha+\beta} \langle \phi_A \phi_B | P_{A\leftrightarrow B}^{(\beta),j} P_{A\leftrightarrow B}^{(\alpha),i} | \phi_A \phi_B \rangle \tag{C.74}$$

In order to avoid the technicality of the development used by Kleinekathöfer [260], it is interesting to dwell on the meaning of this equation: it evaluates the overlap of the wavefunction of each electron of the bra with its equivalent given on the ket. For example

$$\left\langle \begin{array}{ccc|cc} \text{Atom } A & \text{Atom } B & & \text{Atom } A & \text{Atom } B \\ 1_A & 1_B & & 2_A & 3_A \\ 2_A & 2_B & & 2_B & 1_B \\ 3_A & & & 1_A & \end{array} \right\rangle \tag{C.75}$$

amounts to calculate

$$\langle 1_A | 2_A \rangle \langle 2_A | 2_B \rangle \langle 3_A | 1_A \rangle \langle 1_B | 3_A \rangle \langle 1_B | 1_B \rangle . \tag{C.76}$$

As the order of the brakets does not influence the result, it is then not difficult to convince oneself that for each combination of the bra (of the equation C.75), there is a ket which gives the same result (for the equation C.76). Thus, since there exists a number $C_{N_A}^{N_A+N_B}$ of possible permutations on the bra, the equation C.74 becomes:

$$\begin{aligned} 1 &= \langle \psi | \psi \rangle \\ &= (\mathscr{N} N_A! N_B!)^2 C_{N_A}^{N_A+N_B} \sum_{\alpha,i} (-1)^{\alpha} \langle \phi_A \phi_B | P_{A\leftrightarrow B}^{(\alpha),i} | \phi_A \phi_B \rangle \end{aligned} \tag{C.77}$$

Moreover, all the electrons of the same valence shell are similar (1_A, 2_A and 3_A or 1_B and 2_B in the example). Thus, each number of interatomic permutations of α electrons gives a similar result. Since there are $C_\alpha^{N_A} C_\alpha^{N_B}$ possible exchange combinations of α electrons and all these permutations lead to the same result, let us define $P_{A\leftrightarrow B}^{(\alpha)}$ as representing the exchanges $(1_A, 1_B)(2_A, 2_B) \ldots (\alpha_A, \alpha_b)$. Thus, the previous equation reduces to:

$$\begin{aligned} 1 &= \langle \psi | \psi \rangle \\ &= (\mathscr{N} N_A! N_B!)^2 C_{N_A}^{N_A+N_B} \sum_{\alpha=0}^{\min(N_A,N_B)} (-1)^{\alpha} C_\alpha^{N_A} C_\alpha^{N_B} \langle \phi_A \phi_B | P_{A\leftrightarrow B}^{(\alpha)} | \phi_A \phi_B \rangle \end{aligned} \tag{C.78}$$

It remains only to evaluate each term resulting from the sum. To achieve this, we must once again remember the meaning of $\langle \phi_A \phi_B | P_{A\leftrightarrow B}^{(\alpha)} | \phi_A \phi_B \rangle$: This term evaluates individually the overlap of each electron of the bra with its equivalent (after permutation) of the ket. Thus, by taking up the reasoning carried out during C.76: If an electron is on the same atom after permutation then the overlap is 1 (because atomic orbitals are normalized) . On the other

hand, if the electron is on another atom after permutation, then the overlap is given by the overlap of the wavefunction before permutation and after atom permutation. In the framework of the asymptotic model, the overlap of two wavefunctions of electrons located on two different atoms is assumed to be very low [5]. Therefore,

$$\langle\phi_A\phi_B|\,P^{(0)}_{A\leftrightarrow B}\,|\phi_A\phi_B\rangle >> \langle\phi_A\phi_B|\,P^{(1)}_{A\leftrightarrow B}\,|\phi_A\phi_B\rangle >> \langle\phi_A\phi_B|\,P^{(2)}_{A\leftrightarrow B}\,|\phi_A\phi_B\rangle >> \dots \tag{C.80}$$

Additionally, when no electron permutation is applied (and using the fact that atomic wavefunctions are normalized), the 0-order term is given by:

$$\langle\phi_A\phi_B|\,P^{(0)}_{A\leftrightarrow B}\,|\phi_A\phi_B\rangle = 1, \tag{C.81}$$

Therefore, the normalization of the wavefunction becomes:

$$\begin{aligned} 1 &= \langle\psi|\psi\rangle \\ &\simeq (\mathscr{N}N_A!N_B!)^2\, C_{N_A}^{N_A+N_B}\left[1 - N_A N_B\,\langle\phi_A\phi_B|\,P^{(1)}_{A\leftrightarrow B}\,|\phi_A\phi_B\rangle + \dots\right] \\ &\simeq (\mathscr{N}N_A!N_B!)^2\, C_{N_A}^{N_A+N_B} \end{aligned} \tag{C.82}$$

hence

$$\mathscr{N} \simeq \frac{\left(C_{N_A}^{N_A+N_B}\right)^{-1/2}}{N_A!N_B!} = \sqrt{\frac{1}{N_A!N_B!(N_A+N_B)!}}. \tag{C.83}$$

[5] The evaluation of this overlap can be estimated within the framework of the asymptotic model. To achieve this, we have to take the equation 3.132 and replace the Wronskian term with a radial integral:

$$\begin{aligned} \left\langle \phi_{cov}^{l_{A0},m_{mlA0}} \middle|\, \phi_{ion}^{l_{B^-},m_{mlB^-}} \right\rangle \simeq & \\ & -\frac{1}{2}\int_{-1}^{1} \mathrm{d}\cos\theta_B \int_0^{2\pi} \mathrm{d}\varphi_B \;\; Y_{l_B,m_B}(\theta_B,\varphi_B) Y_{l,m_A}(\theta_B,\varphi_B) \\ & \times \frac{\gamma_A(2\gamma_A)^{1/\gamma_A} R^{-1+1/\gamma_{A0}} \exp(-\gamma_{A0}R)}{\sqrt{\Gamma\left(\gamma_A^{-1}+l_A+1\right)\Gamma\left(\gamma_A^{-1}-l_A\right)}} \frac{N_{B^-}\gamma_B}{(2\beta R)^{|m_A|}\;|m_A|!} \sqrt{(2l_A+1)\frac{(l_A+|m_A|)!}{(l_A-|m_A|)!}} \\ & \times \sum_{l=|m_A|}^{\infty} \sqrt{(2l+1)\frac{(l+|m_A|)!}{(l-|m_A|)!}} \int_0^{\infty} \mathrm{d}r_B \;\; \frac{2r_B^2}{\pi}\mathsf{k}_{l_B}(\gamma_B r_B)\left(\mathsf{i}_l^{(2)}(\beta r_B) + \frac{C_l}{\pi}\mathsf{k}_l(\beta r_B)\right) \end{aligned} \tag{C.79}$$

where the result of the integral of Bessel functions is obtained using tables of integrals.

Assuming that this is unitary, it is easy to see that in the framework of the asymptotic model ($\gamma_{A0}R >> 1$), this term becomes exponentially small. However, it would be interesting to add this term to the normalization of the wavefunction in order to obtain a first order correction.

Normalization applied to ionic and covalent wavefunctions

This equation applied to the covalent state gives

$$\mathscr{N}_{cov} \simeq \sqrt{\frac{1}{N_{A0}!N_{B0}!(N_{A0}+N_{B0})!}}. \tag{C.84}$$

and for the ionic state, the equation gives

$$\mathscr{N}_{ion} \simeq \sqrt{\frac{1}{N_{A+}!N_{B-}!(N_{A+}+N_{B-})!}}. \tag{C.85}$$

Note that the result is effectively identical when the ion wavefunction is subdivided into three components $(\phi_{A+})(\phi_{B0}\phi_{ion})$. Indeed, it is possible to decompose g_{B^-}. Therefore:

$$g_{A^+\cup B^-} = P^{(\alpha),i}_{A+\leftrightarrow B^-}\left(P^{(\beta),j}_{B^0\leftrightarrow e^-} g_{B^0} g_{e^-}\right) g_{A^+} \tag{C.86}$$

where g_e is the set of permutations of the isolated electron with itself.

Since B^- is totally antisymmetric, $P^{(\alpha),i}_{B^0\leftrightarrow e^-}|\phi_{B0}\phi_{ion}\rangle = (-1)^\alpha|\phi_{B0}\phi_{ion}\rangle$, with $C^{N_{B0}+1}_1 = N_{B^-}$ equivalent possible permutations (as all these permutations are equivalent, the hypothesis C.80 is not valid). Therefore,

$$\sum_{\alpha',i'}\sum_{\alpha,i}\langle\phi_{B0}\phi_{ion}|P^{(\alpha'),i'}_{B^0\leftrightarrow e^-}P^{(\alpha),i}_{B^0\leftrightarrow e^-}|\phi_{B0}\phi_{ion}\rangle = N^2_{B^-}\langle\phi_{B0}\phi_{ion}|\phi_{B0}\phi_{ion}\rangle \tag{C.87}$$

Thus, the normalization of the ionic state is written, remembering that $N!(N+1) = (N+1)!$:

$$\begin{aligned}
1 &= \langle\psi_{ion}|\psi_{ion}\rangle \\
&\simeq \mathscr{N}^2_{ion}\left[C^{N_{A+}+N_{B-}}_{N_{A+}}(1-\ldots)\right](N_{B-})^2 N_{B0}!^2 N_{A+}!^2 \\
&\simeq \mathscr{N}^2_{ion} N_{A+}!^2 N_{B-}!^2 C^{N_{A+}+N_{B-}}_{N_{A+}}
\end{aligned} \tag{C.88}$$

and leads to the same result for the normalization of the wavefunction.

Before continuing, one point is important to note: No matter what steps are used to decompose the permutations of the wavefunction, the normalization should always be the same. Thus, if the set of permutations initially separates the isolated electron then the atoms:

$$g_{A^+\cup B^-} = P^{(\alpha),i}_{A^+B^0\leftrightarrow e^-}\left(P^{(\beta),j}_{A^+\leftrightarrow B^0}\, g_{A^+} g_{B^0}\right) g_{e^-}, \tag{C.89}$$

the normalization must be identical. Therefore, by developing

$$1 = \langle\psi_{ion}|\psi_{ion}\rangle$$

$$
\begin{aligned}
&\simeq \mathcal{N}_{ion}^2 \left[C_{N_{A+}}^{N_{A+}+N_{B0}} (1-\ldots) \right] N_{B0}!^2 N_{A+}!^2 \\
&\quad \times \sum_{\alpha',i'} \sum_{\alpha,i} \langle \phi_{A+}\phi_{B0}\phi_{ion} | \, P^{(\alpha)',i'}_{A^+B^0\leftrightarrow e^-} P^{(\alpha),i}_{A^+B^0\leftrightarrow e^-} \, | \phi_{A+}\phi_{B0}\phi_{ion} \rangle \\
&= \mathcal{N}_{ion}^2 (N_{A+}+N_{B0})! N_{B0}! N_{A+}! \\
&\quad \times \sum_{\alpha',i'} \sum_{\alpha,i} \langle \phi_{A+}\phi_{B0}\phi_{ion} | \, P^{(\alpha)',i'}_{A^+B^0\leftrightarrow e^-} P^{(\alpha),i}_{A^+B^0\leftrightarrow e^-} \, | \phi_{A+}\phi_{B0}\phi_{ion} \rangle \,, \qquad \text{(C.90)}
\end{aligned}
$$

it is found that

$$
\sum_{\alpha',i'} \sum_{\alpha,i} \langle \phi_{A+}\phi_{B0}\phi_{ion} | \, P^{(\alpha'),i'}_{A^+B^0\leftrightarrow e^-} P^{(\alpha),i}_{A^+B^0\leftrightarrow e^-} \, | \phi_{A+}\phi_{B0}\phi_{ion} \rangle \equiv N_{B-} \, (N_{A+}+N_{B-}) \qquad \text{(C.91)}
$$

This result can be explained by the following reasoning: On the one hand, the double permutation gives a term $C_1^{N_{A+}+N_{B0}+1}$ (each permutation on the bra corresponds to a permutation on the ket). Then, since the relation C.80 is not always valid, the expansion according to the permutations is written as

$$
\sum_{\alpha,i} (-1)^{\alpha} P^{(\alpha),i}_{A^+B^0\leftrightarrow e^-} = P^{(0)}_{A^+B^0\leftrightarrow e^-} - C_1^{N_{B0}} C_1^1 P^{(1)}_{B^0\leftrightarrow e^-} - C_1^{N_{A+}} C_1^1 P^{(1)}_{A^+\leftrightarrow e^-} \qquad \text{(C.92)}
$$

Therefore, neglecting the permutation term between the isolated electron and the ion A^+ and using $P^{(1)}_{B^0\leftrightarrow e^-} |\phi_{A+}\phi_{B0}\phi_{ion}\rangle = -|\phi_{A+}\phi_{B0}\phi_{ion}\rangle$ because B^- is totally antisymmetric, the term N_{B-} appears. Note that the exchange between the isolated electron and an electron of B^0 is always possible, because this permutation operator is applied after the exchange of electrons between A^+ and B^0 as well as the permutations within these two valence shells.

Antisymmetrization of ionic and covalent wavefunctions

The normalization described above does not take into account the decomposition according to the different atomic and molecular angular momenta. When these are taken into account, the wavefunction of the ionic state given by the combined equations 3.97 and 3.98 is of the form:

$$
|\psi_{ion}\rangle = \mathcal{N} N_{A+}! N_{B-}! \hat{A} \sum [\cdots] \, |\phi_{A^+}\phi_{B^-}\phi_{ion}\rangle \qquad \text{(C.93)}
$$

where $[\cdots]$ includes all the other factors related to the different atomic and molecular angular momenta. It is then possible to develop the antisymmetrization operator by using the decomposition of the groups of permutations given by the equation C.67

$$
g_{A^+B^-} = P^{(\alpha),i}_{A^+B^0\leftrightarrow e^-_{ion}} \; g_{A^+B^0} g_{e^-} = P^{(\alpha),i}_{A^+B^0\leftrightarrow e^-_{ion}} \left[P^{(\beta),j}_{A^+\leftrightarrow B^0} \; g_{A^+} g_{B^0} \right] g_{e^-}, \qquad \text{(C.94)}
$$

the wavefunction of the ionic state becomes:

$$\begin{aligned}|\psi_{ion}\rangle &= \sum[\cdots]\mathscr{N}_{ion}\hat{A}\,|\phi_{A^+}\phi_{B^-}\phi_{ion}\rangle \\ &= \sum[\cdots]\mathscr{N}_{ion}\sum_{g_{ion}\in A^+\cup B^-}(-1)^{n_{gion}}g_{ion}\,|\phi_{A^+}\phi_{B^-}\phi_{ion}\rangle \\ &= \sum[\cdots]\mathscr{N}_{ion}\sum_{g_{ion}}(-1)^{n_{gion}}P^{(\alpha),i}_{A^+B^0\leftrightarrow e^-_{ion}}\left[P^{(\beta),j}_{A^+\leftrightarrow B^0}\;g_{A^+}g_{B^0}\right]g_{e^-}\,|\phi_{A^+}\phi_{B^-}\phi_{ion}\rangle\end{aligned} \tag{C.95}$$

where $\mathscr{N}_{ion}$ is the normalization of the ion wavefunction obtained according to the method established previously. Since the wavefunctions of A^+ and B^- are totally antisymmetric and the separated electron only permutes with itself, then:

$$\begin{aligned}|\psi_{ion}\rangle = &\sum[\cdots]\mathscr{N}_{ion}N_{A+}!N_{B-}! \\ &\times\sum_{\alpha,i}\sum_{\beta,j}(-1)^{\alpha+\beta}P^{(\alpha),i}_{A^+B^0\leftrightarrow e^-_{ion}}\;P^{(\beta),j}_{A^+\leftrightarrow B^0}\;|\phi_{A^+}\phi_{B^-}\phi_{ion}\rangle\end{aligned} \tag{C.96}$$

The same reasoning applies to the wavefunction of the covalent state, this one gives:

$$\begin{aligned}|\psi_{cov}\rangle = &\sum[\cdots]\mathscr{N}_{cov}N_{A+}!N_{B-}! \\ &\times\sum_{\alpha,i}\sum_{\beta,j}(-1)^{\alpha+\beta}P^{(\alpha),i}_{A^+B^0\leftrightarrow e^-_{cov}}\;P^{(\beta),j}_{A^+\leftrightarrow B^0}\;|\phi_{A^+}\phi_{B^-}\phi_{ion}\rangle\end{aligned} \tag{C.97}$$

It is then possible to evaluate the interaction term:

$$\begin{aligned}E_{ic} &= \langle\psi_{ion}|\,H\,|\psi_{cov}\rangle \\ &= \sum_{ion}\sum_{cov}[\cdots]_{ion}[\cdots]_{cov}\times\mathscr{N}_{ion}\mathscr{N}_{cov}(N_{A+}!N_{B0}!)^2 \\ &\times\sum_{\alpha,i}\sum_{\beta,j}\sum_{\alpha',i'}\sum_{\beta',j'}(-1)^{\alpha+\beta+\alpha'+\beta'} \\ &\quad\langle\phi_{A^+}\phi_{B^0}\phi_{ion}|\,P^{(\beta),j}_{A^+\leftrightarrow B^0}\;P^{(\alpha),i}_{A^+B^0\leftrightarrow e^-_{ion}}\;HP^{(\alpha'),i'}_{A^+B^0\leftrightarrow e^-_{cov}}\;P^{(\beta'),j'}_{A^+\leftrightarrow B^0}\;|\phi_{A^+}\phi_{B^0}\phi_{ion}\rangle\end{aligned} \tag{C.98}$$

As the permutation operators commute with the Hamiltonian operator, it is possible to apply the same logic used for the normalization (passing from C.74 to C.77).

$$\begin{aligned}\langle\psi_{ion}|\,H\,|\psi_{cov}\rangle = &\sum_{ion}\sum_{cov}[\cdots]_{ion}[\cdots]_{cov}\times\mathscr{N}_{ion}\mathscr{N}_{cov}(N_{A+}!N_{B0}!)^2 \\ &\times C^{N_{A+}+N_{B0}}_{N_{A+}}\left[\sum_{\beta}(-1)^{\beta}C^{N_{A+}}_{\beta}C^{N_{A+}}_{\beta}\;\langle\phi_{A^+}\phi_{B^0}|\,P^{(\beta)}_{A^+\leftrightarrow B^0}\;|\phi_{A^+}\phi_{B^0}\rangle\right]\end{aligned}$$

$$\begin{aligned}
&\times \sum_{\alpha,i}\sum_{\alpha',i'}(-1)^{\alpha+\alpha'}\,\langle\phi_{ion}|\,P^{(\alpha),i}_{A^+B^0\leftrightarrow e^-_{ion}}\,HP^{(\alpha'),i'}_{A^+B^0\leftrightarrow e^-_{cov}}\,|\phi_{cov}\rangle \\
\simeq &\sum_{ion}\sum_{cov}[\cdots]_{ion}[\cdots]_{cov}\times\mathscr{N}_{ion}\mathscr{N}_{cov}(N_{A+}!N_{B0}!)^2C^{N_{A+}+N_{B0}}_{N_{A+}} \\
&\times \sum_{\alpha,i}\sum_{\alpha',i'}(-1)^{\alpha+\alpha'}\,\langle\phi_{ion}|\,P^{(\alpha),i}_{A^+B^0\leftrightarrow e^-_{ion}}\,HP^{(\alpha'),i'}_{A^+B^0\leftrightarrow e^-_{cov}}\,|\phi_{cov}\rangle
\end{aligned} \tag{C.99}$$

taking only the zero-th order of the expansion according to α.

Thus, only the following term $\langle\phi_{ion}|\,P''^{(\beta')}_{j'}HP''^{(\beta)}_{j}\,|\phi_{cov}\rangle$ remains to be determined. To achieve this, let us take the example given above – A^+ has 3 valence electrons and B^0 has only one valence electron – by naming each of the possible permutations (arbitrarily):

$$a:\left|\begin{matrix}1_A & 1_B\\ 2_A & 1_e\\ 3_A & \end{matrix}\right\rangle;b:\left|\begin{matrix}1_A & 1_e\\ 2_A & 1_B\\ 3_A & \end{matrix}\right\rangle;c:\left|\begin{matrix}1_e & 1_B\\ 2_A & 1_A\\ 3_A & \end{matrix}\right\rangle;d:\left|\begin{matrix}1_A & 1_B\\ 1_e & 2_A\\ 3_A & \end{matrix}\right\rangle;e:\left|\begin{matrix}1_A & 1_B\\ 2_A & 3_A\\ 1_e & \end{matrix}\right\rangle \tag{C.100}$$

and

$$a':\left|\begin{matrix}1_A & 1_B\\ 2_A & \\ 3_A & \\ 1_e & \end{matrix}\right\rangle;b':\left|\begin{matrix}1_A & 1_e\\ 2_A & \\ 3_A & \\ 1_B & \end{matrix}\right\rangle;c':\left|\begin{matrix}1_e & 1_B\\ 2_A & \\ 3_A & \\ 1_A & \end{matrix}\right\rangle;d':\left|\begin{matrix}1_A & 1_B\\ 1_e & \\ 3_A & \\ 2_A & \end{matrix}\right\rangle;e':\left|\begin{matrix}1_A & 1_B\\ 2_A & \\ 1_e & \\ 3_A & \end{matrix}\right\rangle \tag{C.101}$$

Thus, the interaction term is non-zero if the permutation on ϕ_{ion} exchanges 1_e with an electron of B_0 and if the permutation on ϕ_{cov} exchanges 1_e with an electron of A^+. Therefore, the interaction term following these permutations is (following every possible permutation):

$$\langle\phi_{ion}|\,P^{(\alpha),i}_{A^+B^0\leftrightarrow e^-_{ion}}\,HP^{(\alpha'),i'}_{A^+B^0\leftrightarrow e^-_{cov}}\,|\phi_{cov}\rangle = \left[\begin{array}{c|ccccc} & a' & b' & c' & d' & e' \\ \hline a & \tilde{E}_{ic} & \sim 0 & \tilde{E}_{ic} & \tilde{E}_{ic} & \tilde{E}_{ic} \\ b & \tilde{E}_{ic} & \sim 0 & \tilde{E}_{ic} & \tilde{E}_{ic} & \tilde{E}_{ic} \\ c & \sim 0 & \sim 0 & \sim 0 & \sim 0 & \sim 0 \\ d & \sim 0 & \sim 0 & \sim 0 & \sim 0 & \sim 0 \\ e & \sim 0 & \sim 0 & \sim 0 & \sim 0 & \sim 0 \end{array}\right] \tag{C.102}$$

We then see that there exists $(N_{B0}+1)(N_{A+}+1)$ permutations of non-zero value.

In addition, we must not forget that all these terms are initially mixed (as in the reasoning applied to the normalization of the wavefunction). This mixture of states then brings $(N_{A+}+N_{B0}+1)$ equivalent terms for each of the permutations indicated above. Which give :

$$\sum_{\alpha,i}\sum_{\alpha',i'}(-1)^{\alpha+\alpha'}\,\langle\phi_{ion}|\,P^{(\alpha),i}_{A^+B^0\leftrightarrow e^-_{ion}}\,HP^{(\alpha'),i'}_{A^+B^0\leftrightarrow e^-_{cov}}\,|\phi_{cov}\rangle$$

$$\simeq (N_{B0}+1)(N_{A+}+1)(N_{A+}+N_{B0}+1)\,\langle\phi_{ion}|\,H\,|\phi_{cov}\rangle \tag{C.103}$$

And by combining the previous equations, and remembering $N_{A+}+1=N_{A0}$ and $N_{B0}+1=N_{B-}$:

$$\begin{aligned}
\langle\psi_{ion}|\,H\,|\psi_{cov}\rangle =& \sum_{ion}\sum_{cov}[\cdots]_{ion}[\cdots]_{cov} \\
& \times \mathscr{N}_{ion}\mathscr{N}_{cov}\ \ (N_{A+}!N_{B0}!)^2\ \ C_{N_{A+}}^{N_{A+}+N_{B0}} \\
& \times N_{A0}\ N_{B-}\ (N_{A+}+N_{B0}+1)\,\langle\phi_{ion}|\,H\,|\phi_{cov}\rangle \\
=& \sum_{ion}\sum_{cov}[\cdots]_{ion}[\cdots]_{cov} \\
& \times \sqrt{\left(\frac{1}{N_{A+}!N_{B-}!(N_{A+}+N_{B-})!}\right)\left(\frac{1}{N_{A0}!N_{B0}!(N_{A0}+N_{B0})!}\right)} \\
& \times (N_{A+}!N_{B0}!)^2\left(\frac{(N_{A+}+N_{B0})!}{N_{A+}!N_{B0}!}\right) \\
& \times N_{A0}\ N_{B-}\ (N_{A+}+N_{B0}+1)\,\langle\phi_{ion}|\,H\,|\phi_{cov}\rangle \\
=& \sum_{ion}\sum_{cov}[\cdots]_{ion}[\cdots]_{cov} \\
& \times \sqrt{N_{A0}\ N_{B-}}\,\langle\phi_{ion}|\,H\,|\phi_{cov}\rangle
\end{aligned} \tag{C.104}$$

which is the result obtained by Nikitin [153] [6] and allows to establish the factor

$$A_{antisym} = \sqrt{N_{A0}N_{B-}} \tag{C.105}$$

defined in equation 3.107.

Core electrons effect

A final aspect of development remains to be clarified: The fact that only valence electrons are taken into account during this development. However, taking into account the other shells does not change the result obtained here. To be convinced of this, we can remember that any permutation group can be decomposed according to the relation C.67. Thus, if ϕ_{core} represents the wavefunction of the set of core electrons of the two atoms A and B (as opposed to valence electrons), the set of permutations of electrons of the molecule g_{mol} can be written in the form

$$g_{mol} = P_i^{c-v:(\alpha)}\,g_{val}\,g_{core} \tag{C.106}$$

[6] This result is similar to that presented (without detail) for two similar atoms by Duman and Smirnov [261, 262] then extended by transforming the number of valence electrons "N" for two identical atoms into "$\sqrt{N_{A0}N_{B-}}$" by Smirnov in 1973 [263], the result of which is taken up by Nikitin [153]. The latter serves as a reference (other articles and books are written in Russian).

where $P_i^{c-v:(\alpha)}$ is the permutation operator of α electrons between one of the valence shells and one of the core shells. The treatment of g_{val} is treated in detail above, it only remains to process the permutations of cores and the permutations between the cores and the valence layers.

Nevertheless, it is not necessary to treat them in detail: As the configurations of the cores are identical for the ionic state and the covalent state, their contributions in $\langle \psi_{ion} | \psi_{ion} \rangle$, $\langle \psi_{cov} | \psi_{cov} \rangle$ and $\langle \psi_{ion} | H | \psi_{cov} \rangle$ are identical. Thus, once placed in the equation C.104, this contribution adds a term

$$\frac{\langle \psi_{ion,core} | H | \psi_{cov,core} \rangle}{\sqrt{\langle \psi_{ion,core} | \psi_{ion,core} \rangle \langle \psi_{cov,core} | \psi_{cov,core} \rangle}} = 1 \tag{C.107}$$

which is omitted in the development (for better readability).

The same argument applies for $P_i^{c-v:(\alpha)}$. Indeed, it breaks down into two components during the evaluation of

$$\sum_{\alpha,i} \sum_{\beta,j} \left\langle \psi_{ion,core} | P_j^{c-v:(\beta)} P_i^{c-v:(\alpha)} | \psi_{ion,core} \right\rangle \tag{C.108}$$

On the one hand, the number of possible combinations is identical between the two wavefunctions (ionic and covalent). Therefore, the combinatorial term disappears when evaluating C.104. On the other hand, since the asymptotic model assumes that molecular orbitals are atomic orbitals and atomic orbitals are constructed to be linearly independent, if an electron from a valence shell is swapped with a core electron from the same atom, then the overlap of the two wavefunctions is zero. It only remains to evaluate the overlap between a valence electron exchanged with a core electron of the other atom: As the core electrons are even more localized around their atom, the overlap between the wavefunction of valence of one atom and the core wavefunction of the other atom is even smaller than the overlap between the wavefunctions of two valence electrons. Therefore, it is reasonable to keep only the zero-th order of the development

$$\sum_{\beta} \left\langle \psi_{ion,core} | P^{c-v:(\beta)} | \psi_{ion,core} \right\rangle \simeq \langle \psi_{ion,core} | \psi_{ion,core} \rangle . \tag{C.109}$$

This component therefore has no influence either on the result obtained in C.104.

C.2.5 Electron wavefunction for the covalent state around atom B

Following this logic, the kinetic term of the Schrödinger equation is expressed as:

$$\nabla^2_{\vec{r}_A} = \nabla^2_{\vec{R}} + \nabla^2_{\vec{r}_B} + \vec{\nabla}_{\vec{r}_B} \cdot \vec{\nabla}_{\vec{R}} + \vec{\nabla}_{\vec{R}} \cdot \vec{\nabla}_{\vec{r}_B} \tag{C.110}$$

As the time scales between the variation of interatomic distance and the distance to the atom B are very different. If there is a variation of the wavefunction according to the interatomic distance, then the component according to the distance to the nucleus B will balance automatically. If there is a variation of the wavefunction according to the distance to the nucleus B, this one is too fast to influence the variation according to the interatomic distance. Therefore, if $\vec{\nabla}_{\vec{r}_B}\tilde{\phi}(\vec{r}_B) \neq 0$ then $\vec{\nabla}_{\vec{R}}\chi_A(\vec{R}) = 0$ and vice versa.

This makes it possible to neglect the cross terms of the preceding equation. Therefore, the term kinetics is expressed as:

$$\nabla^2_{\vec{r}_A} \simeq \nabla^2_{\vec{R}} + \nabla^2_{\vec{r}_B} \tag{C.111}$$

Therefore, the Schrödinger equation

$$\left[\nabla^2_{\vec{r}_A} + 2V_{A^+}(r_A) + 2V_B(r_B) - 2E_{\text{cov}}(R)\right]\phi_{\text{cov}}(\vec{r}_A) = 0 \tag{C.112}$$

becomes:

$$\frac{\left[\nabla^2_{\vec{R}} + 2V_{A^+}(R) - 2E_{A0}\right]\chi_A(\vec{R})}{\chi_A(\vec{R})} = -\frac{\left[\nabla^2_{\vec{r}_B} + 2V_B(r_B) - 2\tilde{\beta}^2\right]\tilde{\phi}(\vec{r}_B)}{\tilde{\phi}(\vec{r}_B)} \tag{C.113}$$

assuming $V_{A^+}(r_A) \simeq V_{A^+}(R)$, and $E_{\text{cov}} = E_A + \tilde{\beta}^2/2$ where $E_{A0} = \gamma^2_{A0}/2$ is the electron binding energy for atom A [7] and $\tilde{\beta}^2/2$ is the energy of the supernumerary electron linked to the perturbative potential of the atom B. This energy $\tilde{\beta}^2/2$ is determined by the asymptotic behavior of the wavefunction.

The term on the left is the Schrödinger equation for the undisturbed atom A [8]. This term is zero – by definition of χ_A.

The term on the right depends only on the distance between the electron and the atom B, however with the interatomic distance used as a parameter included in $E_{\text{cov}}(R)$. Therefore, $\tilde{\phi}(\vec{r}_B)$ satisfies the equation:

$$\left[\nabla^2_{\vec{r}_B} + 2V_B(r_B) - \tilde{\beta}^2\right]\tilde{\phi}(\vec{r}_B) = 0 \tag{C.114}$$

whose boundary conditions are determined later.

In order to simplify the solution of this equation, it is useful to decompose it on a basis separating the radial term r_B and the angular terms (θ_B, φ_B).

Thus, the solution of the Schrödinger equation is a linear combination of the set of radial and angular solutions:

$$\tilde{\phi}(r_B, \theta_B, \varphi_B) = \sum_{l=0}^{\infty}\sum_{m=-l}^{+l} A_{l,m}\frac{U_l(r_B)}{r_B}Y_{l,m}(\theta_B, \varphi_B) \tag{C.115}$$

[7] This energy E_{A0} corresponds to the difference between the ionization potential $IP(A^0)$ and the excitation energy of the state of the atom A^*: $E_{A0} = IP(A^0) - E_{lev}(A^0)$.

[8] This term depends only on the interatomic distance R whose solution is the wavefunction of a valence electron, the atomic state χ_A. The wavefunction χ_A evaluated at the position of the nucleus B.

where $A_{l,m}$ are coefficients determined using the asymptotic behavior of the wavefunction [264, Chap. 5] and the terms $Y_{l,m}(\theta,\varphi)$ represent the basis of the spherical harmonics [9], and the radial functions $U_l(r_B)$ satisfy the equation

$$-\frac{1}{2}\frac{\mathrm{d}^2 U_{l_B}}{\mathrm{d}r_B^2}+\left[\frac{l(l+1)}{2r_B^2}+V_B(r_B)-\frac{\beta^2}{2}\right]U_{l_B}=0 \tag{C.116}$$

Moreover, the radial component of the wavefunction must decrease exponentially when r_B is large (on the sphere of integration described above). Meaning

$$U_l(r_B\to\infty)\sim\exp\left(-\bar{\beta}r_B\right). \tag{C.117}$$

Asymptotic development in the absence of atom B

In order to determine the coefficients $A_{l,m}$ as well as the boundary conditions of equation C.116, a method consists in carrying out the asymptotic expansion of the atomic wavefunction around the atom B.

[9] In order to obtain the decomposition of the wavefunction in spherical harmonics, it is necessary to start by decomposing the kinetic term in spherical coordinates

$$\nabla^2_{\vec{r}_B}\tilde{\phi}=\frac{1}{r_B}\frac{\partial^2}{\partial r_B^2}\left(r_B\tilde{\phi}\right)+\frac{1}{r_B^2}\frac{\partial}{\partial\cos\theta_B}\left(\frac{1}{\sin^2\theta_B}\frac{\partial\tilde{\phi}}{\partial\cos\theta_B}\right)+\frac{1}{r_B^2\sin^2\theta_B}\frac{\partial^2\tilde{\phi}}{\partial\varphi_B^2}$$

As the potential terms do not depend on (θ_B,φ_B), then the angular part of the Schrödinger equation reduces to [186]:

$$\frac{\partial}{\partial\cos\theta_B}\left(\frac{1}{\sin^2\theta_B}\frac{\partial\tilde{\phi}}{\partial\cos\theta_B}\right)+\frac{1}{\sin^2\theta_B}\frac{\partial^2\tilde{\phi}}{\partial\varphi_B^2}=0$$

The azimuthal component of the equation can be expressed as

$$\frac{1}{Q}\frac{\mathrm{d}^2Q}{\mathrm{d}\varphi_B^2}=-m_B^2$$

whose solution is

$$Q(\varphi_B)=e^{im_B\varphi_B}$$

which – once inserted in the previous equation – gives the equation according to the polar angle

$$\frac{\mathrm{d}}{\mathrm{d}\cos\theta_B}\left[\left(1-\cos^2\theta_B\right)\frac{\mathrm{d}P}{\mathrm{d}\cos\theta_B}\right]+\left[l(l+1)-\frac{m^2}{1-\cos^2\theta_B}\right]P=0$$

The set of solutions of this equation are the associated Legendre polynomials $P_l^m(\cos\theta_B)$. However, despite the fact that the associated Legendre polynomials form a basis of space, this basis is not orthonormal.

In order to overcome this problem, it is practical to define an orthonormal basis of functions of (θ_B,φ_B). This orthonormal basis is formed by spherical harmonics. These are written as a function of the associated Legendre polynomials as follows

$$Y_{l,m}(\theta,\varphi)=\sqrt{\frac{2l+1}{4\pi}\,\frac{(l-m)!}{(l+m)!}}\,{P_l}^m(\cos\theta)\,e^{im\varphi}$$

As the two atoms are far from each other, the atomic wavefunction χ_A is exponentially decreasing near the nucleus B.

Thus, for a given covalent state, the wavefunction of the covalent state ϕ_{cov} is approximately the wavefunction of the atom A χ_A without the presence of the atom B:

$$\phi_{\text{cov}} \simeq \chi_A(\vec{r}_A) \tag{C.118}$$

where this atomic wavefunction is a solution of the left member of the equation C.113. It breaks down into radial and angular components according to:

$$\chi_A(\vec{r}_A) = \chi_A(r_A) Y_{l_A,m_A}(\theta_A, \phi_A) \tag{C.119}$$

with the radial component given by [10]:

$$\begin{aligned}\chi_A(r_A) = {} & \mathscr{N}_A r_A^{-1+Z_{A+}/\gamma_{A0}} \exp(-\gamma_{A0} r_A) \\ & \times \left[1 + \frac{l_{A0}(l_{A0}+1) - (Z_{A+}/\gamma_{A0})[(Z_{A+}/\gamma_{A0})-1]}{2\gamma_{A0} r_A} + \mathscr{O}\left(r_A^{-2}\right)\right]\end{aligned} \tag{C.120}$$

where $Z_{A+} = 1$ the charge of the atom A without its valence electron and $\mathscr{N}_A$is the normalization factor. When the atom A is a highly excited atom, this factor approaches the Coulomb normalization factor [11]

$$\mathscr{N}_A^{\text{Coul}} = \gamma_A (2\gamma_A)^{1/\gamma_A} \left[\Gamma\left(\frac{1}{\gamma_A} + l_A + 1\right) \Gamma\left(\frac{1}{\gamma_A} - l_A\right)\right]^{-1/2} \tag{C.121}$$

To obtain the wavefunction of the valence electron located around A^+ in a coordinate system located around B^0, we must remember the coordinate system given by figure 3.10 from which we deduce that when $R >> r_B$:

$$r_A \simeq R - r_B \sin\theta_B \tag{C.122}$$

[10] This expression is the asymptotic power series expansion of the Whittaker functions $W_{Z/\gamma,l+1/2}(2\gamma r)$ [178].

These functions are asymptotic solutions of the equation

$$\left[\frac{1}{2}\nabla^2 + \frac{Z}{r} + \frac{\gamma^2}{2}\right]\left\{W_{Z/\gamma,l+1/2}(2\gamma r) Y_{lm}(\theta,\phi)\right\} = 0$$

Their power series development is [171, §13.19.2]

$$W_{\kappa,\mu}(z) \sim e^{-\frac{1}{2}x} x^{\kappa} \sum_{s=0}^{\infty} \frac{\left(\frac{1}{2}+\mu-\kappa\right)_s \left(\frac{1}{2}-\mu-\kappa\right)_s}{s!} (-z)^{-s},$$

or

$$W_{Z/\gamma,l+1/2}(2\gamma r) = A r^{(Z/\gamma)-1} e^{-\gamma r} \sum_{n=0}^{\infty} \frac{1}{(2\gamma r)^n n!} \prod_{k=1}^{n} (l - Z/\gamma + k)(l + Z/\gamma + 1 - k)$$

The solution given below is that given by Chibisov [167]. This is similar, but only gives the first orders of development.

[11] If this is not the case, the normalization factor must be adjusted with a more rigorous determination of the wavefunction.

thereby

$$\begin{aligned}\chi_A(r_A) &\simeq \chi_A(R - r_B\cos\theta_B)\\ &= \mathscr{N}_A(R - r_B\cos\theta_B)^{-1+1/\gamma_{A0}}e^{-\gamma_A(R-r_B\cos\theta_B)}\\ &= \mathscr{N}_A R^{-1+1/\gamma_{A0}}e^{-\gamma_A R}\left(\frac{R - r_B\cos\theta_B}{R}\right)^{-1+1/\gamma_{A0}} e^{\gamma_{A0}r_B\cos\theta_B}\\ &= \chi_A(R)\ \exp\left\{\gamma_A r_B\cos\theta_B + \left(\frac{1}{\gamma_{A0}} - 1\right)\ln\left(1 - \frac{r_B\cos\theta_B}{R}\right)\right\}\\ &\equiv \chi_A(R)\ e^{\beta r_B\cos\theta_B}\end{aligned} \tag{C.123}$$

where

$$\begin{aligned}\beta &= \gamma_A + \left(\frac{1}{\gamma_{A0}} - 1\right)\left(\frac{1}{r_B\cos\theta_B}\right)\ln\left(1 - \frac{r_B\cos\theta_B}{R}\right)\\ &\simeq \gamma_A - \left(\frac{1}{\gamma_{A0}} - 1\right)\frac{1}{R}\\ &\simeq \gamma_A - \frac{1}{\gamma_{A0}R}\end{aligned} \tag{C.124}$$

using the Taylor expansion of the logarithm $\ln(1-x) \simeq -x + \mathscr{O}(x^2)$. Then

$$\left(\frac{\beta}{\gamma_{A0}}\right)^2 = \left(1 - \frac{1}{\gamma_{A0}^2 R}\right)^2 \simeq 1 - \frac{2}{\gamma_{A0}^2 R} + \mathscr{O}(R^{-2}) \tag{C.125}$$

thus the factor β is given by [12]

$$\beta \simeq \sqrt{\gamma_{A0}^2 - \frac{2}{R}} \tag{C.126}$$

It is therefore possible to express this term according to a series of Bessel functions [171, §10.60E8],

$$e^{\beta r_B\cos\theta_B} = \sum_{l=0}^{\infty}(2l+1)\ \mathrm{i}_l^{(1)}(\beta r_B)\ P_l(\cos\theta_B) \tag{C.127}$$

with $\mathrm{i}_l^{(1)}$ the modified spherical Bessel function [13].

[12] In the first version of the development for the interaction between ionic and covalent state [149], Janev takes the results obtained by [85] and [265] for $Z = 0$ and finds $\beta = \gamma_{A0} + 1/R$. In his following article on the subject [163], he corrects this error without mentioning it, without detailing the reasoning, nor detailing its validity: It requires that $\gamma_{A0} << 1$. Hence the detail of the reasoning given here.

[13] This function is defined by

$$\mathrm{i}_l^{(1)}(\beta r_B) = \sqrt{\frac{\pi}{2\beta r_B}}\ I_{l+1/2}(\beta r_B)$$

If only the zero-th order (asymptotic term) is kept, the equation becomes [14]:

$$e^{\beta r_B \cos\theta_B} = \sum_{l=0}^{\infty} (2l+1) \frac{e^{\beta r_B}}{2\beta r_B} P_l(\cos\theta_B) \tag{C.128}$$

which can be inserted into C.123 and C.119, assuming that the two atoms are far enough from each other so that the angular representation along the interatomic axis is similar to the representation in the reference frame of the atom A,

$$\begin{aligned} \chi_A(\vec{r}_A) &\simeq \chi_A(R) Y_{l_A,m_A}(\theta_A,\varphi_A) e^{\beta r_B \cos\theta_B} \\ &\simeq \chi_A(\vec{R}) \sum_{l=k}^{\infty} (2l+1) \frac{e^{\beta r_B}}{2\beta r_B} P_l(\cos\theta_B) \end{aligned} \tag{C.129}$$

It should be noted that this development does not take into account the atom B. It describes only the atomic wavefunction of an electron located around the atom A^+ at the edge of a position which would correspond to the presence of an atom B. This equation C.129 simply gives the asymptotic conditions that the wavefunction disturbed by the atom B must satisfy.

These asymptotic conditions allow us to compare the initial development of χ_A around B given by C.115 with its asymptotic expansion C.129.

This comparison implies, on the one hand, that only the term with $m = 0$ is possible. This condition amounts to imposing $\varphi_A = \varphi_B$. Indeed, when the two ions approach, a projection axis appears: the interatomic axis $\vec{R}$. Thus, the projection of the angular momentum is defined along this axis. Therefore, as φ_A does not depends on the interatomic axis (the only coordinate which have a physical meaning), any the definitions of φ perpendicular to this axis is valid.

---

and $I_n(x)$ is the modified Bessel function of the first type, whose asymptotic expansion is[171, §10.40E1] :

$$I_l(z) = \frac{e^z}{\sqrt{2\pi z}} \sum_{k=0}^{\infty} (-1)^k \frac{a_k(l)}{z^k}$$

where $a_k(0) = 1$ and

$$a_k(l) = \frac{(4l^2-1^2)(4l^2-3^2)\cdots(4l^2-(2k-1)^2)}{k!8^k}$$

[14] Before continuing, it is important to note that $\mathrm{i}_l(z)$ is solution of the equation [171, §10.47Eq2]:

$$z^2 \frac{\mathrm{d}^2 \mathrm{i}_l}{\mathrm{d}z^2} + 2z \frac{\mathrm{d}\mathrm{i}_l}{\mathrm{d}z} - (l(l+1)+z^2)\mathrm{i}_l(z) = 0$$

which is equivalent to the radial part of the Schrödinger equation for a particle in a central potential. This equation gives the asymptotic solution of the wavefunction of the valence electron when it is located around the ion A^+.

The equation C.115 then becomes:

$$\tilde{\phi}(r_B,\theta_B,\varphi_B)=\sum_{l=0}^{\infty}A_{l,0}\frac{U_l(r_B)}{r_B}\sqrt{\frac{2l+1}{4\pi}}P_l(\cos\theta_B) \tag{C.130}$$

with the following asymptotic condition on $U_l(r_B)$:

$$U_l(r_B\to\infty)=e^{-\beta r_B} \tag{C.131}$$

Moreover, in order to equal these two equations, the parameters $A_{l,m}$ must be equal to:

$$A_{l,m}=(2\beta)^{-1}\sqrt{4\pi(2l+1)}\delta_{m,0}, \tag{C.132}$$

Once this parameter is replaced in the expression C.115, it gives:

$$\chi_A(\vec{r}_A)\simeq\chi_A(\vec{R})\sum_{l=0}^{\infty}\frac{(2l+1)}{2\beta r_B}U_{l_B}(r_B)P_l(\cos\theta_B) \tag{C.133}$$

where $U_{l_B}(r_B)$ satisfies the equation C.116.

Before continuing with our development, and determining $U_{l_B}(r_B)$, it is useful to modify the previous expression slightly. Indeed, a term in $(\sin\theta_B)^m$ will appear later. The idea here is to modify the expression above to make a term appear in $(\sin\theta_B)^{-m}$. To get there, we must first recall the definition of associated Legendre polynomials:

$$P_l^m(\cos\theta)=(-\sin\theta)^m\left(\frac{\partial}{\partial\cos\theta_B}\right)^m P_l(\cos\theta) \tag{C.134}$$

then to derive $k\geq 0$ times the expression C.128 according to $\cos\theta_B$. Which gives, for a k chosen arbitrarily:

$$\begin{aligned}\left(\frac{\partial}{\partial\cos\theta_B}\right)^k e^{\beta r_B\cos\theta_B}&=\sum_{l=0}^{\infty}(2l+1)\frac{e^{\beta r_B}}{2\beta r_B}\left(\frac{\partial}{\partial\cos\theta_B}\right)^k P_l(\cos\theta_B)\\ (\beta r_B)^k e^{\beta r_B\cos\theta_B}&=\sum_{l=0}^{\infty}(2l+1)\frac{e^{\beta r_B}}{2\beta r_B}\left(\frac{-1}{\sin\theta_B}\right)^k P_l^k(\cos\theta_B)\end{aligned} \tag{C.135}$$

consequently,

$$e^{\beta r_B\cos\theta_B}=\sum_{l=0}^{\infty}(2l+1)\frac{e^{\beta r_B}}{2\beta r_B}\left(\frac{-1}{\beta r_B\sin\theta_B}\right)^k P_l^k(\cos\theta_B) \tag{C.136}$$

The equation C.133 then becomesusing $P_l^k(x)=0$ if $k>l$:

$$\chi_A(\vec{r}_A)\simeq\chi_A(\vec{R})\sum_{l=k}^{\infty}(2l+1)\left(\frac{-1}{\beta r_B\sin\theta_B}\right)^k\frac{e^{\beta r_B}}{2\beta r_B}P_l^k(\cos\theta_B) \tag{C.137}$$

because the associated Legendre polynomials are zero if $k>l$. And so C.115 becomes:

$$\tilde{\phi}\,(r_B,\theta_B,\varphi_B)\simeq\sum_{l=k}^{\infty}(2l+1)\left(\frac{-1}{\beta r_B\sin\theta_B}\right)^k\frac{e^{\beta r_B}}{2\beta r_B}P_l^k(\cos\theta_B) \tag{C.138}$$

Perturbative component: Solution with the potential of atom B

The radial perturbative wavefunction U_{l_B}, is solution of the equation C.116, where the potential term is a short-range potential.

This potential is assumed to be dipolar:

$$V_B(r_B) = -\frac{\alpha}{r_B^4} \tag{C.139}$$

where α is the polarizability of the atom B. Therefore, the Schrödinger equation becomes:

$$\left(\frac{\mathrm{d}^2}{\mathrm{d}r_B^2} - \frac{l_B(l_B+1)}{r_B^2} + \frac{2\alpha}{r_B^4} - \beta^2\right) U_{l_B}(r_B) = 0 \tag{C.140}$$

whose solution is given by O'Malley [266] and Smirnov [83]. Its asymptotic value is

$$U_{l_B}(r_B) = (2\beta r_B)\left[\mathrm{i}_{l_B}^{(2)}(\beta r_B) + \frac{C_{l_B}}{\pi}\mathrm{k}_{l_B}(\beta r_B)\right] \tag{C.141}$$

where i_l and k_l are modified Bessel functions, and where the coefficients C_{l_B} vary in the literature [15]. However, these coefficients will disappear when calculating the integral 3.83 [16].

Thus, the equation C.138 becomes:

$$\tilde{\phi}(r_B,\theta_B,\varphi_B) = \sum_{l=k}^{\infty}(2l+1)\left(\frac{-1}{\beta r_B\sin\theta_B}\right)^k\left[\mathrm{i}_l^{(2)}(\beta r_B) + \frac{C_l}{\pi}\mathrm{k}_l(\beta r_B)\right]P_l^k(\cos\theta_B) \tag{C.142}$$

Combination of components

Now that the different components of the wavefunction of the covalent state are determined, it is possible to combine them:

$$\begin{aligned}\phi_{\mathrm{cov}} &\simeq \chi_A(\vec{R})\tilde{\phi}(\vec{r}_B)\\ &\simeq \chi_A(R)\sqrt{\frac{(2l_A+1)}{2}\frac{(l_A-m_A)!}{(l_A+m_A)!}}P_{l_A}^{m_A}(\cos\theta_A)\frac{e^{im_A\varphi}}{\sqrt{2\pi}}\\ &\times\sum_{l=k}^{\infty}(2l+1)\left[\mathrm{i}_l^{(2)}(\beta r_B) + \frac{C_l}{\pi}\mathrm{k}_l(\beta r_B)\right]\left(\frac{-1}{\beta r_B\sin\theta_B}\right)^k P_l^k(\cos\theta_B)\end{aligned} \tag{C.143}$$

[15] For Smirnov [83], $C_l = (2\pi\alpha\beta)/[(2l+3)(2l+1)(2l-1)]$. While for O'Malley [266], the coefficients are slightly different. Which is not a problem, as this coeficient will disappears later.

[16] Indeed, the wavefunction of the ionic state is of the form $a\mathrm{k}_l$. Therefore, the Wronskian is zero for the component of the equation which includes the terms C_l.

The interatomic distance being a parameter instead of a variable, the term $\chi_A(R)$ does not pose a problem to remain as it is. However, the angular term varies non-trivially around the B atom. This implies the need to re-express the angular term according to the angular coordinates (θ_B, φ_B).

Since $R >> r_B$ then $\theta_A \to 0$ and $R\sin\theta_A \simeq r_A \sin\theta_A = r_B \sin\theta_B$ and it is possible to approximate the associated Legendre polynomials, using [254, Eq. 8.812], by:

$$\lim_{\theta\to 0} P_l^m(\cos\theta) = \frac{(-1)^m (l+m)!}{2^m\, m!(n-m)!} \sin^m\theta \times \Big[1 - \mathscr{O}(1-\cos\theta)\Big] \tag{C.144}$$

Therefore, if $m_A \geq 0$,

$$Y_{l_A,m_A}(\cos\theta_A) \simeq \frac{(-1)^{m_A}}{2^{m_A}\, m_A!} \sqrt{\frac{(2l_A+1)}{2}\frac{(l_A+m_A)!}{(l_A-m_A)!}} \left(\frac{r_B\sin\theta_B}{R}\right)^{m_A} \frac{e^{im_A\varphi_A}}{\sqrt{2\pi}} \tag{C.145}$$

If $m_A \geq 0$, then, we can choose $k = m_A$, which gives

$$\begin{aligned}
\phi_{\text{cov}} &\simeq \chi_A(R) \frac{(-1)^{m_A}}{2^{m_A}\, m_A!} \sqrt{\frac{(2l_A+1)}{2}\frac{(l_A+m_A)!}{(l_A-m_A)!}} \left(\frac{r_B\sin\theta_B}{R}\right)^{m_A} \frac{e^{im_A\varphi_A}}{\sqrt{2\pi}} \\
&\quad \times \left(\frac{-1}{\beta r_B \sin\theta_B}\right)^{m_A} \sum_{l=m_A}^{\infty} (2l+1) \left[\mathsf{i}_l^{(2)}(\beta r_B) + \frac{C_l}{\pi}\mathsf{k}_l(\beta r_B)\right] P_l^{m_A}(\cos\theta_B) \\
&\simeq \chi_A(R) \frac{1}{(2\beta R)^{m_A}\, m_A!} \sqrt{\frac{(2l_A+1)}{2}\frac{(l_A+m_A)!}{(l_A-m_A)!}} \\
&\quad \times \sum_{l=m_A}^{\infty} \left[\mathsf{i}_l^{(2)}(\beta r_B) + \frac{C_l}{\pi}\mathsf{k}_l(\beta r_B)\right] (2l+1) P_l^{m_A}(\cos\theta_B) \frac{e^{im_A\varphi_B}}{\sqrt{2\pi}} \\
&= \chi_A(R) \frac{1}{(2\beta R)^{m_A}\, m_A!} \sqrt{\frac{(2l_A+1)}{2}\frac{(l_A+m_A)!}{(l_A-m_A)!}} \\
&\quad \times \sum_{l=m_A}^{\infty} \left[\mathsf{i}_l^{(2)}(\beta r_B) + \frac{C_l}{\pi}\mathsf{k}_l(\beta r_B)\right] 2\sqrt{\frac{(2l+1)}{2}\frac{(l+m_A)!}{(l-m_A)!}} Y_{l,m_A}(\theta_B,\varphi_B)
\end{aligned} \tag{C.146}$$

If $m_A < 0$, then, we can choose $k = |m_A| = -m_A$, and remember that [171, §14.6.13] :

$$P_l^{-|m|}(\cos\theta) = (-1)^{|m|} \frac{(l-|m|)!}{(l+|m|)!} P_l^{|m|}(\cos\theta) \tag{C.147}$$

thus, the asymptotic development of spherical harmonics becomes:

$$Y_{l_A,m_A}(\cos\theta_A) \simeq \frac{1}{2^{|m_A|}\, |m_A|!} \sqrt{\frac{(2l_A+1)}{2}\frac{(l_A+|m_A|)!}{(l_A-|m_A|)!}} \left(\frac{r_B\sin\theta_B}{R}\right)^{|m_A|} \frac{e^{im_A\varphi_A}}{\sqrt{2\pi}} \tag{C.148}$$

which once inserted into the previous development becomes:

$$
\begin{aligned}
&\phi_{\text{cov}} \\
&\simeq \chi_A(R) Y_{l_A,m_A}(\cos\theta_A)\tilde{\phi}(\vec{r}_B) \\
&\simeq \chi_A(R)\frac{1}{2^{|m_A|}\,|m_A|!}\sqrt{\frac{(2l_A+1)}{2}\frac{(l_A+|m_A|)!}{(l_A-|m_A|)!}}\left(\frac{r_B\sin\theta_B}{R}\right)^{|m_A|}\frac{e^{im_A\varphi_A}}{\sqrt{2\pi}} \\
&\times\left(\frac{-1}{\beta r_B\sin\theta_B}\right)^{|m_A|}\sum_{l=|m_A|}^{\infty}(2l+1)\left[\mathsf{i}_l^{(2)}(\beta r_B)+\frac{C_l}{\pi}\mathsf{k}_l(\beta r_B)\right]P_l^{|m_A|}(\cos\theta_B) \\
&\simeq \chi_A(R)\frac{(-1)^{|m_A|}}{(2\beta R)^{|m_A|}\,|m_A|!}\sqrt{\frac{(2l_A+1)}{2}\frac{(l_A+|m_A|)!}{(l_A-|m_A|)!}} \\
&\times\sum_{l=|m_A|}^{\infty}\left[\mathsf{i}_l^{(2)}(\beta r_B)+\frac{C_l}{\pi}\mathsf{k}_l(\beta r_B)\right](2l+1)(-1)^{|m_A|}\frac{(l+|m_A|)!}{(l-|m_A|)!} \\
&\qquad\times P_l^{m_A}(\cos\theta_B)\frac{e^{im_A\varphi_A}}{\sqrt{2\pi}} \\
&\simeq \chi_A(R)\frac{1}{(2\beta R)^{|m_A|}\,|m_A|!}\sqrt{\frac{(2l_A+1)}{2}\frac{(l_A+|m_A|)!}{(l_A-|m_A|)!}} \\
&\times\sum_{l=|m_A|}^{\infty}\left[\mathsf{i}_l^{(2)}(\beta r_B)+\frac{C_l}{\pi}\mathsf{k}_l(\beta r_B)\right]2\sqrt{\frac{(2l+1)}{2}\frac{(l+|m_A|)!}{(l-|m_A|)!}}Y_{l,m_A}(\theta_B,\varphi_B)
\end{aligned}
\tag{C.149}
$$

using:

$$
(2l+1)\frac{(l+|m_A|)!}{(l-|m_A|)!}=2\sqrt{\frac{(2l+1)}{2}\frac{(l+m_A)!}{(l-m_A)!}}\sqrt{\frac{(2l+1)}{2}\frac{(l+|m_A|)!}{(l-|m_A|)!}} \tag{C.150}
$$

The result of this expansion for $m_A<0$ is therefore also valid for $m_A\geq 0$ by adding absolute values to it where necessary. This equation therefore gives the shape of the wavefunction of the covalent state (electron centered around the atom A) measured in the coordinates of the atom B. This expression is similar to that obtained by Janev [149, 163, 265].

Thus, by expliciting the factor $\chi_A(R)$:

$$
\begin{aligned}
\phi_{\text{cov}} \simeq\ & \frac{\gamma_A(2\gamma_A)^{1/\gamma_A}R^{-1+1/\gamma_{A0}}\exp(-\gamma_{A0}R)}{\sqrt{\Gamma\left(\frac{1}{\gamma_A}+l_A+1\right)\Gamma\left(\frac{1}{\gamma_A}-l_A\right)}} \\
&\times\frac{1}{(2\beta R)^{|m_A|}\,|m_A|!}\sqrt{(2l_A+1)\frac{(l_A+|m_A|)!}{(l_A-|m_A|)!}}
\end{aligned}
$$

$$\times \sum_{l=|m_A|}^{\infty} \left[\mathsf{i}_l^{(2)}(\beta r_B) + \frac{C_l}{\pi} \mathsf{k}_l(\beta r_B) \right] \sqrt{(2l+1)\frac{(l+|m_A|)!}{(l-|m_A|)!}} Y_{l,m_A}(\theta_B, \varphi_B) \tag{C.151}$$

C.2.6 Alternate resolution of the ionic wavefunction

Another method of resolution only considers the negative ion and neglects the effects of the positive ion. This other resolution modifies the radial Schrödinger equation. However, the asymptotic behavior of the wavefunctions obtained in each case coincides with the other.

In this case, the radial Schrödinger equation reduces to (by averaging the charge of the other electrons around the nucleus):

$$\left(\frac{1}{2} \frac{\partial^2}{\partial r_B^2} - \frac{Z}{r_B} + \frac{\gamma_{B^-}^2}{2} \right) (r_B \phi_{\text{ion}}) = 0 \tag{C.152}$$

In the case of negative ions $Z = 0$, the solutions of this equation are the Whittaker functions [178, 179]

$$W_{Z/\gamma_B, l_B+1/2}(2\gamma_B r_B) \tag{C.153}$$

which can be written as a spherical Bessel function when $Z = 0$ as [171, §13.18.9 et §10.47.9]:

$$W_{0,l_B+1/2}(2\gamma_B r_B) = \frac{2\gamma_B r_B}{\pi} \mathsf{k}_l(\gamma_B r_B) \tag{C.154}$$

whose asymptotic development is given by Vitanov [178] and NIST [171, §13.19.3]. Nevertheless, Vitanov adds an additional normalization term A in order to take into account the error related to the average potential of the electrons around the nucleus.

$$\phi_{\text{ion}}(r_B \to \infty) = A \frac{e^{-\gamma_B r_B}}{r_B} \sum_{n=0}^{\infty} \frac{(l)_n (l+1)_n}{n!(2\gamma_B r)^n}, \tag{C.155}$$

If only the term in $n = 0$ is kept, it is possible to obtain a sufficiently simple formulation of the wavefunction to normalize it using $\int \phi \; r \mathrm{d}r = 1$:

$$\phi_{\text{ion}}(r_B) \simeq N_{B^-} \frac{1}{r_B} e^{-\gamma_{B^-} r_B} \tag{C.156}$$

where $N_{B^-} = A$ is the normalization of the wavefunction obtained using more complex numerical methods.

C.2.7 Comment on the selection rules

If the development of the Legendre polynomial differed when processing the insertion of C.136 in the equation C.115 , this difference would reveal a term $e^{im\varphi_B}$ linked to the associated Legendre polynomials. In this case, the wave-function expansion $\tilde{\phi}$ should include spherical harmonics (where $m \neq 0$).

In this case, the angular integral which gave the relation

$$\int Y_{l_A,m_A} Y_{l_B,m_B} = \delta_{m_A,m_B} \delta_{l_A,l_B} \tag{C.157}$$

would turn into

$$\begin{aligned} &\int Y_{l_1 m_1} Y_{l_2 m_2} Y_{l_3 m_3} \, \mathrm{d}\Omega \\ &= \sqrt{\frac{(2l_1+1)(2l_2+1)(2l_3+1)}{4\pi}} \begin{pmatrix} l_1 & l_2 & l_3 \\ 0 & 0 & 0 \end{pmatrix} \begin{pmatrix} l_1 & l_2 & l_3 \\ m_1 & m_2 & m_3 \end{pmatrix} \end{aligned} \tag{C.158}$$

where $(:::)$ are the Wigner $3-j$ symbols.

It should be noted that if this reflection is valid, then it calls into question the selection rules on molecular symmetry. It is therefore unlikely that this argument is actually valid. Therefore, the relationship C.138 seems appropriate.

Appendix D

Theory: Asymptotic model parameters

This appendix contains all the theoretical inputs used in the ACAM model.

Anion	EA	A_{B^-}
S	2.077	1.14/2.7
O	1.461	0.64/2.1
Si	1.385	1.17×1.4
C	1.263	0.74×1.5
D	0.754	2.63/4
P	0.747	0.87/2

Cation	IP	A_{A^+} [1]
C	11.2603	1
N	14.5402	1
O	13.6181	1.8
Li	5.3917	1
Na	5.1391	1
Ne	21.5645	1
He	24.5874	1

Table D.1: Anions and cations parameters used by the model. Ionization potentials are from [199], A_{B^-} (without post-factor) are from [178, 179], Electron affinities are from [268]

Atom	Configuration	Term	Energy
D	$1s$	^2S	0.0000
	2ℓ	^2L	10.2016
	3ℓ	^2L	12.0908
	4ℓ	^2L	12.7520
	5ℓ	^2L	13.0581
C	$2s^2 2p^2$	^3P	0.0000
	$2s^2 2p^2$	^1D	1.2601
	$2s^2 2p^2$	^1S	2.6803
O	$2s^2 2p^4$	^3P	0.0000
	$2s^2 2p^4$	^1D	1.9577
	$2s^2 2p^4$	^1S	4.1801
Si	$3s^2 3p^2$	^3P	0.0000
	$3s^2 3p^2$	^1D	0.7624
	$3s^2 3p^2$	^1S	1.8901
P	$3s^2 3p^3$	$^4S^o$	0.0000
	$3s^2 3p^3$	$^2D^o$	1.4097
	$3s^2 3p^3$	$^2P^o$	2.3234
S	$3s^2 3p^4$	^3P	0.0000
	$3s^2 3p^4$	^1D	1.1212
	$3s^2 3p^4$	^1S	2.7257
	$3s^2 3p^3(4S^o)4s$	$^5S^o$	6.5002
	$3s^2 3p^3(4S^o)4s$	$^3S^o$	6.8359

Table D.2: Neutralized anions configurations, terms and energy levels (no J) [199]

Atom	Configuration	Term	Energy
P^-[269]	$3s^2 3p^4$	$^3P_2$	0.0000
	$3s^2 3p^4$	$^3P_1$	0.0225
	$3s^2 3p^4$	$^3P_0$	0.0327
S^-[270, 271]	$3s^2 3p^5$	$^2P^o_{3/2}$	0.0000
	$3s^2 3p^4$	$^2P^o_{1/2}$	0.0600
S	$3s^2 3p^4$	$^3P_2$	0.0000
		$^3P_1$	0.0491
		$^3P_0$	0.0711

Table D.3: Neutralized anions configurations, terms and energy levels (with J)

Configuration	Term	Energy	Configuration	Term	Energy
$1s^2$	^1S	0.0000	$1s3p$	$^1P^o$	23.0870
$1s2s$	^3S	19.8196	$1s4s$	^3S	23.5940
$1s2s$	^1S	20.6159	$1s4s$	^1S	23.6736
$1s2p$	$^3P^o$	20.9641	$1s4p$	$^3P^o$	23.7079
$1s2p$	$^1P^o$	21.2180	$1s4d$	^3D	23.7361
$1s3s$	^3S	22.7185	$1s4d$	^1D	23.7363
$1s3s$	^1S	22.9203	$1s4f$	$^3F^o$	23.7370
$1s3p$	$^3P^o$	23.0071	$1s4f$	$^1F^o$	23.7370
$1s3d$	^3D	23.0737	$1s4p$	$^1P^o$	23.7421
$1s3d$	^1D	23.0741			

Table D.4: Helium energy levels [199]

Configuration	Term	Energy	Configuration	Term	Energy
$1s^22s$	^2S	0.0000	$1s^24d$	^2D	4.5407
$1s^22p$	$^2P^o$	1.8478	$1s^24f$	$^2F^o$	4.5416
$1s^23s$	^2S	3.3731	$1s^25s$	^2S	4.7485
$1s^23p$	$^2P^o$	3.8343	$1s^25p$	$^2P^o$	4.8373
$1s^23d$	^2D	3.8786	$1s^25d$	^2D	4.8472
$1s^24s$	^2S	4.3409	$1s^25f$	$^2F^o$	4.8483
$1s^24p$	$^2P^o$	4.5216			

Table D.5: Lithium energy levels [199]

Configuration	Term	Energy	Configuration	Term	Energy
$2p^63s$	^2S	0.0000	$2p^64p$	$^2P^o$	3.7531
$2p^63p$	$^2P^o$	2.1037	$2p^65s$	^2S	4.1164
$2p^64s$	^2S	3.1914	$2p^64d$	^2D	4.2835
$2p^63d$	^2D	3.6170	$2p^64f$	$^2F^o$	4.2882

Table D.6: Sodium energy levels [199]

Configuration	Term	Energy	Configuration	Term	Energy
$2s^2 2p^2$	^3P	0.0000	$2s^2 2p3d$	$^3D^o$	9.7055
$2s^2 2p^2$	^1D	1.2601	$2s^2 2p4s$	$^1P^o$	9.7093
$2s^2 2p^2$	^1S	2.6803	$2s^2 2p3d$	$^1F^o$	9.7328
$2s2p^3$	$^5S^o$	4.1790	$2s^2 2p3d$	$^1P^o$	9.7578
$2s^2 2p3s$	$^3P^o$	7.4816	$2s^2 2p3d$	$^3P^o$	9.8301
$2s^2 2p3s$	$^1P^o$	7.6811	$2s^2 2p4p$	^1P	9.9846
$2s2p^3$	$^3D^o$	7.9423	$2s^2 2p4p$	^3D	10.0159
$2s^2 2p3p$	^1P	8.5334	$2s^2 2p4p$	^3S	10.0521
$2s^2 2p3p$	^3D	8.6408	$2s^2 2p4p$	^3P	10.0805
$2s^2 2p3p$	^3S	8.7675	$2s^2 2p4p$	^1D	10.1345
$2s^2 2p3p$	^3P	8.8457	$2s^2 2p4p$	^1S	10.1943
$2s^2 2p3p$	^1D	8.9989	$2s^2 2p4d$	$^1D^o$	10.3487
$2s^2 2p3p$	^1S	9.1682	$2s^2 2p5s$	$^3P^o$	10.3828
$2s2p^3$	$^3P^o$	9.3268	$2s^2 2p4d$	$^3F^o$	10.3830
$2s^2 2p3d$	$^1D^o$	9.6274	$2s^2 2p4d$	$^3D^o$	10.3911
$2s^2 2p4s$	$^3P^o$	9.6836	$2s^2 2p5s$	$^1P^o$	10.3958
$2s^2 2p3d$	$^3F^o$	9.6952			

Table D.7: Carbon energy levels [198, 199]

Configuration	Term	Energy	Configuration	Term	Energy
$2s^2 2p^3$	$^4S^o$	0.0000	$2s^2 2p^2(^3P)3d$	^2F	12.9999
$2s^2 2p^3$	$^2D^o$	2.3840	$2s^2 2p^2(^3P)3d$	^4P	12.9993
$2s^2 2p^3$	$^2P^o$	3.5756	$2s^2 2p^2(^3P)3d$	^4D	13.0192
$2s^2 2p^2(^3P)3s$	^4P	10.3323	$2s^2 2p^2(^3P)3d$	^2D	13.0350
$2s^2 2p^2(^3P)3s$	^2P	10.6865	$2s^2 2p^2(^3P)4p$	$^2S^o$	13.2016
$2s2p^4$	^4P	10.9270	$2s^2 2p^2(^3P)4p$	$^4D^o$	13.2444
$2s^2 2p^2(^3P)3p$	$^2S^o$	11.6026	$2s^2 2p^2(^3P)4p$	$^4P^o$	13.2680
$2s^2 2p^2(^3P)3p$	$^4D^o$	11.7584	$2s^2 2p^2(^3P)4p$	$^2D^o$	13.2942
$2s^2 2p^2(^3P)3p$	$^4P^o$	11.8417	$2s^2 2p^2(^3P)4p$	$^4S^o$	13.3216
$2s^2 2p^2(^3P)3p$	$^4S^o$	11.9956	$2s^2 2p^2(^3P)4p$	$^2P^o$	13.3426
$2s^2 2p^2(^3P)3p$	$^2D^o$	12.0058	$2s^2 2p^2(^3P)5s$	^4P	13.6239
$2s^2 2p^2(^3P)3p$	$^2P^o$	12.1249	$2s^2 2p^2(^3P)5s$	^2P	13.6483
$2s^2 2p^2(^1D)3s$	^2D	12.3567	$2s^2 2p^2(^3P)4d$	^4F	13.6695
$2s^2 2p^2(^3P)4s$	^4P	12.8564	$2s^2 2p^2(^3P)4d$	^2P	13.6666
$2s^2 2p^2(^3P)4s$	^2P	12.9187	$2s^2 2p^2(^3P)4d$	^2F	13.6792
$2s^2 2p^2(^3P)3d$	^2P	12.9723	$2s^2 2p^2(^3P)4d$	^4P	13.6774
$2s^2 2p^2(^3P)3d$	^4F	12.9836			

Table D.8: Nitrogen energy levels [199]

Configuration	Term	Energy	Configuration	Term	Energy
$2s^2 2p^4$	^3P	0.0000	$2s^2 2p^3(4S^o)6s$	$^5S^o$	13.0111
$2s^2 2p^4$	^1D	1.9577	$2s^2 2p^3(4S^o)6s$	$^3S^o$	13.0292
$2s^2 2p^4$	^1S	4.1801	$2s^2 2p^3(4S^o)5d$	$^5D^o$	13.0565
$2s^2 2p^3(4S^o)3s$	$^5S^o$	9.1364	$2s^2 2p^3(4S^o)5d$	$^3D^o$	13.0594
$2s^2 2p^3(4S^o)3s$	$^3S^o$	9.5117	$2s^2 2p^3(4S^o)5f$	^5F	13.0634
$2s^2 2p^3(4S^o)3p$	^5P	10.7310	$2s^2 2p^3(4S^o)5f$	^3F	13.0634
$2s^2 2p^3(4S^o)3p$	^3P	10.9792	$2s^2 2p^3(4S^o)6p$	^5P	13.1065
$2s^2 2p^3(4S^o)4s$	$^5S^o$	11.8279	$2s^2 2p^3(4S^o)6p$	^3P	13.1218
$2s^2 2p^3(4S^o)4s$	$^3S^o$	11.9207	$2s^2 2p^3(4S^o)7s$	$^5S^o$	13.2003
$2s^2 2p^3(4S^o)3d$	$^5D^o$	12.0690	$2s^2 2p^3(4S^o)7s$	$^3S^o$	13.2105
$2s^2 2p^3(4S^o)3d$	$^3D^o$	12.0774	$2s^2 2p^3(4S^o)6d$	$^5D^o$	13.2258
$2s^2 2p^3(4S^o)4p$	^5P	12.2764	$2s^2 2p^3(4S^o)6d$	$^3D^o$	13.2276
$2s^2 2p^3(4S^o)4p$	^3P	12.3492	$2s^2 2p^3(4S^o)6f$	^5F	13.2300
$2s^2 2p^3(2D^o)3s$	$^3D^o$	12.5305	$2s^2 2p^3(4S^o)6f$	^3F	13.2300
$2s^2 2p^3(4S^o)5s$	$^5S^o$	12.6512	$2s^2 2p^3(4S^o)6g$	$^5G^o$	13.2303
$2s^2 2p^3(4S^o)5s$	$^3S^o$	12.6878	$2s^2 2p^3(4S^o)6g$	$^3G^o$	13.2303
$2s^2 2p^3(2D^o)3s$	$^1D^o$	12.7188	$2s^2 2p^3(4S^o)8s$	$^5S^o$	13.3119
$2s^2 2p^3(4S^o)4d$	$^5D^o$	12.7440	$2s^2 2p^3(4S^o)8s$	$^3S^o$	13.3183
$2s^2 2p^3(4S^o)4d$	$^3D^o$	12.7494	$2s^2 2p^3(4S^o)7d$	$^5D^o$	13.3277
$2s^2 2p^3(4S^o)4f$	^5F	12.7568	$2s^2 2p^3(4S^o)7d$	$^3D^o$	13.3289
$2s^2 2p^3(4S^o)4f$	^3F	12.7568	$2s^2 2p^3(4S^o)7f$	^5F	13.3304
$2s^2 2p^3(4S^o)5p$	^5P	12.8384	$2s^2 2p^3(4S^o)7f$	^3F	13.3304
$2s^2 2p^3(4S^o)5p$	^3P	12.8686			

Table D.9: Oxygen energy levels [199]

Appendix E

Results: Differential cross section

This appendix compiles all the experimental angular distributions measured when the collision energy is higher than the lowest collision energy achievable by the system.

Some theoretical data are attached, the theory used is described in the previous chapters.

E.1 $He^+ + D^-$

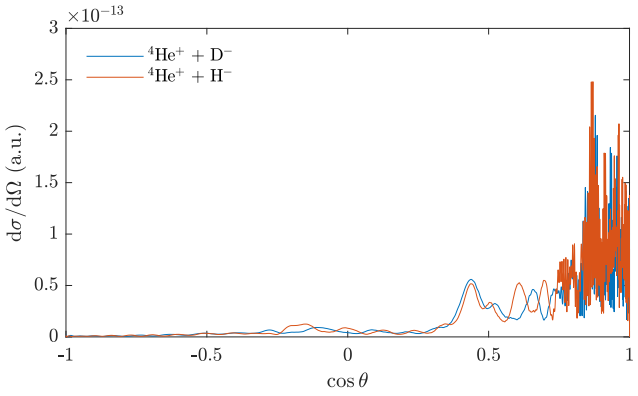

Figure E.1: Differential cross section for $He^+ + H/D^- \rightarrow He + H/D$ with a collision energy of 100 meV [101].

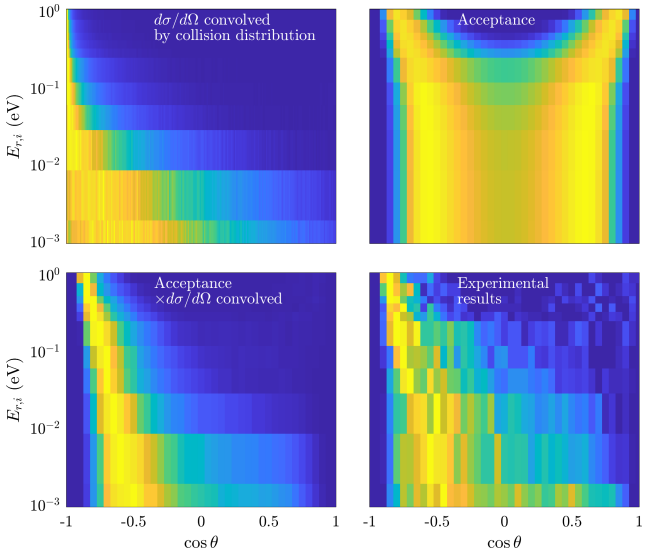

Figure E.2: Differential cross section for $He^+ + D^- \rightarrow He(1s3p\ ^3P^o) + D(1s)$. The simulation is based on the differential cross section for $He^+ + H^- \rightarrow He(1s3p\ ^3P^o) + H(1s)$ [194].

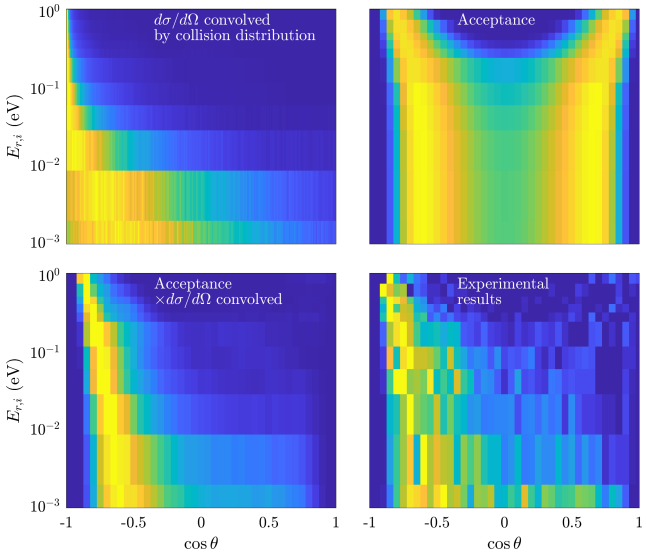

Figure E.3: Differential cross section for $He^+ + D^- \rightarrow He(1s3s\ ^1S) + D(1s)$. The simulation is based on the differential cross section for $He^+ + H^- \rightarrow He(1s3s\ ^1S) + H(1s)$ [194].

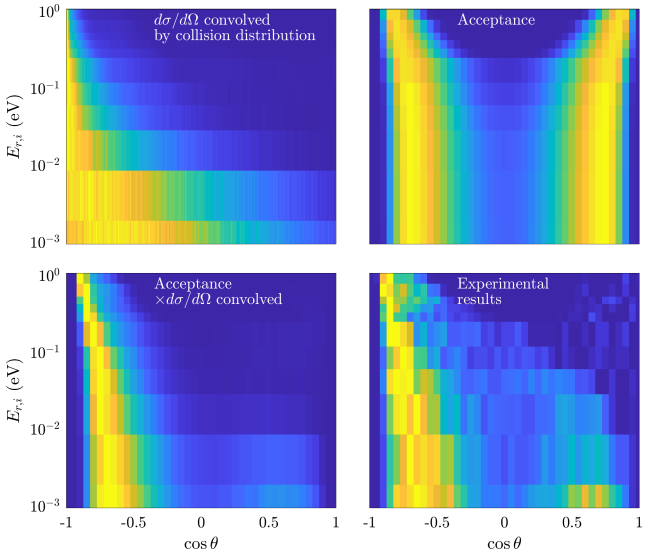

Figure E.4: Differential cross section for $He^+(^2S) + D^-(^1S) \rightarrow He(1s3s\ ^3S) + D(1s)$. The simulation is based on the differential cross section for $He^+(^2S) + H^-(^1S) \rightarrow He(1s3s\ ^3S) + H(1s)$[194].

E.2 $Li^+ + D^-$

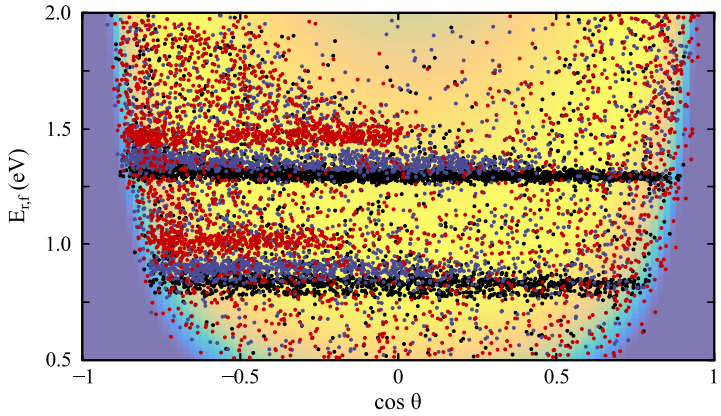

Figure E.5: Experimental events distribution for Li^+ et D^-. Black dots: $E_{r,i}$ =0 meV; violet dots: $E_{r,i}$ =20 meV; red dots: $E_{r,i}$ =200 meV); colormap: acceptance map.

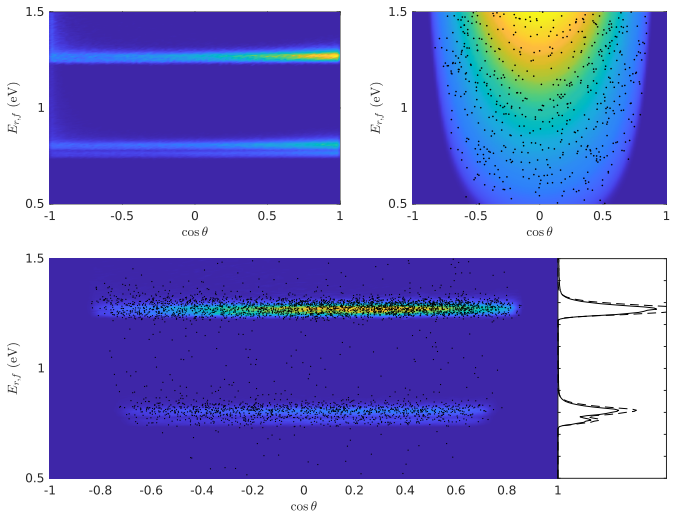

Figure E.6: Differential cross section for $Li^+ + D^- \rightarrow Li + D(1s)$. Top-left: Simulation; Top-right: Acceptance map and background events; Bottom: Product of both. Colormap: Simulation; dots: experiment.

E.3 $Na^+ + O^-$

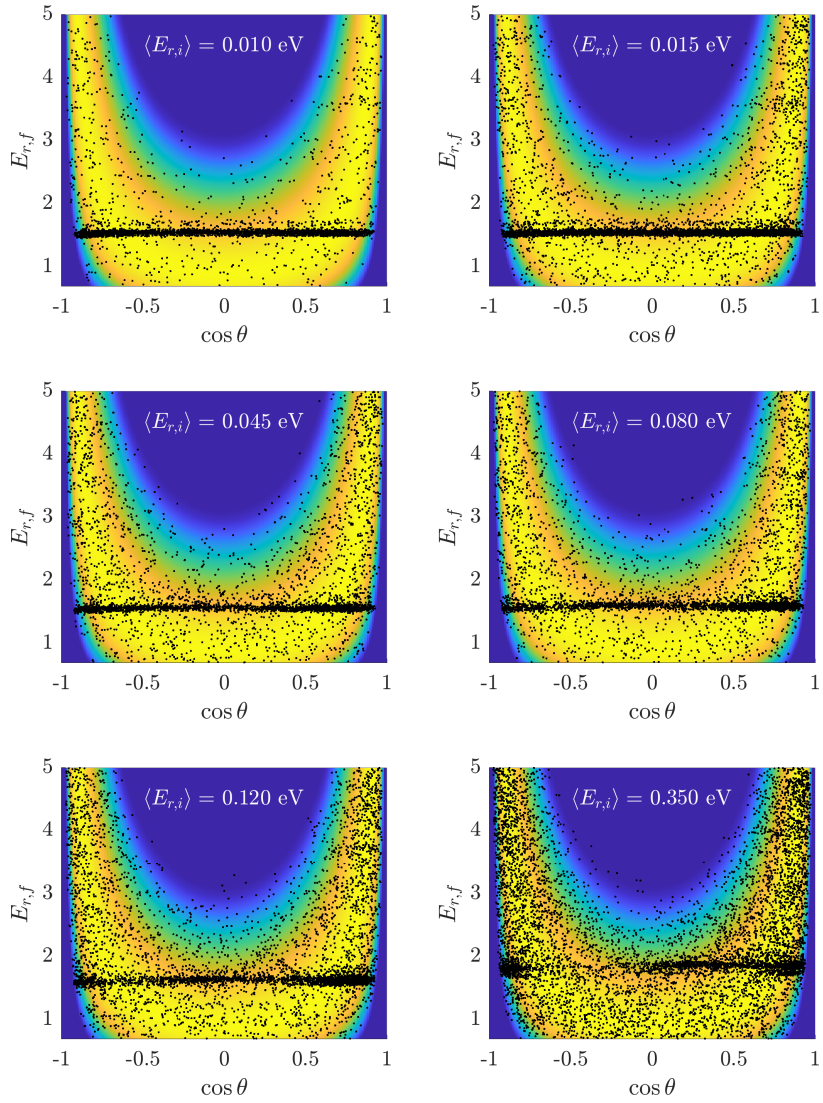

Figure E.7: Experimental events distribution for $Na^+(^1S)$ + O^-. Black dots: experiment; colormap: acceptance map.

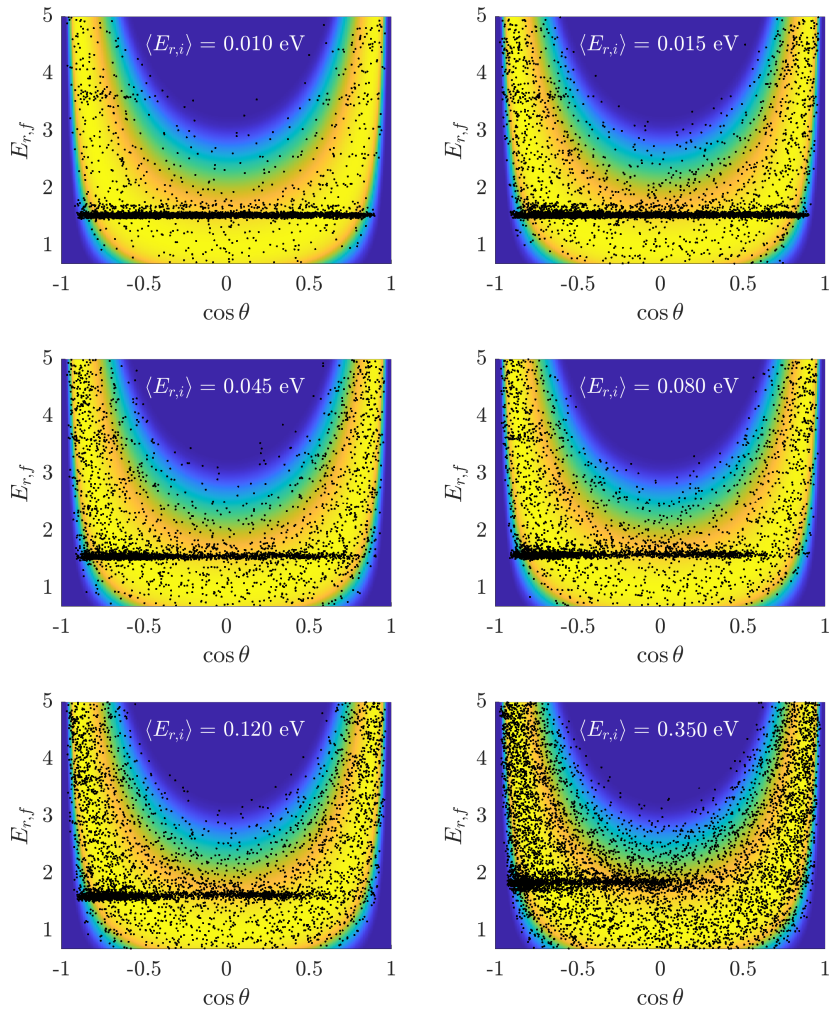

Figure E.8: Experimental events distribution for $Na^+(^1S)$ + O^-. Black dots: experiment; colormap: acceptance map. The masses are exchanged in the analysis compared to Figure E.7.

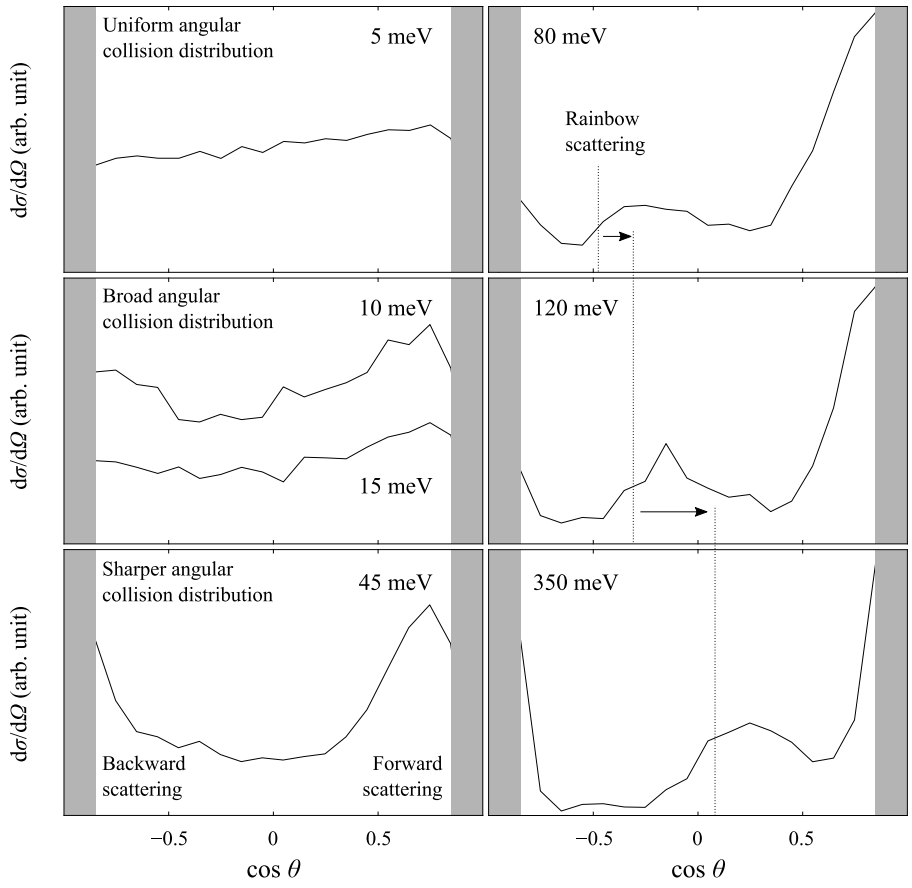

Figure E.9: Differential cross section for $Na^+(^1S) + O^-(^2P^o) \rightarrow Na(3p\ ^2P^o) + O(2p^4\ ^3P)$.

E.4 $C^+ + C^-$

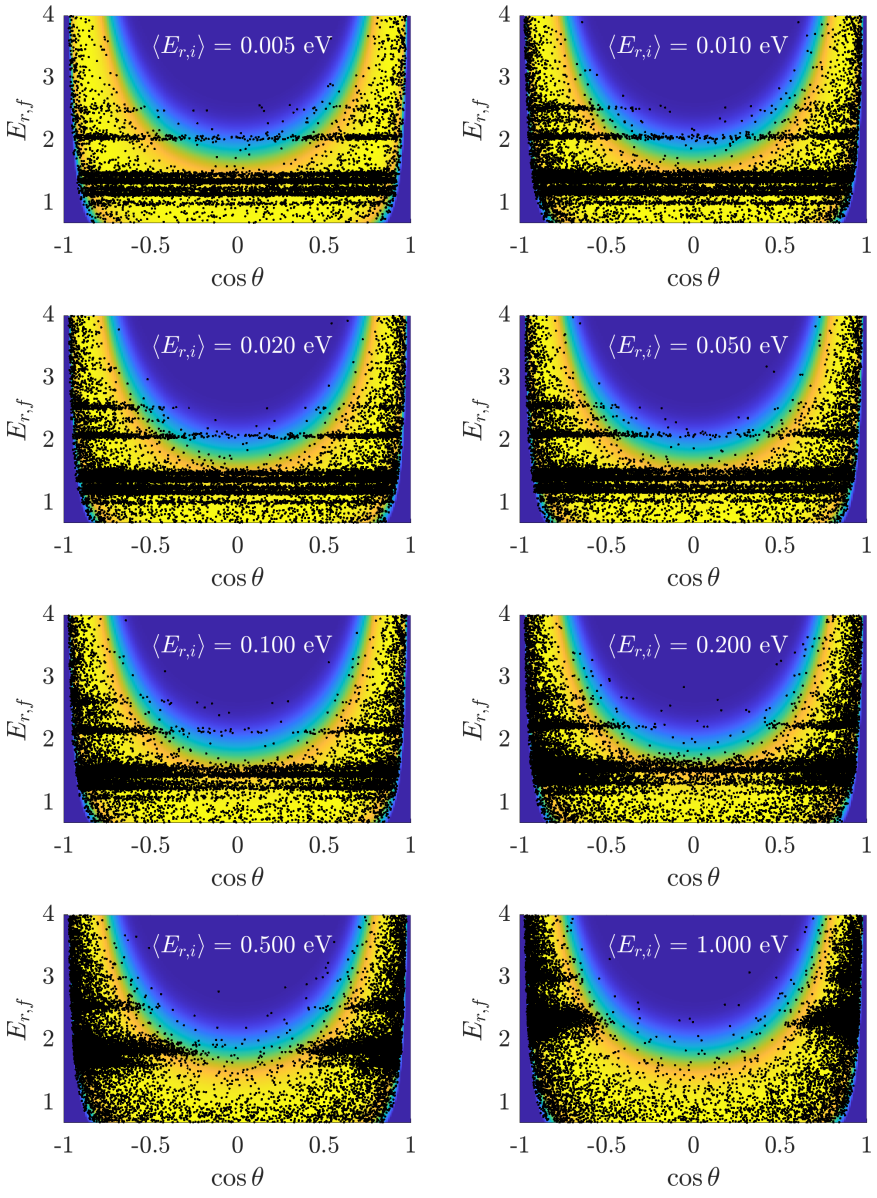

Figure E.10: Experimental events distribution for $C^+(^2P^o) + C^-(^4S^o)$. Black dots: experiment; colormap: acceptance map.

E.5 $C^+ + O^-$

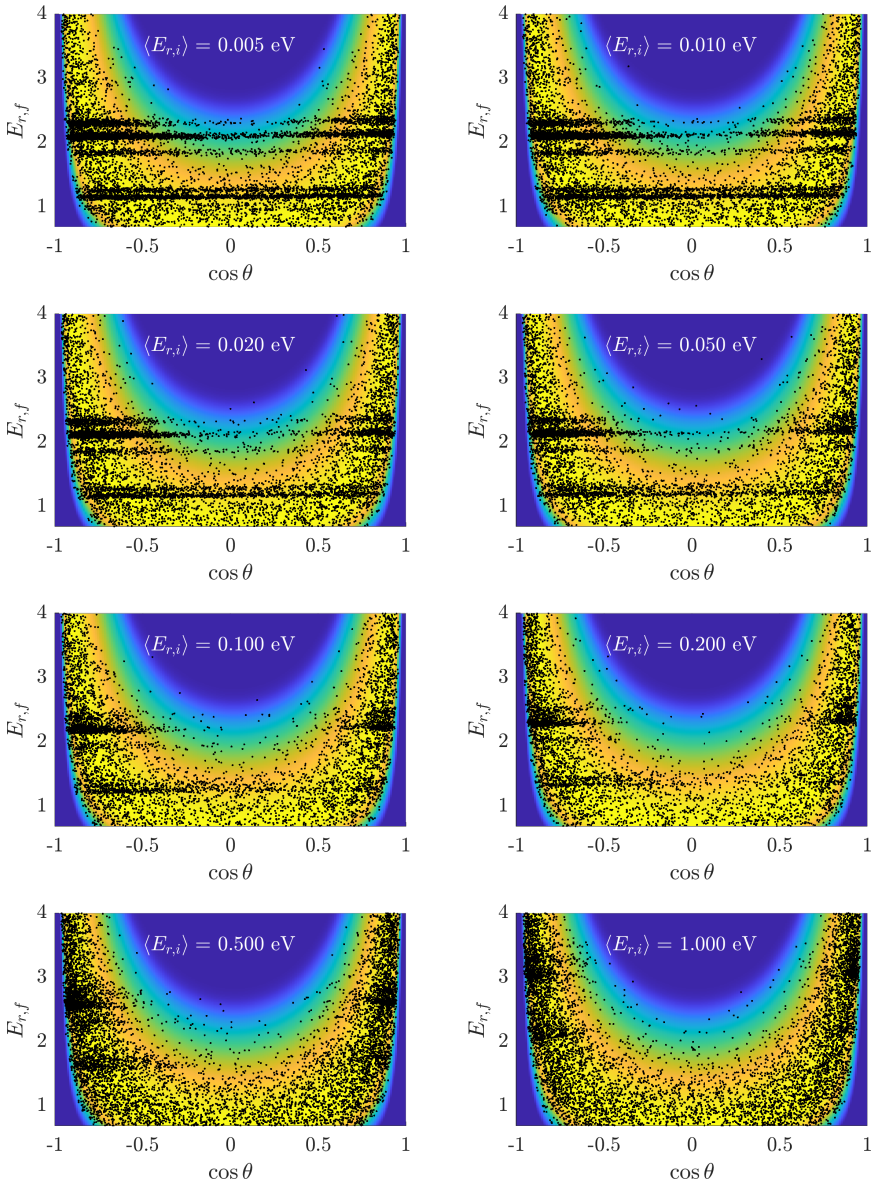

Figure E.11: Experimental events distribution for $C^+(^2P^o) + O^-(^2P^o)$. Black dots: experiment; colormap: acceptance map.

E.6 $N^+ + O^-$

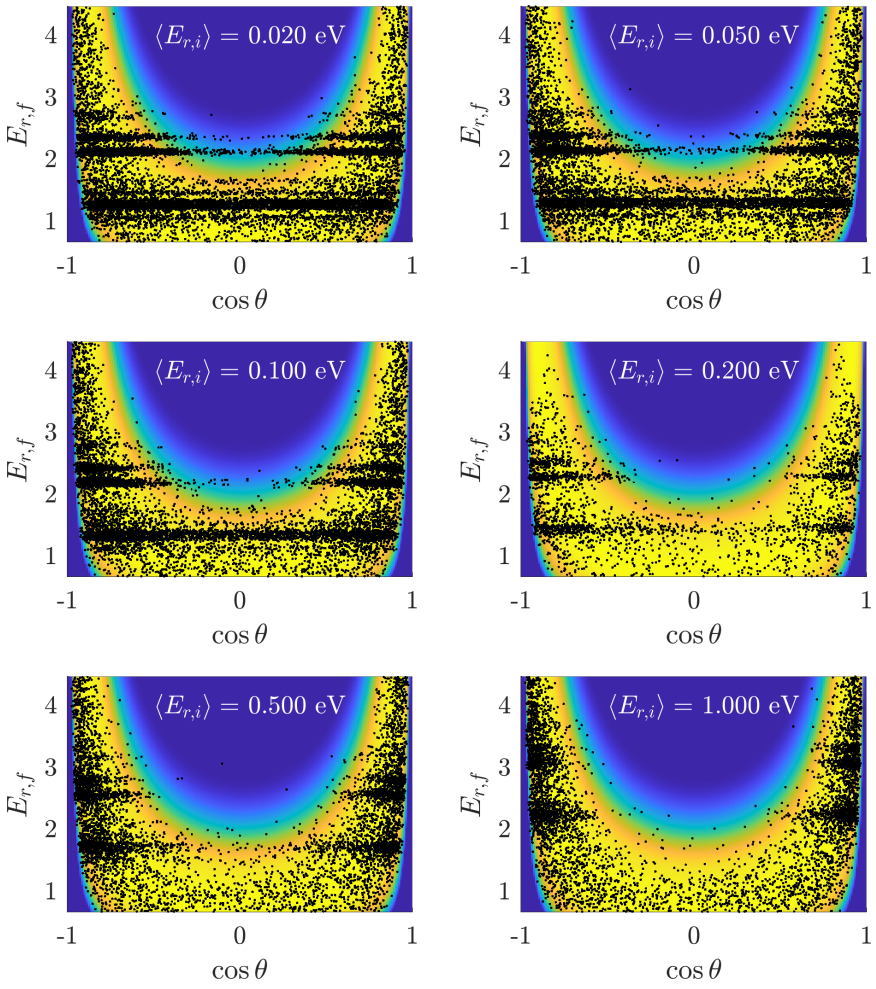

Figure E.12: Experimental events distribution for $N^+(^2P^o) + O^-(^2P^o)$. Black dots: experiment; colormap: acceptance map.

E.7 $O^+ + O^-$

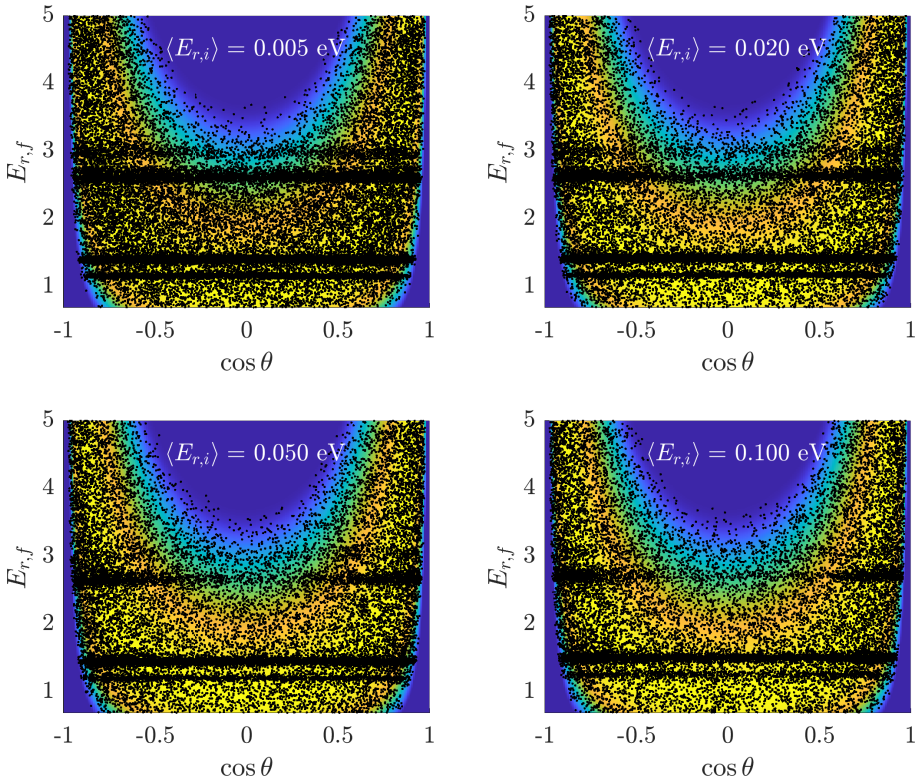

Figure E.13: Experimental events distribution for $O^+(^4S^o) + O^-(^2P^o)$. Black dots: experiment; colormap: acceptance map.

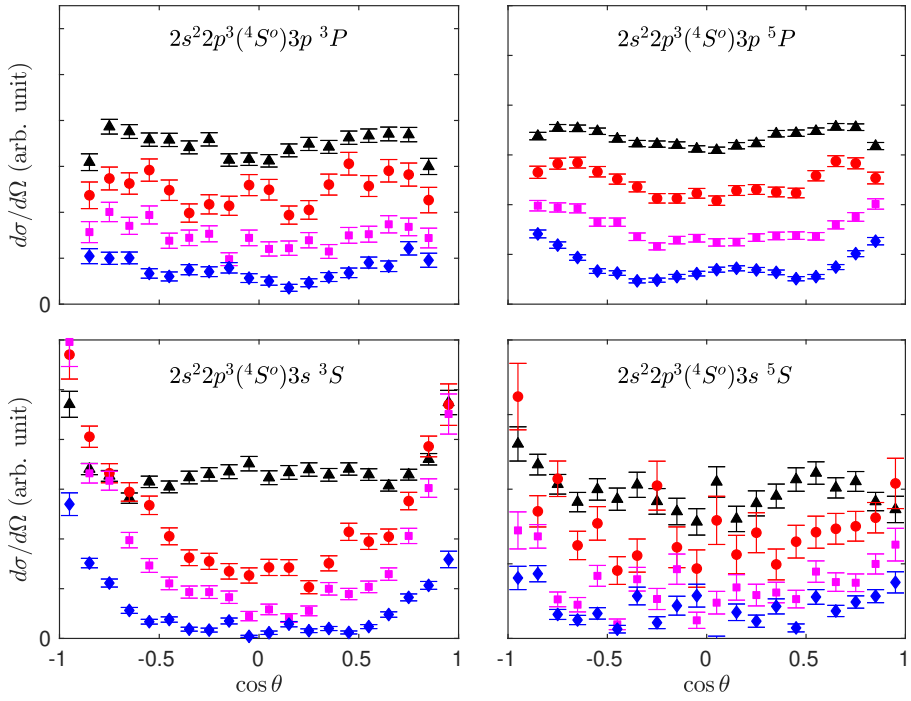

Figure E.14: Differential cross section for $O^+(^4S^o) + O^-(^2P^o) \rightarrow O(3p\ ^2P^o) + O(^{2S+1}L)$. Black triangles: $\langle E_{r,i} \rangle$ =5 meV; Red circles: $\langle E_{r,i} \rangle$ =20 meV; Magenta squares: $\langle E_{r,i} \rangle$ =50 meV; Blue diamonds: $\langle E_{r,i} \rangle$ =100 meV.

E.8 $Ne^+ + C^-$

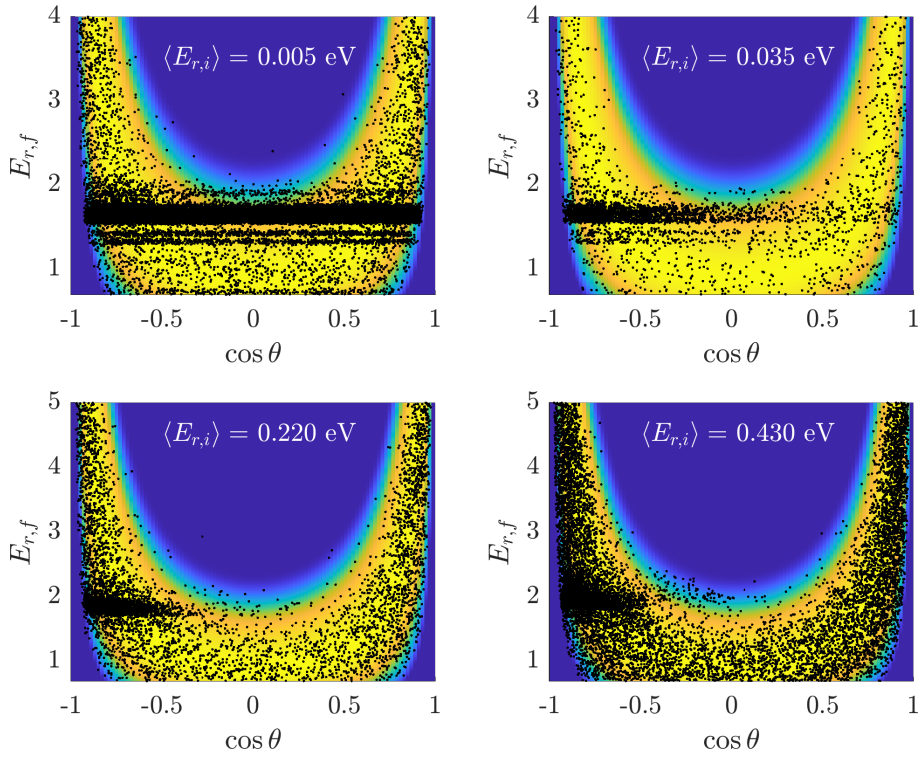

Figure E.15: Experimental events distribution for $Ne^+(^2P^o)$ + $C^-(^4S^o)$. Black dots: experiment; colormap: acceptance map.

Appendix F

Results: Branching ratios

This appendix compiles all the experimental branching ratio measurements: The semilog $E_{r,f}$ spectra treated as described in chapters 4 and B.1; the branching ratios in tabular form; the fit of the KER spectra (Gaussian fit); the interaction potentials in tabular form and a simulation of the spectra using the single-electron asymptotic method 3, using Gaussians to reproduce the spectra.

Note that the width of each (Gaussian) peak is constrained (fit and simulation), being fixed at $\Delta E = 20$ meV for $E_{r,f} = 1$ eV. This width increases with the kinetic energy as follows (section 4.4.3):

$$\Delta E(E_{r,f}) = 0.02 \times \sqrt{E_{r,f}}$$

The normalization of the Gaussian peak is ensured by reducing its amplitude accordingly. The average collision energy is fixed at 20 meV for the simulations.

The ion source used and the beam kinetic energy are indicated for each reaction as well as the mean collision energy (with an error bar of ~ 5 meV). The beam current within the observation cell is not indicated, but goes from 30 to 100 nA for the cation beam and from 10 to 30 nA for the anion beam.

Black:	$A^+ + B^- \rightarrow A^{0*} + B^0$
	$A^+ + B^- \rightarrow A^0 + B^0$
Blue:	$A^+ + B^- \rightarrow A^{0*} + B^{0*}$
	$A^+ + B^- \rightarrow A^0 + B^{0*}$
Red:	$A^{+*} + B^- \rightarrow A^{0*} + B^0$
	$A^{+*} + B^- \rightarrow A^0 + B^0$
Green:	$A^{+*} + B^- \rightarrow A^{0*} + B^{0*}$
	$A^{+*} + B^- \rightarrow A^0 + B^{0*}$
Gray:	$A^+ + B^{-*} \rightarrow A^{0*} + B^0$
	$A^+ + B^{-*} \rightarrow A^{0*} + B^{0*}$
	$A^+ + B^{-*} \rightarrow A^0 + B^0$
	$A^+ + B^{-*} \rightarrow A^0 + B^{0*}$

Table F.1: Color scheme used for the KER spectra fit.

F.1 Helium

F.1.1 Deuterium

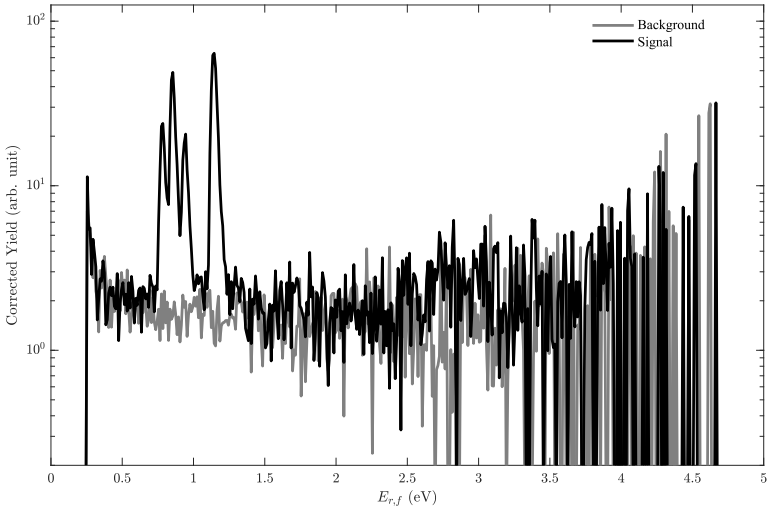

Figure F.1: Experiment: $He^+ + D^- \rightarrow He + D$

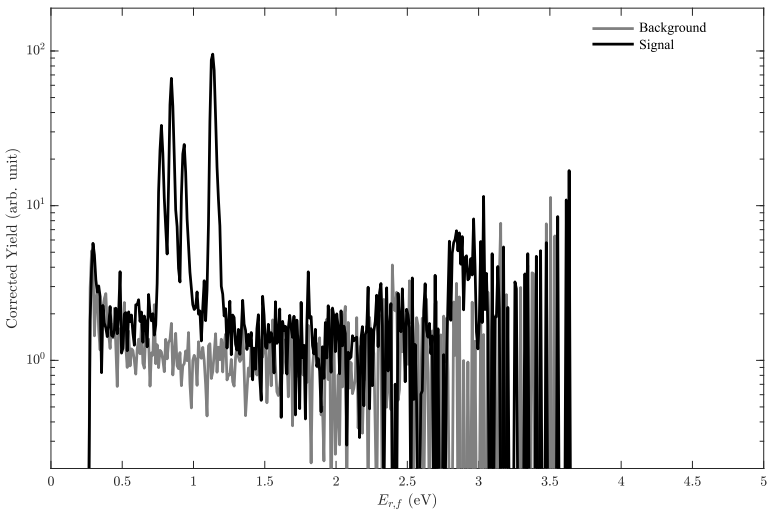

Figure F.2: Experiment: $He^+ + D^- \rightarrow He + D$ (another measurement).

He^+ beam	
Beam energy	11,500 eV
Ion source	ECR (He)
D^- beam	
Beam energy	6,500 eV
Ion source	Duoplasmatron (D_2)
Mean collision energy	$\sim$ 24 meV

Table F.2: He^+ + D^- MN experimental setup parameters.

	$D(1s\ ^2S)$
$He(2s\ ^3S)$	0,027(11)
$He(2p\ ^3P^o)$	0,009(3)
$He(2p\ ^1P^o)$	0,016(3)
$He(3s\ ^3S)$	0,428(8)
$He(3s\ ^1S)$	0,114(4)
$He(3p\ ^3P^o)$	0,271(5)
$He(3d\ ^{1,3}D)$	0,090(3)
$He(3p\ ^1P^o)$	0,043(2)
$He(4s\ ^3S)$	0,004(4)

Table F.3: Branching ratio fit: $He^+(^1S)$ + $D^-(^1S)$.

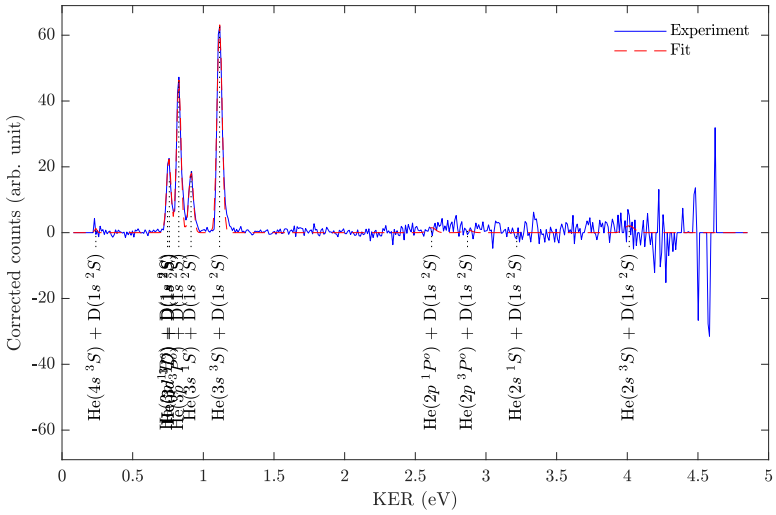

Figure F.3: Branching ratio fit: $He^+(^2S) + D^-(^1S)$.

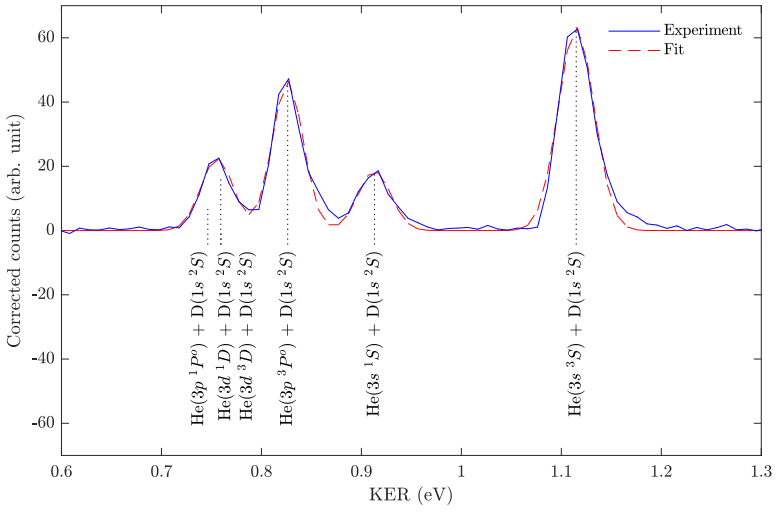

Figure F.4: Branching ratio fit: $He^+(^2S) + D^-(^1S)$ – zoom.

He	D	$^2\Sigma^+$
$1s^2\ ^1S$	$1s\ ^2S$	1.806e-01
$1s^2\ ^1S$	$2s\ ^2S$	4.965e-02
$1s^2\ ^1S$	$3s\ ^2S$	3.104e-02
$1s^2\ ^1S$	$4s\ ^2S$	2.540e-02
$1s^2\ ^1S$	$5s\ ^2S$	2.297e-02
$2s\ ^3S$	$1s\ ^2S$	1.819e-02
$2s\ ^1S$	$1s\ ^2S$	7.183e-03
$2p\ ^3P^o$	$1s\ ^2S$	9.835e-03
$2p\ ^1P^o$	$1s\ ^2S$	4.847e-03
$3s\ ^3S$	$1s\ ^2S$	7.030e-04
$3s\ ^1S$	$1s\ ^2S$	1.591e-04
$3p\ ^3P^o$	$1s\ ^2S$	1.931e-04
$3d\ ^3D$	$1s\ ^2S$	6.729e-05
$3d\ ^1D$	$1s\ ^2S$	3.873e-05
$3p\ ^1P^o$	$1s\ ^2S$	6.019e-05

Table F.4: Interaction potentials E_{ic} (a.u.): $He^+(1s\ ^2S)$ + $D^-(1s^2\ ^1S)$

Cation	Anion	Center-of-mass collision energy (eV)					
He	D	0.002	0.005	0.02	0.05	0.2	0.5
$1s^2\ ^1S$	$1s\ ^2S$	1.07e-29	4.32e-30	1.15e-30	5.17e-31	2.29e-31	2.6e-31
$1s^2\ ^1S$	$2s\ ^2S$	4e-24	1.62e-24	4.29e-25	1.93e-25	8.41e-26	9.19e-26
$2s\ ^3S$	$1s\ ^2S$	2.5e-22	1.01e-22	2.68e-23	1.21e-23	5.28e-24	5.82e-24
$2s\ ^1S$	$1s\ ^2S$	1.32e-17	5.33e-18	1.39e-18	6.02e-19	2.21e-19	1.76e-19
$2p\ ^3P^o$	$1s\ ^2S$	2.71e-16	1.09e-16	2.82e-17	1.21e-17	4.19e-18	2.99e-18
$2p\ ^1P^o$	$1s\ ^2S$	7.09e-13	2.85e-13	7.24e-14	2.99e-14	8.71e-15	4.55e-15
$3s\ ^3S$	$1s\ ^2S$	1.11e-11	4.47e-12	1.13e-12	4.66e-13	1.32e-13	6.49e-14
$3s\ ^1S$	$1s\ ^2S$	2.79e-12	1.12e-12	2.83e-13	1.16e-13	3.21e-14	1.51e-14
$3p\ ^3P^o$	$1s\ ^2S$	5.62e-12	2.25e-12	5.7e-13	2.34e-13	6.54e-14	3.12e-14
$3d\ ^3D$	$1s\ ^2S$	1.13e-12	4.54e-13	1.15e-13	4.72e-14	1.31e-14	6.2e-15
$3d\ ^1D$	$1s\ ^2S$	3.85e-13	1.54e-13	3.9e-14	1.6e-14	4.44e-15	2.09e-15
$3p\ ^1P^o$	$1s\ ^2S$	9.87e-13	3.96e-13	1e-13	4.11e-14	1.14e-14	5.4e-15
$4s\ ^3S$	$1s\ ^2S$	9.45e-24	3.81e-24	9.83e-25	4.17e-25	1.3e-25	6.79e-26

Table F.5: Partial cross section (cm^2) for the He^++D^- MN reaction computed with the ACAM.

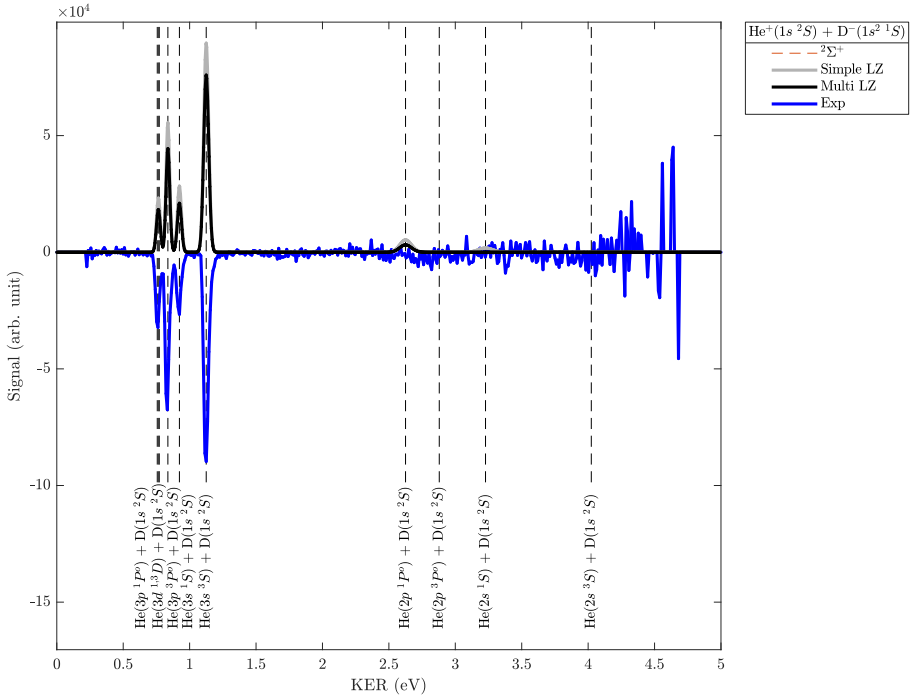

Figure F.5: Simulation: $He^+(^2S) + D^-(^1S)$

F.2 Lithium

	D^- (full) D(1s)	D^- (redu) D(1s)	H^- (full) D(1s)	H^- (redu) D(1s)
Li($2p\ ^2P^o$)	0,001(1)	0,001(1)	0,004(4)	0,004(4)
Li($3s\ ^2S$)	0,522(5)	0,676(21)	0,639(19)	0,626(20)
Li($3p\ ^2P^o$)	0,341(1)	0,226(13)	0,280(11)	0,252(11)
Li($3d\ ^2D$)	0,136(3)	0,098(9)	0,077(6)	0,095(7)

Table F.6: Branching ratio fit: $Li^+(^1S) + X^-$.

F.2.1 Hydrogen

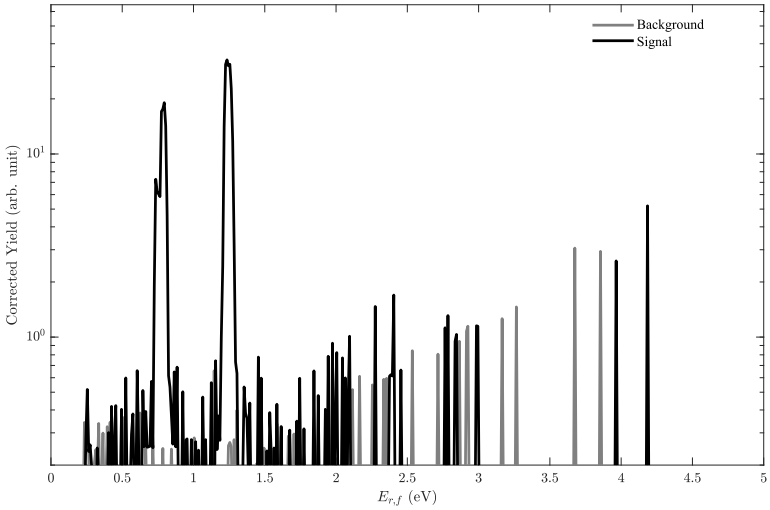

Figure F.6: Experiment: $He^+ + H^- \rightarrow He + H$ – full observation length.

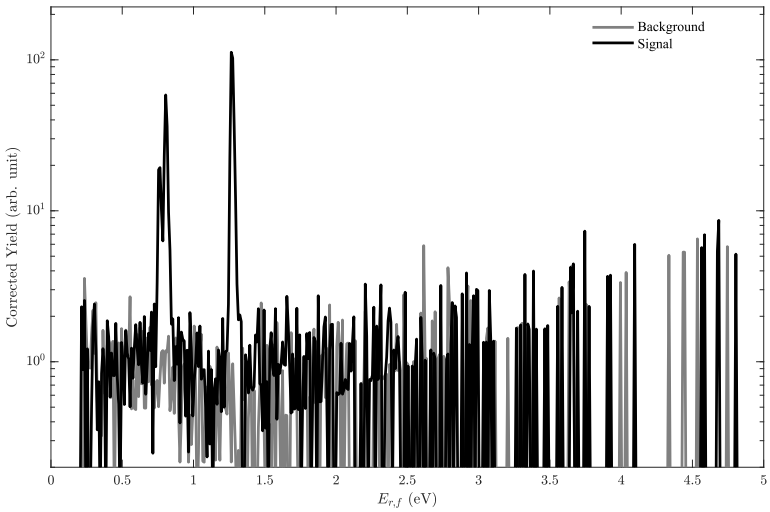

Figure F.7: Experiment: $He^+ + H^- \rightarrow He + H$ – reduced observation length.

Li^+ beam	
Beam energy:	13,500 eV
Ion source:	Thermionic, ^{7}Li enriched
H^- beam	
Beam energy:	2,500 eV
Ion source:	Duoplasmatron (H_2)
Mean collision energy:	$\sim$ 7 meV

Table F.7: Li^+ + H^- MN experimental setup parameters.

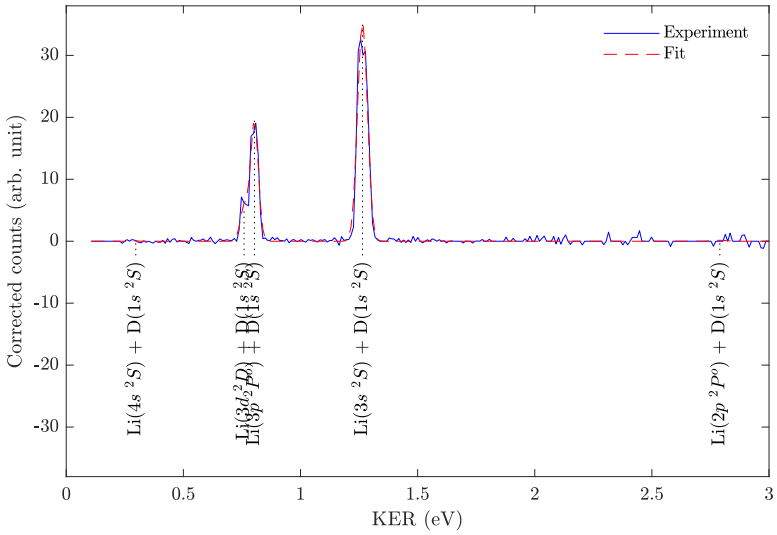

Figure F.8: Branching ratio fit: $Li^+(^1S)$ + $D^-(^1S)$ – full observation length.

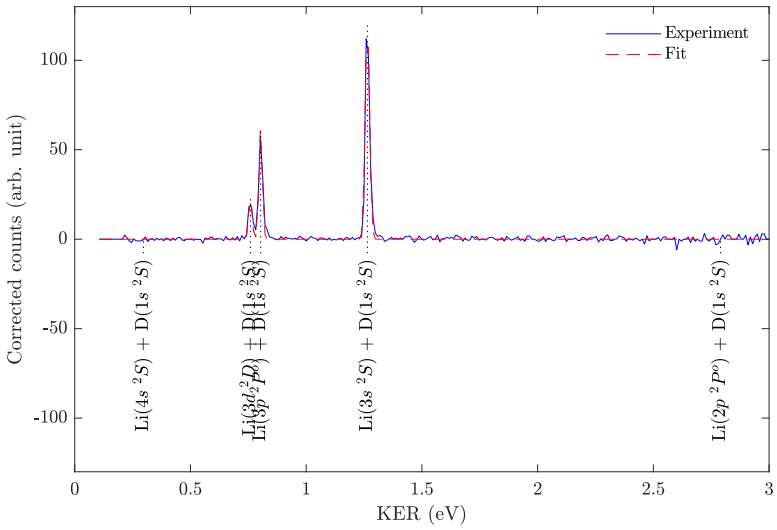

Figure F.9: Branching ratio fit: $Li^+(^1S)$ + $D^-(^1S)$ – reduced observation length.

F.2.2 Deuterium

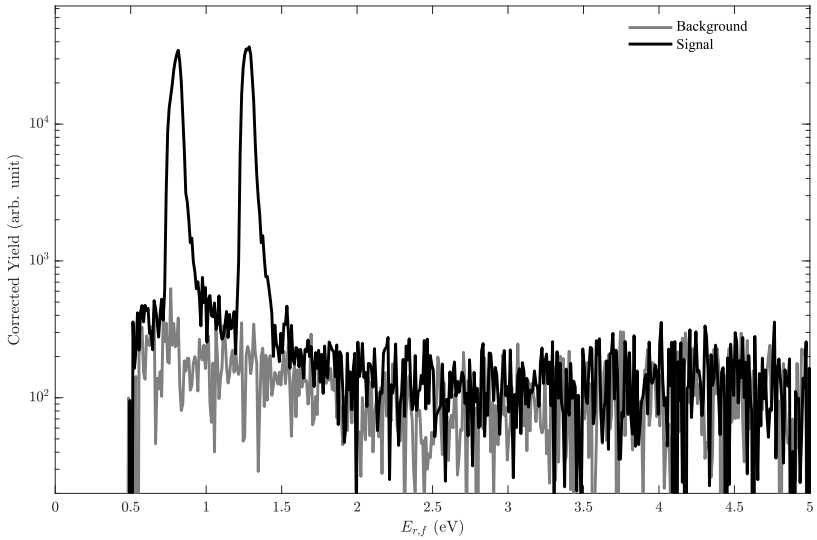

Figure F.10: Experiment: $Li^+ + D^- \rightarrow Li + D$ – full observation length.

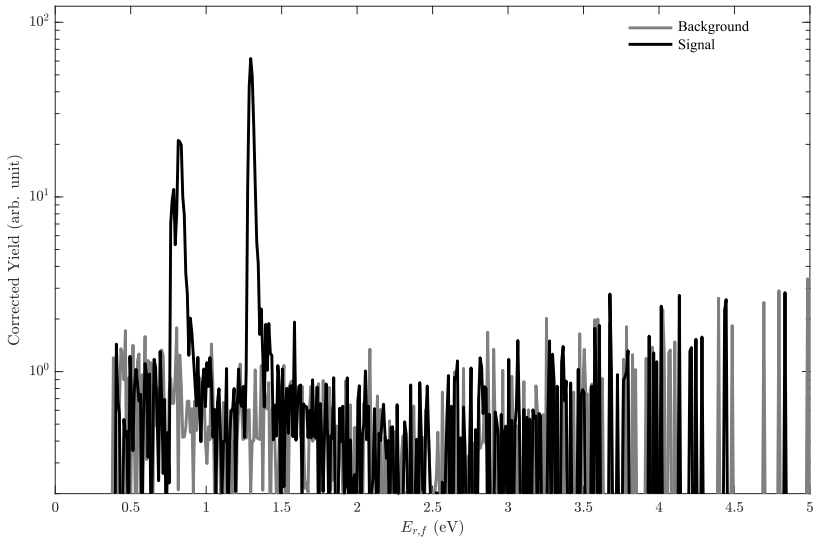

Figure F.11: Experiment: $Li^+ + D^- \rightarrow Li + D$ – reduced observation length.

Li^+ beam	
Beam energy:	12,000 eV
Ion source:	Thermionic
D^- beam	
Beam energy:	3,750 eV
Ion source:	Duoplasmatron (D_2)
Mean collision energy:	$\sim$ 11 meV

Table F.8: Li^+ + D^- MN experimental setup parameters.

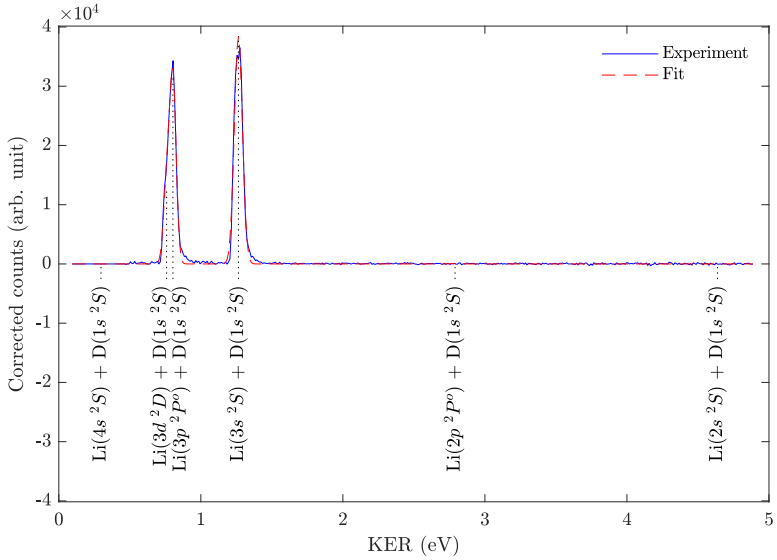

Figure F.12: Branching ratio fit: $Li^+(^1S)$ + $H^-(^1S)$ – full observation length.

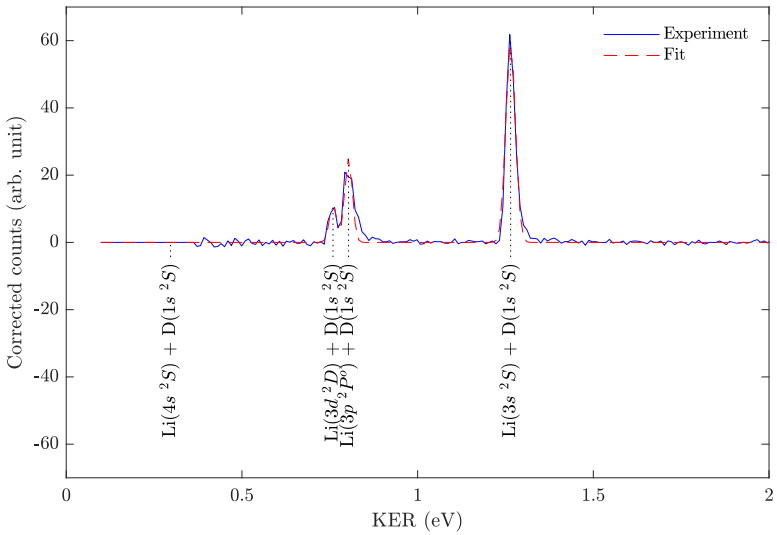

Figure F.13: Branching ratio fit: $Li^+(^1S)$ + $H^-(^1S)$ – reduced observation length.

Li	D	$^1\Sigma^+$
$2s\ ^2S$	$1s\ ^2S$	2.645e-02
$2p\ ^2P^o$	$1s\ ^2S$	1.084e-02
$3s\ ^2S$	$1s\ ^2S$	1.335e-03
$3p\ ^2P^o$	$1s\ ^2S$	1.894e-04
$3d\ ^2D$	$1s\ ^2S$	7.733e-05
$4s\ ^2S$	$1s\ ^2S$	2.395e-09

Table F.9: Interaction potentials E_{ic} (a.u.): $Li^+(^1S)$ + $D^-(^1S)$

Cation Li	Anion D	Center-of-mass collision energy (eV) 0.002	0.005	0.02	0.05	0.2	0.5
$2s\ ^2S$	$1s\ ^2S$	1.19e-22	4.82e-23	1.27e-23	5.69e-24	2.42e-24	2.52e-24
$2p\ ^2P^o$	$1s\ ^2S$	3.89e-16	1.57e-16	4.06e-17	1.74e-17	6.09e-18	4.4e-18
$3s\ ^2S$	$1s\ ^2S$	8.22e-12	3.3e-12	8.39e-13	3.47e-13	1.01e-13	5.22e-14
$3p\ ^2P^o$	$1s\ ^2S$	6.26e-12	2.51e-12	6.35e-13	2.6e-13	7.2e-14	3.39e-14
$3d\ ^2D$	$1s\ ^2S$	1.5e-12	6.01e-13	1.52e-13	6.22e-14	1.72e-14	8.01e-15
$4s\ ^2S$	$1s\ ^2S$	4.58e-20	1.84e-20	4.73e-21	1.98e-21	5.98e-22	3.05e-22

Table F.10: Partial cross section (cm^2) for the Li^++D^- MN reaction computed with the ACAM.

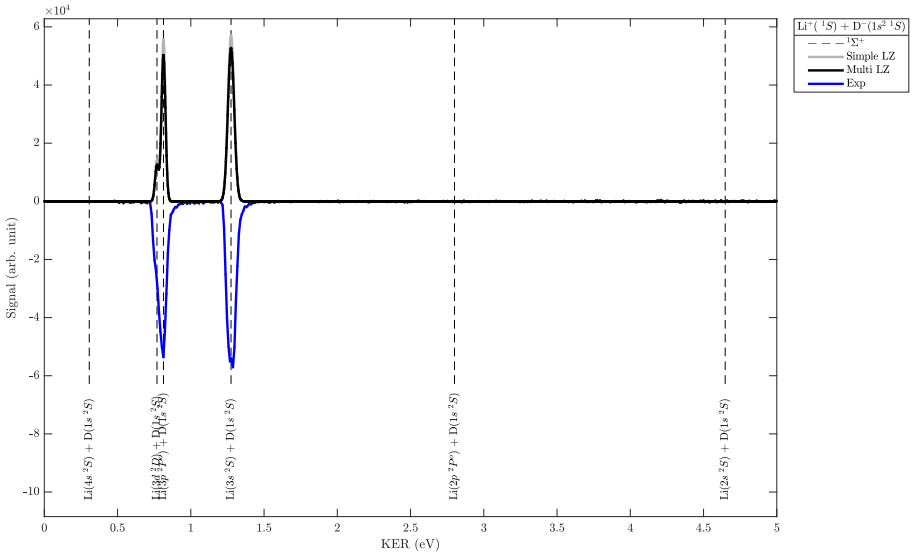

Figure F.14: Simulation: $Li^+(^1S)$ + $D^-(1^1S)$

F.3 Sodium

	$O^-(^2P^o)$		$S^-(^2P^o)$		
	$O(^3P)$	$O(^1D)$	$S(^3P)$	$S(^1D)$	$S(^1S)$
$Na(3s\ ^2S)$	0,011(1)	0,037(1)	0,049(2)	0,926(5)	0,013(2)
$Na(3p\ ^2P^o)$	0,952(6)		0,012(1)		
$Na(4s\ ^2S)$	0,000(1)				

Table F.11: Branching ratio fit: $Na^+(^1S) + X^-$.

F.3.1 Deuterium

Na	D	$^1\Sigma^+$
$3s\ ^2S$	$1s\ ^2S$	2.422e-02
$3p\ ^2P^o$	$1s\ ^2S$	7.494e-03
$4s\ ^2S$	$1s\ ^2S$	1.072e-03
$3d\ ^2D$	$1s\ ^2S$	8.295e-05
$4p\ ^2P^o$	$1s\ ^2S$	3.708e-05

Table F.12: Interaction potentials E_{ic} (a.u.): $Na^+(^1S)$ + $D^-(^1S)$

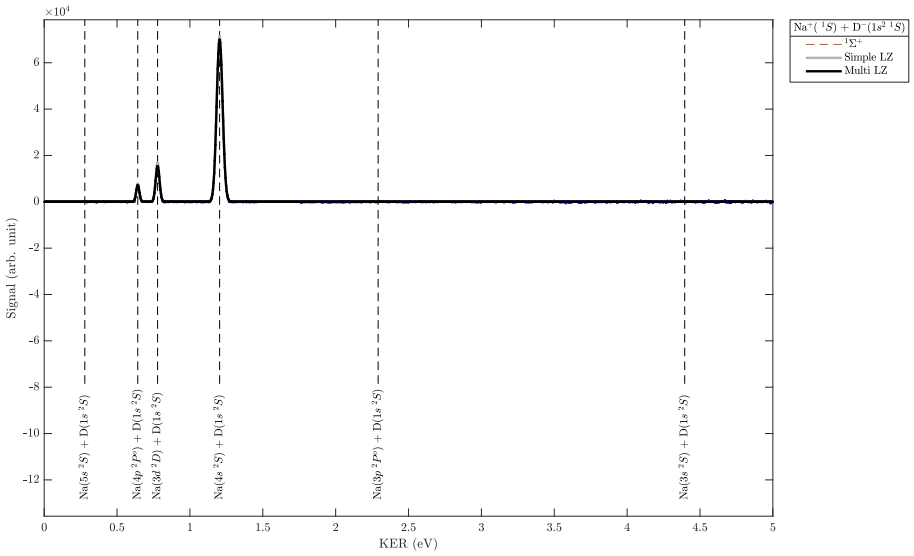

Figure F.15: Simulation: $Na^+(^1S)$ + $D^-(^1S)$

Cation	Anion	Center-of-mass collision energy (eV)					
Na	D	0.002	0.005	0.02	0.05	0.2	0.5
$3s\ ^2S$	$1s\ ^2S$	2.63e-22	1.06e-22	2.82e-23	1.27e-23	5.5e-24	5.93e-24
$3p\ ^2P^o$	$1s\ ^2S$	2.12e-15	8.56e-16	2.22e-16	9.56e-17	3.38e-17	2.47e-17
$4s\ ^2S$	$1s\ ^2S$	1.06e-11	4.25e-12	1.08e-12	4.46e-13	1.28e-13	6.5e-14
$3d\ ^2D$	$1s\ ^2S$	1.88e-12	7.52e-13	1.9e-13	7.77e-14	2.13e-14	9.9e-15
$4p\ ^2P^o$	$1s\ ^2S$	7.92e-13	3.17e-13	8.04e-14	3.3e-14	9.18e-15	4.33e-15
$5s\ ^2S$	$1s\ ^2S$	1.43e-21	5.75e-22	1.48e-22	6.23e-23	1.9e-23	9.78e-24

Table F.13: Partial cross section (cm^2) for the Na^++D^- MN reaction computed with the ACAM.

F.3.2 Oxygen

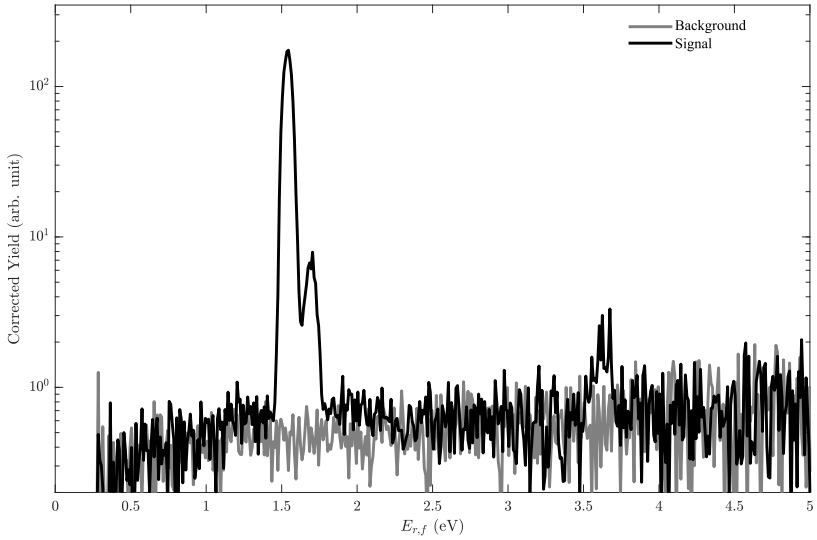

Figure F.16: Experiment: $Na^+ + O^- \rightarrow Na + O$.

Na^+ beam	
Beam energy:	10,500 eV
Ion source:	Thermionic
O^- beam	
Beam energy:	7,700 eV
Ion source:	Duoplasmatron (CO_2)
Mean collision energy:	$\sim$ 7 meV

Table F.14: $Na^+ + O^-$ MN experimental setup parameters.

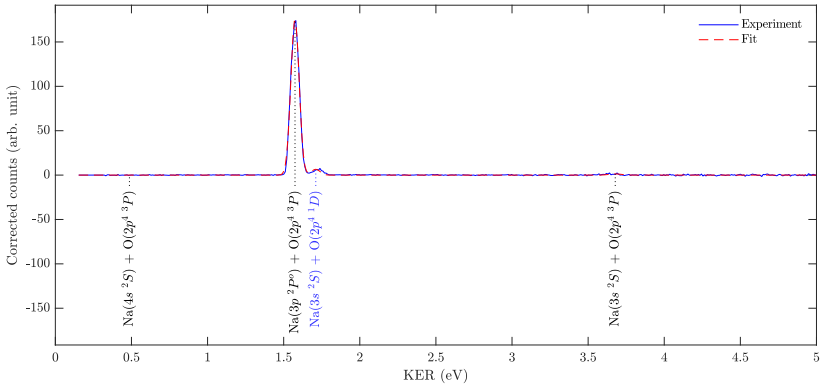

Figure F.17: Branchin ratio fit: $Na^+(^1S) + O^-(^2P^o)$. The color code for the products is given in table F.1.

Na	O	$^2\Sigma^+$	$^2\Pi$
$3s\ ^2S$	$2p^4\ ^3P$		9.034e-03
$3s\ ^2S$	$2p^4\ ^1D$	5.218e-05	4.519e-05
$3p\ ^2P^o$	$2p^4\ ^3P$	1.903e-04	1.109e-04
$4s\ ^2S$	$2p^4\ ^3P$		1.178e-08

Table F.15: Interaction potentials E_{ic} (a.u.): $Na^+(^1S) + O^-(^2P^o)$

Cation	Anion	Center-of-mass collision energy (eV)					
Na	O	0.002	0.005	0.02	0.05	0.2	0.5
$3s\ ^2S$	$2p^4\ ^3P$	1.95e-15	7.84e-16	2e-16	8.32e-17	2.52e-17	1.44e-17
$3s\ ^2S$	$2p^4\ ^1D$	1.05e-13	4.21e-14	1.06e-14	4.27e-15	1.11e-15	4.81e-16
$3p\ ^2P^o$	$2p^4\ ^3P$	1.08e-12	4.32e-13	1.09e-13	4.39e-14	1.15e-14	5.01e-15
$4s\ ^2S$	$2p^4\ ^3P$	3.34e-19	1.34e-19	3.4e-20	1.4e-20	3.97e-21	1.9e-21

Table F.16: Partial cross section (cm^2) for the Na^++O^- MN reaction computed with the ACAM.

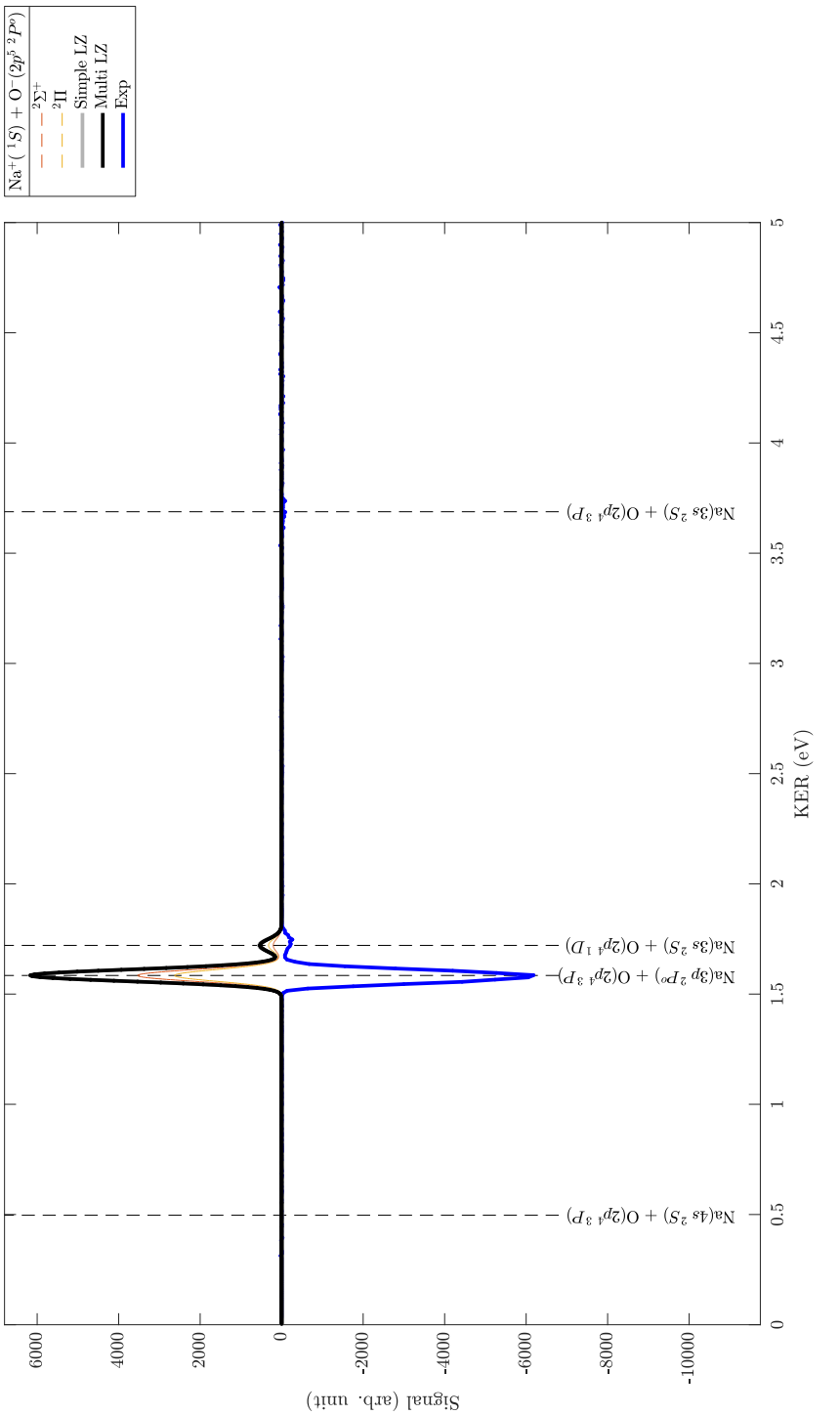

Figure F.18: Simulation: $Na^+(^1S) + O^-(^2P^o)$

F.3.3 Sulfur

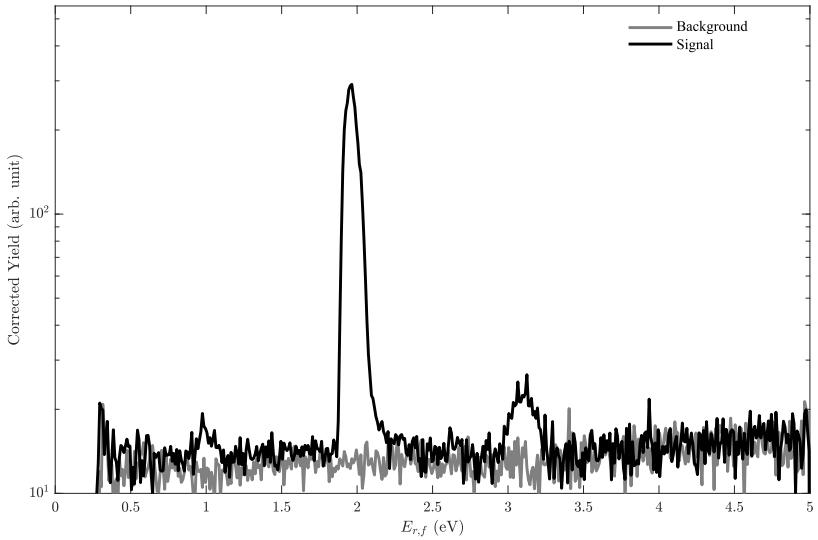

Figure F.19: Experiment: $Na^+ + S^- \rightarrow Na + S$

Na^+ beam	
Beam energy:	10,500 eV
Ion source:	Thermionic
S^- beam	
Beam energy:	7,700 eV
Ion source:	Sputtering (FeS)
Mean collision energy:	$\sim$ 12 meV

Table F.17: $Na^+ + S^-$ MN experimental setup parameters.

Na	S	$^2\Sigma^+$	$^2\Pi$
$3s\ ^2S$	$3p^4\ ^3P$		5.625e-03
$3s\ ^2S$	$3p^4\ ^1D$	1.924e-04	1.666e-04
$3p\ ^2P^o$	$3p^4\ ^3P$	1.233e-06	7.190e-07

Table F.18: Interaction potentials E_{ic} (a.u.): $Na^+(^1S) + S^-(^2P^o)$

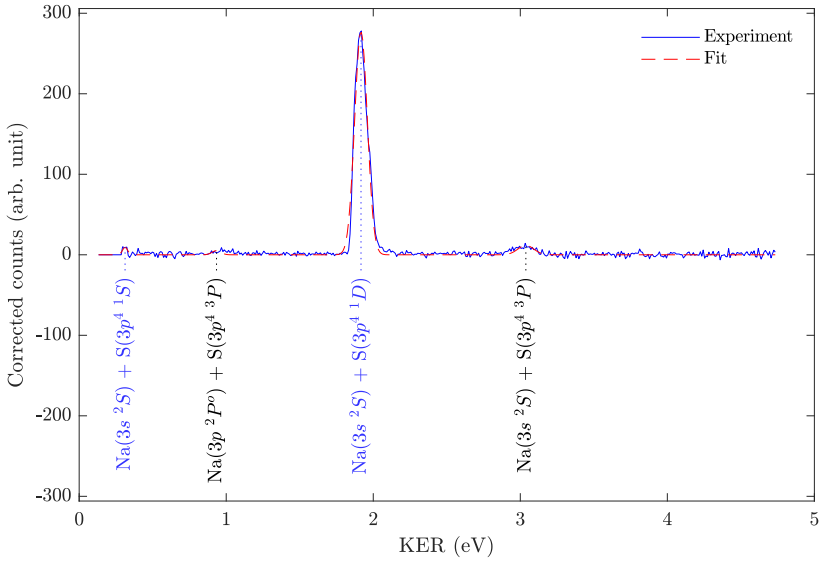

Figure F.20: Branching ratio fit: $Na^+(^1S)$ + $S^-(^2P^o)$. The color code for the products is given in table F.1.

Cation	Anion	Center-of-mass collision energy (eV)					
Na	S	0.002	0.005	0.02	0.05	0.2	0.5
$3s\ ^2S$	$3p^4\ ^3P$	2.06e-14	8.26e-15	2.1e-15	8.74e-16	2.62e-16	1.46e-16
$3s\ ^2S$	$3p^4\ ^1D$	1.05e-12	4.19e-13	1.05e-13	4.25e-14	1.1e-14	4.75e-15
$3p\ ^2P^o$	$3p^4\ ^3P$	3.37e-16	1.35e-16	3.4e-17	1.38e-17	3.71e-18	1.67e-18

Table F.19: Partial cross section (cm^2) for the Na^++S^- MN reaction computed with the ACAM.

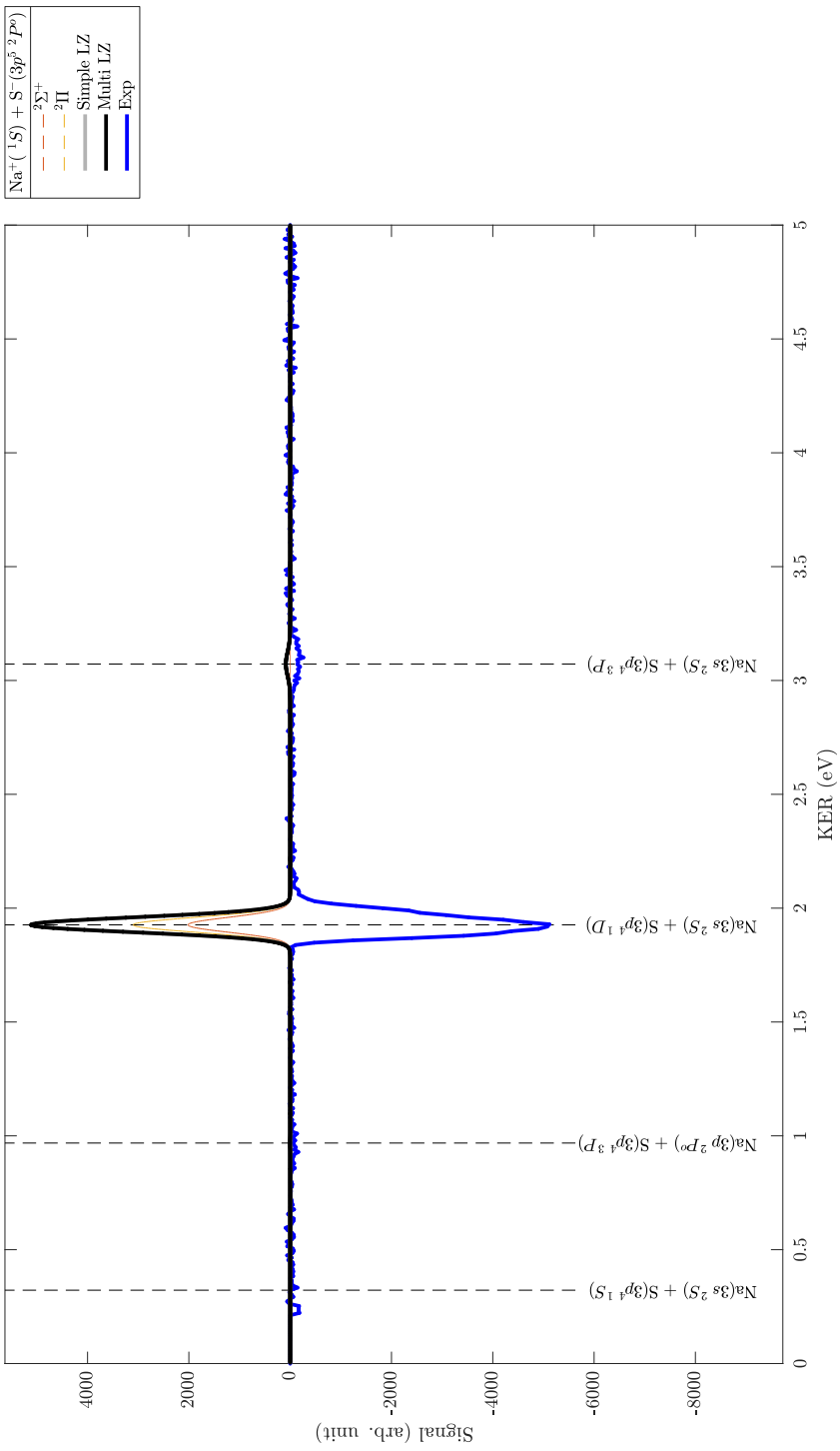

Figure F.21: Simulation: $Na^+(^1S) + S^-(^2P^o)$

F.4 Carbon

	$P^-(^3P)$ $P(^4S^o)$	$D^-(^1S)$ $D(1s)$	$Si^-(^3P)$ $Si(^4S^o)$	$C^-(^4S^o)$ $C(^3P)$	$O^-(^2P^o)$ $O(^3P)$	$S^-(^2P_o)$ $S(^3P)$	OH^- $OH(X)$
$C(3s\,^3P^o)$	0,009(1)	0,001(1)	0,009(1)	0,019(2)	0,156(3)	0,675(4)	0,613(56)
$C(3s\,^1P^o)$	0,006(1)	0,003(1)	0,030(1)	0,012(2)	0,410(5)	0,186(2)	0,308(36)
$C(2s2p^3\,^3D^o)$	0,015(2)	0,005(1)	0,103(2)	0,078(3)	0,082(2)	0,018(1)	0,036(12)
$C(3p\,^1P)$	0,017(1)	0,007(1)	0,155(2)	0,115(3)	0,087(2)	0,005(0)	0,016(13)
$C(3p\,^3D)$	0,059(2)	0,017(1)	0,499(3)	0,444(6)	0,197(3)	0,004(0)	0,009(4)
$C(3p\,^3S)$	0,026(2)	0,026(1)	0,062(1)	0,081(3)	0,017(1)	0,002(0)	0,001(2)
$C(3p\,^3P)$	0,060(2)	0,049(2)	0,109(2)	0,140(3)	0,024(1)	0,002(0)	0,002(2)
$C(3p\,^1D)$	0,123(3)	0,284(4)	0,018(1)	0,029(2)	0,007(1)		0,000(50)
$C(3p\,^1S)$	0,051(2)	0,081(2)	0,009(1)	0,003(1)	0,007(1)		0,016(16)
$C(2s2p^3\,^3P^o)$	0,104(2)	0,141(3)	0,008(1)	0,005(1)	0,004(1)		
$C(3d\,^1D^o)$	0,039(1)	0,035(1)		0,006(1)			
$C(4s\,^3P^o)$	0,142(3)	0,065(3)		0,005(1)			
$C(3d\,^3F^o)$	0,009(4)	0,199(17)		0,003(1)			
$C(3d\,^3D^o)$	0,046(46)	0,02(39)		0,053(15)			
$C(3d\,^1F^o)$		0,000(10)		0,006(3)			
$C(3d\,^1P^o)$	0,014(1)	0,016(1)		0,003(1)			
$C(3d\,^3P^o)$	0,011(1)	0,015(1)					
$C(4p\,^1P)$	0,003(1)	0,002(1)					
$C(4p\,^3D)$		0,005(1)					
$C(4p\,^3S)$	0,002(3)	0,002(1)					
$C(4p\,^3P)$	0,001(1)	0,003(1)					
$C(4p\,^1D)$	0,008(1)	0,005(1)					
$C(4p\,^1S)$	0,001(1)						

Table F.20: Branching ratio fit (simplified): $C^+(^2P^o)$ + X^-.

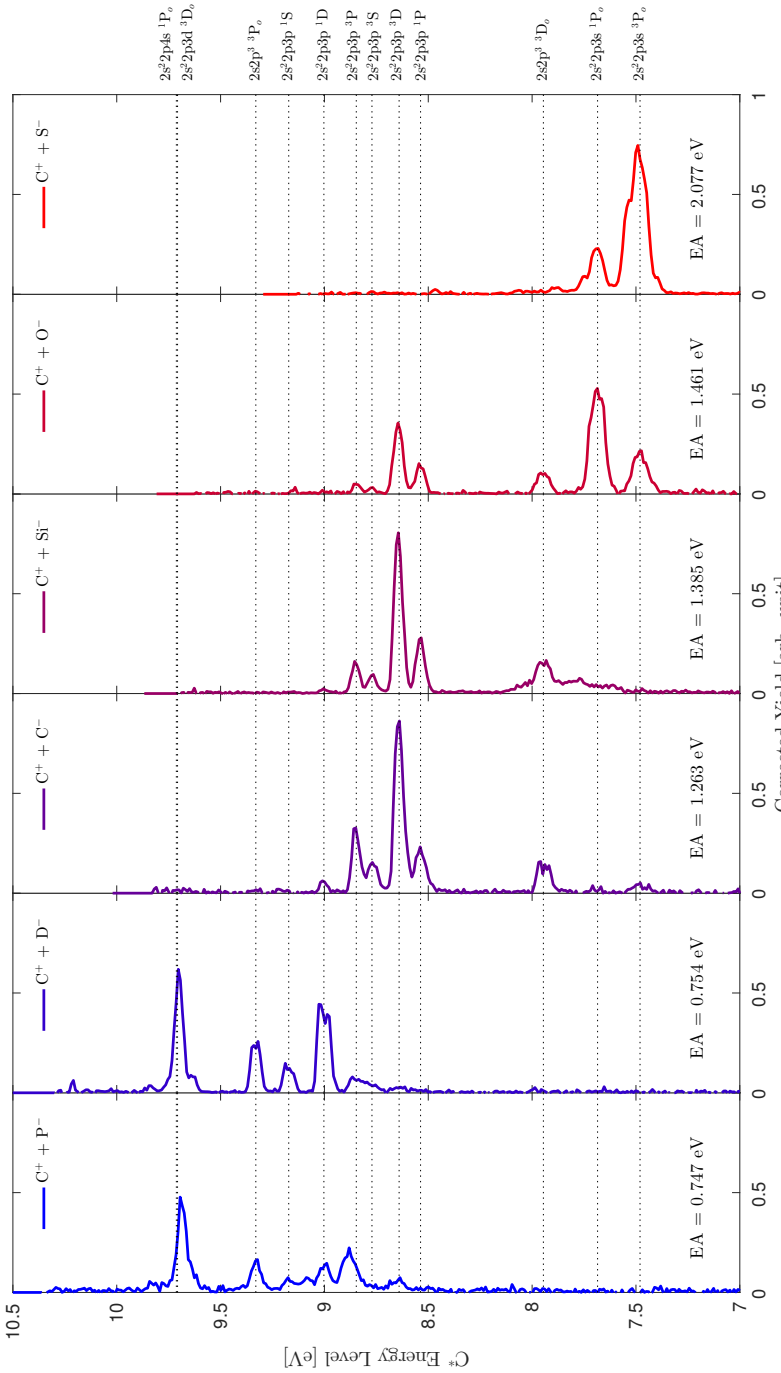

Figure F.22: Combined experiments : $C^+ + X^-$ (peak attributions).

F.4.1 Phosphorus

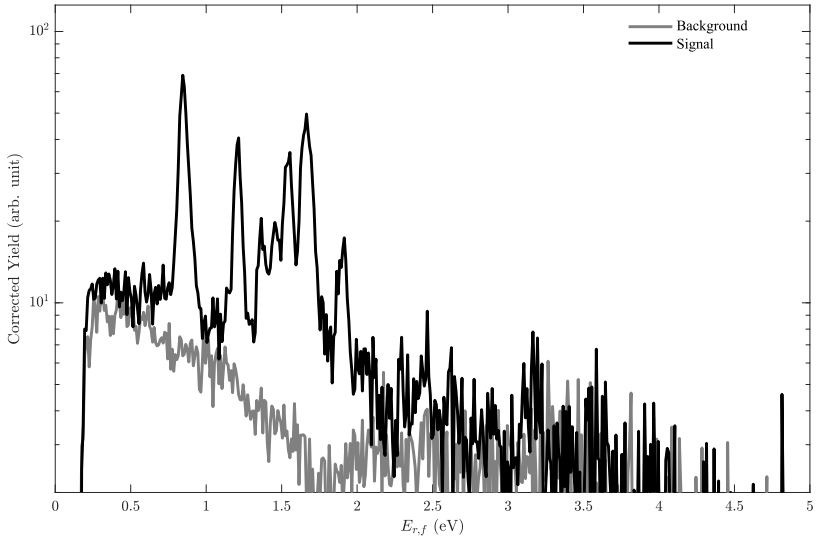

Figure F.23: Experiment: $C^+ + P^- \rightarrow C + P$

C^+ beam	
Beam energy:	4,750 eV
Ion source:	ECR (CO)
P^- beam	
Beam energy:	11,500 eV
Ion source:	Sputtering (Fe_2P)
Mean collision energy:	$\sim$ 5 meV

Table F.21: $C^+ + P^-$ MN experimental setup parameters.

	$P^-(^3P)$ $P(^4S^o)$	$P(^2D^o)$	$P(^2P^o)$
$C(2s2p^3\ ^5S^o)$			0,003(1)
$C(3s\ ^3P^o)$	0,009(1)	0,155(3)	0,005(1)
$C(3s\ ^1P^o)$	0,006(1)	0,056(2)	0,003(1)
$C(2s2p^3\ ^3D^o)$	0,015(2)	0,011(1)	
$C(3p\ ^1P)$	0,017(1)	0,009(1)	
$C(3p\ ^3D)$	0,059(2)	0,004(3)	
$C(3p\ ^3S)$	0,026(2)	0,007(1)	
$C(3p\ ^3P)$	0,060(2)	0,004(1)	
$C(3p\ ^1D)$	0,123(3)		
$C(3p\ ^1S)$	0,051(2)		
$C(2s2p^3\ ^3P^o)$	0,104(2)		
$C(3d\ ^1D^o)$	0,039(1)		
$C(4s\ ^3P^o)$	0,142(3)		
$C(3d\ ^3F^o)$	0,009(4)		
$C(3d\ ^3D^o)$	0,046(46)		
$C(3d\ ^1P^o)$	0,014(1)		
$C(3d\ ^3P^o)$	0,011(1)		
$C(4p\ ^1P)$	0,003(1)		
$C(4p\ ^3S)$	0,002(3)		
$C(4p\ ^3P)$	0,001(1)		
$C(4p\ ^1D)$	0,008(1)		
$C(4p\ ^1S)$	0,001(1)		

Table F.22: Branching ratio fit: $C^+(^2P^o)$ + $P^-(^3P)$.

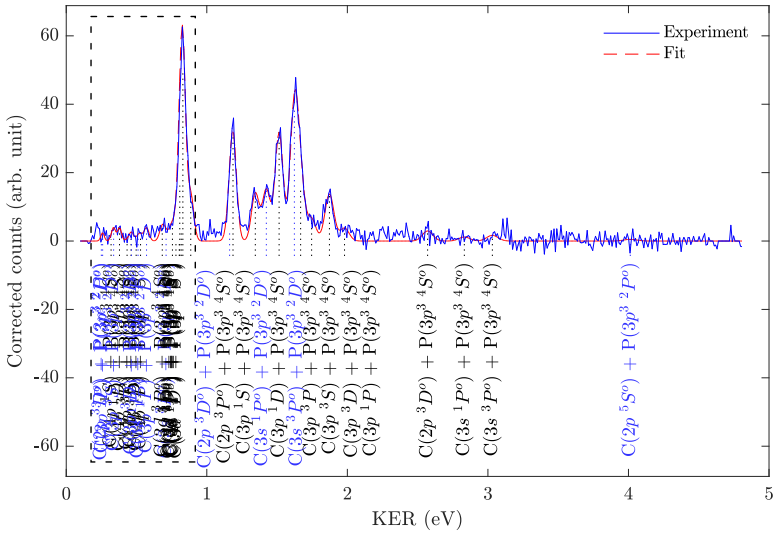

Figure F.24: Branching ratio fit: $C^+(^2P^o)$ + $P^-(^3P)$. The color code for the products is given in table F.1. A zoom of the framed area is given in figure F.25.

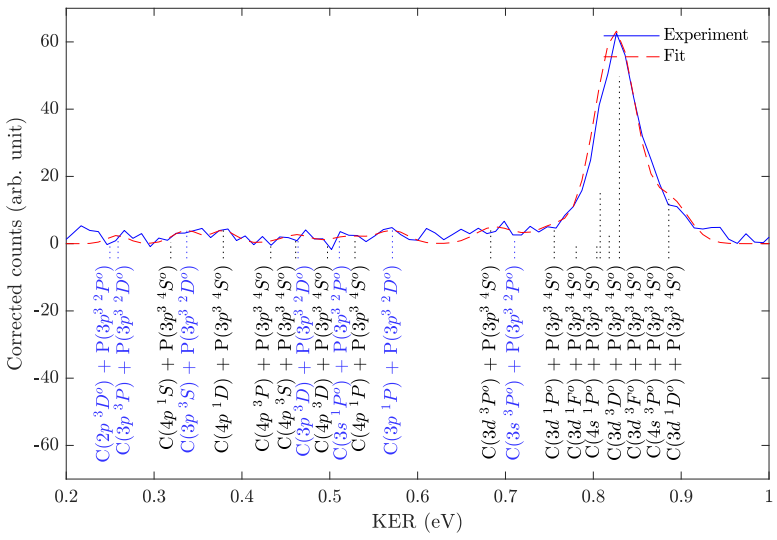

Figure F.25: Branching ratio fit: $C^+(^2P^o)$ + $P^-(^3P)$ – zoom. The color code for the products is given in table F.1.

Cation C	Anion P	Center-of-mass collision energy (eV) 0.002	0.005	0.02	0.05	0.2	0.5
$2p^2\ ^3P$	$3p^3\ ^4S^o$	6e-29	2.45e-29	6.73e-30	3.25e-30	1.98e-30	3.85e-30
$2p^2\ ^3P$	$3p^3\ ^2D^o$	1.72e-14	6.89e-15	1.74e-15	7.04e-16	1.89e-16	8.56e-17
$2p^2\ ^3P$	$3p^3\ ^2P^o$	8.16e-14	3.27e-14	8.21e-15	3.32e-15	8.77e-16	3.87e-16
$2p^2\ ^1D$	$3p^3\ ^4S^o$	5.68e-21	2.28e-21	5.81e-22	2.41e-22	7.22e-23	4.06e-23
$2p^2\ ^1D$	$3p^3\ ^2D^o$	5.67e-15	2.27e-15	5.73e-16	2.33e-16	6.28e-17	2.89e-17
$2p^2\ ^1D$	$3p^3\ ^2P^o$	1.39e-14	5.58e-15	1.41e-15	5.71e-16	1.54e-16	7.05e-17
$2p^2\ ^1S$	$3p^3\ ^4S^o$	6.68e-17	2.68e-17	6.79e-18	2.79e-18	7.93e-19	4.04e-19
$2p^2\ ^1S$	$3p^3\ ^2D^o$	7.29e-14	2.92e-14	7.36e-15	2.99e-15	8e-16	3.62e-16
$2p^2\ ^1S$	$3p^3\ ^2P^o$	3.95e-14	1.58e-14	3.98e-15	1.61e-15	4.31e-16	1.93e-16
$3s\ ^3P^o$	$3p^3\ ^4S^o$	3.67e-13	1.47e-13	3.72e-14	1.52e-14	4.14e-15	1.94e-15
$3s\ ^3P^o$	$3p^3\ ^2D^o$	1.34e-12	5.37e-13	1.35e-13	5.49e-14	1.47e-14	6.67e-15
$3s\ ^3P^o$	$3p^3\ ^2P^o$	2.8e-20	1.12e-20	2.84e-21	1.16e-21	3.22e-22	1.51e-22
$3s\ ^1P^o$	$3p^3\ ^4S^o$	2.25e-13	9.03e-14	2.28e-14	9.26e-15	2.51e-15	1.15e-15
$3s\ ^1P^o$	$3p^3\ ^2D^o$	2.81e-13	1.13e-13	2.84e-14	1.15e-14	3.06e-15	1.36e-15
$3s\ ^1P^o$	$3p^3\ ^2P^o$	4.44e-26	1.78e-26	4.52e-27	1.86e-27	5.29e-28	2.54e-28
$3p\ ^1P$	$3p^3\ ^4S^o$	2.14e-13	8.57e-14	2.17e-14	8.91e-15	2.51e-15	1.23e-15
$3p\ ^1P$	$3p^3\ ^2D^o$	7.36e-21	2.95e-21	7.49e-22	3.08e-22	8.65e-23	4.12e-23
$3p\ ^3D$	$3p^3\ ^4S^o$	2.07e-12	8.28e-13	2.09e-13	8.55e-14	2.36e-14	1.12e-14
$3p\ ^3D$	$3p^3\ ^2D^o$	7.93e-25	3.18e-25	8.1e-26	3.35e-26	9.61e-27	4.68e-27
$3p\ ^3S$	$3p^3\ ^4S^o$	1.04e-12	4.16e-13	1.05e-13	4.27e-14	1.16e-14	5.38e-15
$3p\ ^3P$	$3p^3\ ^4S^o$	7.46e-13	2.99e-13	7.59e-14	3.13e-14	9.02e-15	4.64e-15
$3p\ ^1D$	$3p^3\ ^4S^o$	2.66e-12	1.07e-12	2.7e-13	1.11e-13	3.09e-14	1.5e-14
$3p\ ^1S$	$3p^3\ ^4S^o$	3.35e-13	1.34e-13	3.38e-14	1.37e-14	3.69e-15	1.67e-15
$3d\ ^1D^o$	$3p^3\ ^4S^o$	5.05e-13	2.02e-13	5.12e-14	2.1e-14	5.82e-15	2.74e-15
$4s\ ^3P^o$	$3p^3\ ^4S^o$	3.43e-12	1.37e-12	3.48e-13	1.43e-13	4e-14	1.91e-14
$3d\ ^3F^o$	$3p^3\ ^4S^o$	7.6e-13	3.05e-13	7.71e-14	3.16e-14	8.74e-15	4.11e-15
$3d\ ^3D^o$	$3p^3\ ^4S^o$	8.41e-13	3.37e-13	8.53e-14	3.49e-14	9.68e-15	4.56e-15
$4s\ ^1P^o$	$3p^3\ ^4S^o$	1.01e-12	4.06e-13	1.03e-13	4.21e-14	1.17e-14	5.55e-15
$3d\ ^1F^o$	$3p^3\ ^4S^o$	1.91e-13	7.66e-14	1.94e-14	7.93e-15	2.19e-15	1.03e-15
$3d\ ^1P^o$	$3p^3\ ^4S^o$	4.1e-14	1.65e-14	4.16e-15	1.7e-15	4.71e-16	2.21e-16
$3d\ ^3P^o$	$3p^3\ ^4S^o$	5.08e-14	2.04e-14	5.16e-15	2.12e-15	5.89e-16	2.77e-16
$4p\ ^1P$	$3p^3\ ^4S^o$	8.02e-15	3.22e-15	8.18e-16	3.37e-16	9.59e-17	4.63e-17
$4p\ ^3D$	$3p^3\ ^4S^o$	9.36e-15	3.76e-15	9.54e-16	3.94e-16	1.13e-16	5.46e-17
$4p\ ^3S$	$3p^3\ ^4S^o$	2.96e-17	1.19e-17	3.03e-18	1.25e-18	3.59e-19	1.75e-19
$4p\ ^3P$	$3p^3\ ^4S^o$	6.99e-16	2.81e-16	7.15e-17	2.97e-17	8.59e-18	4.22e-18
$4p\ ^1D$	$3p^3\ ^4S^o$	1.22e-17	4.89e-18	1.25e-18	5.2e-19	1.53e-19	7.63e-20
$4p\ ^1S$	$3p^3\ ^4S^o$	1.21e-21	4.86e-22	1.24e-22	5.21e-23	1.56e-23	7.92e-24

Table F.23: Partial cross section (cm^2) for the C^++P^- MN reaction computed with the ACAM.

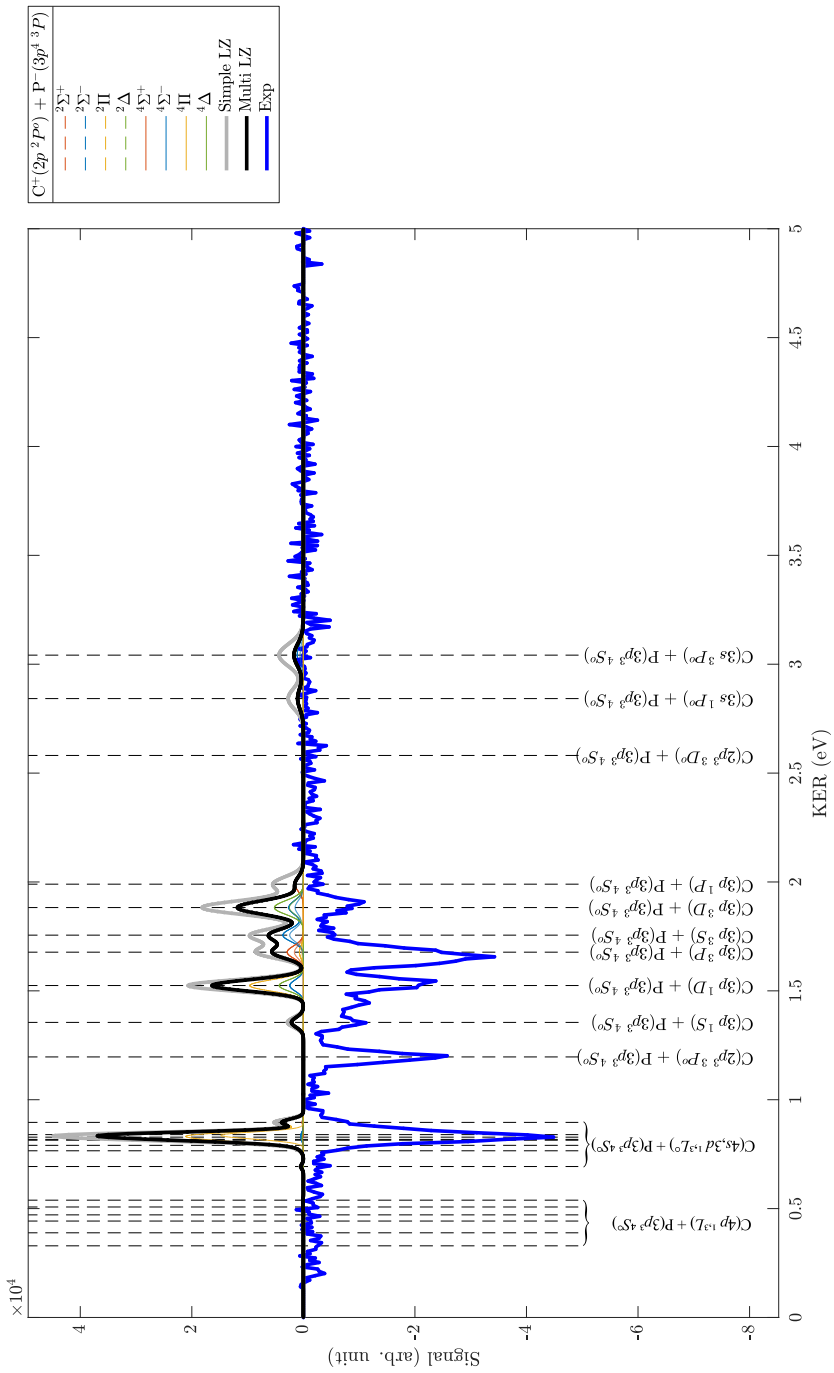

Figure F.26: Simulation: $C^+(^2P^o) + P^-(^3P)$ – Excluding P^*

C	P	$^2\Sigma^+$	$^2\Sigma^-$	$^2\Pi$	$^2\Delta$	$^4\Sigma^+$	$^4\Sigma^-$	$^4\Pi$	$^4\Delta$
$2p^2\ ^3P$	$3p^3\ ^4S^o$	8.512e-02		3.008e-02		6.729e-02		2.378e-02	
$2p^2\ ^1D$	$3p^3\ ^4S^o$						2.043e-02	1.974e-02	4.052e-02
$2p^2\ ^1S$	$3p^3\ ^4S^o$						2.347e-02		
$3s\ ^3P^o$	$3p^3\ ^4S^o$		2.048e-03	1.211e-02			1.619e-03	9.574e-03	
$3s\ ^1P^o$	$3p^3\ ^4S^o$						1.103e-03	6.520e-03	
$3p\ ^1P$	$3p^3\ ^4S^o$					1.208e-03		2.268e-03	
$3p\ ^3D$	$3p^3\ ^4S^o$		9.230e-04	3.254e-03	1.352e-03		7.297e-04	2.573e-03	1.069e-03
$3p\ ^3S$	$3p^3\ ^4S^o$		8.337e-04				6.591e-04		
$3p\ ^3P$	$3p^3\ ^4S^o$	1.091e-03		2.431e-03		8.626e-04		1.922e-03	
$3p\ ^1D$	$3p^3\ ^4S^o$						2.918e-04	1.137e-03	3.822e-04
$3p\ ^1S$	$3p^3\ ^4S^o$						1.969e-04		
$3d\ ^1D^o$	$3p^3\ ^4S^o$					3.102e-05		7.509e-05	1.476e-05
$4s\ ^3P^o$	$3p^3\ ^4S^o$		3.073e-05	1.817e-04			2.430e-05	1.437e-04	
$3d\ ^3F^o$	$3p^3\ ^4S^o$		2.051e-05	7.286e-05	2.092e-05		1.622e-05	5.760e-05	1.653e-05
$3d\ ^3D^o$	$3p^3\ ^4S^o$	2.863e-05		7.602e-05	1.363e-05	2.264e-05		6.010e-05	1.077e-05
$4s\ ^1P^o$	$3p^3\ ^4S^o$						1.566e-05	9.260e-05	
$3d\ ^1F^o$	$3p^3\ ^4S^o$						9.463e-06	3.433e-05	9.401e-06
$3d\ ^1P^o$	$3p^3\ ^4S^o$						7.775e-06	1.418e-05	
$3d\ ^3P^o$	$3p^3\ ^4S^o$		6.296e-06	1.219e-05			4.978e-06	9.640e-06	
$4p\ ^1P$	$3p^3\ ^4S^o$					4.859e-07		3.413e-06	
$4p\ ^3D$	$3p^3\ ^4S^o$		6.203e-07	3.059e-06	3.378e-07		4.904e-07	2.418e-06	2.670e-07
$4p\ ^3S$	$3p^3\ ^4S^o$		2.130e-07				1.684e-07		
$4p\ ^3P$	$3p^3\ ^4S^o$	7.668e-08		6.579e-07		6.062e-08		5.201e-07	
$4p\ ^1D$	$3p^3\ ^4S^o$						1.438e-08	7.202e-08	6.057e-09
$4p\ ^1S$	$3p^3\ ^4S^o$						7.507e-10		

Table F.24: Interaction potentials E_{ic} (a.u.): $C^+(^2P^o) + P^-(^3P)$ – Excluding P^*

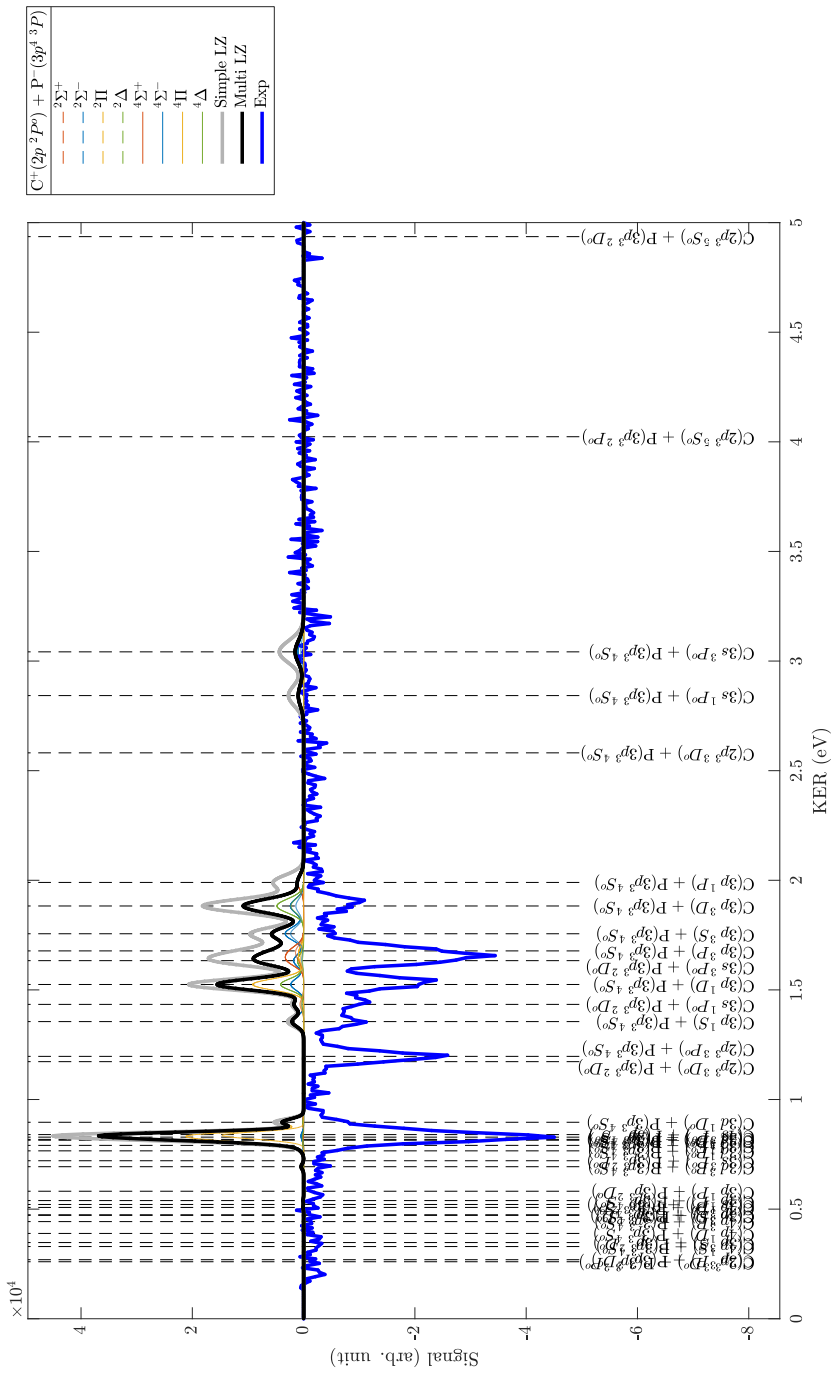

Figure F.27: Simulation: $C^+(^2P^o) + P^-(^3P)$ – Including P^*

C	P	$^2\Sigma^+$	$^2\Sigma^-$	$^2\Pi$	$^2\Delta$	$^4\Sigma^+$	$^4\Sigma^-$	$^4\Pi$	$^4\Delta$
$2p^2\ ^3P$	$3p^3\ ^4S^o$	8.512e-02		3.008e-02		6.729e-02		2.378e-02	
$2p^2\ ^3P$	$3p^3\ ^2D^o$	1.324e-02	1.332e-02	7.201e-03	6.529e-03	2.648e-02	2.665e-02	1.440e-02	1.306e-02
$2p^2\ ^3P$	$3p^3\ ^2P^o$	1.389e-02	7.001e-03		4.845e-03	2.778e-02	1.400e-02		9.691e-03
$2p^2\ ^1D$	$3p^3\ ^4S^o$						2.043e-02	1.974e-02	4.052e-02
$2p^2\ ^1D$	$3p^3\ ^2D^o$	4.056e-02	2.347e-02	1.118e-02	6.629e-03				
$2p^2\ ^1D$	$3p^3\ ^2P^o$	1.572e-02	1.576e-02	5.448e-03	5.911e-03				
$2p^2\ ^1S$	$3p^3\ ^4S^o$						2.347e-02		
$2p^2\ ^1S$	$3p^3\ ^2D^o$		3.577e-03	4.622e-03	6.537e-03				
$2p^2\ ^1S$	$3p^3\ ^2P^o$	3.399e-03		1.982e-03					
$3s\ ^3P^o$	$3p^3\ ^4S^o$		2.048e-03	1.211e-02			1.619e-03	9.574e-03	
$3s\ ^3P^o$	$3p^3\ ^2D^o$	3.091e-04	1.546e-04	1.184e-04	1.057e-04	6.182e-04	3.091e-04	2.368e-04	2.114e-04
$3s\ ^3P^o$	$3p^3\ ^2P^o$	5.400e-09	5.400e-09		2.664e-09	1.080e-08	1.080e-08		5.329e-09
$3s\ ^1P^o$	$3p^3\ ^4S^o$						1.103e-03	6.520e-03	
$3s\ ^1P^o$	$3p^3\ ^2D^o$	2.389e-04	1.195e-04	9.150e-05	8.170e-05				
$3s\ ^1P^o$	$3p^3\ ^2P^o$	1.116e-11	1.116e-11		5.506e-12				
$3p\ ^1P$	$3p^3\ ^4S^o$					1.208e-03		2.268e-03	
$3p\ ^1P$	$3p^3\ ^2D^o$	4.831e-09	4.831e-09	2.616e-09	2.336e-09				
$3p\ ^3D$	$3p^3\ ^4S^o$		9.230e-04	3.254e-03	1.352e-03		7.297e-04	2.573e-03	1.069e-03
$3p\ ^3D$	$3p^3\ ^2D^o$	1.799e-11	1.056e-11	4.131e-12	1.602e-12	3.598e-11	2.113e-11	8.262e-12	3.204e-12
$3p\ ^3S$	$3p^3\ ^4S^o$		8.337e-04				6.591e-04		
$3p\ ^3P$	$3p^3\ ^4S^o$	1.091e-03		2.431e-03		8.626e-04		1.922e-03	
$3p\ ^1D$	$3p^3\ ^4S^o$						2.918e-04	1.137e-03	3.822e-04
$3p\ ^1S$	$3p^3\ ^4S^o$						1.969e-04		

Table F.25: Interaction potentials E_{ic} (a.u.): $C^+(^2P^o)$ + $P^-(^3P)$ – Including P^*

C	P	$^2\Sigma^+$	$^2\Sigma^-$	$^2\Pi$	$^2\Delta$	$^4\Sigma^+$	$^4\Sigma^-$	$^4\Pi$	$^4\Delta$
$3d\ ^1D^o$	$3p^3\ ^4S^o$					3.102e-05		7.509e-05	1.476e-05
$4s\ ^3P^o$	$3p^3\ ^4S^o$		3.073e-05	1.817e-04			2.430e-05	1.437e-04	
$3d\ ^3F^o$	$3p^3\ ^4S^o$		2.051e-05	7.286e-05	2.092e-05		1.622e-05	5.760e-05	1.653e-05
$3d\ ^3D^o$	$3p^3\ ^4S^o$	2.863e-05		7.602e-05	1.363e-05	2.264e-05		6.010e-05	1.077e-05
$4s\ ^1P^o$	$3p^3\ ^4S^o$						1.566e-05	9.260e-05	
$3d\ ^1F^o$	$3p^3\ ^4S^o$						9.463e-06	3.433e-05	9.401e-06
$3d\ ^1P^o$	$3p^3\ ^4S^o$						7.775e-06	1.418e-05	
$3d\ ^3P^o$	$3p^3\ ^4S^o$		6.296e-06	1.219e-05			4.978e-06	9.640e-06	
$4p\ ^1P$	$3p^3\ ^4S^o$					4.859e-07		3.413e-06	
$4p\ ^3D$	$3p^3\ ^4S^o$		6.203e-07	3.059e-06	3.378e-07		4.904e-07	2.418e-06	2.670e-07
$4p\ ^3S$	$3p^3\ ^4S^o$		2.130e-07				1.684e-07		
$4p\ ^3P$	$3p^3\ ^4S^o$	7.668e-08		6.579e-07		6.062e-08		5.201e-07	
$4p\ ^1D$	$3p^3\ ^4S^o$						1.438e-08	7.202e-08	6.057e-09
$4p\ ^1S$	$3p^3\ ^4S^o$						7.507e-10		

Table F.26: Interaction potentials $E_{i\bar{c}}$ (a.u.): $C^+(^2P^o) + P^-(^3P)$ – Including P^*

F.4.2 Deuterium

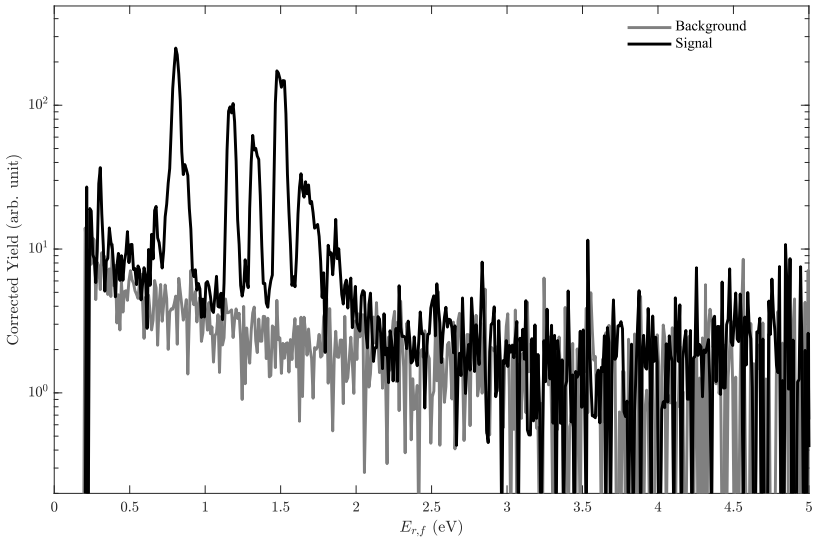

Figure F.28: Experiment: $C^+ + D^- \rightarrow C + D$

C^+ beam	
Beam energy:	13,000 eV
Ion source:	ECR (CO)
D^- beam	
Beam energy:	2,750 eV
Ion source:	Duoplasmatron (D_2)
Mean collision energy:	$\sim$ 5 meV

Table F.27: $C^+ + D^-$ MN experimental setup parameters.

	$D^-(^1S)$	
	$D(1s)$	$D(2\ell)$
$C(2p^2\ ^3P)$		0,021(2)
$C(3s\ ^3P^o)$	0,001(1)	
$C(3s\ ^1P^o)$	0,003(1)	
$C(2s2p^3\ ^3D^o)$	0,005(1)	
$C(3p\ ^1P)$	0,007(1)	
$C(3p\ ^3D)$	0,017(1)	
$C(3p\ ^3S)$	0,026(1)	
$C(3p\ ^3P)$	0,049(2)	
$C(3p\ ^1D)$	0,284(4)	
$C(3p\ ^1S)$	0,081(2)	
$C(2s2p^3\ ^3P^o)$	0,141(3)	
$C(3d\ ^1D^o)$	0,035(1)	
$C(4s\ ^3P^o)$	0,065(3)	
$C(3d\ ^3F^o)$	0,199(17)	
$C(3d\ ^3D^o)$	0,02(39)	
$C(3d\ ^1F^o)$	0,000(10)	
$C(3d\ ^1P^o)$	0,016(1)	
$C(3d\ ^3P^o)$	0,015(1)	
$C(4p\ ^1P)$	0,002(1)	
$C(4p\ ^3D)$	0,005(1)	
$C(4p\ ^3S)$	0,002(1)	
$C(4p\ ^3P)$	0,003(1)	
$C(4p\ ^1D)$	0,005(1)	

Table F.28: Branching ratio fit: $C^+(^2P^o) + D^-$.

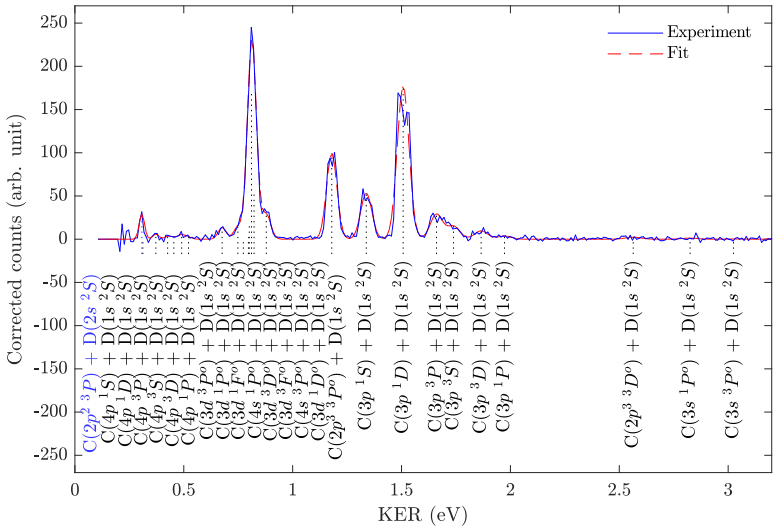

Figure F.29: Branching ratio fit: $C^+(^2P^o) + D^-(^1S)$.

Cation	Anion	Center-of-mass collision energy (eV)					
C	D	0.002	0.005	0.02	0.05	0.2	0.5
$2p^2\ ^3P$	$1s\ ^2S$	3.57e-20	1.44e-20	3.78e-21	1.66e-21	6.55e-22	5.85e-22
$2p^2\ ^1D$	$1s\ ^2S$	3.49e-19	1.41e-19	3.7e-20	1.63e-20	6.38e-21	5.64e-21
$2p^2\ ^1S$	$1s\ ^2S$	1.84e-19	7.42e-20	1.95e-20	8.56e-21	3.36e-21	2.98e-21
$3s\ ^3P^o$	$1s\ ^2S$	2.43e-18	9.8e-19	2.58e-19	1.14e-19	4.54e-20	4.14e-20
$3s\ ^1P^o$	$1s\ ^2S$	1.06e-14	4.26e-15	1.1e-15	4.68e-16	1.57e-16	1.04e-16
$3p\ ^1P$	$1s\ ^2S$	5.95e-14	2.39e-14	6.14e-15	2.59e-15	8.22e-16	4.96e-16
$3p\ ^3D$	$1s\ ^2S$	2.3e-13	9.23e-14	2.37e-14	9.95e-15	3.14e-15	1.87e-15
$3p\ ^3S$	$1s\ ^2S$	8.81e-13	3.54e-13	8.99e-14	3.71e-14	1.08e-14	5.54e-15
$3p\ ^3P$	$1s\ ^2S$	1.73e-12	6.93e-13	1.76e-13	7.28e-14	2.13e-14	1.11e-14
$3p\ ^1D$	$1s\ ^2S$	7.33e-12	2.94e-12	7.42e-13	3.03e-13	8.27e-14	3.85e-14
$3p\ ^1S$	$1s\ ^2S$	1.82e-12	7.31e-13	1.84e-13	7.51e-14	2.04e-14	9.34e-15
$3d\ ^1D^o$	$1s\ ^2S$	3.71e-13	1.49e-13	3.76e-14	1.54e-14	4.23e-15	1.97e-15
$4s\ ^3P^o$	$1s\ ^2S$	4.05e-12	1.63e-12	4.11e-13	1.69e-13	4.68e-14	2.21e-14
$3d\ ^3F^o$	$1s\ ^2S$	8.78e-13	3.52e-13	8.9e-14	3.64e-14	1.01e-14	4.72e-15
$3d\ ^3D^o$	$1s\ ^2S$	5.79e-13	2.32e-13	5.88e-14	2.4e-14	6.65e-15	3.12e-15
$4s\ ^1P^o$	$1s\ ^2S$	1.16e-12	4.63e-13	1.17e-13	4.8e-14	1.33e-14	6.22e-15
$3d\ ^1F^o$	$1s\ ^2S$	2.16e-13	8.64e-14	2.19e-14	8.95e-15	2.47e-15	1.16e-15
$3d\ ^1P^o$	$1s\ ^2S$	7.11e-14	2.85e-14	7.22e-15	2.95e-15	8.19e-16	3.84e-16
$3d\ ^3P^o$	$1s\ ^2S$	8.4e-14	3.37e-14	8.54e-15	3.5e-15	9.77e-16	4.62e-16
$4p\ ^1P$	$1s\ ^2S$	4.47e-15	1.79e-15	4.55e-16	1.88e-16	5.34e-17	2.58e-17
$4p\ ^3D$	$1s\ ^2S$	7.99e-15	3.21e-15	8.16e-16	3.37e-16	9.65e-17	4.69e-17
$4p\ ^3S$	$1s\ ^2S$	3.93e-16	1.58e-16	4.02e-17	1.66e-17	4.8e-18	2.35e-18
$4p\ ^3P$	$1s\ ^2S$	3.26e-16	1.31e-16	3.34e-17	1.38e-17	4.02e-18	1.98e-18
$4p\ ^1D$	$1s\ ^2S$	7.98e-18	3.21e-18	8.19e-19	3.41e-19	1.01e-19	5.02e-20
$4p\ ^1S$	$1s\ ^2S$	1.13e-20	4.55e-21	1.17e-21	4.89e-22	1.47e-22	7.49e-23

Table F.29: Partial cross section (cm^2) for the C^++D^- MN reaction computed with the ACAM.

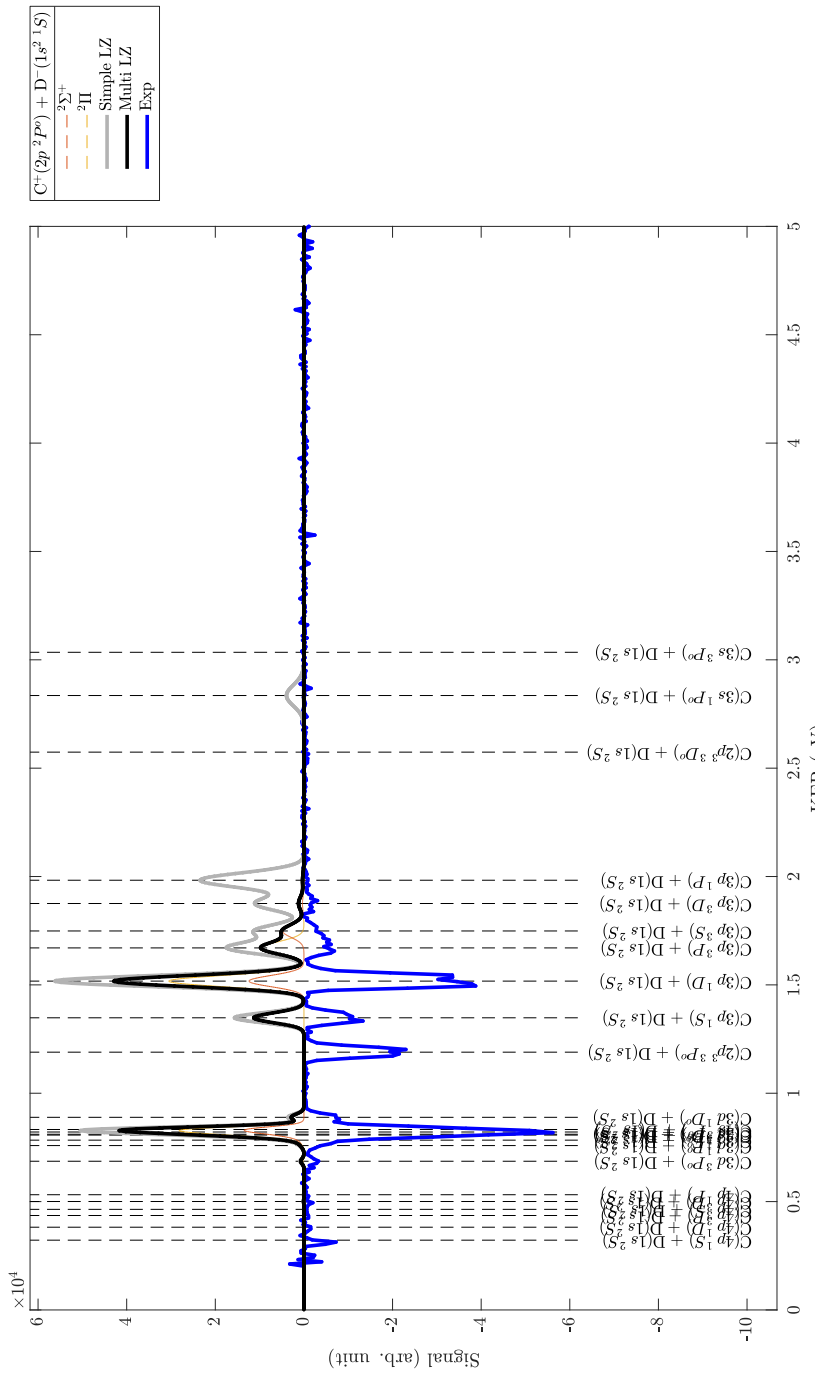

Figure F.30: Simulation: $C^+(^2P^o) + D^-(^1S)$.

C	D	$^2\Sigma^+$	$^2\Pi$
$2p^2\ ^3P$	$1s\ ^2S$		2.780e-02
$2p^2\ ^1D$	$1s\ ^2S$	1.985e-02	1.719e-02
$2p^2\ ^1S$	$1s\ ^2S$	1.362e-02	
$3s\ ^3P^o$	$1s\ ^2S$	1.111e-02	1.111e-02
$3s\ ^1P^o$	$1s\ ^2S$	5.632e-03	5.632e-03
$3p\ ^1P$	$1s\ ^2S$		1.943e-03
$3p\ ^3D$	$1s\ ^2S$	3.409e-03	2.952e-03
$3p\ ^3S$	$1s\ ^2S$	2.024e-03	
$3p\ ^3P$	$1s\ ^2S$		2.196e-03
$3p\ ^1D$	$1s\ ^2S$	1.114e-03	9.646e-04
$3p\ ^1S$	$1s\ ^2S$	5.408e-04	
$3d\ ^1D^o$	$1s\ ^2S$		6.093e-05
$4s\ ^3P^o$	$1s\ ^2S$	1.550e-04	1.550e-04
$3d\ ^3F^o$	$1s\ ^2S$	7.593e-05	6.200e-05
$3d\ ^3D^o$	$1s\ ^2S$		6.457e-05
$4s\ ^1P^o$	$1s\ ^2S$	7.409e-05	7.409e-05
$3d\ ^1F^o$	$1s\ ^2S$	3.348e-05	2.733e-05
$3d\ ^1P^o$	$1s\ ^2S$	2.246e-05	1.123e-05
$3d\ ^3P^o$	$1s\ ^2S$	2.008e-05	1.004e-05
$4p\ ^1P$	$1s\ ^2S$		2.466e-06
$4p\ ^3D$	$1s\ ^2S$	2.645e-06	2.290e-06
$4p\ ^3S$	$1s\ ^2S$	8.099e-07	
$4p\ ^3P$	$1s\ ^2S$		4.619e-07
$4p\ ^1D$	$1s\ ^2S$	5.077e-08	4.397e-08
$4p\ ^1S$	$1s\ ^2S$	2.214e-09	

Table F.30: Interaction potentials E_{ic} (a.u.): $C^+(^2P^o)$ + $D^-(^1S)$.

F.4.3 Silicon

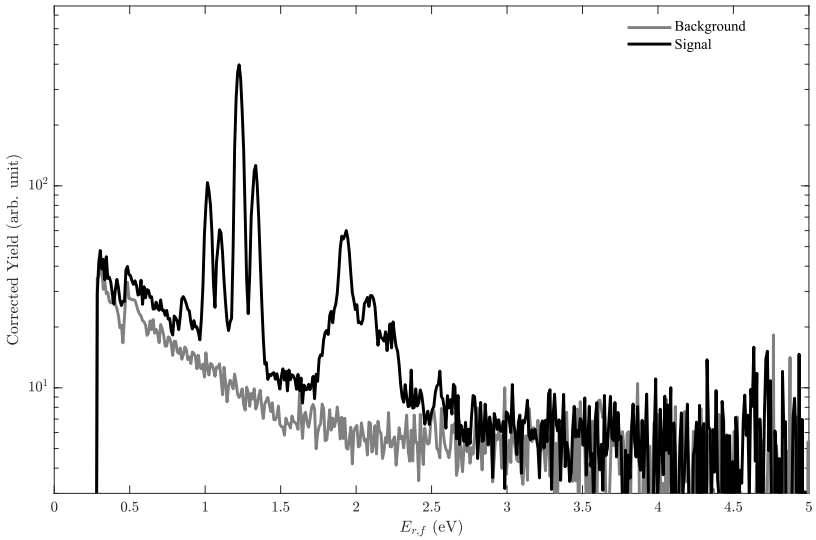

Figure F.31: Experiment: $C^+ + Si^- \rightarrow C + Si$.

C^+ beam	
Beam energy:	5,500 eV
Ion source:	ECR (CO)
Si^- beam	
Beam energy:	11,500 eV
Ion source:	Sputtering (Silicon wafer)
Mean collision energy:	$\sim$ 5 meV

Table F.31: $C^+ + Si^-$ MN experimental setup parameters.

	$Si^-(^4S^o)$ $Si(^3P)$
$C(3s\ ^3P^o)$	0,009(1)
$C(3s\ ^1P^o)$	0,030(1)
$C(2s2p^3\ ^3D^o)$	0,103(2)
$C(3p\ ^1P)$	0,155(2)
$C(3p\ ^3D)$	0,499(3)
$C(3p\ ^3S)$	0,062(1)
$C(3p\ ^3P)$	0,109(2)
$C(3p\ ^1D)$	0,018(1)
$C(3p\ ^1S)$	0,009(1)
$C(2s2p^3\ ^3P^o)$	0,008(1)

Table F.32: Branching ratio fit: $C^+(^2P^o)$ + $Si^-(^4S^o)$.

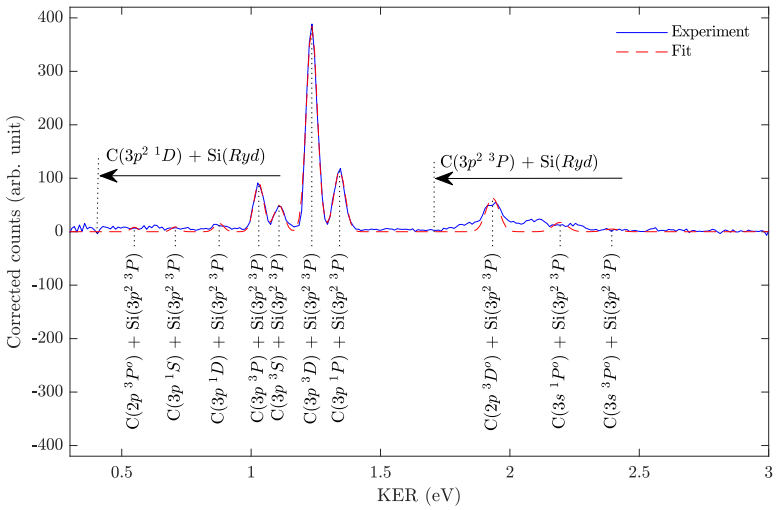

Figure F.32: Branching ratio fit: $C^+(^2P^o)$ + $Si^-(^4S^o)$.

Cation	Anion	Center-of-mass collision energy (eV)					
C	Si	0.002	0.005	0.02	0.05	0.2	0.5
$2p^2\ ^3P$	$3p^2\ ^3P$	1.52e-55	6.32e-56	1.9e-56	1.1e-56	1.58e-56	1.48e-55
$2p^2\ ^1D$	$3p^2\ ^3P$	1.95e-67	7.98e-68	2.25e-68	1.14e-68	9.18e-69	3.44e-68
$2p^2\ ^1S$	$3p^2\ ^3P$	2.46e-34	9.94e-35	2.62e-35	1.17e-35	4.98e-36	5.46e-36
$3s\ ^3P^o$	$3p^2\ ^3P$	8.29e-13	3.32e-13	8.41e-14	3.44e-14	9.55e-15	4.6e-15
$3s\ ^1P^o$	$3p^2\ ^3P$	5.34e-13	2.14e-13	5.4e-14	2.2e-14	5.98e-15	2.78e-15
$3p\ ^1P$	$3p^2\ ^3P$	2.6e-12	1.04e-12	2.65e-13	1.09e-13	3.07e-14	1.51e-14
$3p\ ^3D$	$3p^2\ ^3P$	3.14e-12	1.26e-12	3.18e-13	1.29e-13	3.5e-14	1.59e-14
$3p\ ^3S$	$3p^2\ ^3P$	2.29e-12	9.17e-13	2.32e-13	9.44e-14	2.58e-14	1.19e-14
$3p\ ^3P$	$3p^2\ ^3P$	3.75e-12	1.5e-12	3.79e-13	1.55e-13	4.23e-14	1.96e-14
$3p\ ^1D$	$3p^2\ ^3P$	3.92e-14	1.57e-14	3.96e-15	1.61e-15	4.39e-16	2.01e-16
$3p\ ^1S$	$3p^2\ ^3P$	3.67e-15	1.47e-15	3.72e-16	1.52e-16	4.22e-17	1.97e-17

Table F.33: Partial cross section (cm^2) for the C^++Si^- MN reaction computed with the ACAM.

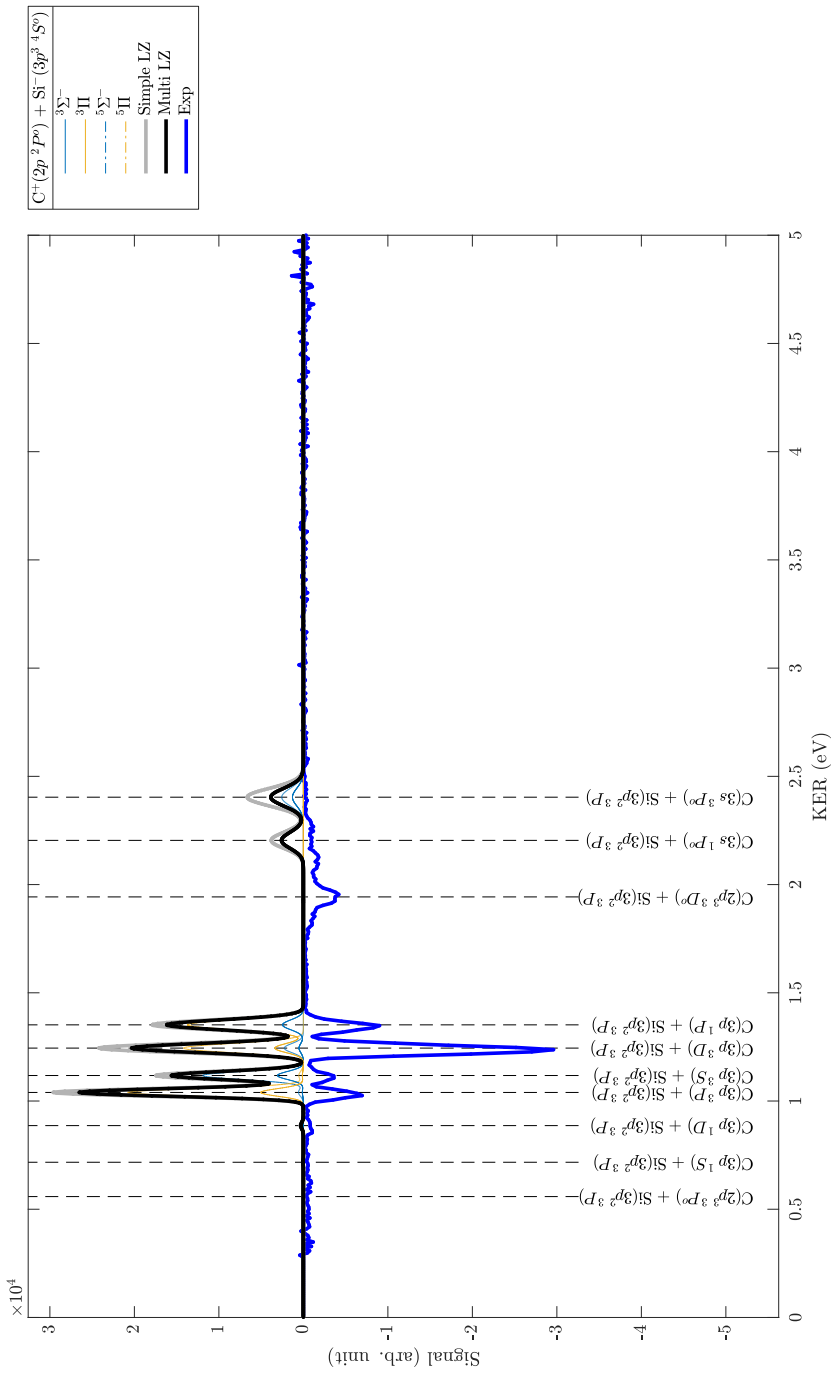

Figure F.33: Simulation: $C^+(^2P^o) + Si^-(^4S^o)$.

C	Si	$^3\Sigma^-$	$^3\Pi$	$^5\Sigma^-$	$^5\Pi$
$2p^2\ ^3P$	$3p^2\ ^3P$	9.551e-02	4.895e-02	1.654e-01	8.478e-02
$2p^2\ ^1D$	$3p^2\ ^3P$	8.767e-02	9.732e-02		
$2p^2\ ^1S$	$3p^2\ ^3P$	5.446e-02	4.513e-02		
$3s\ ^3P^o$	$3p^2\ ^3P$	1.351e-03	7.987e-03	2.339e-03	1.383e-02
$3s\ ^1P^o$	$3p^2\ ^3P$	1.457e-03	8.617e-03		
$3p\ ^1P$	$3p^2\ ^3P$	2.265e-04	8.541e-04		
$3p\ ^3D$	$3p^2\ ^3P$	8.069e-05	1.504e-04	1.398e-04	2.605e-04
$3p\ ^3S$	$3p^2\ ^3P$	1.656e-04	2.113e-05	2.869e-04	3.661e-05
$3p\ ^3P$	$3p^2\ ^3P$	2.549e-05	1.253e-04	4.415e-05	2.170e-04
$3p\ ^1D$	$3p^2\ ^3P$	8.940e-06	1.934e-05		
$3p\ ^1S$	$3p^2\ ^3P$	5.881e-06	4.790e-07		

Table F.34: Interaction potentials E_{ic} (a.u.): $C^+(^2P^o)$ + $Si^-(^4S^o)$.

F.4.4 Carbon

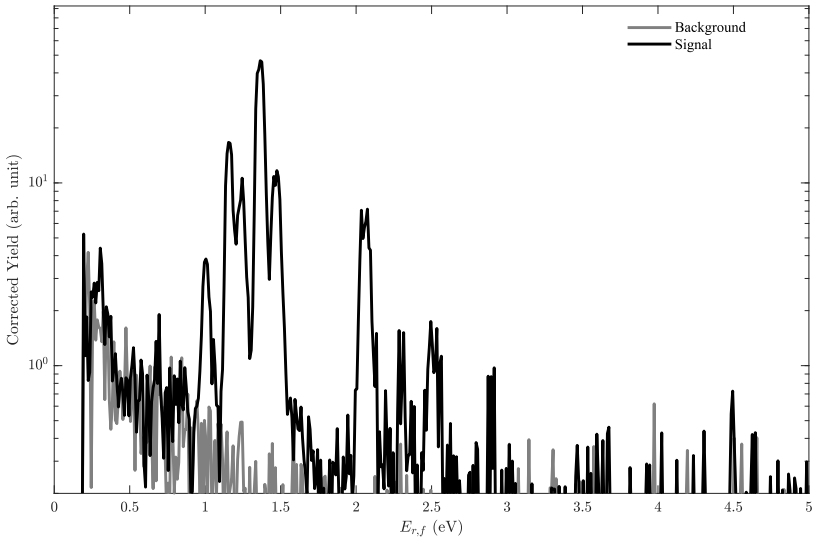

Figure F.34: Experiment: $C^+ + C^- \rightarrow C + C$.

C^+ beam	
Beam energy:	6,500 eV
Ion source:	ECR (CO)
C^- beam	
Beam energy:	7,500 eV
Ion source:	Sputtering (graphite)
Mean collision energy:	$\sim$ 7 meV

Table F.35: $C^+ + C^-$ MN experimental setup parameters.

	$C^-(^4S^o)$ $C(^3P)$
$C(3s\ ^3P^o)$	0,019(2)
$C(3s\ ^1P^o)$	0,012(2)
$C(2s2p^3\ ^3D^o)$	0,078(3)
$C(3p\ ^1P)$	0,115(3)
$C(3p\ ^3D)$	0,444(6)
$C(3p\ ^3S)$	0,081(3)
$C(3p\ ^3P)$	0,140(3)
$C(3p\ ^1D)$	0,029(2)
$C(3p\ ^1S)$	0,003(1)
$C(2s2p^3\ ^3P^o)$	0,005(1)
$C(3d\ ^1D^o)$	0,006(1)
$C(4s\ ^3P^o)$	0,005(1)
$C(3d\ ^3F^o)$	0,003(1)
$C(3d\ ^3D^o)$	0,053(15)
$C(3d\ ^1F^o)$	0,006(3)
$C(3d\ ^1P^o)$	0,003(1)

Table F.36: Branching ratio fit: $C^+(^2P^o) + C^-(^4S^o)$.

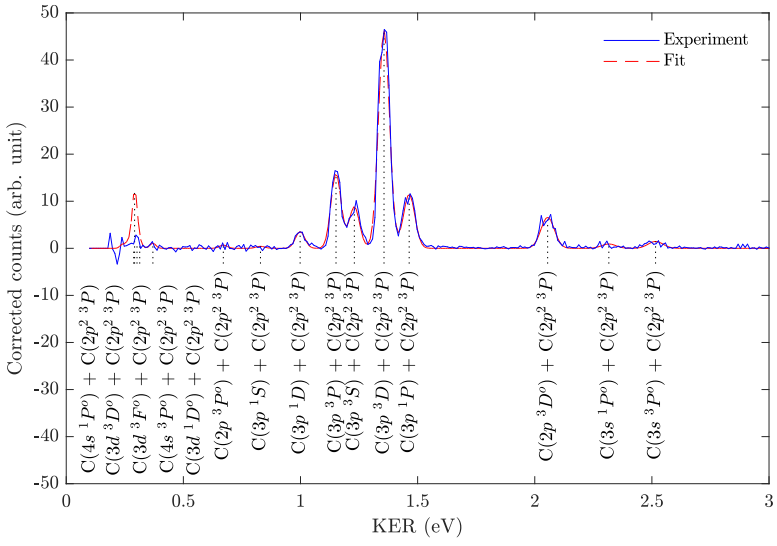

Figure F.35: Branching ratio fit: $C^+(^2P^o) + C^-(^4S^o)$.

Cation C	Anion C	Center-of-mass collision energy (eV) 0.002	0.005	0.02	0.05	0.2	0.5
$2p^2\ ^3P$	$2p^2\ ^3P$	1.85e-33	7.55e-34	2.08e-34	1.01e-34	6.29e-35	1.3e-34
$2p^2\ ^1D$	$2p^2\ ^3P$	2.21e-37	8.94e-38	2.36e-38	1.05e-38	4.44e-39	4.85e-39
$2p^2\ ^1S$	$2p^2\ ^3P$	4.01e-22	1.61e-22	4.13e-23	1.74e-23	5.53e-24	3.5e-24
$3s\ ^3P^o$	$2p^2\ ^3P$	1.06e-12	4.25e-13	1.07e-13	4.37e-14	1.19e-14	5.55e-15
$3s\ ^1P^o$	$2p^2\ ^3P$	5.1e-13	2.04e-13	5.15e-14	2.09e-14	5.64e-15	2.57e-15
$3p\ ^1P$	$2p^2\ ^3P$	2.17e-12	8.7e-13	2.2e-13	9.05e-14	2.56e-14	1.26e-14
$3p\ ^3D$	$2p^2\ ^3P$	3.24e-12	1.3e-12	3.28e-13	1.34e-13	3.65e-14	1.68e-14
$3p\ ^3S$	$2p^2\ ^3P$	2.67e-12	1.07e-12	2.7e-13	1.1e-13	3.04e-14	1.43e-14
$3p\ ^3P$	$2p^2\ ^3P$	5.41e-12	2.17e-12	5.48e-13	2.24e-13	6.15e-14	2.88e-14
$3p\ ^1D$	$2p^2\ ^3P$	1.46e-13	5.86e-14	1.48e-14	6.01e-15	1.63e-15	7.38e-16
$3p\ ^1S$	$2p^2\ ^3P$	4.02e-14	1.61e-14	4.07e-15	1.66e-15	4.57e-16	2.11e-16
$3d\ ^1D^o$	$2p^2\ ^3P$	3.72e-23	1.49e-23	3.81e-24	1.59e-24	4.66e-25	2.32e-25
$4s\ ^3P^o$	$2p^2\ ^3P$	5.1e-24	2.05e-24	5.25e-25	2.2e-25	6.59e-26	3.34e-26
$3d\ ^3F^o$	$2p^2\ ^3P$	1.06e-26	4.25e-27	1.07e-27	4.29e-28	1.07e-28	4.27e-29
$3d\ ^3D^o$	$2p^2\ ^3P$	2.21e-27	8.85e-28	2.21e-28	8.84e-29	2.21e-29	8.73e-30
$4s\ ^1P^o$	$2p^2\ ^3P$	3.03e-26	1.22e-26	3.12e-27	1.3e-27	3.91e-28	2.07e-28

Table F.37: Partial cross section (cm^2) for the C^++C^- MN reaction computed with the ACAM.

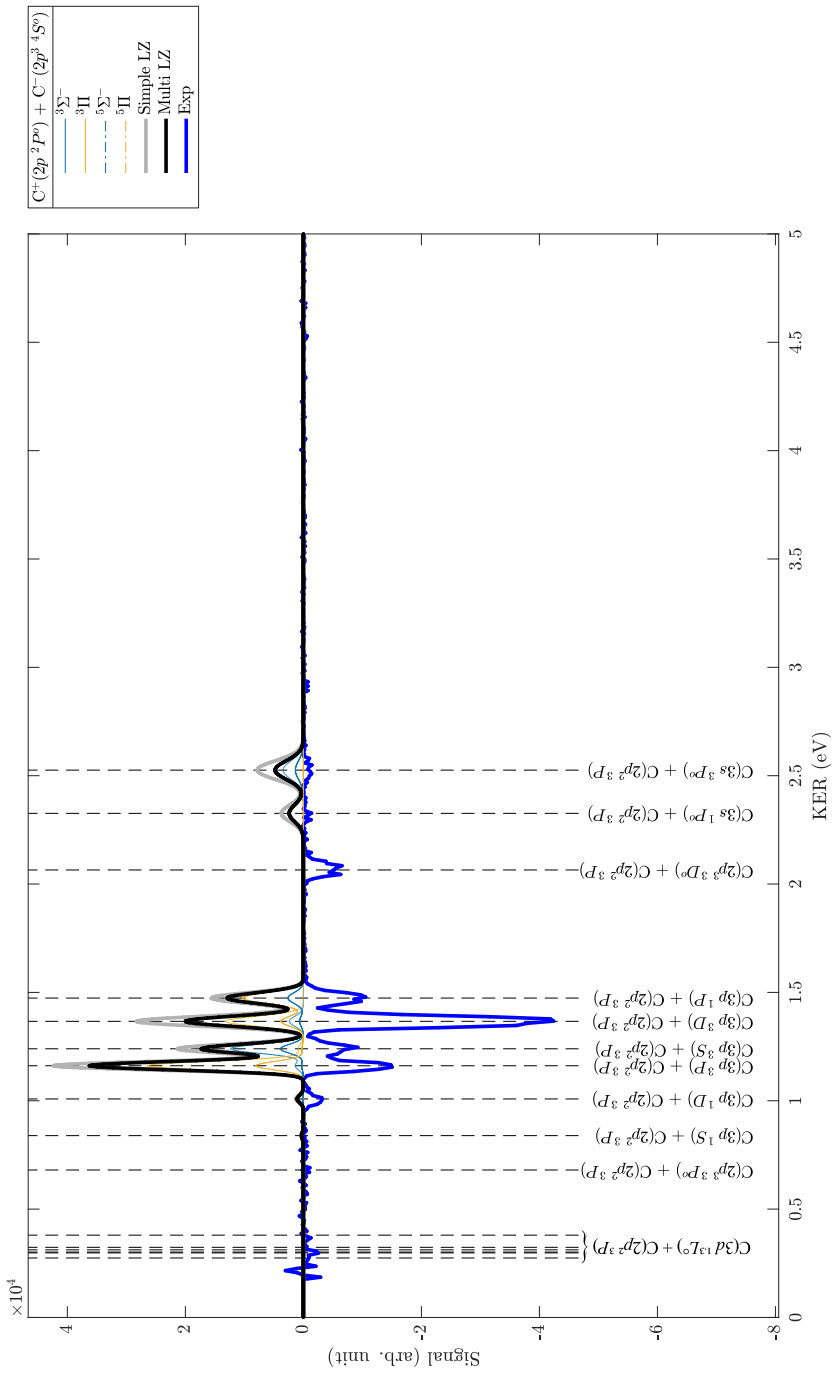

Figure F.36: Simulation: $C^+(^2P^o) + C^-(^4S^o)$.

C	C	$^3\Sigma^-$	$^3\Pi$	$^5\Sigma^-$	$^5\Pi$
$2p^2\ ^3P$	$2p^2\ ^3P$	7.066e-02	3.416e-02	1.224e-01	5.916e-02
$2p^2\ ^1D$	$2p^2\ ^3P$	6.534e-02	7.231e-02		
$2p^2\ ^1S$	$2p^2\ ^3P$	3.863e-02	3.409e-02		
$3s\ ^3P^o$	$2p^2\ ^3P$	1.170e-03	6.921e-03	2.027e-03	1.199e-02
$3s\ ^1P^o$	$2p^2\ ^3P$	1.311e-03	7.754e-03		
$3p\ ^1P$	$2p^2\ ^3P$	3.355e-04	1.108e-03		
$3p\ ^3D$	$2p^2\ ^3P$	1.280e-04	2.236e-04	2.217e-04	3.872e-04
$3p\ ^3S$	$2p^2\ ^3P$	2.770e-04	4.109e-05	4.798e-04	7.117e-05
$3p\ ^3P$	$2p^2\ ^3P$	5.642e-05	2.368e-04	9.772e-05	4.101e-04
$3p\ ^1D$	$2p^2\ ^3P$	2.605e-05	5.232e-05		
$3p\ ^1S$	$2p^2\ ^3P$	2.868e-05	2.868e-06		
$3d\ ^1D^o$	$2p^2\ ^3P$	3.156e-11	1.419e-10		
$4s\ ^3P^o$	$2p^2\ ^3P$	2.722e-12	1.610e-11	4.714e-12	2.788e-11
$3d\ ^3F^o$	$2p^2\ ^3P$	3.456e-13	6.793e-13	5.985e-13	1.177e-12
$3d\ ^3D^o$	$2p^2\ ^3P$	7.754e-14	4.395e-13	1.343e-13	7.612e-13

Table F.38: Interaction potentials E_{ic} (a.u.): $C^+(^2P^o) + C^-(^4S^o)$.

F.4.5 Oxygen

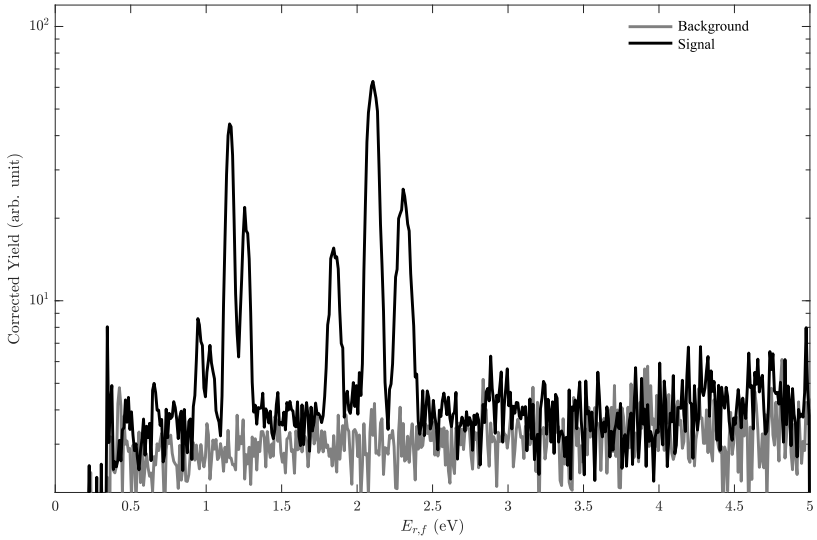

Figure F.37: Experiment: $C^+ + O^- \rightarrow C + O$.

C^+ beam	
Beam energy:	6,700 eV
Ion source:	ECR (CO)
O^- beam	
Beam energy:	7,700 eV
Ion source:	Sputtering (Fe_2O_3)
Mean collision energy:	$\sim$ 12 meV

Table F.39: $C^+ + O^-$ MN experimental setup parameters.

	$O^-(^2P^o)$	
	$O(^3P)$	$O(^1D)$
$C(3s\ ^3P^o)$	0,156(3)	0,009(2)
$C(3s\ ^1P^o)$	0,410(5)	
$C(2s2p^3\ ^3D^o)$	0,082(2)	
$C(3p\ ^1P)$	0,087(2)	
$C(3p\ ^3D)$	0,197(3)	
$C(3p\ ^3S)$	0,017(1)	
$C(3p\ ^3P)$	0,024(1)	
$C(3p\ ^1D)$	0,007(1)	
$C(3p\ ^1S)$	0,007(1)	
$C(2s2p^3\ ^3P^o)$	0,004(1)	

Table F.40: Branching ratio fit: $C^+(^2P^o)$ + $O^-(^2P^o)$.

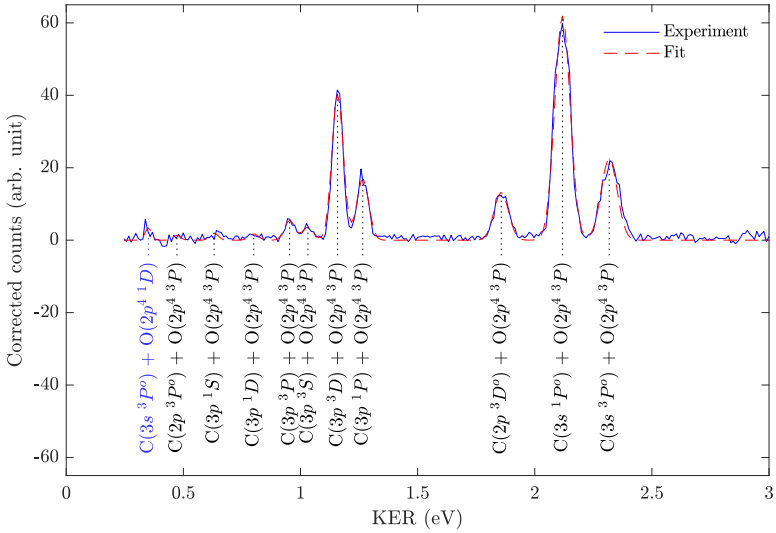

Figure F.38: Branching ratio fit: $C^+(^2P^o)$ + $O^-(^2P^o)$. The color code for the products is given in table F.1.

Cation	Anion	Center-of-mass collision energy (eV)					
C	O	0.002	0.005	0.02	0.05	0.2	0.5
$2p^2\ ^3P$	$2p^4\ ^3P$	3.24e-15	1.3e-15	3.28e-16	1.34e-16	3.68e-17	1.75e-17
$2p^2\ ^3P$	$2p^4\ ^1D$	2.75e-13	1.1e-13	2.76e-14	1.11e-14	2.89e-15	1.24e-15
$2p^2\ ^3P$	$2p^4\ ^1S$	2.69e-13	1.08e-13	2.7e-14	1.08e-14	2.75e-15	1.13e-15
$2p^2\ ^1D$	$2p^4\ ^3P$	4.68e-14	1.88e-14	4.71e-15	1.91e-15	5.04e-16	2.24e-16
$2p^2\ ^1D$	$2p^4\ ^1D$	2.06e-13	8.23e-14	2.06e-14	8.28e-15	2.12e-15	8.84e-16
$2p^2\ ^1D$	$2p^4\ ^1S$	6.84e-14	2.74e-14	6.86e-15	2.76e-15	7.04e-16	2.94e-16
$2p^2\ ^1S$	$2p^4\ ^3P$	4.46e-13	1.79e-13	4.47e-14	1.8e-14	4.62e-15	1.94e-15
$2p^2\ ^1S$	$2p^4\ ^1D$	8.38e-14	3.36e-14	8.41e-15	3.38e-15	8.7e-16	3.67e-16
$2p^2\ ^1S$	$2p^4\ ^1S$	3.74e-20	1.5e-20	3.87e-21	1.64e-21	5.44e-22	3.57e-22
$3s\ ^3P^o$	$2p^4\ ^3P$	4.67e-13	1.87e-13	4.74e-14	1.94e-14	5.47e-15	2.71e-15
$3s\ ^1P^o$	$2p^4\ ^3P$	1.61e-12	6.44e-13	1.62e-13	6.62e-14	1.8e-14	8.45e-15
$3p\ ^1P$	$2p^4\ ^3P$	7.08e-13	2.84e-13	7.14e-14	2.9e-14	7.74e-15	3.47e-15
$3p\ ^3D$	$2p^4\ ^3P$	9.61e-13	3.85e-13	9.7e-14	3.94e-14	1.06e-14	4.74e-15
$3p\ ^3S$	$2p^4\ ^3P$	1.78e-15	7.14e-16	1.8e-16	7.3e-17	1.96e-17	8.78e-18
$3p\ ^3P$	$2p^4\ ^3P$	1.61e-13	6.47e-14	1.63e-14	6.63e-15	1.79e-15	8.13e-16
$3p\ ^1D$	$2p^4\ ^3P$	4.54e-15	1.82e-15	4.6e-16	1.87e-16	5.11e-17	2.35e-17
$3p\ ^1S$	$2p^4\ ^3P$	1.18e-19	4.71e-20	1.19e-20	4.89e-21	1.36e-21	6.36e-22

Table F.41: Partial cross section (cm^2) for the C^++O^- MN reaction computed with the ACAM.

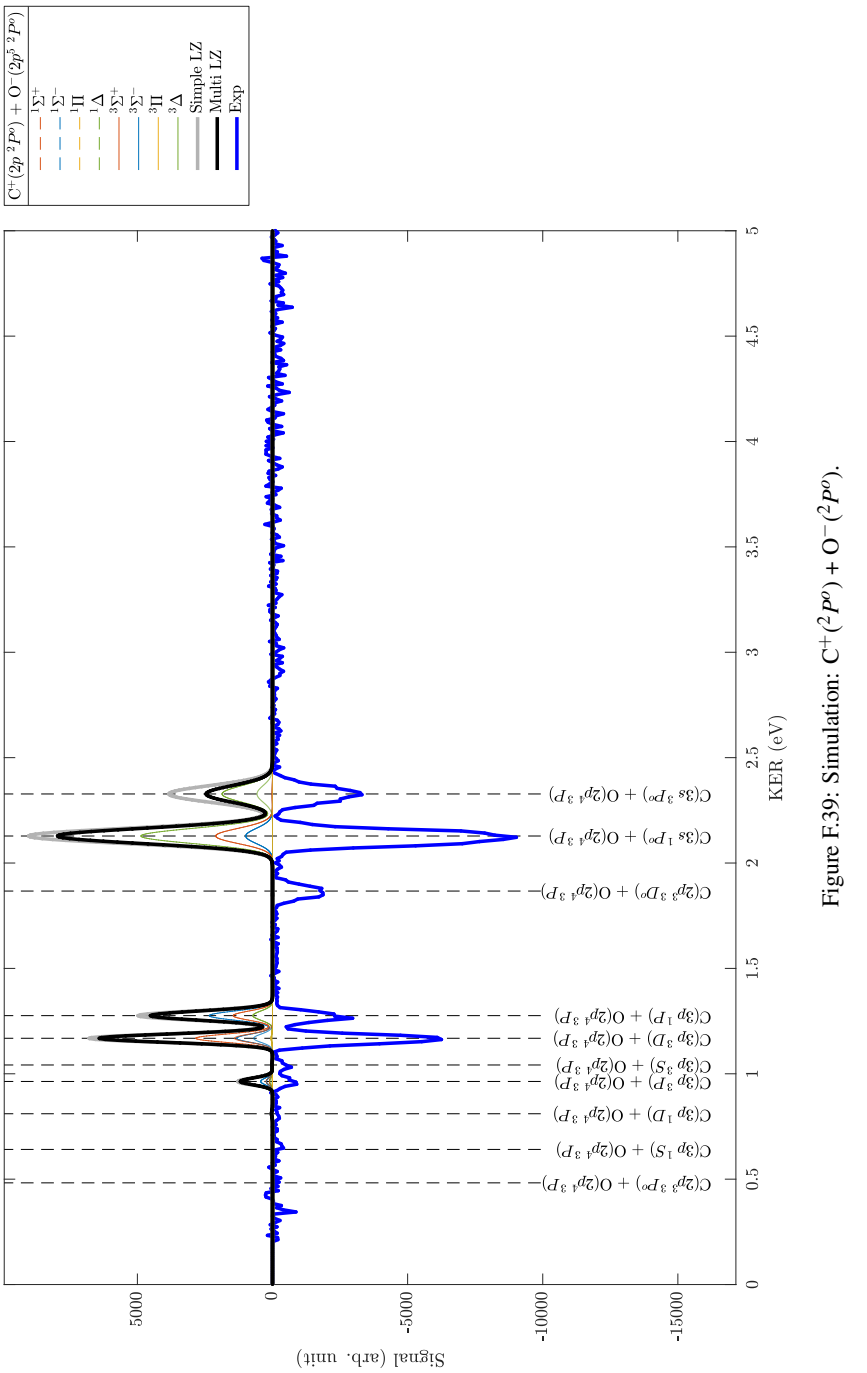

Figure F.39: Simulation: $C^+(^2P^o) + O^-(^2P^o)$.

C	O	$^1\Sigma^+$	$^1\Sigma^-$	$^1\Pi$	$^1\Delta$	$^3\Sigma^+$	$^3\Sigma^-$	$^3\Pi$	$^3\Delta$
$2p^2\ ^3P$	$2p^4\ ^3P$	2.784e-02	5.435e-02		1.896e-02	2.273e-02	4.438e-02		1.548e-02
$2p^2\ ^1D$	$2p^4\ ^3P$					2.335e-02	2.315e-02	1.432e-02	1.527e-02
$2p^2\ ^1S$	$2p^4\ ^3P$						1.167e-02	6.803e-03	
$3s\ ^3P^o$	$2p^4\ ^3P$	5.404e-03	5.404e-03		2.666e-03	4.412e-03	4.412e-03		2.177e-03
$3s\ ^1P^o$	$2p^4\ ^3P$					2.316e-03	2.316e-03		1.143e-03
$3p\ ^1P$	$2p^4\ ^3P$					1.229e-04	2.458e-04		8.574e-05
$3p\ ^3D$	$2p^4\ ^3P$	1.788e-04	1.788e-04	1.501e-05	2.174e-05	1.460e-04	1.460e-04	1.226e-05	1.775e-05
$3p\ ^3S$	$2p^4\ ^3P$		6.578e-06	3.834e-06			5.371e-06	3.131e-06	
$3p\ ^3P$	$2p^4\ ^3P$	3.243e-05	6.484e-05		2.262e-05	2.648e-05	5.294e-05		1.847e-05
$3p\ ^1D$	$2p^4\ ^3P$					5.949e-06	5.948e-06	3.451e-07	6.139e-07
$3p\ ^1S$	$2p^4\ ^3P$						2.230e-08	1.300e-08	

Table F.42: Interaction potentials E_{ic} (a.u.): $C^+(2P^o) + O^-(^2P^o)$.

F.4.6 Sulfur

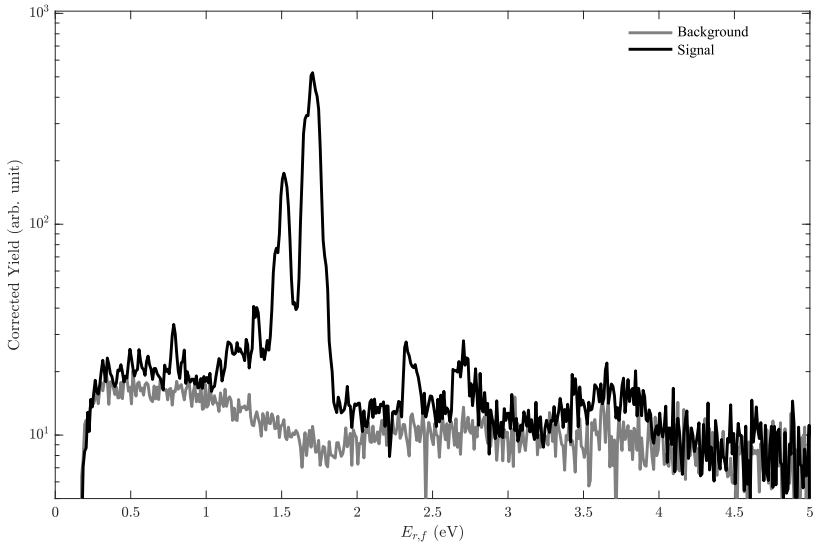

Figure F.40: Experiment: $C^+ + S^- \rightarrow C + S$.

C^+ beam	
Beam energy:	5,000 eV
Ion source:	ECR (CO)
S^- beam	
Beam energy:	11,500 eV
Ion source:	Sputtering (FeS)
Mean collision energy:	$\sim$ 15 meV

Table F.43: $C^+ + S^-$ MN experimental setup parameters.

	S($3p^4\ ^3P$)	S($3p^4\ ^1D$)	S($3p^4\ ^1S$)	S($4s\ ^5S^o$)	S($4s\ ^3S^o$)	S($4p\ ^5P$)
C($2p^2\ ^3P$)				0,022(1)	0,022(1)	0,032(1)
C($2p^2\ ^1D$)				0,000(131)	0,009(0)	
C($2p^2\ ^1S$)			0,014(1)			
C($2p^3\ ^5S^o$)		0,006(1)				
C($3s\ ^3P^o$)	0,675(4)	0,003(0)				
C($3s\ ^1P^o$)	0,186(2)	0,001(0)				
C($2s2p^3\ ^3D^o$)	0,018(1)					
C($3p\ ^1P$)	0,005(0)					
C($3p\ ^3D$)	0,004(0)					
C($3p\ ^3S$)	0,002(0)					
C($3p\ ^3P$)	0,002(0)					

Table F.44: Branching ratio fit: $C^+(^2P^o)$ + $S^-(^2P^o)$.

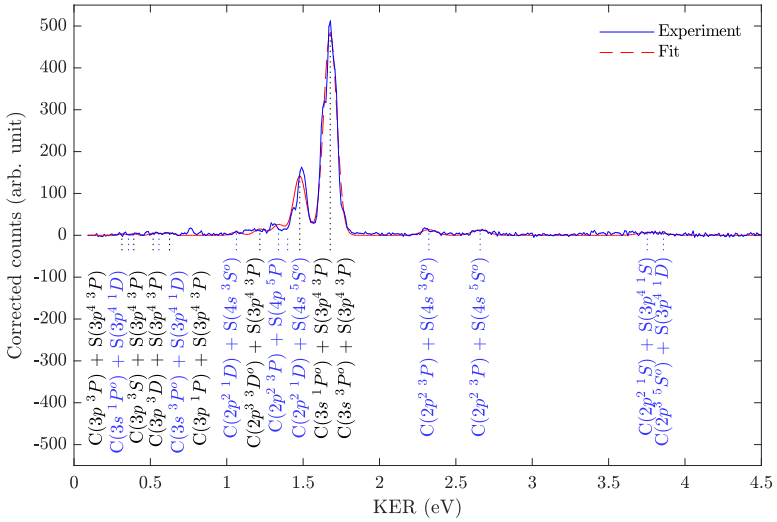

Figure F.41: Branching ratio fit: $C^+(^2P^o)$ + $S^-(^2P^o)$. The color code for the products is given in table F.1.

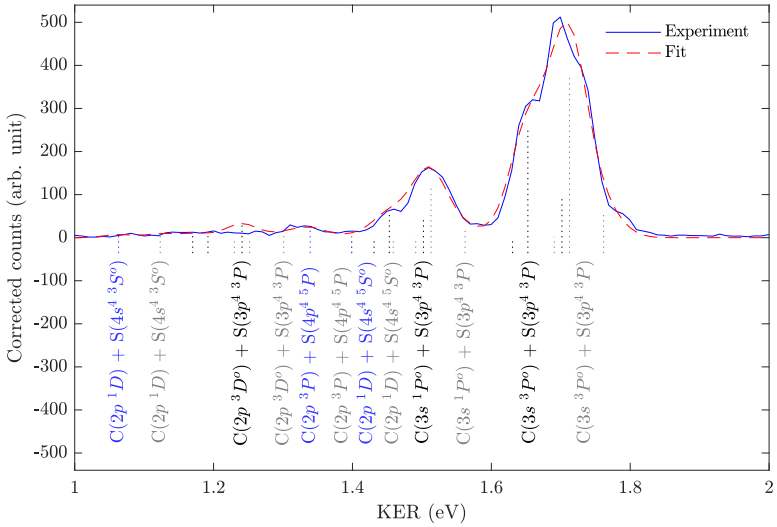

Figure F.42: Branching ratio fit: $C^+(^2P^o)$ + $S^-(^2P^o)$ – zoom. The color code for the products is given in table F.1.

Cation	Anion	Center-of-mass collision energy (eV)					
C	S	0.002	0.005	0.02	0.05	0.2	0.5
$2p^2\ ^3P$	$3p^4\ ^3P$	1.47e-15	5.88e-16	1.48e-16	6.01e-17	1.62e-17	7.42e-18
$2p^2\ ^3P$	$3p^4\ ^1D$	2.31e-14	9.26e-15	2.33e-15	9.42e-16	2.49e-16	1.11e-16
$2p^2\ ^3P$	$3p^4\ ^1S$	6.04e-13	2.42e-13	6.05e-14	2.43e-14	6.2e-15	2.58e-15
$2p^2\ ^3P$	$4p\ ^3P$	1.24e-23	4.95e-24	1.25e-24	5.06e-25	1.35e-25	6.01e-26
$2p^2\ ^1D$	$3p^4\ ^3P$	8.6e-14	3.44e-14	8.65e-15	3.49e-15	9.16e-16	4.02e-16
$2p^2\ ^1D$	$3p^4\ ^1D$	2.17e-13	8.7e-14	2.18e-14	8.79e-15	2.27e-15	9.65e-16
$2p^2\ ^1D$	$3p^4\ ^1S$	2.35e-13	9.41e-14	2.36e-14	9.49e-15	2.43e-15	1.02e-15
$2p^2\ ^1S$	$3p^4\ ^3P$	4.95e-13	1.98e-13	4.97e-14	2e-14	5.16e-15	2.19e-15
$2p^2\ ^1S$	$3p^4\ ^1D$	2.41e-13	9.65e-14	2.42e-14	9.74e-15	2.51e-15	1.07e-15
$2p^2\ ^1S$	$3p^4\ ^1S$	3.87e-15	1.55e-15	3.9e-16	1.58e-16	4.19e-17	1.86e-17
$3s\ ^3P^o$	$3p^4\ ^3P$	3.71e-12	1.49e-12	3.75e-13	1.53e-13	4.13e-14	1.9e-14
$3s\ ^3P^o$	$3p^4\ ^1D$	4.18e-24	1.68e-24	4.25e-25	1.75e-25	4.9e-26	2.33e-26
$3s\ ^1P^o$	$3p^4\ ^3P$	1.09e-12	4.36e-13	1.1e-13	4.45e-14	1.18e-14	5.25e-15
$3p\ ^1P$	$3p^4\ ^3P$	1.23e-18	4.94e-19	1.25e-19	5.12e-20	1.42e-20	6.68e-21
$3p\ ^3D$	$3p^4\ ^3P$	1.66e-20	6.67e-21	1.69e-21	6.96e-22	1.96e-22	9.36e-23
$3p\ ^3S$	$3p^4\ ^3P$	2.21e-29	8.9e-30	2.18e-30	8.25e-31	2.1e-31	8.08e-32

Table F.45: Partial cross section (cm^2) for the C^++S^- MN reaction computed with the ACAM.

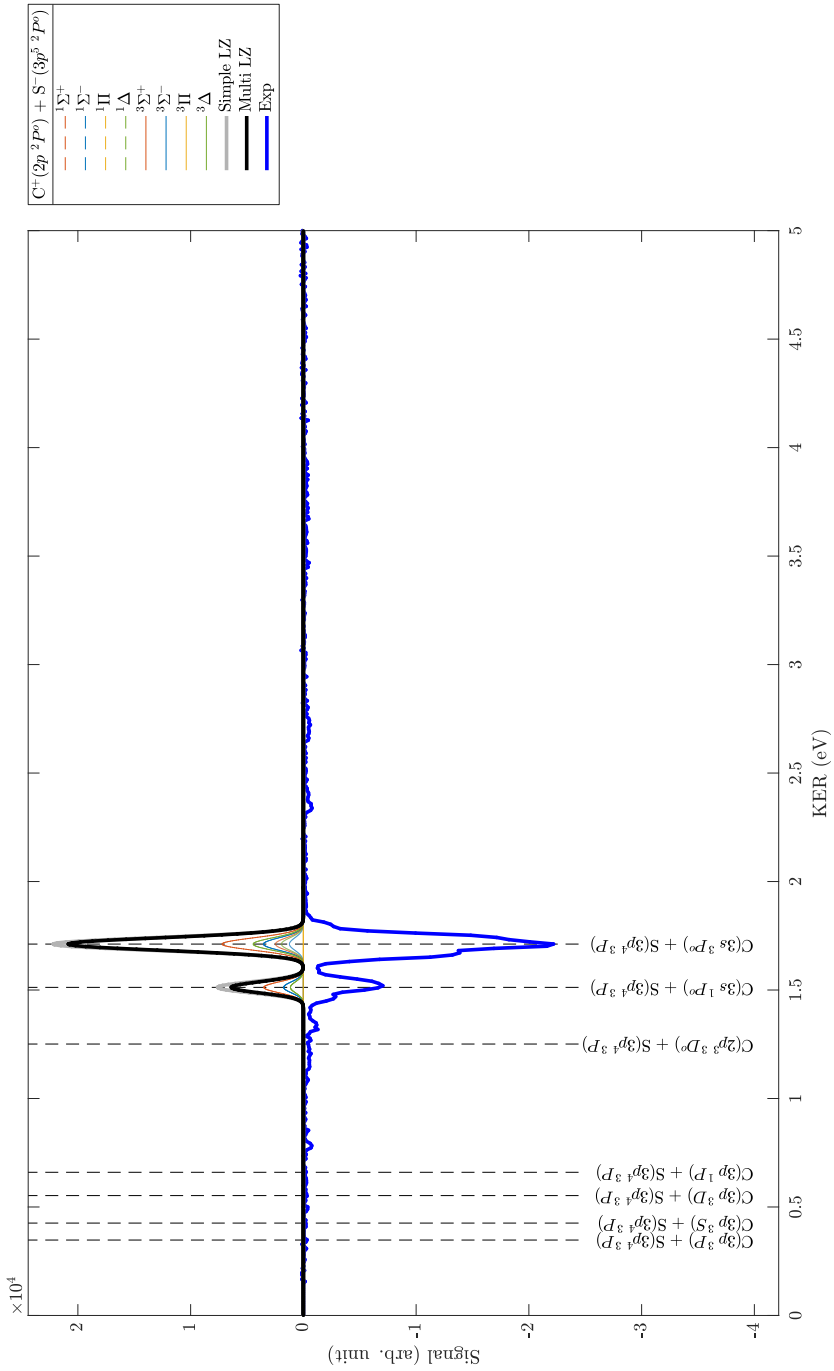

Figure F.43: Simulation: $C^+(^2P^o) + S^-(^2P^o)$.

C	S	$^1\Sigma^+$	$^1\Sigma^-$	$^1\Pi$	$^1\Delta$	$^3\Sigma^+$	$^3\Sigma^-$	$^3\Pi$	$^3\Delta$
$2p^2\,^3P$	$3p^4\,^3P$	3.247e-02	6.397e-02		2.232e-02	2.651e-02	5.223e-02		1.822e-02
$2p^2\,^1D$	$3p^4\,^3P$					2.639e-02	2.625e-02	1.264e-02	1.355e-02
$2p^2\,^1S$	$3p^4\,^3P$						9.512e-03	5.545e-03	
$3s\,^3P^o$	$3p^4\,^3P$	1.052e-03	1.052e-03		5.190e-04	8.589e-04	8.589e-04		4.238e-04
$3s\,^1P^o$	$3p^4\,^3P$					2.983e-04	2.983e-04		1.472e-04
$3p\,^1P$	$3p^4\,^3P$					4.236e-08	8.472e-08		2.956e-08
$3p\,^3D$	$3p^4\,^3P$	5.407e-09	5.407e-09	1.783e-10	4.867e-10	4.415e-09	4.415e-09	1.456e-10	3.974e-10
$3p\,^3S$	$3p^4\,^3P$		5.662e-13	3.301e-13			4.623e-13	2.695e-13	

Table F.46: Interaction potentials E_{ic} (a.u.): $C^+(^2P^o) + S^-(^2P^o)$.

F.4.7 Hydroxide

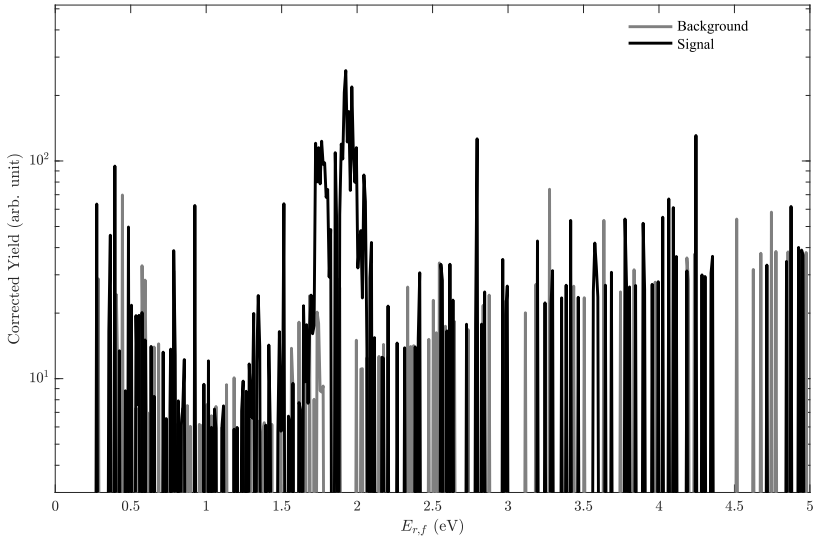

Figure F.44: Experiment: $C^+ + OH^- \rightarrow C + OH$

C^+ beam	
Beam energy:	6,500 eV
Ion source:	ECR (CO)
OH^- beam	
Beam energy:	7,500 eV
Ion source:	Sputtering (Fe_2O_3)
Mean collision energy:	$\sim$ 20 meV

Table F.47: $C^+ + OH^-$ MN experimental setup parameters.

	OH^- $OH(X)$
$C(3s\ ^3P^o)$	0,613(56)
$C(3s\ ^1P^o)$	0,308(36)
$C(2s2p^3\ ^3D^o)$	0,036(12)
$C(3p\ ^1P)$	0,016(13)
$C(3p\ ^3D)$	0,009(4)

Table F.48: Branching ratio fit: $C^+(^2P^o)$ + OH^-.

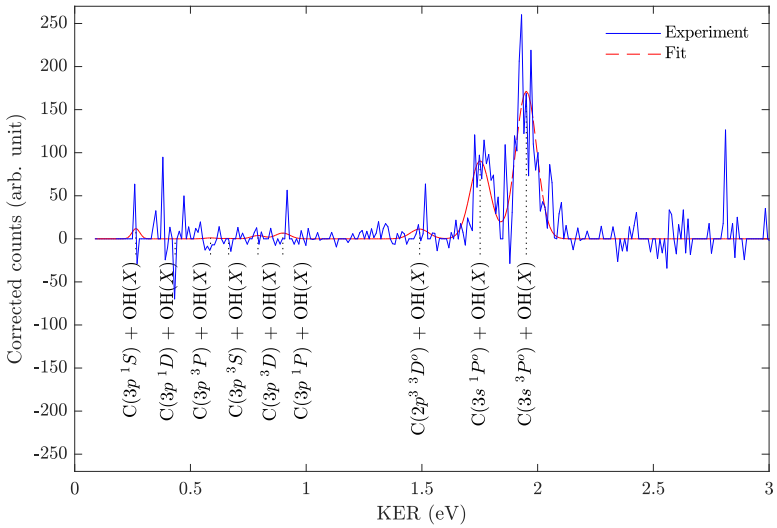

Figure F.45: Branching ratio fit: $C^+(^2P^o)$ + $OH^-(X)$.

F.5 Nitrogen

	$P^-(^3P)$ $P(^4S^o)$	$D^-(^1S)$ $D(1s)$	$Si^-(^4S^o)$ $Si(^3P)$	$C^-(^4S^o)$ $C(^3P)$	$O^-(^2P^o)$ $O(^3P)$	$S^-(^2P^o)$ $S(^3P)$
$N(2p\ ^4S^o)$						
$N(2p\ ^2D^o)$						
$N(3s\ ^4P)$	0,005(2)	0,006(3)	0,002(1)	0,006(1)	0,042(1)	0,302(3)
$N(3s\ ^2P)$	0,007(1)	0,002(1)	0,004(1)	0,012(1)	0,142(2)	0,558(3)
$N(2s2p^4\ ^4P)$	0,006(1)		0,044(3)	0,112(2)	0,268(2)	0,140(2)
$N(3p\ ^2S^o)$	0,011(2)	0,011(2)	0,054(2)	0,050(1)	0,051(1)	
$N(3p\ ^4D^o)$	0,039(2)	0,010(1)	0,253(4)	0,264(3)	0,218(2)	
$N(3p\ ^4P^o)$	0,079(3)	0,014(2)	0,266(4)	0,290(3)	0,140(1)	
$N(3p\ ^4S^o)$		0,066(3)	0,085(3)	0,015(1)	0,016(1)	
$N(3p\ ^2D^o)$	0,158(4)	0,017(2)	0,115(2)	0,189(3)	0,025(1)	
$N(3p\ ^2P^o)$	0,224(5)	0,110(4)	0,042(2)	0,059(2)	0,011(1)	
$N(3s\ ^2D)$	0,055(2)	0,019(1)			0,002(2)	
$N(4s\ ^4P)$	0,179(4)	0,328(5)	0,003(1)			
$N(4s\ ^2P)$	0,065(3)	0,117(3)	0,006(2)			
$N(3d\ ^{2,4}P,D,F)$	0,144*	0,158*				
$N(4p\ ^2S^o)$	0,008(1)	0,003(1)				
$N(4p\ ^4D^o)$	0,009(1)	0,010(1)				
$N(4p\ ^4P^o)$	0,010(2)	0,00(2)				
$N(4p\ ^2D^o)$		0,003(1)				
$N(4p\ ^4S^o)$						
$N(4p\ ^2P^o)$		0,006(1)				
$N(5s\ ^{2,4}P)$						
$N(4d\ ^{2,4}P,F)$						

Table F.49: Branching ratio fit (simplified): $N^+(^3P)$ + X^-.

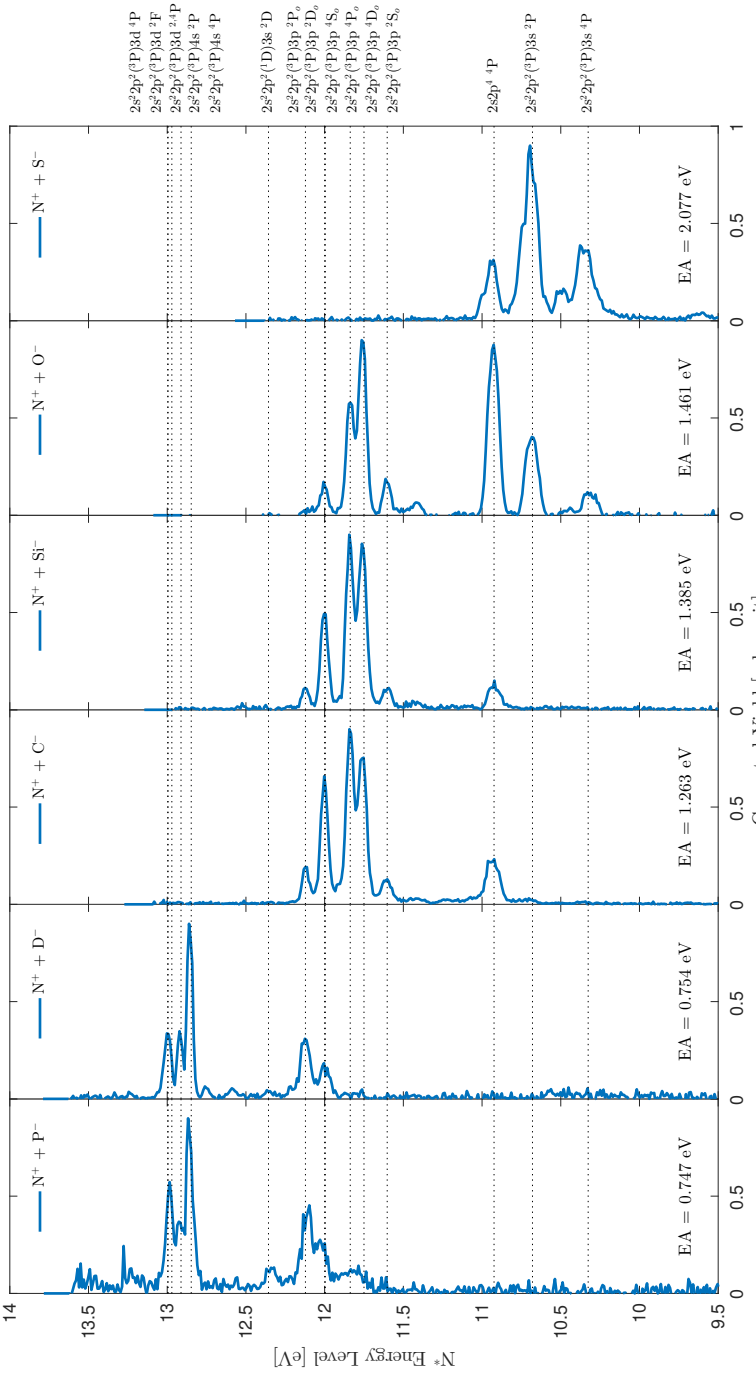

Figure F.46: Combined experiments : $N^+ + X^-$ (peak attributions).

F.5.1 Phosphorus

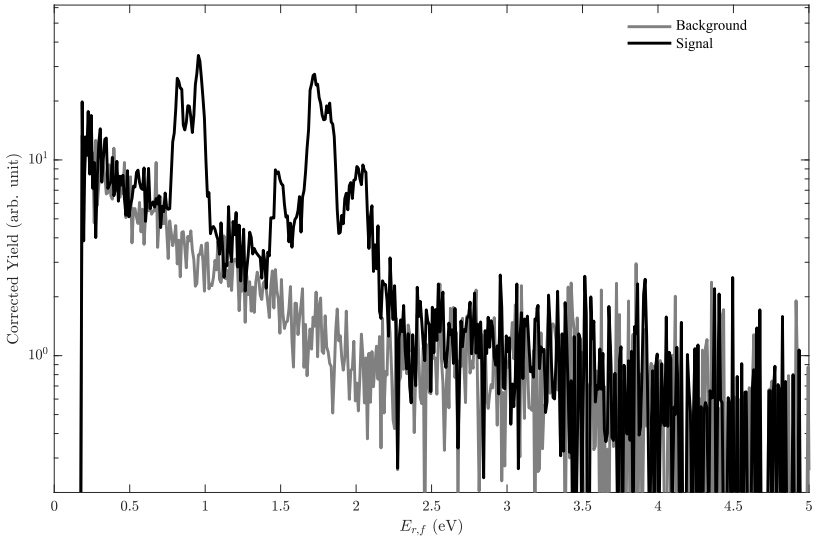

Figure F.47: Experiment: $N^+ + P^- \rightarrow N + P$.

N^+ beam	
Beam energy:	5,500 eV
Ion source:	ECR (N_2)
P^- beam	
Beam energy:	11,500 eV
Ion source:	Sputtering (Fe_2P)
Mean collision energy:	$\sim$ 5 meV

Table F.50: $N^+ + P^-$ MN experimental setup parameters.

	P^- – simple $P(^4S^o)$	$P^-(^3P)$ – all $P(^4S^o)$	$P(^2D^o)$	$P(^2P^o)$
$N(3s\ ^4P)$	0,005(2)	0,006(2)		0,010(1)
$N(3s\ ^2P)$	0,007(1)	0,006(1)	0,138(4)	
$N(2s2p^4\ ^4P)$	0,006(1)	0,005(1)	0,044(2)	0,018(9)
$N(3p\ ^2S^o)$	0,011(2)	0,011(2)		
$N(3p\ ^4D^o)$	0,039(2)	0,050(3)		
$N(3p\ ^4P^o)$	0,079(3)	0,070(3)		
$N(3p\ ^4S^o)$		0,010(2)		
$N(3p\ ^2D^o)$	0,158(4)	0,131(5)		
$N(3p\ ^2P^o)$	0,224(5)	0,090(3)		
$N(3s\ ^2D)$	0,055(2)	0,009(1)		
$N(4s\ ^4P)$	0,179(4)	0,174(4)		
$N(4s\ ^2P)$	0,065(3)	0,069(3)		
$N(3d\ ^{2,4}P,D,F)$	0,144*	0,143(15)		
$N(4p\ ^2S^o)$	0,008(1)	0,007(1)		
$N(4p\ ^4D^o)$	0,009(1)			
$N(4p\ ^4P^o)$	0,010(2)			

Table F.51: Branching ratio fit: $N^+(^3P)$ + $P^-(^3P)$. "P^- – simple" takes only "$P(^4S^o)$" into account. "$P^-(^3P)$ – all" takes all the P^* into account. Both fits take $N^+(^2D^o)$ and $N^+(^2P^o)$ into account but not included in the table.

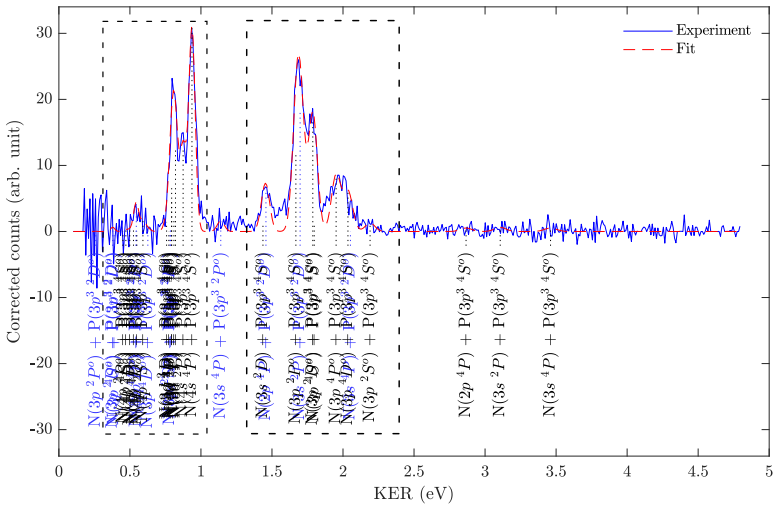

Figure F.48: Branching ratio fit: $N^+(^3P)$ + $P^-(^3P)$. The color code for the products is given in table F.1. A zoom for the framed areas are shown in figures F.49 and F.50.

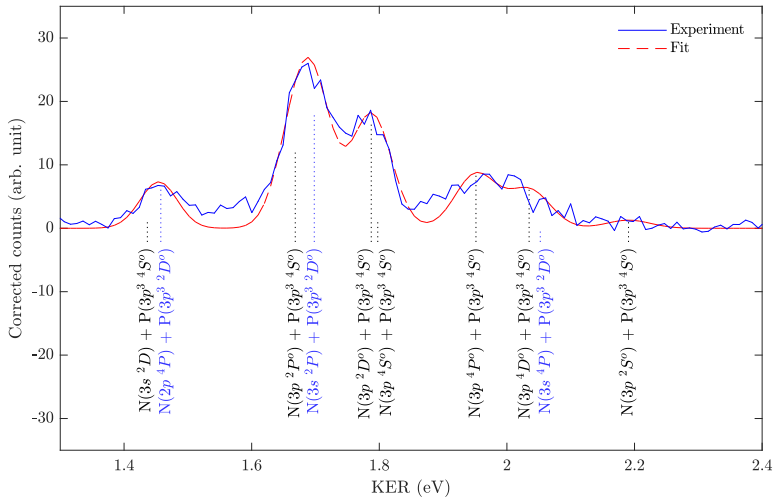

Figure F.49: Branching ratio fit: $N^+(^3P)$ + $P^-(^3P)$ – zoom 1. The color code for the products is given in table F.1.

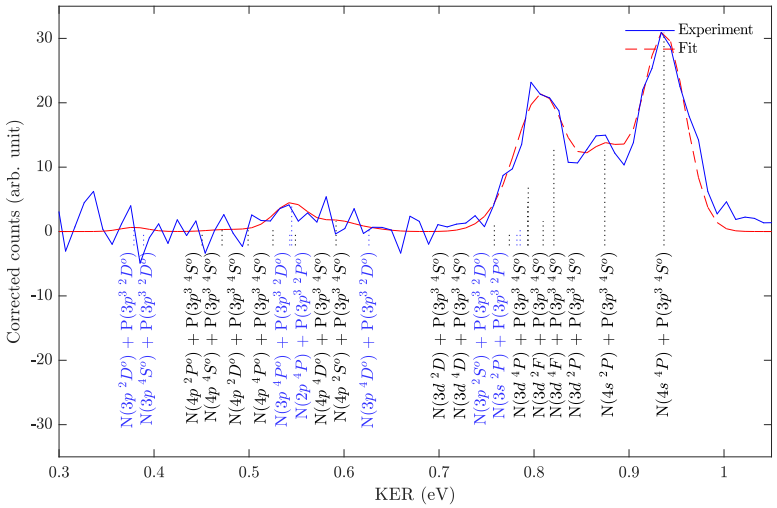

Figure F.50: Branching ratio fit: $N^+(^3P)$ + $P^-(^3P)$ – zoom 2. The color code for the products is given in table F.1.

Cation	Anion	Center-of-mass collision energy (eV)					
N	P	0.002	0.005	0.02	0.05	0.2	0.5
$2p^3\ ^4S^o$	$3p^3\ ^4S^o$	5.44e-29	2.18e-29	5.51e-30	2.25e-30	6.22e-31	2.97e-31
$2p^3\ ^4S^o$	$3p^3\ ^2D^o$	3.36e-30	1.35e-30	3.41e-31	1.39e-31	3.84e-32	1.83e-32
$2p^3\ ^4S^o$	$3p^3\ ^2P^o$	3.94e-38	1.58e-38	4.06e-39	1.71e-39	5.47e-40	3.46e-40
$2p^3\ ^2D^o$	$3p^3\ ^4S^o$	3.85e-15	1.54e-15	3.9e-16	1.59e-16	4.4e-17	2.11e-17
$2p^3\ ^2D^o$	$3p^3\ ^2D^o$	2.6e-15	1.04e-15	2.63e-16	1.07e-16	2.9e-17	1.34e-17
$2p^3\ ^2D^o$	$3p^3\ ^2P^o$	3.81e-15	1.53e-15	3.85e-16	1.57e-16	4.24e-17	1.96e-17
$2p^3\ ^2P^o$	$3p^3\ ^4S^o$	2.12e-23	8.51e-24	2.18e-24	9.2e-25	2.96e-25	1.88e-25
$2p^3\ ^2P^o$	$3p^3\ ^2D^o$	9.93e-15	3.98e-15	1e-15	4.08e-16	1.1e-16	5.08e-17
$2p^3\ ^2P^o$	$3p^3\ ^2P^o$	4.76e-14	1.91e-14	4.8e-15	1.95e-15	5.27e-16	2.42e-16
$3s\ ^4P$	$3p^3\ ^4S^o$	1.39e-13	5.56e-14	1.41e-14	5.76e-15	1.61e-15	7.83e-16
$3s\ ^4P$	$3p^3\ ^2D^o$	5.5e-13	2.2e-13	5.58e-14	2.28e-14	6.37e-15	3.09e-15
$3s\ ^4P$	$3p^3\ ^2P^o$	1.61e-15	6.46e-16	1.63e-16	6.6e-17	1.77e-17	7.91e-18
$3s\ ^2P$	$3p^3\ ^4S^o$	1.01e-13	4.04e-14	1.02e-14	4.19e-15	1.17e-15	5.68e-16
$3s\ ^2P$	$3p^3\ ^2D^o$	9.14e-13	3.66e-13	9.22e-14	3.74e-14	1e-14	4.5e-15
$3s\ ^2P$	$3p^3\ ^2P^o$	2.42e-19	9.68e-20	2.45e-20	9.99e-21	2.74e-21	1.27e-21
$3p\ ^2S^o$	$3p^3\ ^4S^o$	2e-13	8e-14	2.03e-14	8.32e-15	2.35e-15	1.16e-15
$3p\ ^2S^o$	$3p^3\ ^2D^o$	1.48e-19	5.95e-20	1.5e-20	6.14e-21	1.69e-21	7.83e-22
$3p\ ^4D^o$	$3p^3\ ^4S^o$	1.33e-12	5.33e-13	1.35e-13	5.51e-14	1.52e-14	7.28e-15
$3p\ ^4D^o$	$3p^3\ ^2D^o$	1.94e-20	7.76e-21	1.97e-21	8.07e-22	2.25e-22	1.06e-22
$3p\ ^4P^o$	$3p^3\ ^4S^o$	3.19e-13	1.28e-13	3.24e-14	1.33e-14	3.75e-15	1.86e-15
$3p\ ^4P^o$	$3p^3\ ^2D^o$	3.96e-21	1.59e-21	4.03e-22	1.66e-22	4.69e-23	2.25e-23
$3p\ ^4S^o$	$3p^3\ ^4S^o$	9.06e-13	3.63e-13	9.15e-14	3.72e-14	1.01e-14	4.65e-15
$3p\ ^2D^o$	$3p^3\ ^4S^o$	2.08e-12	8.32e-13	2.1e-13	8.54e-14	2.32e-14	1.07e-14
$3p\ ^2D^o$	$3p^3\ ^2D^o$	4.73e-31	1.91e-31	4.95e-32	1.49e-32	4.31e-33	8.73e-34
$3p\ ^2P^o$	$3p^3\ ^4S^o$	1.64e-12	6.59e-13	1.67e-13	6.85e-14	1.94e-14	9.6e-15
$4s\ ^4P$	$3p^3\ ^4S^o$	4.87e-12	1.95e-12	4.96e-13	2.04e-13	5.79e-14	2.83e-14
$4s\ ^2P$	$3p^3\ ^4S^o$	2.25e-12	9.01e-13	2.28e-13	9.35e-14	2.61e-14	1.24e-14
$3d\ ^2P$	$3p^3\ ^4S^o$	1.04e-13	4.17e-14	1.05e-14	4.31e-15	1.19e-15	5.56e-16
$3d\ ^4F$	$3p^3\ ^4S^o$	6.67e-13	2.67e-13	6.76e-14	2.77e-14	7.66e-15	3.6e-15
$3d\ ^2F$	$3p^3\ ^4S^o$	2.93e-13	1.18e-13	2.98e-14	1.22e-14	3.38e-15	1.59e-15
$3d\ ^4P$	$3p^3\ ^4S^o$	1.63e-13	6.54e-14	1.65e-14	6.77e-15	1.87e-15	8.77e-16
$3d\ ^4D$	$3p^3\ ^4S^o$	5.87e-13	2.36e-13	5.96e-14	2.44e-14	6.78e-15	3.19e-15
$3d\ ^2D$	$3p^3\ ^4S^o$	2.56e-13	1.03e-13	2.6e-14	1.07e-14	2.96e-15	1.39e-15
$4p\ ^2S^o$	$3p^3\ ^4S^o$	7.96e-16	3.19e-16	8.09e-17	3.32e-17	9.33e-18	4.44e-18
$4p\ ^4D^o$	$3p^3\ ^4S^o$	3.97e-14	1.59e-14	4.05e-15	1.67e-15	4.73e-16	2.28e-16
$4p\ ^4P^o$	$3p^3\ ^4S^o$	2.01e-14	8.07e-15	2.05e-15	8.46e-16	2.41e-16	1.17e-16
$4p\ ^2D^o$	$3p^3\ ^4S^o$	4.53e-15	1.82e-15	4.63e-16	1.91e-16	5.47e-17	2.66e-17
$4p\ ^4S^o$	$3p^3\ ^4S^o$	4.24e-17	1.7e-17	4.33e-18	1.79e-18	5.13e-19	2.49e-19
$4p\ ^2P^o$	$3p^3\ ^4S^o$	7.14e-16	2.87e-16	7.3e-17	3.02e-17	8.75e-18	4.3e-18

Table F.52: Partial cross section (cm^2) for the $N^+(^3P)$+$P^-(^3P)$ MN reaction computed with the ACAM.

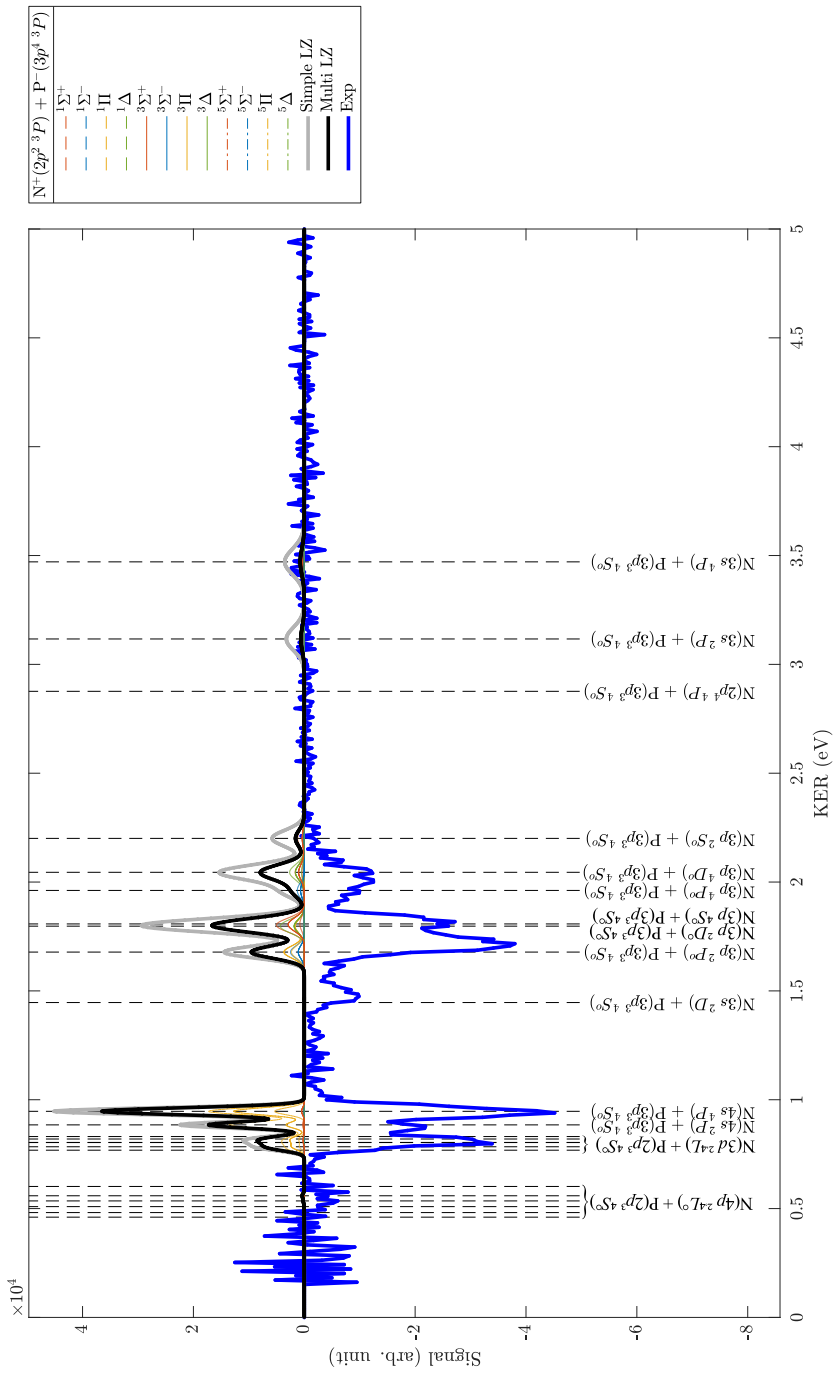

Figure F.51: Simulation: $N^+(^3P) + P^-(^3P)$ - without P^*

N	P	$^1\Sigma^+$	$^1\Sigma^-$	$^1\Pi$	$^1\Delta$	$^3\Sigma^+$	$^3\Sigma^-$
$2p^3\ ^4S^o$	$3p^3\ ^4S^o$	2.522e-09				2.302e-09	
$2p^3\ ^2D^o$	$3p^3\ ^4S^o$					1.163e-02	
$2p^3\ ^2P^o$	$3p^3\ ^4S^o$						3.005e-02
$3s\ ^4P$	$3p^3\ ^4S^o$	2.597e-03		1.536e-02		2.371e-03	
$3s\ ^2P$	$3p^3\ ^4S^o$					8.746e-04	
$3p\ ^2S^o$	$3p^3\ ^4S^o$					6.907e-04	
$3p\ ^4D^o$	$3p^3\ ^4S^o$	1.168e-03		3.936e-03	1.777e-03	1.067e-03	
$3p\ ^4P^o$	$3p^3\ ^4S^o$		1.882e-03	3.583e-03			1.718e-03
$3p\ ^4S^o$	$3p^3\ ^4S^o$	9.183e-04				8.383e-04	
$3p\ ^2D^o$	$3p^3\ ^4S^o$					3.286e-04	
$3p\ ^2P^o$	$3p^3\ ^4S^o$						4.461e-04
$4s\ ^4P$	$3p^3\ ^4S^o$	5.904e-05		3.491e-04		5.390e-05	
$4s\ ^2P$	$3p^3\ ^4S^o$					1.683e-05	
$3d\ ^2P$	$3p^3\ ^4S^o$					8.757e-06	
$3d\ ^4F$	$3p^3\ ^4S^o$	1.929e-05		6.883e-05	1.955e-05	1.761e-05	
$3d\ ^2F$	$3p^3\ ^4S^o$					6.970e-06	
$3d\ ^4P$	$3p^3\ ^4S^o$	1.746e-05		3.087e-05		1.594e-05	
$3d\ ^4D$	$3p^3\ ^4S^o$		2.155e-05	5.972e-05	1.026e-05		1.967e-05
$3d\ ^2D$	$3p^3\ ^4S^o$						7.635e-06
$4p\ ^2S^o$	$3p^3\ ^4S^o$					1.026e-06	
$4p\ ^4D^o$	$3p^3\ ^4S^o$	1.611e-06		7.882e-06	9.601e-07	1.470e-06	
$4p\ ^4P^o$	$3p^3\ ^4S^o$		7.399e-07	5.232e-06			6.754e-07
$4p\ ^2D^o$	$3p^3\ ^4S^o$					2.617e-07	
$4p\ ^4S^o$	$3p^3\ ^4S^o$	2.733e-07				2.495e-07	
$4p\ ^2P^o$	$3p^3\ ^4S^o$						5.219e-08

Table F.53: Interaction potentials E_{ic} (a.u.): $N^+(^3P) + P^-(^3P)$ - without P^*.

N	P	$^3\Pi$	$^3\Delta$	$^5\Sigma^+$	$^5\Sigma^-$	$^5\Pi$	$^5\Delta$
$2p^3\ ^4S^o$	$3p^3\ ^4S^o$			1.783e-09			
$2p^3\ ^2D^o$	$3p^3\ ^4S^o$	9.169e-03	2.321e-02	2.015e-02		1.588e-02	4.020e-02
$2p^3\ ^2P^o$	$3p^3\ ^4S^o$	1.093e-02			5.204e-02	1.893e-02	
$3s\ ^4P$	$3p^3\ ^4S^o$	1.402e-02		1.837e-03		1.086e-02	
$3s\ ^2P$	$3p^3\ ^4S^o$	5.172e-03		1.515e-03		8.958e-03	
$3p\ ^2S^o$	$3p^3\ ^4S^o$			1.196e-03			
$3p\ ^4D^o$	$3p^3\ ^4S^o$	3.593e-03	1.622e-03	8.262e-04		2.783e-03	1.257e-03
$3p\ ^4P^o$	$3p^3\ ^4S^o$	3.271e-03			1.331e-03	2.534e-03	
$3p\ ^4S^o$	$3p^3\ ^4S^o$			6.494e-04			
$3p\ ^2D^o$	$3p^3\ ^4S^o$	1.186e-03	4.705e-04	5.691e-04		2.055e-03	8.149e-04
$3p\ ^2P^o$	$3p^3\ ^4S^o$	9.935e-04			7.727e-04	1.721e-03	
$4s\ ^4P$	$3p^3\ ^4S^o$	3.187e-04		4.175e-05		2.469e-04	
$4s\ ^2P$	$3p^3\ ^4S^o$	9.951e-05		2.914e-05		1.723e-04	
$3d\ ^2P$	$3p^3\ ^4S^o$	1.515e-05		1.517e-05		2.624e-05	
$3d\ ^4F$	$3p^3\ ^4S^o$	6.283e-05	1.785e-05	1.364e-05		4.867e-05	1.383e-05
$3d\ ^2F$	$3p^3\ ^4S^o$	2.510e-05	6.987e-06	1.207e-05		4.347e-05	1.210e-05
$3d\ ^4P$	$3p^3\ ^4S^o$	2.818e-05		1.235e-05		2.183e-05	
$3d\ ^4D$	$3p^3\ ^4S^o$	5.452e-05	9.364e-06		1.524e-05	4.223e-05	7.254e-06
$3d\ ^2D$	$3p^3\ ^4S^o$	2.160e-05	3.634e-06		1.322e-05	3.741e-05	6.294e-06
$4p\ ^2S^o$	$3p^3\ ^4S^o$			1.777e-06			
$4p\ ^4D^o$	$3p^3\ ^4S^o$	7.195e-06	8.765e-07	1.139e-06		5.573e-06	6.789e-07
$4p\ ^4P^o$	$3p^3\ ^4S^o$	4.776e-06			5.232e-07	3.700e-06	
$4p\ ^2D^o$	$3p^3\ ^4S^o$	1.290e-06	1.429e-07	4.533e-07		2.235e-06	2.475e-07
$4p\ ^4S^o$	$3p^3\ ^4S^o$			1.933e-07			
$4p\ ^2P^o$	$3p^3\ ^4S^o$	4.301e-07			9.040e-08	7.450e-07	

Table F.54: Interaction potentials E_{ic} (a.u.): $N^+(^3P) + P^-(^3P)$ - without P* (continued).

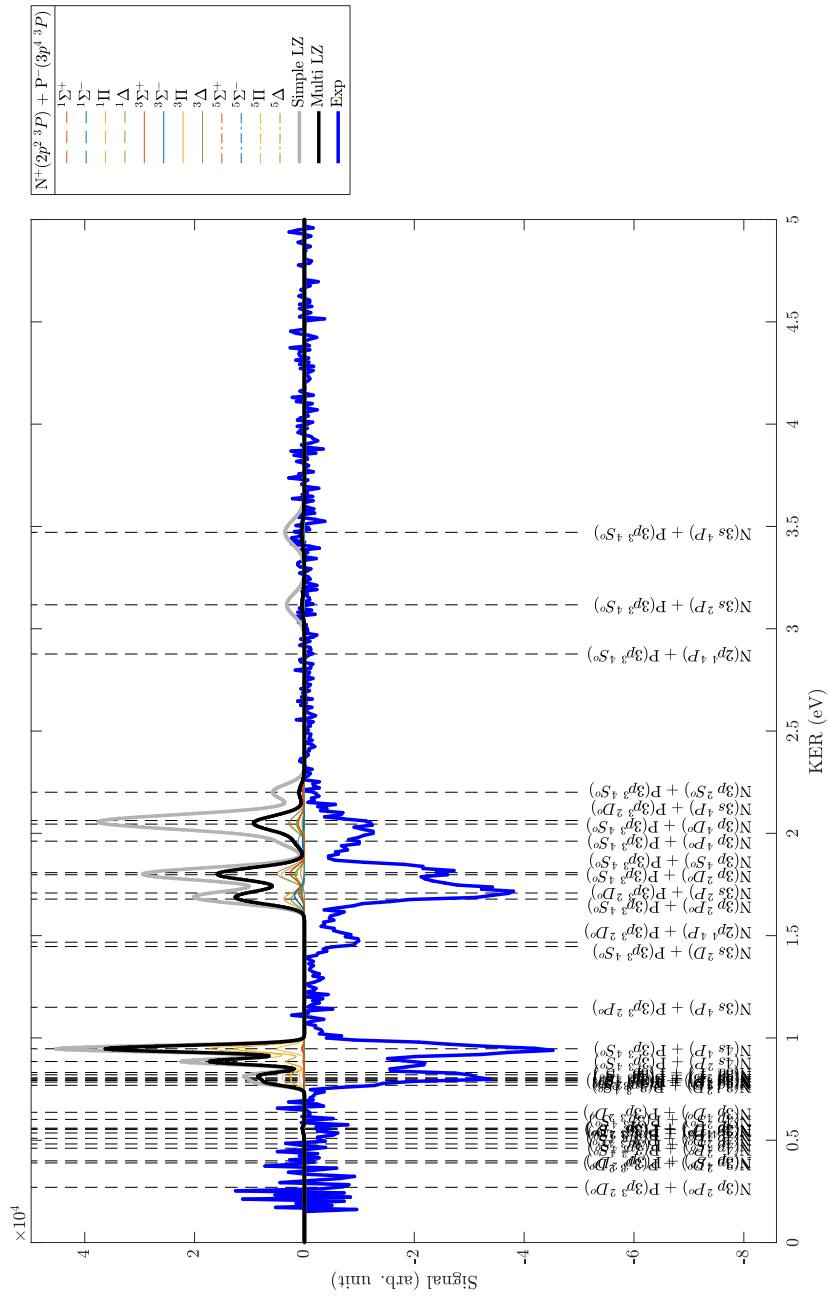

Figure F.52: Simulation: $N^+(^3P) + P^-(^3P)$ - with P*

N	P	$^1\Sigma^+$	$^1\Sigma^-$	$^1\Pi$	$^1\Delta$
$2p^3\ ^4S^o$	$3p^3\ ^4S^o$	2.522e-09			
$2p^3\ ^4S^o$	$3p^3\ ^2D^o$				
$2p^3\ ^4S^o$	$3p^3\ ^2P^o$				
$2p^3\ ^2D^o$	$3p^3\ ^4S^o$				
$2p^3\ ^2D^o$	$3p^3\ ^2D^o$	2.680e-02	4.632e-02	1.281e-02	7.617e-03
$2p^3\ ^2D^o$	$3p^3\ ^2P^o$	1.605e-02	1.598e-02	7.259e-03	7.795e-03
$2p^3\ ^2P^o$	$3p^3\ ^4S^o$				
$2p^3\ ^2P^o$	$3p^3\ ^2D^o$	2.334e-02	2.320e-02	1.261e-02	1.143e-02
$2p^3\ ^2P^o$	$3p^3\ ^2P^o$	1.207e-02	2.396e-02		8.359e-03
$3s\ ^4P$	$3p^3\ ^4S^o$	2.597e-03		1.536e-02	
$3s\ ^4P$	$3p^3\ ^2D^o$				
$3s\ ^4P$	$3p^3\ ^2P^o$				
$3s\ ^2P$	$3p^3\ ^4S^o$				
$3s\ ^2P$	$3p^3\ ^2D^o$	3.983e-04	7.964e-04	3.050e-04	2.724e-04
$3s\ ^2P$	$3p^3\ ^2P^o$	5.505e-08	5.505e-08		2.716e-08
$3p\ ^2S^o$	$3p^3\ ^4S^o$				
$3p\ ^2S^o$	$3p^3\ ^2D^o$	4.670e-08		1.672e-08	2.365e-08
$3p\ ^4D^o$	$3p^3\ ^4S^o$	1.168e-03		3.936e-03	1.777e-03
$3p\ ^4D^o$	$3p^3\ ^2D^o$				
$3p\ ^4P^o$	$3p^3\ ^4S^o$		1.882e-03	3.583e-03	
$3p\ ^4P^o$	$3p^3\ ^2D^o$				
$3p\ ^4S^o$	$3p^3\ ^4S^o$	9.183e-04			
$3p\ ^2D^o$	$3p^3\ ^4S^o$				
$3p\ ^2P^o$	$3p^3\ ^4S^o$				
$4s\ ^4P$	$3p^3\ ^4S^o$	5.904e-05		3.491e-04	
$4s\ ^2P$	$3p^3\ ^4S^o$				
$3d\ ^2P$	$3p^3\ ^4S^o$				
$3d\ ^4F$	$3p^3\ ^4S^o$	1.929e-05		6.883e-05	1.955e-05
$3d\ ^2F$	$3p^3\ ^4S^o$				
$3d\ ^4P$	$3p^3\ ^4S^o$	1.746e-05		3.087e-05	
$3d\ ^4D$	$3p^3\ ^4S^o$		2.155e-05	5.972e-05	1.026e-05
$3d\ ^2D$	$3p^3\ ^4S^o$				
$4p\ ^2S^o$	$3p^3\ ^4S^o$				
$4p\ ^4D^o$	$3p^3\ ^4S^o$	1.611e-06		7.882e-06	9.601e-07
$4p\ ^4P^o$	$3p^3\ ^4S^o$		7.399e-07	5.232e-06	
$4p\ ^2D^o$	$3p^3\ ^4S^o$				
$4p\ ^4S^o$	$3p^3\ ^4S^o$	2.733e-07			
$4p\ ^2P^o$	$3p^3\ ^4S^o$				

Table F.55: Interaction potentials E_{ic} (a.u.): $N^+(^3P)$ + $P^-(^3P)$ - with P^*.

N	P	$^3\Sigma^+$	$^3\Sigma^-$	$^3\Pi$	$^3\Delta$
$2p^3\ ^4S^o$	$3p^3\ ^4S^o$	2.302e-09			
$2p^3\ ^4S^o$	$3p^3\ ^2D^o$	2.208e-10		3.063e-10	4.332e-10
$2p^3\ ^4S^o$	$3p^3\ ^2P^o$		3.397e-10	1.980e-10	
$2p^3\ ^2D^o$	$3p^3\ ^4S^o$	1.163e-02		9.169e-03	2.321e-02
$2p^3\ ^2D^o$	$3p^3\ ^2D^o$	2.188e-02	3.782e-02	1.046e-02	6.219e-03
$2p^3\ ^2D^o$	$3p^3\ ^2P^o$	1.310e-02	1.305e-02	5.927e-03	6.365e-03
$2p^3\ ^2P^o$	$3p^3\ ^4S^o$		3.005e-02	1.093e-02	
$2p^3\ ^2P^o$	$3p^3\ ^2D^o$	1.905e-02	1.894e-02	1.030e-02	9.330e-03
$2p^3\ ^2P^o$	$3p^3\ ^2P^o$	9.855e-03	1.956e-02		6.825e-03
$3s\ ^4P$	$3p^3\ ^4S^o$	2.371e-03		1.402e-02	
$3s\ ^4P$	$3p^3\ ^2D^o$	5.911e-04	1.182e-03	4.527e-04	4.042e-04
$3s\ ^4P$	$3p^3\ ^2P^o$	3.630e-06	3.630e-06		1.791e-06
$3s\ ^2P$	$3p^3\ ^4S^o$	8.746e-04		5.172e-03	
$3s\ ^2P$	$3p^3\ ^2D^o$	3.252e-04	6.503e-04	2.491e-04	2.224e-04
$3s\ ^2P$	$3p^3\ ^2P^o$	4.495e-08	4.495e-08		2.218e-08
$3p\ ^2S^o$	$3p^3\ ^4S^o$	6.907e-04			
$3p\ ^2S^o$	$3p^3\ ^2D^o$	3.813e-08		1.365e-08	1.931e-08
$3p\ ^4D^o$	$3p^3\ ^4S^o$	1.067e-03		3.593e-03	1.622e-03
$3p\ ^4D^o$	$3p^3\ ^2D^o$	3.349e-09	5.708e-09	1.328e-09	5.439e-10
$3p\ ^4P^o$	$3p^3\ ^4S^o$		1.718e-03	3.271e-03	
$3p\ ^4P^o$	$3p^3\ ^2D^o$	1.292e-09	1.292e-09	7.000e-10	6.250e-10
$3p\ ^4S^o$	$3p^3\ ^4S^o$	8.383e-04			
$3p\ ^2D^o$	$3p^3\ ^4S^o$	3.286e-04		1.186e-03	4.705e-04
$3p\ ^2P^o$	$3p^3\ ^4S^o$		4.461e-04	9.935e-04	
$4s\ ^4P$	$3p^3\ ^4S^o$	5.390e-05		3.187e-04	
$4s\ ^2P$	$3p^3\ ^4S^o$	1.683e-05		9.951e-05	
$3d\ ^2P$	$3p^3\ ^4S^o$	8.757e-06		1.515e-05	
$3d\ ^4F$	$3p^3\ ^4S^o$	1.761e-05		6.283e-05	1.785e-05
$3d\ ^2F$	$3p^3\ ^4S^o$	6.970e-06		2.510e-05	6.987e-06
$3d\ ^4P$	$3p^3\ ^4S^o$	1.594e-05		2.818e-05	
$3d\ ^4D$	$3p^3\ ^4S^o$		1.967e-05	5.452e-05	9.364e-06
$3d\ ^2D$	$3p^3\ ^4S^o$		7.635e-06	2.160e-05	3.634e-06
$4p\ ^2S^o$	$3p^3\ ^4S^o$	1.026e-06			
$4p\ ^4D^o$	$3p^3\ ^4S^o$	1.470e-06		7.195e-06	8.765e-07
$4p\ ^4P^o$	$3p^3\ ^4S^o$		6.754e-07	4.776e-06	
$4p\ ^2D^o$	$3p^3\ ^4S^o$	2.617e-07		1.290e-06	1.429e-07
$4p\ ^4S^o$	$3p^3\ ^4S^o$	2.495e-07			
$4p\ ^2P^o$	$3p^3\ ^4S^o$		5.219e-08	4.301e-07	

Table F.56: Interaction potentials E_{ic} (a.u.): $N^+(^3P)$ + $P^-(^3P)$ - with P^* (continued).

N	P	$^5\Sigma^+$	$^5\Sigma^-$	$^5\Pi$	$^5\Delta$
$2p^3\ ^4S^o$	$3p^3\ ^4S^o$	1.783e-09			
$2p^3\ ^4S^o$	$3p^3\ ^2D^o$	3.824e-10		5.305e-10	7.503e-10
$2p^3\ ^4S^o$	$3p^3\ ^2P^o$		5.883e-10	3.430e-10	
$2p^3\ ^2D^o$	$3p^3\ ^4S^o$	2.015e-02		1.588e-02	4.020e-02
$2p^3\ ^2D^o$	$3p^3\ ^2D^o$				
$2p^3\ ^2D^o$	$3p^3\ ^2P^o$				
$2p^3\ ^2P^o$	$3p^3\ ^4S^o$		5.204e-02	1.893e-02	
$2p^3\ ^2P^o$	$3p^3\ ^2D^o$				
$2p^3\ ^2P^o$	$3p^3\ ^2P^o$				
$3s\ ^4P$	$3p^3\ ^4S^o$	1.837e-03		1.086e-02	
$3s\ ^4P$	$3p^3\ ^2D^o$	1.024e-03	2.047e-03	7.841e-04	7.001e-04
$3s\ ^4P$	$3p^3\ ^2P^o$	6.288e-06	6.288e-06		3.102e-06
$3s\ ^2P$	$3p^3\ ^4S^o$	1.515e-03		8.958e-03	
$3s\ ^2P$	$3p^3\ ^2D^o$				
$3s\ ^2P$	$3p^3\ ^2P^o$				
$3p\ ^2S^o$	$3p^3\ ^4S^o$	1.196e-03			
$3p\ ^2S^o$	$3p^3\ ^2D^o$				
$3p\ ^4D^o$	$3p^3\ ^4S^o$	8.262e-04		2.783e-03	1.257e-03
$3p\ ^4D^o$	$3p^3\ ^2D^o$	5.801e-09	9.887e-09	2.301e-09	9.421e-10
$3p\ ^4P^o$	$3p^3\ ^4S^o$		1.331e-03	2.534e-03	
$3p\ ^4P^o$	$3p^3\ ^2D^o$	2.238e-09	2.238e-09	1.212e-09	1.083e-09
$3p\ ^4S^o$	$3p^3\ ^4S^o$	6.494e-04			
$3p\ ^2D^o$	$3p^3\ ^4S^o$	5.691e-04		2.055e-03	8.149e-04
$3p\ ^2P^o$	$3p^3\ ^4S^o$		7.727e-04	1.721e-03	
$4s\ ^4P$	$3p^3\ ^4S^o$	4.175e-05		2.469e-04	
$4s\ ^2P$	$3p^3\ ^4S^o$	2.914e-05		1.723e-04	
$3d\ ^2P$	$3p^3\ ^4S^o$	1.517e-05		2.624e-05	
$3d\ ^4F$	$3p^3\ ^4S^o$	1.364e-05		4.867e-05	1.383e-05
$3d\ ^2F$	$3p^3\ ^4S^o$	1.207e-05		4.347e-05	1.210e-05
$3d\ ^4P$	$3p^3\ ^4S^o$	1.235e-05		2.183e-05	
$3d\ ^4D$	$3p^3\ ^4S^o$		1.524e-05	4.223e-05	7.254e-06
$3d\ ^2D$	$3p^3\ ^4S^o$		1.322e-05	3.741e-05	6.294e-06
$4p\ ^2S^o$	$3p^3\ ^4S^o$	1.777e-06			
$4p\ ^4D^o$	$3p^3\ ^4S^o$	1.139e-06		5.573e-06	6.789e-07
$4p\ ^4P^o$	$3p^3\ ^4S^o$		5.232e-07	3.700e-06	
$4p\ ^2D^o$	$3p^3\ ^4S^o$	4.533e-07		2.235e-06	2.475e-07
$4p\ ^4S^o$	$3p^3\ ^4S^o$	1.933e-07			
$4p\ ^2P^o$	$3p^3\ ^4S^o$		9.040e-08	7.450e-07	

Table F.57: Interaction potentials E_{ic} (a.u.): $N^+(^3P)$ + $P^-(^3P)$ - with P^* (continued).

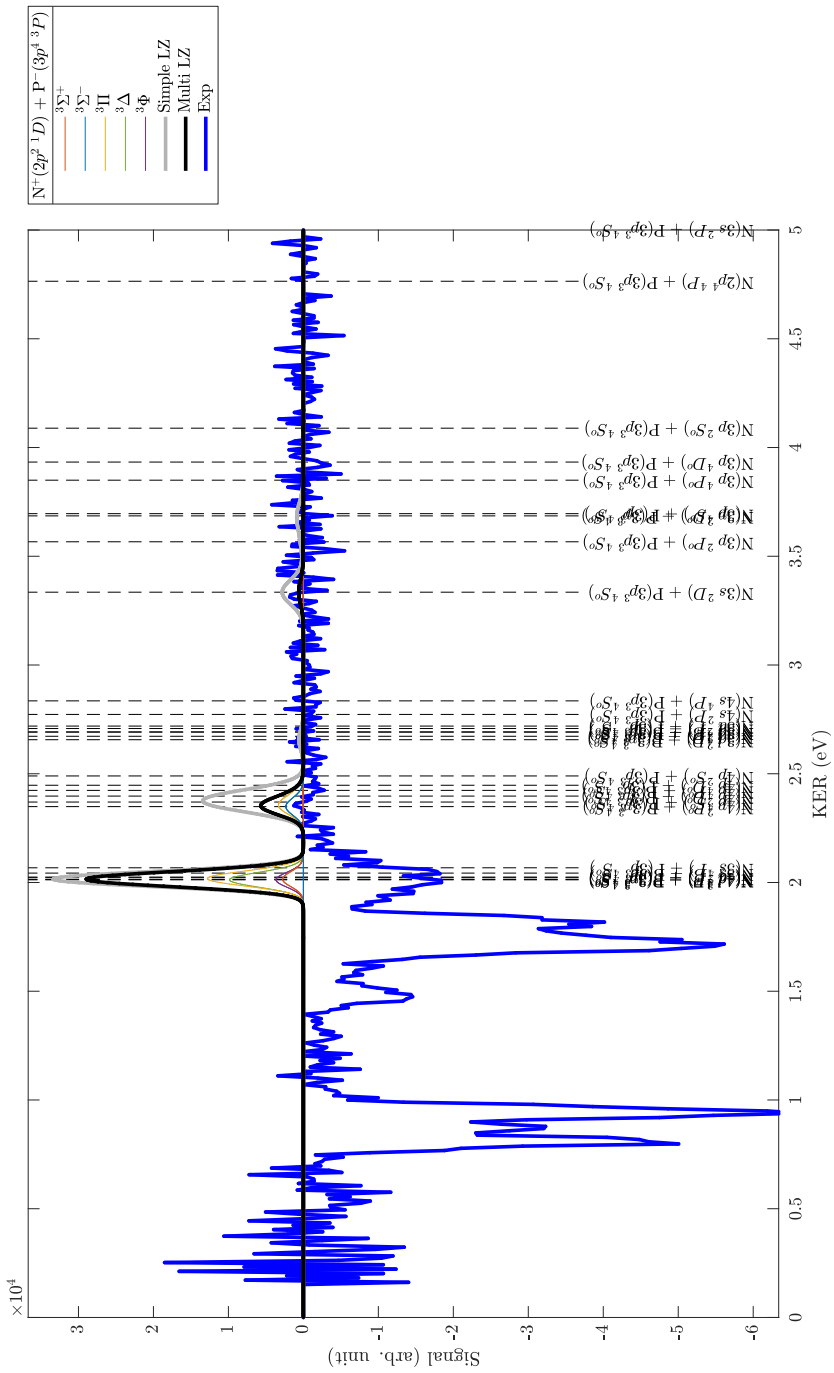

Figure F.53: Simulation: $N^+(^1D) + P^-(^3P)$.

N	P	$^3\Sigma^+$	$^3\Sigma^-$	$^3\Pi$	$^3\Delta$	$^3\Phi$
$2p^3\ ^2D^o$	$3p^3\ ^4S^o$	2.905e-09		1.308e-09	9.471e-10	
$2p^3\ ^2P^o$	$3p^3\ ^4S^o$		2.318e-02	2.521e-02		
$3p\ ^2D^o$	$3p^3\ ^4S^o$	1.086e-02		5.310e-03	1.245e-02	
$3p\ ^2P^o$	$3p^3\ ^4S^o$		5.584e-03	6.549e-03		
$3s\ ^2D$	$3p^3\ ^4S^o$		1.439e-03	4.883e-03	1.411e-02	
$3d\ ^2P$	$3p^3\ ^4S^o$	2.397e-10		2.165e-10		
$3d\ ^2F$	$3p^3\ ^4S^o$	4.730e-10		2.400e-10	4.144e-10	3.064e-10
$3d\ ^2D$	$3p^3\ ^4S^o$		7.104e-05	1.322e-04	1.573e-04	
$4p\ ^2D^o$	$3p^3\ ^4S^o$	3.530e-03		1.910e-03	6.221e-03	
$4p\ ^2P^o$	$3p^3\ ^4S^o$		1.881e-03	2.405e-03		
$4d\ ^2P$	$3p^3\ ^4S^o$	4.792e-04		4.769e-04		
$4d\ ^2F$	$3p^3\ ^4S^o$	9.495e-04		5.084e-04	1.114e-03	6.150e-04

Table F.58: Interaction potentials E_{ic} (a.u.): $N^+(^1D) + P^-(^3P)$.

F.5.2 Deuterium

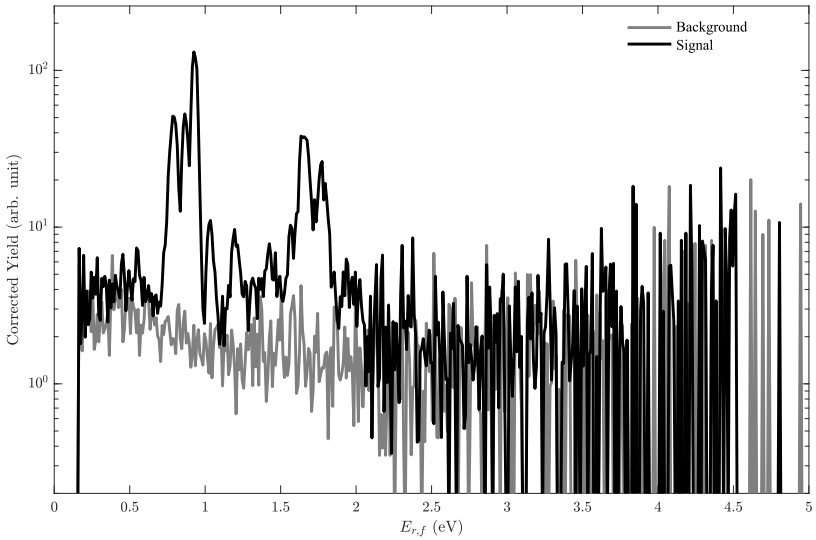

Figure F.54: Experiment: $N^+ + D^- \rightarrow N + D$.

N^+ beam	
Beam energy:	13,500 eV
Ion source:	ECR (N_2)
D^- beam	
Beam energy:	2,500 eV
Ion source:	Duoplasmatron (D_2)
Mean collision energy:	$\sim$ 16 meV

Table F.59: $N^+ + D^-$ MN experimental setup parameters.

	$D^-(^1S)$ $D(1s)$	$D(2\ell)$	$D(3\ell)$	$D(4\ell)$	$D(5\ell)$
$N(2p\ ^4S^o)$		0,007(3)	0,054(3)	0,025(1)	0,008(1)
$N(2p\ ^2D^o)$		0,024(1)			
$N(3s\ ^4P)$	0,006(3)				
$N(3s\ ^2P)$	0,002(1)				
$N(2s2p^4\ ^4P)$					
$N(3p\ ^2S^o)$	0,011(2)				
$N(3p\ ^4D^o)$	0,010(1)				
$N(3p\ ^4P^o)$	0,014(2)				
$N(3p\ ^4S^o)$	0,066(3)				
$N(3p\ ^2D^o)$	0,017(2)				
$N(3p\ ^2P^o)$	0,110(4)				
$N(3s\ ^2D)$	0,019(1)				
$N(4s\ ^4P)$	0,328(5)				
$N(4s\ ^2P)$	0,117(3)				
$N(3d\ ^{2,4}P,D,F)$	0,158*				
$N(4p\ ^2S^o)$	0,003(1)				
$N(4p\ ^4D^o)$	0,010(1)				
$N(4p\ ^4P^o)$	0,00(2)				
$N(4p\ ^2D^o)$	0,003(1)				
$N(4p\ ^4S^o)$					
$N(4p\ ^2P^o)$	0,006(1)				

Table F.60: Branching ratio fit: $N^+(^3P)$ + $D^-(^1S)$.

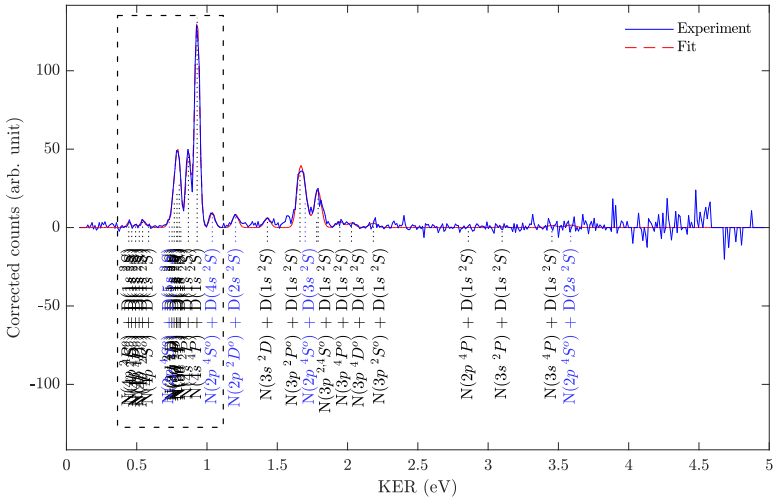

Figure F.55: Branching ratio fit: $N^+(^3P)$ + $D^-(^1S)$. The color code for the products is given in table F.1. A zoom of the framed area is given in figure F.56.

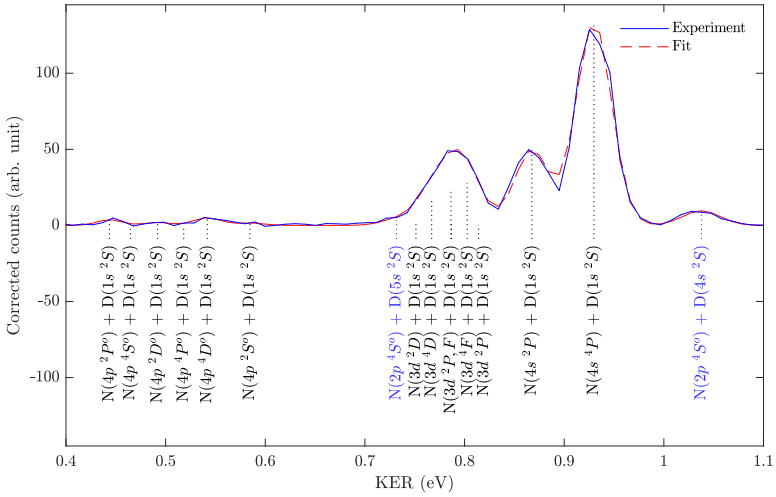

Figure F.56: Branching ratio fit: $N^+(^3P)$ + $D^-(^1S)$ – zoom. The color code for the products is given in table F.1.

Cation	Anion	Center-of-mass collision energy (eV)					
N	D	0.002	0.005	0.02	0.05	0.2	0.5
$2p^3\ ^4S^o$	$1s\ ^2S$	3.14e-35	1.27e-35	3.34e-36	1.48e-36	6.05e-37	5.78e-37
$2p^3\ ^2D^o$	$1s\ ^2S$	2.34e-20	9.47e-21	2.49e-21	1.1e-21	4.47e-22	4.21e-22
$2p^3\ ^2D^o$	$2s\ ^2S$	3.26e-25	1.31e-25	3.3e-26	1.34e-26	3.62e-27	1.64e-27
$2p^3\ ^2P^o$	$1s\ ^2S$	2.24e-20	9.06e-21	2.38e-21	1.06e-21	4.27e-22	4.02e-22
$3s\ ^4P$	$1s\ ^2S$	1.4e-19	5.64e-20	1.49e-20	6.61e-21	2.72e-21	2.64e-21
$3s\ ^2P$	$1s\ ^2S$	8.64e-16	3.48e-16	9.03e-17	3.88e-17	1.37e-17	9.94e-18
$3p\ ^2S^o$	$1s\ ^2S$	7.85e-15	3.16e-15	8.13e-16	3.44e-16	1.12e-16	7.14e-17
$3p\ ^4D^o$	$1s\ ^2S$	5.58e-14	2.25e-14	5.78e-15	2.45e-15	7.99e-16	5.06e-16
$3p\ ^4P^o$	$1s\ ^2S$	2.73e-13	1.1e-13	2.81e-14	1.17e-14	3.59e-15	2.04e-15
$3p\ ^4S^o$	$1s\ ^2S$	4.7e-13	1.89e-13	4.8e-14	1.99e-14	5.82e-15	3.05e-15
$3p\ ^2D^o$	$1s\ ^2S$	3.13e-12	1.26e-12	3.18e-13	1.31e-13	3.71e-14	1.84e-14
$3p\ ^2P^o$	$1s\ ^2S$	3.75e-12	1.5e-12	3.8e-13	1.56e-13	4.31e-14	2.05e-14
$4s\ ^4P$	$1s\ ^2S$	7.31e-12	2.93e-12	7.41e-13	3.03e-13	8.43e-14	3.99e-14
$4s\ ^2P$	$1s\ ^2S$	2.78e-12	1.11e-12	2.82e-13	1.15e-13	3.18e-14	1.49e-14
$3d\ ^2P$	$1s\ ^2S$	1.81e-13	7.24e-14	1.83e-14	7.49e-15	2.06e-15	9.63e-16
$3d\ ^4F$	$1s\ ^2S$	7.48e-13	3e-13	7.58e-14	3.1e-14	8.57e-15	4.01e-15
$3d\ ^2F$	$1s\ ^2S$	3.26e-13	1.31e-13	3.31e-14	1.35e-14	3.74e-15	1.75e-15
$3d\ ^4P$	$1s\ ^2S$	2.81e-13	1.13e-13	2.85e-14	1.17e-14	3.22e-15	1.51e-15
$3d\ ^4D$	$1s\ ^2S$	3.81e-13	1.53e-13	3.86e-14	1.58e-14	4.38e-15	2.05e-15
$3d\ ^2D$	$1s\ ^2S$	1.63e-13	6.54e-14	1.65e-14	6.77e-15	1.88e-15	8.8e-16
$4p\ ^2S^o$	$1s\ ^2S$	1.05e-14	4.21e-15	1.07e-15	4.39e-16	1.24e-16	5.91e-17
$4p\ ^4D^o$	$1s\ ^2S$	3.56e-14	1.43e-14	3.62e-15	1.49e-15	4.24e-16	2.04e-16
$4p\ ^4P^o$	$1s\ ^2S$	1.07e-14	4.29e-15	1.09e-15	4.5e-16	1.28e-16	6.2e-17
$4p\ ^2D^o$	$1s\ ^2S$	3.79e-15	1.52e-15	3.87e-16	1.6e-16	4.58e-17	2.22e-17
$4p\ ^4S^o$	$1s\ ^2S$	5.48e-16	2.2e-16	5.59e-17	2.31e-17	6.65e-18	3.25e-18
$4p\ ^2P^o$	$1s\ ^2S$	3.35e-16	1.34e-16	3.42e-17	1.42e-17	4.1e-18	2.01e-18

Table F.61: Partial cross section (cm^2) for the $N^+(^3P)$+$D^-(^1S)$ MN reaction computed with the ACAM.

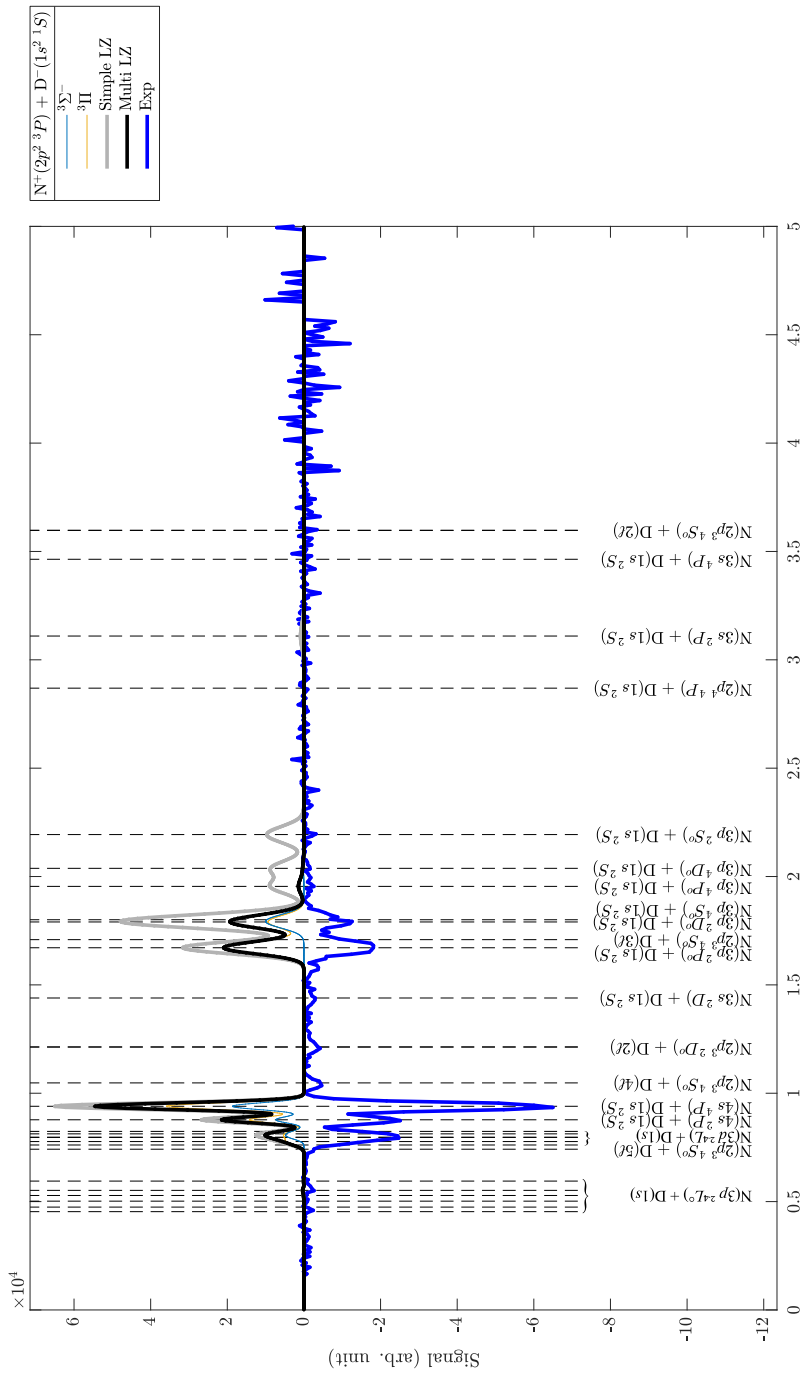

Figure F.57: Simulation: $N^+(^3P) + D^-(^1S)$.

N	D	$^3\Sigma^-$	$^3\Pi$
$2p^3\ ^4S^o$	$1s\ ^2S$	8.358e-10	
$2p^3\ ^2D^o$	$1s\ ^2S$	1.598e-02	1.384e-02
$2p^3\ ^2P^o$	$1s\ ^2S$		1.649e-02
$3s\ ^4P$	$1s\ ^2S$	1.330e-02	1.330e-02
$3s\ ^2P$	$1s\ ^2S$	7.748e-03	7.748e-03
$3p\ ^2S^o$	$1s\ ^2S$	2.285e-03	
$3p\ ^4D^o$	$1s\ ^2S$	3.898e-03	3.376e-03
$3p\ ^4P^o$	$1s\ ^2S$		3.069e-03
$3p\ ^4S^o$	$1s\ ^2S$	2.056e-03	
$3p\ ^2D^o$	$1s\ ^2S$	2.026e-03	1.755e-03
$3p\ ^2P^o$	$1s\ ^2S$		1.466e-03
$4s\ ^4P$	$1s\ ^2S$	2.853e-04	2.853e-04
$4s\ ^2P$	$1s\ ^2S$	1.396e-04	1.396e-04
$3d\ ^2P$	$1s\ ^2S$	4.212e-05	2.106e-05
$3d\ ^4F$	$1s\ ^2S$	6.753e-05	5.514e-05
$3d\ ^2F$	$1s\ ^2S$	4.251e-05	3.471e-05
$3d\ ^4P$	$1s\ ^2S$	4.931e-05	2.465e-05
$3d\ ^4D$	$1s\ ^2S$		4.749e-05
$3d\ ^2D$	$1s\ ^2S$		2.964e-05
$4p\ ^2S^o$	$1s\ ^2S$	6.552e-06	
$4p\ ^4D^o$	$1s\ ^2S$	6.660e-06	5.768e-06
$4p\ ^4P^o$	$1s\ ^2S$		3.771e-06
$4p\ ^2D^o$	$1s\ ^2S$	1.824e-06	1.580e-06
$4p\ ^4S^o$	$1s\ ^2S$	9.852e-07	
$4p\ ^2P^o$	$1s\ ^2S$		5.033e-07

Table F.62: Interaction potentials E_{ic} (a.u.): $N^+(^3P) + D^-(^1S)$.

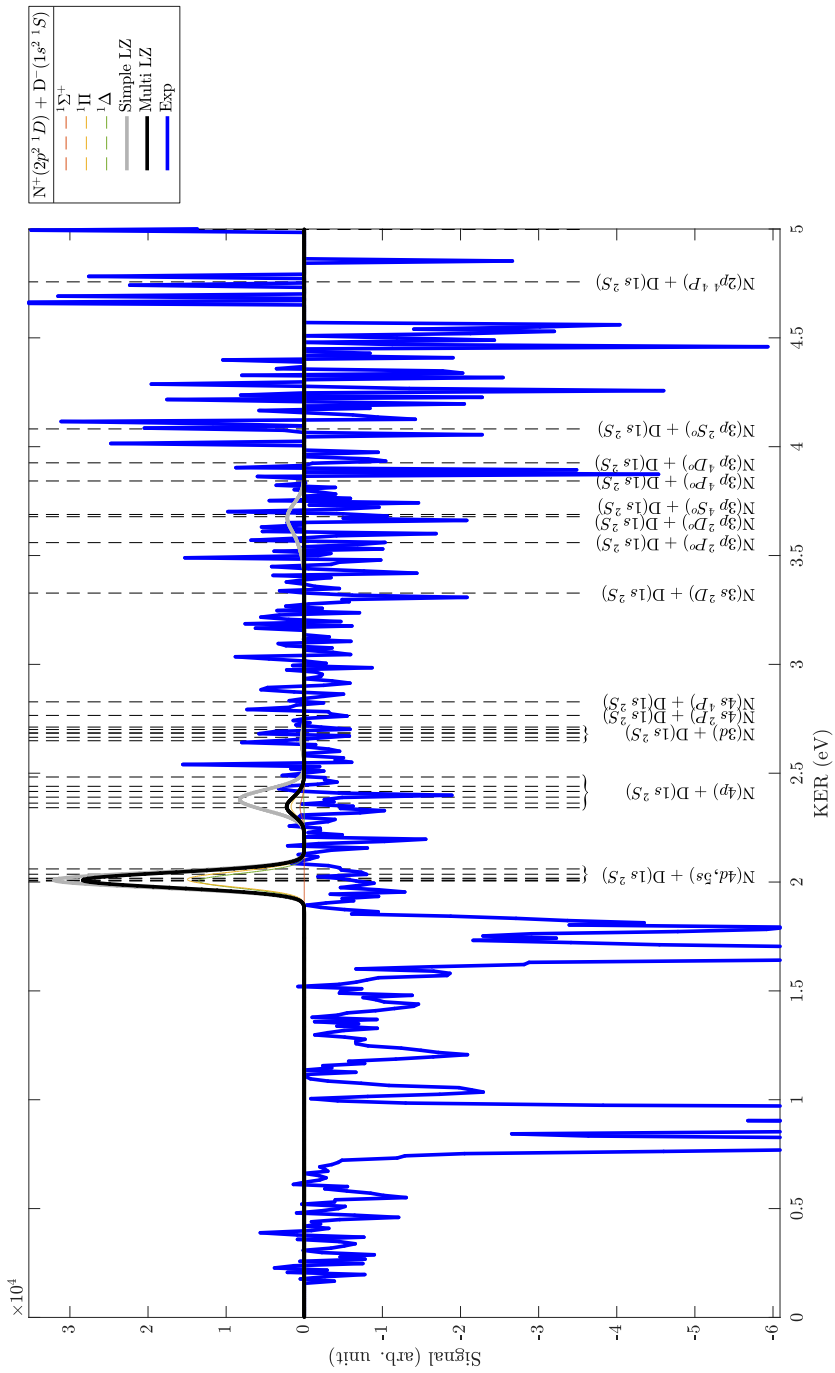

Figure F.58: Simulation: $N^+(^1D) + D^-(^1S)$.

N	D	$^1\Sigma^+$	$^1\Pi$	$^1\Delta$
$2p^3\ ^2D^o$	$1s\ ^2S$		4.973e-10	9.945e-10
$2p^3\ ^2P^o$	$1s\ ^2S$	1.231e-02	1.066e-02	
$3p\ ^2D^o$	$1s\ ^2S$		6.688e-03	1.338e-02
$3p\ ^2P^o$	$1s\ ^2S$	9.903e-03	8.576e-03	
$3s\ ^2D$	$1s\ ^2S$	1.518e-02	1.518e-02	1.518e-02
$3d\ ^2P$	$1s\ ^2S$		3.453e-10	
$3d\ ^2F$	$1s\ ^2S$		2.811e-10	4.444e-10
$3d\ ^2D$	$1s\ ^2S$	1.667e-04	8.336e-05	1.667e-04
$4p\ ^2D^o$	$1s\ ^2S$		3.324e-03	6.649e-03
$4p\ ^2P^o$	$1s\ ^2S$	4.948e-03	4.285e-03	
$4d\ ^2P$	$1s\ ^2S$		9.223e-04	
$4d\ ^2F$	$1s\ ^2S$		7.505e-04	1.187e-03

Table F.63: Interaction potentials E_{ic} (a.u.): $N^+(^1D)$ + $D^-(^1S)$.

F.5.3 Silicon

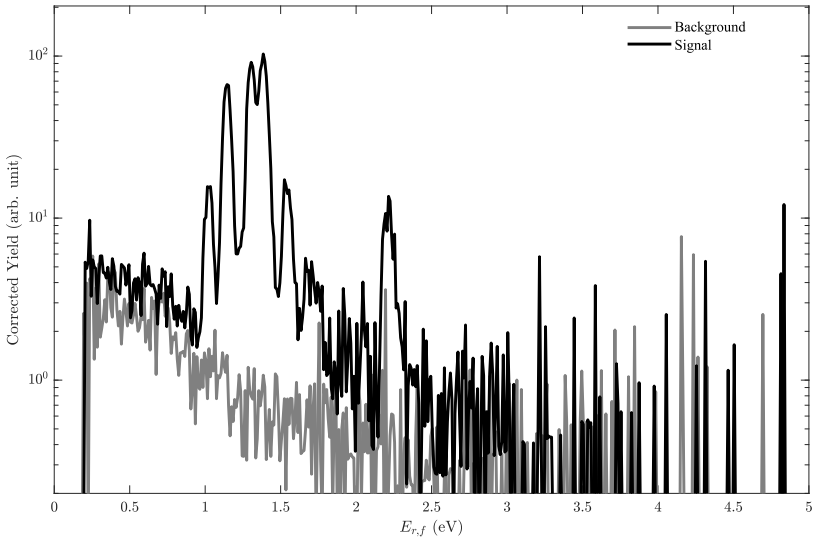

Figure F.59: Experiment: $N^+ + Si^- \rightarrow N + Si$.

N^+ beam	
Beam energy:	5,500 eV
Ion source:	ECR (N_2)
Si^- beam	
Beam energy:	11,500 eV
Ion source:	Sputtering (silicon wafer)
Mean collision energy:	$\sim$ 5 meV

Table F.64: $N^+ + Si^-$ MN experimental setup parameters.

	$Si^{-}(^4S^o)$ $Si(^3P)$
$N(3s\ ^4P)$	0,002(1)
$N(3s\ ^2P)$	0,004(1)
$N(2s2p^4\ ^4P)$	0,044(3)
$N(3p\ ^2S^o)$	0,054(2)
$N(3p\ ^4D^o)$	0,253(4)
$N(3p\ ^4P^o)$	0,266(4)
$N(3p\ ^4S^o)$	0,085(3)
$N(3p\ ^2D^o)$	0,115(2)
$N(3p\ ^2P^o)$	0,042(2)
$N(4s\ ^4P)$	0,003(1)
$N(4s\ ^2P)$	0,006(2)

Table F.65: Branching ratio fit: $N^{+}(^3P)$ + $Si^{-}(^4S^o)$.

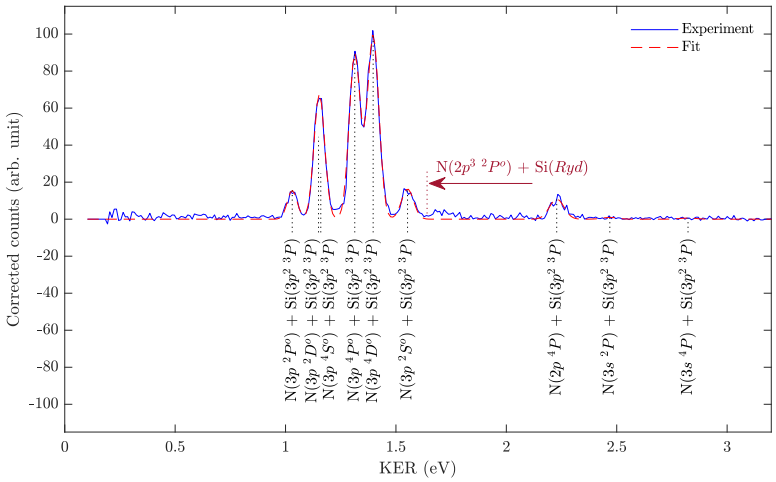

Figure F.60: Branching ratio fit: $N^+(^3P)$ + $Si^-(^4S^o)$ – explaining the low signal with Rydberg series.

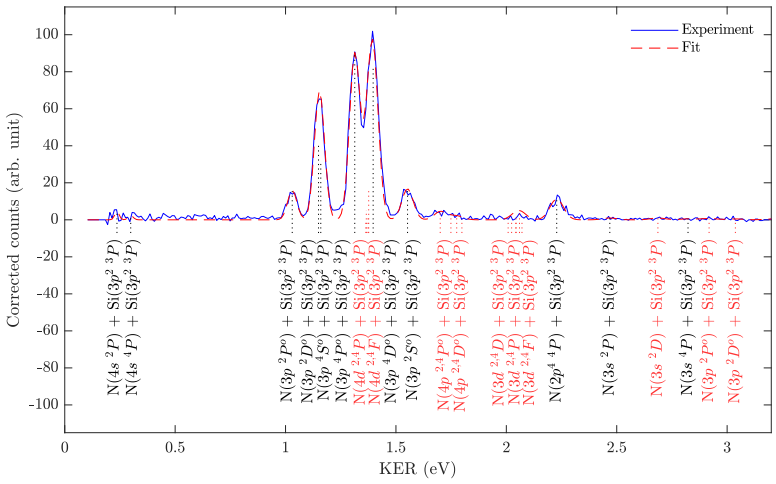

Figure F.61: Branching ratio fit: $N^+(^3P)$ + $Si^-(^4S^o)$ – explaining the low signal with N^+ excited states (which is not perfectly working). The color code for the products is given in table F.1.

Cation N	Anion Si	Center-of-mass collision energy (eV) 0.002	0.005	0.02	0.05	0.2	0.5
$2p^3\ ^4S^o$	$3p^2\ ^3P$	2.63e-27	1.05e-27	2.66e-28	1.09e-28	2.99e-29	1.42e-29
$2p^3\ ^2D^o$	$3p^2\ ^3P$	4.54e-68	1.86e-68	5.16e-69	2.55e-69	1.83e-69	6.72e-69
$2p^3\ ^2P^o$	$3p^2\ ^3P$	1.99e-53	8.27e-54	2.52e-54	1.5e-54	2.63e-54	3.76e-53
$3s\ ^4P$	$3p^2\ ^3P$	1.33e-13	5.34e-14	1.36e-14	5.6e-15	1.63e-15	8.48e-16
$3s\ ^2P$	$3p^2\ ^3P$	1.02e-13	4.11e-14	1.04e-14	4.32e-15	1.27e-15	6.68e-16
$3p\ ^2S^o$	$3p^2\ ^3P$	1.02e-12	4.09e-13	1.04e-13	4.26e-14	1.21e-14	6.07e-15
$3p\ ^4D^o$	$3p^2\ ^3P$	2.28e-12	9.16e-13	2.32e-13	9.51e-14	2.66e-14	1.29e-14
$3p\ ^4P^o$	$3p^2\ ^3P$	5.21e-12	2.09e-12	5.3e-13	2.18e-13	6.18e-14	3.06e-14
$3p\ ^4S^o$	$3p^2\ ^3P$	2.49e-12	9.97e-13	2.52e-13	1.03e-13	2.82e-14	1.32e-14
$3p\ ^2D^o$	$3p^2\ ^3P$	8.11e-13	3.25e-13	8.2e-14	3.34e-14	9.05e-15	4.14e-15
$3p\ ^2P^o$	$3p^2\ ^3P$	1.67e-12	6.69e-13	1.69e-13	6.89e-14	1.89e-14	8.78e-15
$4s\ ^4P$	$3p^2\ ^3P$	8.41e-26	3.38e-26	8.67e-27	3.64e-27	1.09e-27	5.49e-28

Table F.66: Partial cross section (cm^2) for the $N^+(^3P)$+$Si^-(^4S^o)$ MN reaction computed with the ACAM.

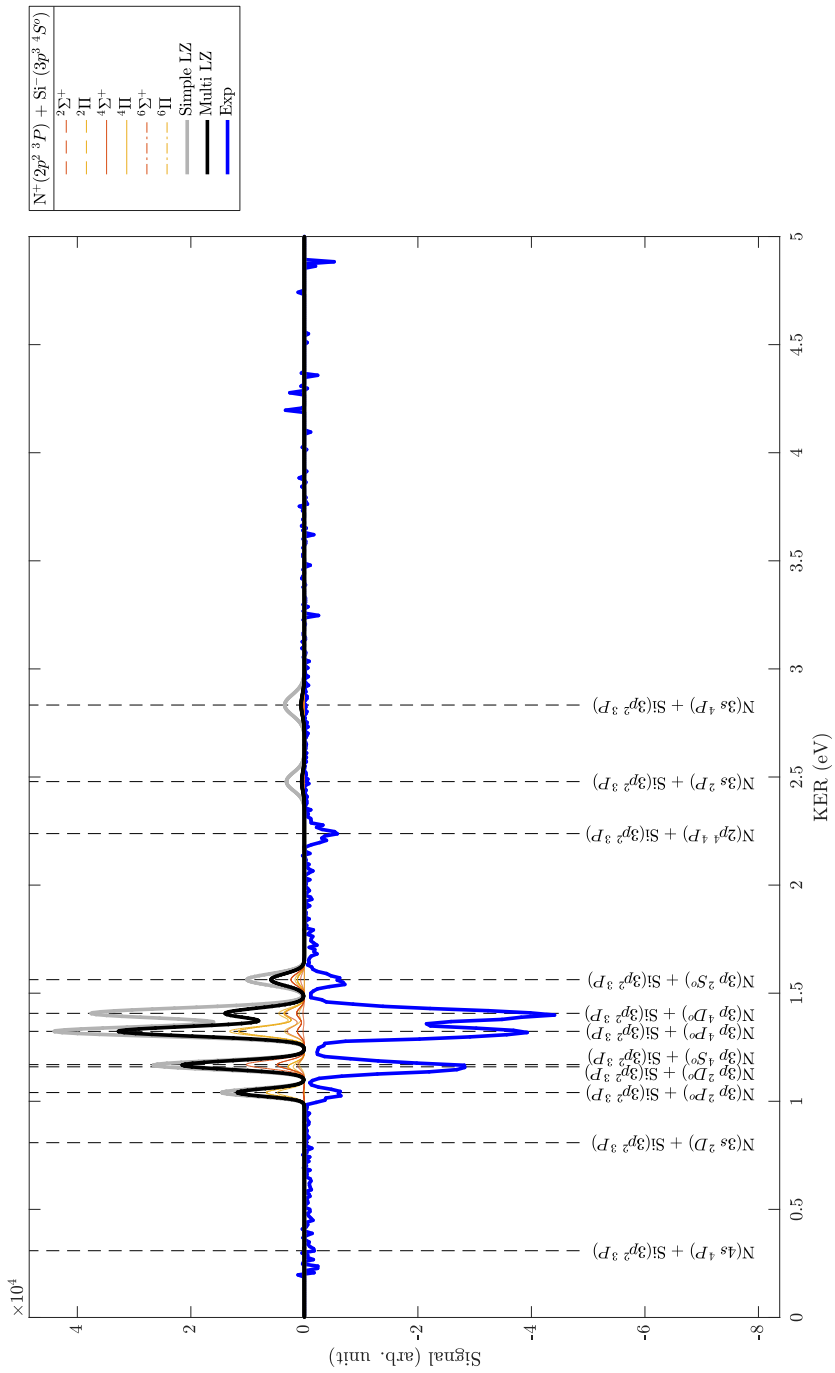

Figure F.62: Simulation: $N^+(^3P) + Si^-(^4S^o)$.

N	Si	$^2\Sigma^+$	$^2\Pi$	$^4\Sigma^+$	$^4\Pi$	$^6\Sigma^+$	$^6\Pi$
$2p^3\,^4S^o$	$3p^2\,^3P$	9.426e-10	1.428e-09	1.885e-09	2.856e-09	2.828e-09	4.285e-09
$2p^3\,^2D^o$	$3p^2\,^3P$	9.207e-02	1.012e-01	7.279e-02	8.000e-02		
$2p^3\,^2P^o$	$3p^2\,^3P$	1.338e-01	7.069e-02	1.058e-01	5.589e-02		
$3s\,^4P$	$3p^2\,^3P$	1.236e-03	7.310e-03	2.472e-03	1.462e-02	3.709e-03	2.193e-02
$3s\,^2P$	$3p^2\,^3P$	2.416e-03	1.429e-02	1.910e-03	1.129e-02		
$3p\,^2S^o$	$3p^2\,^3P$	1.603e-03	2.867e-04	1.267e-03	2.266e-04		
$3p\,^4D^o$	$3p^2\,^3P$	9.718e-05	1.711e-04	1.944e-04	3.422e-04	2.915e-04	5.132e-04
$3p\,^4P^o$	$3p^2\,^3P$	8.102e-05	3.122e-04	1.620e-04	6.243e-04	2.431e-04	9.365e-04
$3p\,^4S^o$	$3p^2\,^3P$	1.267e-04	1.693e-05	2.534e-04	3.385e-05	3.802e-04	5.078e-05
$3p\,^2D^o$	$3p^2\,^3P$	8.280e-05	1.594e-04	6.546e-05	1.260e-04		
$3p\,^2P^o$	$3p^2\,^3P$	4.184e-05	2.055e-04	3.308e-05	1.625e-04		
$4s\,^4P$	$3p^2\,^3P$	1.758e-13	1.039e-12	3.516e-13	2.079e-12	5.273e-13	3.118e-12

Table F.67: Interaction potentials E_{ic} (a.u.): $N^+(^3P) + Si^-(^4S^o)$.

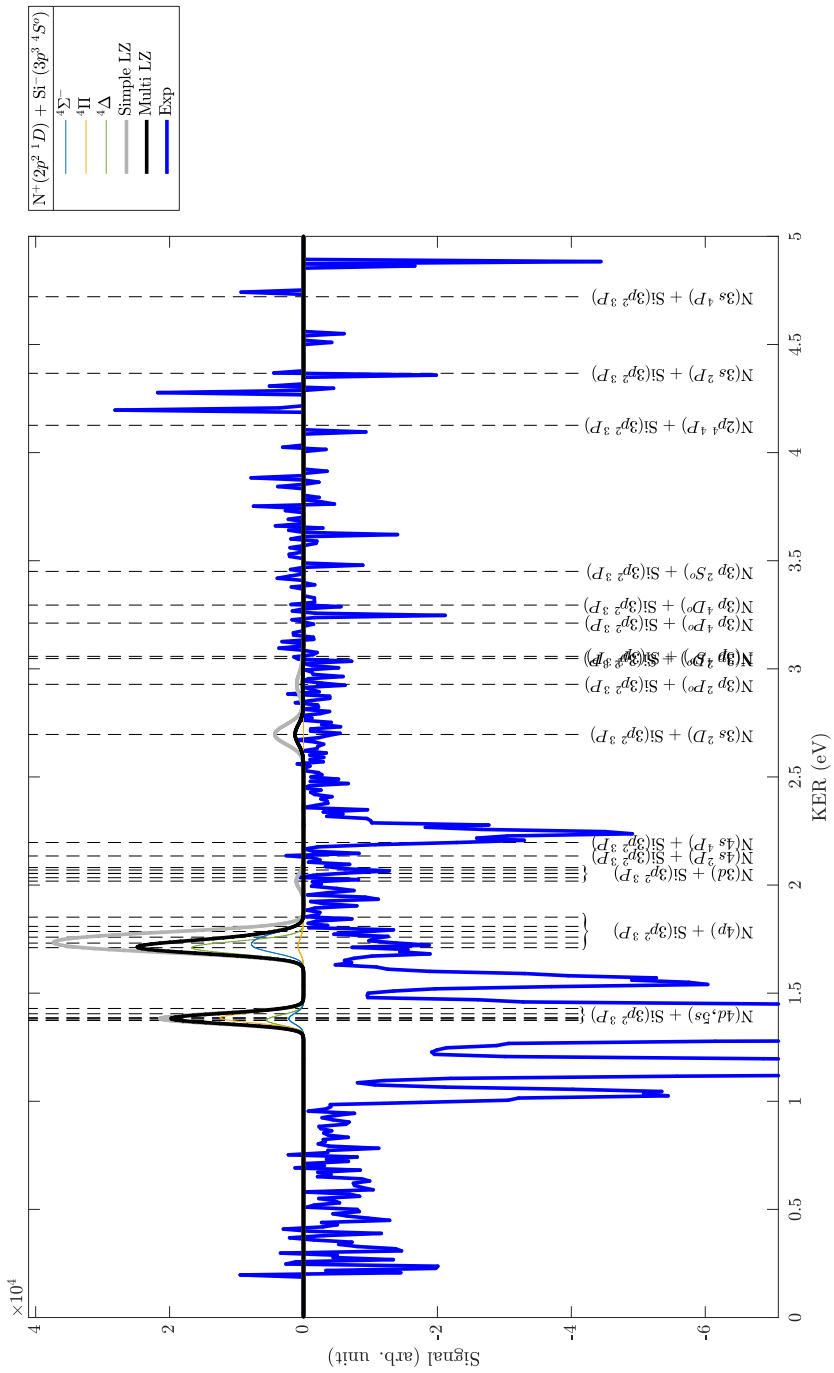

Figure F.63: Simulation: $N^+(^1D) + Si^-(^4S^o)$.

N	Si	$^4\Sigma^-$	$^4\Pi$	$^4\Delta$
$2p^3\ ^2D^o$	$3p^2\ ^3P$	5.959e-09	2.704e-09	2.736e-09
$2p^3\ ^2P^o$	$3p^2\ ^3P$	2.731e-02	2.888e-02	5.395e-02
$3p\ ^2D^o$	$3p^2\ ^3P$	1.022e-02	5.656e-03	1.928e-02
$3p\ ^2P^o$	$3p^2\ ^3P$	3.669e-03	1.200e-02	5.703e-03
$3s\ ^2D$	$3p^2\ ^3P$	1.932e-03	6.557e-03	1.894e-02
$3d\ ^2P$	$3p^2\ ^3P$	2.066e-10	2.916e-10	9.835e-11
$3d\ ^2F$	$3p^2\ ^3P$	1.630e-10	5.770e-11	2.062e-10
$3d\ ^2D$	$3p^2\ ^3P$	3.507e-05	6.472e-05	1.312e-04
$4p\ ^2D^o$	$3p^2\ ^3P$	1.178e-03	8.500e-04	3.857e-03
$4p\ ^2P^o$	$3p^2\ ^3P$	5.615e-04	2.353e-03	6.518e-04
$4d\ ^2P$	$3p^2\ ^3P$	1.279e-04	2.714e-04	6.085e-05
$4d\ ^2F$	$3p^2\ ^3P$	1.007e-04	5.143e-05	1.671e-04

Table F.68: Interaction potentials E_{ic} (a.u.): $N^+(^1D)$ + $Si^-(^4S^o)$.

F.5.4 Carbon

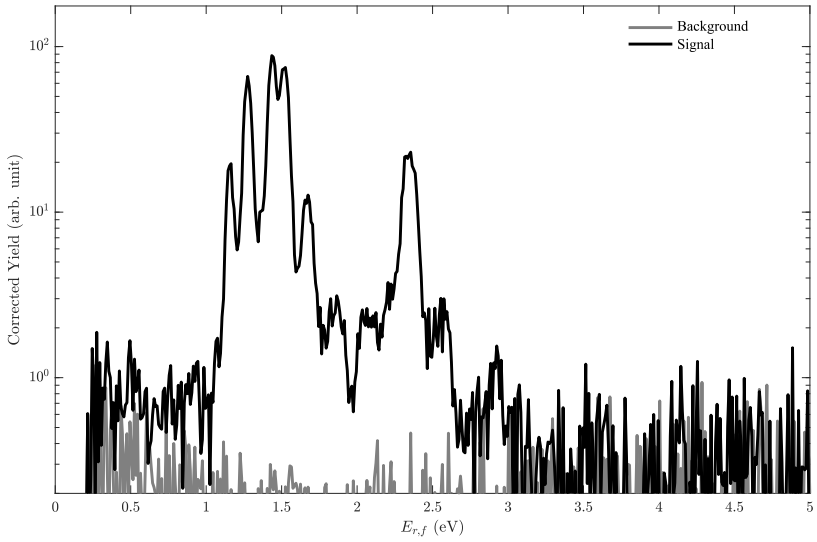

Figure F.64: Experiment: $N^+ + C^- \rightarrow N + C$.

N^+ beam	
Beam energy:	7,900 eV
Ion source:	ECR (N_2)
C^- beam	
Beam energy:	7,700 eV
Ion source:	Sputtering (graphite)
Mean collision energy:	$\sim$ 12 meV

Table F.69: $N^+ + C^-$ MN experimental setup parameters.

	$C^-(^4S^o)$ $C(^3P)$
$N(3s\ ^4P)$	0,006(1)
$N(3s\ ^2P)$	0,012(1)
$N(2s2p^4\ ^4P)$	0,112(2)
$N(3p\ ^2S^o)$	0,050(1)
$N(3p\ ^4D^o)$	0,264(3)
$N(3p\ ^4P^o)$	0,290(3)
$N(3p\ ^4S^o)$	0,015(1)
$N(3p\ ^2D^o)$	0,189(3)
$N(3p\ ^2P^o)$	0,059(2)

Table F.70: Branching ratio fit: $N^+(^3P)$ + $C^-(^4S^o)$.

Cation	Anion	Center-of-mass collision energy (eV)					
N	C	0.002	0.005	0.02	0.05	0.2	0.5
$2p^3\ ^4S^o$	$2p^2\ ^3P$	2.87e-27	1.15e-27	2.9e-28	1.18e-28	3.15e-29	1.42e-29
$2p^3\ ^2D^o$	$2p^2\ ^3P$	2.82e-38	1.14e-38	3e-39	1.33e-39	5.48e-40	5.75e-40
$2p^3\ ^2P^o$	$2p^2\ ^3P$	4.01e-32	1.62e-32	4.26e-33	1.89e-33	8.09e-34	1.06e-33
$3s\ ^4P$	$2p^2\ ^3P$	3.44e-13	1.38e-13	3.49e-14	1.43e-14	4.02e-15	1.97e-15
$3s\ ^2P$	$2p^2\ ^3P$	1.31e-13	5.27e-14	1.34e-14	5.51e-15	1.58e-15	8.07e-16
$3p\ ^2S^o$	$2p^2\ ^3P$	8.69e-13	3.49e-13	8.84e-14	3.64e-14	1.04e-14	5.18e-15
$3p\ ^4D^o$	$2p^2\ ^3P$	1.82e-12	7.3e-13	1.85e-13	7.58e-14	2.13e-14	1.04e-14
$3p\ ^4P^o$	$2p^2\ ^3P$	4.23e-12	1.7e-12	4.3e-13	1.77e-13	5.02e-14	2.49e-14
$3p\ ^4S^o$	$2p^2\ ^3P$	2.62e-12	1.05e-12	2.65e-13	1.08e-13	2.98e-14	1.4e-14
$3p\ ^2D^o$	$2p^2\ ^3P$	1.03e-12	4.11e-13	1.04e-13	4.23e-14	1.15e-14	5.29e-15
$3p\ ^2P^o$	$2p^2\ ^3P$	2.45e-12	9.82e-13	2.48e-13	1.01e-13	2.79e-14	1.3e-14
$4s\ ^4P$	$2p^2\ ^3P$	3.21e-19	1.29e-19	3.28e-20	1.36e-20	3.92e-21	1.92e-21
$4s\ ^2P$	$2p^2\ ^3P$	5.89e-22	2.37e-22	6.05e-23	2.52e-23	7.45e-24	3.73e-24
$3d\ ^2P$	$2p^2\ ^3P$	3.12e-26	1.25e-26	3.22e-27	1.36e-27	3.98e-28	2e-28
$3d\ ^4F$	$2p^2\ ^3P$	6.13e-28	2.45e-28	6.17e-29	2.44e-29	6.03e-30	2.4e-30
$3d\ ^4P$	$2p^2\ ^3P$	3.49e-29	1.41e-29	3.53e-30	1.42e-30	3.68e-31	1.29e-31

Table F.71: Partial cross section (cm^2) for the $N^+(^3P)$+$C^-(^4S^o)$ MN reaction computed with the ACAM.

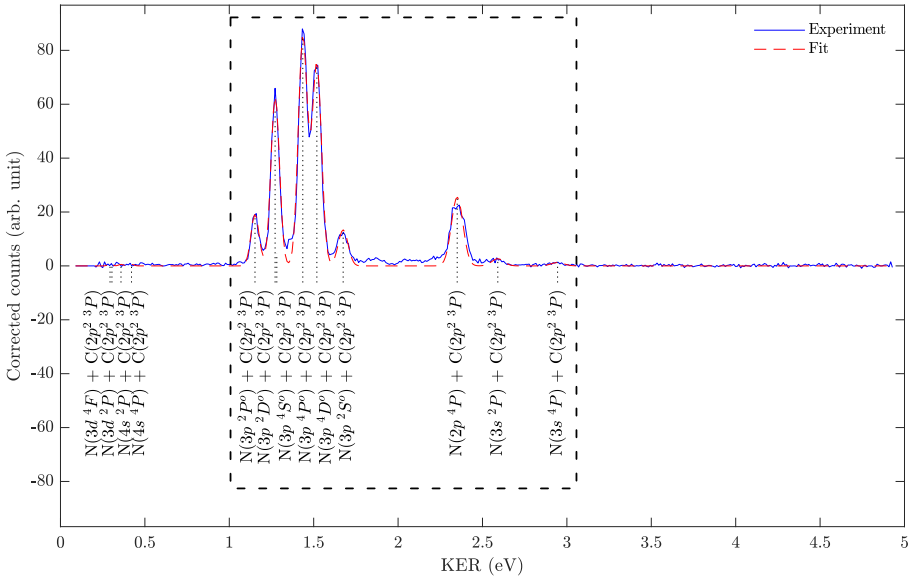

Figure F.65: Branching ratio fit: $N^+(^3P) + C^-(^4S^o)$. The color code for the products is given in table F.1. A zoom of the framed area is given in figure F.66.

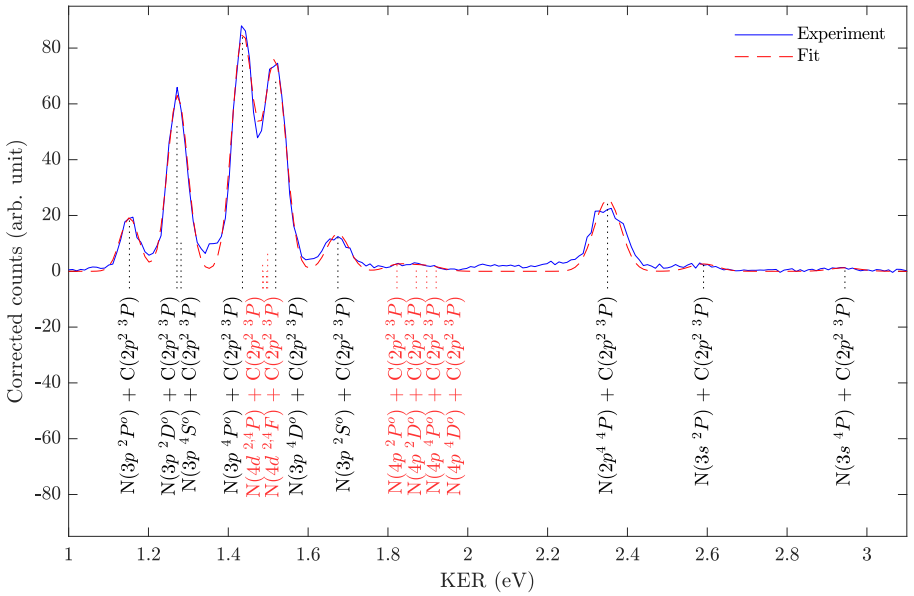

Figure F.66: Branching ratio fit: $N^+(^3P) + C^-(^4S^o)$ – zoom. The color code for the products is given in table F.1.

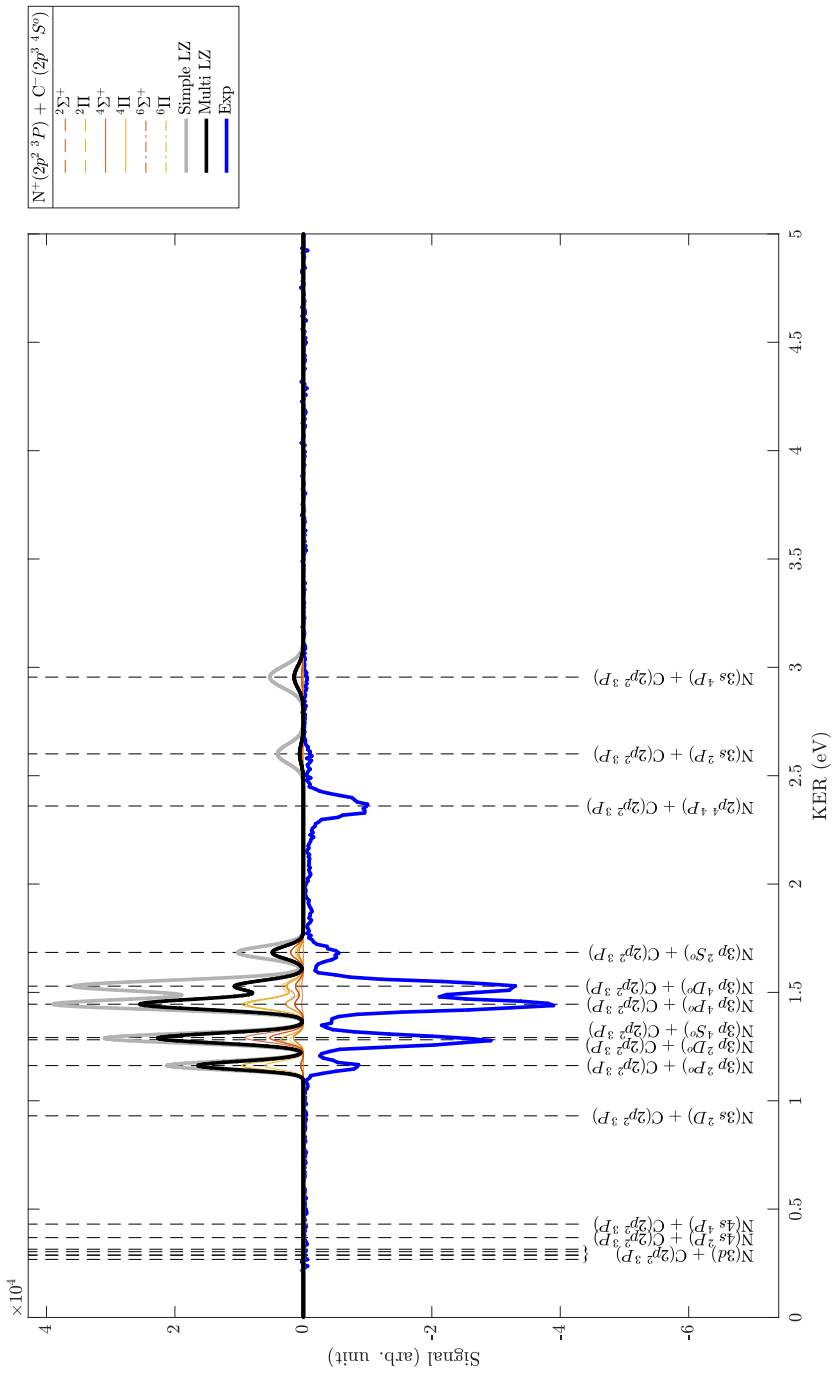

Figure F.67: Simulation: $N^+(^3P) + C^-(^4S^o)$.

N	C	$^2\Sigma^+$	$^2\Pi$	$^4\Sigma^+$	$^4\Pi$	$^6\Sigma^+$	$^6\Pi$
$2p^3\ ^4S^o$	$2p^2\ ^3P$	6.516e-10	1.044e-09	1.303e-09	2.087e-09	1.955e-09	3.131e-09
$2p^3\ ^2D^o$	$2p^2\ ^3P$	6.780e-02	7.438e-02	5.360e-02	5.880e-02		
$2p^3\ ^2P^o$	$2p^2\ ^3P$	9.915e-02	4.939e-02	7.839e-02	3.905e-02		
$3s\ ^4P$	$2p^2\ ^3P$	1.011e-03	5.981e-03	2.023e-03	1.196e-02	3.034e-03	1.794e-02
$3s\ ^2P$	$2p^2\ ^3P$	2.068e-03	1.223e-02	1.635e-03	9.670e-03		
$3p\ ^2S^o$	$2p^2\ ^3P$	1.802e-03	3.640e-04	1.425e-03	2.877e-04		
$3p\ ^4D^o$	$2p^2\ ^3P$	1.333e-04	2.211e-04	2.667e-04	4.423e-04	4.000e-04	6.634e-04
$3p\ ^4P^o$	$2p^2\ ^3P$	1.232e-04	4.149e-04	2.464e-04	8.297e-04	3.697e-04	1.245e-03
$3p\ ^4S^o$	$2p^2\ ^3P$	1.979e-04	3.059e-05	3.957e-04	6.118e-05	5.936e-04	9.176e-05
$3p\ ^2D^o$	$2p^2\ ^3P$	1.450e-04	2.610e-04	1.146e-04	2.063e-04		
$3p\ ^2P^o$	$2p^2\ ^3P$	9.251e-05	3.880e-04	7.313e-05	3.067e-04		
$4s\ ^4P$	$2p^2\ ^3P$	6.852e-10	4.052e-09	1.370e-09	8.105e-09	2.056e-09	1.216e-08
$4s\ ^2P$	$2p^2\ ^3P$	8.960e-11	5.299e-10	7.083e-11	4.189e-10		
$3d\ ^2P$	$2p^2\ ^3P$	1.033e-12	2.839e-12	8.164e-13	2.244e-12		
$3d\ ^4F$	$2p^2\ ^3P$	9.525e-14	1.894e-13	1.905e-13	3.788e-13	2.858e-13	5.682e-13

Table F.72: Interaction potentials E_{ic} (a.u.): $N^+(^3P)$ + $C^-(^4S^o)$.

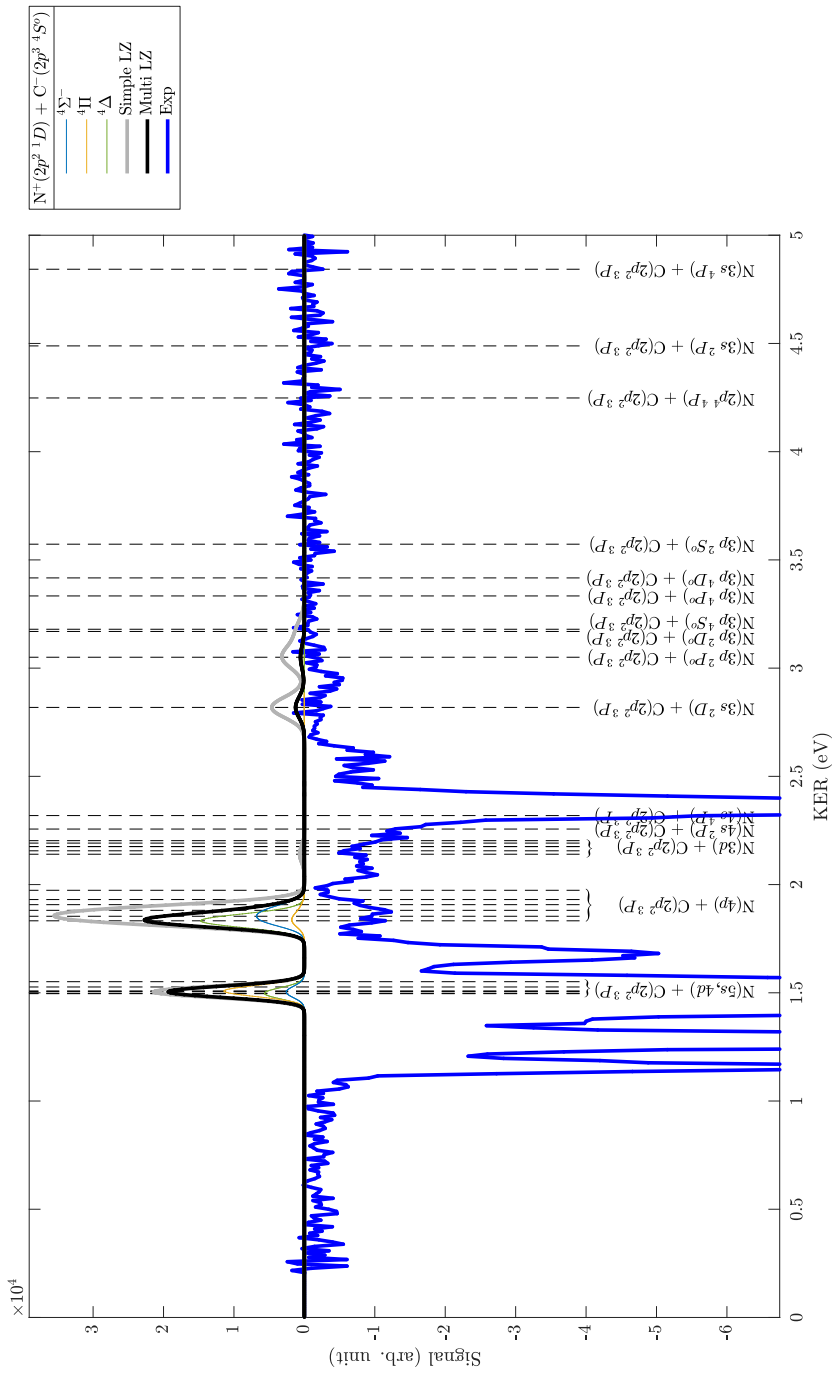

Figure F.68: Simulation: $N^+(^1D) + C^-(^4S^o)$.

N	C	$^4\Sigma^-$	$^4\Pi$	$^4\Delta$
$2p^3\ ^2D^o$	$2p^2\ ^3P$	4.360e-09	1.976e-09	1.897e-09
$2p^3\ ^2P^o$	$2p^2\ ^3P$	2.001e-02	2.005e-02	3.963e-02
$3p\ ^2D^o$	$2p^2\ ^3P$	8.921e-03	4.800e-03	1.545e-02
$3p\ ^2P^o$	$2p^2\ ^3P$	3.135e-03	9.718e-03	5.040e-03
$3s\ ^2D$	$2p^2\ ^3P$	1.605e-03	5.448e-03	1.574e-02
$3d\ ^2P$	$2p^2\ ^3P$	2.122e-10	2.699e-10	1.010e-10
$3d\ ^2F$	$2p^2\ ^3P$	1.687e-10	5.459e-11	2.014e-10
$3d\ ^2D$	$2p^2\ ^3P$	3.616e-05	6.687e-05	1.236e-04
$4p\ ^2D^o$	$2p^2\ ^3P$	1.353e-03	9.129e-04	3.953e-03
$4p\ ^2P^o$	$2p^2\ ^3P$	6.118e-04	2.461e-03	7.650e-04
$4d\ ^2P$	$2p^2\ ^3P$	1.839e-04	3.423e-04	8.751e-05
$4d\ ^2F$	$2p^2\ ^3P$	1.463e-04	6.613e-05	2.206e-04

Table F.73: Interaction potentials E_{ic} (a.u.): $N^+(^1D) + C^-(^4S^o)$.

F.5.5 Oxygen

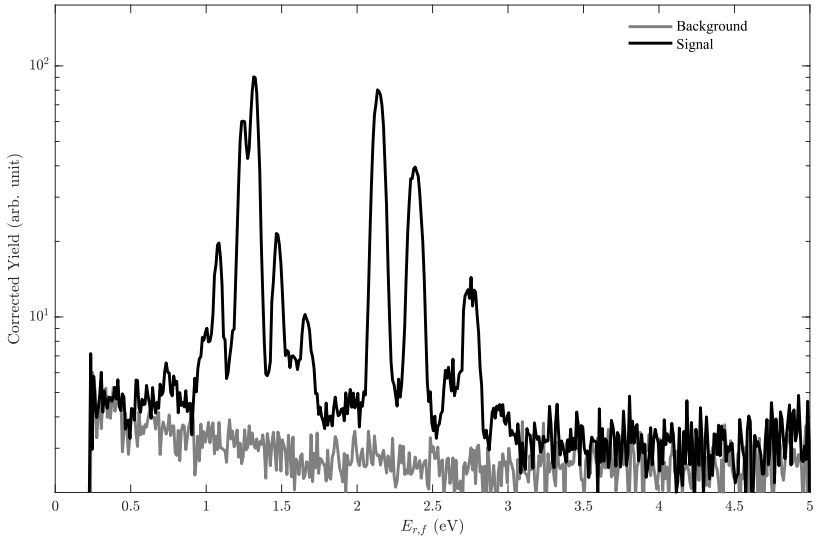

Figure F.69: Experiment: $N^+ + O^- \rightarrow N + O$.

N^+ beam	
Beam energy:	7,900 eV
Ion source:	ECR (N_2)
O^- beam	
Beam energy:	7,700 eV
Ion source:	Sputtering (Fe_2O_3)
Mean collision energy:	$\sim$ 7 meV

Table F.74: $N^+ + O^-$ MN experimental setup parameters.

	O^- – simple $O(^3P)$	$O^-(^2P^o)$ – all $O(^3P)$	$O(^1D)$
$N(3s\ ^4P)$	0,042(1)	0,041(1)	0,005(1)
$N(3s\ ^2P)$	0,142(2)	0,138(2)	0,001(1)
$N(2s2p^4\ ^4P)$	0,268(2)	0,262(2)	
$N(3p\ ^2S^o)$	0,051(1)	0,050(1)	
$N(3p\ ^4D^o)$	0,218(2)	0,210(2)	
$N(3p\ ^4P^o)$	0,140(1)	0,001(17)	
$N(3p\ ^4S^o)$	0,016(1)	0,020(1)	
$N(3p\ ^2D^o)$	0,025(1)	0,019(1)	
$N(3p\ ^2P^o)$	0,011(1)	0,006(1)	
$N(3s\ ^2D)$	0,002(2)	0,002(2)	

Table F.75: Branching ratio fit: $N^+(^3P)$ + $O^-(^2P^o)$. "O^- – simple" takes only "$O(^3P)$" into account. "$O^-(^2P^o)$ – all" takes all the O^0 into account. Both fits take $N^+(^2D^o)$ and $N^+(^2P^o)$ into account but not included in the table.

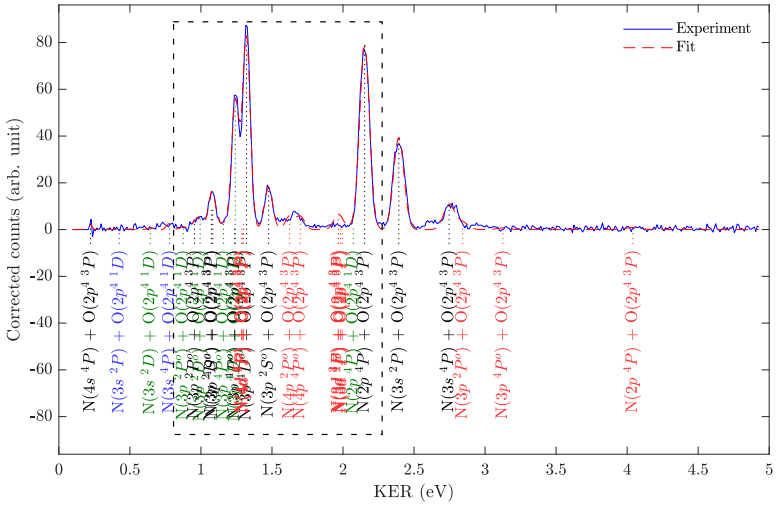

Figure F.70: Branching ratio fit: $N^+(^3P) + O^-(^2P^o)$. The color code for the products is given in table F.1. A zoom of the framed area is given in figure F.71.

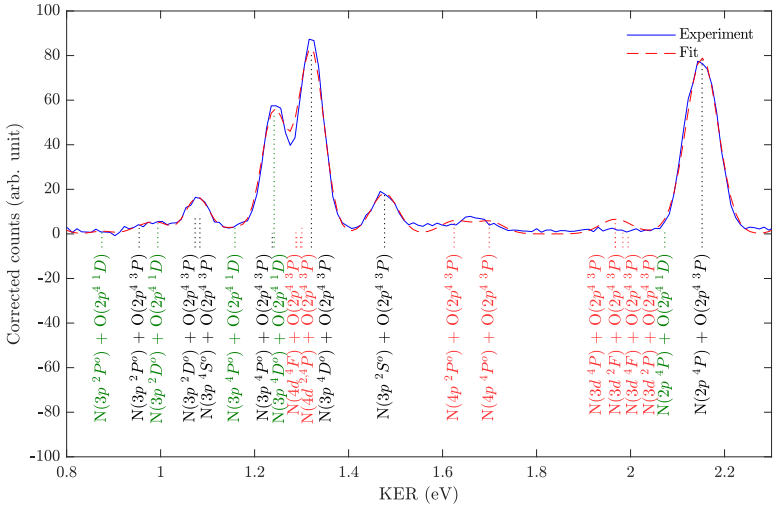

Figure F.71: Branching ratio fit: $N^+(^3P) + O^-(^2P^o)$ – zoom. The color code for the products is given in table F.1.

Cation	Anion	Center-of-mass collision energy (eV)					
N	O	0.002	0.005	0.02	0.05	0.2	0.5
$2p^3\ ^4S^o$	$2p^4\ ^3P$	1.64e-27	6.55e-28	1.64e-28	6.6e-29	1.68e-29	7.01e-30
$2p^3\ ^4S^o$	$2p^4\ ^1D$	7.98e-29	3.19e-29	8e-30	3.22e-30	8.23e-31	3.45e-31
$2p^3\ ^4S^o$	$2p^4\ ^1S$	3.59e-34	1.45e-34	3.77e-35	1.63e-35	5.96e-36	4.63e-36
$2p^3\ ^2D^o$	$2p^4\ ^3P$	3.15e-13	1.26e-13	3.16e-14	1.27e-14	3.25e-15	1.36e-15
$2p^3\ ^2D^o$	$2p^4\ ^1D$	7.84e-14	3.14e-14	7.86e-15	3.16e-15	8.09e-16	3.38e-16
$2p^3\ ^2D^o$	$2p^4\ ^1S$	7.33e-14	2.93e-14	7.35e-15	2.95e-15	7.49e-16	3.09e-16
$2p^3\ ^2P^o$	$2p^4\ ^3P$	1.14e-14	4.58e-15	1.16e-15	4.73e-16	1.31e-16	6.31e-17
$2p^3\ ^2P^o$	$2p^4\ ^1D$	1.94e-13	7.78e-14	1.95e-14	7.84e-15	2.01e-15	8.43e-16
$2p^3\ ^2P^o$	$2p^4\ ^1S$	9.22e-14	3.69e-14	9.24e-15	3.71e-15	9.45e-16	3.92e-16
$3s\ ^4P$	$2p^4\ ^3P$	1.03e-13	4.12e-14	1.05e-14	4.3e-15	1.24e-15	6.38e-16
$3s\ ^4P$	$2p^4\ ^1D$	5.08e-20	2.04e-20	5.14e-21	2.1e-21	5.73e-22	2.64e-22
$3s\ ^2P$	$2p^4\ ^3P$	1.49e-12	5.97e-13	1.51e-13	6.12e-14	1.66e-14	7.64e-15
$3p\ ^2S^o$	$2p^4\ ^3P$	2.93e-14	1.17e-14	2.95e-15	1.19e-15	3.16e-16	1.39e-16
$3p\ ^4D^o$	$2p^4\ ^3P$	1.85e-12	7.43e-13	1.87e-13	7.62e-14	2.05e-14	9.33e-15
$3p\ ^4P^o$	$2p^4\ ^3P$	1.39e-12	5.58e-13	1.41e-13	5.72e-14	1.54e-14	6.99e-15
$3p\ ^4S^o$	$2p^4\ ^3P$	2.92e-15	1.17e-15	2.95e-16	1.2e-16	3.2e-17	1.43e-17
$3p\ ^2D^o$	$2p^4\ ^3P$	2.26e-13	9.07e-14	2.29e-14	9.29e-15	2.5e-15	1.13e-15
$3p\ ^2P^o$	$2p^4\ ^3P$	7.36e-14	2.95e-14	7.44e-15	3.03e-15	8.19e-16	3.73e-16

Table F.76: Partial cross section (cm^2) for the $N^+(^3P)$+$O^-(^2P^o)$ MN reaction computed with the ACAM.

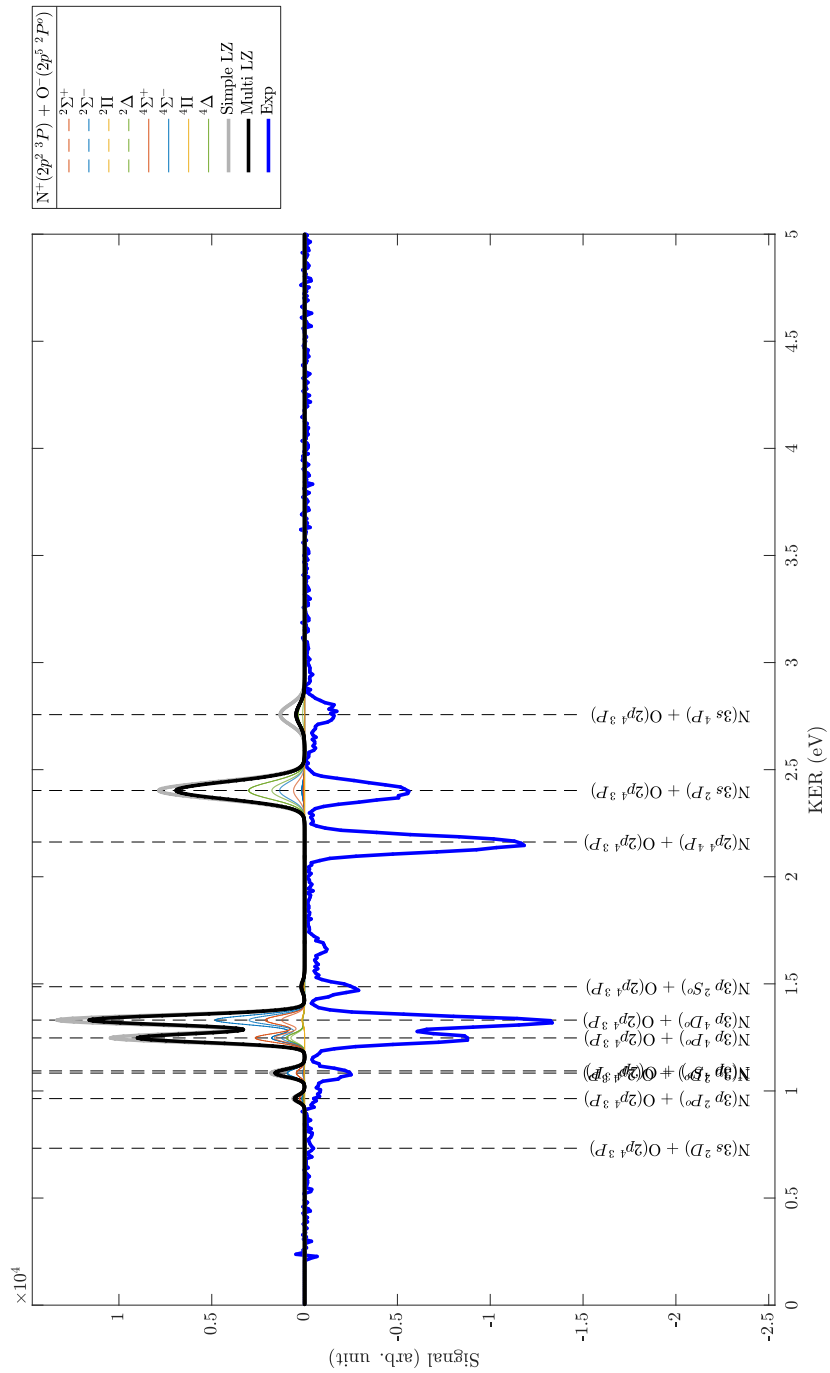

Figure F.72: Simulation: $N^+(^3P) + O^-(^2P^o)$.

N	O	$^2\Sigma^+$	$^2\Sigma^-$	$^2\Pi$	$^2\Delta$	$^4\Sigma^+$	$^4\Sigma^-$	$^4\Pi$	$^4\Delta$
$2p^3\,^4S^o$	$2p^4\,^3P$	1.509e-09		8.799e-10		1.193e-09		6.956e-10	
$2p^3\,^2D^o$	$2p^4\,^3P$	9.807e-03	9.933e-03	7.589e-03	8.072e-03	1.961e-02	1.987e-02	1.518e-02	1.614e-02
$2p^3\,^2P^o$	$2p^4\,^3P$	1.601e-02	8.189e-03		5.585e-03	3.202e-02	1.638e-02		1.117e-02
$3s\,^4P$	$2p^4\,^3P$	8.415e-03	8.415e-03		4.152e-03	6.652e-03	6.652e-03		3.282e-03
$3s\,^2P$	$2p^4\,^3P$	1.990e-03	1.990e-03		9.819e-04	3.980e-03	3.980e-03		1.964e-03
$3p\,^2S^o$	$2p^4\,^3P$	2.556e-05		1.490e-05		5.112e-05		2.980e-05	
$3p\,^4D^o$	$2p^4\,^3P$	3.607e-04	3.608e-04	3.453e-05	4.724e-05	2.852e-04	2.852e-04	2.730e-05	3.734e-05
$3p\,^4P^o$	$2p^4\,^3P$	3.525e-04	1.763e-04		1.230e-04	2.786e-04	1.394e-04		9.721e-05
$3p\,^4S^o$	$2p^4\,^3P$	9.133e-06		5.324e-06		7.221e-06		4.209e-06	
$3p\,^2D^o$	$2p^4\,^3P$	3.627e-05	3.628e-05	2.822e-06	4.240e-06	7.254e-05	7.255e-05	5.644e-06	8.480e-06
$3p\,^2P^o$	$2p^4\,^3P$	2.174e-05	1.087e-05		7.584e-06	4.347e-05	2.174e-05		1.517e-05

Table F.77: Interaction potentials E_{ic} (a.u.): $N^+(^3P) + O^-(^2P^o)$.

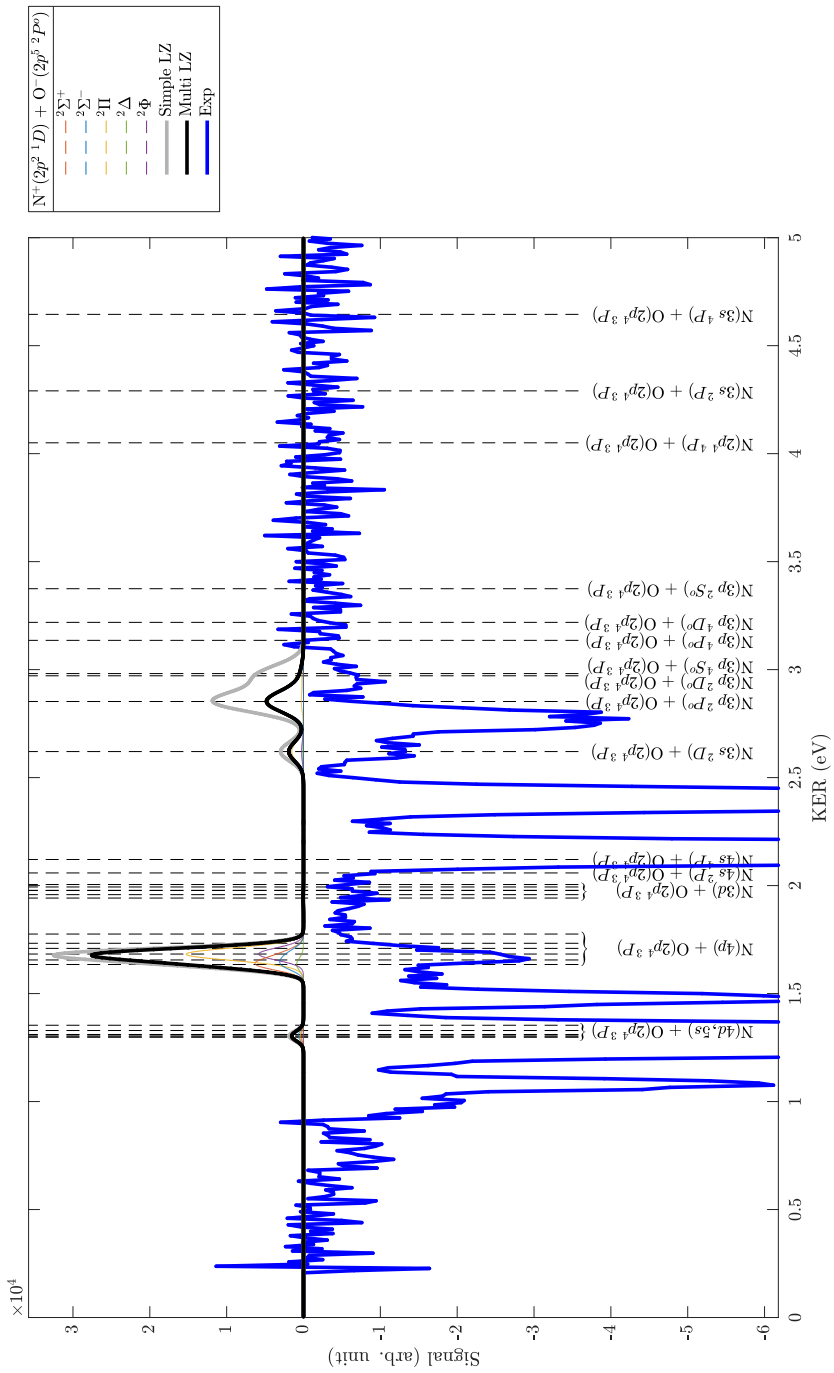

Figure F.73: Simulation: $N^+(^1D) + O^-(^2P^o)$.

N	O	$^2\Sigma^+$	$^2\Sigma^-$	$^2\Pi$	$^2\Delta$	$^2\Phi$
$2p^3\ ^2D^o$	$2p^4\ ^3P$	4.640e-10	8.907e-10	6.003e-10	1.448e-10	6.147e-10
$2p^3\ ^2P^o$	$2p^4\ ^3P$	1.324e-02	1.343e-02	1.091e-02	1.159e-02	
$3p\ ^2D^o$	$2p^4\ ^3P$	2.892e-03	5.770e-03	3.467e-03	2.276e-04	3.982e-03
$3p\ ^2P^o$	$2p^4\ ^3P$	4.943e-03	4.948e-03	1.018e-03	1.153e-03	
$3s\ ^2D$	$2p^4\ ^3P$	7.823e-03	7.823e-03	3.300e-03	1.092e-04	3.817e-03
$3d\ ^2P$	$2p^4\ ^3P$	7.726e-11	1.544e-10	1.602e-11	1.900e-11	
$3d\ ^2F$	$2p^4\ ^3P$	6.141e-11	1.227e-10	5.982e-11	2.259e-11	3.013e-11
$3d\ ^2D$	$2p^4\ ^3P$	2.469e-05	2.469e-05	2.140e-05	2.632e-06	2.408e-05
$4p\ ^2D^o$	$2p^4\ ^3P$	4.831e-04	9.655e-04	5.772e-04	2.291e-05	6.663e-04
$4p\ ^2P^o$	$2p^4\ ^3P$	8.045e-04	8.048e-04	9.473e-05	1.204e-04	
$4d\ ^2P$	$2p^4\ ^3P$	5.678e-05	1.135e-04	7.679e-06	1.042e-05	
$4d\ ^2F$	$2p^4\ ^3P$	4.473e-05	8.942e-05	4.353e-05	1.080e-05	1.725e-05

Table F.78: Interaction potentials E_{ic} (a.u.): $N^+(2p^2\ ^1D) + O^-(2p^5\ ^2P^o)$.

F.5.6 Sulfur

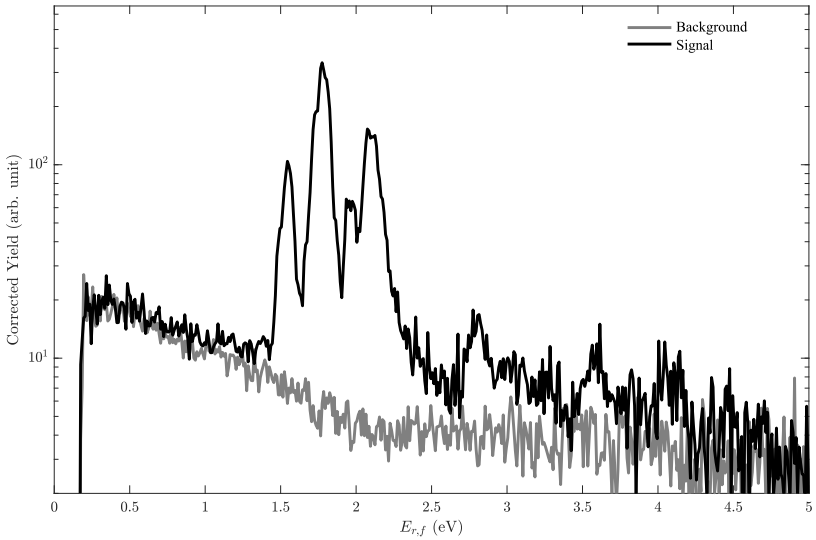

Figure F.74: Experiment: $N^+ + S^- \rightarrow N + S$.

N^+ beam	
Beam energy:	5,500 eV
Ion source:	ECR (N_2)
S^- beam	
Beam energy:	11,500 eV
Ion source:	Sputtering (FeS)
Mean collision energy:	$\sim$ 15 meV

Table F.79: $N^+ + S^-$ MN experimental setup parameters.

	$N^+(^3P) + S^-(^2P^o)$ $S(^3P)$	$N^+(^1D) + S^-(^2P^o)$ $S(^3P)$
$N(3s\ ^4P)$	0.302(3)	
$N(3s\ ^2P)$	0.558(3)	0.080(6)
$N(2s2p^4\ ^4P)$	0.140(2)	0.031(31)
$N(3p\ ^2S^o)$		0.062(6)
$N(3p\ ^4D^o)$		0.031(6)
$N(3p\ ^4P^o)$		0.024(6)
$N(3p\ ^4S^o)$		0.167(31)
$N(3p\ ^2D^o)$		0.000(6)
$N(3p\ ^2P^o)$		0.006(6)
$N(3s\ ^2D)$		0.599(6)

Table F.80: Branching ratio fit: $N^+(^3P) + S^-(^2P^o)$ and $N^+(^1D) + S^-(^2P^o)$.

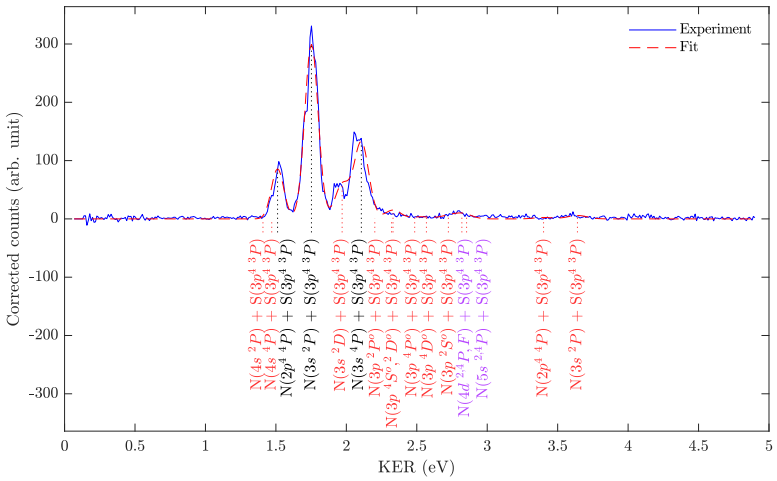

Figure F.75: Branching ratio fit: $N^+(^3P) + S^-(^2P^o)$. The color code for the products is given in table F.1.

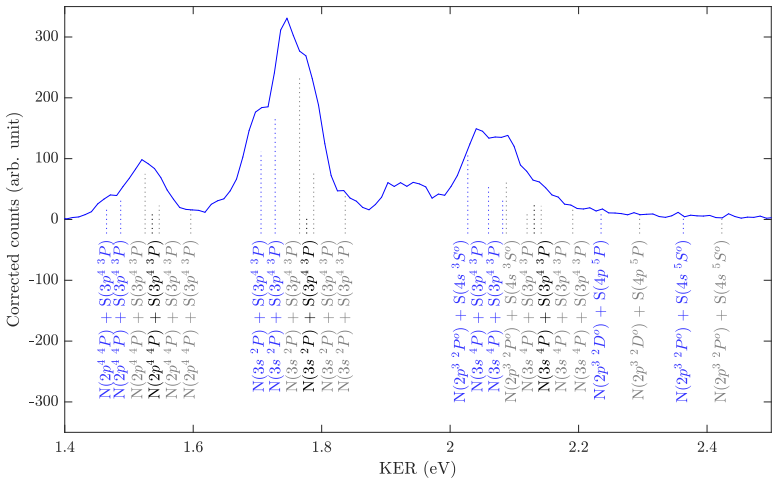

Figure F.76: Branching ratio fit: $N^+(^3P) + S^-(^2P^o)$ – zoom. The color code for the products is given in table F.1. This figure show the effect of the J splitting of S and S^-.

Cation	Anion	Center-of-mass collision energy (eV)					
N	S	0.002	0.005	0.02	0.05	0.2	0.5
$2p^3\ ^4S^o$	$3p^4\ ^3P$	9.39e-28	3.76e-28	9.42e-29	3.79e-29	9.75e-30	4.12e-30
$2p^3\ ^4S^o$	$3p^4\ ^1D$	1.72e-28	6.9e-29	1.73e-29	6.96e-30	1.79e-30	7.55e-31
$2p^3\ ^4S^o$	$3p^4\ ^1S$	2.44e-31	9.79e-32	2.48e-32	1.01e-32	2.83e-33	1.37e-33
$2p^3\ ^4S^o$	$4p\ ^3P$	1.89e-34	7.58e-35	1.94e-35	8.16e-36	2.55e-36	1.49e-36
$2p^3\ ^2D^o$	$3p^4\ ^3P$	2.25e-13	9.01e-14	2.26e-14	9.09e-15	2.34e-15	9.91e-16
$2p^3\ ^2D^o$	$3p^4\ ^1D$	3.73e-14	1.49e-14	3.75e-15	1.51e-15	3.92e-16	1.69e-16
$2p^3\ ^2D^o$	$3p^4\ ^1S$	1.65e-13	6.61e-14	1.66e-14	6.65e-15	1.7e-15	7.08e-16
$2p^3\ ^2D^o$	$4p\ ^3P$	5.11e-18	2.05e-18	5.15e-19	2.09e-19	5.55e-20	2.47e-20
$2p^3\ ^2P^o$	$3p^4\ ^3P$	5.81e-14	2.33e-14	5.85e-15	2.36e-15	6.24e-16	2.75e-16
$2p^3\ ^2P^o$	$3p^4\ ^1D$	1.24e-13	4.95e-14	1.24e-14	5.01e-15	1.3e-15	5.61e-16
$2p^3\ ^2P^o$	$3p^4\ ^1S$	2.29e-13	9.18e-14	2.3e-14	9.24e-15	2.36e-15	9.82e-16
$2p^3\ ^2P^o$	$4p\ ^3P$	2.45e-31	4.92e-32	1.25e-32	5.17e-33	1.5e-33	7.68e-34
$3s\ ^4P$	$3p^4\ ^3P$	1.61e-12	6.43e-13	1.62e-13	6.63e-14	1.82e-14	8.66e-15
$3s\ ^4P$	$3p^4\ ^1D$	9.49e-17	3.8e-17	9.59e-18	3.89e-18	1.05e-18	4.7e-19
$3s\ ^2P$	$3p^4\ ^3P$	2.96e-12	1.19e-12	2.99e-13	1.21e-13	3.24e-14	1.45e-14
$3s\ ^2P$	$3p^4\ ^1D$	2.35e-22	9.4e-23	2.38e-23	9.74e-24	2.7e-24	1.26e-24
$3p\ ^2S^o$	$3p^4\ ^3P$	1.87e-18	7.5e-19	1.89e-19	7.7e-20	2.08e-20	9.47e-21
$3p\ ^4D^o$	$3p^4\ ^3P$	2.34e-17	9.38e-18	2.37e-18	9.69e-19	2.66e-19	1.24e-19
$3p\ ^4P^o$	$3p^4\ ^3P$	1.07e-18	4.28e-19	1.08e-19	4.44e-20	1.23e-20	5.8e-21
$3p\ ^4S^o$	$3p^4\ ^3P$	5.8e-26	2.33e-26	5.91e-27	2.44e-27	6.96e-28	3.39e-28
$3p\ ^2D^o$	$3p^4\ ^3P$	1.68e-23	6.76e-24	1.72e-24	7.1e-25	2.03e-25	9.85e-26

Table F.81: Partial cross section (cm^2) for the $N^+(^3P)$+$S^-(^2P^o)$ MN reaction computed with the ACAM.

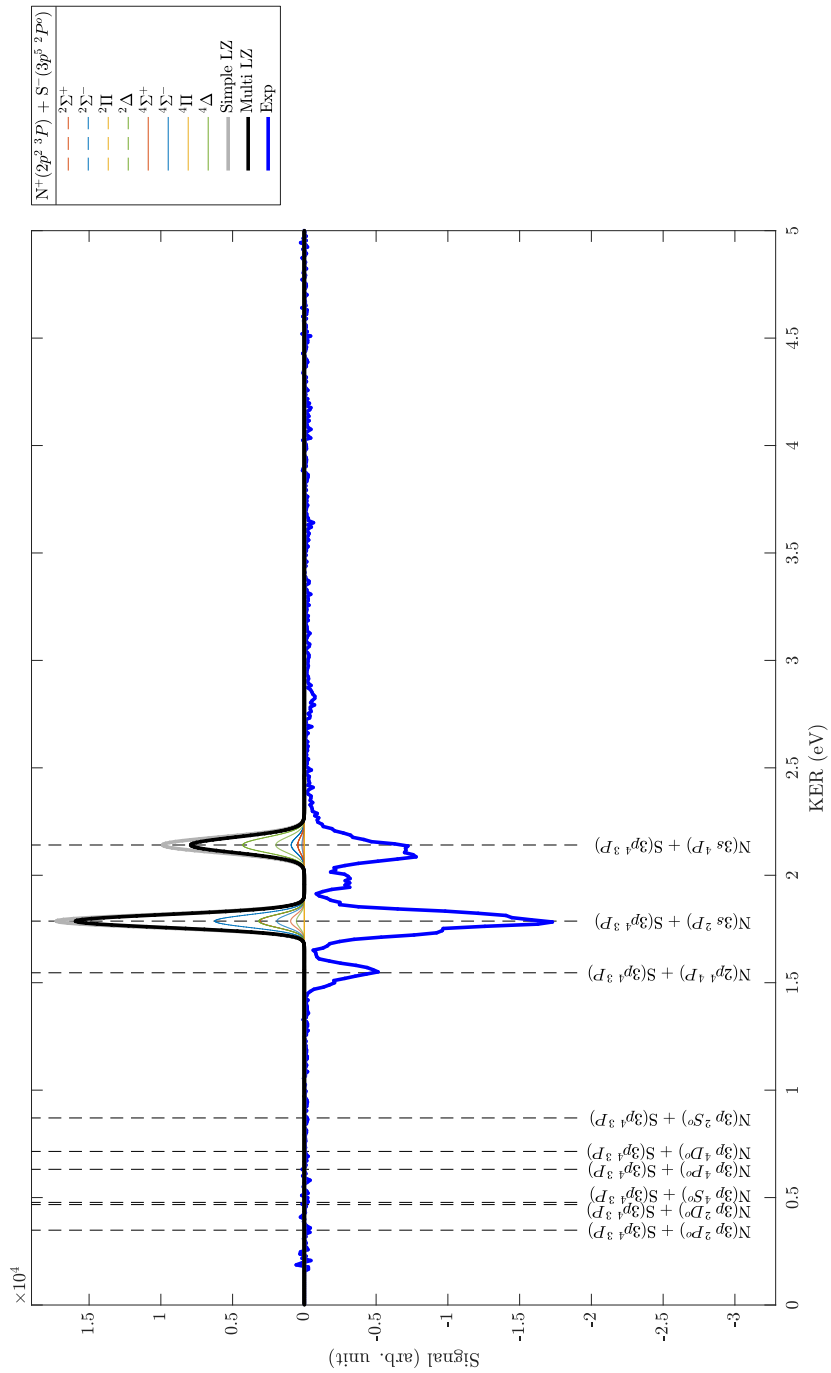

Figure F.77: Simulation: $N^+(^3P) + S^-(^2P^o)$.

N	S	$^2\Sigma^+$	$^2\Sigma^-$	$^2\Pi$	$^2\Delta$	$^4\Sigma^+$	$^4\Sigma^-$	$^4\Pi$	$^4\Delta$
$2p^3\,^4S^o$	$3p^4\,^3P$	1.500e-09		8.746e-10		1.186e-09		6.914e-10	
$2p^3\,^2D^o$	$3p^4\,^3P$	1.176e-02	1.186e-02	7.199e-03	7.680e-03	2.352e-02	2.371e-02	1.440e-02	1.536e-02
$2p^3\,^2P^o$	$3p^4\,^3P$	1.870e-02	9.484e-03		6.525e-03	3.740e-02	1.897e-02		1.305e-02
$3s\,^4P$	$3p^4\,^3P$	2.904e-03	2.904e-03		1.433e-03	2.296e-03	2.296e-03		1.133e-03
$3s\,^2P$	$3p^4\,^3P$	4.393e-04	4.393e-04		2.167e-04	8.785e-04	8.785e-04		4.335e-04
$3p\,^2S^o$	$3p^4\,^3P$	7.024e-08		4.094e-08		1.405e-07		8.188e-08	
$3p\,^4D^o$	$3p^4\,^3P$	3.113e-07	3.114e-07	1.334e-08	2.944e-08	2.461e-07	2.461e-07	1.055e-08	2.327e-08
$3p\,^4P^o$	$3p^4\,^3P$	7.013e-08	3.507e-08		2.447e-08	5.544e-08	2.772e-08		1.934e-08
$3p\,^4S^o$	$3p^4\,^3P$	8.444e-12		4.923e-12		6.676e-12		3.892e-12	
$3p\,^2D^o$	$3p^4\,^3P$	6.162e-11	6.162e-11	1.713e-12	5.425e-12	1.232e-10	1.232e-10	3.427e-12	1.085e-11

Table F.82: Interaction potentials E_{ic} (a.u.): $N^+(^3P) + S^-(^2P^o)$.

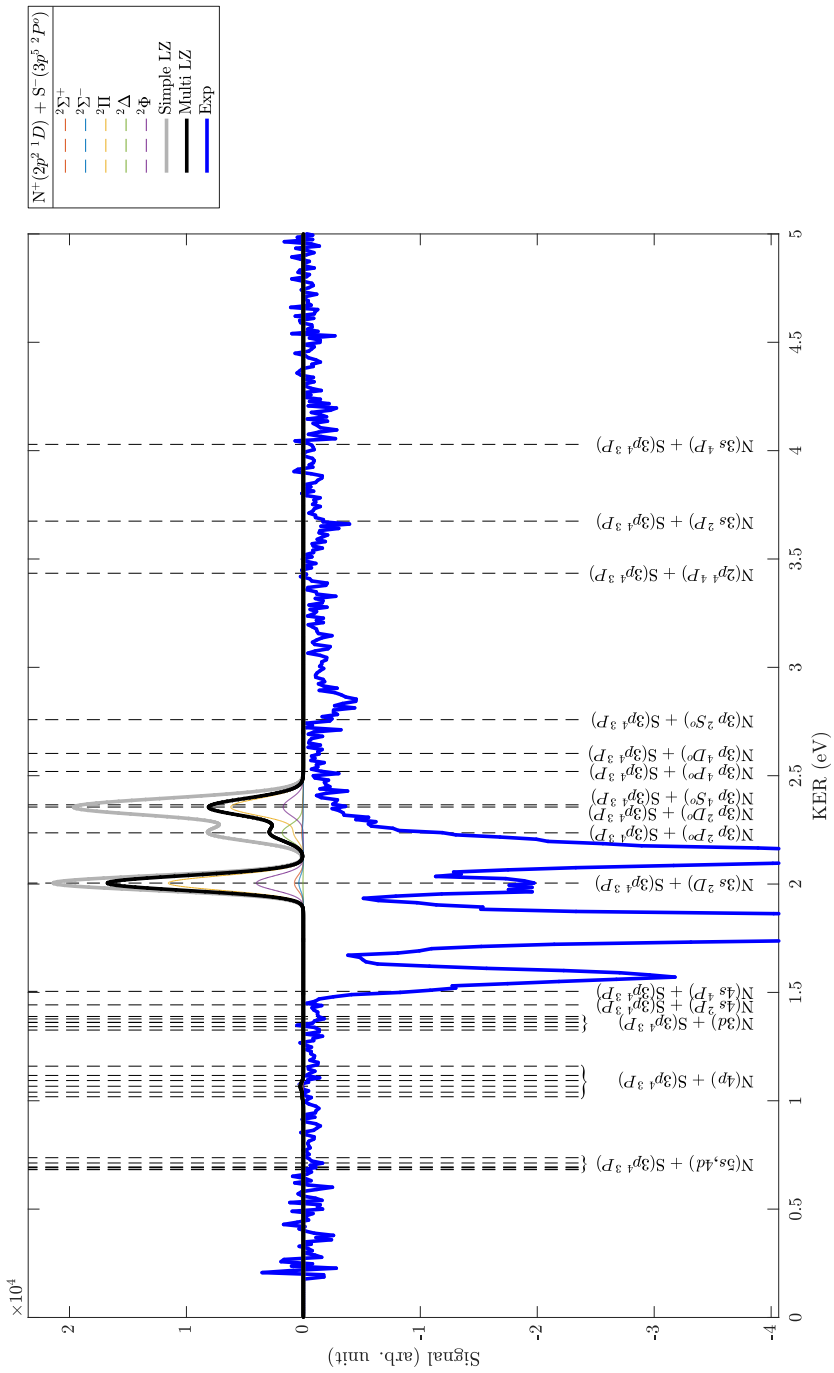

Figure F.78: Simulation: $N^+(^1D) + S^-(^2P^o)$.

N	S	$^2\Sigma^+$	$^2\Sigma^-$	$^2\Pi$	$^2\Delta$	$^2\Phi$
$2p^3\ ^2D^o$	$3p^4\ ^3P$	5.654e-10	1.101e-09	7.123e-10	1.430e-10	7.599e-10
$2p^3\ ^2P^o$	$3p^4\ ^3P$	1.607e-02	1.622e-02	1.052e-02	1.121e-02	
$3p\ ^2D^o$	$3p^4\ ^3P$	1.205e-03	2.408e-03	1.441e-03	6.554e-05	1.661e-03
$3p\ ^2P^o$	$3p^4\ ^3P$	1.867e-03	1.868e-03	2.526e-04	3.090e-04	
$3s\ ^2D$	$3p^4\ ^3P$	2.327e-03	2.327e-03	9.817e-04	3.248e-05	1.136e-03
$3d\ ^2P$	$3p^4\ ^3P$	7.134e-12	1.426e-11	8.579e-13	1.225e-12	
$3d\ ^2F$	$3p^4\ ^3P$	5.209e-12	1.042e-11	5.069e-12	1.108e-12	1.901e-12
$3d\ ^2D$	$3p^4\ ^3P$	1.869e-06	1.869e-06	1.591e-06	1.158e-07	1.823e-06
$4p\ ^2D^o$	$3p^4\ ^3P$	1.163e-05	2.326e-05	1.388e-05	3.514e-07	1.605e-05
$4p\ ^2P^o$	$3p^4\ ^3P$	1.442e-05	1.443e-05	8.844e-07	1.519e-06	
$4d\ ^2P$	$3p^4\ ^3P$	3.566e-08	7.131e-08	2.129e-09	4.736e-09	
$4d\ ^2F$	$3p^4\ ^3P$	2.278e-08	4.555e-08	2.215e-08	2.445e-09	6.938e-09

Table F.83: Interaction potentials E_{ic} (a.u.): $N^+(^1D) + S^-(^2P^o)$.

F.6 Oxygen

	$P^-(^3P)$ $P(^4S^o)$	$D^-(^1S)$ $D(1s)$	$Si^-(^4S^o)$ $Si(^3P)$	$C^-(^4S^o)$ $C(^3P)$	$O^-(^2P^o)$ $O(^3P)$	S^- $S(3p^4\ ^3P)$
$O(3s\ ^5S^o)$	0,007(5)	0,002(3)	0,005(1)	0,003(1)	0,033(1)	0,150(3)
$O(3s\ ^3S^o)$	0,000(37)	0,003(3)	0,002(1)	0,006(85)	0,114(1)	0,842(6)
$O(3p\ ^5P)$	0,015(3)	0,002(1)	0,454(7)	0,415(6)	0,579(3)	0,003(1)
$O(3p\ ^3P)$	0,109(7)	0,013(2)	0,422(6)	0,436(6)	0,120(1)	0,006(1)
$O(4s\ ^5S^o)$	0,001(24)	0,466(9)	0,026(2)		0,001(1)	
$O(4s\ ^3S^o)$	0,212(8)	0,280(7)	0,030(3)			
$O(3d\ ^5D^o)$	0,105(5)					
$O(3d\ ^3D^o)$	0,089(6)	0,216(7)				
$O(4p\ ^5P)$	0,043(4)	0,005(1)				
$O(4p\ ^3P)$	0,035(3)	0,002(2)				

Table F.84: Branching ratio fit (simplified): $O^+(^4S^o)$ + X^-.

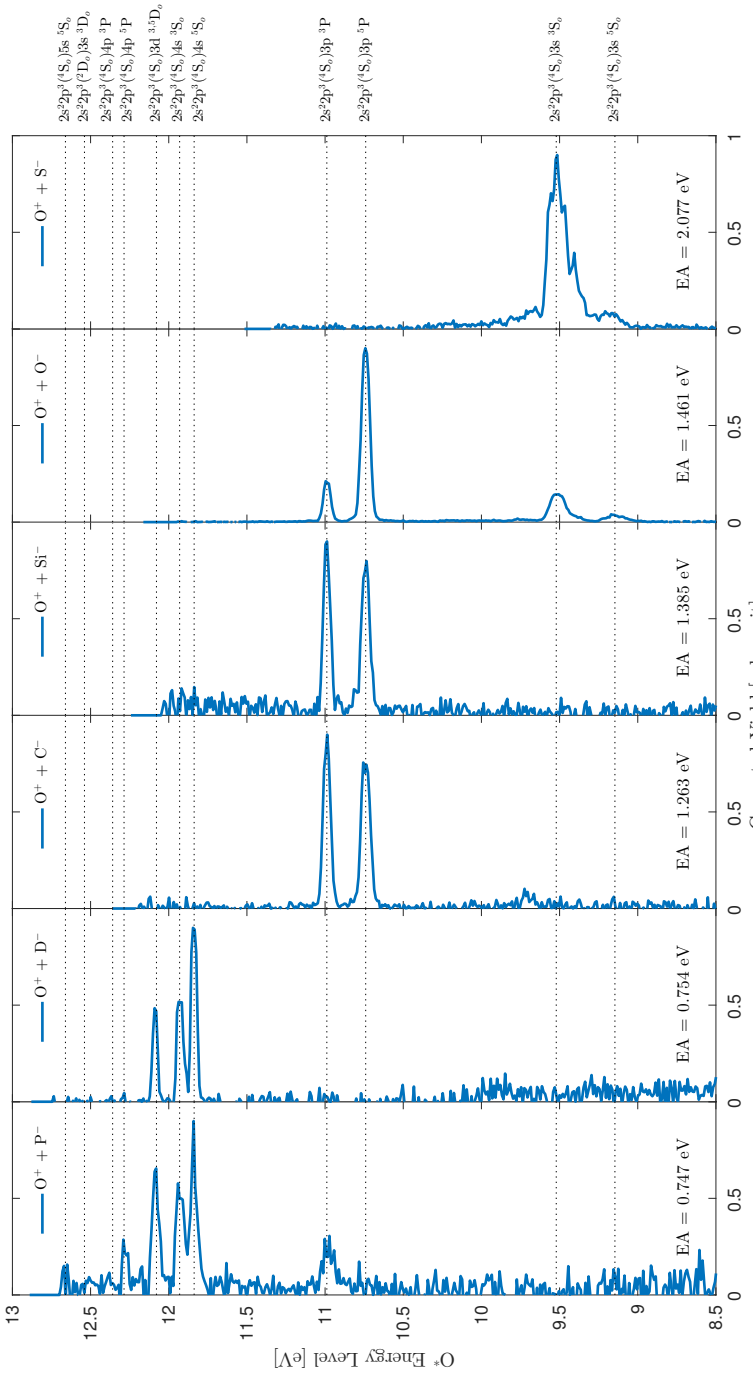

Figure F.79: Combined experiments : $O^+ + X^-$ (peak attributions).

F.6.1 Phosphorus

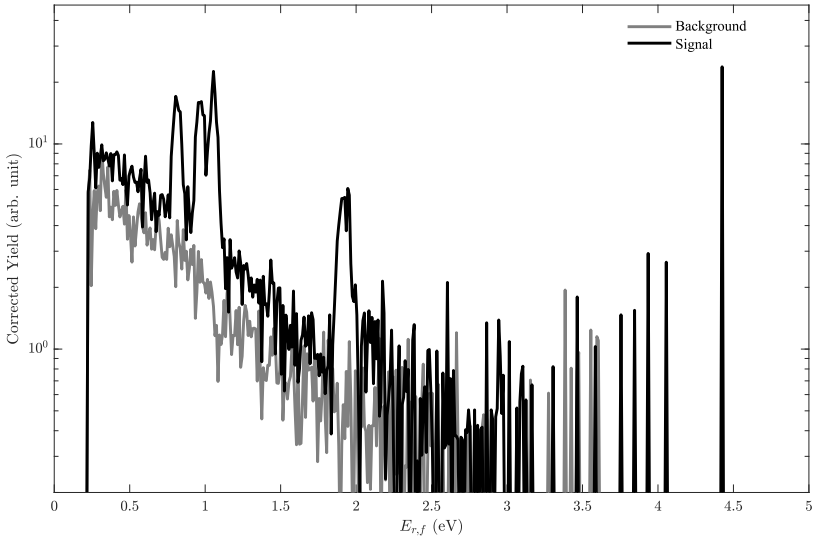

Figure F.80: Experiment: $O^+ + P^- \rightarrow O + P$.

O^+ beam	
Beam energy:	5,500 eV
Ion source:	ECR (CO)
P^- beam	
Beam energy:	11,500 eV
Ion source:	Sputtering (Fe_2P)
Mean collision energy:	$\sim$ 5 meV

Table F.85: $O^+ + P^-$ MN experimental setup parameters.

	$P^-(^3P)$ $P(^4S^o)$	$P(^2D^o)$	$P(^2P^o)$
$O(3s\ ^5S^o)$	0,007(5)	0,007(3)	0,024(3)
$O(3s\ ^3S^o)$	0,000(37)	0,005(2)	0,262(9)
$O(3p\ ^5P)$	0,015(3)	0,024(3)	
$O(3p\ ^3P)$	0,109(7)	0,028(3)	
$O(4s\ ^5S^o)$	0,001(24)		
$O(4s\ ^3S^o)$	0,212(8)		
$O(3d\ ^5D^o)$	0,105(5)		
$O(3d\ ^3D^o)$	0,089(6)		
$O(4p\ ^5P)$	0,043(4)		
$O(4p\ ^3P)$	0,035(3)		

Table F.86: Branching ratio fit: $O^+(^4S^o) + P^-(^3P)$.

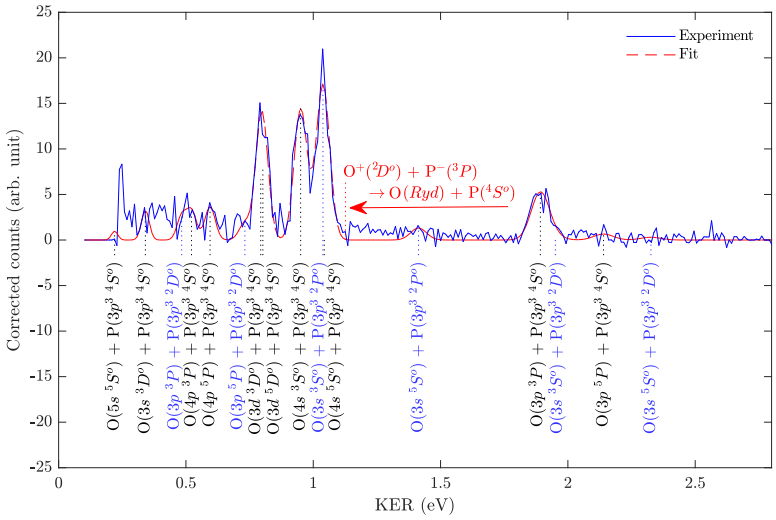

Figure F.81: Branching ratio fit: $O^+(^4S^o) + P^-(^3P)$. The color code for the products is given in table F.1.

Cation	Anion	Center-of-mass collision energy (eV)					
O	P	0.002	0.005	0.02	0.05	0.2	0.5
$2p^4\ ^3P$	$3p^3\ ^4S^o$	5.29e-28	2.13e-28	5.44e-29	2.27e-29	6.99e-30	3.99e-30
$2p^4\ ^3P$	$3p^3\ ^2D^o$	2.07e-29	8.32e-30	2.13e-30	8.9e-31	2.75e-31	1.58e-31
$2p^4\ ^3P$	$3p^3\ ^2P^o$	2.31e-29	9.26e-30	2.37e-30	9.92e-31	3.07e-31	1.77e-31
$3s\ ^5S^o$	$3p^3\ ^4S^o$	1.14e-68	4.91e-69	1.74e-69	1.38e-69	9e-69	1.17e-66
$3s\ ^5S^o$	$3p^3\ ^2D^o$	1.37e-14	5.53e-15	1.42e-15	5.99e-16	1.92e-16	1.19e-16
$3s\ ^5S^o$	$3p^3\ ^2P^o$	6.11e-14	2.45e-14	6.15e-15	2.49e-15	6.53e-16	2.84e-16
$3s\ ^3S^o$	$3p^3\ ^4S^o$	1.8e-36	7.48e-37	2.27e-37	1.33e-37	2e-37	1.77e-36
$3s\ ^3S^o$	$3p^3\ ^2D^o$	1.11e-12	4.43e-13	1.12e-13	4.56e-14	1.25e-14	5.86e-15
$3s\ ^3S^o$	$3p^3\ ^2P^o$	2.49e-16	9.96e-17	2.51e-17	1.02e-17	2.73e-18	1.23e-18
$3p\ ^5P$	$3p^3\ ^4S^o$	6.45e-14	2.59e-14	6.64e-15	2.78e-15	8.69e-16	5.13e-16
$3p\ ^5P$	$3p^3\ ^2D^o$	9.37e-19	3.76e-19	9.49e-20	3.88e-20	1.06e-20	4.93e-21
$3p\ ^3P$	$3p^3\ ^4S^o$	2.5e-12	1e-12	2.53e-13	1.03e-13	2.87e-14	1.38e-14
$3p\ ^3P$	$3p^3\ ^2D^o$	1.96e-24	7.88e-25	2e-25	8.26e-26	2.36e-26	1.14e-26
$4s\ ^5S^o$	$3p^3\ ^4S^o$	9.52e-13	3.83e-13	9.88e-14	4.2e-14	1.37e-14	8.42e-15
$4s\ ^3S^o$	$3p^3\ ^4S^o$	3.18e-12	1.28e-12	3.25e-13	1.35e-13	3.92e-14	2e-14
$3d\ ^5D^o$	$3p^3\ ^4S^o$	2.81e-12	1.13e-12	2.86e-13	1.17e-13	3.29e-14	1.57e-14
$3d\ ^3D^o$	$3p^3\ ^4S^o$	1.73e-12	6.93e-13	1.75e-13	7.18e-14	1.99e-14	9.4e-15
$4p\ ^5P$	$3p^3\ ^4S^o$	5.23e-13	2.1e-13	5.32e-14	2.19e-14	6.2e-15	2.98e-15
$4p\ ^3P$	$3p^3\ ^4S^o$	5.14e-14	2.06e-14	5.24e-15	2.16e-15	6.17e-16	2.98e-16
$5s\ ^5S^o$	$3p^3\ ^4S^o$	5.11e-25	2.06e-25	5.33e-26	2.27e-26	7.15e-27	3.78e-27

Table F.87: Partial cross section (cm^2) for the $O^+(^4S^o)$+$P^-(^3P)$ MN reaction computed with the ACAM.

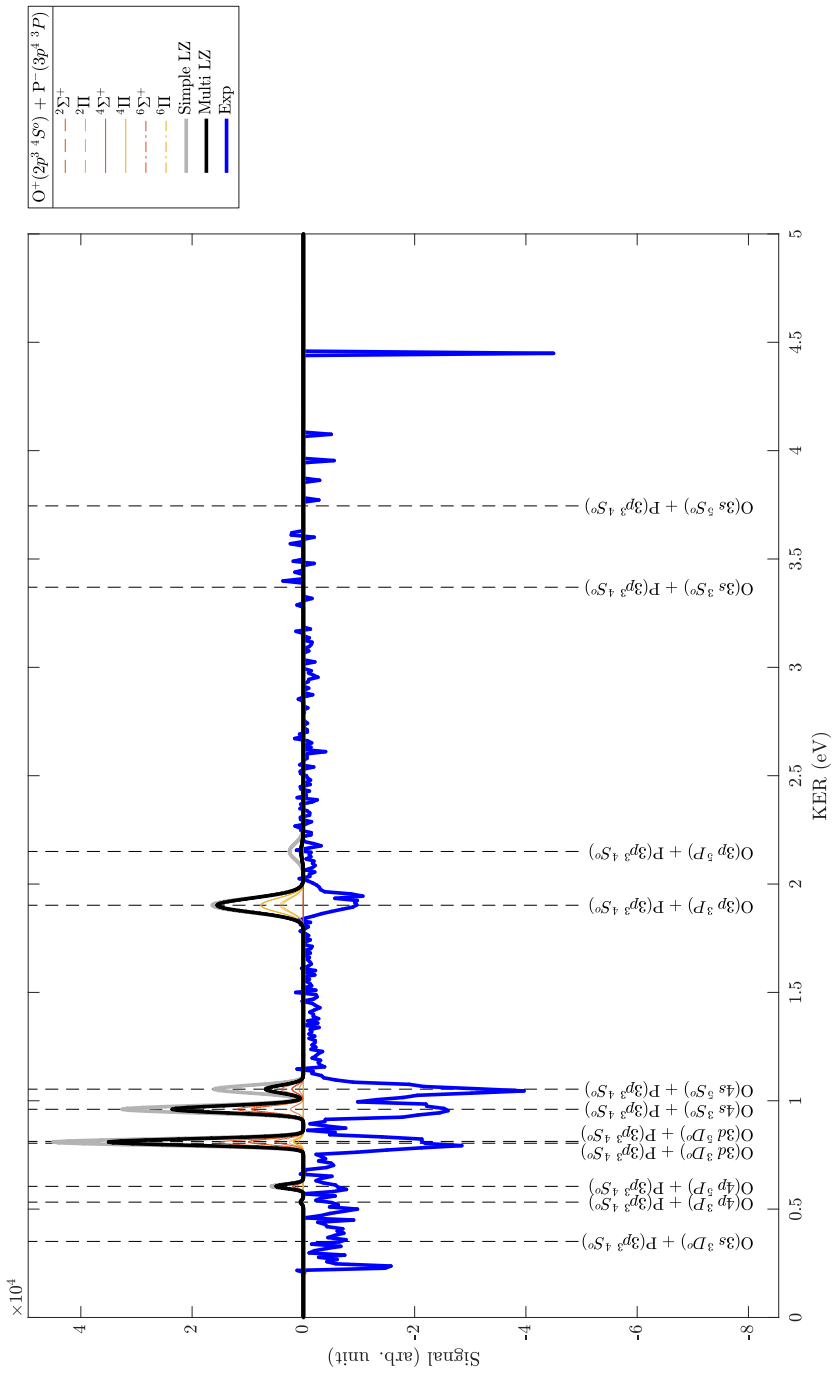

Figure F.82: Simulation: $O^+(^4S^o) + P^-(^3P)$.

O	P	$^2\Sigma^+$	$^2\Pi$	$^4\Sigma^+$	$^4\Pi$	$^6\Sigma^+$	$^6\Pi$
$2p^4\,^3P$	$3p^3\,^4S^o$	4.721e-10	9.532e-10	9.442e-10	1.906e-09	1.416e-09	2.860e-09
$3s\,^5S^o$	$3p^3\,^4S^o$	3.049e-02		2.727e-02		2.083e-02	
$3s\,^3S^o$	$3p^3\,^4S^o$	6.561e-03		1.312e-02		1.968e-02	
$3p\,^5P$	$3p^3\,^4S^o$	1.081e-02	3.631e-03	9.672e-03	3.248e-03	7.387e-03	2.480e-03
$3p\,^3P$	$3p^3\,^4S^o$	2.122e-03	6.299e-04	4.244e-03	1.260e-03	6.366e-03	1.890e-03
$4s\,^5S^o$	$3p^3\,^4S^o$	1.014e-03		9.073e-04		6.929e-04	
$4s\,^3S^o$	$3p^3\,^4S^o$	1.688e-04		3.377e-04		5.065e-04	
$3d\,^5D^o$	$3p^3\,^4S^o$	1.802e-04	3.928e-05	1.612e-04	3.514e-05	1.231e-04	2.684e-05
$3d\,^3D^o$	$3p^3\,^4S^o$	4.387e-05	9.464e-06	8.774e-05	1.893e-05	1.316e-04	2.839e-05
$4p\,^5P$	$3p^3\,^4S^o$	3.900e-05	3.641e-06	3.489e-05	3.256e-06	2.664e-05	2.487e-06
$4p\,^3P$	$3p^3\,^4S^o$	3.134e-06	2.567e-07	6.268e-06	5.135e-07	9.403e-06	7.702e-07

Table F.88: Interaction potentials E_{ic} (a.u.): $O^+(^4S^o) + P^-(^3P)$.

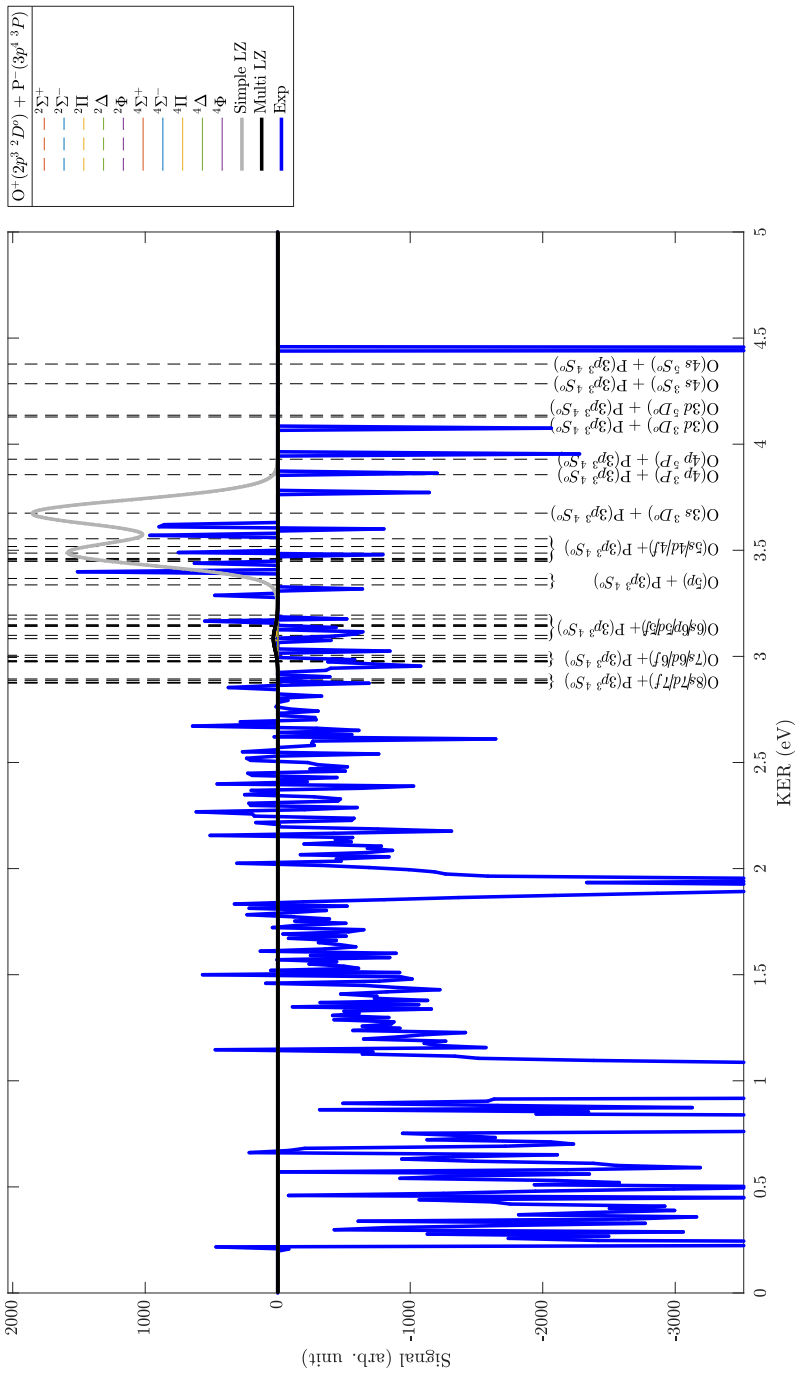

Figure F.83: Simulation: $O^+(^2D^o) + P^-(^3P)$.

O	P	$^2\Sigma^+$	$^2\Sigma^-$	$^2\Pi$	$^2\Delta$	$^2\Phi$	$^4\Sigma^+$	$^4\Sigma^-$	$^4\Pi$	$^4\Delta$	$^4\Phi$
$2p^4\,^3P$	$3p^3\,^4S^o$	4.325e-09		4.688e-09			3.419e-09		3.706e-09		
$2p^4\,^1D$	$3p^3\,^4S^o$							5.118e-09	2.303e-09	1.565e-09	
$3p\,^3P$	$3p^3\,^4S^o$	2.299e-02		2.585e-02			1.817e-02		2.043e-02		
$3d\,^3D^o$	$3p^3\,^4S^o$	4.422e-10		8.249e-10	6.486e-10		3.496e-10		6.522e-10	5.128e-10	
$4p\,^3P$	$3p^3\,^4S^o$	1.204e-02		1.397e-02			9.521e-03		1.104e-02		
$3s\,^3D^o$	$3p^3\,^4S^o$	3.066e-03		1.040e-02	3.006e-02		2.424e-03		8.225e-03	2.377e-02	
$3s\,^1D^o$	$3p^3\,^4S^o$						1.715e-03		5.820e-03	1.682e-02	
$4d\,^3D^o$	$3p^3\,^4S^o$	3.550e-10		6.618e-10	6.147e-10		2.807e-10		5.232e-10	4.859e-10	
$4f\,^3F$	$3p^3\,^4S^o$	4.048e-10		1.060e-09	7.851e-10	7.303e-10	3.200e-10		8.376e-10	6.207e-10	5.773e-10
$5p\,^3P$	$3p^3\,^4S^o$	8.572e-03		1.016e-02			6.777e-03		8.031e-03		
$5d\,^3D^o$	$3p^3\,^4S^o$	3.165e-10		5.896e-10	5.982e-10		2.502e-10		4.661e-10	4.730e-10	
$5f\,^3F$	$3p^3\,^4S^o$	3.612e-10		9.431e-10	7.643e-10	6.496e-10	2.855e-10		7.456e-10	6.042e-10	5.136e-10
$6p\,^3P$	$3p^3\,^4S^o$	7.053e-03		8.475e-03			5.576e-03		6.700e-03		
$6d\,^3D^o$	$3p^3\,^4S^o$	2.958e-10		5.509e-10	5.887e-10		2.339e-10		4.355e-10	4.654e-10	
$6f\,^3F$	$3p^3\,^4S^o$	3.378e-10		8.806e-10	7.522e-10	6.063e-10	2.670e-10		6.961e-10	5.946e-10	4.793e-10
$6g\,^3G^o$	$3p^3\,^4S^o$	3.780e-10		1.270e-09	8.747e-10	1.077e-09	2.988e-10		1.004e-09	6.915e-10	8.514e-10
$7d\,^3D^o$	$3p^3\,^4S^o$	2.834e-10		5.277e-10	5.826e-10		2.241e-10		4.172e-10	4.606e-10	
$7f\,^3F$	$3p^3\,^4S^o$	3.238e-10		8.430e-10	7.444e-10	5.802e-10	2.560e-10		6.665e-10	5.885e-10	4.587e-10

Table F.89: Interaction potentials E_{ic} (a.u.): $O^+(^2D^o) + P^-(^3P)$.

F.6.2 Deuterium

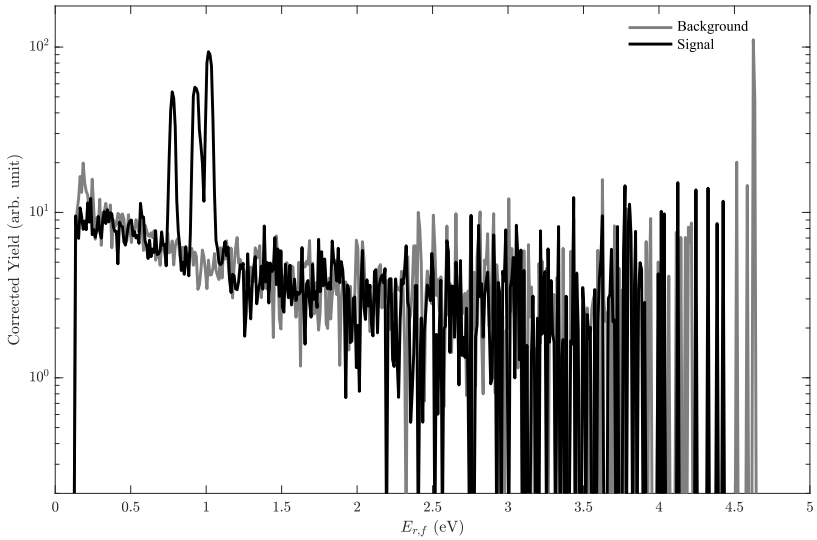

Figure F.84: Experiment: $O^+ + D^- \rightarrow O + D$.

O^+ beam	
Beam energy:	13,500 eV
Ion source:	ECR (CO)
D^- beam	
Beam energy:	2,250 eV
Ion source:	Duoplasmatron (D_2)
Mean collision energy:	$\sim$ 12 meV

Table F.90: $O^+ + D^-$ MN experimental setup parameters.

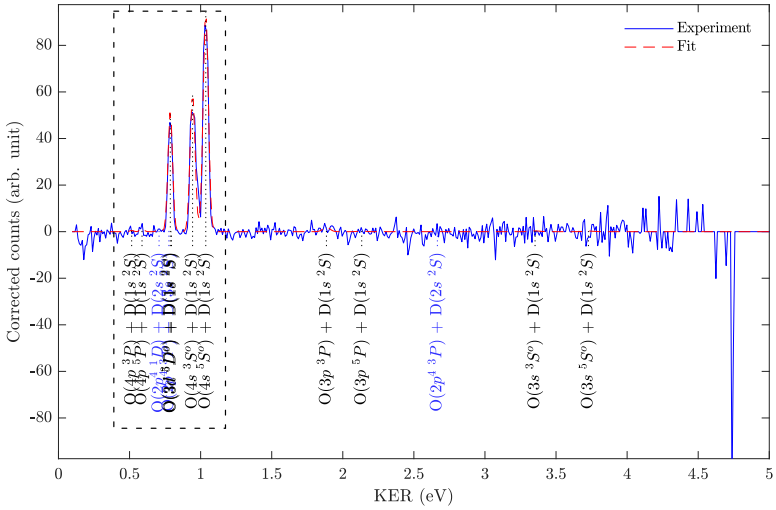

Figure F.85: Branching ratio fit: $O^+(^4S^o) + D^-(^1S)$. The color code for the products is given in table F.1. A zoom of the framed area is given in figure F.86.

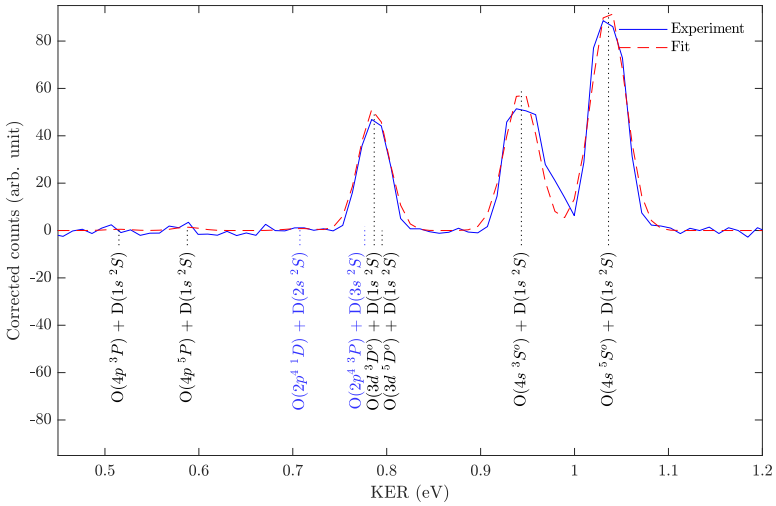

Figure F.86: Branching ratio fit: $O^+(^4S^o) + D^-(^1S)$ – zoom. The color code for the products is given in table F.1.

	$D^-(^1S)$		
	D($1s$)	D(2ℓ)	D(3ℓ)
O($2p^4\ ^3P$)			0,007(9)
O($2p^4\ ^1D$)		0,004(1)	
O($3s\ ^5S^o$)	0,002(3)		
O($3s\ ^3S^o$)	0,003(3)		
O($3p\ ^5P$)	0,002(1)		
O($3p\ ^3P$)	0,013(2)		
O($4s\ ^5S^o$)	0,466(9)		
O($4s\ ^3S^o$)	0,280(7)		
O($3d\ ^3D^o$)	0,216(7)		
O($4p\ ^5P$)	0,005(1)		
O($4p\ ^3P$)	0,002(2)		

Table F.91: Branching ratio fit: $O^+(^4S^o)$ + $D^-(^1S)$.

Cation	Anion	Center-of-mass collision energy (eV)					
O	D	0.002	0.005	0.02	0.05	0.2	0.5
$2p^4\ ^3P$	$1s\ ^2S$	4.84e-53	2e-53	5.89e-54	3.26e-54	3.78e-54	2.31e-53
$3s\ ^5S^o$	$1s\ ^2S$	1.78e-38	7.34e-39	2.16e-39	1.19e-39	1.38e-39	8.45e-39
$3s\ ^3S^o$	$1s\ ^2S$	4.36e-27	1.79e-27	5e-28	2.5e-28	1.8e-28	4.56e-28
$3p\ ^5P$	$1s\ ^2S$	9.23e-21	3.75e-21	1.02e-21	4.83e-22	2.64e-22	4.08e-22
$3p\ ^3P$	$1s\ ^2S$	8.09e-15	3.26e-15	8.5e-16	3.69e-16	1.34e-16	1.02e-16
$4s\ ^5S^o$	$1s\ ^2S$	9.47e-12	3.8e-12	9.69e-13	4.03e-13	1.2e-13	6.3e-14
$4s\ ^3S^o$	$1s\ ^2S$	9.68e-12	3.88e-12	9.83e-13	4.04e-13	1.13e-13	5.46e-14
$3d\ ^5D^o$	$1s\ ^2S$	3.67e-12	1.47e-12	3.73e-13	1.53e-13	4.26e-14	2.02e-14
$3d\ ^3D^o$	$1s\ ^2S$	2.18e-12	8.74e-13	2.21e-13	9.05e-14	2.51e-14	1.18e-14
$4p\ ^5P$	$1s\ ^2S$	5.8e-13	2.33e-13	5.9e-14	2.43e-14	6.87e-15	3.3e-15
$4p\ ^3P$	$1s\ ^2S$	5.15e-14	2.07e-14	5.25e-15	2.17e-15	6.2e-16	3.01e-16
$5s\ ^5S^o$	$1s\ ^2S$	1.03e-25	4.17e-26	1.09e-26	4.62e-27	1.4e-27	7.46e-28

Table F.92: Partial cross section (cm^2) for the $O^+(^4S^o)$+$D^-(^1S)$ MN reaction computed with the ACAM.

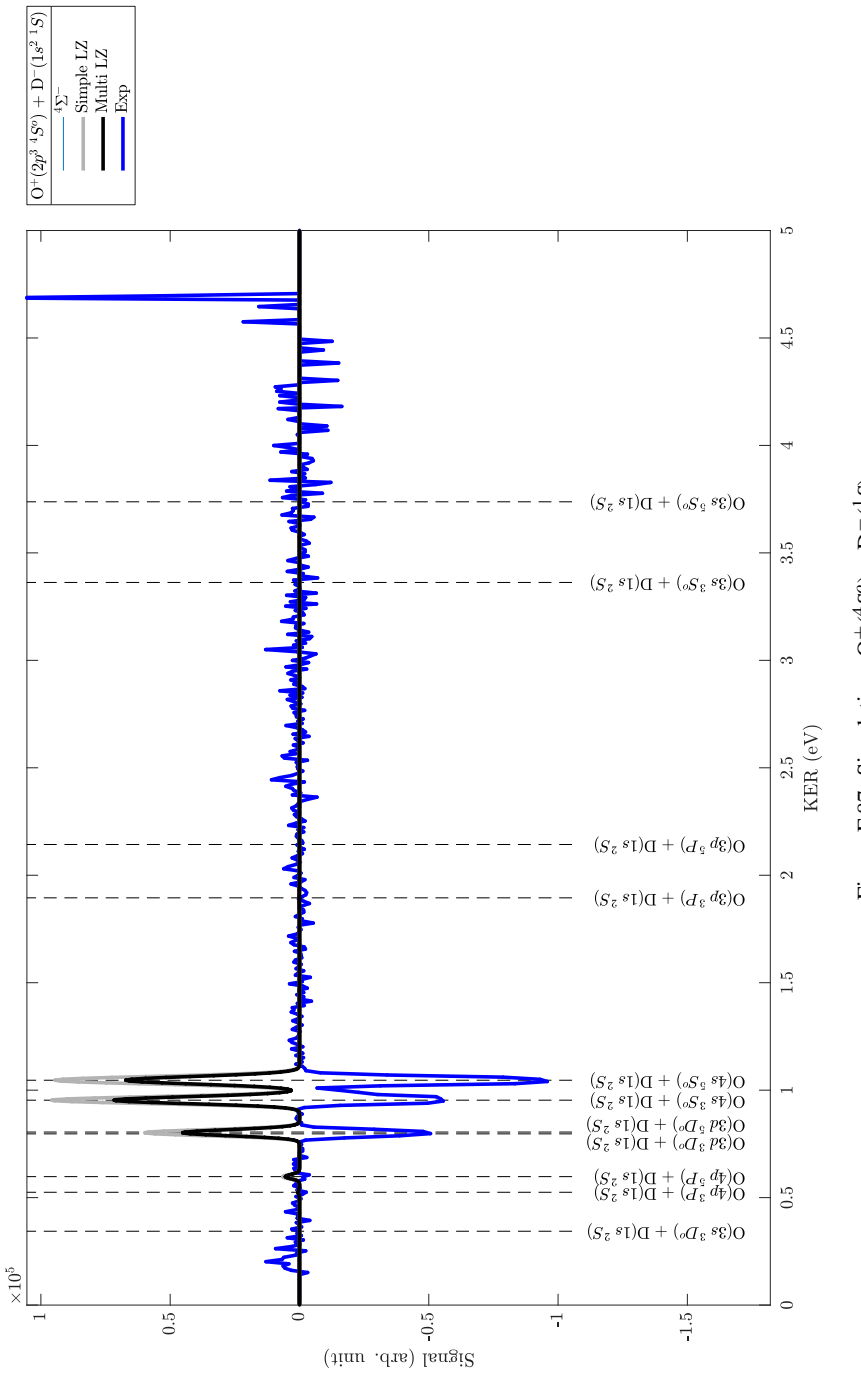

Figure F.87: Simulation: $O^+(^4S^o) + D^-(^1S)$.

O	D	$^4\Sigma^-$
$2p^4\ ^3P$	$1s\ ^2S$	1.234e-09
$3s\ ^5S^o$	$1s\ ^2S$	2.643e-02
$3s\ ^3S^o$	$1s\ ^2S$	1.704e-02
$3p\ ^5P$	$1s\ ^2S$	9.287e-03
$3p\ ^3P$	$1s\ ^2S$	5.448e-03
$4s\ ^5S^o$	$1s\ ^2S$	8.384e-04
$4s\ ^3S^o$	$1s\ ^2S$	4.146e-04
$3d\ ^5D^o$	$1s\ ^2S$	1.441e-04
$3d\ ^3D^o$	$1s\ ^2S$	1.051e-04
$4p\ ^5P$	$1s\ ^2S$	2.925e-05
$4p\ ^3P$	$1s\ ^2S$	6.761e-06

Table F.93: Interaction potentials E_{ic} (a.u.): $O^+(^4S^o)$ + $D^-(^1S)$.

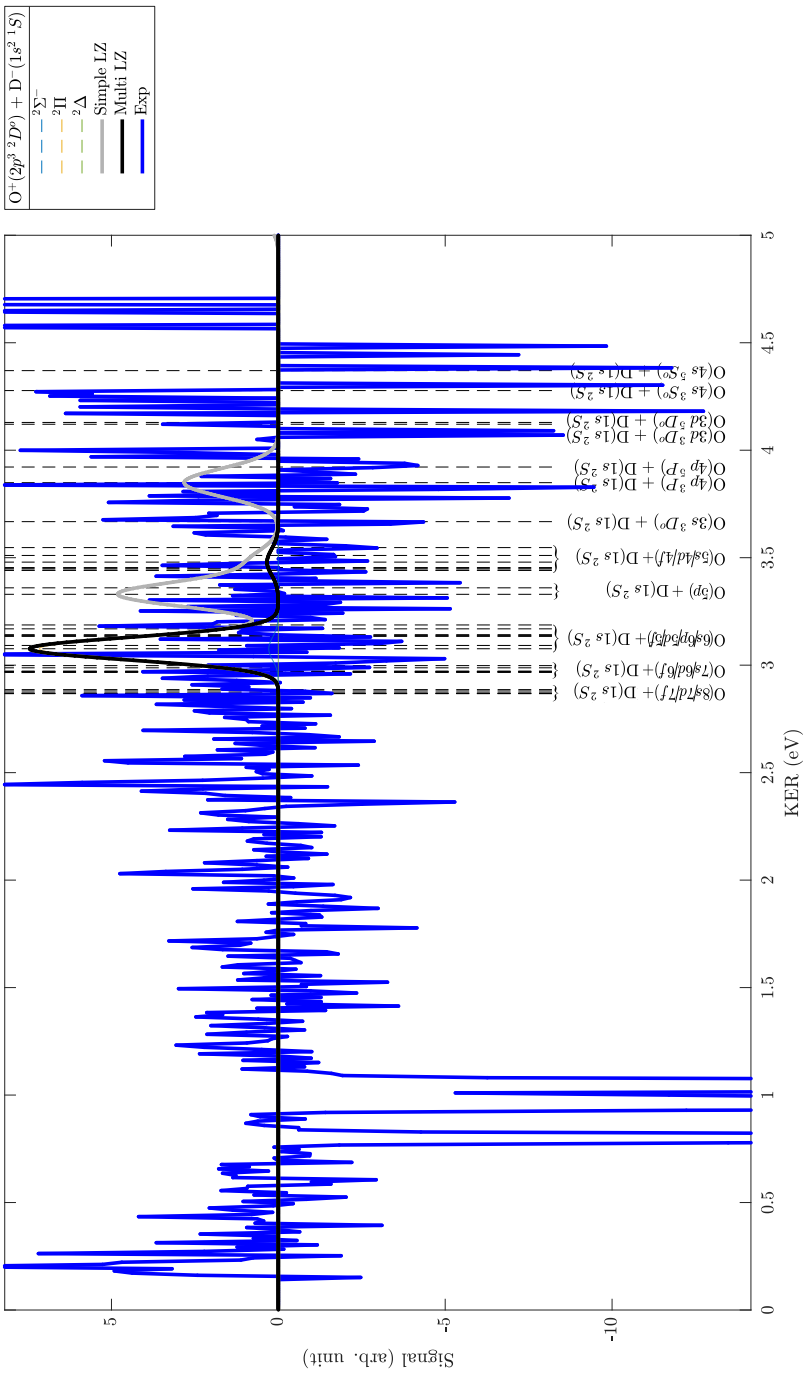

Figure F.88: Simulation: $O^+(^2D^o) + D^-(^1S)$.

O	D	$^2\Sigma^-$	$^2\Pi$	$^2\Delta$
$2p^4\ ^3P$	$1s\ ^2S$	1.488e-09	1.289e-09	
$2p^4\ ^1D$	$1s\ ^2S$		6.682e-10	1.336e-09
$3p\ ^3P$	$1s\ ^2S$	2.433e-02	2.107e-02	
$3d\ ^3D^o$	$1s\ ^2S$	5.895e-10	2.948e-10	5.895e-10
$4p\ ^3P$	$1s\ ^2S$	1.715e-02	1.485e-02	
$3s\ ^3D^o$	$1s\ ^2S$	2.804e-02	2.804e-02	2.804e-02
$3s\ ^1D^o$	$1s\ ^2S$	1.478e-02	1.478e-02	1.478e-02
$4d\ ^3D^o$	$1s\ ^2S$	5.621e-10	2.811e-10	5.621e-10
$4f\ ^3F$	$1s\ ^2S$	6.422e-10	2.270e-10	7.180e-10
$5p\ ^3P$	$1s\ ^2S$	1.404e-02	1.216e-02	
$5d\ ^3D^o$	$1s\ ^2S$	5.482e-10	2.741e-10	5.482e-10
$5f\ ^3F$	$1s\ ^2S$	6.264e-10	2.215e-10	7.004e-10
$6p\ ^3P$	$1s\ ^2S$	1.245e-02	1.078e-02	
$6d\ ^3D^o$	$1s\ ^2S$	5.399e-10	2.699e-10	5.399e-10
$6f\ ^3F$	$1s\ ^2S$	6.170e-10	2.181e-10	6.898e-10
$6g\ ^3G^o$	$1s\ ^2S$	6.904e-10	1.891e-10	8.022e-10
$7d\ ^3D^o$	$1s\ ^2S$	5.345e-10	2.672e-10	5.345e-10
$7f\ ^3F$	$1s\ ^2S$	6.109e-10	2.160e-10	6.830e-10

Table F.94: Interaction potentials E_{ic} (a.u.): $O^+(^2D^o)$ + $D^-(^1S)$.

F.6.3 Silicon

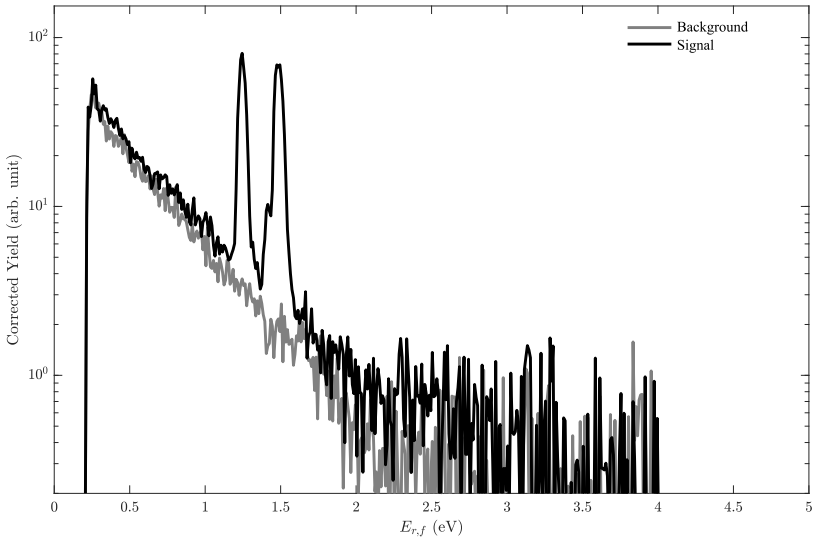

Figure F.89: Experiment: $O^+ + Si^- \rightarrow O + Si$.

O^+ beam	
Beam energy:	5,500 eV
Ion source:	ECR (CO)
Si^- beam	
Beam energy:	11,500 eV
Ion source:	Sputtering (silicon wafer)
Mean collision energy:	$\sim$ 26 meV

Table F.95: $O^+ + Si^-$ MN experimental setup parameters.

	$Si^-(^4S^o)$ $Si(^3P)$	$Si(^1D)$	$Si(^1S)$
$O(3s\ ^5S^o)$	0,005(1)	0,006(1)	0,00(14
$O(3s\ ^3S^o)$	0,002(1)	0,007(1)	0,015(1)
$O(3p\ ^5P)$	0,454(7)	0,020(1)	
$O(3p\ ^3P)$	0,422(6)	0,013(1)	
$O(4s\ ^5S^o)$	0,026(2)		
$O(4s\ ^3S^o)$	0,030(3)		

Table F.96: Branching ratio fit: $O^+(^4S^o)$ + $Si^-(^4S^o)$.

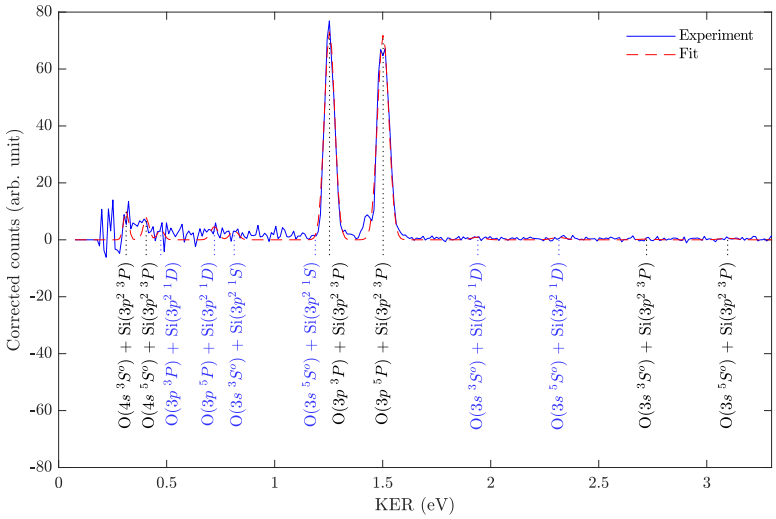

Figure F.90: Branching ratio fit: $O^+(^4S^o)$ + $Si^-(^4S^o)$. The color code for the products is given in table F.1.

Cation O	Anion Si	Center-of-mass collision energy (eV) 0.002	0.005	0.02	0.05	0.2	0.5
$2p^4\ ^3P$	$3p^2\ ^3P$	3.63e-134	1.67e-134	8.26e-135	1.28e-134	2e-132	7.97e-128
$3s\ ^5S^o$	$3p^2\ ^3P$	1.4e-128	6.47e-129	3.29e-129	5.37e-129	1.1e-126	7.24e-122
$3s\ ^3S^o$	$3p^2\ ^3P$	1.69e-67	7.23e-68	2.56e-68	2.05e-68	1.37e-67	1.97e-65
$3p\ ^5P$	$3p^2\ ^3P$	5.79e-12	2.32e-12	5.89e-13	2.42e-13	6.86e-14	3.4e-14
$3p\ ^3P$	$3p^2\ ^3P$	4.46e-12	1.79e-12	4.51e-13	1.84e-13	5.02e-14	2.33e-14
$4s\ ^5S^o$	$3p^2\ ^3P$	1.61e-19	6.47e-20	1.65e-20	6.82e-21	1.98e-21	9.7e-22
$4s\ ^3S^o$	$3p^2\ ^3P$	2.1e-24	8.45e-25	2.16e-25	9.06e-26	2.71e-26	1.38e-26

Table F.97: Partial cross section (cm^2) for the $O^+(^4S^o)$+$Si^-(^4S^o)$ MN reaction computed with the ACAM.

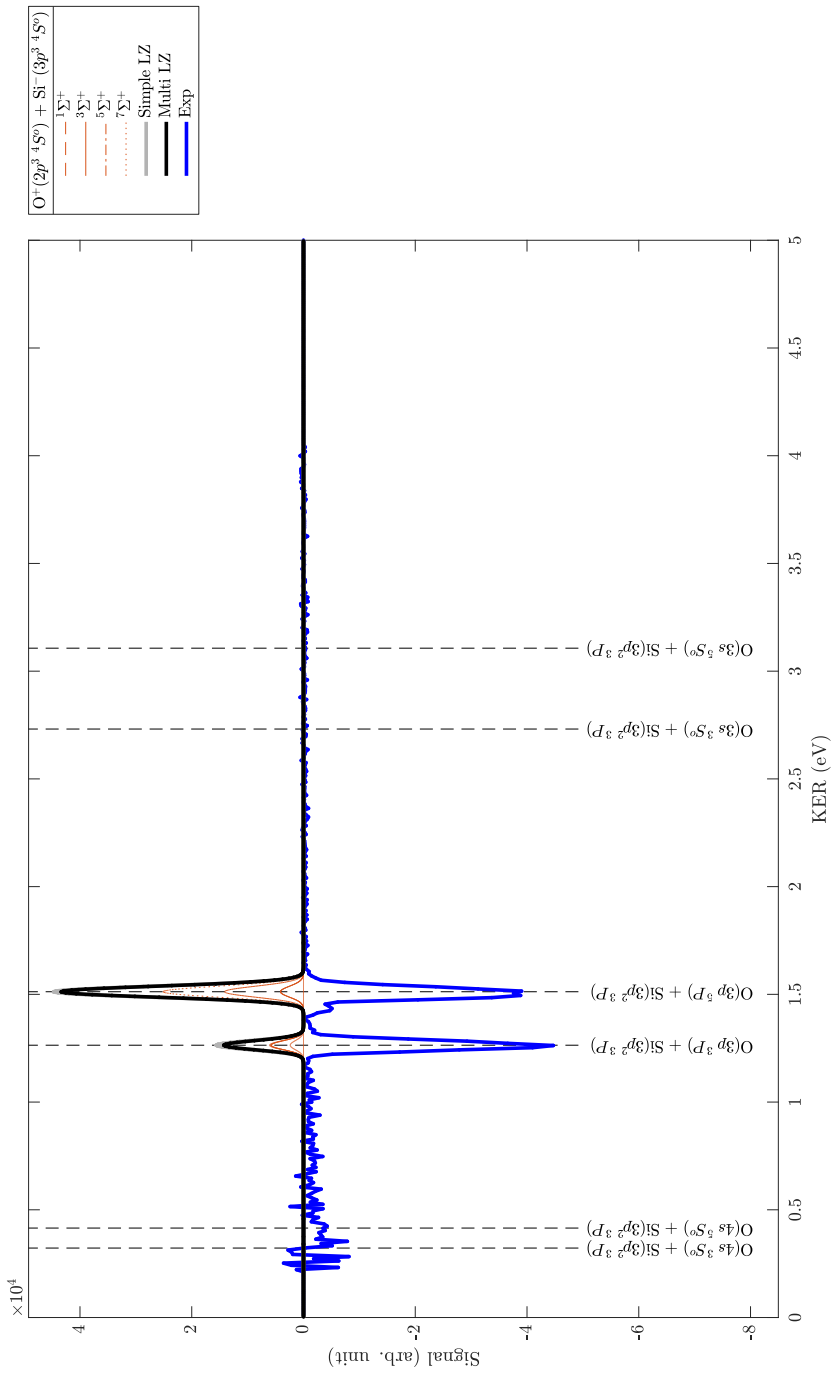

Figure F.91: Simulation: $O^+(^4S^o) + Si^-(^4S^o)$.

O	Si	$^1\Sigma^+$	$^3\Sigma^+$	$^5\Sigma^+$	$^7\Sigma^+$
$2p^4\,^3P$	$3p^2\,^3P$	9.471e-09	8.646e-09	6.697e-09	
$3s\,^5S^o$	$3p^2\,^3P$		2.035e-02	3.525e-02	4.985e-02
$3s\,^3S^o$	$3p^2\,^3P$	3.583e-02	3.271e-02	2.533e-02	
$3p\,^5P$	$3p^2\,^3P$		5.037e-04	8.724e-04	1.234e-03
$3p\,^3P$	$3p^2\,^3P$	4.524e-04	4.130e-04	3.199e-04	
$4s\,^5S^o$	$3p^2\,^3P$		2.483e-09	4.301e-09	6.083e-09
$4s\,^3S^o$	$3p^2\,^3P$	1.808e-11	1.650e-11	1.278e-11	

Table F.98: Interaction potentials E_{ic} (a.u.): $O^+(^4S^o)$ + $Si^-(^4S^o)$.

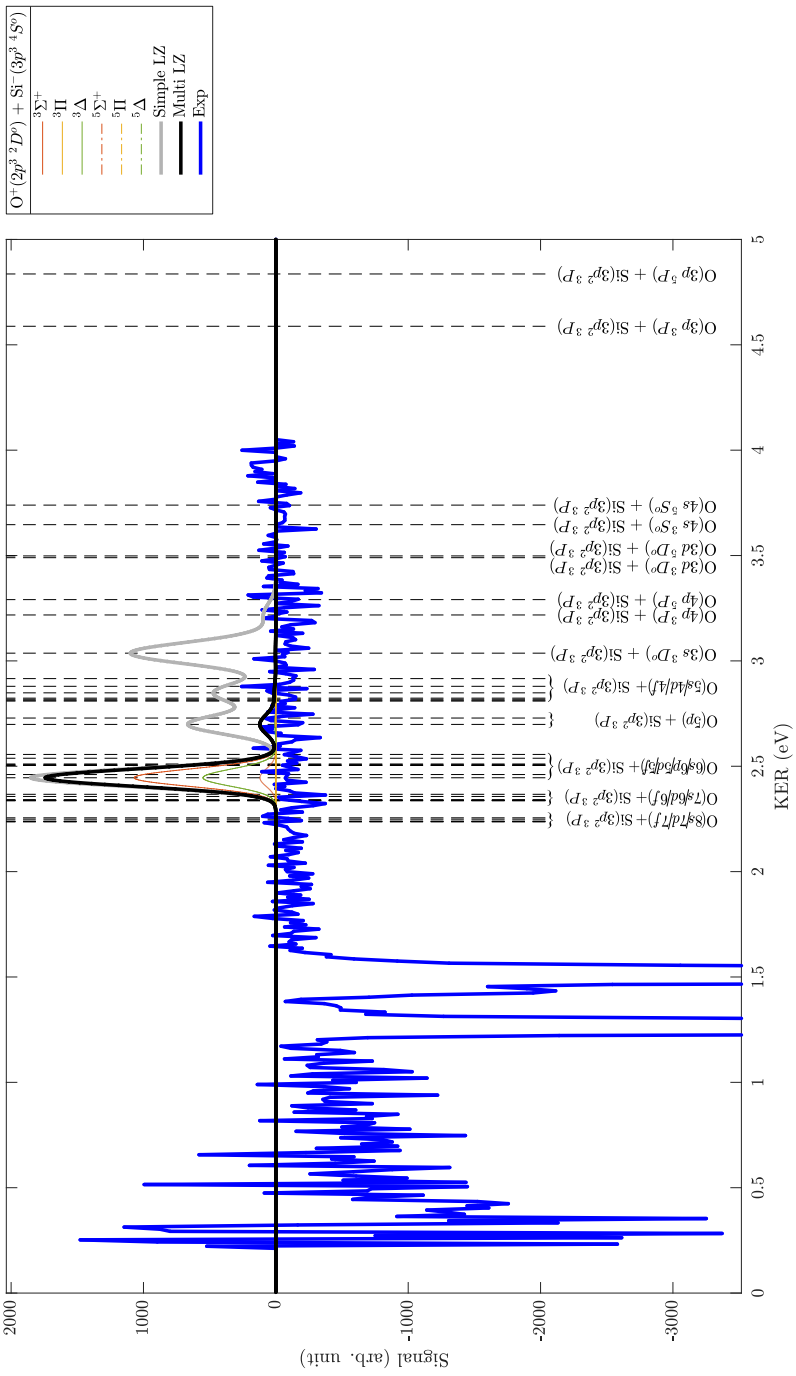

Figure F.92: Simulation: $O^+(^2D^o) + Si^-(^4S^o)$.

O	Si	$^3\Sigma^+$	$^3\Pi$	$^3\Delta$	$^5\Sigma^+$	$^5\Pi$	$^5\Delta$
$2p^4\ ^3P$	$3p^2\ ^3P$	3.073e-09	2.419e-09	6.131e-09	5.322e-09	4.191e-09	1.062e-08
$2p^4\ ^1D$	$3p^2\ ^3P$	1.418e-08	6.421e-09	6.073e-09			
$3p\ ^3P$	$3p^2\ ^3P$	1.188e-02	2.843e-02	2.120e-02	2.057e-02	4.924e-02	3.672e-02
$3d\ ^3D^o$	$3p^2\ ^3P$	2.849e-10	5.301e-10	6.518e-10	4.935e-10	9.181e-10	1.129e-09
$4p\ ^3P$	$3p^2\ ^3P$	4.960e-03	1.530e-02	7.995e-03	8.591e-03	2.650e-02	1.385e-02
$3s\ ^3D^o$	$3p^2\ ^3P$	2.735e-03	9.282e-03	2.682e-02	4.737e-03	1.608e-02	4.645e-02
$3s\ ^1D^o$	$3p^2\ ^3P$	3.286e-03	1.115e-02	3.222e-02			
$4d\ ^3D^o$	$3p^2\ ^3P$	1.786e-10	3.315e-10	4.974e-10	3.093e-10	5.741e-10	8.615e-10
$4f\ ^3F$	$3p^2\ ^3P$	4.156e-10	4.226e-10	4.293e-10	7.198e-10	7.319e-10	7.436e-10
$5p\ ^3P$	$3p^2\ ^3P$	2.998e-03	1.027e-02	4.499e-03	5.193e-03	1.779e-02	7.793e-03
$5d\ ^3D^o$	$3p^2\ ^3P$	1.344e-10	2.490e-10	4.158e-10	2.328e-10	4.313e-10	7.203e-10
$5f\ ^3F$	$3p^2\ ^3P$	3.106e-10	3.159e-10	3.371e-10	5.379e-10	5.472e-10	5.838e-10
$6p\ ^3P$	$3p^2\ ^3P$	2.204e-03	7.958e-03	3.157e-03	3.818e-03	1.378e-02	5.468e-03
$6d\ ^3D^o$	$3p^2\ ^3P$	1.120e-10	2.073e-10	3.687e-10	1.940e-10	3.591e-10	6.385e-10
$6f\ ^3F$	$3p^2\ ^3P$	2.575e-10	2.620e-10	2.887e-10	4.461e-10	4.539e-10	5.001e-10
$6g\ ^3G^o$	$3p^2\ ^3P$	4.197e-10	3.062e-10	3.586e-10	7.269e-10	5.303e-10	6.211e-10
$7d\ ^3D^o$	$3p^2\ ^3P$	9.918e-11	1.834e-10	3.393e-10	1.718e-10	3.176e-10	5.877e-10
$7f\ ^3F$	$3p^2\ ^3P$	2.272e-10	2.312e-10	2.603e-10	3.935e-10	4.004e-10	4.509e-10

Table F.99: Interaction potentials E_{ic} (a.u.): $O^+(^2D^o)$ + $Si^-(^4S^o)$.

F.6.4 Carbon

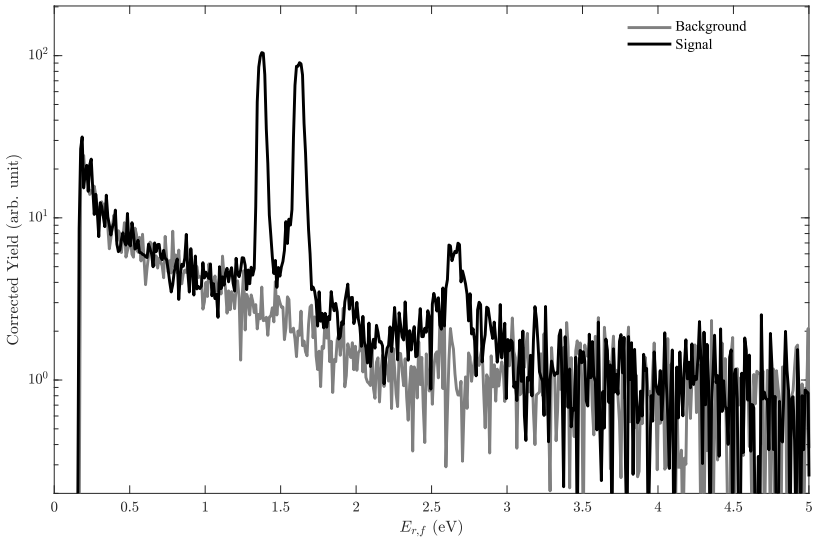

Figure F.93: Experiment: $O^+ + C^- \rightarrow O + C$.

O^+ beam	
Beam energy:	7,500 eV
Ion source:	ECR (CO)
C^- beam	
Beam energy:	6,500 eV
Ion source:	Sputtering (graphite)
Mean collision energy:	$\sim$ 5 meV

Table F.100: $O^+ + C^-$ MN experimental setup parameters.

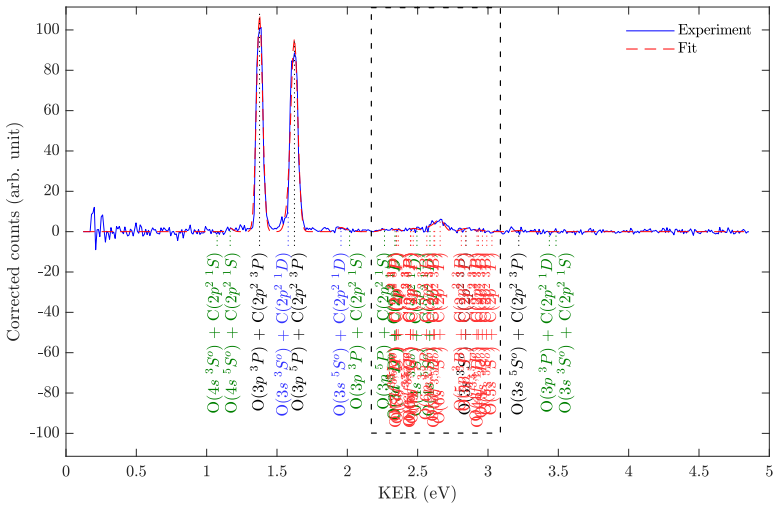

Figure F.94: Branching ratio fit: $O^+(^4S^o) + C^-(^4S^o)$. The color code for the products is given in table F.1. A zoom of the framed area is given in figure F.95.

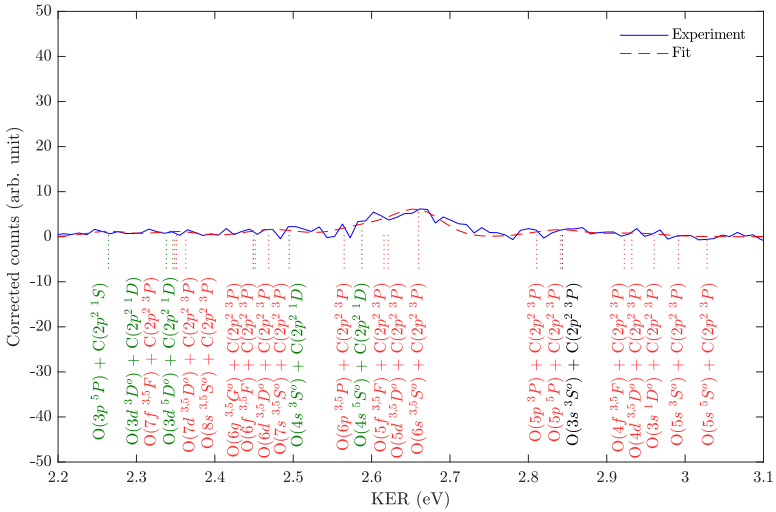

Figure F.95: Branching ratio fit: $O^+(^4S^o) + C^-(^4S^o)$ – zoom. The color code for the products is given in table F.1.

	$C^-(^4S^o)$	
	$C(^3P)$	$C(^1D)$
$O(3s\ ^5S^o)$	0,003(1)	0,010(1)
$O(3s\ ^3S^o)$	0,006(85)	0,042(2)
$O(3p\ ^5P)$	0,415(6)	
$O(3p\ ^3P)$	0,436(6)	

Table F.101: Branching ratio fit: $O^+(^4S^o)$ + $C^-(^4S^o)$.

Cation	Anion	Center-of-mass collision energy (eV)					
O	C	0.002	0.005	0.02	0.05	0.2	0.5
$2p^4\ ^3P$	$2p^2\ ^3P$	3.49e-81	1.49e-81	5.21e-82	4.04e-82	2.39e-81	2.78e-79
$3s\ ^5S^o$	$2p^2\ ^3P$	6.38e-71	2.74e-71	9.66e-72	7.64e-72	4.96e-71	6.96e-69
$3s\ ^3S^o$	$2p^2\ ^3P$	1.03e-40	4.25e-41	1.26e-41	7.14e-42	9.29e-42	7.15e-41
$3p\ ^5P$	$2p^2\ ^3P$	4.82e-12	1.93e-12	4.9e-13	2.01e-13	5.7e-14	2.82e-14
$3p\ ^3P$	$2p^2\ ^3P$	4.67e-12	1.87e-12	4.72e-13	1.92e-13	5.26e-14	2.45e-14
$4s\ ^5S^o$	$2p^2\ ^3P$	7.5e-16	3.01e-16	7.63e-17	3.14e-17	8.84e-18	4.22e-18
$4s\ ^3S^o$	$2p^2\ ^3P$	2.36e-18	9.46e-19	2.41e-19	9.97e-20	2.88e-20	1.41e-20
$3d\ ^5D^o$	$2p^2\ ^3P$	2.83e-28	1.14e-28	2.83e-29	1.12e-29	2.79e-30	1.06e-30
$3d\ ^3D^o$	$2p^2\ ^3P$	4.91e-30	1.99e-30	3.14e-31	1.38e-31	2.8e-32	1.46e-32

Table F.102: Partial cross section (cm^2) for the $O^+(^4S^o)$+$C^-(^4S^o)$ MN reaction computed with the ACAM.

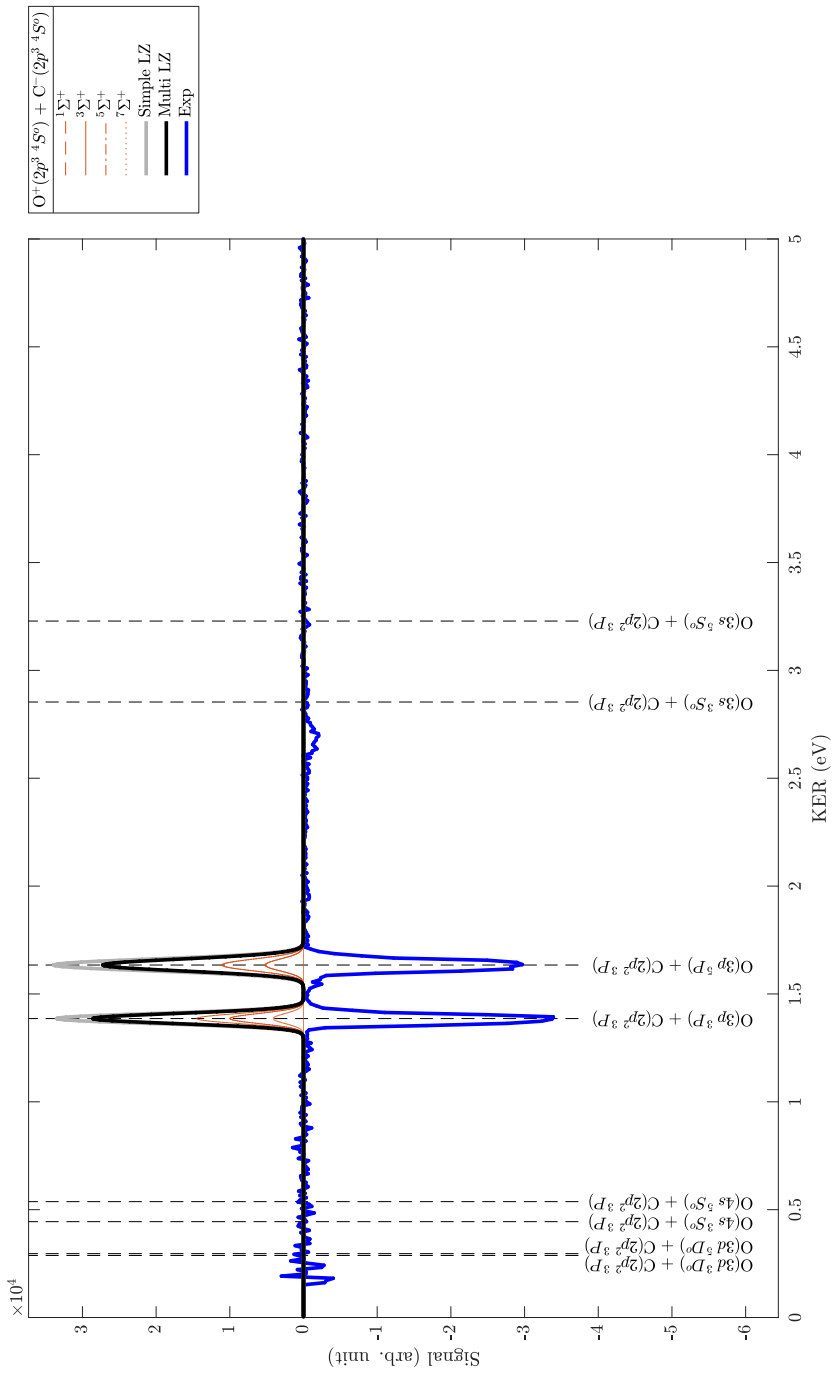

Figure F.96: Simulation: $O^+(^4S^o) + C^-(^4S^o)$.

O	C	$^1\Sigma^+$	$^3\Sigma^+$	$^5\Sigma^+$	$^7\Sigma^+$
$2p^4\,^3P$	$2p^2\,^3P$	6.935e-09	6.331e-09	4.904e-09	
$3s\,^5S^o$	$2p^2\,^3P$		1.622e-02	2.810e-02	3.974e-02
$3s\,^3S^o$	$2p^2\,^3P$	2.965e-02	2.706e-02	2.096e-02	
$3p\,^5P$	$2p^2\,^3P$		6.309e-04	1.093e-03	1.545e-03
$3p\,^3P$	$2p^2\,^3P$	6.866e-04	6.268e-04	4.855e-04	
$4s\,^5S^o$	$2p^2\,^3P$		2.974e-07	5.151e-07	7.285e-07
$4s\,^3S^o$	$2p^2\,^3P$	3.788e-08	3.458e-08	2.679e-08	

Table F.103: Interaction potentials $E_{i\mathcal{C}}$ (a.u.): $O^+(^4S^o) + C^-(^4S^o)$.

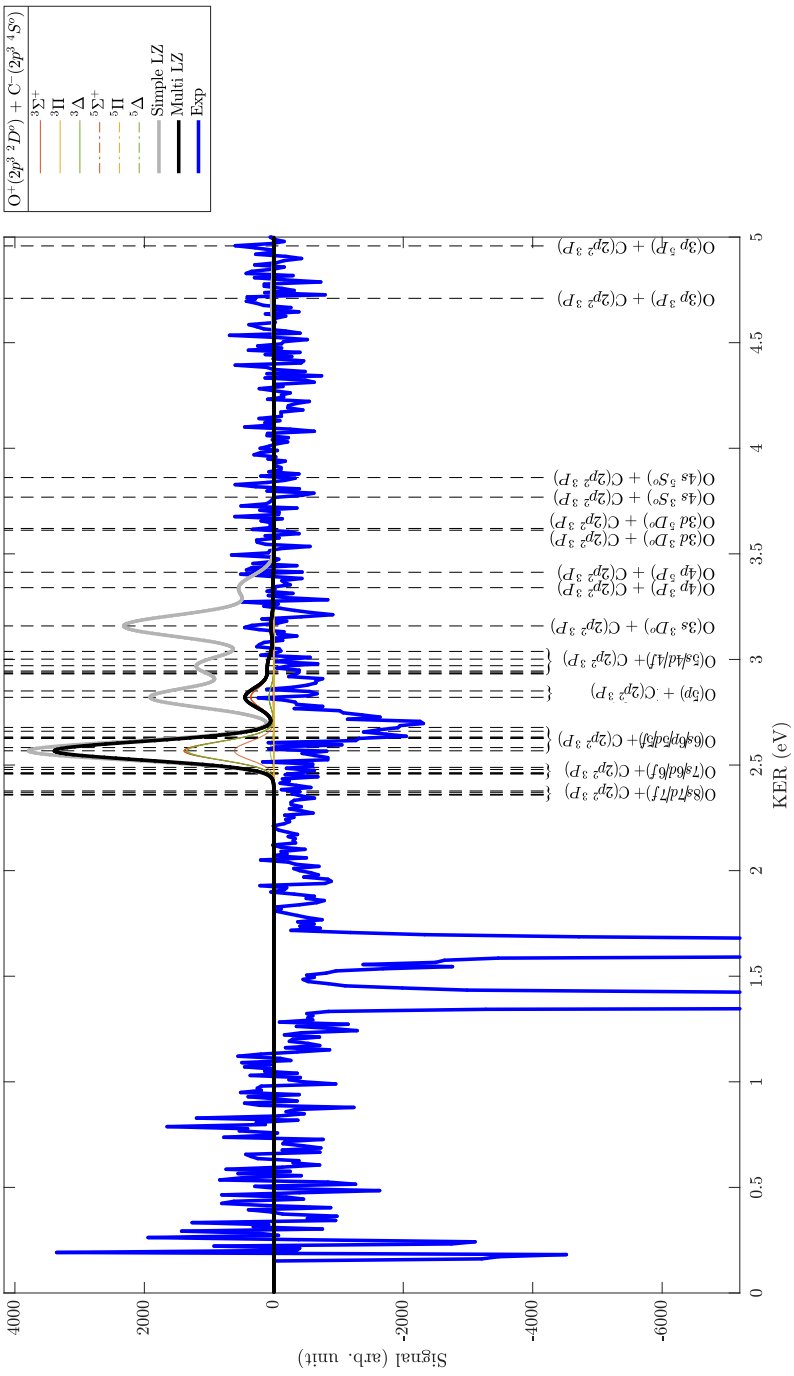

Figure F.97: Simulation: $O^+(^2D^o) + C^-(^4S^o)$.

O	C	$^3\Sigma^+$	$^3\Pi$	$^3\Delta$	$^5\Sigma^+$	$^5\Pi$	$^5\Delta$
$2p^4\,^3P$	$2p^2\,^3P$	2.230e-09	1.666e-09	4.456e-09	3.863e-09	2.886e-09	7.718e-09
$2p^4\,^1D$	$2p^2\,^3P$	1.035e-08	4.680e-09	4.203e-09			
$3p\,^3P$	$2p^2\,^3P$	9.314e-03	2.105e-02	1.688e-02	1.613e-02	3.646e-02	2.923e-02
$3d\,^3D^o$	$2p^2\,^3P$	2.386e-10	4.442e-10	5.065e-10	4.133e-10	7.694e-10	8.773e-10
$4p\,^3P$	$2p^2\,^3P$	4.140e-03	1.209e-02	6.867e-03	7.170e-03	2.094e-02	1.189e-02
$3s\,^3D^o$	$2p^2\,^3P$	2.193e-03	7.444e-03	2.151e-02	3.799e-03	1.289e-02	3.725e-02
$3s\,^1D^o$	$2p^2\,^3P$	2.684e-03	9.109e-03	2.632e-02			
$4d\,^3D^o$	$2p^2\,^3P$	1.589e-10	2.952e-10	4.081e-10	2.752e-10	5.113e-10	7.069e-10
$4f\,^3F$	$2p^2\,^3P$	3.721e-10	3.783e-10	3.718e-10	6.445e-10	6.553e-10	6.439e-10
$5p\,^3P$	$2p^2\,^3P$	2.624e-03	8.535e-03	4.092e-03	4.544e-03	1.478e-02	7.087e-03
$5d\,^3D^o$	$2p^2\,^3P$	1.248e-10	2.315e-10	3.549e-10	2.161e-10	4.010e-10	6.147e-10
$5f\,^3F$	$2p^2\,^3P$	2.907e-10	2.956e-10	3.030e-10	5.034e-10	5.120e-10	5.248e-10
$6p\,^3P$	$2p^2\,^3P$	1.994e-03	6.849e-03	2.988e-03	3.454e-03	1.186e-02	5.175e-03
$6d\,^3D^o$	$2p^2\,^3P$	1.071e-10	1.985e-10	3.234e-10	1.855e-10	3.439e-10	5.601e-10
$6f\,^3F$	$2p^2\,^3P$	2.485e-10	2.528e-10	2.664e-10	4.305e-10	4.378e-10	4.614e-10
$6g\,^3G^o$	$2p^2\,^3P$	4.054e-10	2.957e-10	3.409e-10	7.022e-10	5.121e-10	5.905e-10
$7d\,^3D^o$	$2p^2\,^3P$	9.681e-11	1.793e-10	3.035e-10	1.677e-10	3.106e-10	5.256e-10
$7f\,^3F$	$2p^2\,^3P$	2.240e-10	2.278e-10	2.446e-10	3.879e-10	3.946e-10	4.237e-10

Table F.104: Interaction potentials E_{ic} (a.u.): $O^+(^2D^o) + C^-(^4S^o)$.

Possible link between Rydberg series of the neutralized anion and transfer ionization

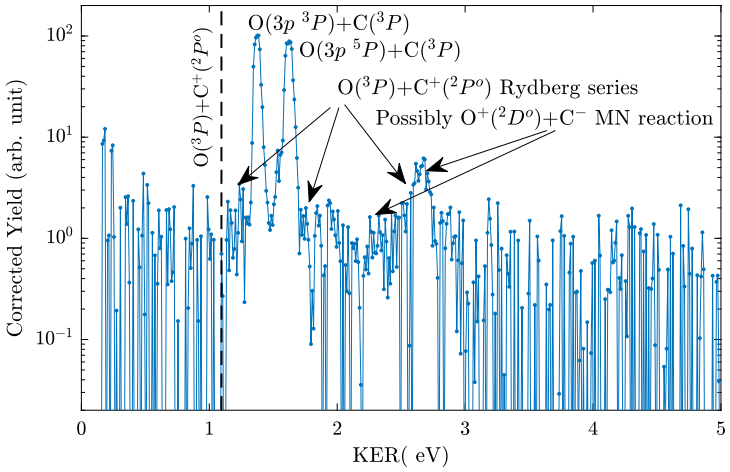

Figure F.98: $O^+ + C^- \rightarrow O + C$ kinetic energy release spectra at $\langle E_{r,i} \rangle = 5$ meV.

It was stated that the appearance of Rydberg series in O^++C^- MN spectra (figure F.98) might be a sign of a possible transfer ionization process. Following the description given in [267], the transfer ionization follows the sequence shown in figure F.99;

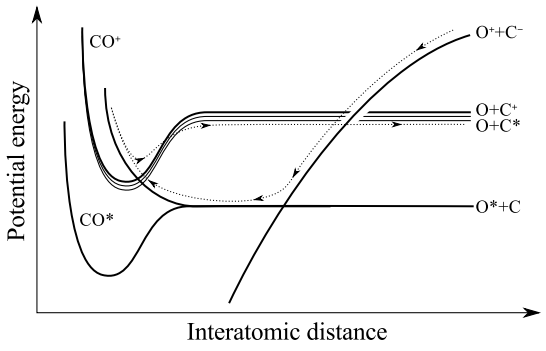

Figure F.99: Sketch of the potential energy curves involved in the O^++C^- transfer ionization.

This process happens at short interatomic distance meaning that it is far less probable than the mutual neutralization process. In their study of the H^++H^- transfer ionization, Schön *et al.* [267] show that this process has a cross section two orders of magnitude lower than mutual neutralization. It corresponds to the signal ratio measured for O^++C^- (figure F.98).

F.6.5 Oxygen

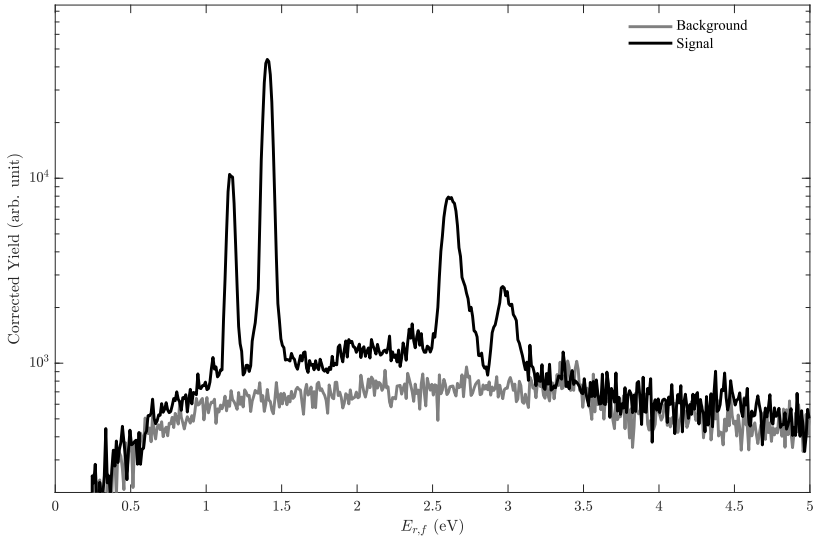

Figure F.100: Experiment: $O^+ + O^- \rightarrow O + O$.

O^+ beam	
Beam energy:	8,700 eV
Ion source:	ECR (CO)
O^- beam	
Beam energy:	7,700 eV
Ion source:	Sputtering (Fe_2O_3)
Mean collision energy:	$\sim$ 7 meV

Table F.105: $O^+ + O^-$ MN experimental setup parameters.

	$O^-(^2P^o)$ $O(^3P)$
$O(3s\ ^5S^o)$	0,033(1)
$O(3s\ ^3S^o)$	0,114(1)
$O(3p\ ^5P)$	0,579(3)
$O(3p\ ^3P)$	0,120(1)
$O(4s\ ^5S^o)$	0,001(1)

Table F.106: Branching ratio fit: $O^+(^4S^o) + O^-(^2P^o)$.

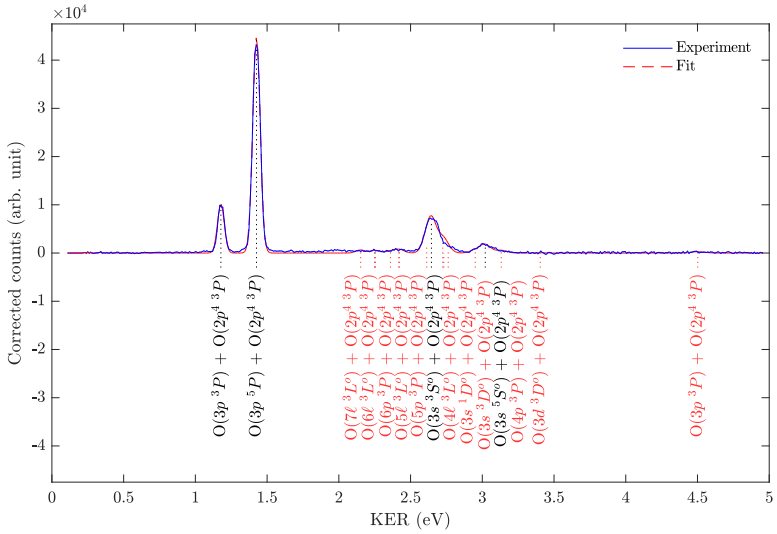

Figure F.101: Branching ratio fit: $O^+(^4S^o) + O^-(^2P^o)$. The color code for the products is given in table F.1.

Cation O	Anion O	Center-of-mass collision energy (eV) 0.002	0.005	0.02	0.05	0.2	0.5
$2p^4\ ^3P$	$2p^4\ ^3P$	4.4e-26	1.76e-26	4.4e-27	1.76e-27	4.44e-28	1.8e-28
$2p^4\ ^3P$	$2p^4\ ^1D$	1.76e-27	7.05e-28	1.76e-28	7.06e-29	1.78e-29	7.24e-30
$2p^4\ ^3P$	$2p^4\ ^1S$	7.42e-28	2.97e-28	7.43e-29	2.98e-29	7.52e-30	3.07e-30
$3s\ ^5S^o$	$2p^4\ ^3P$	1.56e-17	6.29e-18	1.63e-18	7.03e-19	2.51e-19	1.91e-19
$3s\ ^5S^o$	$2p^4\ ^1D$	1.3e-16	5.21e-17	1.31e-17	5.32e-18	1.42e-18	6.32e-19
$3s\ ^3S^o$	$2p^4\ ^3P$	5.78e-13	2.32e-13	5.86e-14	2.39e-14	6.64e-15	3.21e-15
$3s\ ^3S^o$	$2p^4\ ^1D$	6.72e-22	2.69e-22	6.81e-23	2.78e-23	7.64e-24	3.54e-24
$3p\ ^5P$	$2p^4\ ^3P$	9.33e-13	3.73e-13	9.39e-14	3.8e-14	1e-14	4.38e-15
$3p\ ^3P$	$2p^4\ ^3P$	9.71e-14	3.89e-14	9.79e-15	3.96e-15	1.05e-15	4.65e-16
$4s\ ^5S^o$	$2p^4\ ^3P$	2.83e-25	1.14e-25	2.91e-26	1.21e-26	3.58e-27	1.79e-27

Table F.107: Partial cross section (cm^2) for the $O^+(^4S^o)$+$O^-(^2P^o)$ MN reaction computed with the ACAM.

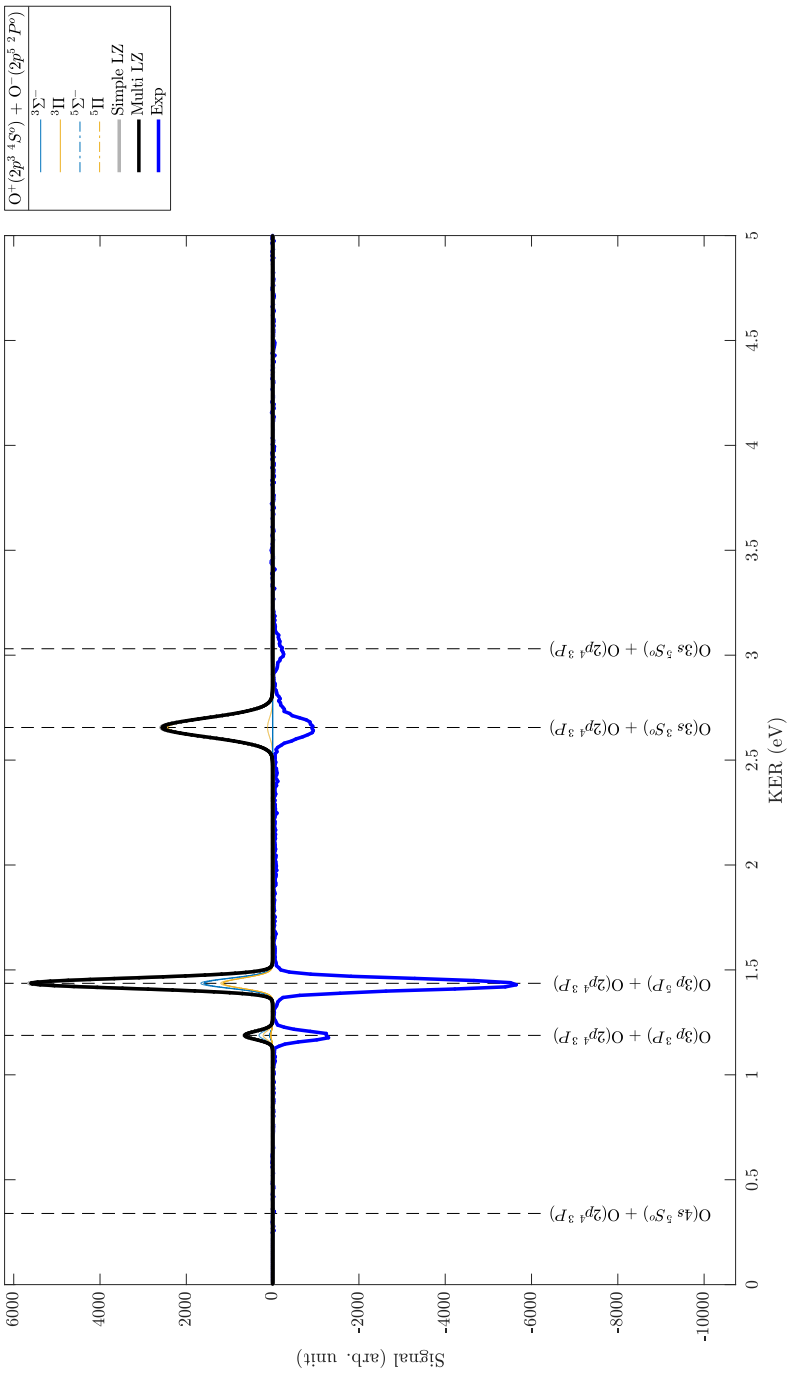

Figure F.102: Simulation: $O^+(^4S^o) + O^-(^2P^o)$.

O	O	$^3\Sigma^-$	$^3\Pi$	$^5\Sigma^-$	$^5\Pi$
$2p^4\ ^3P$	$2p^4\ ^3P$	5.522e-10	3.219e-10	9.564e-10	5.575e-10
$3s\ ^5S^o$	$2p^4\ ^3P$		4.342e-03		3.363e-03
$3s\ ^3S^o$	$2p^4\ ^3P$		1.360e-03		2.355e-03
$3p\ ^5P$	$2p^4\ ^3P$	8.305e-05	4.841e-05	6.433e-05	3.750e-05
$3p\ ^3P$	$2p^4\ ^3P$	1.068e-05	6.227e-06	1.850e-05	1.079e-05
$4s\ ^5S^o$	$2p^4\ ^3P$		3.071e-12		2.379e-12

Table F.108: Interaction potentials E_{ic} (a.u.): $O^+(^4S^o) + O^-(^2P^o)$.

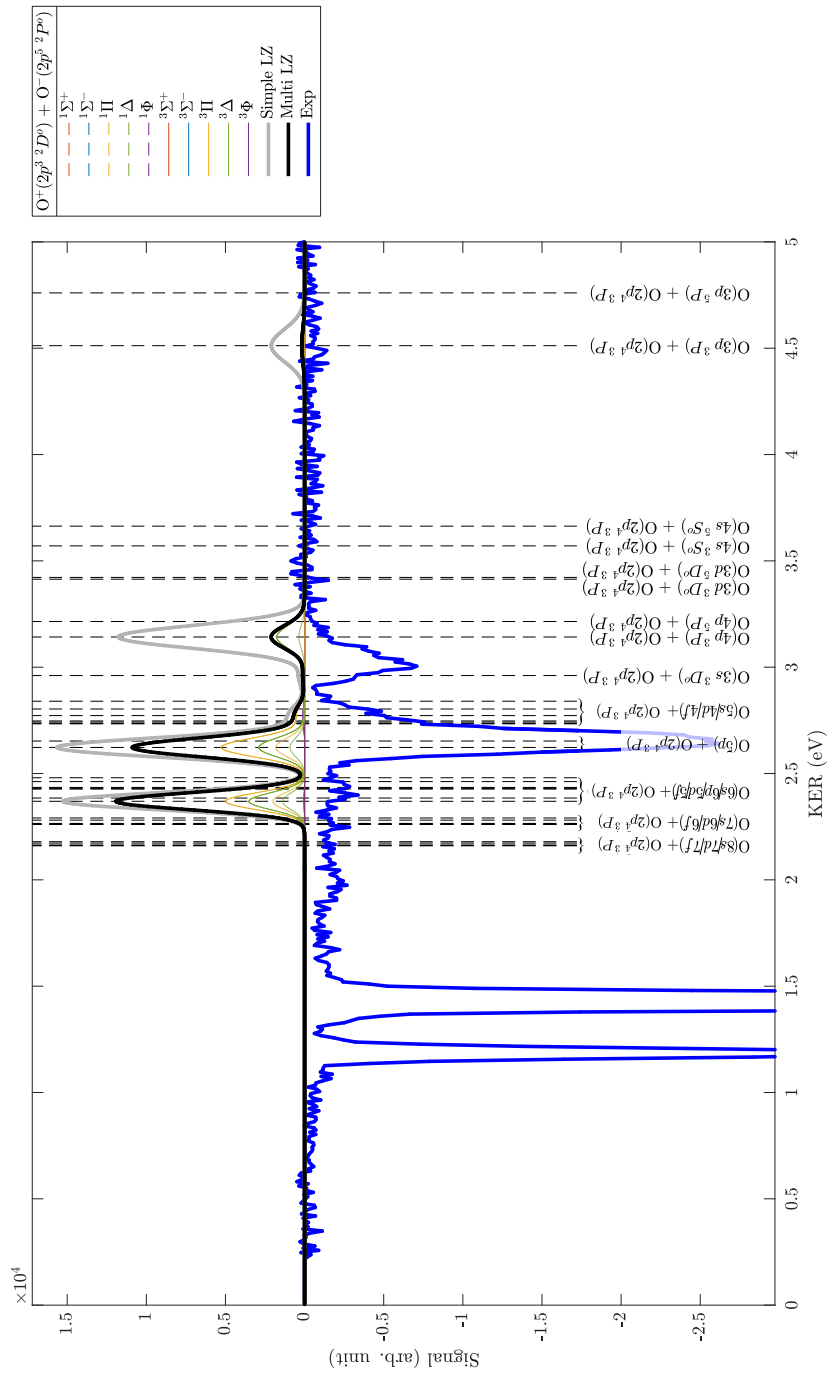

Figure F.103: Simulation: $O^+(^2D^o) + O^-(^2P^o)$.

O	O	$^1\Sigma^+$	$^1\Sigma^-$	$^1\Pi$	$^1\Delta$	$^1\Phi$	$^3\Sigma^+$	$^3\Sigma^-$	$^3\Pi$	$^3\Delta$	$^3\Phi$
$2p^4\ ^3P$	$2p^4\ ^3P$	1.985e-09	1.934e-09	2.162e-09	2.293e-09		1.621e-09	1.579e-09	1.765e-09	1.872e-09	
$2p^4\ ^1D$	$2p^4\ ^3P$						1.396e-09	7.320e-10	9.569e-10	2.440e-10	9.637e-10
$3p\ ^3P$	$2p^4\ ^3P$	2.164e-02	2.159e-02	7.042e-03	7.664e-03		1.767e-02	1.763e-02	5.750e-03	6.258e-03	
$3d\ ^3D^o$	$2p^4\ ^3P$	2.423e-10	2.423e-10	2.215e-10	4.520e-11	2.361e-10	1.979e-10	1.979e-10	1.808e-10	3.690e-11	1.928e-10
$4p\ ^3P$	$2p^4\ ^3P$	1.112e-02	1.111e-02	2.522e-03	2.824e-03		9.082e-03	9.072e-03	2.059e-03	2.305e-03	
$3s\ ^3D^o$	$2p^4\ ^3P$	1.966e-02	1.966e-02	8.294e-03	2.744e-04	9.595e-03	1.606e-02	1.606e-02	6.772e-03	2.240e-04	7.835e-03
$3s\ ^1D^o$	$2p^4\ ^3P$						9.524e-03	9.524e-03	4.017e-03	1.329e-04	4.647e-03
$4d\ ^3D^o$	$2p^4\ ^3P$	1.786e-10	1.786e-10	1.589e-10	2.679e-11	1.741e-10	1.458e-10	1.458e-10	1.297e-10	2.187e-11	1.422e-10
$4f\ ^3F$	$2p^4\ ^3P$	1.439e-10	1.451e-10	2.071e-10	1.076e-10	1.269e-10	1.175e-10	1.185e-10	1.691e-10	8.787e-11	1.036e-10
$5p\ ^3P$	$2p^4\ ^3P$	7.210e-03	7.204e-03	1.364e-03	1.562e-03		5.887e-03	5.882e-03	1.114e-03	1.276e-03	
$5d\ ^3D^o$	$2p^4\ ^3P$	1.454e-10	1.454e-10	1.279e-10	1.936e-11	1.417e-10	1.187e-10	1.187e-10	1.044e-10	1.580e-11	1.157e-10
$5f\ ^3F$	$2p^4\ ^3P$	1.173e-10	1.180e-10	1.672e-10	7.785e-11	9.432e-11	9.578e-11	9.638e-11	1.366e-10	6.357e-11	7.701e-11
$6p\ ^3P$	$2p^4\ ^3P$	5.444e-03	5.441e-03	9.304e-04	1.083e-03		4.445e-03	4.443e-03	7.596e-04	8.844e-04	
$6d\ ^3D^o$	$2p^4\ ^3P$	1.264e-10	1.264e-10	1.106e-10	1.568e-11	1.233e-10	1.032e-10	1.032e-10	9.032e-11	1.280e-11	1.007e-10
$6f\ ^3F$	$2p^4\ ^3P$	1.021e-10	1.027e-10	1.449e-10	6.310e-11	7.788e-11	8.337e-11	8.382e-11	1.183e-10	5.152e-11	6.359e-11
$6g\ ^3G^o$	$2p^4\ ^3P$	8.853e-11	9.040e-11	1.701e-10	9.983e-11	6.975e-11	7.229e-11	7.381e-11	1.389e-10	8.151e-11	5.695e-11
$7d\ ^3D^o$	$2p^4\ ^3P$	1.148e-10	1.148e-10	1.001e-10	1.360e-11	1.119e-10	9.370e-11	9.370e-11	8.175e-11	1.111e-11	9.139e-11
$7f\ ^3F$	$2p^4\ ^3P$	9.275e-11	9.321e-11	1.313e-10	5.477e-11	6.847e-11	7.573e-11	7.611e-11	1.072e-10	4.472e-11	5.591e-11

Table F.109: Interaction potentials E_{ic} (a.u.): $O^+(^2D^o) + O^-(^2P^o)$.

F.6.6 Sulfur

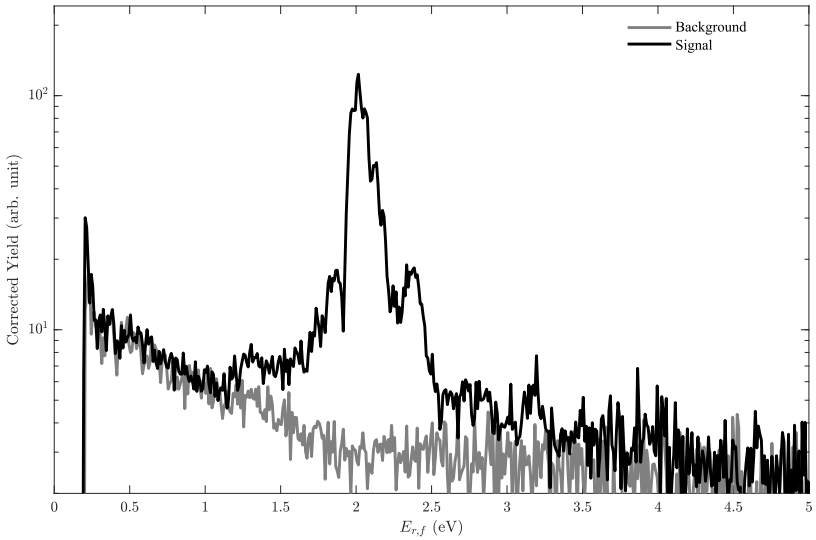

Figure F.104: Experiment: $O^+ + S^- \rightarrow O + S$.

O^+ beam	
Beam energy:	5,000 eV
Ion source:	ECR (CO)
S^- beam	
Beam energy:	11,500 eV
Ion source:	Sputtering (FeS)
Mean collision energy:	$\sim$ 5 meV

Table F.110: $O^+ + S^-$ MN experimental setup parameters.

	$S^-(^2P^o)$ $S(3p^4\ ^3P)$	$S(3p^4\ ^1D)$	$S(4s\ ^5S^o)$	$S(4s\ ^3S^o)$	$S(4p\ ^5P)$	$S(4p\ ^3P)$
$O(2p^4\ ^3P)$				0,008	0,009	0,009
$O(2p^4\ ^1D)$			0,018	0,021	0,067	0,028
$O(2p^4\ ^1S)$			0,003	0,001		
$O(3s\ ^5S^o)$	0,105	0,017				
$O(3s\ ^3S^o)$	0,697	0,001				
$O(3p\ ^5P)$	0,008					
$O(3p\ ^3P)$	0,009					

Table F.111: Branching ratio fit E_{ic} (a.u.): $O^+(^4S^o)$ + $S^-(^2P^o)$.

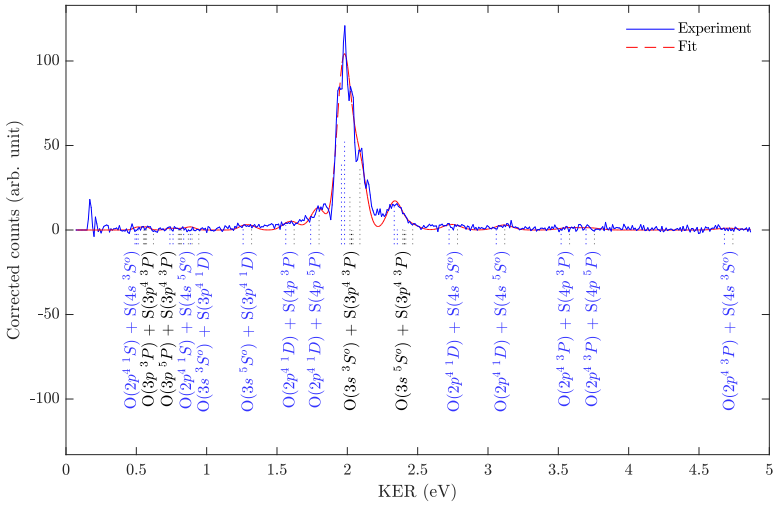

Figure F.105: Branching ratio fit: $O^+(^4S^o)$ + $S^-(^2P^o)$. The color code for the products is given in table F.1.

Cation O	Anion S	Center-of-mass collision energy (eV) 0.002	0.005	0.02	0.05	0.2	0.5
$2p^4\ ^3P$	$3p^4\ ^3P$	6e-26	2.4e-26	6.01e-27	2.41e-27	6.07e-28	2.47e-28
$2p^4\ ^3P$	$3p^4\ ^1D$	4.6e-27	1.84e-27	4.6e-28	1.84e-28	4.65e-29	1.89e-29
$2p^4\ ^3P$	$3p^4\ ^1S$	2.26e-27	9.06e-28	2.27e-28	9.08e-29	2.29e-29	9.33e-30
$3s\ ^5S^o$	$3p^4\ ^3P$	1.11e-13	4.47e-14	1.14e-14	4.75e-15	1.44e-15	8.06e-16
$3s\ ^5S^o$	$3p^4\ ^1D$	1.36e-14	5.46e-15	1.37e-15	5.55e-16	1.47e-16	6.44e-17
$3s\ ^3S^o$	$3p^4\ ^3P$	3.85e-12	1.54e-12	3.89e-13	1.58e-13	4.29e-14	1.99e-14
$3s\ ^3S^o$	$3p^4\ ^1D$	8.51e-18	3.41e-18	8.59e-19	3.5e-19	9.44e-20	4.28e-20
$3p\ ^5P$	$3p^4\ ^3P$	2.16e-17	8.65e-18	2.18e-18	8.89e-19	2.41e-19	1.1e-19
$3p\ ^3P$	$3p^4\ ^3P$	6.26e-22	2.51e-22	6.36e-23	2.61e-23	7.29e-24	3.45e-24

Table F.112: Partial cross section (cm^2) for the $O^+(^4S^o)$+$S^-(^2P^o)$ MN reaction computed with the ACAM.

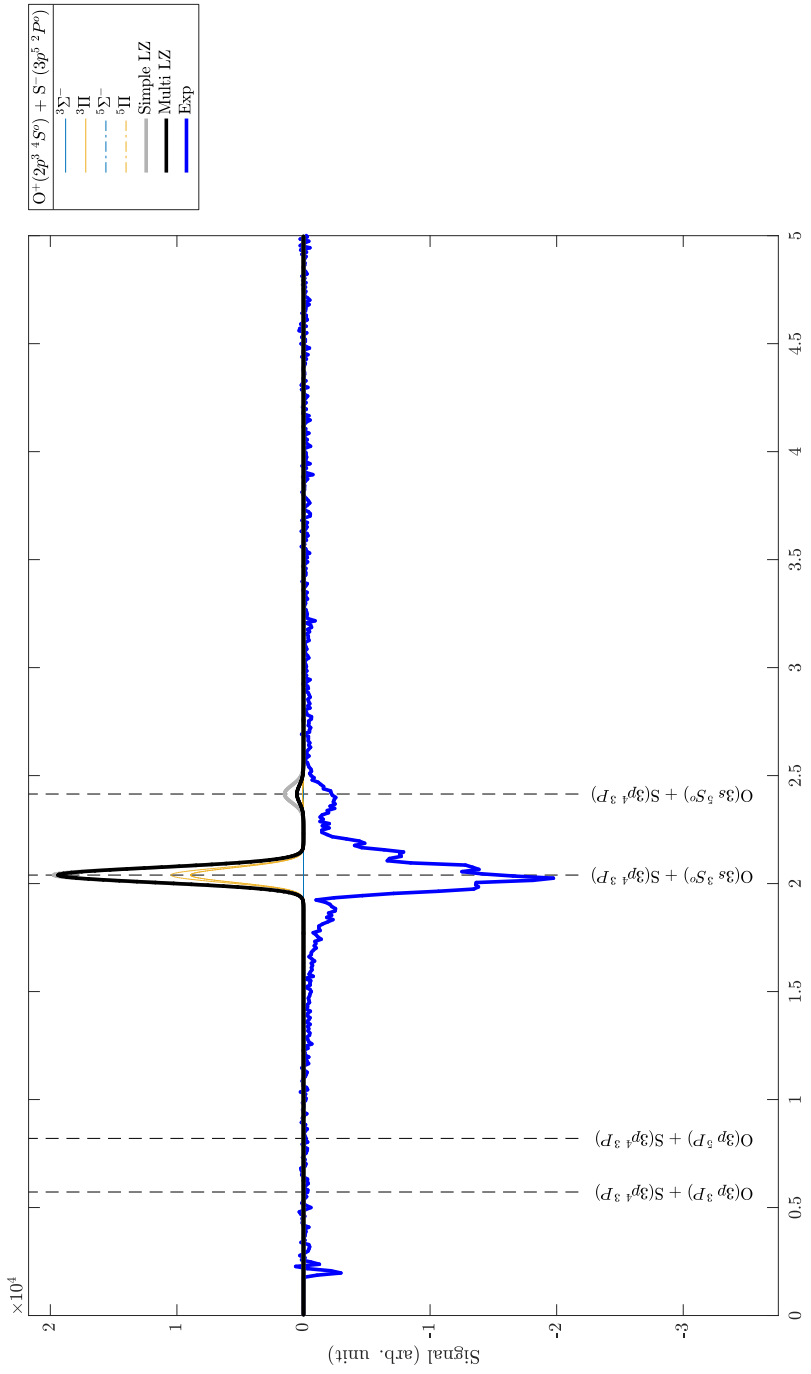

Figure F.106: Simulation: $O^+(^4S^o) + S^-(^2P^o)$.

O	S	$^3\Sigma^-$	$^3\Pi$	$^5\Sigma^-$	$^5\Pi$
$2p^4\,^3P$	$3p^4\,^3P$	1.158e-09	6.751e-10	2.006e-09	1.169e-09
$3s\,^5S^o$	$3p^4\,^3P$		4.061e-03		3.145e-03
$3s\,^3S^o$	$3p^4\,^3P$		9.025e-04		1.563e-03
$3p\,^5P$	$3p^4\,^3P$	2.850e-07	1.661e-07	2.207e-07	1.287e-07
$3p\,^3P$	$3p^4\,^3P$	4.655e-10	2.714e-10	8.063e-10	4.700e-10

Table F.113: Interaction potentials E_{ic} (a.u.): $O^+(^4S^o) + S^-(^2P^o)$.

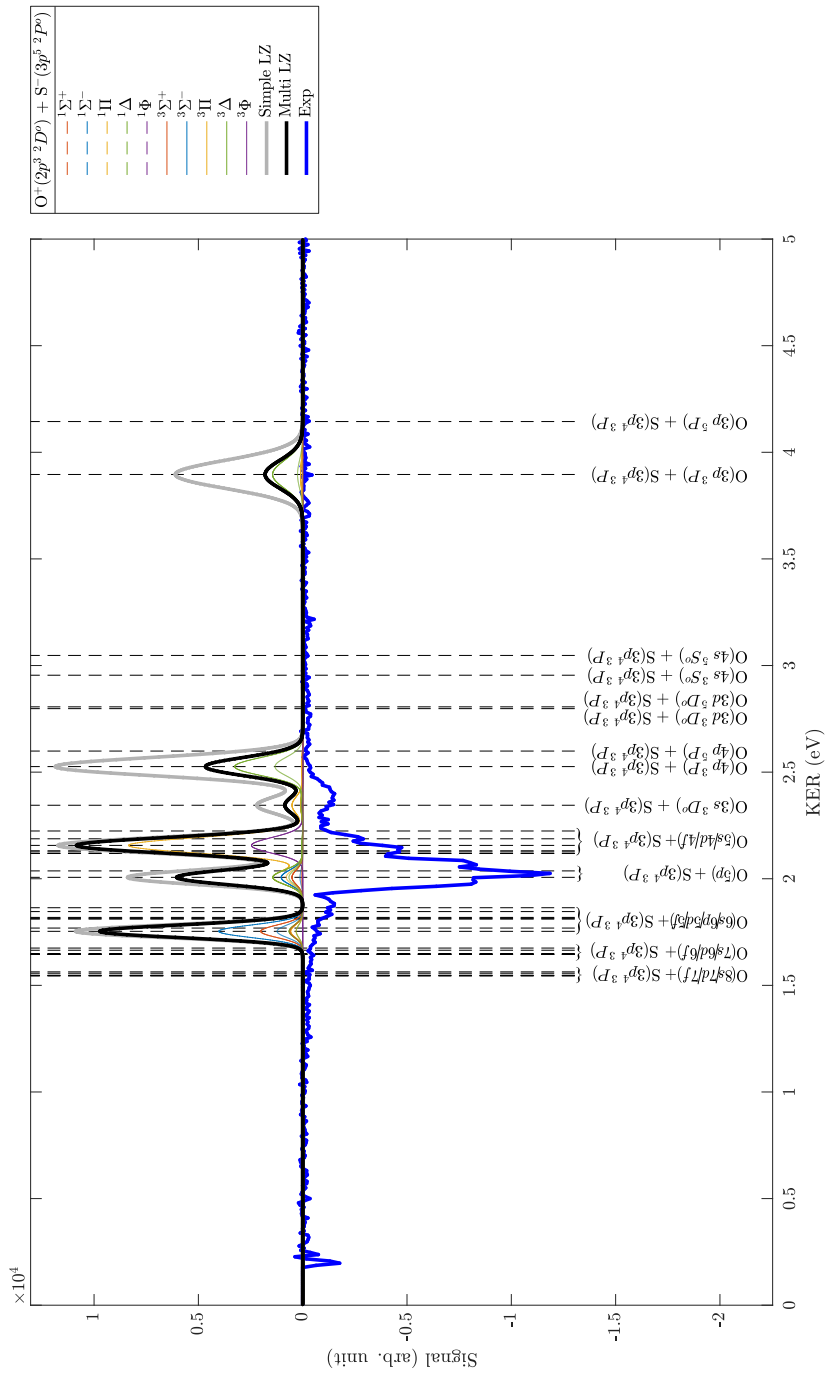

Figure F.107: Simulation: $O^+(^2D^o) + S^-(^2P^o)$.

O	S	$^1\Sigma^+$	$^1\Sigma^-$	$^1\Pi$	$^1\Delta$	$^1\Phi$	$^3\Sigma^+$	$^3\Sigma^-$	$^3\Pi$	$^3\Delta$	$^3\Phi$
$2p^4\ ^3P$	$3p^4\ ^3P$	2.499e-09	2.456e-09	2.214e-09	2.352e-09		2.040e-09	2.005e-09	1.808e-09	1.920e-09	
$2p^4\ ^1D$	$3p^4\ ^3P$						1.745e-09	8.999e-10	1.143e-09	2.443e-10	1.204e-09
$3p\ ^3P$	$3p^4\ ^3P$	1.712e-02	1.709e-02	4.038e-03	4.502e-03		1.397e-02	1.396e-02	3.297e-03	3.676e-03	
$3d\ ^3D^o$	$3p^4\ ^3P$	1.334e-10	1.334e-10	1.171e-10	1.716e-11	1.301e-10	1.089e-10	1.089e-10	9.559e-11	1.401e-11	1.062e-10
$4p\ ^3P$	$3p^4\ ^3P$	5.240e-03	5.238e-03	8.010e-04	9.526e-04		4.279e-03	4.277e-03	6.540e-04	7.778e-04	
$3s\ ^3D^o$	$3p^4\ ^3P$	8.136e-03	8.136e-03	3.432e-03	1.135e-04	3.970e-03	6.643e-03	6.643e-03	2.802e-03	9.270e-05	3.242e-03
$3s\ ^1D^o$	$3p^4\ ^3P$						3.338e-03	3.338e-03	1.408e-03	4.657e-05	1.629e-03
$4d\ ^3D^o$	$3p^4\ ^3P$	6.066e-11	6.066e-11	5.237e-11	5.949e-12	5.918e-11	4.953e-11	4.953e-11	4.276e-11	4.857e-12	4.832e-11
$4f\ ^3F$	$3p^4\ ^3P$	4.853e-11	4.869e-11	6.807e-11	2.357e-11	3.145e-11	3.962e-11	3.976e-11	5.557e-11	1.924e-11	2.568e-11
$5p\ ^3P$	$3p^4\ ^3P$	2.149e-03	2.149e-03	2.608e-04	3.285e-04		1.755e-03	1.754e-03	2.129e-04	2.682e-04	
$5d\ ^3D^o$	$3p^4\ ^3P$	3.355e-11	3.355e-11	2.879e-11	2.819e-12	3.273e-11	2.739e-11	2.739e-11	2.350e-11	2.302e-12	2.673e-11
$5f\ ^3F$	$3p^4\ ^3P$	2.691e-11	2.698e-11	3.755e-11	1.117e-11	1.591e-11	2.197e-11	2.203e-11	3.066e-11	9.123e-12	1.299e-11
$6p\ ^3P$	$3p^4\ ^3P$	1.138e-03	1.138e-03	1.206e-04	1.587e-04		9.291e-04	9.289e-04	9.844e-05	1.296e-04	
$6d\ ^3D^o$	$3p^4\ ^3P$	2.184e-11	2.184e-11	1.868e-11	1.669e-12	2.131e-11	1.783e-11	1.783e-11	1.525e-11	1.363e-12	1.740e-11
$6f\ ^3F$	$3p^4\ ^3P$	1.756e-11	1.759e-11	2.444e-11	6.616e-12	9.870e-12	1.433e-11	1.436e-11	1.995e-11	5.402e-12	8.059e-12
$6g\ ^3G^o$	$3p^4\ ^3P$	1.521e-11	1.533e-11	2.869e-11	1.046e-11	8.987e-12	1.242e-11	1.252e-11	2.343e-11	8.537e-12	7.338e-12
$7d\ ^3D^o$	$3p^4\ ^3P$	1.601e-11	1.601e-11	1.367e-11	1.150e-12	1.562e-11	1.307e-11	1.307e-11	1.116e-11	9.393e-13	1.275e-11
$7f\ ^3F$	$3p^4\ ^3P$	1.289e-11	1.292e-11	1.792e-11	4.562e-12	7.032e-12	1.053e-11	1.055e-11	1.463e-11	3.725e-12	5.741e-12

Table F.114: Interaction potentials E_{ic} (a.u.): $O^+(^2D^o) + S^-(^2P^o)$.

F.7 Neon

	$C^-(^4S^o)$ $C(^3P)$	$O^-(^2P^o)$ $O(^3P)$	$S^-(^2P^o)$ $S(^3P)$	$S(^1D)$
Ne($3s$)	0,009	0,025	0,211	0,789
Ne($3p$)	0,961	0,975		
Ne($4s$)	0,030			

Table F.115: Branching ratio fit: $Ne^+(^2P^o) + X^-$.

The one electron transfer model used was only developped under the *LS* coupling scheme. As the *JJ* coupling cannot be neglected when neon is used, the simulations below only show a simple statistical model using the following selection rule :

If the mutual neutralization reaction can be written as :

$$Ne^+(^2P^o_J) + X^- \rightarrow Ne^+(^2P^o_{J'}\ n\ell\ ^{2S'+1}K''_J) + X$$

where $n\ell$ is $3p$ for carbon and oxygen, and $3s$ for sulphur, then $m_J = m'_J$.

F.7.1 Carbon

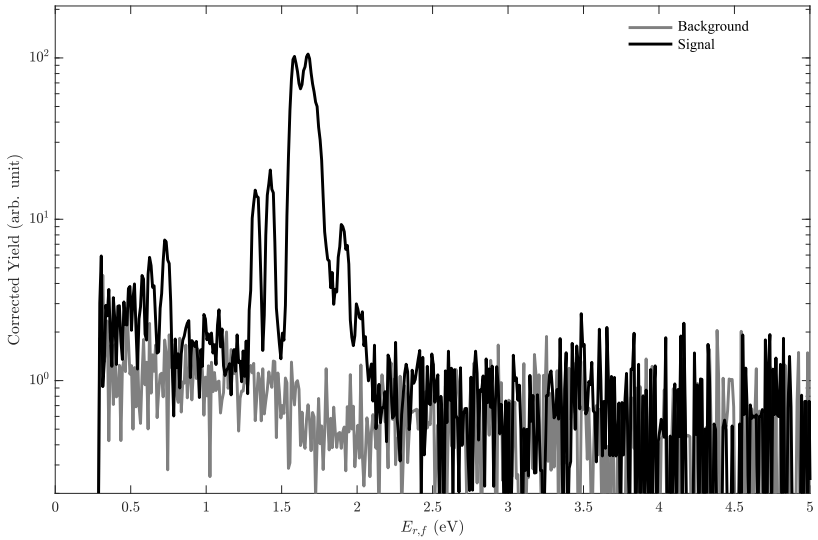

Figure F.108: Experiment: $Ne^+ + C^- \rightarrow Ne + C$ – full observation length.

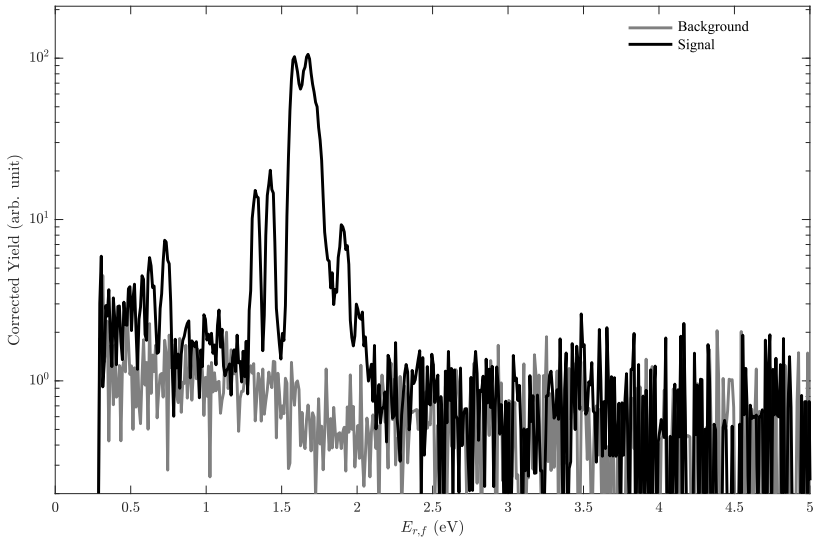

Figure F.109: Experiment: $Ne^+ + C^- \rightarrow Ne + C$ – reduced observation length.

Ne^+ beam	
Beam energy:	11,500 eV
Ion source:	ECR (Ne)
C^- beam	
Beam energy:	7,700 eV
Ion source:	Sputtering (graphite)
Mean collision energy:	$\sim$ 12 meV

Table F.116: Ne^+ + C^- MN experimental setup parameters.

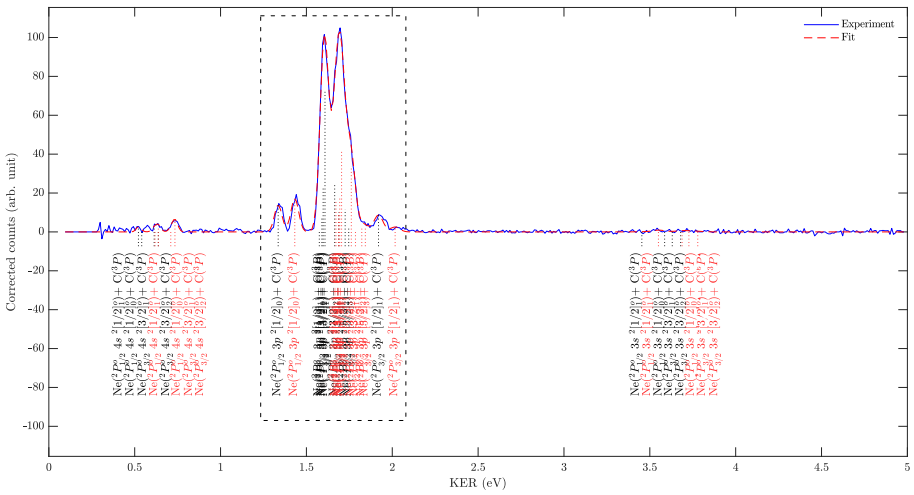

Figure F.110: Branching ratio fit: $Ne^+(^2P^o)$ + $C^-(^4S^o)$ – full observation length. The color code for the products is given in table F.1. A zoom similar to the framed area is given in figure F.112.

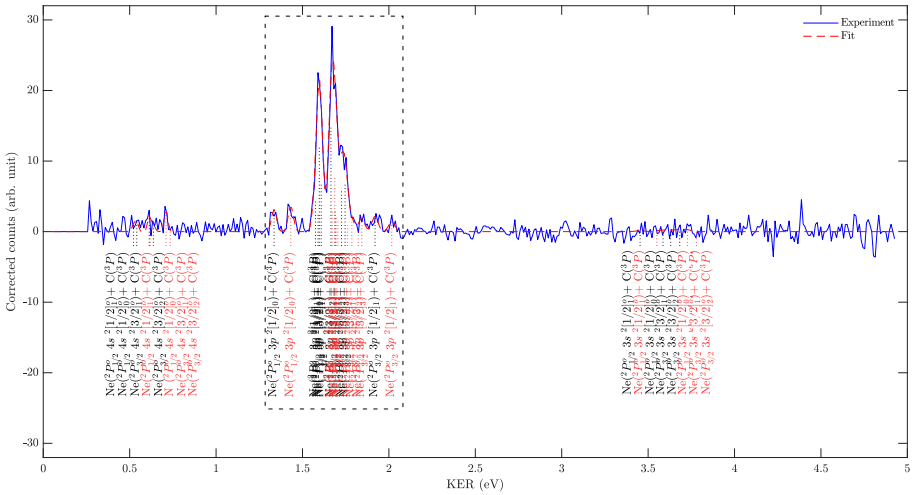

Figure F.111: Branching ratio fit: $Ne^+(^2P^o) + C^-(^4S^o)$ – reduced observation length. The color code for the products is given in table F.1. A zoom of the framed area is given in figure F.112.

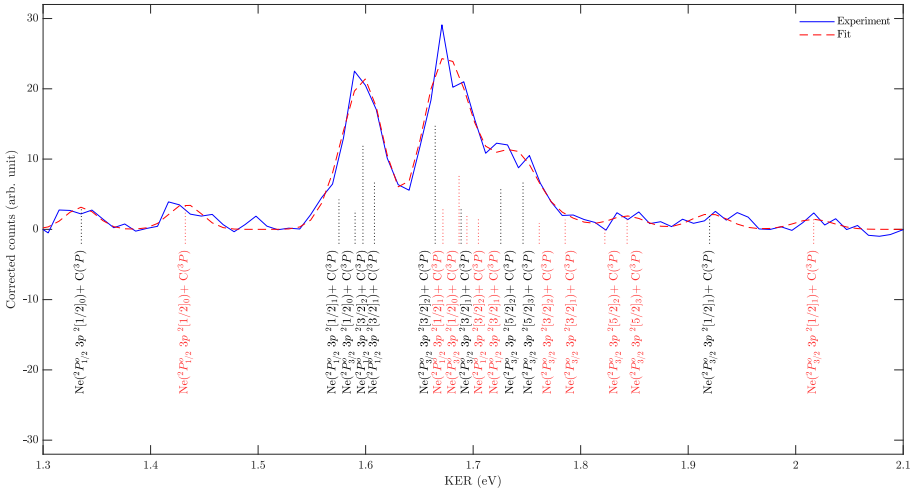

Figure F.112: Branching ratio fit: $Ne^+(^2P^o) + C^-(^4S^o)$ – reduced observation length – zoom. The color code for the products is given in table F.1.

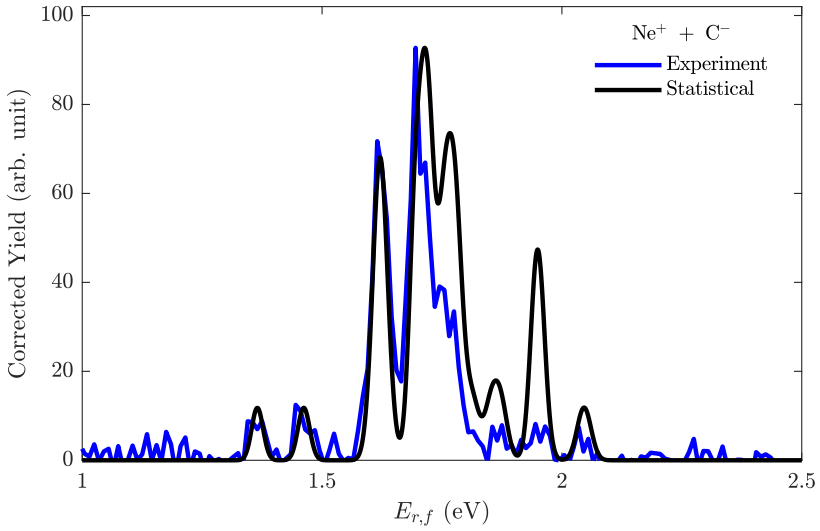

Figure F.113: Simulation (statistical only): $Ne^+(^2P^o)$ + $C^-(^4S^o)$.

F.7.2 Oxygen

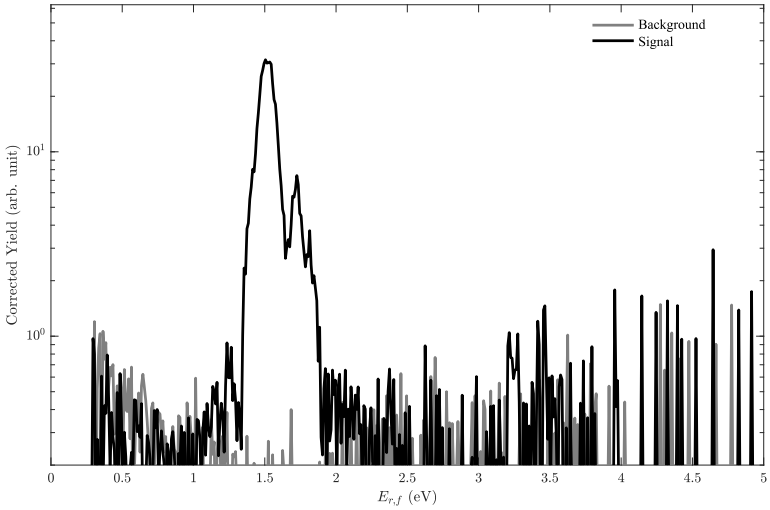

Figure F.114: Experiment: $Ne^+ + O^- \rightarrow Ne + O$ – full observation length.

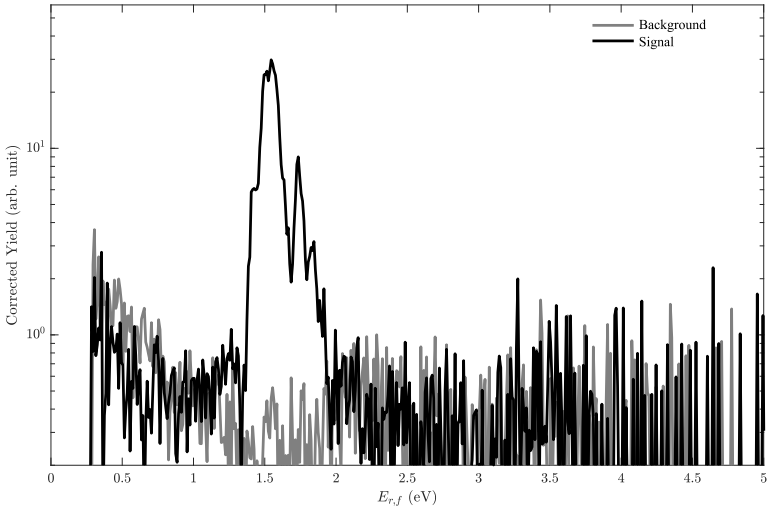

Figure F.115: Experiment: $Ne^+ + O^- \rightarrow Ne + O$ – reduced observation length.

Ne^+ beam	
Beam energy:	11,500 eV
Ion source:	ECR (Ne)
O^- beam	
Beam energy:	7,700 eV
Ion source:	Duoplasmatron (CO_2)
Mean collision energy:	$\sim$ 5 meV

Table F.117: Ne^+ + O^- MN experimental setup parameters.

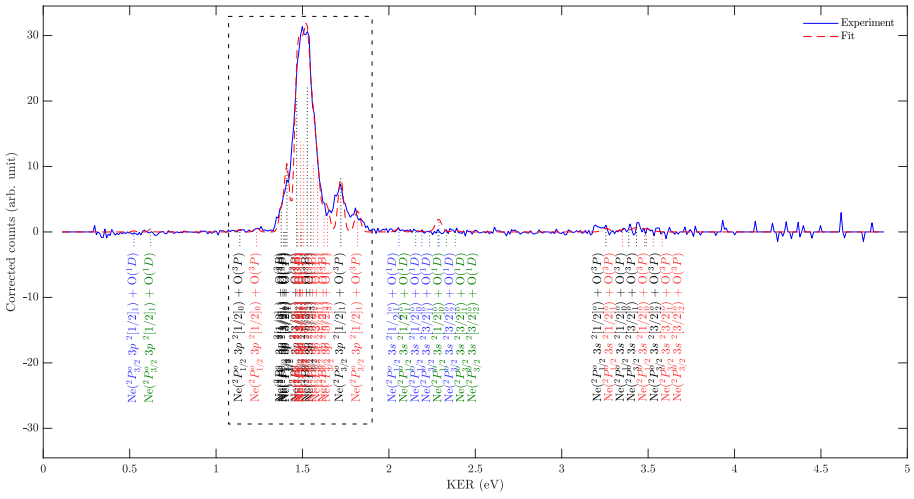

Figure F.116: Branching ratio fit: $Ne^+(^2P^o)$ + $O^-(^2P^o)$ – full observation length. The color code for the products is given in table F.1. A zoom of the framed area is given in figure F.117.

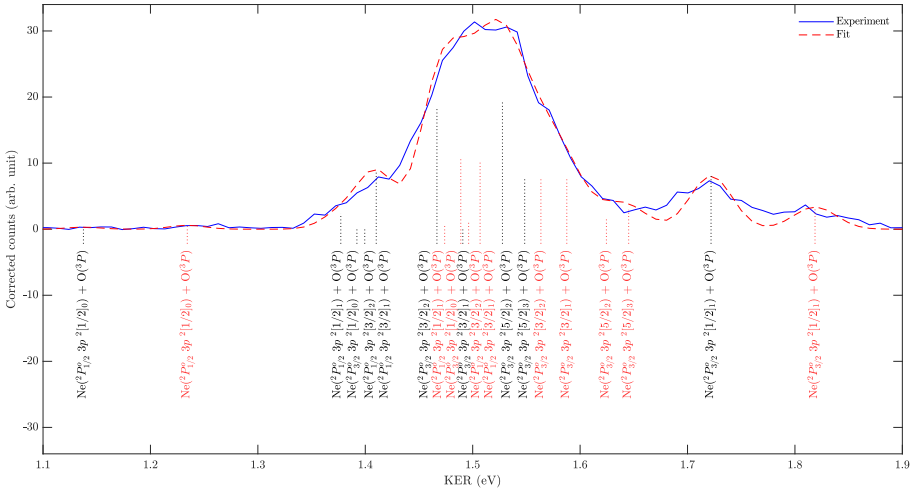

Figure F.117: Branching ratio fit: $Ne^+(^2P^o) + O^-(^2P^o)$ – full observation length – zoom. The color code for the products is given in table F.1.

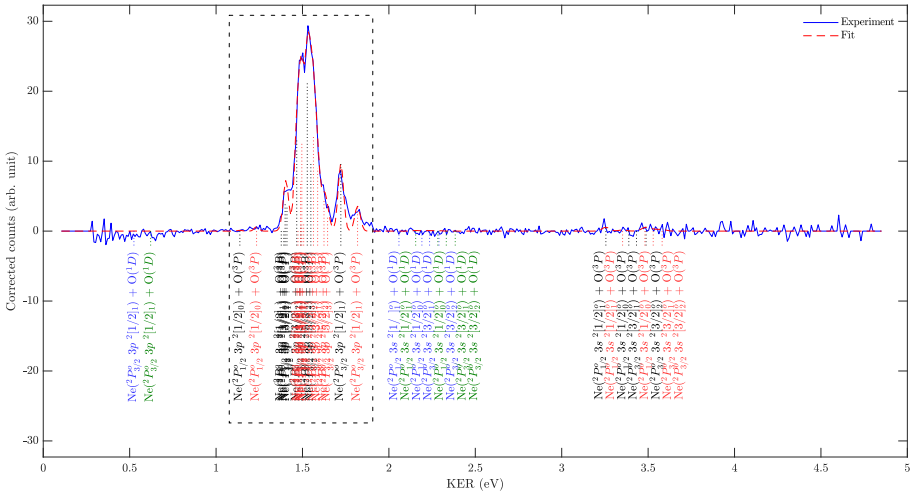

Figure F.118: Branching ratio fit: $Ne^+(^2P^o) + O^-(^2P^o)$ – reduced observation length. The color code for the products is given in table F.1. A zoom similar to the framed area is given in figure F.117.

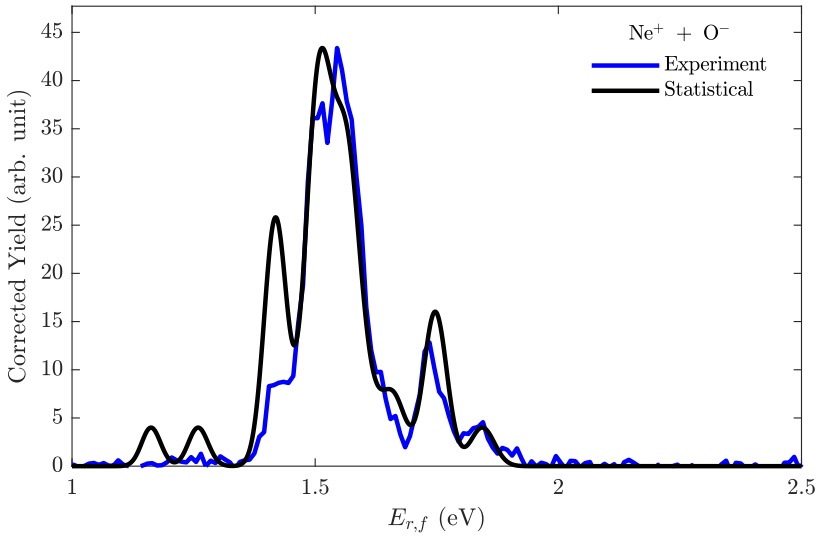

Figure F.119: Simulation (statistical only): $Ne^{+}(^{2}P^{o}) + O^{-}(^{2}P^{o})$.

F.7.3 Sulfur

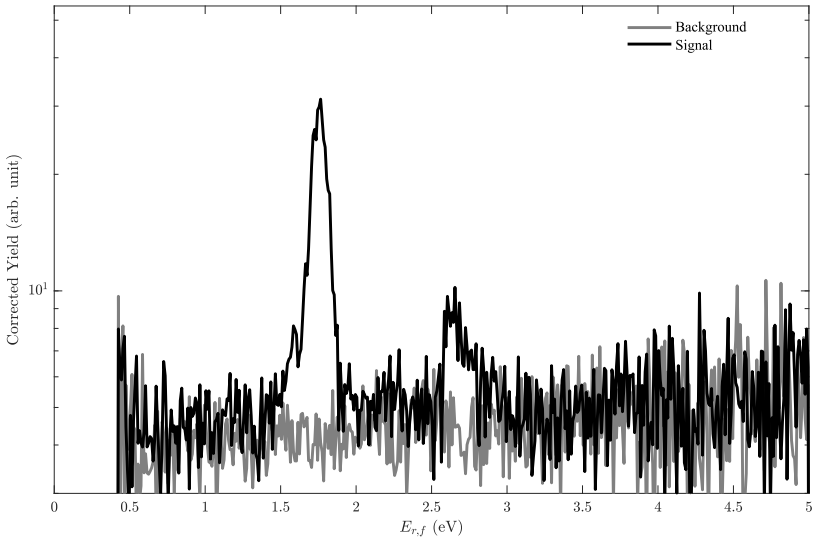

Figure F.120: Experiment: $Ne^+ + S^- \rightarrow Ne + S$ – full observation length.

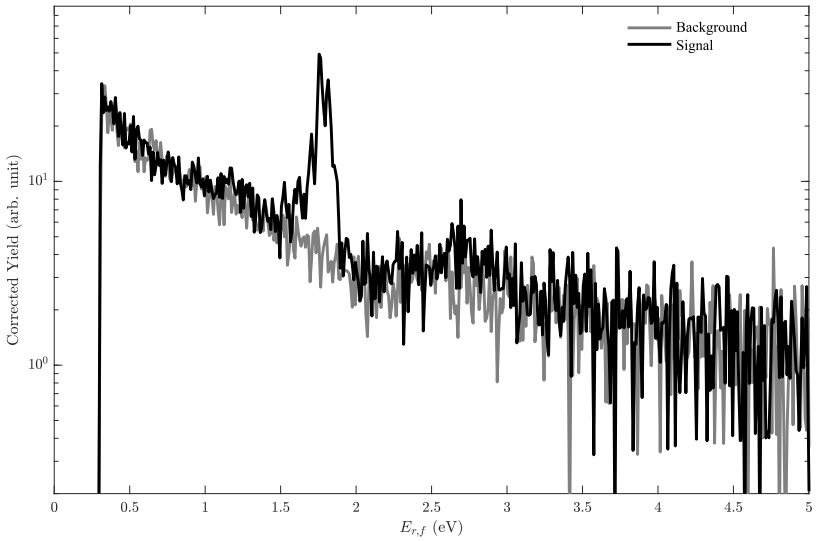

Figure F.121: Experiment: $Ne^+ + S^- \rightarrow Ne + S$ – reduced observation length.

Ne^+ beam	
Beam energy:	11,500 eV
Ion source:	ECR (Ne)
S^- beam	
Beam energy:	7,700 eV
Ion source:	Sputtering (FeS)
Mean collision energy:	$\sim$ 12 meV

Table F.118: Ne^+ + S^- MN experimental setup parameters.

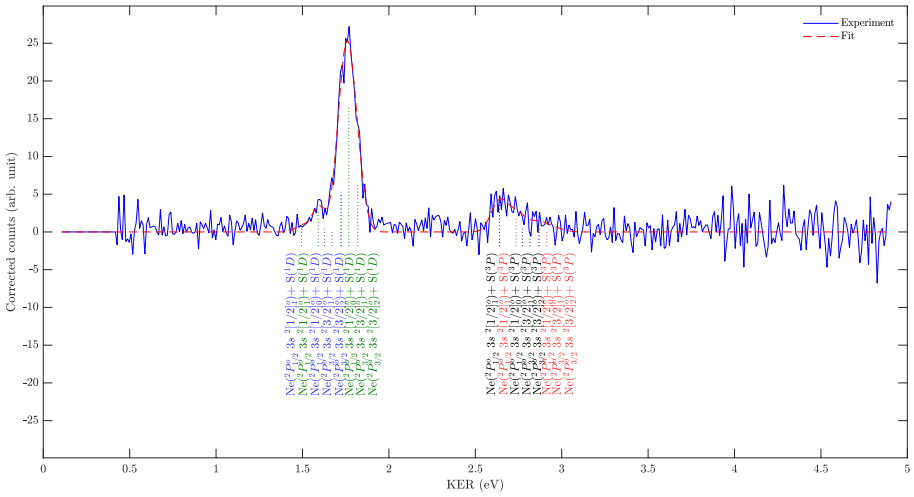

Figure F.122: Branching ratio fit: $Ne^+(^2P^o)$ + $S^-(^2P^o)$ – full observation length. The color code for the products is given in table F.1.

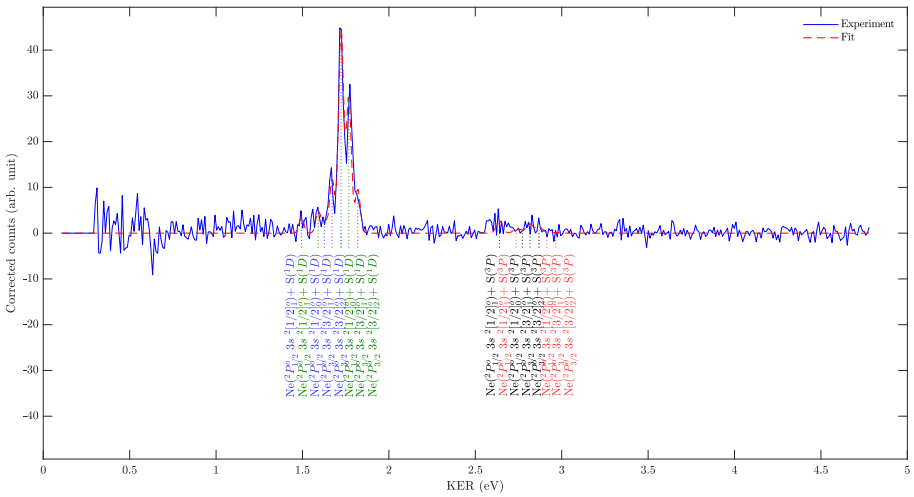

Figure F.123: Branching ratio fit: $Ne^+(^2P^o)$ + $S^-(^2P^o)$ – reduced observation length. The color code for the products is given in table F.1.

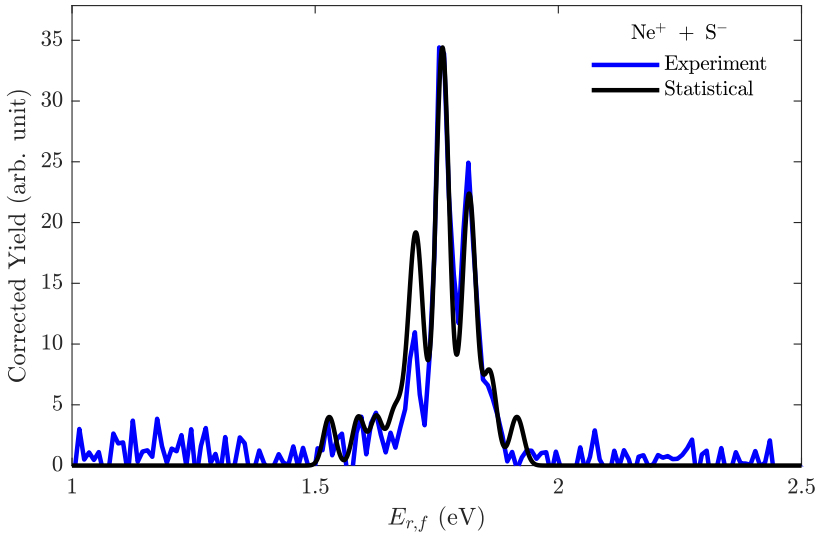

Figure F.124: Simulation (statistical only): $Ne^+(^2P^o)$ + $S^-(^2P^o)$.

List of Figures

1.1 Classical mutual neutralization trajectories as described by the Landau-Zener model 5
1.2 Illustration as curves of potential energy and kinetic energy. . . 7
1.3 Mutual neutralization reaction paths 8
1.4 Illustration in the form of potential energy curves of the kinetic energy release (KER). 9
1.5 Schematic definition fo the kinetic energy released during a mutual neutralization reaction. 10
1.6 Schematic diagram of the Flowing Afterglow/Langmuir Probe apparatus [12] 13
1.7 Representation of the probability of reaction $p(x,y)$ of a particle A^+ with another particle B^- when the latter crosses the plane transverse to its trajectory which includes B^-. 16

2.1 Schematic representation of the experimental setup 39
2.2 Turntable position according to the ratio between the kinetic energy of positive and negative beam 42
2.3 Various cases of beam alignment 45
2.4 Detection efficiency of a channeltron as a function of the incident Ag energy 51
2.5 Histogram of the distribution of τ for the C^++S^- MN at minimal collision energy 54
2.6 Raw histogram of relative kinetic energy after reaction for the C^++S^- MN at minimal collision energy 55

3.1 Potential energy curves in the adiabatic and diabatic representations 60
3.2 Values of the integral $G(\zeta)$ defined in equation 3.62. 70
3.3 Landau-Zener window illustration 71
3.4 Partial (colored curves) and total (black curve) cross sections calculated from the simple Landau-Zener model for the reaction $Li^+ + D^- \rightarrow Li^* + D$. 72

3.5 Mutual neutralization reaction paths - extended version 73
3.6 CCl/CCl^+ potential energy curves [26, 157] 76
3.7 C^++Cl^- MN KER spectrum simulated using the ACAM for a 20 meV collision energy 77
3.8 Example of volume for integral J 81
3.9 Representation of the spherical volume integral used in the anion center asymptotic model. 83
3.10 Representation of the spherical coordinates used. 90
3.11 Isotope effect on the branching ratios of the He^++H^- MN reaction illustrated by the $G(\zeta)$ function (equation 3.62). The values for E_{ic} are given by the anion centered asymptotic model. 103
3.12 Top (reproduced from Larson *et al.* [101, Fig.9]): Calculated cross section of mutual neutralization in collisions of different isotopes of hydrogen and helium ions. Bottom (reproduced from Larson *et al.* [101, Fig.11]): Calculated final-state distributions in mutual neutralization in (a) $^4He^+$+H^- and (b) $^4He^+$+D^- collisions with (dashed lines) and without (solid lines) inclusion of rotational couplings. 104

4.1 Representation of the alignment of the relative velocity $\vec{v}_{f,r}$ with respect to the velocity of the particle A and of the particle B, in the center-of-mass frame 107
4.2 Representation of the trajectory of the ions in the laboratory frame, and in the center-of-mass frame. 108
4.3 Representation of the initial arc. 111
4.4 Acceptance in a simple case 112
4.5 Graphical representation of obtaining the new distances and angles, taking into account the center-of-mass offset (x_{cm}, y_{cm}). 113
4.6 Acceptance when the center-of-mass is off-center. 114
4.7 Opening angle of the acceptance linked to a line. 115
4.8 Acceptances which takes into account an internal/external cut-off 116
4.9 Acceptance map for the N^+ with O^- MN 118
4.10 Acceptance map for the N^+ with O^- MN (details) 119
4.11 Acceptance map for the Li^+ with D^- MN 120
4.12 Diaphragms position in the experimental setup. 122
4.13 Simulated angular distribution of the beams passing the diaphragms (table 4.1) of the experimental setup using a Monte-Carlo method. 122
4.14 Effects of the beams energies and angular distributions for the N^+ + O^- MN as a function of the unspread collision energy . 125
4.15 Simulated distribution of the collision energy when taking into account the $1/\sqrt{E}$ dependence of the rate coefficient 126

4.16 Distribution of the center-of-mass 127
4.17 Scattering angles in the interrupted Rutherford model. 133
4.18 Example of modeled trajectories of a pseudo-particle in the center-of-mass frame 137
4.19 Semi-classical trajectory of the pseudo-particle in the coordinate system of the center-of-mass for the reaction $Li^+ + D^- \rightarrow Li(1s^2 3p) + D$ 138
4.20 Adiabatic potential energy curves for LiH ($^1\Sigma^+$ symmetry, which applies also for LiD) [51]. 140
4.21 Potential energy curves corresponding to the different paths which lead to the mutual neutralization of Li^+ with D^- towards the state $Li(1s^2 3d\ ^2D) + D(1s^2\ ^1S)$ 141
4.22 Set of semi-classical trajectories of the pseudo-particle in the center-of-mass frame for the $Li^+ + D^- \rightarrow Li(1s^2 3p\ ^2P) + D$ reaction 142
4.23 Differential cross section for the Li^++D^- mutual neutralization reaction for an collision energy of 200 meV. 143
4.24 Differential cross section of the reaction $Na + I \rightarrow Na^+ + I^-$ [153] 145
4.25 Normalized partial differential cross section for the Li^++D^- MN 147
4.26 Representation of measured events of mutual neutralization reaction between Li^+ and D^- placed on the acceptance map . . 148
4.27 Coordinate system and representation of the vectors useful for the convolution of the differential cross section by the angular distribution of the beams. 149
4.28 Convolution of the differential cross section with the angular distribution of collisions for the Li^++D^- MN 150
4.29 Comparison between experimental and simulated angular distribution for the Li^++D^- MN 151
4.30 Diagram of the observation cell 152
4.31 Bias potential applied along the axis of the observation cell . . 153
4.32 Representation of the edge effects of the bias potential of the observation cell 154
4.33 Collision behavior for a full and reduced observation cell . . . 155
4.34 Cross section simulated as a function of the observation potential 156
4.35 Comparison between the experimental distribution of events according to $\cos\theta$ and $E_{r,f}$ for the complete and reduced observation cell 158
4.36 Comparison of angular distribution as a function of the beams energy spread 160

4.37 Experimental kinetic energy release histograms for the mutual neutralization reaction of N^+ with O^- at minimal collision energy . . . 163
4.38 KER spectrum for the Li^++D^- MN reaction . . . 165

5.1 Kinetic energy release definition as a function of the energy levels of the initial ions and the final (neutral) products. . . . 168
5.2 Combined experiments : $C^+ + X^-$ . . . 170
5.3 Combined experiments : $N^+ + X^-$ . . . 171
5.4 Combined experiments : $O^+ + X^-$ . . . 172
5.5 Renormalization efect on kinetic energy release spectra . . . 173
5.6 Branching ratio simulation for the reactions : $Li^+ + D^- \rightarrow Li +$ D (top); $He^+ + D^- \rightarrow He + D$ (middle); $Na^+ + D^- \rightarrow Na + D$ (bottom). . . . 175
5.7 Comparison between experimental spectra (shaded areas) and theoretical prediction (black curves) for the $C^+/N^+/O^+$ + $S^-/O^-/Si^-/C^-/D^-/P^-$ mutual neutralisation reaction at low collision energies (5-25 meV). . . . 179
5.8 Convolved partial differential cross section of the reaction Na^+ + O^- MN . . . 185
5.9 NaO differential cross section simulation details . . . 186
5.10 NaO potential energy curves . . . 187
5.11 Experimental and simulated $E_{r,f}$ spectra using the configuration mixing given by the NIST for the $C(2s2p^3\ ^3P^o)$ state . . . 190
5.12 Potential diagram for the $^3\Sigma^+$ symmetry of CS . . . 192
5.13 Relative kinetic energy spectrum after collisions for the O^+ + O^- mutual neutralization reaction . . . 195
5.14 Squared radial wavefunctions of the $3p$ and $6p$ hydrogenic states 198
5.15 Schematic for representation of the validity domain of the Firsov integral . . . 199
5.16 Simulation of the presence of autoionizing states lead by the $O^+(^2D^o)$+$O^-(^2P^o)$ mutual neutralisation reaction. . . . 201

A.1 Illustration of the utility of Pierce geometry . . . 218
A.2 Trajectories of the extracted ions from a plasma . . . 219
A.3 Representation of ion trajectories (green lines) within an Einzel lens . . . 220
A.4 Diagram of deflection by a cylindrical deflector . . . 222
A.5 Focusing effect of a magnetic deflector . . . 224
A.6 Mass spectrum produced using a Wien filter . . . 225
A.7 Simplified diagram of the time and position sensitive detection system [215]. . . . 227

A.8 Resitive anode geometry explanation 228
A.9 Process of ejection of a particle from a surface during the impact of another particle on the same surface [221]. 230
A.10 Extraction function of an electron from a molybdenum surface as a function of the thickness of the cesium layer on this surface (in number of layers) [222]. 231
A.11 Diagram of the sputtering source used at UCLouvain. 231
A.12 Diagram of the ECR source. 238
A.13 Axial magnetic field along the axis of propagation within the ECR source. 239
A.14 Configuration of the permanent magnets around the axis of the ECR source. On the left, the hexapolar field in the plane perpendicular to the axis. On the right, the arrangement of the permanent magnets. 239
A.15 Diagram of the exterior of the ECR source, with its shielding systems. 240
A.16 Schematic profile of a duoplasmatron source used to extract a negative ion beam (compiled from [229]) – Plasma types and electromagnetic fields. 242
A.17 Schematic profile of a duoplasmatron source used to extract a negative ion beam (compiled from [229]) – Electrons density profiles. 243

B.1 Explanation of the apparent "backward scattering" 254

C.1 Convergence domain of asymptotic development of hypergeometric cylinder functions 259
C.2 List of possible paths during a mutual neutralization reaction for a system with four different covalent states. 263

E.1 Differential cross section for $He^+ + H/D^- \rightarrow He + H/D$ with a collision energy of 100 meV [101]. 298
E.2 Differential cross section for $He^+ + D^- \rightarrow He(1s3p\ ^3P^o) + D(1s)$. 298
E.3 Differential cross section for $He^+ + D^- \rightarrow He(1s3s\ ^1S) + D(1s)$. 299
E.4 Differential cross section for $He^+(^2S) + D^-(^1S) \rightarrow He(1s3s\ ^3S) + D(1s)$. 299
E.5 Experimental events distribution for Li^+ et D^-. 300
E.6 Differential cross section for $Li^+ + D^- \rightarrow Li + D(1s)$. 300
E.7 Experimental events distribution for $Na^+(^1S) + O^-$. 301
E.8 Experimental events distribution for $Na^+(^1S) + O^-$. 302
E.9 Differential cross section for $Na^+(^1S) + O^-(^2P^o) \rightarrow Na(3p\ ^2P^o) + O(2p^4\ ^3P)$. 303

E.10 Experimental events distribution for $C^+(^2P^o) + C^-(^4S^o)$. . . . 304
E.11 Experimental events distribution for $C^+(^2P^o) + O^-(^2P^o)$. . . . 305
E.12 Experimental events distribution for $N^+(^2P^o) + O^-(^2P^o)$. . . . 306
E.13 Experimental events distribution for $O^+(^4S^o) + O^-(^2P^o)$. . . . 307
E.14 Differential cross section for $O^+(^4S^o) + O^-(^2P^o) \rightarrow O(3p\,^2P^o)$ + $O(^{2S+1}L)$. 308
E.15 Experimental events distribution for $Ne^+(^2P^o) + C^-(^4S^o)$. . . . 309

F.1 Experiment: $He^+ + D^- \rightarrow He + D$ 313
F.2 Experiment: $He^+ + D^- \rightarrow He + D$ (another measurement). . . 313
F.3 Branching ratio fit: $He^+(^2S) + D^-(^1S)$. 315
F.4 Branching ratio fit: $He^+(^2S) + D^-(^1S)$ – zoom. 315
F.5 Simulation: $He^+(^2S) + D^-(^1S)$ 317
F.6 Experiment: $He^+ + H^- \rightarrow He + H$ – full observation length. . 319
F.7 Experiment: $He^+ + H^- \rightarrow He + H$ – reduced observation length. 319
F.8 Branching ratio fit: $Li^+(^1S) + D^-(^1S)$ – full observation length. 321
F.9 Branching ratio fit: $Li^+(^1S) + D^-(^1S)$ – reduced observation length. 321
F.10 Experiment: $Li^+ + D^- \rightarrow Li + D$ – full observation length. . . 322
F.11 Experiment: $Li^+ + D^- \rightarrow Li + D$ – reduced observation length. 322
F.12 Branching ratio fit: $Li^+(^1S) + H^-(^1S)$ – full observation length. 324
F.13 Branching ratio fit: $Li^+(^1S) + H^-(^1S)$ – reduced observation length. 324
F.14 Simulation: $Li^+(^1S) + D^-(1^1S)$ 325
F.15 Simulation: $Na^+(^1S) + D^-(^1S)$ 327
F.16 Experiment: $Na^+ + O^- \rightarrow Na + O$. 328
F.17 Branchin ratio fit: $Na^+(^1S) + O^-(^2P^o)$. 329
F.18 Simulation: $Na^+(^1S) + O^-(^2P^o)$ 330
F.19 Experiment: $Na^+ + S^- \rightarrow Na + S$ 331
F.20 Branching ratio fit: $Na^+(^1S) + S^-(^2P^o)$. 332
F.21 Simulation: $Na^+(^1S) + S^-(^2P^o)$ 333
F.22 Combined experiments : $C^+ + X^-$ (peak attributions). 335
F.23 Experiment: $C^+ + P^- \rightarrow C + P$ 336
F.24 Branching ratio fit: $C^+(^2P^o) + P^-(^3P)$. 338
F.25 Branching ratio fit: $C^+(^2P^o) + P^-(^3P)$ – zoom. 338
F.26 Simulation: $C^+(^2P^o) + P^-(^3P)$ – Excluding P^* 340
F.27 Simulation: $C^+(^2P^o) + P^-(^3P)$ – Including P^* 342
F.28 Experiment: $C^+ + D^- \rightarrow C + D$ 345
F.29 Branching ratio fit: $C^+(^2P^o) + D^-(^1S)$. 347
F.30 Simulation: $C^+(^2P^o) + D^-(^1S)$. 349
F.31 Experiment: $C^+ + Si^- \rightarrow C + Si$. 351
F.32 Branching ratio fit: $C^+(^2P^o) + Si^-(^4S^o)$. 352

F.33 Simulation: $C^+(^2P^o) + Si^-(^4S^o)$. 354
F.34 Experiment: $C^+ + C^- \rightarrow C + C$. 356
F.35 Branching ratio fit: $C^+(^2P^o) + C^-(^4S^o)$. 357
F.36 Simulation: $C^+(^2P^o) + C^-(^4S^o)$. 359
F.37 Experiment: $C^+ + O^- \rightarrow C + O$. 361
F.38 Branching ratio fit: $C^+(^2P^o) + O^-(^2P^o)$. 362
F.39 Simulation: $C^+(^2P^o) + O^-(^2P^o)$. 364
F.40 Experiment: $C^+ + S^- \rightarrow C + S$. 366
F.41 Branching ratio fit: $C^+(^2P^o) + S^-(^2P^o)$. 368
F.42 Branching ratio fit: $C^+(^2P^o) + S^-(^2P^o)$ – zoom. 368
F.43 Simulation: $C^+(^2P^o) + S^-(^2P^o)$. 370
F.44 Experiment: $C^+ + OH^- \rightarrow C + OH$ 372
F.45 Branching ratio fit: $C^+(^2P^o) + OH^-(X)$. 373
F.46 Combined experiments : $N^+ + X^-$ (peak attributions). 375
F.47 Experiment: $N^+ + P^- \rightarrow N + P$. 376
F.48 Branching ratio fit: $N^+(^3P) + P^-(^3P)$. 377
F.49 Branching ratio fit: $N^+(^3P) + P^-(^3P)$ – zoom 1. 378
F.50 Branching ratio fit: $N^+(^3P) + P^-(^3P)$ – zoom 2. 378
F.51 Simulation: $N^+(^3P) + P^-(^3P)$ - without P^* 380
F.52 Simulation: $N^+(^3P) + P^-(^3P)$ - with P^* 383
F.53 Simulation: $N^+(^1D) + P^-(^3P)$. 387
F.54 Experiment: $N^+ + D^- \rightarrow N + D$. 389
F.55 Branching ratio fit: $N^+(^3P) + D^-(^1S)$. 391
F.56 Branching ratio fit: $N^+(^3P) + D^-(^1S)$ – zoom. 391
F.57 Simulation: $N^+(^3P) + D^-(^1S)$. 393
F.58 Simulation: $N^+(^1D) + D^-(^1S)$. 395
F.59 Experiment: $N^+ + Si^- \rightarrow N + Si$. 397
F.60 Branching ratio fit: $N^+(^3P) + Si^-(^4S^o)$ – explaining the low signal with Rydberg series. 399
F.61 Branching ratio fit: $N^+(^3P) + Si^-(^4S^o)$ – explaining the low signal with N^+ excited states. 399
F.62 Simulation: $N^+(^3P) + Si^-(^4S^o)$. 401
F.63 Simulation: $N^+(^1D) + Si^-(^4S^o)$. 403
F.64 Experiment: $N^+ + C^- \rightarrow N + C$. 405
F.65 Branching ratio fit: $N^+(^3P) + C^-(^4S^o)$. 407
F.66 Branching ratio fit: $N^+(^3P) + C^-(^4S^o)$ – zoom. 407
F.67 Simulation: $N^+(^3P) + C^-(^4S^o)$. 408
F.68 Simulation: $N^+(^1D) + C^-(^4S^o)$. 410
F.69 Experiment: $N^+ + O^- \rightarrow N + O$. 412
F.70 Branching ratio fit: $N^+(^3P) + O^-(^2P^o)$. 414
F.71 Branching ratio fit: $N^+(^3P) + O^-(^2P^o)$ – zoom. 414
F.72 Simulation: $N^+(^3P) + O^-(^2P^o)$. 416

F.73 Simulation: $N^+(^1D) + O^-(^2P^o)$. 418
F.74 Experiment: $N^+ + S^- \rightarrow N + S$. 420
F.75 Branching ratio fit: $N^+(^3P) + S^-(^2P^o)$. 422
F.76 Branching ratio fit: $N^+(^3P) + S^-(^2P^o)$ – zoom. 422
F.77 Simulation: $N^+(^3P) + S^-(^2P^o)$. 424
F.78 Simulation: $N^+(^1D) + S^-(^2P^o)$. 426
F.79 Combined experiments : $O^+ + X^-$ (peak attributions). 429
F.80 Experiment: $O^+ + P^- \rightarrow O + P$. 430
F.81 Branching ratio fit: $O^+(^4S^o) + P^-(^3P)$. 431
F.82 Simulation: $O^+(^4S^o) + P^-(^3P)$. 433
F.83 Simulation: $O^+(^2D^o) + P^-(^3P)$. 435
F.84 Experiment: $O^+ + D^- \rightarrow O + D$. 437
F.85 Branching ratio fit: $O^+(^4S^o) + D^-(^1S)$. 438
F.86 Branching ratio fit: $O^+(^4S^o) + D^-(^1S)$ – zoom. 438
F.87 Simulation: $O^+(^4S^o) + D^-(^1S)$. 440
F.88 Simulation: $O^+(^2D^o) + D^-(^1S)$. 442
F.89 Experiment: $O^+ + Si^- \rightarrow O + Si$. 444
F.90 Branching ratio fit: $O^+(^4S^o) + Si^-(^4S^o)$. 445
F.91 Simulation: $O^+(^4S^o) + Si^-(^4S^o)$. 446
F.92 Simulation: $O^+(^2D^o) + Si^-(^4S^o)$. 448
F.93 Experiment: $O^+ + C^- \rightarrow O + C$. 450
F.94 Branching ratio fit: $O^+(^4S^o) + C^-(^4S^o)$. 451
F.95 Branching ratio fit: $O^+(^4S^o) + C^-(^4S^o)$ – zoom. 451
F.96 Simulation: $O^+(^4S^o) + C^-(^4S^o)$. 453
F.97 Simulation: $O^+(^2D^o) + C^-(^4S^o)$. 455
F.98 $O^+ + C^- \rightarrow O + C$ kinetic energy release spectra at $\langle E_{r,i} \rangle =$ 5 meV. 457
F.99 Sketch of the potential energy curves involved in the O^++C^- transfer ionization. 457
F.100 Experiment: $O^+ + O^- \rightarrow O + O$. 458
F.101 Branching ratio fit: $O^+(^4S^o) + O^-(^2P^o)$. 459
F.102 Simulation: $O^+(^4S^o) + O^-(^2P^o)$. 460
F.103 Simulation: $O^+(^2D^o) + O^-(^2P^o)$. 462
F.104 Experiment: $O^+ + S^- \rightarrow O + S$. 464
F.105 Branching ratio fit: $O^+(^4S^o) + S^-(^2P^o)$. 465
F.106 Simulation: $O^+(^4S^o) + S^-(^2P^o)$. 466
F.107 Simulation: $O^+(^2D^o) + S^-(^2P^o)$. 468
F.108 Experiment: $Ne^+ + C^- \rightarrow Ne + C$ – full observation length. . 471
F.109 Experiment: $Ne^+ + C^- \rightarrow Ne + C$ – reduced observation length. 471
F.110 Branching ratio fit: $Ne^+(^2P^o) + C^-(^4S^o)$ – full observation length. 472

F.111 Branching ratio fit: $Ne^+(^2P^o) + C^-(^4S^o)$ – reduced observation length. 473
F.112 Branching ratio fit: $Ne^+(^2P^o) + C^-(^4S^o)$ – reduced observation length – zoom. 473
F.113 Simulation (statistical only): $Ne^+(^2P^o) + C^-(^4S^o)$. 474
F.114 Experiment: $Ne^+ + O^- \rightarrow Ne + O$ – full observation length. . 475
F.115 Experiment: $Ne^+ + O^- \rightarrow Ne + O$ – reduced observation length. 475
F.116 Branching ratio fit: $Ne^+(^2P^o) + O^-(^2P^o)$ – full observation length. The color code for the products is given in table F.1. A zoom of the framed area is given in figure F.117. 476
F.117 Branching ratio fit: $Ne^+(^2P^o) + O^-(^2P^o)$ – full observation length – zoom. 477
F.118 Branching ratio fit: $Ne^+(^2P^o) + O^-(^2P^o)$ – reduced observation length. 477
F.119 Simulation (statistical only): $Ne^+(^2P^o) + O^-(^2P^o)$. 478
F.120 Experiment: $Ne^+ + S^- \rightarrow Ne + S$ – full observation length. . . 479
F.121 Experiment: $Ne^+ + S^- \rightarrow Ne + S$ – reduced observation length. 479
F.122 Branching ratio fit: $Ne^+(^2P^o) + S^-(^2P^o)$ – full observation length. 480
F.123 Branching ratio fit: $Ne^+(^2P^o) + S^-(^2P^o)$ – reduced observation length. 481
F.124 Simulation (statistical only): $Ne^+(^2P^o) + S^-(^2P^o)$. 481

List of Tables

1.1 Abbreviations for the different models of dynamics used. . . . 32
1.2 Compilation of the methods used to obtain the interaction potential (see text for details). 34

4.1 Position of the apertures defining the beam emittance. 123
4.2 Experimental branching ratios obtained for the Li^++D^- MN reaction [51]. 164

5.1 Summary of reactants used in mutual neutralization measurements. Labels redirect to the appendices. 167
5.2 Branching ratio simulation for the reactions : $Li^+ + D^- \rightarrow Li +$ D (top); $He^+ + D^- \rightarrow He + D$ (middle); $Na^+ + D^- \rightarrow Na + D$ (bottom). 176
5.3 Highest Λ symmetry for a given mutual neutralization reaction. 178
5.4 Branching ratio for the O^+ + H/D^- MN reaction. 180
5.5 Branching ratio for the N^+ + H/D^- MN reaction. 181
5.6 Branching ratio for the Mg^+ + H/D^- MN reaction. 182
5.7 Branching ratio for the C^+ + H/D^- MN reaction. 182
5.8 Fractional parentage coefficients between $np^3n'p$ and np^3 (as described in section C.2.3). 195

6.1 Various total cross sections (in cm^2) computed with the ACAM-MLZ at $E_{r,i} = 20$ meV. REactions measures by VENDAMS are in bold font. 208

D.1 Anions and cations parameters used by the model. 291
D.2 Neutralized anions configurations, terms and energy levels (no J) [199] 292
D.3 Neutralized anions configurations, terms and energy levels (with J) 292
D.4 Helium energy levels [199] 293
D.5 Lithium energy levels [199] 293

D.6 Sodium energy levels [199] . . . 293
D.7 Carbon energy levels [198, 199] . . . 294
D.8 Nitrogen energy levels [199] . . . 294
D.9 Oxygen energy levels [199] . . . 295

F.1 Color scheme used for the KER spectra fit. . . . 312
F.2 $He^+ + D^-$ MN experimental setup parameters. . . . 314
F.3 Branching ratio fit: $He^+(^1S) + D^-(^1S)$. . . . 314
F.4 Interaction potentials E_{ic} (a.u.): $He^+(1s\ ^2S) + D^-(1s^2\ ^1S)$ . . . 316
F.5 Partial cross section (cm^2) for the He^++D^- MN reaction computed with the ACAM. . . . 316
F.6 Branching ratio fit: $Li^+(^1S) + X^-$. . . . 318
F.7 $Li^+ + H^-$ MN experimental setup parameters. . . . 320
F.8 $Li^+ + D^-$ MN experimental setup parameters. . . . 323
F.9 Interaction potentials E_{ic} (a.u.): $Li^+(^1S) + D^-(^1S)$ . . . 325
F.10 Partial cross section (cm^2) for the Li^++D^- MN reaction computed with the ACAM. . . . 325
F.11 Branching ratio fit: $Na^+(^1S) + X^-$. . . . 326
F.12 Interaction potentials E_{ic} (a.u.): $Na^+(^1S) + D^-(^1S)$ . . . 327
F.13 Partial cross section (cm^2) for the Na^++D^- MN reaction computed with the ACAM. . . . 327
F.14 $Na^+ + O^-$ MN experimental setup parameters. . . . 328
F.15 Interaction potentials E_{ic} (a.u.): $Na^+(^1S) + O^-(^2P^o)$ . . . 329
F.16 Partial cross section (cm^2) for the Na^++O^- MN reaction computed with the ACAM. . . . 329
F.17 $Na^+ + S^-$ MN experimental setup parameters. . . . 331
F.18 Interaction potentials E_{ic} (a.u.): $Na^+(^1S) + S^-(^2P^o)$ . . . 331
F.19 Partial cross section (cm^2) for the Na^++S^- MN reaction computed with the ACAM. . . . 332
F.20 Branching ratio fit (simplified): $C^+(^2P^o) + X^-$. . . . 334
F.21 $C^+ + P^-$ MN experimental setup parameters. . . . 336
F.22 Branching ratio fit: $C^+(^2P^o) + P^-(^3P)$. . . . 337
F.23 Partial cross section (cm^2) for the C^++P^- MN reaction computed with the ACAM. . . . 339
F.24 Interaction potentials E_{ic} (a.u.): $C^+(^2P^o) + P^-(^3P)$ – Excluding P^* . . . 341
F.25 Interaction potentials E_{ic} (a.u.): $C^+(^2P^o) + P^-(^3P)$ – Including P^* . . . 343
F.26 Interaction potentials E_{ic} (a.u.): $C^+(^2P^o) + P^-(^3P)$ – Including P^* . . . 344
F.27 $C^+ + D^-$ MN experimental setup parameters. . . . 345
F.28 Branching ratio fit: $C^+(^2P^o) + D^-$. . . . 346

F.29 Partial cross section (cm^2) for the C^++D^- MN reaction computed with the ACAM. 348
F.30 Interaction potentials E_{ic} (a.u.): $C^+(^2P^o)$ + $D^-(^1S)$. 350
F.31 C^+ + Si^- MN experimental setup parameters. 351
F.32 Branching ratio fit: $C^+(^2P^o)$ + $Si^-(^4S^o)$. 352
F.33 Partial cross section (cm^2) for the C^++Si^- MN reaction computed with the ACAM. 353
F.34 Interaction potentials E_{ic} (a.u.): $C^+(^2P^o)$ + $Si^-(^4S^o)$. 355
F.35 C^+ + C^- MN experimental setup parameters. 356
F.36 Branching ratio fit: $C^+(^2P^o)$ + $C^-(^4S^o)$. 357
F.37 Partial cross section (cm^2) for the C^++C^- MN reaction computed with the ACAM. 358
F.38 Interaction potentials E_{ic} (a.u.): $C^+(^2P^o)$ + $C^-(^4S^o)$. 360
F.39 C^+ + O^- MN experimental setup parameters. 361
F.40 Branching ratio fit: $C^+(^2P^o)$ + $O^-(^2P^o)$. 362
F.41 Partial cross section (cm^2) for the C^++O^- MN reaction computed with the ACAM. 363
F.42 Interaction potentials E_{ic} (a.u.): $C^+(2P^o)$ + $O^-(^2P^o)$. 365
F.43 C^+ + S^- MN experimental setup parameters. 366
F.44 Branching ratio fit: $C^+(^2P^o)$ + $S^-(^2P^o)$. 367
F.45 Partial cross section (cm^2) for the C^++S^- MN reaction computed with the ACAM. 369
F.46 Interaction potentials E_{ic} (a.u.): $C^+(^2P^o)$ + $S^-(^2P^o)$. 371
F.47 C^+ + OH^- MN experimental setup parameters. 372
F.48 Branching ratio fit: $C^+(^2P^o)$ + OH^-. 373
F.49 Branching ratio fit (simplified): $N^+(^3P)$ + X^-. 374
F.50 N^+ + P^- MN experimental setup parameters. 376
F.51 Branching ratio fit: $N^+(^3P)$ + $P^-(^3P)$. 377
F.52 Partial cross section (cm^2) for the $N^+(^3P)$+$P^-(^3P)$ MN reaction computed with the ACAM. 379
F.53 Interaction potentials E_{ic} (a.u.): $N^+(^3P)$ + $P^-(^3P)$ - without P^*. 381
F.54 Interaction potentials E_{ic} (a.u.): $N^+(^3P)$ + $P^-(^3P)$ - without P^* (continued). 382
F.55 Interaction potentials E_{ic} (a.u.): $N^+(^3P)$ + $P^-(^3P)$ - with P^*. . . 384
F.56 Interaction potentials E_{ic} (a.u.): $N^+(^3P)$ + $P^-(^3P)$ - with P^* (continued). 385
F.57 Interaction potentials E_{ic} (a.u.): $N^+(^3P)$ + $P^-(^3P)$ - with P^* (continued). 386
F.58 Interaction potentials E_{ic} (a.u.): $N^+(^1D)$ + $P^-(^3P)$. 388
F.59 N^+ + D^- MN experimental setup parameters. 389
F.60 Branching ratio fit: $N^+(^3P)$ + $D^-(^1S)$. 390

F.61 Partial cross section (cm^2) for the $N^+(^3P)$+$D^-(^1S)$ MN reaction computed with the ACAM. 392
F.62 Interaction potentials E_{ic} (a.u.): $N^+(^3P)$ + $D^-(^1S)$. 394
F.63 Interaction potentials E_{ic} (a.u.): $N^+(^1D)$ + $D^-(^1S)$. 396
F.64 N^+ + Si^- MN experimental setup parameters. 397
F.65 Branching ratio fit: $N^+(^3P)$ + $Si^-(^4S^o)$. 398
F.66 Partial cross section (cm^2) for the $N^+(^3P)$+$Si^-(^4S^o)$ MN reaction computed with the ACAM. 400
F.67 Interaction potentials E_{ic} (a.u.): $N^+(^3P)$ + $Si^-(^4S^o)$. 402
F.68 Interaction potentials E_{ic} (a.u.): $N^+(^1D)$ + $Si^-(^4S^o)$. 404
F.69 N^+ + C^- MN experimental setup parameters. 405
F.70 Branching ratio fit: $N^+(^3P)$ + $C^-(^4S^o)$. 406
F.71 Partial cross section (cm^2) for the $N^+(^3P)$+$C^-(^4S^o)$ MN reaction computed with the ACAM. 406
F.72 Interaction potentials E_{ic} (a.u.): $N^+(^3P)$ + $C^-(^4S^o)$. 409
F.73 Interaction potentials E_{ic} (a.u.): $N^+(^1D)$ + $C^-(^4S^o)$. 411
F.74 N^+ + O^- MN experimental setup parameters. 412
F.75 Branching ratio fit: $N^+(^3P)$ + $O^-(^2P^o)$. 413
F.76 Partial cross section (cm^2) for the $N^+(^3P)$+$O^-(^2P^o)$ MN reaction computed with the ACAM. 415
F.77 Interaction potentials E_{ic} (a.u.): $N^+(^3P)$ + $O^-(^2P^o)$. 417
F.78 Interaction potentials E_{ic} (a.u.): $N^+(2p^2\ ^1D)$ + $O^-(2p^5\ ^2P^o)$. . 419
F.79 N^+ + S^- MN experimental setup parameters. 420
F.80 Branching ratio fit: N^+ + $S^-(^2P^o)$. 421
F.81 Partial cross section (cm^2) for the $N^+(^3P)$+$S^-(^2P^o)$ MN reaction computed with the ACAM. 423
F.82 Interaction potentials E_{ic} (a.u.): $N^+(^3P)$ + $S^-(^2P^o)$. 425
F.83 Interaction potentials E_{ic} (a.u.): $N^+(^1D)$ + $S^-(^2P^o)$. 427
F.84 Branching ratio fit (simplified): $O^+(^4S^o)$ + X^-. 428
F.85 O^+ + P^- MN experimental setup parameters. 430
F.86 Branching ratio fit: $O^+(^4S^o)$ + $P^-(^3P)$. 431
F.87 Partial cross section (cm^2) for the $O^+(^4S^o)$+$P^-(^3P)$ MN reaction computed with the ACAM. 432
F.88 Interaction potentials E_{ic} (a.u.): $O^+(^4S^o)$ + $P^-(^3P)$. 434
F.89 Interaction potentials E_{ic} (a.u.): $O^+(^2D^o)$ + $P^-(^3P)$. 436
F.90 O^+ + D^- MN experimental setup parameters. 437
F.91 Branching ratio fit: $O^+(^4S^o)$ + $D^-(^1S)$. 439
F.92 Partial cross section (cm^2) for the $O^+(^4S^o)$+$D^-(^1S)$ MN reaction computed with the ACAM. 439
F.93 Interaction potentials E_{ic} (a.u.): $O^+(^4S^o)$ + $D^-(^1S)$. 441
F.94 Interaction potentials E_{ic} (a.u.): $O^+(^2D^o)$ + $D^-(^1S)$. 443
F.95 O^+ + Si^- MN experimental setup parameters. 444

F.96 Branching ratio fit: $O^+(^4S^o) + Si^-(^4S^o)$. 445
F.97 Partial cross section (cm^2) for the $O^+(^4S^o)$+$Si^-(^4S^o)$ MN reaction computed with the ACAM. 445
F.98 Interaction potentials E_{ic} (a.u.): $O^+(^4S^o) + Si^-(^4S^o)$. 447
F.99 Interaction potentials E_{ic} (a.u.): $O^+(^2D^o) + Si^-(^4S^o)$. 449
F.100 $O^+ + C^-$ MN experimental setup parameters. 450
F.101 Branching ratio fit: $O^+(^4S^o) + C^-(^4S^o)$. 452
F.102 Partial cross section (cm^2) for the $O^+(^4S^o)$+$C^-(^4S^o)$ MN reaction computed with the ACAM. 452
F.103 Interaction potentials E_{ic} (a.u.): $O^+(^4S^o) + C^-(^4S^o)$. 454
F.104 Interaction potentials E_{ic} (a.u.): $O^+(^2D^o) + C^-(^4S^o)$. 456
F.105 $O^+ + O^-$ MN experimental setup parameters. 458
F.106 Branching ratio fit: $O^+(^4S^o) + O^-(^2P^o)$. 459
F.107 Partial cross section (cm^2) for the $O^+(^4S^o)$+$O^-(^2P^o)$ MN reaction computed with the ACAM. 459
F.108 Interaction potentials E_{ic} (a.u.): $O^+(^4S^o) + O^-(^2P^o)$. 461
F.109 Interaction potentials E_{ic} (a.u.): $O^+(^2D^o) + O^-(^2P^o)$. 463
F.110 $O^+ + S^-$ MN experimental setup parameters. 464
F.111 Branching ratio fit E_{ic} (a.u.): $O^+(^4S^o) + S^-(^2P^o)$. 465
F.112 Partial cross section (cm^2) for the $O^+(^4S^o)$+$S^-(^2P^o)$ MN reaction computed with the ACAM. 465
F.113 Interaction potentials E_{ic} (a.u.): $O^+(^4S^o) + S^-(^2P^o)$. 467
F.114 Interaction potentials E_{ic} (a.u.): $O^+(^2D^o) + S^-(^2P^o)$. 469
F.115 Branching ratio fit: $Ne^+(^2P^o) + X^-$. 470
F.116 $Ne^+ + C^-$ MN experimental setup parameters. 472
F.117 $Ne^+ + O^-$ MN experimental setup parameters. 476
F.118 $Ne^+ + S^-$ MN experimental setup parameters. 480

Bibliography

[1] X. Urbain, N. de Ruette, A. Dochain, T. Launoy, R. F. Nascimento, M. Kaminska, M. H. Stockett, J. Loreau, J. Liévin, N. Vaeck, R. Thomas, H. Schmidt, and H. Cederquist, Journal of Physics: Conference Series **1412**, 062009 (2020).

[2] E. P. Wigner, Physical Review **73**, 1002 (1948).

[3] J. Qin, J. J. Makela, F. Kamalabadi, and R. R. Meier, Journal of Geophysical Research: Space Physics **120**, 10116 (2015).

[4] N. de Ruette, A. Dochain, T. Launoy, R. F. Nascimento, M. Kaminska, M. H. Stockett, N. Vaeck, H. T. Schmidt, H. Cederquist, and X. Urbain, Physical Review Letters **121**, 083401 (2018).

[5] P. S. Barklem, A. M. Amarsi, J. Grumer, G. Eklund, S. Rosén, M. Ji, H. Cederquist, H. Zettergren, and H. T. Schmidt, The Astrophysical Journal **908**, 245 (2021).

[6] A. Mitrushchenkov, M. Guitou, A. K. Belyaev, Y. V. Voronov, and N. Feautrier, The Journal of Chemical Physics **150**, 064312 (2019).

[7] A. M. Amarsi and P. S. Barklem, Astronomy & Astrophysics **625**, A78 (2019).

[8] P. S. Barklem, Astronomy and Astrophysics **610**, A57 (2018).

[9] A. M. Amarsi, P. E. Nissen, and A. Skúladóttir, Astronomy & Astrophysics **630**, A104 (2019).

[10] A. M. Amarsi, N. Grevesse, J. Grumer, M. Asplund, P. S. Barklem, and R. Collet, Astronomy & Astrophysics **636**, A120 (2020).

[11] C. Zener, Proceedings of the Royal Society of London. Series A, Mathematical and Physical Sciences **137**, 696 (1932).

[12] D. Smith and N. G. Adams, in *Physics of Ion-Ion and Electron-Ion Collisions*, edited by F. Brouillard and J. W. McGowan (Springer US, Boston, MA, 1983) pp. 501–532.

[13] B. H. Mahan, Recombination of gaseous ions, in *Advances in Chemical Physics* (John Wiley & Sons, Ltd, 1973) Chap. 1, pp. 1–40.

[14] N. S. Shuman, T. M. Miller, A. A. Viggiano, and J. Troe, in *Advances in Atomic, Molecular, and Optical Physics*, Advances In Atomic, Molecular, and Optical Physics, Vol. 61, edited by P. Berman, E. Arimondo, and C. Lin (Academic Press, 2012) pp. 209 – 294.

[15] J. Sayers, Proceedings of the Royal Society of London. Series A, Mathematical and Physical Sciences **169**, 83 (1938).

[16] M. E. Gardner, Physical Review **53**, 75 (1938).

[17] H. G. Ebert, J. Booz, and R. Koepp, Zeitschrift für Physik **181**, 187 (1964).

[18] S. McGowan, Canadian Journal of Physics **45**, 439 (1967).

[19] T. H. Y. Yeung, Proceedings of the Physical Society **71**, 341 (1958).

[20] C. Greaves, Journal of Electronics and Control **17**, 171 (1964).

[21] M. J. Church and D. Smith, Journal of Physics D: Applied Physics **11**, 2199 (1978).

[22] M. J. Church and D. Smith, Journal of Physics D: Applied Physics **11**, 2199 (1978).

[23] N. S. Shuman, T. M. Miller, R. Johnsen, and A. A. Viggiano, The Journal of Chemical Physics **140**, 044304 (2014).

[24] J. P. Wiens, N. S. Shuman, T. M. Miller, and A. A. Viggiano, The Journal of Chemical Physics **144**, 204309 (2016).

[25] J. C. Sawyer, T. M. Miller, B. C. Sweeny, S. G. Ard, A. A. Viggiano, and N. S. Shuman, The Journal of Chemical Physics **149**, 044303 (2018).

[26] J. C. Sawyer, P. Hedvall, T. M. Miller, K. W. Engeling, A. Larson, A. E. Orel, A. A. Viggiano, and N. S. Shuman, The Journal of Chemical Physics **151**, 244301 (2019).

[27] J. C. Sawyer, K. W. Engeling, B. C. Sweeny, D. C. McDonald, S. G. Ard, T. M. Miller, A. A. Viggiano, and N. S. Shuman, Chemical Physics Letters **760**, 137973 (2020).

[28] A. Kuppermann and E. F. Greene, Journal of Chemical Education **45**, 361 (1968).

[29] W. Aberth, J. R. Peterson, D. C. Lorents, and C. J. Cook, V ICPEAC, Abstract of Papers , 162 (1967).

[30] W. Aberth, J. R. Peterson, D. C. Lorents, and C. J. Cook, Physical Review Letters **20**, 979 (1968).

[31] W. Aberth and J. R. Peterson, Review of Scientific Instruments **38**, 745 (1967).

[32] P. Defrance, F. Brouillard, W. Claeys, and G. Van Wassenhove, Journal of Physics B: Atomic and Molecular Physics **14**, 103 (1981).

[33] W. Schön, S. Krüdener, F. Melchert, K. Rinn, M. Wagner, and E. Salzborn, Journal of Physics B: Atomic and Molecular Physics **20**, L759 (1987).

[34] R. D. Rundel, K. L. Aitken, and M. F. A. Harrison, Journal of Physics B: Atomic and Molecular Physics **2**, 954 (1969).

[35] T. D. Gaily and M. F. A. Harrison, Journal of Physics B: Atomic and Molecular Physics **3**, L25 (1970).

[36] T. D. Gaily and M. F. A. Harrison, Journal of Physics B: Atomic and Molecular Physics **3**, 1098 (1970).

[37] B. Peart, R. Grey, and K. T. Dolder, Journal of Physics B: Atomic and Molecular Physics **9**, 3047 (1976).

[38] B. Peart, M. A. Bennett, and K. Dolder, Journal of Physics B: Atomic and Molecular Physics **18**, L439 (1985).

[39] K. Dolder and B. Peart, Reports on Progress in Physics **48**, 1283 (1985).

[40] W. H. Aberth and J. R. Peterson, Physical Review A **1**, 158 (1970).

[41] B. Peart and D. Hayton, Journal of Physics B: Atomic, Molecular and Optical Physics **25**, 5109 (1992).

[42] S. Szucs, M. Karemera, M. Terao, and F. Brouillard, Journal of Physics B: Atomic and Molecular Physics **17**, 1613 (1984).

[43] K. Olamba, S. Szücs, J. Chenu, N. E. Arbi, and F. Brouillard, Journal of Physics B: Atomic, Molecular and Optical Physics **29**, 2837 (1996).

[44] B. Peart, R. Grey, and K. T. Dolder, Journal of Physics B: Atomic and Molecular Physics **9**, L369 (1976).

[45] M. H. Cohen, T. Schwope, M. Tissandier, and J. V. Coe, in *Dissociative Recombination: Theory, Experiment and Applications III* (1996) p. 216.

[46] B. Plastridge, K. Cowen, D. Wood, M. Cohen, and J. Coe, Surface Review and Letters **03**, 655 (1996).

[47] R. D. Thomas, H. T. Schmidt, G. Andler, M. Björkhage, M. Blom, L. Brännholm, E. Bäckström, H. Danared, S. Das, N. Haag, P. Halldén, F. Hellberg, A. I. S. Holm, H. A. B. Johansson, A. Källberg, G. Källersjö, M. Larsson, S. Leontein, L. Liljeby, P. Löfgren, B. Malm, S. Mannervik, M. Masuda, D. Misra, A. Orbán, A. Paál, P. Reinhed, K.-G. Rensfelt, S. Rosén, K. Schmidt, F. Seitz, A. Simonsson, J. Weimer, H. Zettergren, and H. Cederquist, Review of Scientific Instruments **82**, 065112 (2011).

[48] X. Urbain, J. Lecointre, F. Mezdari, K. A. Miller, and D. W. Savin, Journal of Physics: Conference Series **388**, 092004 (2012).

[49] S. M. Nkambule, N. Elander, A. Larson, J. Lecointre, and X. Urbain, Physical Review A **93**, 032701 (2016).

[50] S. Rosén, H. T. Schmidt, P. Reinhed, D. Fischer, R. D. Thomas, H. Cederquist, L. Liljeby, L. Bagge, S. Leontein, and M. Blom, Review of Scientific Instruments **78**, 113301 (2007).

[51] T. Launoy, J. Loreau, A. Dochain, J. Liévin, N. Vaeck, and X. Urbain, The Astrophysical Journal **883**, 85 (2019).

[52] J. Weiner, W. B. Peatman, and R. S. Berry, Physical Review Letters **25**, 79 (1970).

[53] J. Weiner, W. B. Peatman, and R. S. Berry, Physical Review A **4**, 1824 (1971).

[54] P. Taramelli, *Contribution à l'étude de la réaction* $H^+ + H^- \rightarrow H(nl) + H(1s)$, Master's thesis, Université Catholique de Louvain (1981).

[55] M. Bourglia, *Contribution à l'étude de la réaction* $H^+ + H^- \rightarrow H(nl) + H(1s)$, Master's thesis, Université Catholique de Louvain (1981).

[56] M. Cherkani Hassani, *Contribution à l'étude de la réaction* $H^+ + H^- \rightarrow H^0 + H^0$, Master's thesis, Université Catholique de Louvain (1983).

[57] M. Karemera, *Contribution à l'étude de la neutralisation mutuelle des ions* H^+ *et* H^- *de l'hydrogène à basse énergie*, Ph.D. thesis, Université Catholique de Louvain (1983).

[58] W. Schön, S. Krüdener, F. Melchert, K. Rinn, M. Wagner, E. Salzborn, M. Karemera, S. Szücs, M. Terao, D. Fussen, R. Janev, X. Urbain, and F. Brouillard, Physical Review Letters **59**, 1565 (1987).

[59] J. T. Moseley, W. Aberth, and J. R. Peterson, Journal of Geophysical Research **77**, 255 (1972).

[60] G. Eklund, J. Grumer, S. Rosén, M. Ji, N. Punnakayathil, A. Källberg, A. Simonsson, R. D. Thomas, M. H. Stockett, P. Reinhed, P. Löfgren, M. Björkhage, M. Blom, P. S. Barklem, H. Cederquist, H. Zettergren, and H. T. Schmidt, Physical Review A **102**, 012823 (2020).

[61] G. Eklund, J. Grumer, P. S. Barklem, S. Rosén, M. Ji, A. Simonsson, R. D. Thomas, H. Cederquist, H. Zettergren, and H. T. Schmidt, Physical Review A (2021).

[62] G. Eklund, *Experiments on mutual neutralization using storage rings with merged ion beams*, Ph.D. thesis, Stockholm University, Stockholm, Sweden (2021).

[63] A. Dochain and X. Urbain, EPJ Web of Conferences **84**, 05001 (2015).

[64] M. Génévriez and X. Urbain, Physical Review A **91**, 033403 (2015).

[65] M. Génévriez, K. M. Dunseath, M. Terao-Dunseath, A. Hibbert, A. Dochain, R. Marion, and X. Urbain, Phys. Rev. A **98**, 033410 (2018).

[66] R. Marion, K. M. Dunseath, M. Terao-Dunseath, and X. Urbain, Physical Review A **103**, 023115 (2021).

[67] D. Smith and M. Church, International Journal of Mass Spectrometry and Ion Physics **19**, 185 (1976).

[68] J. R. Peterson, W. H. Aberth, J. T. Moseley, and J. R. Sheridan, Physical Review A **3**, 1651 (1971).

[69] J. Moseley, R. Olson, and J. Peterson, in *Case Studies in Atomic Physics*, Vol. 5, edited by E. McDaniel and M. McDowell (Elsevier, 1975) Chap. 1, pp. 1–45.

[70] V. Sidis, C. Kubach, and D. Fussen, Physical Review A **27**, 2431 (1983).

[71] D. Fussen, *Une autre approche de la dynamique des réactions de transfert de charge dans le système H-H*, Ph.D. thesis, Université Catholique de Louvain (1983).

[72] F. T. Smith, Physical Review **179**, 111 (1969).

[73] S. B. Schneiderman and A. Russek, Physical Review **181**, 311 (1969).

[74] C. J. Joachain, *Quantum collision theory*, 3rd ed. (North-Holland Physics Publishing, Amsterdam, 1983).

[75] N. Vaeck, M. Desouter-Lecomte, and J. Liévin, Journal of Physics B: Atomic, Molecular and Optical Physics **32**, 409 (1999).

[76] A. K. Belyaev and O. V. Lebedev, Physical Review A **84**, 014701 (2011).

[77] Y. N. Demkov, Journal of Experimental and Theoretical Physics (JETP) **18**, 138 (1964), russian version: ZhETF, Vol. 45, No. 1, p. 195, January 1964.

[78] A. K. Belyaev, Physical Review A **48**, 4299 (1993).

[79] B. Warner, Monthly Notices of the Royal Astronomical Society **139**, 1 (1968).

[80] D. R. Bates and J. T. Lewis, Proceedings of the Physical Society. Section A **68**, 173 (1955).

[81] C. A. Coulson, Mathematical Proceedings of the Cambridge Philosophical Society **38**, 210–223 (1942).

[82] J. van den Bos, The Journal of Chemical Physics **52**, 3254 (1970).

[83] B. M. Smirnov, Doklady Akademii Nauk SSSR (DAN) **161**, 92 (1965).

[84] B. M. Smirnov, Journal of Experimental and Theoretical Physics (JETP) **24**, 314 (1967).

[85] D. M. Davidović and R. K. Janev, Physical Review **186**, 89 (1969).

[86] D. R. Bates and B. L. Moiseiwitsch, Proceedings of the Physical Society. Section A **67**, 805 (1954).

[87] A. Dalgarno, Proceedings of the Physical Society. Section A **67**, 1010 (1954).

[88] R. Grice and D. Herschbach, Molecular Physics **27**, 159 (1974).

[89] R. K. Janev, The Journal of Chemical Physics **64**, 1891 (1976).

[90] P. S. Barklem, Physical Review A **93**, 042705 (2016).

[91] S. M. Blinder, American Journal of Physics **33**, 431 (1965).

[92] H. Werner and W. Meyer, The Journal of Chemical Physics **74**, 5802 (1981).

[93] R. E. Olson, J. R. Peterson, and J. Moseley, The Journal of Chemical Physics **53**, 3391 (1970).

[94] R. E. Olson, F. T. Smith, and E. Bauer, Applied Optics **10**, 1848 (1971).

[95] D. R. Bates and T. J. M. Boyd, Proceedings of the Physical Society. Section A **69**, 910 (1956).

[96] R. E. Olson, The Journal of Chemical Physics **56**, 2979 (1972).

[97] A. P. Hickman, The Journal of Chemical Physics **70**, 4872 (1979).

[98] W. H. Miller and H. Morgner, The Journal of Chemical Physics **67**, 4923 (1977).

[99] D. Fussen and C. Kubach, Journal of Physics B: Atomic and Molecular Physics **19**, L31 (1986).

[100] M. Stenrup, A. Larson, and N. Elander, Physical Review A **79**, 012713 (2009).

[101] A. Larson, S. M. Nkambule, and A. E. Orel, Physical Review A **94**, 022709 (2016).

[102] S. Adelman and D. Herschbach, Molecular Physics **33**, 793 (1977).

[103] R. K. Janev and Z. M. Radulović, Physical Review A **17**, 889 (1978).

[104] A. Boutalib and F. X. Gadéa, The Journal of Chemical Physics **97**, 1144 (1992).

[105] H. Croft, A. Dickinson, and F. Gadéa, Journal of Physics B: Atomic, Molecular and Optical Physics **32**, 81 (1999).

[106] H. Croft, A. S. Dickinson, and F. X. Gadéa, Monthly Notices of the Royal Astronomical Society **304**, 327 (1999).

[107] A. K. Belyaev and P. S. Barklem, Physical Review A **68**, 062703 (2003).

[108] P. S. Barklem, A. K. Belyaev, and M. Asplund, Astronomy & Astrophysics **409**, L1 (2003).

[109] H. M. Hedberg, S. Nkambule, and Å. Larson, Journal of Physics B: Atomic, Molecular and Optical Physics **47**, 225206 (2014).

[110] S. A. Yakovleva, Y. V. Voronov, and A. K. Belyaev, Astronomy & Astrophysics **593**, A27 (2016).

[111] A. K. Belyaev, Y. V. Voronov, A. Mitrushchenkov, M. Guitou, and N. Feautrier, Monthly Notices of the Royal Astronomical Society **487**, 5097 (2019).

[112] R. E. Olson and M. Kimura, Physical Review A **32**, 3092 (1985).

[113] O. Mó, A. Riera, and M. Yáez, Physical Review A **31**, 3977 (1985).

[114] L. F. Errea, L. Méndez, O. Mó, and A. Riera, The Journal of Chemical Physics **84**, 147 (1986).

[115] A. Dickinson, R. Poteau, and F. Gadéa, Journal of Physics B: Atomic, Molecular and Optical Physics **32**, 5451 (1999).

[116] A. K. Belyaev, P. S. Barklem, A. S. Dickinson, and F. X. Gadéa, Physical Review A **81**, 032706 (2010).

[117] P. S. Barklem, A. K. Belyaev, A. S. Dickinson, and F. X. Gadéa, Astronomy & Astrophysics **519**, A20 (2010).

[118] A. K. Belyaev, P. S. Barklem, A. Spielfiedel, M. Guitou, N. Feautrier, D. S. Rodionov, and D. V. Vlasov, Physical Review A **85**, 032704 (2012).

[119] M. Guitou, A. Belyaev, A. Spielfiedel, N. Feautrier, and P. Barklem, Journal of Physics: Conference Series **397**, 012053 (2012).

[120] P. S. Barklem, A. K. Belyaev, A. Spielfiedel, M. Guitou, and N. Feautrier, Astronomy & Astrophysics **541**, A80 (2012).

[121] M. Guitou, A. Spielfiedel, D. Rodionov, S. Yakovleva, A. Belyaev, T. Merle, F. Thévenin, and N. Feautrier, Chemical Physics **462**, 94 (2015).

[122] A. K. Belyaev and Y. V. Voronov, Astronomy & Astrophysics **606**, A106 (2017).

[123] A. K. Belyaev, Physical Review A **88**, 052704 (2013).

[124] A. K. Belyaev, Astronomy & Astrophysics **560**, A60 (2013).

[125] A. K. Belyaev, S. A. Yakovleva, and P. S. Barklem, Astronomy & Astrophysics **572**, A103 (2014).

[126] A. K. Belyaev and Y. V. Voronov, The Astrophysical Journal **893**, 59 (2020).

[127] S. A. Yakovleva, P. S. Barklem, and A. K. Belyaev, Monthly Notices of the Royal Astronomical Society **473**, 3810 (2017).

[128] A. K. Belyaev, S. A. Yakovleva, M. Guitou, A. O. Mitrushchenkov, A. Spielfiedel, and N. Feautrier, Astronomy & Astrophysics **587**, A114 (2016).

[129] A. Mitrushchenkov, M. Guitou, A. K. Belyaev, S. A. Yakovleva, A. Spielfiedel, and N. Feautrier, The Journal of Chemical Physics **146**, 014304 (2017).

[130] A. K. Belyaev, D. V. Vlasov, A. Mitrushchenkov, and N. Feautrier, Monthly Notices of the Royal Astronomical Society **490**, 3384 (2019).

[131] J. Grumer and P. S. Barklem, Astronomy & Astrophysics **637**, A28 (2020).

[132] S. Yakovleva, A. Belyaev, and W. Kraemer, Chemical Physics **515**, 369 (2018), ultrafast Photoinduced Processes in Polyatomic Molecules:Electronic Structure, Dynamics and Spectroscopy (Dedicated to Wolfgang Domcke on the occasion of his 70th birthday).

[133] R. E. Olson, M. Kimura, and H. Sato, Physical Review A **30**, 1692 (1984).

[134] W. Zrafi, B. Oujia, and F. X. Gadea, Journal of Physics B: Atomic, Molecular and Optical Physics **39**, 3815 (2006).

[135] A. K. Belyaev, B. Lepetit, and F. X. Gadéa, Physical Review A **90**, 062701 (2014).

[136] A. K. Belyaev and S. A. Yakovleva, Monthly Notices of the Royal Astronomical Society **478**, 3952 (2018).

[137] X. Zhou and A. Dickinson, Nuclear Instruments and Methods in Physics Research Section B: Beam Interactions with Materials and Atoms **124**, 5 (1997).

[138] J. van den Bos, The Journal of Chemical Physics **59**, 5358 (1973).

[139] J. van den Bos, Computer Physics Communications **7**, 163 (1974).

[140] X.-X. Zhou and C.-Z. Dong, Chinese Physics Letters **13**, 93 (1996).

[141] R. K. Janev and Z. M. Radulović, The Journal of Chemical Physics **67**, 2856 (1977).

[142] S. Bienstock and A. Dalgarno, The Journal of Chemical Physics **78**, 224 (1983).

[143] J. B. Roos, A. E. Orel, and A. Larson, Physical Review A **79**, 062510 (2009).

[144] J. Z. Mezei, J. B. Roos, K. Shilyaeva, N. Elander, and A. Larson, Physical Review A **84**, 012703 (2011).

[145] S. Nkambule, P. Nurzia, and Å. Larson, Chemical Physics **462**, 23 (2015).

[146] A. Larson, J. Hörnquist, P. Hedvall, and A. E. Orel, The Journal of Chemical Physics **151**, 214305 (2019).

[147] K. Olamba, *Une nouvelle approche de la mesure des sections efficaces absolues en faisceaux confluents et son application à l'étude des réactions :* $H^-(D^-) + He^+ \rightarrow H(D) + He$, Ph.D. thesis, Université Catholique de Louvain (1995).

[148] X. Urbain, D. Bech, J.-P. Van Roy, M. Géléoc, S. J. Weber, A. Huetz, and Y. J. Picard, Review of Scientific Instruments **86**, 023305 (2015).

[149] R. Janev and A. Salin, Journal of Physics B: Atomic and Molecular Physics **5**, 177 (1972).

[150] C. Cohen-Tannoudji, B. Diu, and F. Laloe, *Mécanique quantique, Volume 1* (Hermann, 1998).

[151] C. Wittig, The Journal of Physical Chemistry B **109**, 8428 (2005), pMID: 16851989.

[152] D. Fussen (2004), lecture's notes.

[153] E. E. Nikitin and S. Y. Umanskii, *Theory of Slow Atomic Collisions* (Springer, Berlin, Heidelberg, 1984) pp. 273–312.

[154] J. S. Cohen, Physical Review A **13**, 86 (1976).

[155] J. S. Cohen, Physical Review A **13**, 99 (1976).

[156] T. Launoy, *Étude de réactions astrochimiques impliquant des paires d'ions*, Ph.D. thesis, Université libre de Bruxelles, Faculté des Sciences - Chimie, Bruxelles (2018).

[157] X. Zhang, H. Zhai, Y. Liu, and J. Sun, Journal of Quantitative Spectroscopy and Radiative Transfer **119**, 23 (2013).

[158] T. M. Miller, N. S. Shuman, and A. A. Viggiano, The Journal of Chemical Physics **136**, 204306 (2012).

[159] A. Le Padellec, T. Launoy, A. Dochain, and X. Urbain, Journal of Physics B: Atomic, Molecular and Optical Physics **50**, 095202 (2017).

[160] M. Chibisov, Journal of Experimental and Theoretical Physics (JETP) **49**, 962 (1979).

[161] J. N. Bardsley, T. Holstein, B. R. Junker, and S. Sinha, Physical Review A **11**, 1911 (1975).

[162] L. Gor'kov and L. Pitaevskii, Doklady Akademii Nauk SSSR (DAN) **151**, 822 (1963).

[163] R. Janev, in *Nonadiabatic Transitions Between Ionic and Covalent States*, Advances in Atomic and Molecular Physics, Vol. 12, edited by D. Bates and B. Bederson (Academic Press, 1976) pp. 1–37.

[164] K. Taulbjerg, Journal of Physics B: Atomic and Molecular Physics **19**, L367 (1986).

[165] B. Smirnov, Journal of Experimental and Theoretical Physics (JETP) **22**, 692 (1966).

[166] B. Smirnov and M. I. Chibisov, Journal of Experimental and Theoretical Physics (JETP) **22**, 585 (1966).

[167] M. Chibisov and R. Janev, Physics Reports **166**, 1 (1988).

[168] B. H. Armstrong, Physical Review **131**, 1132 (1963).

[169] M. Chibisov, Teplofizika vysokikh temperatur (TBT) **3**, 775 (1965).

[170] C. Herring, Reviews of Modern Physics **34**, 631 (1962).

[171] NIST digital library of mathematical functions, http://dlmf.nist.gov/, Release 1.0.19 of 2018-06-22, f. W. J. Olver, A. B. Olde Daalhuis, D. W. Lozier, B. I. Schneider, R. F. Boisvert, C. W. Clark, B. R. Miller and B. V. Saunders, eds.

[172] G. Racah, Physical Review **61**, 186 (1942).

[173] G. Racah, Physical Review **62**, 438 (1942).

[174] G. Racah, Physical Review **63**, 367 (1943).

[175] G. Racah, Physical Review **76**, 1352 (1949).

[176] C. W. Nielson and G. F. Koster, *Spectroscopic Coefficients for the pn, dn, and fn Configurations* (M.I.T. Press, 1963).

[177] A. Radtsig and B. Smirnov, Journal of Experimental and Theoretical Physics (JETP) **33**, 282 (1971).

[178] N. Vitanov and G. Panev, Europhysics Letters (EPL) **16**, 159 (1991).

[179] A. A. Radzig and B. M. Smirnov, *Reference Data on Atoms, Molecules, and Ions*, 1st ed., Springer Series in Chemical Physics, Vol. 31 (Springer, Berlin, Heidelberg, 1985).

[180] T. Ohmura and H. Ohmura, Physical Review **118**, 154 (1960).

[181] R. D. Piacentini and A. Salin, Journal of Physics B: Atomic and Molecular Physics **7**, 1666 (1974).

[182] V. Bykhovskii, E. Nikitin, and M. Y. Ovchinnikova, Journal of Experimental and Theoretical Physics (JETP) **20**, 500 (1965).

[183] T. Gould and T. Bučko, Journal of Chemical Theory and Computation **12**, 3603 (2016).

[184] M. Schlagmüller, T. C. Liebisch, F. Engel, K. S. Kleinbach, F. Böttcher, U. Hermann, K. M. Westphal, A. Gaj, R. Löw, S. Hofferberth, T. Pfau, J. Pérez-Ríos, and C. H. Greene, Phys. Rev. X **6**, 031020 (2016).

[185] F. Brouillard and W. Claes, in *Physics of Ion-Ion and Electron-Ion Collisions*, edited by F. Brouillard and J. W. McGowan (Springer US, Boston, MA, 1983) pp. 415–459.

[186] J. D. Jackson, *Électrodynamique classique* (Dunod, 2001).

[187] B. Fabre, *Paquets d'onde vibrationnels créés par ionisation de H_2 en champ laser intense*, Ph.D. thesis, Université Catholique de Louvain (2005).

[188] C. L. Pekeris, Phys. Rev. **112**, 1649 (1958).

[189] S. Chandrasekhar, Astrophysical Journal **100**, 176 (1944).

[190] M. Terao, *Etude expérimentale et théorique de la réaction de capture dans les collision* He^{2+} – H^{-}, Ph.D. thesis, Université Catholique de Louvain (1986).

[191] P. Barklem, Private Communication (2019).

[192] G. Eklund, J. Grumer, S. Rosén, M. Ji, N. Punnakayathil, A. Källberg, A. Simonsson, R. D. Thomas, M. H. Stockett, P. Reinhed, P. Löfgren, M. Björkhage, M. Blom, P. S. Barklem, H. Cederquist, H. Zettergren, and H. T. Schmidt, Phys. Rev. A **102**, 012823 (2020).

[193] P. S. Barklem, Phys. Rev. A **104**, 062806 (2021).

[194] A. Larson and S. M. Nkambule, Private Communication (2019).

[195] S. R. Langhoff, H. Partridge, and C. W. Bauschlicher, Chemical Physics **153**, 1 (1991).

[196] A. Dalgarno, Advances in Physics **11**, 281 (1962).

[197] E. A. Mason and E. W. McDaniel, eds., Appendix III: Tables of properties useful in the estimation of ion-neutral interaction energies, in *Transport Properties of Ions in Gases* (John Wiley & Sons, Ltd, 1988) pp. 531–539.

[198] K. Haris and A. Kramida, The Astrophysical Journal Supplement Series **233**, 16 (2017).

[199] A. Kramida, Y. Ralchenko, J. Reader, and NIST ASD Team, NIST Atomic Spectra Database (ver. 5.8), [Online]. Available: `https://physics.nist.gov/asd` [2021, January 26]. National Institute of Standards and Technology, Gaithersburg, MD. (2020).

[200] W. A. Chupka, The Journal of Chemical Physics **98**, 4520 (1993).

[201] P. Allmendinger, J. Deiglmayr, O. Schullian, K. Höveler, J. A. Agner, H. Schmutz, and F. Merkt, ChemPhysChem **17**, 3596 (2016).

[202] M. Poline, S. Rosén, M.-C. Ji, G. Eklund, A. Dochain, X. Urbain, M. Larsson, N. Shuman, S. Ard, A. A. Viggiano, H. Cederquist, H. T. Schmidt, H. Zettergren, P. S. Barklem, and R. D. Thomas (2021), to be published.

[203] A. Niehaus, Journal of Physics B: Atomic and Molecular Physics **19**, 2925 (1986).

[204] A. Hibbert, Computer Physics Communications **9**, 141 (1975).

[205] É. Biémont, *Spectroscopie atomique: Instrumentation et structures atomiques*, LMD Physique (De Boeck, 2006).

[206] W. Martin and W. Wiese, in *Springer Handbook of Atomic, Molecular, and Optical Physics*, edited by G. Drake (Springer New York, New York, NY, 2006) pp. 175–198.

[207] J.-M. De Conto, Eléments d'optique corpusculaire et introduction à la physique des accélérateurs de particules (1994).

[208] A. Banford, *The Transport of Charged Particle Beams* (Spon, London, 1966).

[209] J. Roth, *Industrial Plasma Engineering: Volume 1: Principles*, Industrial Plasma Engineering (CRC Press, 1995).

[210] J. R. Pierce, Journal of Applied Physics **11**, 548 (1940).

[211] W. S. Cooper, K. Berkner, and R. Pyle, Nuclear Fusion **12**, 263 (1972).

[212] O. Klemperer and M. Barnett, *Electron Optics*, Cambridge Monographs on Physics (Cambridge University Press, 1971).

[213] X. Urbain, *Etude expérimentale et théorique de la réaction H(1s) + H(2s) $\rightarrow H_2^+ + e^-$*, Ph.D. thesis, Université Catholique de Louvain (1990).

[214] M. Génévriez and X. Urbain, Physical Review A **91**, 033403 (2015).

[215] *Quantar Technology: 3300/2400 Series System installaton and operation manual*, Quantar Technology Incorporated, Santa Cruz, CA (2013).

[216] S. Kalbitzer and W. Melzer, Nuclear Instruments and Methods **56**, 301 (1967).

[217] A. Doehring, S. Kalbitzer, and W. Melzer, Nuclear Instruments and Methods **59**, 40 (1968).

[218] J. W. Stumpel, P. W. Sanford, and H. F. Goddard, Journal of Physics E: Scientific Instruments **6**, 397 (1973).

[219] P. Defrance, Sources de particules chargées (1994).

[220] B. Wolf, *Handbook of Ion Sources* (Taylor & Francis, 1995).

[221] G. Alton, in *Electrostatic Accelerators: Fundamentals and Applications*, edited by R. Hellborg (Springer Berlin Heidelberg, Berlin, Heidelberg, 2005) pp. 222–273.

[222] D. Faircloth, Negative Ion Sources: Magnetron and Penning (2014), comments: 26 pages, contribution to the CAS-CERN Accelerator School: Ion Sources, Senec, Slovakia, 29 May - 8 June 2012, edited by R. Bailey, CERN-2013-007.

[223] R. Middleton, A negative-ion cookbook (1990).

[224] J. Delcroix and A. Bers, *Physique des plasmas*, Vol. 1 (EDP Sciences, 1994).

[225] M. Liehr, *Entwicklung und Aufban von Elektron-Zyklotron-Resonanz Ionenquellen (ECRIS) mit Mikrowellenfrequenzen von 10 und 2.45 GHz unter spezieller Berücksichtigung der Plasmaheizung mit Verzögerungsleitungen*, Ph.D. thesis, Justus-Liebig-Universität Giessen (1992).

[226] M. Liehr, R. Trassl, M. Schlapp, and E. Salzborn, Review of Scientific Instruments **63**, 2541 (1992).

[227] unknown, The klystron, https://youtu.be/Fvud81pYGOg.

[228] M. von Ardenne, Atomkernenergie **2**, 121 (1956).

[229] C. Lejeune, Nuclear Instruments and Methods **116**, 417 (1974).

[230] C. Lejeune, Nuclear Instruments and Methods **116**, 429 (1974).

[231] C. Lejeune, *Interprétation des propriétés des sources d'ions du type duoplasmatron à partir du modèle de la décharge*, Ph.D. thesis, Centre d'Orsay, Université Paris-Sud (1971).

[232] X. Urbain and P. Defrance, Méthodes d'analyse en physique atomique et moléculaire (2015).

[233] R. L. Boxman, D. M. Sanders, and P. J. Martin, eds., *Handbook of Vacuum Arc Science and Technology* (William Andrew Publishing, Park Ridge, NJ, 1996).

[234] T. Intrator, M. H. Cho, E. Y. Wang, N. Hershkowitz, D. Diebold, and J. DeKock, Journal of Applied Physics **64**, 2927 (1988).

[235] I. Langmuir, Physical Review **33**, 954 (1929).

[236] P. D. Prewett and J. E. Allen, Proceedings of the Royal Society of London. Series A, Mathematical and Physical Sciences **348**, 435 (1976).

[237] G. Lawrence, R. Beauchamp, and J. McKibben, Nuclear Instruments and Methods **32**, 357 (1965).

[238] L. Collins and R. Gobbett, Nuclear Instruments and Methods **35**, 277 (1965).

[239] M. Bacal and M. Wada, Applied Physics Reviews **2**, 021305 (2015).

[240] M. Rutigliano and M. Cacciatore, Physical Chemistry Chemical Physics (PCCP) **13**, 7475 (2011).

[241] W. H. Weinberg, Accounts of Chemical Research **29**, 479 (1996).

[242] R. Pétuya, P. Larrégaray, C. Crespos, H. F. Busnengo, and A. E. Martínez, The Journal of Chemical Physics **141**, 024701 (2014).

[243] H. Umemoto, S. G. Ansari, and H. Matsumura, Journal of Applied Physics **99**, 043510 (2006).

[244] L. Schiesko, M. Carrère, G. Cartry, and J. M. Layet, Plasma Sources Science and Technology **17**, 035023 (2008).

[245] P. Diomede, S. Longo, and M. Capitelli, The European Physical Journal D - Atomic, Molecular, Optical and Plasma Physics **33**, 243 (2005).

[246] M. Capitelli and C. Gorse, IEEE Transactions on Plasma Science **33**, 1832 (2005).

[247] J. R. Hiskes, Journal of Applied Physics **70**, 3409 (1991).

[248] P. Diomede, S. Longo, and M. Capitelli, Physics of Plasmas **13**, 113505 (2006).

[249] B. Bouchy-Lorentz, M. Remy, and C. Muller, International Journal of Mass Spectrometry and Ion Physics **22**, 147 (1976).

[250] V. M. Andrianarijaona, *Mesure de l'énergie interne d'ions meoléculaires par imagerie à trois dimensions : Application aux réaction d'ionisation associative d'atomes métastables*, Ph.D. thesis, Université Catholique de Louvain (2002).

[251] N. de Ruette, *Sélectivité rovibrationnelle de l'ionisation de H_2 en champ laser intense : Analyse détaillée de la dissociation induite par électron ou photon d'ions H_2^+ préparés par laser*, Ph.D. thesis, Université Catholique de Louvain (2007).

[252] A. Schils, *Atomic collision processes limiting the efficiency of negative ion beam production relevant to fusion plasma heating*, Master's thesis, Université Catholique de Louvain (2019).

[253] E. Stueckelber, Helvetica Physica Acta **5**, 369 (1932).

[254] I. Gradshteyn and I. Ryzhik, in *Table of Integrals, Series, and Products (Seventh Edition)*, edited by A. Jeffrey and D. Zwillinger (Academic Press, Boston, 2007) seventh edition ed., pp. 859 – 1048.

[255] A. Salop and R. E. Olson, Physical Review A **13**, 1312 (1976).

[256] P. Kelly and B. H. Armstrong, Astrophysical Journal **129**, 786 (1959).

[257] E. Wigner and E. E. Witmer, Zeitschrift für Physik **51**, 859 (1928).

[258] R. S. Mulliken, Reviews of Modern Physics **4**, 1 (1932).

[259] G. Herzberg, *Spectra of diatomic molecules*, Molecular spectra and molecular structure (Van Nostrand, 1950).

[260] U. Kleinekathöfer, K. T. Tang, J. P. Toennies, and C. L. Yiu, The Journal of Chemical Physics **103**, 6617 (1995).

[261] E. L. Duman and B. M. Smirnov, Optics and Spectroscopy **29**, 229 (1970).

[262] E. L. Duman and B. M. Smirnov, Soviet Physics - Technical Physics **15**, 61 (1970).

[263] B. Smirnov, *Asymptotic methods in the theory of atomic collisions* (Moscow, Atomizdat, 1973).

[264] L. D. Landau and E. M. Lifshitz, *A Course of Theoretical Physics Vol.3 - Quantum Mechanics: Non-Relativistic Theory*, 2nd ed. (Pergamon Press, London, 1965).

[265] R. Janev, Journal of Physics B: Atomic and Molecular Physics **4**, 215 (1971).

[266] T. F. O'Malley, L. Spruch, and L. Rosenberg, Journal of Mathematical Physics **2**, 491 (1961).

[267] W. Schön, S. Krüdener, F. Melchert, K. Rinn, M. Wagner, E. Salzborn, M. Karemera, S. Szücs, M. Terao, D. Fussen, R. Janev, X. Urbain, and F. Brouillard, Physical Review Letter **59**, 1565 (1987).

[268] J. C. Rienstra-Kiracofe, G. S. Tschumper, H. F. Schaefer, S. Nandi, and G. B. Ellison, Chemical Reviews **102**, 231 (2002), pMID: 11782134.

[269] P. Andersson, A. O. Lindahl, C. Alfredsson, L. Rogström, C. Diehl, D. J. Pegg, and D. Hanstorp, Journal of Physics B: Atomic, Molecular and Optical Physics **40**, 4097 (2007).

[270] E. Bäckström, D. Hanstorp, O. M. Hole, M. Kaminska, R. F. Nascimento, M. Blom, M. Björkhage, A. Källberg, P. Löfgren, P. Reinhed, S. Rosén, A. Simonsson, R. D. Thomas, S. Mannervik, H. T. Schmidt, and H. Cederquist, Phys. Rev. Lett. **114**, 143003 (2015).

[271] C. Blondel, W. Chaibi, C. Delsart, and C. Drag, Journal of Physics B: Atomic, Molecular and Optical Physics **39**, 1409 (2006).